UNIVERSITY OF
Southampton
School of Engineering Sciences

Group Design Project

Concept Design of a Fast Sail Assisted Feeder Container Ship

Aaron Burden,
Thomas Lloyd,
Simon Mockler,
Lorenzo Mortola,
Ie Bum Shin,
Ben Smith

Supervisor: Grant E Hearn

Academic year 2009/2010

Main Report

Acknowledgements

The group members would like to thank a number of people who have helped in the completion of the project.

Firstly to our supervisor, Professor Grant Hearn who has guided the work from day one and pushed us in all aspects of the project. Also to Ian Campbell, the 2nd supervisor whose advice regarding and supervision of towing tank testing proved invaluable.

Other members of the *WUMTIA* who have provided support are Dickon Buckland, Martyn Prince and Chris Harmer. Thanks also to Dr. Dominic Taunton for his advice on tank testing and results processing. Many thanks to the University of Southampton and Southampton Solent University for allowing us to use their respective testing facilities, and to Mike Tudor-Pole for his help with the use of the wind tunnel. Supervision in the towing tank was kindly provided by Dr. Mingyi Tan and Ms. Sally Denchfield, and is greatly appreciated. Many hours of manufacturing time have contributed to the successfully delivery of the test rig and ship models thanks to the members of the *EDMC* namely Mike Sellwood, Tom Roberts, Gordon Mills, Phil Herring, Dave Williams, Richard Dooler and Mike Street.

The kind support of Lloyd's Register is gratefully acknowledged, both for contribution to the budget which allowed the project to achieve a large amount of physical testing, and the advice provided by many employees: Kim Tanneberger, David Tozer, Ed Fort, Rob Dickie, Rhoda Wilson and especially Dr. Fai Cheng for recognising the potential of the project early on. Wind data was kindly supplied by Dr. Elizabeth Kent of the NOCS. ABB are thanked for providing azipod® product data. Finally, thanks go to Christian Mash of Borchard Lines for his insight into the operation of feeder container ships and the impact this had on the design.

Report Contributions

Section:	*Section title:*	*Work undertaken by:*	*Written by:*
1.	Introduction	TL	TL
2.	Design Specification	BS, SM & LM	BS
3.	Initial Development of Fast Feeder Container Ship		
3.1	Basis ships	AB & TL	AB
3.2	Mass and powering estimate		
3.2.1	Mass estimate	BS & SM	BS
3.2.3	Powering	BS & SM	BS
3.2.2	Stability	BS & SM	BS
3.3	Main propulsion and machinery options	TL	TL
4.	Hydrodynamic Design Development		
4.1	Hull form design		
4.1.1	Design for hydrodynamic performance	AB	AB
4.1.2	*Hull A* basis hull form	AB	AB
4.1.3	*Hull B* basis hull form	SM	SM
4.1.4	Bulbous bow optimisation	AB	AB
4.1.5	Results	AB	AB
4.2	Towing tank model design and manufacture		
4.2.1	Introduction	TL	TL
4.2.2	Model design	TL, SM & LM	TL
4.2.3	Model manufacture	TL	TL
4.3	Testing matrix and procedure	AB & TL	TL
4.4	Analysis of results	AB	AB
4.4.1.	Upright condition	AB	AB
4.4.2	Sailing condition	AB	AB
4.4.3	Added resistance in waves	AB	AB
4.4.4	Uncertainty analysis	BS	BS
5.	Sail System Design		
5.1	Initial design		
5.1.1.	Concept review	IBS	IBS
5.1.2	Design	LM & IBS	LM & IBS
	Wind data	BS	BS
5.1.3	Theoretical performance	LM	LM
5.2	Wind tunnel testing		
5.2.1	Introduction	LM & IBS	LM & IBS
5.2.2	Model design	IBS & LM	IBS
5.2.3	Model manufacture	LM & IBS	LM
5.2.4	Experimental setup	LM & IBS	LM
5.2.5	Wind tunnel post processing	LM	LM
5.2.6	Analysis of the results	LM & IBS	LM & IBS
5.3	Computational fluid dynamics study of Multi-wing system	IBS	IBS
6.	Performance Predictions		
6.1	Design selection		
6.1.1	Sailing performance	LM	LM

6.1.2	Propulsive efficiency	TL	TL
6.1.3	Justification of hull form choice	TL	TL
6.2	Design feasibility		
6.2.1	Round-trip evaluation	TL	TL
6.2.2	Economic feasibility of *Multi-wing* system	LM	LM
7.	Design Development		
7.1	Seakeeping		
7.1.1	Modelling	AB	AB
7.1.2	Results	AB	AB
7.1.3	Theoretical added resistance	AB	AB
7.1.4	Absolute motions	BS	BS
7.1.5	Cargo securing	BS	BS
7.1.6	Motions	BS	BS
7.1.7	Roll damping due to sails	LM	LM
7.2	Structural Design		
7.2.1	Midship scantlings	SM	SM
7.2.2	Global strength	SM & BS	SM
7.2.3	Finite element midship section model	BS	BS
7.2.4	Finite element sail rig model	IBS	IBS
7.3	Stability		
7.3.1	Intact stability	IBS	IBS
7.3.2	Damage stability	SM	SM
7.3.3	Freeboard and tonnage	AB	AB
7.4	Layout and arrangement	BS	BS
8.	Conclusions	ALL	TL
9.	Recommendations for Future Work	ALL	TL

Table of Contents

List of Figures

List of Tables

Nomenclature

Symbols:

A	Sail area
A_C	Wind tunnel cross sectional area contraction
A_{SD}	Attained subdivision index
A_W	Windage lateral area
B	Moulded breadth or beam
BM_T	Distance from centre of buoyancy to transverse metacentre
$b_{\psi\varphi}$	yaw damping coefficient induced by roll
C_A	Ship –model correlation allowance
C_B	Block coefficient at design draught
$C_{B0.8}$	Block co-efficient at $0.8D$
C_D	Drag coefficient
$C_{D'}$	Drag coefficient windage correction
$C_{D,cf}$	Cross-flow drag coefficient
C_{DH}	Hull / superstructure drag coefficient for windage
C_{Di}	Drag coefficient due to lift or effective induced drag coefficient
C_{D0}	Minimum or parasitic drag coefficient
C_{D1}	Total drag coefficient at maximum lift
C_F	Frictional resistance coefficient
${C_F}^{15\,deg}$	Frictional resistance coefficient at 15°C
${C_F}^{tw}$	Frictional resistance coefficient at measured water temperature
C_L	Lift coefficient
$C_{L'}$	Lift coefficient windage correction
C_{L0}	Lift coefficient at zero angle of attack
C_P	Prismatic coefficient
C_{Ri}	Induced resistance coefficient, motion damping
C_{RT}	Total resistance coefficient, roll damping
C_T	Total resistance coefficient
${C_T}^{15\,deg}$	Total resistance coefficient at 15°C
${C_T}^{tw}$	Total resistance coefficient at measured water temperature
C_V	Viscous resistance coefficient
C_W	Wave resistance coefficient
C_{WP}	Waterplane area co-efficient
C_X	Sail thrust coefficient
C_Y	Sail heeling coefficient
D	Moulded depth
Df	Drive force
D_M	Measured model drag
D_P	Propeller diameter
D_{SAIL}	Sail drag
d	Water depth
F_{ix}, F_{iy}, F_{iz}	Racking forces at the ith tier of a container stack
$F_{ixRES}, F_{iyRES}, F_{izRES}$	Residual forces at the ith tier of a container stack
F_X	Sail drive force
F_Y	Aerodynamic side force
F_Z	Vertical component of aerodynamic side force
Fn	Froude number
FR_E	Effective aspect ratio
G	Biplane lift constant due to change in angle of attack
G_0	Biplane lift constant due to section curvature
GM	Metacentric height
g	Acceleration due to gravity
H	Wind lever
He	Effective rig height
Hf	Heeling force
H_{max}	Sliding force at top of motions in transverse direction
H_{min}	Sliding force at bottom of motions in transverse direction
H_0	Vertical distance from centre of windage lateral area to half mean draught
h	High speed (when subscript) or height of grit strip
$h_{1/3}$	Significant wave height
I_Y	Ship section second moment of area about the horizontal neutral axis
I_{y_i}	Structural element second moment of area contribution about the transverse neutral axis
I_Z	Ship section second moment of area about the vertical neutral axis
I_ω	Sectional sectorial moment of inertia
J_{max}	Sliding force at top of motions in longitudinal direction
J_{min}	Sliding force at bottom of motions in longitudinal direction
K	Coverage factor for standard deviation
KB	Vertical centre of buoyancy above keel
KG	Vertical centre of gravity above keel
k	Wave number
k_{ix}, k_{iy}, k_{iz}	Equivalent spring stiffness of a container stack at the ith tier
k_L	Lashing stiffness

k_{xx}	Pitch gyradius
ks	Constant for grit strip calculation
L_{BP}	Length between perpendiculars
L_L	Loadline length
L_{OA}	Length overall
L_R	Rule length
L_{SAIL}	Sail lift
L_{SD}	IMO subdivision length
L_{WL}	Length at waterline
M	Model scale (when subscript)
M_H	Wind heeling moment
M_r	Number of test runs
M_S	Still water bending moment
M_{ST}	Static cargo torque
M_{WH}	Horizontal wave bending moment
M_{WT}	Wave hydrodynamic torque
M_{WV}	Wave vertical bending moment
M_x	Resistance mass
M_Θ	Trimming moment
M_ψ	Yaw moment
m_o	Mean square of frequency spectrum
N_C	Cargo capacity (number of TEU)
NB	Number of propeller blades
$N_{\varphi A}$	Total aerodynamic roll damping
$N_{\varphi Aa}$	Aerodynamic roll damping, incidence changes component
$N_{\varphi AV}$	Aerodynamic roll damping, air speed changes component
n	Propeller rps
n_H	Number of holds
n_S	Number of stacks
n_T	Number of tiers
P_B	Brake (installed) power
P_D	Delivered power
P_E	Effective power
P_i	Vertical force at corner posts of containers in a stack at the ith tier
p_i	Probability of damage case i occuring
Q_i	Wind force in one transverse end of a container in a stack at the ith tier
q	Dynamic pressure
R_{AAS}	Air drag
R_{AW}	Added resistance
$\overline{R_{AW}}$	Average added resistance
$\overline{R_{AW}}'$	Average added resistance including weight for ship heading
R_{eft}	Effective Reynolds number
R_F	Frictional resistance
R_H	Resistance due to heel
R_I	Induced resistance
R_{SD}	Required subdivision index
R_T	Total resistance
R_U	Upright resistance
R_V	Viscous resistance
Rn	Reynolds number
S	Ship scale (when subscript) or wetted surface area
S_{ixy}	Transverse shear force at the ith tier in a container stack
S_{ixz}	Longitudinal shear force at the ith tier in a container stack
s	Stiffener spacing
s_i	Probability of survival following damage case i
T	Draught
T_D	Design scantling draught
T_e	Effective draught
T_h	Heave period
T_{Li}	Tension in a lashing at the ith tier in a container stack
T_p	Pitch period
T_r	Roll period
t	Thrust deduction factor
t_P	Plating thickness
V	Wind Speed
V_A	Apparent wind speed
V_a	Advance speed
V_M	Model speed
V_S	Ship speed
V_T	True wind speed
W_{Df}	Windage drive force
W_{Hf}	Windage Heeling force
w_T	Wake fraction
y_i	Structural element distance from vertical neutral axis
Z_i	Stiffener section modulus
z_i	Structural element distance from transverse neutral axis
z_{NA}	Height of transverse neutral axis from base
α	Angle of attack
β	Apparent wind angle
γ	True wind angle
Δ	Mass displacement
$\delta_{ix}, \delta_{iy}, \delta_{iz}$	Displacement of a container stack at the ith tier
ε	Position of torsion neutral axis below section baseline
ζ	Measured wave amplitude
$\zeta_{1/3}$	Significant wave amplitude
η_H	Hull efficiency
η_O	Propeller open water efficiency
η_R	Relative rotative efficiency
Θ	Trim angle
Λ	Model scale factor
λ	Wavelength
μ	Structural mass variation along the ship length

μ_{slide}	Co-efficient of tipping or sliding for calculation of MII
ν	Kinematic viscosity
ν_{φ}	Non – dimensional hydrodynamic roll damping
$\nu_{\varphi A}$	Non – dimensional aerodynamic roll damping
ρ	Mass density of water
ρ_a	Mass density of air
Σ	Summation
σ_{AW}	Added resistance coefficient
σ_{cr}	Buckling stress corrected for plasticity effects
σ_{design}	Midship scantling design stress
σ_L	Permissible design stress
σ_{local}	Stress due to locally applied loads
σ_N	Nominal stress
σ_x	Longitudinal direct stress
σ_y	Transverse direct stress
σ_0	Material yield stress
τ	Shear stress
Φ	Heel angle
$\Phi_{zz}(\omega_e)$	Wave spectrum as a function of wave encounter frequency
φ	Roll angle
X	Ship heading
Ψ	Leeway angle
ψ	Yaw angle
ω	Wave frequency
ω_e	Wave encounter frequency
ω_{n_i}	Normalised sectorial coordinate
∇	Volumetric displacement

Acronyms:

AoA	Angle of attack
AE	Auxiliary engine
AP	Aft perpendicular
AR	Wing aspect ratio
aft	Aft propeller (when subscripted)
CO_2	Carbon dioxide
CNC	Computer numerically controlled
CPP	Controllable pitch propeller
CRP	Contra-rotating propeller
CSR	Common Structural Rules
DF	Dual-fuel
DoF	Degree of freedom
DWT	Deadweight mass
EEDI	Energy Efficiency Design Index
FC	Fuel consumption
FE	Finite element
FEM	Finite element method
FEU	Forty-foot equivalent unit (container)
fwd	Forward propeller (when subscripted)
FP	Forward perpendicular
FPP	Fixed pitch propeller
GL	Germanischer Lloyd
HFO	Heavy fuel oil
IMO	International Maritime Organisation
IRR	Internal return rate
ITTC	International Towing Tank Conference
LCB	Longitudinal centre of buoyancy
LCF	Longitudinal centre of flotation
LCG	Longitudinal centre of gravity
LHV	Lower heating value
LNG	Liquefied natural gas
LR	Lloyd's Register
LR SDA	Lloyds Register ShipRight Primary Structure for Container Ships design procedure
LY2	The Large Commercial Yacht Code
MBtu	Metric British unit
MCA	Maritime Coastguard Agency
MCR	Maximum continuous rating
ME	Main engine
MDO	Marine diesel oil
MGO	Marine gas oil
MII	Motion induced interruption
MSI	Motion sickness index
NACA	National Advisory Committee for Aeronautics
NPV	Net present value
NO_x	Nitrogen oxides
PM	Particulate matter
PPP	Performance prediction program
RAO	Response amplitude operator
$RULE$	Required minimum value from LR's Rules (when subscript)
SECA	SO_x Emission Control Area
SF	Side force
SFC	Specific fuel consumption
SM	Subjective magnitude
SO_x	Sulphur oxides
SWBM	Still water bending moment
TEU	Twenty-foot equivalent unit (container)
TR	Thrust reduction
TF	Turbulence factor
VCB	Vertical centre of buoyancy (from keel)

1. Introduction

1.1 Background

Shipping is currently estimated to contribute 3.3% towards total global emissions [Buhaug *et al.* (2009)]. Of primary concern is carbon dioxide (CO_2), a greenhouse gas (GHG) linked to global warming. An additional consideration is the predicted growth of shipping. Increases in emissions of between 150% and 250% by 2050 are estimated if measures are not taken to improve environmental sustainability [Buhaug *et al.* (2009)].

Whilst legislation to guarantee the long term environmental sustainability of shipping is not currently in place, the industry is certainly addressing this issue from a design perspective, see Wärtsilä Ship Power R&D (2009). The adoption of the IMO Energy Efficiency Design Index [IMO (2005a)] as a means of assessing the environmental performance of existing or future designs is a step towards environmental sustainability becoming a key consideration in ship design and operation. However, economic viability remains the main driver in design. Reluctance of ship owners and operators to adopt new technologies or change operational procedure [Mash (2009)] could slow progress in the development of low-carbon shipping.

Regulation of other ship exhaust emissions is also tightening, characterised by the recent MARPOL Annex VI amendments [IMO (2005b)]. These global regulations limit the levels of certain emitted substances, including sulphur oxides (SO_x), which cause acid rain; and nitrogen oxides (NO_x) and particulate matter (PM), which can worsen or cause conditions such as emphysema and cancer.

Thus there is a strong focus on the maritime industry to address the issue of its emissions, despite shipping remaining the most carbon-efficient form of transport [Buhaug *et al.* (2009)]. The challenge of the naval architect is diversifying, with pressure from both inside and outside of the industry to produce environmentally conscious ships, while maintaining the profitability and familiarity expected by owners.

Container ships are one of the largest contributors to global shipping emissions [Buhaug *et al.* (2009)], largely due to their high speed. This can be up to 26 knots for the largest ships [Wärtsilä Ship Power R&D (2009)]. The 'efficiency of scale' principle alongside increasing demand of containerised transportation has seen an increase in the average size of container ships. The largest are capable of carrying 14,000 twenty-foot equivalent units (TEU), representing a high 'transport efficiency'. Wärtsilä Ship Power R&D (2009) (p.6) state that "a 10% increase in ship size will increase transport efficiency by a 4-5% ".

While 'post-panamax' ships represent high transport efficiency, smaller 'feeder' vessels present an opportunity for significant improvement in both efficiency and sustainability. These ships make up a large proportion of the global container ship fleet, and distribute cargo from mainline 'hubs' to regional ports, not accessible by larger vessels. Measures such as increasing ship size, improving cargo handling and employing 'just in time' arrival techniques are just some of the efficiency improvements suggested for this ship type [Wärtsilä Ship Power R&D (2009)].

Further improvements in efficiency can be achieved through the use of auxiliary propulsion systems. These are particularly applicable to smaller ships, where the benefits can be greater. They include: sail systems, kites; flettner rotors; and air bubble systems. While the latter is a newer technology, wind-assisted propulsion of merchant vessels has been a popular topic of research and development in the past [Smulders (1985); Bergeson & Greenwald (1985)] mainly due to high fuel prices. While interest in wind propulsion has recently been seen to reflect bunker prices, it should be remembered that in the not to distant past, wind power was the primary means of merchant vessel propulsion. The use of wind-assistance devices is becoming more common as a means of reducing emissions as well as saving fuel costs. Designs exist both conceptually [NYK (2010)] and operationally [SkySails (2010)]. Thus the application of technologies such as these has the potential to improve both the efficiency and environmental sustainability of feeder container ships.

This report details the design of such a vessel, taking into account both economic and environmental feasibility. A general approach in reducing emissions and fuel costs can be achieved by lowering operating speed, this project adopts a rather different philosophy. That is that an increase in speed, rather than decrease, is the answer to improving the efficiency of feeder services. By optimising ship design and operation, a viable concept is sought that can meet both future trade predictions and environmental targets.

1.2 Aims and objectives

The aim of this project is to design a fast, sail-assisted feeder container ship that can be considered economically and environmentally sustainable in the future container trade market. Only one iteration of the 'design spiral' is to be considered due to the limited time available.

This will be achieved by addressing the following main objectives, to:

- Make an assessment of future container trade and derive suitable ship particulars;
- Investigate technologies and methods for improving both transport efficiency and environmental sustainability;
- Develop the concept through the use of numerical techniques and physical model testing, focussing on minimising ship resistance and thus power requirement;
- Complete a feasibility study to assess the proposed concept against existing ships and the requirements derived in the initial stages of the project;
- Conduct a full concept design study to assess the impact of the novel design features utilised on vessel performance and prove the viability of the concept in all design areas. This will require considering seakeeping, structural design and stability.

The chapters that follow deal with each of these objectives in turn, which correspond to the natural progression of the design process.

1.3 Outcome and main achievements

The result of the project is a fast feeder container ship that has been designed to enter operation in 2020. The design performs favourably in terms of both transport efficiency and emissions levels compared to existing vessels operating on the routes considered. Emissions reduction targets have been exceeded, implying relevant legislation (MARPOL Annex VI) is also complied with. This is due largely to the use of liquefied natural gas (LNG) as fuel, which contains less carbon than typical fuel oils, and has zero sulphur content. The thrust benefit provided by the installed *Multi-wing* sail system is low at the ship's service speed of 25 knots. However, the feasibility of the design relies on a low power requirement at 15 knots speed, which is in fact lower than typical existing feeder ships, despite an increase in cargo capacity of approximately 40%. The ability to self-berth and load/unload independently of shore-side cranes also plays a major factor in the viability of the design. The unconventional design has also been rigorously assessed in terms of structural design, motion analyses and stability, thus improving the robustness of the proposed fast feeder concept.

2. Design Specification

2.1 Operating principles

The 'efficiencies of scale' principle has seen the size of container ships increase over the past decade, a trend that is set to continue. This poses problems to world shipping as the number of ports capable of accommodating these 'mega' container ships is limited due to draught, length and cargo handling restrictions. The solution to this problem lies with the operation of mega container ships on mainline East-West routes between regional hub ports (Figure 2.1). The transhipment[1] of containers from the regional 'hub ports' to smaller satellite ports is carried out using smaller feeder container ships, a concept that is commonly known as a 'hub and spoke' network [Koi Yu Ng & Kee (2008)].

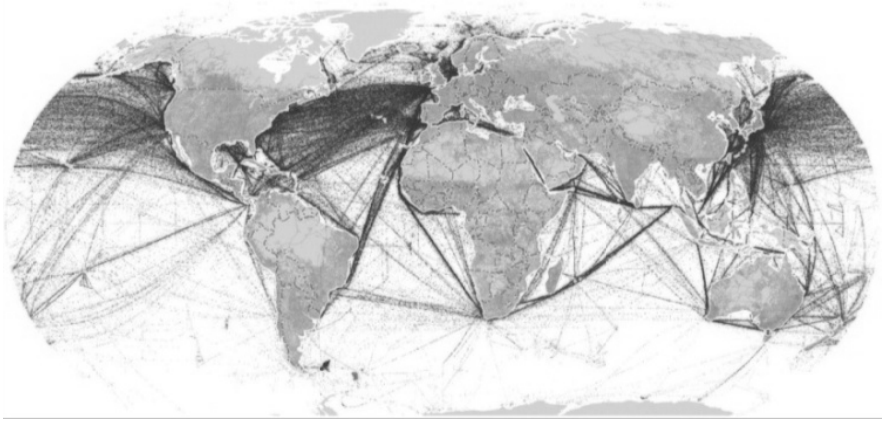

Figure 2.1 – Primary world trade routes [NOAA Satellite and Information Service (2009)]

A 'hub and spoke' network has a number of advantages over traditional networks. Firstly it acts as a means to transport cargo from satellite ports to a hub port for transhipment to a mainline shipping route. Secondly, because it is quicker for a container to be transhipped through a hub port than to wait for a direct ship, it provides quicker inter-regional transport of cargo between satellite ports. Generally, it means far fewer journeys are required, which makes 'hub and spoke' networks economically and environmentally more sustainable. For example, consider a region with sixteen regional ports. Without transhipment, if each port connected to every other port the number of journeys is represented by the left of Figure 2.2. However, with transhipment the same number of ports could be connected more efficiently as shown in the right of Figure 2.2 [PSA Singapore Terminals (2009)].

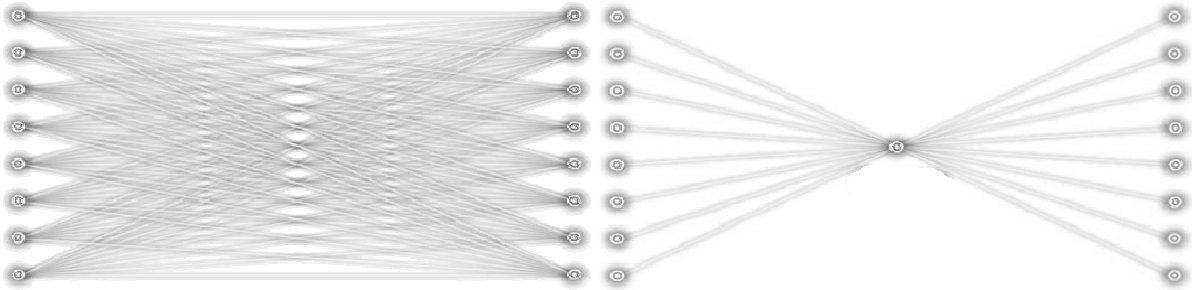

Figure 2.2 – Shipping network without (left) and with (right) transhipment [PSA Singapore Terminals (2009)]

The advantages of transhipment through hub ports meant the transhipment market tripled over the period of 1995-2005 [Ocean Shipping Consultants Ltd (2006)] a trend that is set to continue making it an integral part of the future container shipping market.

[1] Transhipment is the movement of containers to an intermediate location before being moved to their required destination.

2.2 Region analysis

An initial assessment of the current container ship market was made, using various research papers, professional society publications (such as 'The Naval Architect') and container ship operator websites. Seven regions (the Caribbean, Mediterranean, Middle East, Far East as well as South East Asia and the East and West coasts of the USA) were identified as potential areas where a 'hub and spoke' network could be applied. The East and West coasts of the USA were later rejected due to the strong competition from low cost rail transport, making the use of feeder container ships less economically and environmentally viable. Within the five remaining regions, a representative sample of the 60 largest ports were selected for further analysis.

In particular, potential 'hub ports' for the 2020 container ship market were identified based on the minimum combined distance to every other port in the region. This minimises the total distance that cargo needs to be transported, improving the transport chain when considered as a whole rather than on a route by route basis. For a more detailed analysis, consideration needs to be paid to the location of the hub port in relation to mainline services in order to optimise the entire transport chain. For simplicity only the location of the port within the region has been considered in this analysis. A summary of the regional hub ports is given in Table 2.1.

Table 2.1 – Identification of regional hub ports by minimum combined distance to all satellite ports

Region	*Hub port*	*Country*	*Total distance / n. miles*
South East Asia	Singapore[2]	Singapore	11836
Caribbean	Kingston[3]	Jamaica	7870
Far East	Busan	South Korea	5033
Mediterranean / Middle East	Gioia Tauro[4]	Italy	13014

In selecting hub ports consideration was paid to selecting ports that already had sufficient capacity to handle large volumes of cargo. This assumption is important as it is deemed impractical to build a purpose built port facility from scratch within the considered time frame. It would be expected in the longer term that hub port facilities would be custom built (either on land or floating offshore) in optimum locations to optimize the entire transport chain.

2.3 Port analysis

2.3.1 Throughput predictions

In order to dimension a suitable ship for the 2020 market it is necessary to gain an understanding of the container ship market at that time. In order to assess this, historic port throughput data (in terms of TEU) was obtained from Degerlund (2004; 2006; 2008) as well as port websites for a period between 1995 and 2008 for the ports identified in Section 2.2. A linear regression analysis was carried out and used to predict port throughput in 2020 for each of the 60 ports being investigated. The percentage increase on 2009 levels has

[2] Ocean Shipping Consultants Ltd (2006) found that Singapore has a 73.3% share in the South East Asia transhipment market. Container throughput at Singapore rose by 151% over 1995-2005 with a 113% increase in transhipment over the same period. This provides additional justification for its selection as a hub port.

[3] Kingston is identified as a hub port by Frankel (2002) who investigates how the use of mega-container ships on mainline services will affect trans-shipment in the Caribbean.

[4] Gioia Tauro is identified as a hub port by Francesetti & Foschi (2002) who discusses the use of 'hub and spoke' networks in the Mediterranean.

been averaged on a regional basis and is presented in Table 2.2. The author has used his discretion to remove items of data that appeared to be anomalous when making linear regression estimates.

Table 2.2 – Predicted container ship market growth by 2020

Region	*Predicted percentage increase*
Caribbean	83.12%
Mediterranean	100.37%
Far East	159.33%
South East Asia	67.39%
Average	**102.55%**

The historical throughput of containers for the cited regions together with predictions to 2020 are provided in Figure 2.3.

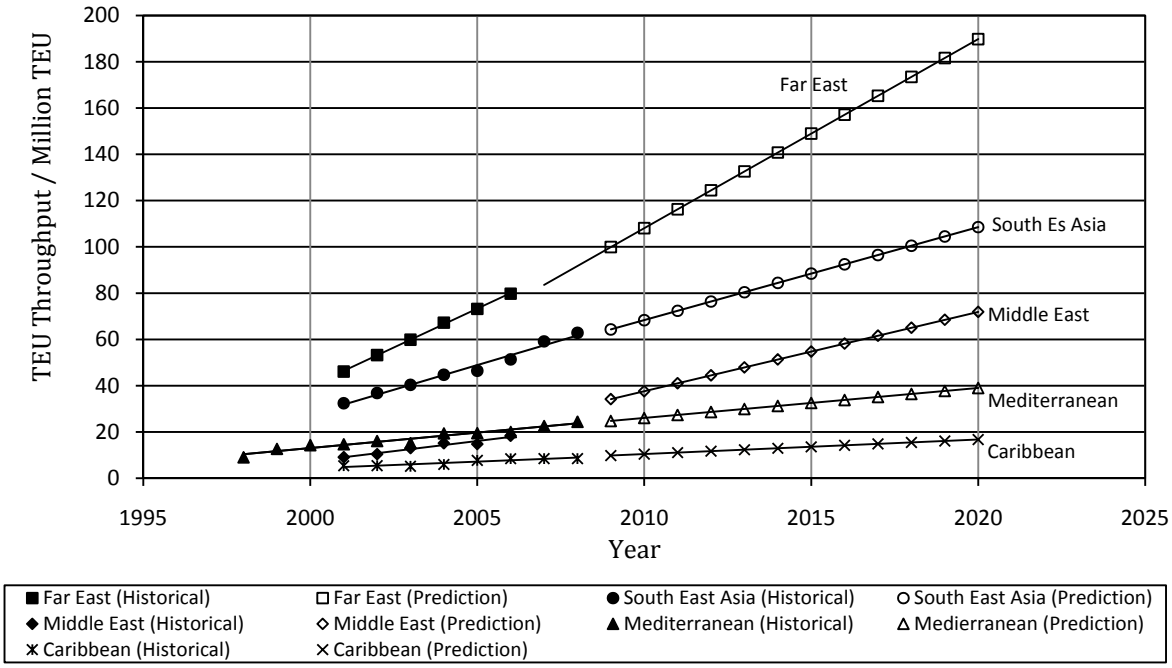

Figure 2.3 – Predicted growth in regional container ship markets by 2020

These estimates of container ship market growth are consistent with research of Ocean Shipping Consultants Ltd (2006) which predicted a 102-126% increase in world container throughput over 2004-2015 and a further 18-24% increase over 2015-2020.

The estimates of Table 2.2 container throughput by 2020 are derived using a linear regression analysis. This is deemed conservative compared to estimates made by other some authors [Cheng (2009)], who base their estimates upon an exponential growth rate. The prediction is also rather simplistic in that the estimate is not linked to the growth of the world economy (or the recent financial crises), nor does it account for scenarios that change trade patterns (such as tariffs) or sudden shocks to the trade patterns.

2.3.2 Port restrictions

One of the key parameters in the design and operation of feeder container ships is the ability to operate between small satellite ports that may have length and draught restrictions. In order to determine the port restriction dimensional restraints, maximum berth length and water depth data was collected from appropriate port websites and Degerlund (2004; 2006; 2008). A summary of this research is presented in Table 2.3.

Table 2.3 – Summary of port restrictions

Draught / m			*No. of ports*	*% of ports*
5	→	6	0	0.00
6	→	7	0	0.00
7	→	8	1	2.04
8	→	9	4	8.16
9	→	10	5	10.20
10	→	12	8	16.33
12	→	13	5	10.20
13	→	14	13	26.53
14	→	15	4	8.16
15	→		9	18.37

Berth length / m			*no. of ports*	*% of ports*
160	→	170	2	4.08
170	→	180	1	2.04
190	→	200	0	0.00
210	→	220	0	0.00
220	→		46	93.88

From discussions with Christian Mash of Borchard Lines Ltd, a feeder container ship operator, it was identified that shorter 'beamy' ships have advantageous operational benefits over larger ships. In ports with length restrictions, two long ships cannot berth at the same time. Consequently, smaller ships are allowed to jump the queue making them more profitable. This improves efficiency by reducing port waiting times.

A third port restriction that can restrict a ship size is air draught. Due to the relatively small size of the proposed ship this constraint is viewed as less onerous, although insufficient data is available to warrant a complete investigation.

2.4 Route analysis

The Datloy voyage management system used by major shipping companies worldwide permitted voyage routes between all of the satellite ports and their corresponding regional hub port to be investigated. The Dataloy voyage management system holds data on more than 7,200 ports and maritime locations, and over 69,000 waypoints to plan ship voyages accurately [Dataloy (2009)]. Hence it was possible to assess the distance between ports and the distance travelled at different headings on a particular route by post processing the longitude and latitude position of the waypoints along the routes considered. This data permits identification of a suitable ship range and allows sailing performance estimates for the ship from the anticipated apparent wind direction.

A summary of the required ship ranges from a cited hub port to the satellite ports is provided in Table 2.4.

Table 2.4 – Summary of required ship range for cited hub ports

Range / nm			*No. of routes*	*% of routes*	*Cum. sum*
0	→	1000	16	30.77	30.77
1000	→	1500	12	23.08	53.85
1500	→	2000	11	21.15	75.00
2000	→	2500	8	15.38	90.38
2500	→	3000	3	5.77	96.15
3000	→	3500	2	3.85	100.00
3500	→	10000	0	0.00	100.00

The distance travelled at a particular heading for the Caribbean, South East Asia and North Atlantic routes is summarised in Table 2.5. The Caribbean and South East Asia are presented as the results of the initial economic analysis (discussed in Section 2.6) these regions are the most viable for the exploitation of transhippment.

In order to also address the feasibility of sail assisted ship propulsion it is pertinent to investigate the ship performance in areas of the world with more favourable wind conditions. For this reason, twelve north transatlantic routes from various ports on the East coast of Canada, USA and the Caribbean to Rotterdam and Gibraltar have been considered. Within these routes, the route that provides the most favourable wind strength and apparent wind angle shall be selected to assess the ship performance in 'ideal' conditions. For this reason Table 2.5 also contains summary route data for North Atlantic routes.

Table 2.5 – Distance travelled on a given heading for the regions being considered

Heading / degrees	*Distance travelled / nm*		*Combined total / nm*	*% of total*	*North Atlantic distance travelled / nm*	*% of total*
	South East Asia	*Caribbean*				
0 → 29	827	1120	1947	5.51	1332	1.53
30 → 59	1330	2307	3637	10.29	1265	1.45
60 → 89	1281	1630	2911	8.24	11463	13.13
90 → 119	1163	1058	2221	6.28	23043	26.39
120 → 149	2424	366	2791	7.90	2257	2.58
150 → 179	3377	781	4158	11.76	4301	4.93
180 → 209	827	1134	1961	5.55	1334	1.53
210 → 239	1330	2307	3637	10.29	1265	1.45
240 → 269	1281	1630	2911	8.24	11463	13.13
270 → 299	1163	1058	2221	6.28	23043	26.39
300 → 329	2424	366	2791	7.90	2257	2.58
330 → 359	3377	781	4158	11.76	4301	4.93

The 'cascade principle' in the operation of container ships says that a new container ship will operate on mainline services until being replaced with a new ship. Once replaced, the old ship will be used on feeder routes until it becomes uneconomical and is scrapped. This progression of container ships from mainline to feeder to scrapping makes feeder ships older and less efficient on average. Hence it is an ideal area of the market to make efficiency savings [Tozer (2009)].

From an analysis of 174 services across the five regions being considered statistics regarding typical ship size, voyage time, speed and age serving each port were investigated [Degerlund (2004; 2006; 2008)]. A summary of typical age of ships operating on the routes being considered is shown in Table 2.6. Other statistics gathered in this exercise are discussed in Section 2.6.

Table 2.6 – Breakdown of basis ships by year built

Year built			*No. of ships*	*% of ships*
1960	→	1970	1	0.68
1971	→	1975	4	2.72
1976	→	1980	16	10.88
1981	→	1985	20	13.61
1986	→	1990	9	6.12
1991	→	1995	20	13.61
1996	→	2000	49	33.33
2001	→	2005	29	19.73

If container ship service life is 30 years then by 2020 ships constructed between 1990 and 2000, that is 46.94% of the feeder fleet, will need replacing. Assuming these ships carry an equivalent share of the total TEU throughput, the amount of cargo the proposed feeder ship will have to carry in a typical year can be estimated by assuming it will replace a certain percentage of these scrapped ships. Initially a 20% target share of the

2020 new build market has been set, which gives a target market share in the 2020 feeder container ship market in the order of 10%. This assumption takes no account of the variations in scrapping and build rates over time, which is heavily influenced by the growth or decline of the global economy.

2.5 Operational analysis

Further discussions with Mash (2009) of Borchard lines Ltd provided insight regarding the feeder container ship's requirements from an operator's perspective.

Fuel efficiency is crucial not just because of rising fuel costs. The amount of tonnage available to charter allows operators to select the ship size that most suits their markets and their service philosophy. Generally, more frequent services satisfy shippers demands for a short transit time. Big ships are only economical if you can fill them. Thus, ship size, speed and fuel efficiency are crucial and will vary heavily from route to route.

Congestion in busy ports can be up to five days and is a major problem for operators. Typically on a 28 day voyage 20 days is spent at sea, eight days in port and usually two to three days is left to account for congestion. Even with this allowance, ships still need to sail faster than their design speed to catch up, which increases fuel costs. Bad weather has significant influences on the ability to maintain schedules and many ships are worse than others at keeping speed in rough weather. Ideally ships need to be able to operate at constant speed up to force five. Currently some ships reduce speed to less than five knots in bad weather when other similar sized/powered ships can still proceed at upwards of 12 knots. Ships spend 75% of their time at a service speed of 90% MCR and sometimes operate at reduced speed e.g. in case of good weather, fast turnaround in port etc. and then MCR is at least 70% because any lower than this engines incur problems. In winter, ships will spend a greater proportion of their time at full speed. Performance of a ship over time is monitored and if a ship does not perform, then it is replaced by more efficient designs. Some shipyards invest little money into achieving an efficient hull and propeller design.

In order to comply with SO_x Emission Control Areas (SECAs) ships need to be able to burn both high and low sulphur fuels. Currently owners are unwilling to invest in fitting scrubbers to reduce emissions given the cost versus return, because they do not pay for the fuel and time charters are not long enough to achieve a saving. Regular bottom cleaning and low friction coefficient paints are regularly used to improve efficiency and can improve performance by two to three nautical miles per ton. Sails and other structures that protrude on a container ship tend to get hit and damaged during cargo operations and anything high tech tends to go wrong and costs money. If the crew can effect repairs without the need for shore based technicians to join the ship then this saves on costs and delays.

Ships that are manoeuvrable with bow and stern thrusters save on tug usage which can be thousands of Euros a time. Ships come under different rules depending on the gross tonnage. For instance, ships with a gross tonnage greater than fifteen thousand tonnes require pilots to pass the Messina straits adding costs and delay.

Ships need to be able to take high cube containers in all positions without loss of slots, with an ability to load cargo for more than one destination in each bay but able to discharge in any order. Open hatch ships are ideal for this. Otherwise split hatch covers are used. Container stacks need to be capable of supporting high container weights which are not reduced because of racking forces. This is a drawback of open hatch designs. For example if you load six high 30 metric tonne 20ft containers then the bottom container can collapse.

2.6 Economic and environmental analysis

A key criterion in container ship operation is to deploy the right size ship to cater for the desired market while minimising excess capacity, since the right size tonnage has significant implications on freight rate. There is no one ship to suit all markets. Thus, in order to determine a suitable capacity and speed for the fast feeder concept an analysis was conducted encompassing all the research discussed in Sections 2.2 to 2.5.

Some key assumptions had to be made initially to control ship operations so as to optimise the transport chain efficiency as a whole, and not just on a ship by ship basis. The assumptions made can be summarised as follows, that:

- In 2020 all containers in a region are transhipped through a hub port with direct return feeder services from hub ports to single satellite ports, i.e. there are no direct services between satellite ports, circular routes or backtracking routes. Frankel (2002) found 'hub and spoke' networks to be the quickest and most economically efficient method of transporting cargo;
- The number of sailings per week is to remain constant at 2009 levels, to maintain the same level of consumer service. The number of sailings is calculated by assuming that operators switch with immediate effect to a hub and spoke network with no services between satellite ports (i.e. all containers are transhipped through a hub port). This assumption will essentially increase the size of feeder container ships in line with the increased growth of the container ship markets predicted by the port analysis;
- The number of ships required on a regional basis is to be halved in order to reduce congestion and time spent waiting to get into port. This is to be achieved by increasing ship speed and port handling capabilities;
- The proposed ship will not experience congestion and will control the loading and unloading of all containers to minimise delays;
- The initial target market share will be to carry approximately 10% of the total container throughput on all routes.

In order to determine suitable dimensions for the ship, the 2009 TEU throughput was divided by the average ship size on a given route to set the number of sailings, assuming a 90% ship utilization [Noteboom & Vernimmen (2009)]. The market growth and target market share was used to calculate required TEU capacity per week per route. On the assumption the number of sailings a week on a route is to remain constant a new ship size could be determined. On the assumption that:

- the ship will have to make at least two voyages in the time it takes a current ship to make one;
- the route length is known;
- an assumed unloading time can be made based on ship size;

the ship speed can be determined. Since the congestion and unloading times varies from port to port the exact number of basis ships the ship will replace is adjusted using the authors discretion to yield realistic and achievable values (i.e. replacing 3 basis ships for 1 concept ship, or 3 basis ships for 2 basis ships instead of 2 for 1 etc. on some routes). The process followed by the author to determine the ship capacity and speed is presented graphically in Figure 2.4. The boxes in grey indicate inputs to the process whereas the highlighted boxes indicate process outputs.

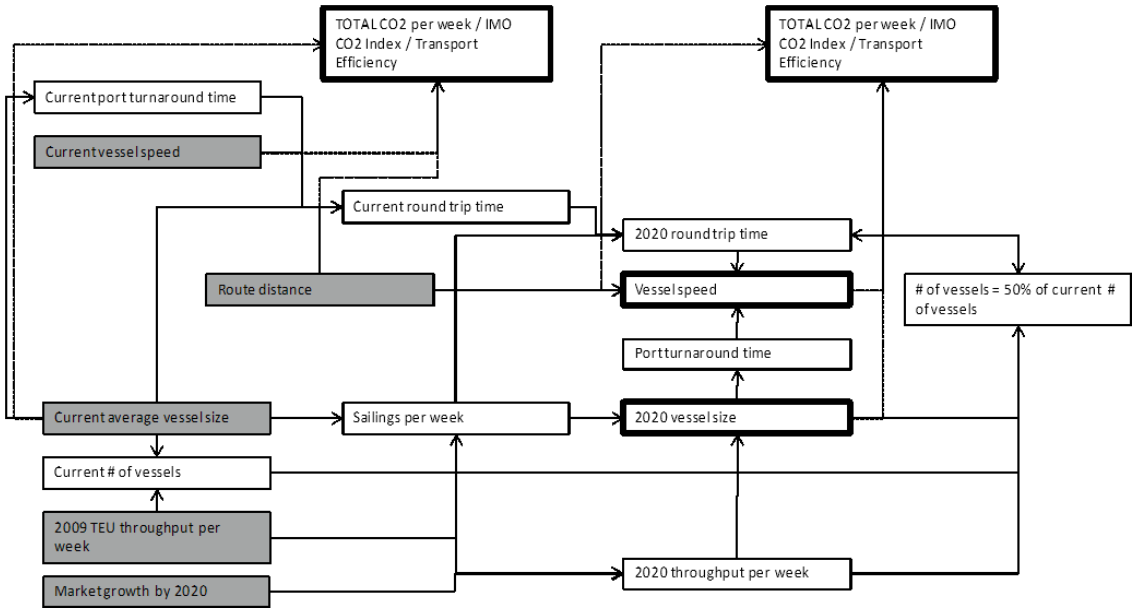

Figure 2.4 – Flow chart used to determine the required ship capacity and speed for a particular route

The process shown in Figure 2.4 was applied to each route to determine an optimum ship size and speed that satisfied the listed assumptions. Statistics were then generated to indicate the proportion of ships of a certain size and speed. These results are summarised in Table 2.7 and Table 2.8.

Table 2.7 – Summary of required speed

Speed / knots	*No. of ships*	*% of ships*	*Cum. sum*
0 → 16	39	38.89	38.89
16 → 17	5	5.05	43.94
17 → 18	12	12.12	56.06
18 → 19	4	4.04	60.10
19 → 20	16	15.66	75.76
20 → 21	8	8.08	83.84
21 → 22	1	1.01	84.85
22 → 23	3	3.03	87.88
23 → 24	0	0.00	87.88
24 → 25	1	1.01	88.89
25 → 26	0	0.00	88.89
26 → 27	8	8.08	96.97
27 → 28	0	0.00	96.97
28 → 29	2	2.02	98.99
29 → 30	0	0.00	98.99
35 → 36	1	1.01	100.00

A rather simplistic estimate of ship speed assumes that the ship advances at its operational speed from leaving port to arriving at their destination. Clearly a proportion of the time is spent at slow speed upon leaving and entering port and also when manoeuvring. Thus, the service speed of the proposed ships will be marginally larger than the values quoted in Table 2.7. Using all the information discussed and the ship requirements analysis for specific routes it was concluded that a service speed of 25 knots would be appropriate. This is approximately ten knots faster than existing ships on routes of interest.

The ship capacity of Table 2.8 suggests that 1200 to 1300 TEU would be suitable for a large proportion of the 2020 container ship market. Thus this is the target capacity for the proposed new design.

Table 2.8 – Summary of required ship capacity

Capacity / TEU			*No. of ships*	*% of ships*	*Cum. sum*
0	→	100	0	0.00	0.00
100	→	200	0	0.00	0.00
200	→	300	2	1.98	1.98
300	→	400	0	0.00	1.98
400	→	500	1	0.99	2.97
500	→	600	1	0.99	3.96
600	→	700	2	1.98	5.94
700	→	800	2	1.98	7.92
800	→	900	6	5.94	13.86
900	→	1000	2	1.98	15.84
1000	→	1100	10	9.90	25.74
1100	→	1200	9	8.91	34.65
1200	→	1300	11	10.40	45.05
1300	→	1400	6	5.94	50.99
1400	→	1500	4	3.96	54.95
1500	→	1600	2	1.98	56.93
1600	→	1700	2	1.98	58.91
1700	→	1800	2	1.98	60.89
1800	→	1900	0	0.00	60.89
1900	→	6000	40	39.11	100.00

Detailed analysis of the South East Asia and the Caribbean routes revealed that the optimum ship size was similar. The optimum ship sizes for the Mediterranean / Middle East and Far East routes are comparable, but a lot larger than the ship for the Caribbean and South East Asia markets. As a consequence of these very distinct differences it was decided to focus on developing a conceptual design for the Caribbean and South East Asia markets.

The basis ship for a particular operational area will be designated “Case A”. The optimal design will be referred to as “Case B”. In each case, and for each region of interest, it is necessary to assess the average weekly CO_2 emissions expected for 2020, when transporting 10% of the total regional container throughput. A comparison of the emissions from the proposed optimum and basis ship is given in Table 2.9.

Table 2.9 – Predicted CO_2 emissions in 2020

Region	*Million tonne CO_2 per week*		
	Case A	*Case B*	*% increase*
South East Asia	976	1262	129.32
Mediterranean	609	982	161.40
Caribbean	243.6	294	120.71

Table 2.9 indicates that by reducing the ship numbers gives a rise in CO_2 of between 20% and 60% due to the increase in speed. However, these increases are expected. The aim of this investigation is to reduce congestion and improve transport efficiency, a strategy that does not reflect well on a tonnes of CO_2 per nautical mile measurement scheme (such as that used for the EEDI The rise in emissions from increasing speed will be recovered using for example, auxiliary propulsion in the form of rigid wind sails; low friction antifouling coatings and alternative fuels.

The predictions of Table 2.9 are rough estimates of average ship speed over the route distances, but are adequate for an initial comparison of the two operational strategies. There is insufficient basis ship data on routes in the two regions not presented (Far East and Middle East) to make a suitable analysis but it is

suspected due to the nature of the container line business that the trend will be similar to the Mediterranean. The greater increase in emissions associated with Mediterranean routes is linked with the larger optimum ship size.

A comparison of the number of ships required by the two assumptions is given in Table 2.10.

Table 2.10 – Number of ships required in 2009 and 2020 by region

Region	*No. of ships*		
	Case A	*Case B*	*% difference*
South East Asia	120	44	36.67
Mediterranean	80	45	56.25
Caribbean	28	12	42.86

It is evident from Table 2.10 that a significant reduction on ship numbers can be achieved with the proposed operational assumptions. Furthermore, Table 2.10 indicates that the ship reduction in South East Asia and the Caribbean is much greater than the 50% set target. The likely cause for this is the average ship size is smaller and older than the other regions being considered. This was discovered by analysis of the route specific basis ship data. Due to lack of port regulation etc. container ship operators use their older and more inefficient ships on South East Asia routes. This means that greater savings can be made in terms of operational efficiency by replacing these ships. In the Mediterranean, the reverse is true. The tighter regulations give rise to ships that are larger, newer and more efficient. This makes it much harder to produce the same efficiency savings. A summary of the average ship sizes operating in the regions being considered currently and predicted in 2020 are given in Table 2.11.

Table 2.11 – Average ship size by region

Region	*Average ship size / TEU (2009)*	*Average ship size / TEU (2020)*	*% increase*
South East Asia	890	1303	146
Mediterranean	1547	2161	139
Caribbean	955	1088	113

2.7 Summary

The proposed fast feeder design will have a service speed of 25 knots and a cargo capacity of 1300 TEU. This is deemed to be suitable for a large proportion of the routes considered in this investigation. It is evident that the concept is most suited to the South East Asia and Caribbean regions, where greater efficiency savings can be made due to the length of the routes (up to 1500 miles) and the inadequacy of the ships currently serving these routes. These regions will be the focus of the remainder of this investigation. Furthermore the use of sail assisted ships on transatlantic passages will also be considered.

3. Initial Development of Fast Feeder Container Ship

3.1 Basis ships

In any design study it is important to assess existing ships undertaking similar operations. In Chapter 2 economic and operational assessments of existing shipping lines facilitated the identity of a feasible concept. Thereafter, basis ships are a good source for the preliminary estimation of a number of basic design parameters. A database of around 170 ships has been created from data primarily sourced online [van Duivendijk (2009) and Svendsen & Tiedemann (2009)] and secondarily from Degerlund (2004; 2006; 2008). Whilst online sources provide a plentiful supply of data, they are often incomplete and potentially inaccurate. However, as the basis ship data is only used to provide initial estimates, the existence of inaccuracies is simply noted. Discretion has been used to illuminate or correct data that is obviously incorrect. Some more reliable sources of data have been found in published technical papers [Kim *et al.* (2003), Sipila & Brown (1997) and BMT Nigel Gee (1998)]. These provide detailed technical information, including indications of layout, however these sources are scarce and thus do not constitute a large proportion of the database.

Information extracted from sources includes, but is not limited to:

- Cargo capacity (N_C);
- Maximum capacity of refrigerated units (Reefers);
- Length overall (L_{OA});
- Beam (B);
- Draught (T);
- Maximum speed;
- Operating speed;
- Year built;
- Installed power (P_B);
- Machinery types;
- Deadweight (DWT).

Dimensions and capacities given are generally maximum values allowing for an estimation of overall dimensions. It is unfortunate that operating speed is only given for a number of ships, as this is of particular interest. Primarily the basis ship data has been used to estimate the required principal dimensions to fulfil the capacity requirement identified in the initial economic evaluation. The basic dimensions will primarily be a function of the cargo carrying capacity of any container ship. By plotting L_{OA}, B and T against N_C , (Figure A.1 and Figure A.2), it is clear the trend is linear.

It is not unusual at this stage to use dimensionless hull form parameters. However if one plots L_{OA}/B and B/T against capacity there is little variance and hence the correlation of the linear regression is weak. Thus this approach is avoided. The results of these regressions are summarised in Table 3.1.

Table 3.1 – Summary of regression analysis results

$L_{OA}\ /\ m$	$0.04391N_C + 105.5358$	162.619
$B/\ m$	$0.005608N_C + 17.898958$	25.189
$T/\ m$	$0.002236N_C + 6.161147$	9.070
L_{OA}/B	$0.093637V_S + 4.738531$	7.079
$DWT\ /\ tonnes$	$14.547N_C - 529.94$	18381.160
$P_B\ /\ kW$	$1.671V_S^3 - 707.4$	25401.980

As expected the trends of the data sets suggest that as the cargo capacity of a container ship increases then so must all of its principal dimensions. When increasing the dimensions one should take note of any operational restrictions placed on the ship such as depth in ports, length of berths and minimum air draught. The influence of changing the parameters upon ship performance need to be appreciated, and hence the effect on efficiency and costs (including those associated with construction).

Most container ships have similar hull form topology. Within the regression analyses this fact is reflected by the number of data points near the mean. However, ships with excessive breadth or draught (Figure A.1 and Figure A.2), compared to their cargo capacity exist. This is interpreted as inefficient design or the impact of restrictions on the other principal dimensions leading to a growth in unrestricted parameters.

In addition to capacity, the hull form 'shape' is a function of the ship operating speed, particularly L_{OA}/B. This is due to minimising resistance of a hull form, see Section 4.1. Generally faster ships, for which wave pattern resistance constitutes a larger proportion of the total resistance, will have larger L_{OA}/B to minimise this component of resistance. This is evident in Figure A.2 with the lower speed set having this general trend and the higher speed ships showing a more significant increase in L_{OA}/B. Ideally the slenderness ratio L_{WL}/∇^3 would be used but almost all of the basis ship data lacks information regarding the displacement and waterline length. Regression of the data in Figure A.2 leads to the results presented in Table 3.1. One can compare the result from this regression to the result obtained from the regressions for L_{OA} and B giving $L_{OA}/B = 6.456$. There is an 8.8% decrease from the original result, such a difference is expected when dealing with regression analysis of data.

Estimating the mass of a ship is important. From the basis ship database information regarding deadweight is abundant. As deadweight is almost purely a function of cargo capacity it can be estimated using the regression formula of Table 3.1. Similarly the installed power can be estimated by deriving a regression equation dependent upon cube of the required maximum speed. This gives the linear trend of Figure 3.1. It is important to note the significance of the build year field when filtering this data. Ships in the database built in the 1970s and 1980s, which must be nearing or have come to the end of their operational life, tend to have large installed powers for the speed achieved and the capacity of cargo carried when compared to more modern ships. This indicates inefficient ship design. These data points have been eliminated from this analysis as they do not provide data of relevance to future designs.

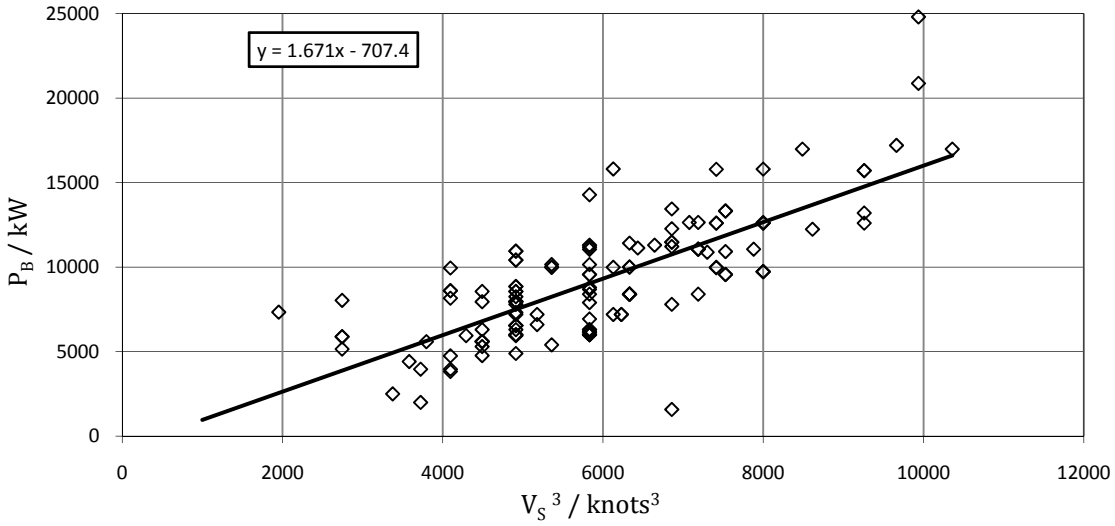

Figure 3.1 – P_B as a function of the cube of ship speed (V_s^3)

The lower speed ships of 15 knots cannot be excluded, since data relevant to the 25 knot design target are very limited, see [Kim *et al.* (2003), Sipila & Brown (1997) and BMT Nigel Gee (1998)].

Further analysis could be carried out using the basis ship data. However it is important to remember the approximate nature of this analysis and hence its applicability. The derived data are to be used to aid further development of the design but will not be used as absolute values for design parameters. Absolute values will be determined using technical and logical design methods. In short, extensive basis ship analysis is not an efficient use of time. The basic design parameters to be used are those already suggested by the initial economic analysis namely, ship speed and cargo capacity.

3.2 Initial mass, powering and stability estimates

The processes in which preliminary dimensions are determined for a container ship are very different to that of a conventional ship. Since container ships carry a significant proportion of their cargo on deck, cargo volume is indeterminate, which means it is not possible to base the design on the required cargo volume. The design is principally driven by stability considerations, which controls the limiting height to which containers can be stacked. To help stability and maximise capacity the top container slots are reserved for lightly loaded containers. Heavy containers are located lower down and typically ballast water is carried permanently to help improve stability. For a given stacking height there will be a minimum ship breadth in order to guarantee stability. Within this, to ensure longitudinal and torsional structural strength, a proportion of the breadth has to be devoted to structural decks. Thus the number of container tiers determines the number of container rows in the breadth. Length is determined by the technically desirable length to breadth ratio and also limiting port constraints. These dimensions are heavily influenced by ship speed, because of its effect on C_B and installed power [Watson & Gilfillan (1977)].

With this in mind the determination of the ship dimensions is principally found to reflect multiples of container height, width and length with an allowance for sail stowage, machinery (determined from basis ships), fore and aft peak volumes, bilge volume and fuel volume. The requirement for hydrostatic equilibrium is heavily dependent on ship dimensions and carrying capacity.

Using the initial principal particulars as a starting point, an iterative approach is adopted to determine suitable dimensions. The approach can summarised as follows:

1. Define the ship beam and depth as a function of container dimensions and then select ship length in terms of the number of cargo holds required to achieve the required capacity with consideration to relevant port restrictions;
2. Estimate ship power required to obtain design speed using basis ship data;
3. Estimate ship mass using the Watson and Schneekluth empirical methods as well as basis ship scaling methods;
4. Demonstrate a balance of weight and buoyancy at a draught within the port restrictions.
5. Ensure the ship has adequate stability;
6. Alter dimensions and repeat until a satisfactory dimensions, balance of forces and stability is achieved.

What follows is a brief description of some of the methods employed in the cited steps.

3.2.1 Mass estimate

An initial estimate of ship mass was made during each iteration using three different methods, namely:

- A general empirical estimate using the method described by Watson & Gilfillan (1977) based on Lloyd's equipment numeral with constants prescribed for container ships;
- A more detailed empirical estimate described by Schneekluth & Bertram (1987) to estimate the lightship mass of container ships;
- By scaling of basis ships with corrections allowing for a change in dimensions and a change in scantlings.

The two empirical methods use regression equations based on statistical data from basis ships to provide an estimate of lightship mass for various weight groups, which include the;

- Weight of hull steel;
- Weight of steel superstructure and deckhouses;
- Weight of equipment and outfit;
- Weight of engine (propulsion plant);
- Weight of cranes;
- Weight margin to account for material tolerance, design details and tolerances in design;
- Total deadweight including payload, ballast water, provisions, fuel, lubricants, water, persons and personal effects.

The method given by Schneekluth & Bertram (1987) is more detailed and more specifically tailored to the design of container ships and includes estimates for:

- Lashings, cell guides and refrigeration equipment;
- The breakdown of engine mass into separate masses to account for engine, gearbox, generators, propeller, shafting and miscellaneous items;
- The mass of tanks;
- The dependence of the ship mass on size and type of container carried (TEU, FEU, reefer etc.).

When employing empirical methods in ship design it is important that the ship particulars are within the prescribed limits of the original data collected. Generally the form of the proposed ship lies within these limits, except for the high Froude number required. However, in the absence of more accurate empirical methods the procedures followed here were deemed adequate as an initial estimate. For the authors, the greatest concern of uncertainty was the estimate of masses. The empirical equations were based on installed power, and the relatively high speed of the concept design is much larger than basis ships.

A key criterion in the determination of machinery mass is the choice of propulsion system. At the point of determining initial dimensions a number of different propulsion systems were under consideration, as well as the use of alternative fuels such as LNG and hydrogen. Each will require different machinery installations requiring different space and mass allowances. Initially an LNG plant with a contra-rotating pod has been assumed. This initial mass estimate was an attempt to second guess the results of more detailed propulsion research to follow.

The empirical estimates of ship mass were backed up with lightship estimates provided by the scaling of basis ships following the method of Molland (2008). The method includes corrections to the lightship mass of the basis ships due to changes in dimension through the determination of mass per metre of length, depth and beam,: this is then multiplied by correction factors to obtain a dimensional changes in lightship mass. A correction is then applied in a similar manner to account for the changes in scantlings. The limitation of this method was being able to find basis ships with similar dimensions and known lightship mass. The method of

basis ship scaling was applied to four ships of the International Shipping Corporation (2010). The results of which are summarised in Table 3.2.

Table 3.2 – Summary of mass estimates based on scaling basis ships

Ship	*Lightship / tonnes*	*LOA / m*	*B / m*	*D / m*	*Dimensional correction / tonnes*	*Scantling correction / tonnes*	*Total correction / tonnes*	*Lightship estimate / tonnes*
Intra Bhum	9825	182	30.55	16.2	-2601	-1021	-3623	6202
Maersk Alabama	6120	155	25	9.52	+586	+166	+752	6872
Java Sea	1702	91	14.7	4.97	+2411	+812	+3224	4926
-	3283	116	18	7	+2409	+782	+3191	6474

A summary of the mass estimates produced by the three different methods is given in Table 3.3. The maximum variation in mass estimate between the various methods employed is 14%.

Table 3.3 – Summary of mass estimates

Method	*Steel mass / tonnes*	*Outfit mass / tonnes*	*Machinery mass / tonnes*	*Lightship mass (tonnes)*	*Deadweight / tonnes*	*Total / tonnes*
Watson and Gilfillan (1977)	4670	1430	1121	7366	12842	20208
Schneeluth and Bertram (1985)	4326	2489	1144	8962	12842	21629
Scaling basis ships	-	-	-	6119	12842	18961

As well as providing empirical estimates of mass, the method of Schneekluth & Bertram (1987) provides empirical estimates for vertical centre of gravity of the various weight groups (i.e. ship steel mass, outfit and propulsion). When combined with known estimates of the vertical centre of gravity of the deadweight components an initial estimate of ship centre of gravity can be made, thus allowing an assessment of the ship stability.

3.2.2 Powering

Within the empirical methods employed, there are equations to provide estimates of machinery mass. These are principally a function of installed power and thus require an initial estimate of powering to be made. In order to gain a rough approximation of installed power the basis ship data was used to estimate ship power as a function of ship speed using a $P \propto V^3$ relationship (Figure 3.1). The estimate is rather crude as it does not account for hull form changes, however there was a good fit to the basis ship data; the ship installed power was found as 25 MW. This is very close to the BMT fast feeder "Norasia" [BMT Nigel Gee (1998)].

As previously mentioned, it was anticipated that in order to meet emission reduction targets an alternative fuel such as LNG or hydrogen would need to be employed. Initially it is assumed that LNG would be the propulsion fuel although allowances were made to select another fuel source later in the design process. An estimate of fuel and tank mass, and tank volume, were made assuming the use of LNG and a voyage profile. A range of 3000 nautical miles (nm) was assumed, with 2% of voyage time spent manoeuvring, 23% of voyage time in port, 46% of voyage time at lower operational speed and 29% of time at service speed [Mash (2009)]. An auxiliary power allowance of 1.5MW was assumed to be required throughout the entire voyage. A summary of the assumed voyage profile is given in Table 3.4 A summary of the fuel and tank mass estimate with an estimate of emissions and a comparison to standard MDO is given in Table 3.5.

Table 3.4 – Assumed operational profile for fuel and tank mass estimates

	Service speed	*Slow speed*	*Cruise auxiliary*	*Manoeuvring*	*Port auxiliary*	*Total*
Speed / knots	25.00	15.00	-	-	-	-
Dist. travelled / n.miles	1537.00	1462.89	-	-	-	3000.00
Time spent / hours	61.48	97.52	163.25	4.24	48.76	212.00
% time spent	29.00	46.00	-	2.00	23.00	-
Power req. / MW	25.03	4.60	1.20	5.00	0	26.23
Energy req. / MWh	1538.60	448.60	195.90	21.20	0	2204.45

Table 3.5 – Capacity and emission per trip

	LNG	*MDO*	*% diff.*
Mass / tonnes	343	479	-28.47
Tank mass / tonnes	302		
CO_2 / tonnes	1090	1597	-31.75
NO_x / tonnes	4	29	-87.83

Table 3.5 indicates that the use LNG for propulsion leads to substantial emissions and fuel mass savings.

3.2.3 Stability

An initial stability check was conducted using an approximate stability formula [Molland (2008)]. The minimum limiting GM_T was estimated at 0.5 metres and the maximum GM_T to be limited by a minimum roll period of ten seconds (which is equivalent to a maximum GM_T of 1.2681 metres).

The water plane area coefficient (C_{WP}) was estimated using the 'Baker', 'Munro-Smith' and 'BSRA' methods [Molland (2008)]. The sensitivity of the solution to these parameters investigated. The Baker method was used in the final estimates of stability, as this was deemed the more representative of the proposed hull form[5]. The KB of the ship was estimated using Morrish's formula. A summary of the final iteration stability check for the proposed concept is given in Table 3.6

Table 3.6 – Summary of initial stability check

Parameter	*Method employed*	*Value*
C_{WP}	Baker	0.7988
C_{WP}	Munro-Smith	0.6700
C_{WP}	BSRA	0.7020
KB/ m	Morrish's Formula	5.5500
BM_T / m		7.2910
BM_L / m		8.010
KG / m		12.956
GM_T / m		0.601
T_r / s		14.520

A summary of the initial principal particulars of the ship is given in Table 3.7.

[5] This was validated later with waterplane area calculated from the *Maxsurf* model, which was very close to the Baker estimate.

Table 3.7 – Summary of principle particulars

Particular	*Dimension*
L_{OA} / m	170.70
L_{WL} / m	155.40
B /m	26.19
D / m	18.97
T / m	9.00
C_B	0.57
$C_{B0.8D}$	0.64
Δ / tonnes	21402.00

3.3 Main propulsion and machinery options

The two main elements of the propulsion system are the *propulsor* and the *plant.* When choosing an appropriate propulsion solution, it is necessary to take into account: the range of operating speeds; the overall efficiency of the system; initial cost and bunker prices; complexity and ease of maintenance; manoeuvring requirements; and emissions. Potential options for both the propulsor and plant are considered next.

3.3.1 Propulsor

Fixed pitch propeller

This is the most common propulsion device amongst merchant ships, especially for low speed operation. It provides the optimum efficiency when a ship operates predominantly at one speed only. In addition, fixed pitch propellers (FPPs) feature simple design and thus reduce construction and maintenance costs.

Controllable pitch propeller

The controllable pitch propeller (CPP) provides a number of advantages over the FPP: firstly, one can achieve greater control over the thrust generated, aiding in manoeuvring situations; this also allows (where appropriate) the propulsion machinery to stay running at a constant speed, to maintain efficiency, even when variable thrust is required during a voyage; lastly, the blades can be feathered to reduce hydrodynamic drag, should the propeller not be rotating. Since the boss diameter increases slightly compared to the FPP, a 2-3% reduction in efficiency can be expected [Molland (2009)]. An additional consideration is the complex mechanism used to control the blades' pitch, which means a CPP requires more maintenance than an FPP.

Waterjets

A waterjet consists of a pump which draws water through a ducting system before expelling it at high velocity near the waterline, thus generating thrust. Waterjets are best employed on ships operating at speeds between 30 and 45 knots [Molland (2009)], and suffer from poor efficiency at low speeds. High manoeuvrability, as well as stopping ability, can be achieved using 'deflector' units. It should be noted that the weight of a complete waterjet unit is generally more than that of a propeller arrangement, although no rudder is required, thus saving weight and appendage drag. Waterjets also require significant modification of the stern layout of the ship, which may impact other design considerations.

Azimuthing drives

This propulsion solution is commonly seen in two main forms, namely the 'Z-drive' and the 'podded drive', each of which is discussed separately next.

(i) Z-drive

Allowing high levels of manouevrability, the Z-drive is so-called due to the shape of the mechanical linkage between plant and propulsor. Bevel gears transfer power through a shaft mounted within the bearing of the azimuthing unit to the propeller. This device is a popular installation on tugs, where ducted units are often used due to high thrust loadings. They have the advantage of relatively low drag since the unit is smaller than an equivalent podded drive. However, the complex gearing can lead to an increase in maintenance costs. They are not best suited to use in combination with electric propulsion, due to the shafting arrangement and main plant location. Thus some of the efficiency gains and layout flexibility of electric propulsion are lost.

(ii) Podded drive

This propulsion arrangement is a development of the Z-drive concept, mounting an electric motor inside the pod housing to power the propeller, instead of using a mechanical drive. This improves the flexibility of power distribution and machinery layout. A large range of such devices, up to 23 Megawatts (MW) installed power per pod is available [Carlton (2007)]. They are suitable even for large ships where manoeuvrability is important, such as cruise ships. Generally the propeller is mounted on the front of the pod, offering a cleaner inflow to the propeller due to an absence of shafting and bracketing, resulting in higher efficiency. Reductions in appendage drag (by removing shafting brackets and rudders) are offset by the drag of the pod unit itself. A further consideration is the large mass supported by the stern framing, which includes a large amount of additional machinery as seen in Figure 3.2. An additional consideration is the complex bearing units required to rotate the pods, which are required to transmit large thrust loadings to the hull and as a result can suffer from low service lives. Where multiple units are used, their interaction can cause significant hull vibration as well as damage to the pod housings themselves, and thus careful design is essential.

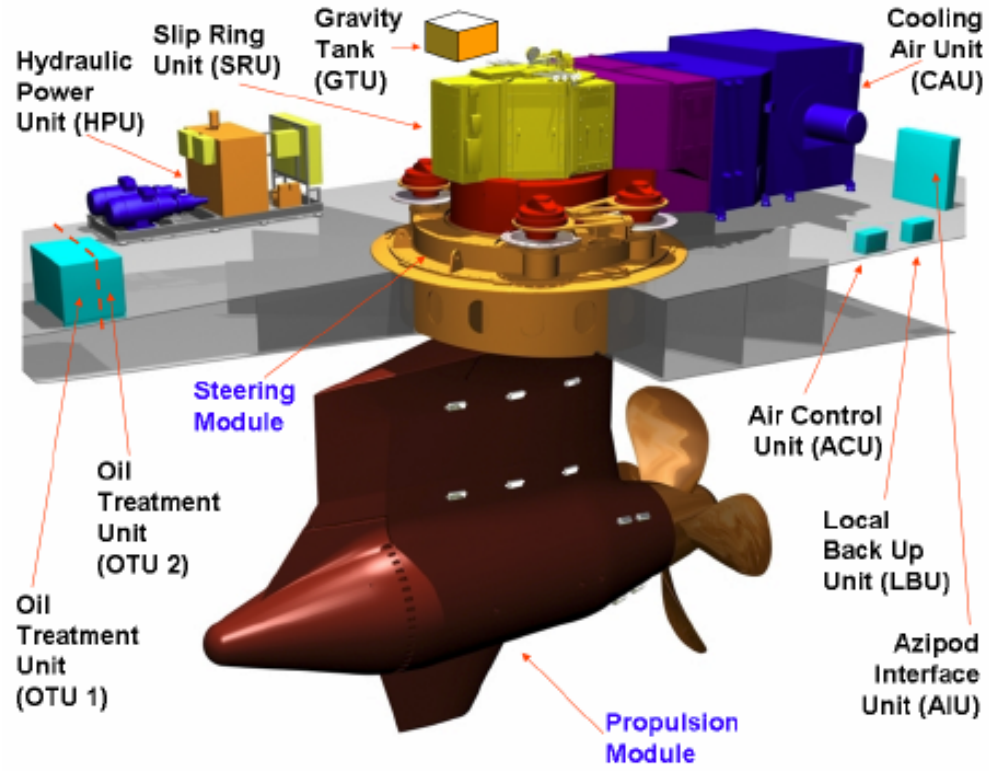

Figure 3.2 – Typical podded drive (ABB VO series) and associated machinery [ABB (2009)]

Contra-rotating propellers

A contra-rotating propeller (CRP) consists of two propellers mounted along the same shaft axis but rotating in opposite directions. One shaft turns inside the other. This system has the advantage of recovering some of the rotational energy lost in the propeller slipstream. The aft propeller is generally smaller to accommodate slipstream contraction, and the two propellers may have a different number of blades so as to avoid inducing large hull vibrations. Improvement in efficiency is of the order of 5-7% [Molland (2009)]. Their mechanical complexity makes them unpopular for use on merchant ships.

A development of the CRP, popularised by Wärtsilä [Levander (2002)] is the CRP-pod concept, which mounts the aft propeller on a podded drive, as presented in Figure 3.3. This removes the complex shafting arrangement and allows the advantages of using a podded drive to be combined with the efficiency gains of a CRP. For a ship with two or more distinct operating conditions, such as is being considered here, this arrangement has the additional advantage of allowing the forward propeller to be feathered when operating at lower speeds without any loss of manoeuvrability. This propulsion layout is popular in fast RoPax designs. RoPax ships have a similar fine form to, and operate at speeds close to the fast feeder concept. Fuel savings of 16% have been quoted by operators using this system, having switched from a twin-screw layout [Levander (2002)]. A disadvantage of this arrangement is the impingement of the forward propeller slipstream onto the pod housing during course-keeping. This could induce significant hull vibration or surface damage.

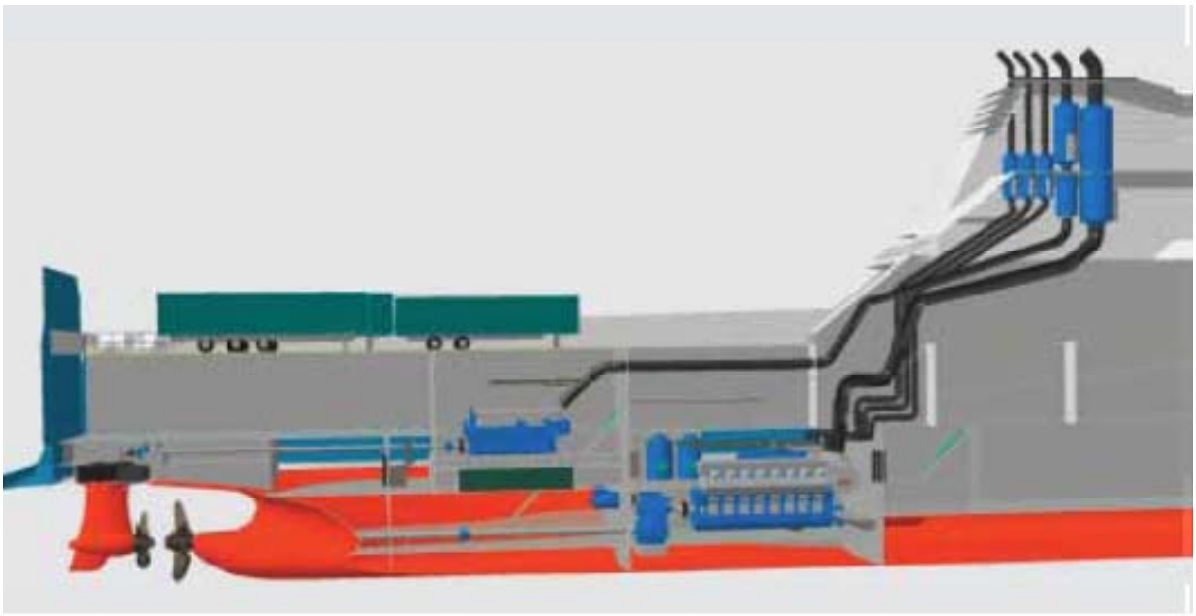

Figure 3.3 – Contra-rotating propeller-pod layout on fast RoPax ship [Levander (2009)]

3.3.2 Plant and fuels

Diesel engines

Diesel engines are the most commonly seen plant in merchant ships. They are generally classed as *low speed* and *medium speed*. Low speed diesels offer the best efficiency in terms of specific fuel consumption (SFC), with values as low as 154 grams per kilowatt-hour [Carlton (2007)], although 165 g.$(kWh)^{-1}$ is a more typical figure [MAN Diesel (2010)]. Power outputs of almost 100 MW are seen from the largest units. These engines are best suited to direct drive arrangements with constant operating speed for much of the voyage to maintain optimal efficiency. Consequently they are not suitable for use with podded drives.

Other disadvantages of low speed diesel engines concern the size and weight of the plant. The dimensions, particularly height, of a typical unit place significant restrictions on layout. In addition, low speeds typically

weigh more than other plant of equivalent power output, and have the further limitation that this weight cannot be re-distributed easily for the purposes of mass distribution calculations. As an example, a typical low speed engine of suitable size for application in this design, the MAN ME-C8, rated at 25 MW [MAN Diesel (2010)] has an overall mass of 820 tonnes and a height of 13 metres. By way of comparison, a medium speed diesel propulsion solution, giving 26.6 MW [Wärtsilä Ship Power Technology (2009a)], weights approximately 450 tonnes and has a maximum height of five metres. Since it consists of four separate units, this solution also provides flexibility in terms of engine room layout and mass distribution.

As well as the cited advantages, medium speed engines would provide considerable redundancy and flexibility in power output to the fast feeder concept. For a ship operating at multiple speeds, demanding vastly varying power requirements, the medium speed engines readily facilitate demands and maintain the efficiency of running at high maximum continuous rating (MCR) by turning unwanted plant off and running with fewer units at normal operating conditions. This would not be possible with a low speed engine where typically only one unit is installed. Medium speed also allows auxiliary load to be handled more easily, without the need for separate generators, and thus lends itself to use in conjunction with electric propulsion power distribution, also allowing a more flexible layout of machinery spaces. The main disadvantage of medium speed diesel engines is their SFC, which is typically 180 g.(kWh)$^{-1}$, or 9% higher than the comparable low speed engine.

Steam Turbine

The steam turbine features low weight and space requirements, as well as low maintenance costs. The freedom to burn a variety of fuels in order to generate steam can be attractive in some cases, such as LNG carriers using boil-off gas from the cargo tanks to fuel the boiler. However, steam turbines have poor SFC when compared to diesel engines, and as such cannot be considered the best option from an emissions standpoint.

Gas Turbine

Gas turbines are popular in naval ships, where sprint ability is important, and cruise ships, which take advantage of the vast space savings possible to incorporate additional cabins. Gas turbines offer high power-to-weight and power-to-volume ratios, typically four times higher than medium speed diesels [Carlton (2007)]. Other advantages are low maintenance, low manning requirements, and lower nitrogen oxide (NO_x) and sulphur oxide (SO_x) emissions, burning marine gas oil (MGO) fuel. If used in conjunction with diesel engines, in a so-called Combined Diesel and Gas (CODAG) arrangement, gas turbines can provide rapid increases in delivered power when required for high speed transit. Since gas turbine efficiencies are low when not run at the design MCR and their power outputs are extremely large, they are switched off for low speed cruising and diesels alone are used. One disadvantage of this system however is the need to carry two fuel types.

It is also noted that operation in regions of high ambient temperature reduces the efficiency of gas turbines, the reverse of which is true for diesel plant. Since the fast feeder concept is to be designed primarily for tropical operation, this factor presents a large disadvantage.

Hydrogen

The idea of using hydrogen fuel in high-speed marine applications is a common one. Veldhuis (2007) proposes a high-speed hydrofoil-assisted feeder container ship powered using modified gas turbines burning hydrogen fuel. A key point is the reduction in mass of hydrogen fuel required, estimated as 2.8 times less compared to normal gas turbine fuel. This allows a significant improvement in transport efficiency for high-speed ships. However, this solution is recommended for power requirements greater than 36 MW, and as such is not considered suitable for this concept, where the ship is classed as ‘fast’ rather than ‘high-speed’.

Fuel cells

Fuel cells use a chemical reaction between hydrogen and oxygen to produce energy, with the main ‘emission’ being water. In the case of the *solid oxide* fuel cell, the fuel used is methane and water. Fuel cells have high

efficiencies compared to engines, with greater than 50% electrical efficiency [Wärtsilä Corporation (2010)]. Despite their potential to drastically reduce emissions, in terms of merchant shipping, fuel cells are still essentially at a prototype stage, with small 20 kW units installed on some ships. Although five MW units are planned [Wärtsilä Corporation (2010)] these are far from being operational and thus current commercially available cells would not even provide adequate auxiliary power for a typical merchant ship. Whether or not fuel cell technology will have matured sufficiently by 2020 to provide significant power is hard to predict, yet it is almost certain that using fuel cells as the sole means of power would entail large volume and weight penalties on ships with large power requirements.

Natural gas

Liquefied natural gas (LNG), the main constituent of which is methane, offers large savings in emissions, particularly sulphur oxides (SO_x) and particulate matter (PM) [Levander (2008a)]. Table 3.8 summarises these benefits compared to Marine Diesel Oil (MDO). The use of a dual-fuel engine, such as the Wärtsilä 50DF [Wärtsilä Ship Power Technology (2009b)] allows LNG fuel to be burnt, and offers much higher efficiency (SFC = 135 $g.kWh^{-1}$) compared to diesel operation, meaning a lower fuel mass is required. Wärtsilä Ship Power Technology (2009b) also claim a 50% increase in the service life of engine components when using LNG instead of MDO. This is a significant advantage in terms of reducing maintenance costs and increasing the service life of the ship.

The main disadvantage of this fuel is its low density, even in liquid form, which doubles the storage volume for an equivalent operational range. Whilst Levander (2008b) advocates the use of such engines on container ships in order to reduce coastal and port emissions, there is no reason to use LNG as the primary fuel, as long as the required storage volume is feasible.

Table 3.8 – Estimated emissions reduction using LNG compared to MDO [Levander (2008a)]

Emission	*Percentage reduction*
CO_2	25-30
NO_x	85
SO_x	100
PM	99

Fuel price makes up a large part of the operational costs of a ship, and with fast ships being particularly sensitive to fluctuations in bunker price, this must be considered at an early stage in the design. Table 3.9 compares the three main fuels under consideration here, including current (2010) bunker prices.

Table 3.9 – Comparison of marine fuels by density, lower heating value and cost [MDO and MGO prices obtained online[6], correct on 23rd March 2010, Singapore; LNG price estimated by Levander (2008b)]

Fuel type	*Density / kgm^{-3}*	*LHV / $MJ.kg^{-1}$*	*LHV / $kWh.kg^{-1}$*	*Cost / $US.ton^{-1}$*	*Cost / $USD.MBtu^{-1}$*
MDO	900	42.7	11.9	643	15.9
MGO	875	42.7	11.9	656	16.1
LNG	410	28.0	7.8	465	10.0

The cost per Metric British unit (MBtu) gives a relative cost per energy content, and shows LNG to be vastly superior to the more common fuels in this respect. Levander (2008b) also notes a downturn in the price of LNG circa January 2008, yet it is naïve to assume that the price of LNG will continue to decrease into the 2020 market. There are many factors that make it hard to predict future fuel prices, such as political relations with oil-producing nations, yet as the drive towards cleaner shipping continues LNG may become more desired and

[6] http://www.bunkerworld.com/prices/

as such, more expensive, before production and bunkering infrastructure can develop sufficiently to accommodate demand. Whilst it is vastly beyond the scope of this report to investigate future trends in fuel prices, it is assumed that LNG fuel will be commonplace in the marine industry in 2020, and thus a viable option. In addition, any economic calculations involving fuel prices will use current figures for simplicity.

Electric propulsion

Electric propulsion uses main engines to drive generators that provide electrical power where required on the ship through a distribution system. This is particularly useful on ships with large hotel loads, such as cruise ships, and those powered by podded drives, where power is transmitted to a motor in the pod housing. Such propulsion systems are often referred to as diesel-electric, or DF-electric, where dual-fuel main engines are used. Since there is no mechanical connection between main engine(s) and propulsor, the designer has flexibility in terms of the location and layout of the propulsion machinery, which can improve the cargo capacity of the ship. It should be noted that efficiency gains from running the main engines at constant rating are offset by losses in the electrical distribution system. Wärtsilä Corporation (2009a) claim potential reductions in fuel consumption of between 5-8% in addition to a reduction in installed power of 10% owing to more efficient load distribution throughout operation.

An example of a complete propulsion system utilising a number of the technologies discussed in this section is illustrated in Figure 3.4.

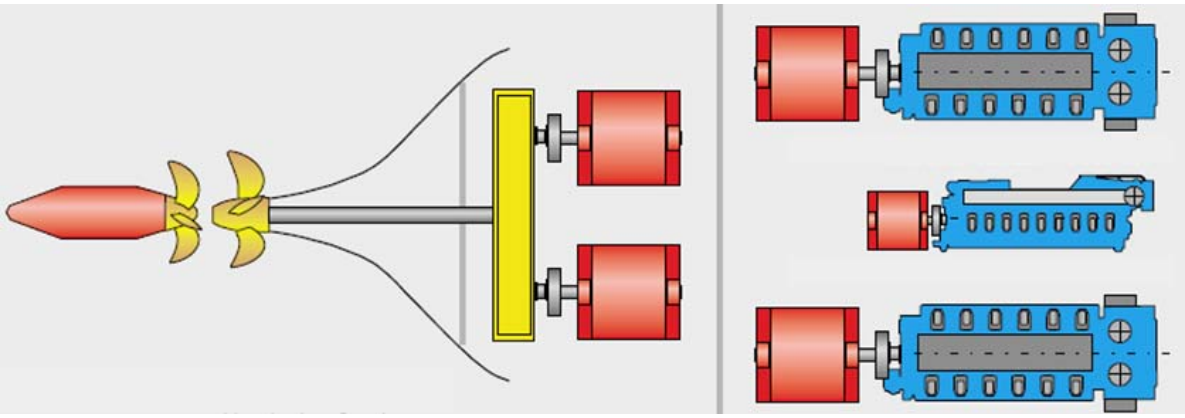

Figure 3.4 – Example LNG-electric Contra-rotating propeller-pod propulsion system arrangement: plant are shown in blue with generators and motors in red [Levander (2002)]

Summary

Considering all the propulsor and plant options discussed here, the main driver in selecting an appropriate solution is the need to maximise efficiency at both service and sailing speeds and reduce emissions levels. The most efficient propulsion system for this ship is thus a podded drive or CRP-pod arrangement, which has the added advantage of providing high levels of manoeuvrability and layout flexibility through the use of an electric power distribution system. If this system were combined with plant burning LNG fuel, it is anticipated that the 'emissions deficit' presented in Table 2.9 can be easily recovered, based on the values given in Table 3.8. This is before any other form of emissions reduction or improvement in efficiency has been made.

4. Hydrodynamic Design Development

4.1 Hull form design

The hull form development must fulfil the operational requirements of the shipping routes selected whilst being economically and environmentally efficient. Fortunately, on a fundamental level, these requirements complement one another; if a ship is efficient in terms of reducing operational costs by reducing fuel consumption then it must be said that this will also reduce the operational environmental impact. Ultimately the overall efficiency is considered to be a combination of the efficiencies of the hull form hydrodynamics and the propulsion system, which are of course interdependent.

To increase the comprehension of this study two hull forms are to be developed to house different propulsion system designs. The first (*Hull A*) is designed for a contra rotating CPP azimuthing pod combination. The second design (*Hull B*) is developed to accommodate twin azimuthing podded propulsors. These propulsion options have been selected as a result of an initial evaluation of propulsion and machinery options (see Section 3.3). It is expected that these two concepts will perform best in terms of efficiency and operational flexibility. One would expect the hydrodynamic performance of these two hulls to be somewhat different, as a result of the significantly different 'standard' stern forms needed to house the relevant propulsors. This highlights the need to assess the overall efficiency of both the hull and propulsor.

4.1.1 Design for hydrodynamic performance

This section outlines the design of *Hull A* and *Hull B* to optimise hydrodynamic efficiency and to provide a performance prediction for each form. The hull forms are optimised to reduce the hydrodynamic drag in calm water, aiming to minimise the energy demand to attain the operational speed of 25 knots. The proportion of time a ship spends operating in calm water is of course minimal. Thus, the performance in waves is an important consideration. Optimising a ship for added resistance in waves is much more complex and numerical methods are only useful when supported by model tests. Both of the forms will be analysed to assess performance in waves in Sections 4.4.3 and 7.1.3.

It is important to carry out hull form design early in the project as most subsequent design stages are dependent on the finalisation of the ship lines. One must however be confident in the design in terms of creating something that is 'optimal' as it is difficult to make subsequent changes to the lines. In terms of economics, design decisions made in the first few weeks of the project account for 70% to 80% of the costs associated with the design [Harries (2006)]. It is therefore important to have confidence in the procedures and methods applied at this stage of the project. Whilst this section focuses on hydrodynamic performance it is important to consider other implications of the optimisation. The preferred design solution to improve hydrodynamics is to obtain an optimum form that neither requires additional production costs nor entails any operational complications [Harries *et al.* (2006)].

Hydrodynamic optimisation is not trivial by any means. Harries *et al.* (2006) states 'to realise a 1% increase in speed one needs to lower the total resistance by around 4% to 5%, provided propulsive efficiency is constant'. This level of resistance reduction is significant, especially at the early stage of a concept design when extensive time cannot be spared for detailed hull hydrodynamic analysis. Note that with regards to this concept the aim is to reduce the power requirement not increase the speed, the benefits are equivalent.

The primary source for the estimation of the calm water resistance is the Holtrop regression [Holtrop & Mennen (1982) and Holtrop (1984)]. This is a regression method based on 334 ship model experiments, carried out at *MARIN* in the Netherlands, and results from sea trials. The hull forms tested in these instances are not vastly dissimilar to the fast feeder ship forms. Hence this regression provides realistic estimates of the naked

hull resistance for each design. This is contrary to others' expectations who comment that such regression analyses they are 'outdated' and thus found to underestimate the resistance of modern ships [Bertram (2000)]. The Holtrop regression is however the best method available; allowing comparison of hull form designs. Ultimately the final values of resistance will be determined from the model tests presented in Section 4.4.

4.1.2 *Hull A* basis hull form

Although the propulsion system utilised with this design is somewhat unique there are not that many differences with other fast container ship hull forms. Therefore a 'library' hull form of a larger container ship has been used as a starting point. This hull form has been scaled to match the required dimensions specified in Section 3.2. The fullness of the hull form is adjusted and the draught calculated, with restrictions in mind, to give the required displacement and block coefficient C_B. The 'Hogner' stern form has been modified to ensure there is enough space available for the propulsion system and the associated controls. The bow form, including bulbous bow, have at this stage been left to resemble the 'library' hull. Initially the mid body has been designed to maximise the amount of parallel mid body, to attain the required displacement, and so to increase the cargo capacity. The cargo delimitation on a container ship is discrete and thus a small change in hull dimensions can result in large changes to the cargo capacity.

The resistance was evaluated and found to be much larger than expected from initial estimates, almost twice the expected value. This drastic increase in resistance would mean that the ship would not be economically viable to operate. It was clear that the ship could not operate efficiently with this level of parallel mid body at 25 knots. In particular, the prismatic coefficient was observed as being very large, this is defined as $C_p = \nabla / L_{WL} A_M$. Increasing C_p increases the resistance of a hull form and it is expected that as Froude number increases C_p should decrease [Schneekluth & Bertram (1987)]. As the maximum sectional area A_M is fixed by the preliminary dimensions and the waterline length L_{WL} cannot change significantly it must be the displacement ∇ that is changed. The displacement must hence be reduced slightly by reducing the length of the parallel mid body. Hence the entrance and run increase. These modifications reduce C_P from 0.765 to 0.620. This is consistent inline with the recommendations of Comstock (1967) (Figure 56 p345) at this Froude number. The result of this is a reduction in resistance to a value comparable to basis ships (see Section 3.1). This inevitably leads to a lower cargo carrying capacity. The hull form changes have been accommodated so as not to lose a whole row of containers. The loss in displacement is 992 tonnes, which equates to 100 TEU. This cargo capacity reduction still leaves the design within the limits for economic operation.

It is possible to equate this change in hull form shape to changes in block coefficient C_B rather than C_P. This is arbitrary however and the author feels the point is better illustrated in terms of C_P. A decrease in volume has the same effect on the frictional resistance by reducing the wetted surface area. Aside from this the ship is becoming more slender in the entrance and the run and hence the disturbance of the free surface is reduced. Physically, due to a reduction in the flow pressure, the wave pattern resistance is reduced. Prior to the C_P reduction the parallel mid body was large and hence there was a large gradient between the stem/stern and the mid body resulting in high pressure in these areas. This constitutes a large wave pattern resistance. When the mid body length was decreased this gradient reduced significantly, hence lowering the wave pattern and overall resistance. In addition the waterline length L_{WL} has been increased by around two metres. This will of course increase the friction resistance, but this is far outweighed by the reduction in the wave pattern resistance. This can also be attributed to a lower value of C_P. The increase in L_{WL} has been achieved by adjusting the stem and stern profiles, thus bringing L_{WL} closer to L_{BP}.

When optimising the hull form at constant displacement one considers the effect of moving the longitudinal centre of buoyancy (LCB), hence adjusting the distribution of the displacement volume. Schneekluth & Bertram (1987) state that the optimal position of the LCB is a function of Fn and C_B, and provides an estimation

procedure. However for reduced resistance the longitudinal centre of gravity (LCG) must coincide with the LCB to facilitate level keel operation. The position of the LCB often needs to be a compromise between the hydrodynamic optimum position and coincide with the mass distribution dependant LCG. Figure 4.1 illustrates how the optimum LCB varies with C_B.

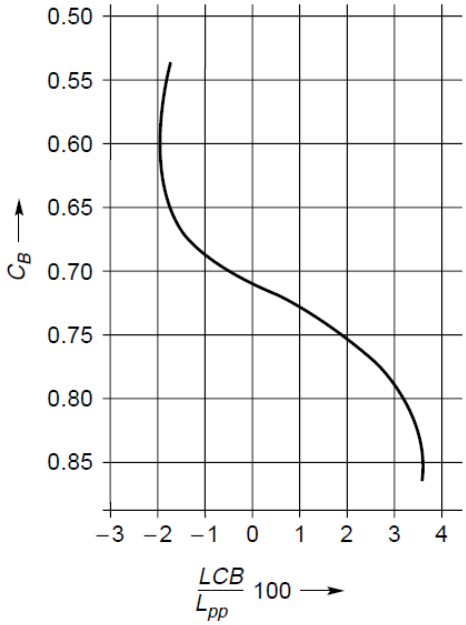

Figure 4.1 – Variation of optimum LCB with C_B, Schneekluth & Bertram (1987)

The block coefficient for the basis hull is $C_B = 0.547$; this equates approximately to $LCB = -2.88$ metres from amidships. On observation of the LCB value in Table 4.3 it can be seen that this value is closer to amidships. The LCB has been moved forward from the 'optimal' location to accommodate the ship's unconventional layout. Ultimately, having superstructure and large generators positioned forward, the LCG will be located further forward than in a conventional container ship. With the position of LCB nearer to amidships it should be possible to adjust the mass distribution so the LCG coincides with this point and thus the ship can operate on an even keel. The final position of LCB presented in Table 4.3 is not random but a consequence of fine tuning the displacement distribution. It is common practice to design the sectional area curve to be smooth except for one inflection between the forward perpendicular and the stem [Harries *et al.* (2006)], to generate a hull that exhibits good resistance characteristics. Final adjustments to the hull form have been made to achieve this and Figure 4.2 exhibits this with inflections at the forward and aft end. This illustrates a rapid change in sectional area in these regions.

Design considerations other than hydrodynamic optimisation have been made. The accommodation block is to be located forward to improve aerodynamics, cargo stowage efficiency and line of sight. The bow has sufficient flare to produce a deck area consistent with housing the required superstructure. Whilst increased flare could result in heavy slamming the additional buoyancy will act to reduce the amplitude of the pitch motions, which is important given most of the working spaces are located at the forward end. A seakeeping analysis of the design is provided in Section 7.1.

4.1.3 *Hull B* basis hull form

The form for *Hull B* was developed from the C_P optimised version of *Hull A*, to maintain a basis of comparison. The only notable design difference is the selected propulsion method, so the aim was to optimise the form for use with twin azipods. In practice, this meant that the optimisation effort was focused on the aft form.

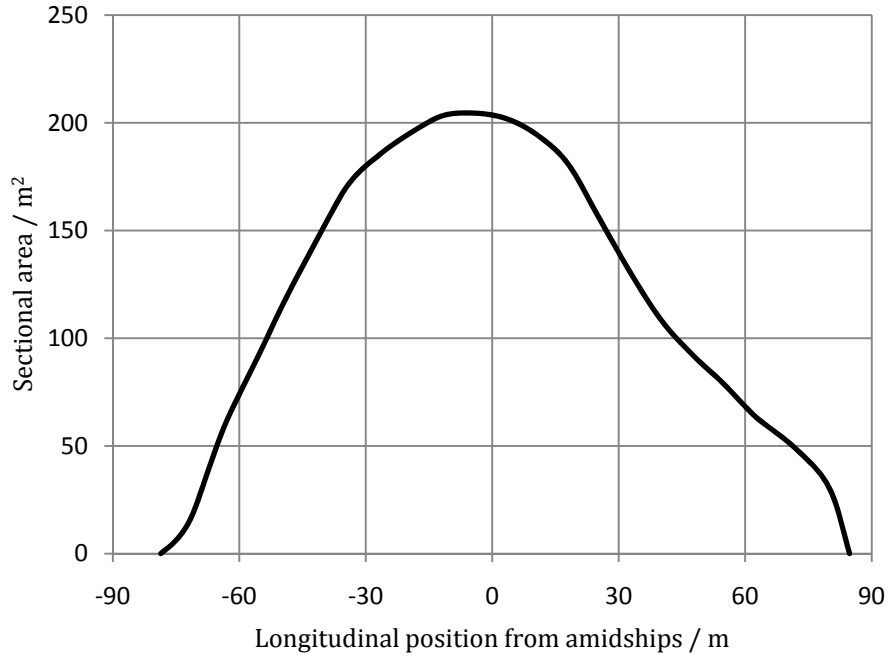

Figure 4.2 – *Hull A* basis sectional area curve

Given the draught restriction (Section 3.2) the pods were to be mounted relatively high above the baseline. This, coupled with a desire to maximise pod efficiency, (Section 3.3.1) by allowing them to operate in clean flow outside of the turbulent wake required a gradual rise of stern aft of amidships. The computational time available for the analysis was limited by model production considerations, so the design process was driven by a simple minimum resistance optimisation. This would be carried out through use of the Australian freeware packages *Michlet* and *Godzilla*.

Software

Michlet [Cyberiad (2009)] provides the user with predictions of the hull form wave resistance by applying Michell's thin ship theory based wave resistance integral from a user defined hull underwater form. The method cited was implemented by Tuck *et al.* (1999). Tuck & Lazaukas (2008) have demonstrated that it remains a good general indicator of wave resistance trends, correlating with experimental and CFD results, so it was felt that it would be a reasonable indicator of hull performance. Estimates of total resistance are obtained by use of ITTC '57 correlation line and a user-input viscous form factor.

The freeware package is supplied with an integral genetic algorithm add-on, *Godzilla*. An explanation of the search methodology employed is provided by Tuck & Lazaukas (1996).

Methodology

The practical application of the software requires definition of the underwater form of the basis hull. Since re-entrant sections at bow and stern could not be modelled, the match was based on maximum waterline dimensions, form coefficients and the underwater midship section.

Once satisfied with this initial form, the optimisation procedure was constrained with regards to overall dimensions and form parameters (see Table 4.1) and the parametric definition of the forward form was effectively fixed. While some particulars such as C_M were very tightly constrained to maintain compatibility with the forward form, others such as LCB and S were relatively loosely fixed, so as to give the best possible freedom to the optimisation. The principal dimensions were allowed to vary slightly to permit a broad population range. The optimisation algorithm was then run with the objective of minimising total resistance at speeds of 25 and 15 knots.

Table 4.1 – Basis estimates and *Godzilla* optimisation constraints on principal particulars

Particulars and constraints					*Seed value*
155	≤	L / m	≤	160	(157.0)
25.6	≤	B / m	≤	25.8	(25.7)
8.75	≤	T / m	≤	9.0	(8.94)
0.54	≤	C_B	≤	0.57	(0.554)
0.58	≤	C_P	≤	0.67	(0.620)
-4	≤	LCB (% L from midships)	≤	0	(-2.0)
4000	≤	S / m^2	≤	5000	(4679)

Results

The aft-body plan of the optimised form from *Godzilla* as compared to the basis approximation and the improvement in wave resistance demonstrated are shown in Figure 4.3. It must be stressed at this point that the resistance comparison is for comparative and qualitative purposes only and is intended to be indicative of the optimising trend, not of the performance of the final *Hull B* or of any quantitative decrease, especially in the speed region above 20 knots.

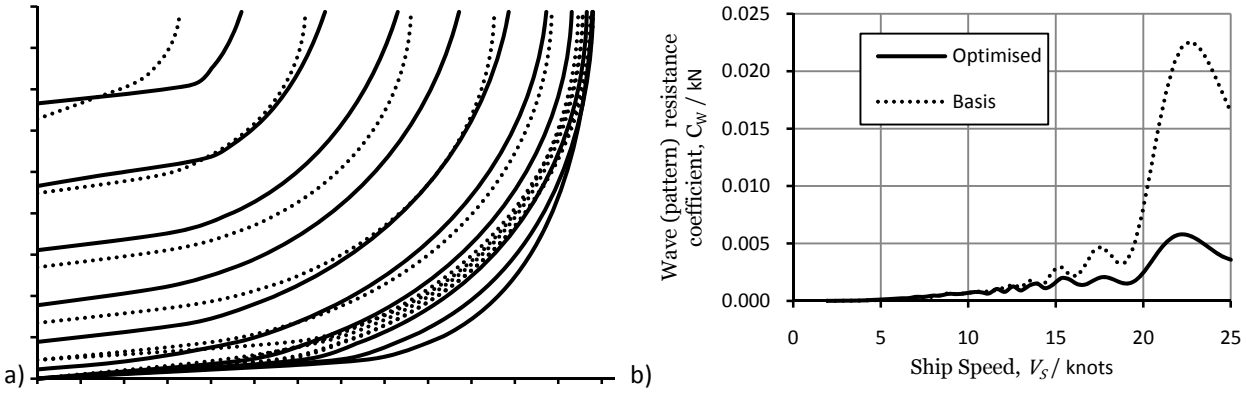

Figure 4.3 –Body plans for the aft sections of *Hull B*, *Michlet* basis and *Godzilla* optimised (left); and variation in wave resistance coefficient C_W with ship speed (right)

4.1.4 Bulbous bow optimisation

Now that basis hulls have been developed to exhibit good resistance characteristics one can focus on the optimisation of these designs. Comstock (1967) (Table 18, p.346) states that for ships operating at the selected Froude number a bulbous bow is beneficial. Bulb design is ship dependant and is not trivial, as a badly designed bulb will increase resistance. Unfortunately it is impossible to associate standard design 'guidelines' for a bulbous bow. To select bulbs for the basis forms developed in Sections 4.1.2 and 4.1.3 an optimisation process was implemented to generate bulbs that lead to increased hydrodynamic efficiency.

In accordance with Harries *et al.* (2006), a parent bulb was developed. However, the bulb design has not yet been considered and so instead of comparing to one baseline hull the two hull forms with a number of bulb options are to be compared with one another. It is important to note that it is only the bulbous bow that is being optimised. The mid body has already been designed to reduce resistance as far as possible, subject to required cargo capacity, and the stern forms are optimised to exhibit good flow characteristic into the propulsors. Thus the optimisation was limited to the bulb as significant savings can be made with little effect on the hydrostatics. Kracht (1978) suggests that there are no significant adverse effects of a bulbous bow in

terms of motions and added resistance in waves below Beaufort eight wind, so the bulb was optimised for calm water resistance.

A bulbous bow reduces the wave pattern and wave breaking resistance. For fast slender ships the main reduction is in the wave pattern resistance [Hoyle *et al.* (1986)] due to interference effects, as the wave resistance constitutes a large proportion of the total resistance. The bulb must create a cancellation effect between the wave systems created by the bulb and hull. A ship moving through a free surface creates two wave systems attributed to two high pressure locations in the flow around the hull, at the bow and stern. The purpose of the bulb is to modify the location and magnitude of the high pressure at the bow. The longitudinal position of the bulb is a measure of the phasing between to two wave systems. The size of the bulb is related to the amplitude of the waves generated at the bow [Kracht (1978)]. Unfortunately it is only practically possible to optimise a bulb for one speed. Complete cancellation of wave peaks and troughs from the two systems can be achieved with the correct phasing of the bow and stern wave systems. In reality complete cancellation is unlikely, and in attempting this one may have to create a large bow wave system that will create significant drag before cancellation effects take hold. Hence for cancellation the wave system generated at the stern must already be reasonably small.

Wave breaking resistance is much more difficult to quantify. However, its occurrence is apparent. It is broadly associated with waves created by the ship breaking and spray from these waves resulting in a net energy loss downstream that must be attributed to a resistance component. The only way to reduce this component, in terms of bulb design, is to ensure that the bow waves are not steep enough to break [Kracht (1978)]. The introduction of a bulb on a ship increases the frictional resistance due to the increased wetted surface area. However, it is expected that this will be small compared to the reduction in wave resistance, especially for a fast ship. A bulb does not, in general, affect course stability or manoeuvrability and is the ideal place to locate bow thrusters [Kyriazis (1996)].

Fifteen bulb combinations of varying dimensions, as defined in Table 4.2, which have been analysed. The dimensions have been chosen to cover the range that is practically achievable in terms of construction and operation and based on proportions that have been observed on basis ships. Figure 4.4 describes how the dimensions are defined.

Table 4.2 – Topology of bulb variants

Bulb variant	$\frac{L_B}{L_{BP}} / \%$	L_B / m	$\frac{B_B}{B} / \%$	B_B / m
1	4.5	7.168	25.6	6.712
2	4.5	7.168	21.4	5.600
3	4.5	7.168	18.3	4.800
4	3.9	6.253	25.6	6.712
5	3.9	6.253	21.4	5.600
6	3.9	6.253	18.3	4.800
7	2.9	4.689	25.6	6.712
8	2.9	4.689	21.4	5.600
9	2.9	4.689	18.3	4.800
10	2.0	3.126	25.6	6.712
11	2.0	3.126	21.4	5.600
12	2.0	3.126	18.3	4.800
13	1.0	1.563	25.6	6.712
14	1.0	1.563	21.4	5.600
15	1.0	1.563	18.3	4.800

By studying different bulb lengths and breadths it will be possible to assess when the interference relationship between the wave systems is destructive. This allows for the most suitable bulb for each of the hull forms to be selected. Since the bulb design is specific to a particular ship design the optimal bulb will not be the same for both *Hull A* and *Hull B*. The bulb dimensions have been defined based on a method presented by Kracht (1978) where the length of the bulb L_B is non-dimensionalised with respect to L_{BP} and the bulb breadth B_B with respect to B (Table 4.2). The bulb depth is constant and always below the waterline.

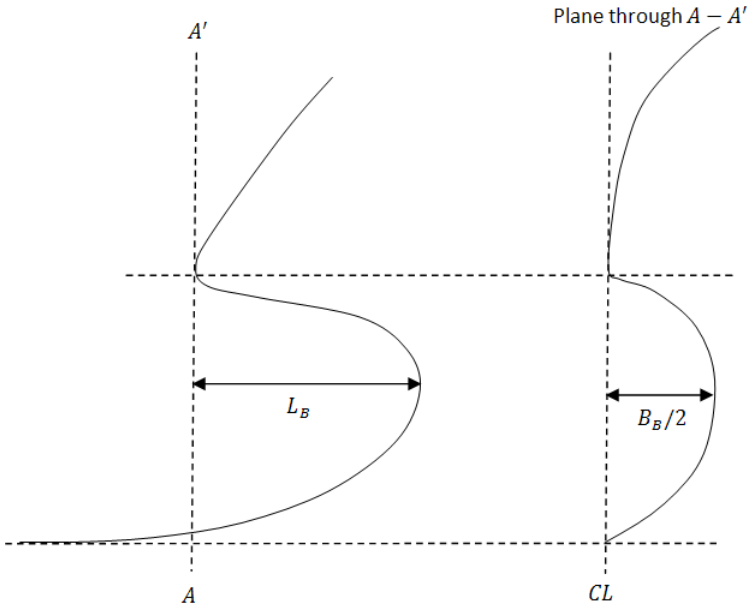

Figure 4.4 – Schematic showing bulbous bow dimension definitions

The bulb cross sections fit into a category termed 'nabla' type by Kracht (1978). This type of bulb has its centre of volume toward the top of the bulb giving favourable seakeeping characteristics, it is for this reason that this is the most common type of bulb and why it has been chosen for development in this concept. In previous studies, Percival *et al.* (2001), Kyriazis (1996), Hoyle *et al.* (1986) and Kracht (1978) have all drawn significant benefits from using 'nabla' type bulbs and so it seems reasonable to develop 'nabla' bulbs for the two basis hull forms.

4.1.5 Results

The Holtrop regression series is used to analyse the calm water resistance of the two hull forms for each of the 15 bulb combinations. This regression analysis is implemented through the software package *Hullspeed*, part of the *Formation Systems* design suite. *Hullspeed* takes the 3D NURBS surface from *Maxsurf* and calculates the particulars of the ship required to carry out the regression. In terms of the bulb definition the Holtrop regression series uses the transverse bulb area and the bulb depth from the keel. Implementing the regression series requires the application of many equations to determine the coefficients of resistance. On implementing this for all 30 hull form variants the results may be represented in terms of the total resistance coefficient. Figure 4.5 presents C_{TS} for each hull for an operating speed of 25 knots.

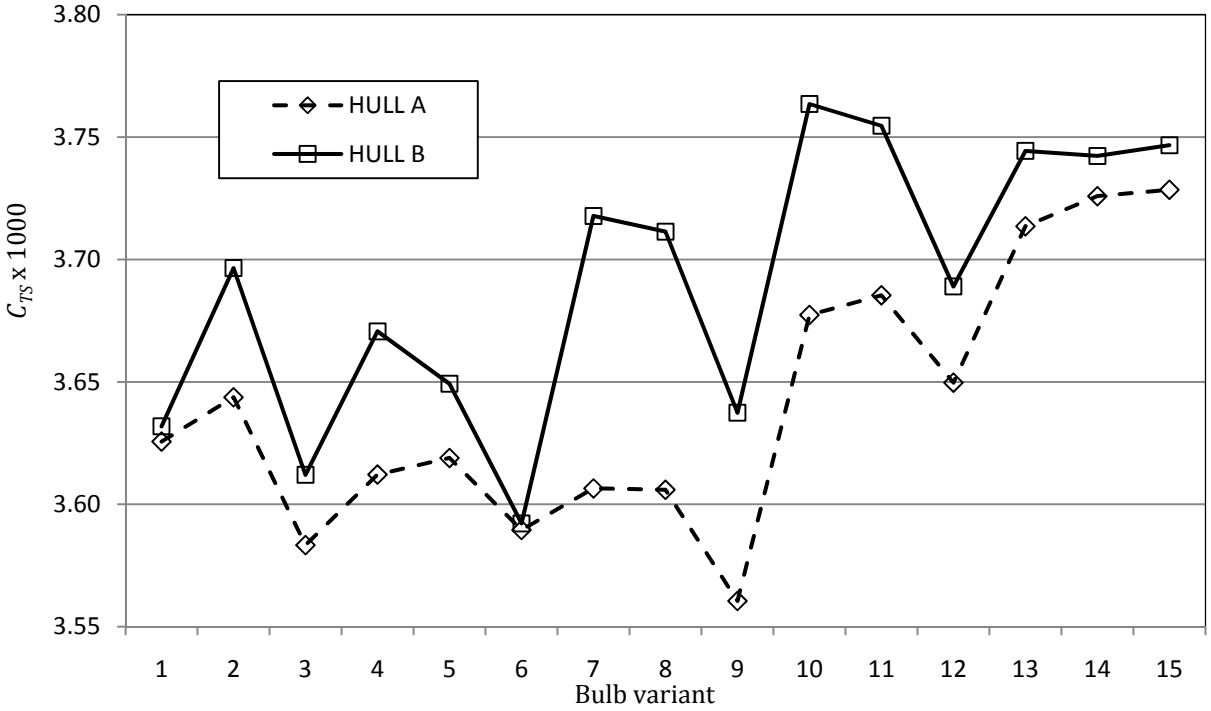

Figure 4.5 – Variation of C_T at 25 knots for all bulb variants

Caution is required when comparing dimensionless resistance. In particular we note that resistance is non-dimensionalised with respect to wetted surface area. The variation in bulb dimensions means the wetted area is not constant which will affect the frictional resistance. Fortunately the area fluctuation in all of these cases is small and presentation of the total resistance, instead of the total resistance coefficient, indicates the same trend as observed in Figure 4.5. Full details of the variation in C_{TS} over a range of speeds for each variant are given in Table B.1 and Table B.2. The variation of C_{TS} essentially represents the variation of C_W as the frictional C_{FS} (and viscous C_{VS}) is almost constant. This is due to the implementation of the ITTC'57 correlation lines to estimate C_{FS}. Hence one can deduce that variation of the resistance at the design speed is due to changes in wave pattern resistance.

Figure 4.5 shows that the optimal bulb variant for *Hull A* is number 9 and for *Hull B* is number 6. Figure 4.5 also indicates that bulbs 3, 6, 9 and 12 for which $B_B = 4.80\ m$, have a low resistance compared to other bulb variants of the same length. This suggests that these bulbs are leading to destructive interference and reductions in the wave pattern. From these bulbs the optimum for each hull is decided by the phasing they introduce between the bow and stern wave systems. *Hull A* is optimal for a shorter bulb ($L_B = 4.689\ m$) than *Hull B* ($L_B = 6.253\ m$). This is a function of the distances between the sources and the wavelength generated by those sources.

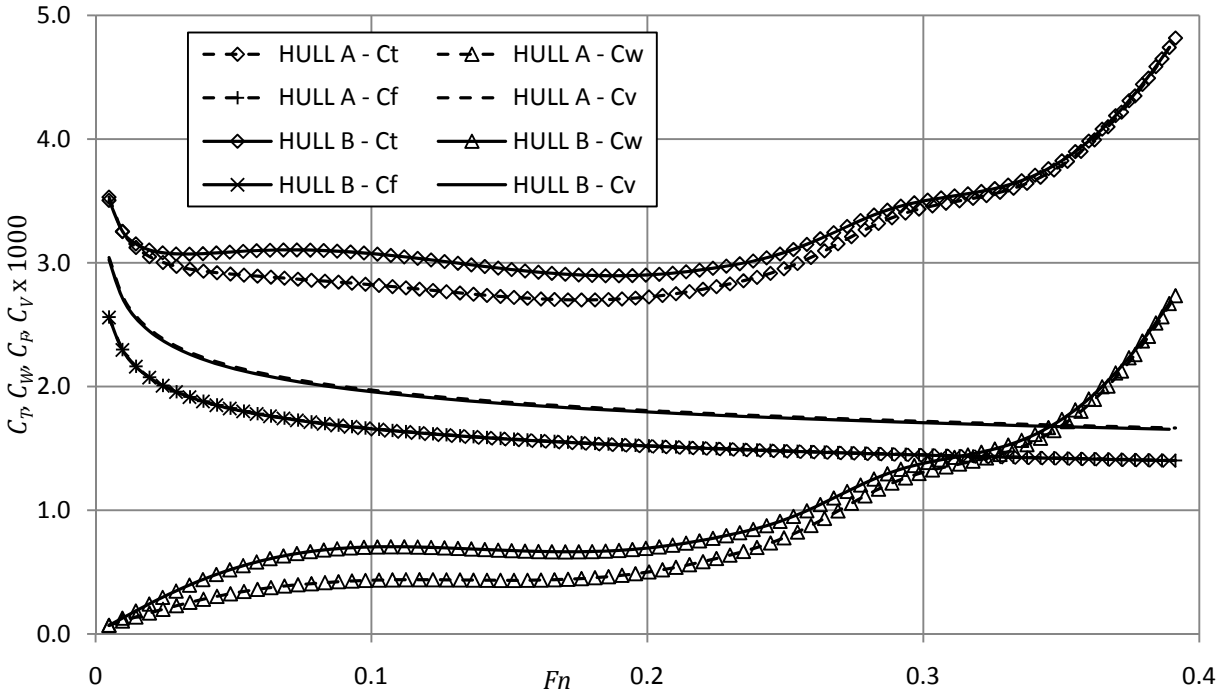

Figure 4.6 – Breakdown of resistance components as a function of Fn for both *Hull A* and *Hull B*

Figure 4.6 presents the breakdown of the resistance into its components. The Holtrop regression essentially determines the total resistance using

$$C_T = C_W + C_V + C_A = C_W + C_F(1+k) + C_A\,. \tag{4.1}$$

The where the frictional coefficient is determined using the ITTC'57 correlation line

$$C_F = \frac{0.075}{(log_{10}Re - 2)^2}\,. \tag{4.2}$$

The form factors $(1+k)$, determined in the regression analysis, equal 1.1878 for *Hull A* and 1.1819 for *Hull B*. The coefficient of wave making resistance C_W and the correlation allowance C_A are also determined in the regression analysis. The correlation allowance represents the differences in full scale results from towing tank measurements and sea trials. For *Hull A* $C_A = 0.416694$ and for *Hull B* $C_A = 0.414195$.

From Holtrop & Mennen (1982) there are two additional resistance terms, accounting for the additional pressure resulting from the bulbous bow and an immersed transom. In this case they are both zero.

As already observed from the bulb optimisation *Hull A* has a lower total resistance coefficient. Having studied the lines plans, this is surprising. As *Hull B* would be expected to have a lower naked hull resistance. It is only when the dimensional form of the resistance is plotted, Figure 4.7, that the lower naked hull resistance of *Hull B* is observable above 20 knots of advance. Reverting to Table 4.3, one notes that *Hull A* does have a larger wetted surface and the slight differences in L_{WL} mean that each design will not have identical ship speeds at identical Froude number. Hence this will cause some shifting of the coefficient of resistance curves in Figure 4.6. Full details of the coefficient breakdown and effective power of both hulls is given in Table B.3.

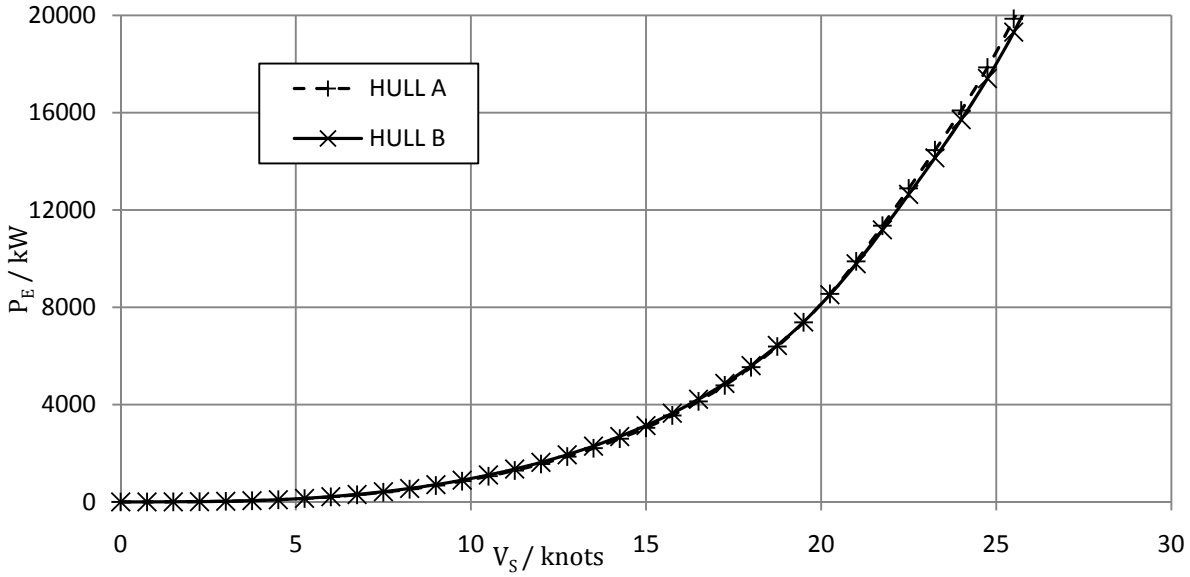

Figure 4.7 – Effective power against ship speed for *Hull A* and *Hull B*

In addition to using the Holtrop regression, the wavemaking resistance was determined using Thin Ship theory [Michell (1898)] via *Hullspeed*. Thin Ship theory vastly overestimated the total resistance, although the slenderness and Fn are within the claimed ranges of applicability [Formation Design Systems (2005a)].

Figure B.1 shows a comparison of the results from the regression and Thin Ship theory. There is good correlation at low speed. This is likely due to the fact that the wave pattern resistance is negligible. There is increasing disagreement with higher Fn, where the Thin Ship Theory results should become more realistic. Due to poor representation at the operating Fn the results from Thin Ship Theory have been neglected.

The lines plans for the optimised *Hull A* and *Hull B* are presented in Appendices B.3 and B.4 respectively. The principal particulars and hydrostatics are presented in Table 4.3. The power prediction allows other aspects of the design to progress including the design of models for towing tank testing (Section 4.2), which are used to verify the calculated resistance results.

Table 4.3 – Summary of principal particulars and hydrostatics

	Hull A	*Hull B*
L_{OA} / m	170.7	170.7
L_{BP} / m	160.09	160.09
B / m	26.2	26.2
D / m	18.97	18.97
T / m	8.94	8.72
$\Delta / tonne$	20466	20344
∇ / m^3	19966.88	19847.58
L_{WL} / m	158.47	160.301
S / m^2	4847.188	4633.287
A_M / m^2	203.315	203.335
A_W / m^2	3224.507	3113.071
C_P	0.62	0.609
C_B	0.547	0.55
$LCB\ (amidships) / m$	0.604	-0.893
$LCF\ (amidships) / m$	5.833	-4.214
KB / m	5.213	5.082
BM_T / m	7.236	6.533
BM_L / m	242.742	233.462
$TPC / tonne/cm$	33.051	31.909
$MCT / tonne.m$	316.98	303.126

4.2 Towing tank model design and manufacture

4.2.1 Introduction

Model tests were carried out in order to support the existing design work, and validate numerical predictions of hull form resistance and added resistance in waves. In addition, tests were undertaken to assess sail-hull interaction and allow comparison of the sailing performance of each hull form, which cannot be so readily achieved using the numerical resistance prediction methods. In order to guide the design, manufacture and testing of the models, ITTC recommended procedures were followed as closely as possible, to improve confidence in the test results.

The facility available for conducting the tests was the Southampton Solent University (SSU) Towing Tank, the principal dimensions and capabilities are summarised in Table 4.4.

Table 4.4 – Summary of Southampton Solent University Towing Tank facility

Dimension	*Value*
Length / m	60.0
Breadth / m	3.7
Depth / m	1.85
Max. carriage speed / ms^{-1}	4.5
Frequency range of wavemaker / Hz	0.25 – 2.00

4.2.2 Model design

Choice of scale

There are a number of considerations to be made in selecting an appropriate scale for a ship model. Maximising model size is important in order to reduce the percentage experimental error and give more accurate results when using resistance scaling techniques. However practical restrictions are imposed by:

- The size of the tank: breadth is most important in this case to avoid tank wall interference when testing in waves. Depth is less important since the Froude number (Fn) is likely to be low. This is confirmed by the fact that the depth Froude number (Fn_D) only becomes critical for a model length of 17.38 metres, as calculated in Appendix C;
- The maximum carriage speed: due to Froude scaling, the required model-scale speed increases with model size, and this must stay below the safe operating limit of the carriage;
- Budget constraints: the choice, quantity and price of material all have to be considered within any financial limitations;
- Manufacturing capability: The tools and expertise available to the designer must be taken in account.

ITTC (2005b) provide a function to ensure that, when testing in waves, tank wall interference does not occur. This requires consideration of the likely wavelengths to be tested, which are normally taken as a percentage of the ship length, and therefore unknown. The process adopted was to:

- Assume a scale factor and model length from the full scale particulars;
- Calculate the upper limit of wave frequency that will cause tank wall interference;
- Simultaneously calculate the required wavemaker wave frequencies and check that they lie above the established limit; and within the capabilities of the wavemaker itself;
- Calculate the required carriage speed for the highest Froude number to be tested and check against the maximum carriage speed.

Following this approach, assuming the wavelengths of 50, 100, 150 and 200 % of the model length, the maximum model size that can be tested has a waterline length of six metres, corresponding to a carriage speed of approximately 2.5 metres per second. Whilst this gives an agreeable scale factor of 26.4, the model displacement would be of the order of 1.1 tonnes, which is simply not practical, and would make handling and transportation difficult.

To reduce the size of the models, attention was shifted towards material selection and manufacturing process. The University's Engineering Design and Manufacturing Centre (EDMC) was approached to carry out the work, since labour cost was not charged directly to the project, and the location made communication easier. Based on previous experience, it was recommended that the hulls be manufactured using high density foam (HDF) cut on a Computer-Numerically Controlled (CNC) milling machine. This was considered cheaper and less labour intensive than the proposed alternative, using fibre-reinforced plastic (FRP), and could offer a higher quality surface finish. These two manufacturing methods are recommended by ITTC (2002), who also suggest wax and wood as potential construction materials. These had however been discounted since the former would be too heavy, and the later too hard to construct in areas of high hull curvature such as at the bulbous bow.

Having chosen HDF as the construction material, the main limitation was the size of the material block that the CNC milling machine could accommodate. This was limited to 1.25 metres in length, and thus it was decided that the overall length of both models must fit within two foam blocks of 1.25 metre length, so as to reduce the total cost and machining time. Allowing 50 millimetres of waste material at either end of the block for the machining head to manoeuvre, the overall length (L_{OA}) of the models was restricted to 2.3 metres. Using this limit, a scale factor of 1:75 between ship and model scale was derived. Details of the two models are summarised in Table 4.5.

Table 4.5 – Summary of model scale hulls at design speed

	Hull A	*Hull B*
L_{BP} / m	2.113	2.127
B_{WL} / m	0.344	0.344
T / m	0.119	0.116
Δ/kg	48.5	48.2
Fn @ 25 knots	0.326	0.324
V_M/ ms^{-1}	1.484	1.483

Using the recommended supplier, *Homeblown,* the cost of foam required was estimated along with additional materials. This is included as part of the budget summary in Appendix N The total estimated cost of materials for the two towing tank models was £1045.45. Note that in order to save costs, 120 kg/m^3 density foam was specified for the aft sections, while 200 kg/m^3 density foam was used for the bow sections where the detail of the hull forms was more intricate, because of the bulbous bow.

Mass distribution for tests in waves

In order to obtain accurate results of added resistance when testing in waves, the pitch gyradius (k_{xx}) had to be modelled to represent that expected on the full-scale ship. As recommended by ITTC (2005b), k_{xx} was estimated as 0.25 $L_{BP}$and the necessary mass distribution calculated using :

$$k_{xx} = \frac{\sum m_i({x_i}^2 + {z_i}^2)}{\Delta}, \tag{4.3}$$

where m_i is the component mass, and x_i and z_i are the longitudinal and vertical centroids of m_i. This requirement also had to be balanced against the need to achieve the correct trim. The process was carried out for *Hull A* only, assuming *Hull B* to be similar, using a spreadsheet. The foam cross-section was assumed solid at bow and stern in order to retain strength in these finer regions of the hull form, whilst the mid-body was designed to be hollowed out to save weight and allow more flexibility in the positioning of the ballasting weights (Figure C.1 and Figure C.2). Bulkheads were located either side of the tow post plate in order to give the mid-body torsional strength. The mass and centroid of the hollowed sections was estimated using the 'area inspection' tool in *AutoCAD*. The ballasting weight masses used were based on the actual weights that were available at the SSU Towing Tank. A break-down of the mass components is given in Table 4.6.

Table 4.6 – Component masses used in estimation of model longitudinal centre of gravity and pitch gyradius

Component	*Mass / kg*
Foam	10.9
Plywood	0.225
Heel fitting	1.5
Tow post	1
Resin and paint	2
Ballast weight forward	2 x 9.07
Ballast weight aft	9.07
Ballast weight aft	5
Ballast weight aft	0.665
Total mass	48.5

Based on this, the predicted values of longitudinal centre of gravity (LCG) and k_{xx} are 0.0042 metres aft and 0.577 metres (or 0.27 L_{BP}). These compare favourably with the required values of 0.0040 metres aft and 0.534 metres respectively. Whilst it is recognised that this approach early on in the design is very approximate, since the true mass distribution of the manufactured hull is not known accurately, it provides some confidence that

the model may be ballasted in the towing tank to the correct draught and trim, and still achieve a pitch gyradius close to the value assumed, thus improving confidence in the results of any seakeeping tests.

Turbulence stimulation studs

Turbulence stimulation studs were fitted to the model to approximate the effect of a full scale boundary layer. Initially it was planned to fit the studs at one inch intervals around the girth in accordance with the method due to Hughes & Allan (1951) as recommended by ITTC (2008b). However, on consultation with Campbell (2010b) it was suggested that these stud positions were too far forward and that a uniform arrangement at 10% L_{WL} aft of the forward perpendicular (FP) would be more appropriate. Dimensions of the studs used and a comparison of the alternative positions are shown in Figure 4.8.

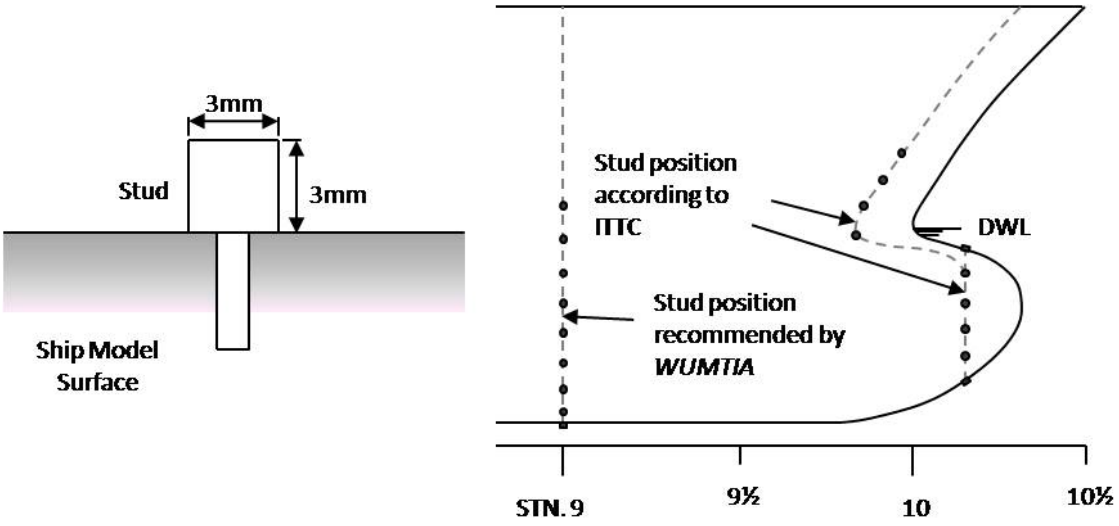

Figure 4.8 – (a) Turbulence stimulation stud dimensions; and (b) comparison of the ITTC and WUMTIA recommended positions

Model plans

The two models were designed using the 3-D NURBS software package *Rhino,* using the hull form definitions exported from *Maxsurf.* In *Rhino,* the internal shape of the models was defined so as to allow the 'hollowing out' codes for the CNC milling machine to be created. In addition, 2-D plans were also drawn up using *AutoCAD,* describing internal features which were not clear from the 3-D files. 2-D drawings and 3-D models of both hulls are included in Appendix C.

4.2.3 Model manufacture

Stages of manufacture

The manufacturing process can be summarised in the following stages:

1. Drill holes in foam blocks to mount on CNC milling machine.
2. Size foam blocks to correct breadth and depth, and hollow out all internal pockets.
3. Cut stern hull forms of both models from above. Cut 'jigsaw' locking holes in keel.
4. Cut bow hull forms of both models from port and starboard sides. This takes longer since the foam block must be re-oriented halfway through the cutting process due to the three-axis limitation of the CNC milling machine. Cut 'jigsaw' locking holes in keel.

5. Remove all excess material manually. Cut 'jigsaw' locking pins to join the two halves of the hulls.
6. Glue the two halves of the hull, clamping them overnight.
7. Fill surface deviations with filler and sand hull smooth with 400 grit wet and dry paper [ITTC (2002)].
8. Coat hulls in a thin layer of '*Ampreg 22*' resin to seal and add strength. Leave to dry overnight.
9. Further light sanding followed by two coats of grey car body primer spray paint.
10. Mark design waterline using a height gauge on a flat surface. Install turbulence stimulators in desired location.
11. Use epoxy resin to glue in plywood plate for mounting heel fitting.

High manufacturing tolerances are specified by ITTC (2002) so as to achieve the correct displacement during testing. Due to the high accuracy of the CNC milling machine, both models were produced to within the required $\pm$ one millimetre in length, beam and depth. The resin and paint finish did not add significantly to the overall dimensions. The draught marks were measured using a height gauge, with an accuracy of $\pm$ one hundredth of a millimetre, although they are marked by hand using a permanent marker pen which has a thickness of 0.5 millimetres, thus losing some of this accuracy. Photographs of the models at varying stages of completion are included in Figure C.3.

Model quality

Whilst ITTC procedures were taken into account, the models produced did not adhere perfectly to the recommendations. The main concern was the quality of the surface finish exhibited, especially on the stern sections of both models. Numerous pores in the foam were noticed, due to the low quality of foam specified in as a cost-saving measure, which would contribute to increased drag during testing and thus inaccuracies in results. Despite the application of filler and coats of resin and paint, these holes could not be entirely removed and thus the model surface finish is sub-standard in terms of ITTC requirements. Whilst an allowance is made for surface roughness in the post-processing of test results, quantifying the effect of these pores on the data is not well documented and as such is not addressed in this project.

An additional concern regarded the hull fairness, especially at the join of the bulbous bow with the hull. Here it was noted that the desired continuity of hull lines was not exhibited, and that flow separation was possible, which would again lead to inaccuracies in the measured data. However, this issue cannot be attributed to the manufacturing process, due to the high accuracy of the CNC milling machine, and is instead traced to the original design of hull lines in *Maxsurf*, where 'perfect' fairing was not achieved. The effect of this on the measured resistance is again hard to quantify, or even qualify, without the use of flow visualisation techniques and more detailed analysis than is possible within the scope of this work.

4.3 Preparations for testing

Test matrix

The main considerations in planning the required tests were the total time available, which was limited to three days, and the time required for each run. Both 'conservative' and 'optimistic' test schedules were drawn up, with the time allowed for each run modified between the two, as shown in Table 4.7. The main difference between the two schedules is the ability to complete the sailing condition runs with both port and starboard leeway angles. A full breakdown of the 'conservative' and 'optimistic' schedules is given in Table C.1 and Table C.2. Note that both schedules allow extra time so that the number of runs would not be compromised if delays were experienced. During actual testing this spare time was used to test the models in the 'sailing condition' at an additional speed.

Table 4.7 – Time allowed per run in minutes for both 'conservative' and 'optimistic' schedules

Run Type	*Conservative*	*Optimistic*
Calm water	10	7
Sailing condition	15	10
In waves	20	15

The models were prepared for testing following the recommendations of the ITTC (2002,(2008b), requiring that:

- They be loaded to within 0.2% of the design displacement. This was carried out by first weighing the model without ballast and then applying the appropriate amount of ballasting weight;
- The mean of the draughts forward and aft, port and starboard be within two millimetres of the design draught;
- The tow force be applied at the LCB and in line with the propeller shaft.

It is recognised that the accuracy with which these guidelines were followed was not entirely satisfactory for commercial testing purposes. Acknowledging the recommendations when preparing the models for testing was considered important in order to give the best possible confidence in the quality of results obtained.

Moment corrections

Various corrections were applied to the models in order to simulate the full scale ship more closely, including compliance with the ITTC requirements already described.

(i) Skin friction correction

The skin friction coefficient at model scale is always larger than for the full scale ship, as the Reynolds number is lower at model scale. If the towing point is above the centre of wetted area, this will result in a bow down trim moment which must be corrected by applying ballast aft. The skin friction correction, ΔR_F, is calculated as shown in Equation (4.4).

$$\Delta R_F = R_{FM} - R_{FS} / \Lambda^3 \tag{4.4}$$

(ii) Thrust line correction

In addition, if the model is towed from a point which above the thrust line, a second correction aft of the centre of gravity has to be applied to correct the resulting bow down trim moment. If the total drag of the model is known beforehand, the total correction can be calculated as (refer to Figure 4.9):

$$Total\ correction = \Delta R_F \bar{a} + R_{TM} \bar{b}\,, \tag{4.5}$$

where a and b are the lever arms between the towing point, and the centre of wetted area and thrust line respectively.

The total trim moment correction was calculated for the appropriate range of test speeds, as seen in Figure C.4. The corrections were applied using a sliding weight mounted on a guide rail screwed to the model's deck (see Figure C.3 (f)).

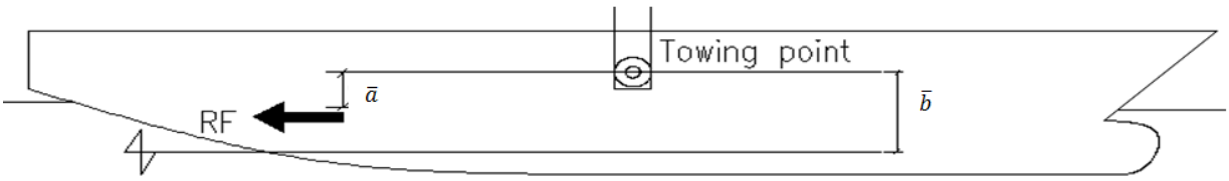

Figure 4.9 – Schematic showing total trim moment correction levers $\bar{a}$ and $\bar{b}$

(iii) Sail drive force correction

The drive force generated by the sails will also cause a bow down moment; to represent this change in trim, ballast is added forward of the centre of gravity of the model. The drive force generated by the sails at the same scale of the model can be calculated using average values for apparent wind angle and speed; the drive force is then multiplied by the levers from the centre of effort to the centre of gravity to find the required correction of 15.5 Nm.

(iv) Sail heel force correction

When operating at an angle of heel the aerodynamic sideforce will have a vertical component acting downwards and equal to $F_Z = F_Y \sin\varphi$. This force is simulated by adding a weight on top of the towing post, however due to the small magnitude of the predicted angle of heel, the correction amounts to only 3.2 N.

Measurement system

The experimental setup at the SSU towing tank consisted of a *WUMTIA* single tow post dynamometer constraining the model in surge, sway and yaw, and a 'Large Yacht heel fitting' which is a heel- and trim-able tow post fitting. When testing the models in the upright condition, resistance and side force measurements were obtained from the dynamometer, with yaw moment measurements taken from the tow post and heave measured from the position of the model relative to the dynamometer. For tests in the heeled and yawed conditions, the tow post assembly was rotated within the dynamometer to the desired leeway angle and ballast shifted in the model to achieve suitable heel before locking the heel fitting in that position, thus minimising the roll moment and removing any influence of the flexibility of the system on the angle of heel [Campbell & Claughton (1987)].

When testing in waves a sword-type wave probe was used to monitor the form of the generated waves. The probe was mounted as far from the model as possible towards the front right corner of the carriage so as to avoid measuring a wave signal from the model's own wave pattern, and to avoid the wave pattern of the probe impinging on the model.

All data acquisition was through the *WUMTIA* software *LASSO*, via an analogue to digital converter. For the wave probe trace a *Churchill* signal processing unit was also employed. Calibration of the system components was conducted on the carriage, during which time it became apparent that the roll moment output from the heel fitting was unsteady. As it was judged non-critical to the testing, roll moment measurements were not recorded.

Wavemaker

The wave frequencies to be input into the wavemaker computer were calculated using simple wave theory and the values of model length given in Table 4.5. From the dispersion relation, assuming deep water[7]:

$$\omega^2 = gk = \frac{2\pi g}{\lambda}, \tag{4.6}$$

[7] $d > \frac{\lambda}{2}$, Bertram (2000)

and the wave frequency (f) in Hertz is derived to be:

$$f = \frac{1}{2\pi}\sqrt{\frac{2\pi g}{\lambda}}. \tag{4.7}$$

The resulting frequencies input are given in Table 4.8. The wave amplitude was constant for all runs, and chosen as an approximately one quarter of the ship draught, equal to three centimetres. Only one value was tested since the results can be scaled to any wave amplitude during post-processing.

Table 4.8 – Wave frequencies input into wavemaker

Wavelength	*Frequency / Hz*	
/ %L_{WL}	*Hull A*	*Hull B*
50	1.209	1.215
100	0.855	0.859
150	0.698	0.702
200	0.604	0.608

4.4 Analysis of results

Throughout the course of testing a total of 112 measured runs were completed. Of these 83 are deemed to be useful for further analysis. The useful data is almost equally divided between each hull, with *Hull A* and *Hull B* having 43 and 40 runs respectively. Increasing the size of the data set and repeating runs increases confidence in the results by reducing random and systematic error.

The majority of the runs that do not yield meaningful results represent runs corresponding to unsatisfactory calibration of the dynamometer. Some problems were encountered when trying to achieve an almost constant 'zero' value between runs. This led to recalibration until the problem had been rectified, wasting valuable testing time. In some cases corrections have been applied to results. When an unexpectedly large drag measurement is observed due to a shifting zero value, an acquisition can be made with the model in the same condition but with zero carriage speed. This effectively defines the actual zero and hence the drag is obtained by differencing the measured drag and the 'measured zero'. Although this correction has been applied in a few instances this is not an efficient use of time. Thus time was spent recalibrating to avoid this. The parameters measured by the various channels of the dynamometer and output by *LASSO* are as follows:

- Model speed, V_M ;
- Drag force, D_M ;
- Side force, SF;
- Trim angle, θ ;
- Heave ;
- Roll moment ;
- Yaw moment, M_Ψ;
- Wave amplitude, ζ;
- Drag zero.

Not all of these data channel outputs are used in the analysis. This is either because these values are not needed or the results are not reliable. This is probably due to the instrumentation on the dynamometer and the heel fitting not working correctly. In some cases connection problems to the signal box occurred.

Fortunately, all the variables that are needed for the analysis produce reliable results i.e. V_M, D_M, SF, M_Ψ and ζ provide sufficient information required for the post processing of the result data.

4.4.1 Upright condition

Processing of model scale data

Testing procedure and data analysis have been carried out for the upright condition in line with ITTC recommended procedures [ITTC (2008b)]. The upright condition results do indicate a misalignment of the model from the centreline of the tank. All the tests in this condition are required to be carried out at zero leeway angle, however, the results show non-zero yaw moment and hence indicate model misalignment. Alternatively this could suggest asymmetry in the model about the centre plane. The alignment was simply conducted by sighting the model from the end of the tank and from the carriage. This is not the most rigorous approach, but was the best method available during testing. A correction needs to be applied to the resistance results to account for this misalignment. Fortunately this can be achieved with relative ease as the model has been tested at a number of leeway angles to assess the effects of the sail system (Section 4.4.2). From this data the misalignment can be determined. Consider *Hull A* as an example. Table 4.9 shows the measured yaw moment at a range of leeway angles for the high speed sailing condition (approximately 25 knots ship speed).

Table 4.9 – Model misalignment correction to yaw moment – *Hull A*

$\Psi\ /\ deg$	$M_\Psi\ /\ Nm$	$Corrected\ M_\Psi\ /\ Nm$	$C_{TM,Measured}$	$Corrected - best\ fit\ M_\Psi\ /\ Nm$	$Best\ fit\ C_{TM}$
-5.0	10.16	11.07	8.159E-03	11.36	8.340E-03
-2.5	5.07	5.97	7.266E-03	5.68	7.284E-03
0.0	-0.58	0.32	6.878E-03	0.00	6.900E-03
2.5	-6.94	-6.04	7.749E-03	-5.68	7.702E-03
5.0	-12.22	-11.32	8.820E-03	-11.36	8.956E-03

One expects a linear relationship between yaw moment and leeway angle passing through the origin. Figure 4.10 (left) shows the actual relationship. One can appreciate the linearity, however the trend does not pass through the origin (further illustrated by the equation of the best fit line) indicating the magnitude of the misalignment. The corrected yaw moment in Table 4.9 is obtained by adding a factor to the yaw moment data so that the best fit line [Figure 4.10 (left)] intersects the origin. To account for the fact that this data only represents one speed the resistance is non-dimensionalised using

$$C_{TMMeasured} = \frac{D_M}{{}^1/_2\,\rho S V_M^2}. \tag{4.8}$$

This allows for the correction to be applied to any speed. The yaw moment is then adjusted to coincide with the new best fit line, giving symmetry port and starboard. Now this corrected yaw from the best fit line is plotted against $C_{TM,Measured}$ and a fourth order polynomial is fitted through the data [see Figure 4.10 (right)]. This allows for the C_{TM} values on the best fit line to be obtained. These values of C_{TM} are subsequently averaged to obtain symmetry for positive and negative yaw moment. These average values are plotted and a quadratic polynomial is fitted through the data. It is this equation that provides the correction to the upright cases. $C_{TM\psi}$, resulting from leeway, is given in the form

$$C_{TM\psi} = aM_\psi^2 + bM_\psi + c \tag{4.9}$$

where a, b and c are constants determined during the curve fitting operation. Thus the corrected coefficient of total resistance is

$$C_{TM} = C_{TMMeasured} - (C_{TM\Psi} - c)\,. \tag{4.10}$$

as c is the corrected coefficient of total resistance when the yaw moment is zero. Then clearly the corrected model drag is given by

$$R_{TM} = {}^{1}/_{2}\,\rho S V_M^2 C_{TM}\,. \tag{4.11}$$

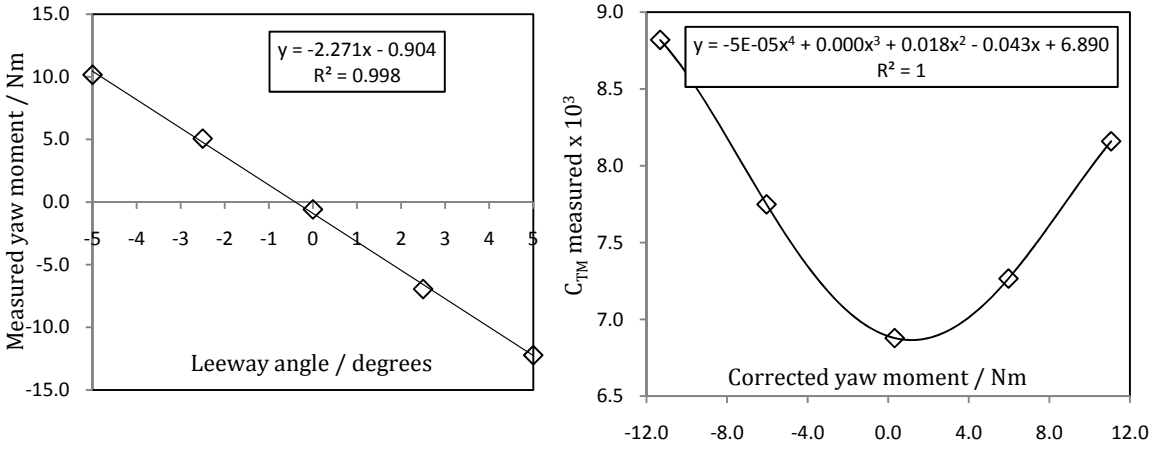

Figure 4.10 – Illustration of misalignment (left); and yaw moment correction (right)

Figure 4.11 presents the corrected model resistance over the range of tested speeds and allows an initial comparison of *Hull A* and *Hull B* before any scaling procedures have been implemented.

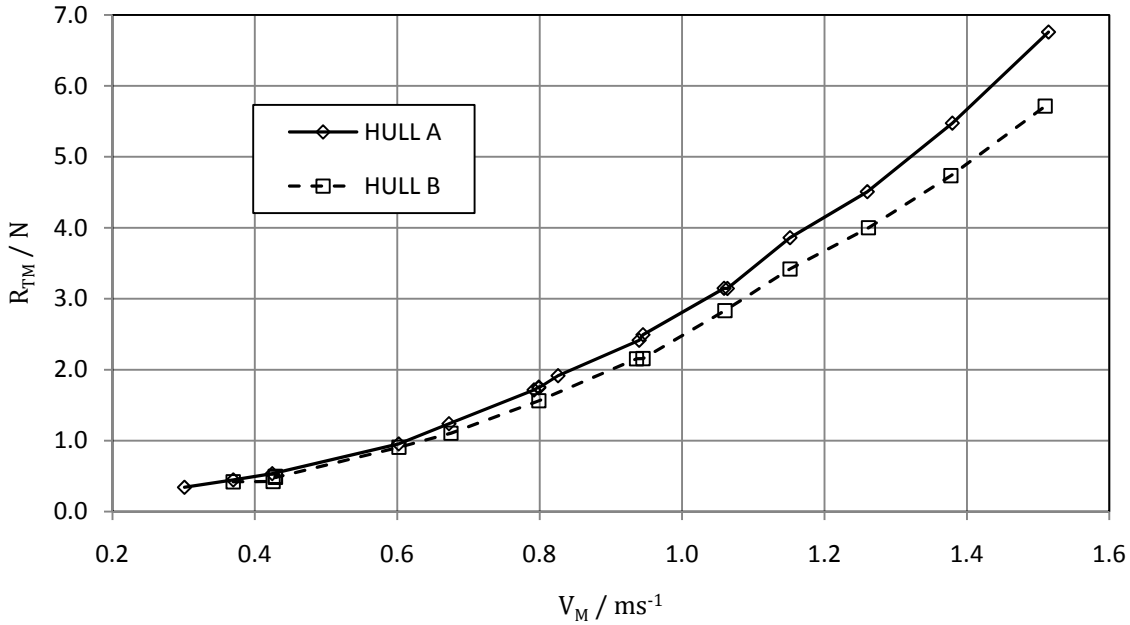

Figure 4.11 – Corrected model resistance for *Hull A* and *Hull B*

Implementation of ITTC 1978 Performance Prediction Method

The ITTC '78 Performance Prediction Method [ITTC (2008d)] is currently the recognised procedure for scaling model test results for commercial ships to predict full scale performance. In terms of resistance this method divides the components of resistance as follows

$$C_{TS} = (1+k)C_{FS} + \Delta C_{FS} + C_A + C_W + C_{AAS}\,, \tag{4.12}$$

where

$$C_W = C_{TM} - (1+k)C_{FM}; \tag{4.13}$$

$$\Delta C_{FS} = 0.044\left[\left(\frac{k_{SS}}{L_{WLS}}\right)^{1/3} - 10Re_S^{-1/3}\right] + 0.000125; \tag{4.14}$$

$$C_A = (5.68 - 0.6logRe) \times 10^{-3}; \tag{4.15}$$

and

$$C_{AAS} = \frac{1}{2}\rho_A V_S^2 C_{DA}\frac{A_{TS}}{S_S}. \tag{4.16}$$

represent, in coefficient form, the wave making resistance; resistance allowance for hull roughness; correlation allowance between model and ship and the still air drag resistance respectively. C_F is determined using the ITTC '57 correlation line defined in Equation (4.2). The ITTC '78 method has been assessed and is reasonable to apply in this instance, except for the following, that:

- An allowance for model roughness will need to be introduced;
- A reasonable formulation for the still air resistance must be derived.

Allowance for model roughness

Due to budget constraints and limitations in manufacturing techniques the models produced were not 'glass smooth' as is assumed in the ITTC '78 method. Consequently if one commences the analysis without accounting for model roughness the power requirement is overestimated. This problem is apparent when observing the form factor determined from the Prohaska plot [ITTC (2008d)].

Variations in C_{FM} affect the form factor and ultimately the ship resistance. To account for the model roughness, enabling a realistic power estimate, a factor ΔC_{FM} must be introduced. In this case it does not make sense to use Equation (4.14), the formula proposed by Townsin (2003), as this is applied at full scale alongside the correlation allowance. If one applies it without the correlation factor at model scale ΔC_{FM} is predominately negative which makes no physical sense. Applying it with the correlation factor at model scale is not reasonable; it would mean using the correlation allowance twice and applying it to adjust model scale values before scaling. For these reasons a formula has been used from a previous revision of the ITTC '78 method, known as the Bowden-Davison equation:

$$\Delta C_{FM} = \left[105\left(\frac{k_{SM}}{L_M}\right)^{1/3} - 0.64\right] \times 10^{-3}. \tag{4.17}$$

The final complexity is in determining or estimating the model surface roughness. Measuring the roughness is not impossible, but requires specialist methods that are not available to the authors. Having a roughness value for the HDF would not help matters as it is coated in resin and painted, as explained in Section 4.2.3, and thus a standard value is of no use. This process is incredibly easy for the ship hull roughness as a value quoted by *International Paints* [Willsher & Solomon (2010)] is used ($k_{SS} = 80.5 \times 10^{-6}$ metres).

The model roughness then must be estimated. It is expected that it must lie in the range $0.1 - 50 \times 10^{-6}$ metres which represents the roughness boundary between plate glass and bare steel plate [Molland (2009)]. In the absence of any definite information it seems reasonable that as the form factor is a measure of hull drag and that as ΔC_{FM} changes so will the form factor (determined from the Prohaska plot), that ΔC_{FM} can be varied in the range defined to achieve a reasonable form factor. As it is believed that the hull forms are well represented by the Holtrop regression it is expected that the form factors determined in Section 4.1.5 should be fairly close to the actual values. These values are used as an approximate target to determine the

roughness of the model. Table 4.10 illustrates the sensitivity of the form factor when varying the surface roughness.

Table 4.10 – Sensitivity of form factor due to varying surface roughness

	$k_{SM} \times 10^6$	0.1	1	2	3	4	6	8	10	30	50
	$(1+k)$ Holtrop	$(1+k)$ Prohaska									
Hull A	1.188	1.349	1.229	1.178	1.145	1.120	1.083	1.055	1.032	0.911	0.851
Hull B	1.182	1.351	1.230	1.179	1.145	1.120	1.082	1.054	1.031	0.909	0.849
Hull A	$C_{TS} \times 10^3$ @ 25 knots	4.048	3.777	3.662	3.587	3.530	3.445	3.382	3.330	3.057	2.920
Hull B		3.297	3.030	2.918	2.844	2.788	2.705	2.643	2.592	2.325	2.192

Although the regression analysis value is thought to be reasonable it would be questionable to blindly select the roughness value giving the closest form factor result of two microns. It is however expected that model surface roughness is towards the lower end of the suggested range. Two microns seems a very low roughness for the surface, and hence to be more conservative a roughness of three microns was selected for the model surface.

The ultimate dependence of the ship resistance on the changes in $(1+k)$ and ΔC_{FM} is not straight forward, as when the latter is increasing the former is decreasing. In the determination of C_W [Equation (4.13)**]** the term C_{FM} must be replaced with $C_{FM} + \Delta C_{FM}$. It must of course depend on the magnitudes of $(1+k)$ and ΔC_{FM} as to whether there is a net increase or decrease in C_W. The complexity is further increased by the dependence of C_{TS} on $(1+k)$ and C_W. The simplest way to evaluate this then is to study the numerical results at the design speed. This data is presented in Table 4.10 alongside the form factors. This variance is better illustrated graphically (Figure 4.12). The non-dimensional form provides no real comparison between *Hull A* and *Hull B* as the wetted surface areas are somewhat different. The resistance of each hull is however decreasing as the model roughness is increased. This is a consequence of the scaling procedure and illustrates that the ship resistance significantly varies with the model roughness, highlighting the importance of formulating a reasonable estimate.

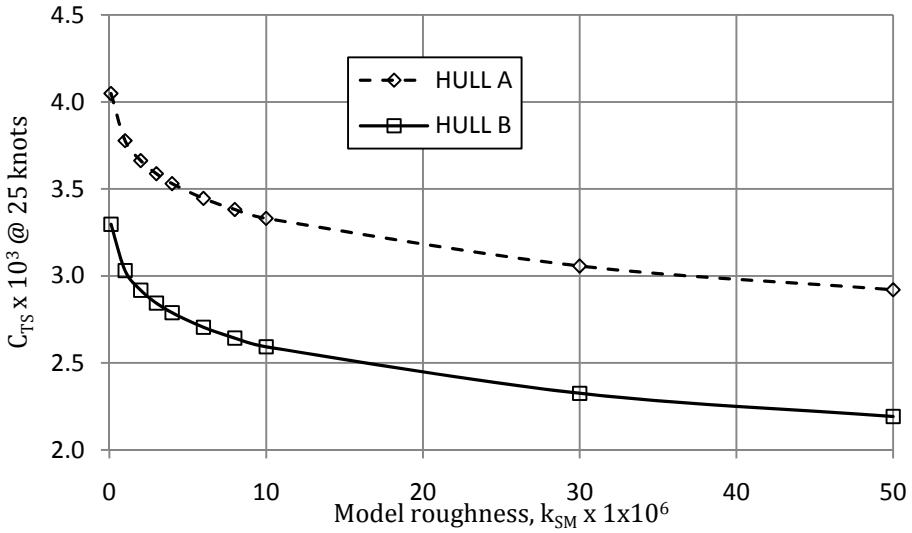

Figure 4.12 – Variation of C_{TS} with surface roughness

A final correction that has been applied to the model resistance accounts for the additional drag resulting from the trip studs. This has been done in accordance with a procedure outlined by Molland *et al.* (1994) and is represented by a further increase of C_{FM} (see Appendix D.1).

Correction of still air resistance expression

The ITTC '78 method provides a formula for the determination of the still air resistance of the ship [Equation (4.16]. If one considers the structure of this equation and assesses the dimensions it is fundamentally incorrect. It has dimensions of $mass/(length \times time^2)$ when this coefficient should be dimensionless. In particular it should represent an air drag non-dimensionalised by the standard 'hydrodynamic' parameters $^1/_2\,\rho_S S_S V_S^2$ as it is simply summed with the other coefficients [Equation (4.16)]. If one follows these steps the air resistance coefficient is represented as

$$C_{AAS} = \frac{\rho_a A_{TS}}{\rho_S S_S} C_D. \tag{4.18}$$

For all the analysis in this section, Equation (4.18**)** replaces Equation (4.16**)**. Attempting to utilise Equation (4.16**)** further confirms its incorrectness as the results are unreasonably large. C_D is chosen in line with Molland (2009) and taken as 0.5, which is a low value associated with the aerodynamic characteristics of having a sloped forward superstructure. The transverse area above the waterline A_{TS} is determined from the layout as $616.23\ m^2$; the air and sea water density are calculated for a temperature of 25^oC as $1.1855\ kgm^{-3}$ and $1023.38\ kgm^{-3}$ respectfully and the wetted surface areas are given in Table 4.3. This results in $C_{AAS} = 7.364 \times 10^{-5}$ for *Hull A* and $C_{AAS} = 7.7304 \times 10^{-5}$ for *Hull B*.

Upright condition results

One can now begin to evaluate the resistance characteristics of the hull designs. The effective power is given over the range of tested speeds in Figure 4.13, full details are provided in Table D.2 and Table D.3.

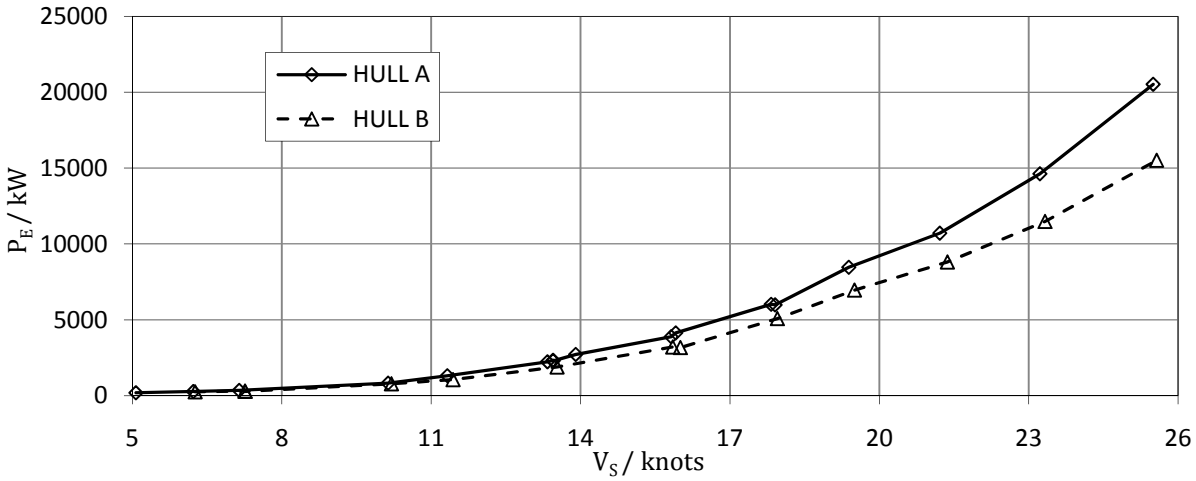

Figure 4.13 – Effective power comparison

The first conclusion to draw from Figure 4.13 is that the effective power of *Hull B* is less than *Hull A* across the entire speed range. This is a trend that has also been observed in Section 4.1.5 and is due to the difference in (naked) wetted surface area between the two hulls. In terms of dimensionless resistance components, by comparing results in Figure 4.14, *Hull B's* total resistance coefficient is the lesser over the Froude number range; the converse of what was observed using the Holtrop regression.

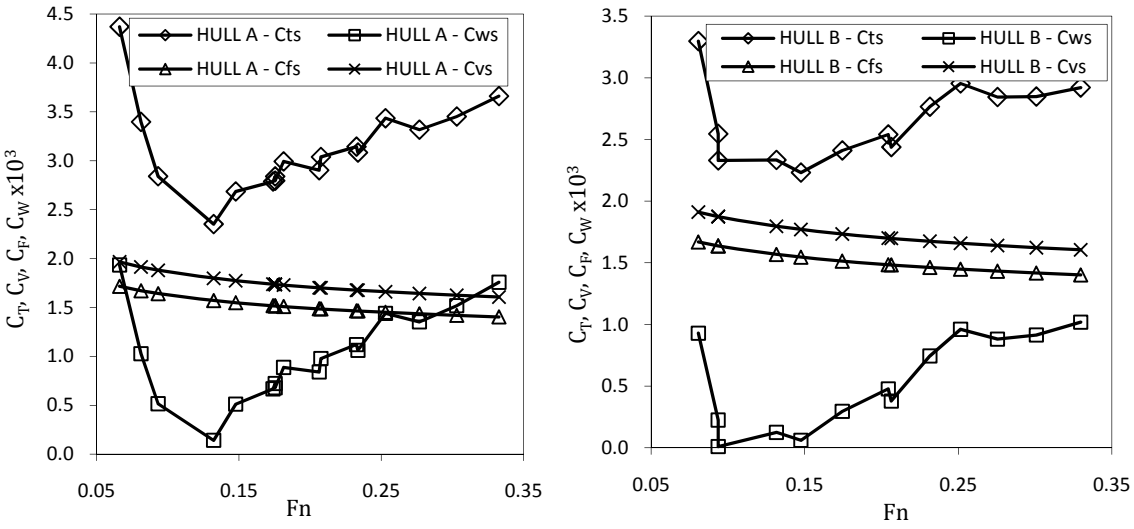

Figure 4.14 – Breakdown of resistance components for (a) *Hull A;* and (b) *Hull B*

From Figure 4.14 one can appreciate the effect of the form factor, the difference between C_{FS} and C_{VS}. The reason *Hull A* has a larger C_{TS} is due to the C_W being around twice the magnitude of the C_W for *Hull B*. C_{FS} and C_{VS} are similar for each hull due to the fact that L_{WL} is similar, the only variable affecting C_{FS}, and also the form factors are very similar. The variation of these components with Froude number is not substantial. The wave resistance never constitutes more that 50% of the total resistance. It is somewhat expected that for the concept operating at the design Froude number that viscous and wave pattern resistance are comparable in magnitude, as observed. One expects *Hull B* to have lower wave making resistance as it is designed to reduce the wave pattern generated by the stern, see Section 4.1.3. It may be noticed that the viscous and wave pattern components do not seem to sum to give the total. One should consult Equations (4.15) and (4.16) and notice that C_{AAS} and C_A are not presented in Figure 4.14 however they still contribute to C_{TS}.

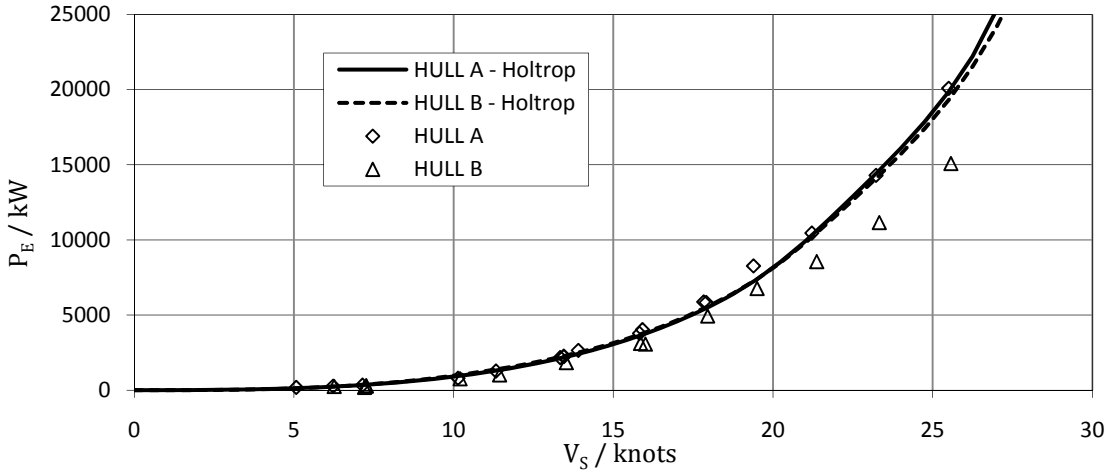

Figure 4.15 – Comparison to Holtrop effective power for *Hull A* and *Hull B*

Figure 4.15 and Figure 4.16 present comparisons between resistance measurements obtained from models tests and those estimated in Section 4.1.5. Note that in these instances C_{AAS} is not included as no allowance for air resistance is accounted for in the Holtrop regression. From Figure 4.15 it can be seen that the predictions and the measurements are fairly similar especially at low speed. The prediction for *Hull A* is better than it is for *Hull B*. It is likely that *Hull B* is not well represented by the Holtrop regression as its stern form is not standard for merchant ships. This would affect the validity of the coefficient of wave resistance, as seen in Figure 4.16(b), and suggests why the power estimate for *Hull A* is closer to the measured value than for *Hull B*

(Figure 4.15). It also seems reasonable that the Holtrop regression over predicts the resistance further as the speed increases. At higher speed the proportion of resistance attributed to the wave pattern increases and hence as it is this part of the total resistance that is being overestimated, the difference becomes greater. This can be observed in Figure 4.16 (a) and (b).

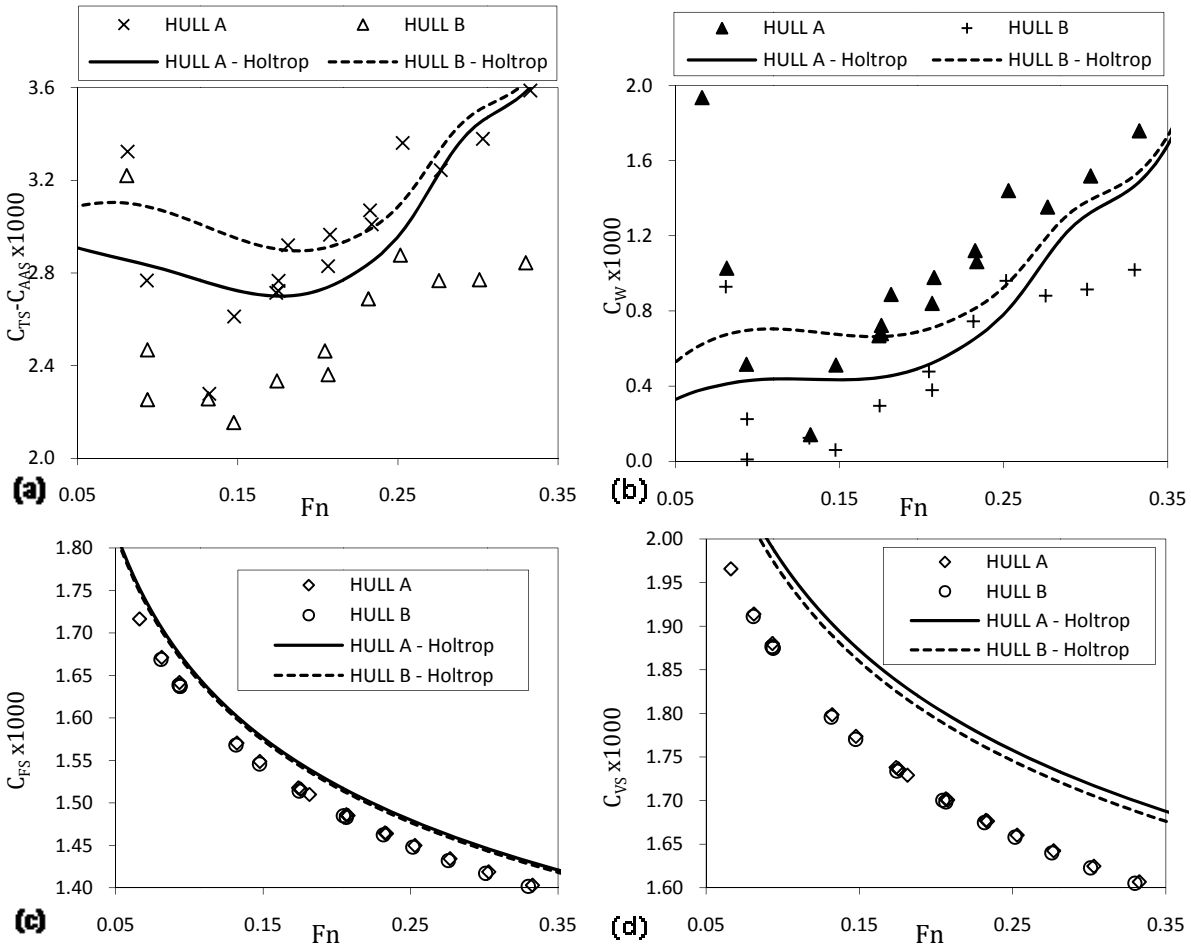

Figure 4.16 – Comparison of individual resistance components to those obtained using the Holtrop regression. (a) $C_{TS} - C_{AAS}$; (b) C_{WS}; (c) C_{FS} and (d) C_{VS}

There is a small difference in the C_{FS} values obtained from the predictions and the model tests. This is unexpected as in both instances ITTC '57 friction line has been used. It is thought that *Hullspeed* must have used the incorrect L_{WL}, or more likely, a different value of the kinematic viscosity, as no account is taken for sea surface temperature, when determining the ship Reynolds number. This of course affects the values of C_{VS}, which are further augmented from one another by the fact that the form factors used in each method are different. One can also see how the Holtrop form factors are different for each hull. Other than the differences in magnitudes the trends of the results are very similar.

These results are considered when selecting the most suitable hull form (see Section 6.1). It is important to be clear in the mind of the reader that the testing in this section only considers the performance of the naked hull. Although there are appreciable differences in the performance of the hulls there may be benefits currently unaccounted for that can outweigh this.

4.4.2 Assessment of hydrodynamic forces resulting from use of sails

An amount of heel and leeway will be experienced in all wind conditions, except for running dead before the wind, by any ship that uses sails for propulsion when underway. Heel and leeway produce forces and moments

that balance the aerodynamic sideforce generated by the sails [Kirkman & Pedrick (1974)]. The underwater body operates like a lifting surface which generates an amount of sideforce SF which balances the force of the sails. Associated with this lift force there is an induced drag component. It is important that the hull form is able to generate enough sideforce at small leeway angles in order to minimise this component and hence increase the thrust reduction from the sails. These forces must be quantified by running the models at a number of heel and leeway angles. This of course is not a standard practice in a ship concept design and hence knowledge must be taken from the design of sailing yachts with regards to testing procedures and evaluation of performance. The forces resulting from the changes in orientation are namely a resistance component and a side force component, acting in orthogonal planes. The resistance measured of course is the total drag force however a portion of this is attributed to the use of sails. The magnitude of the sideforce will determine how much the orientation of the ship changes due to a force on the sails and hence the magnitude of the induced resistance that is experienced. Being able to estimate this is very important as it will allow for an assessment as to whether the benefit of the sails outweighs the induced resistance due to the leeway and a component due to heel (Section 6.1.1).

Corrections have been made to the measurements of resistance and sideforce similar to those made in Section 4.4.1. In this instance the resistance has been corrected so that the value at zero heel and zero leeway is the same as the upright resistance measured (after being corrected for misalignment) in Section 4.4.1. The sideforce has been corrected so that it is zero in the upright condition. In any instance these errors are small with the measured sideforce at zero heel and zero leeway at 15.9 knots being 0.02 N. These corrections have been applied by considering a linear fit of data through a graph of resistance versus sideforce squared for each heel angle. There are many areas of uncertainty and sources of error that could have caused these problems. Uncertainty is quantified in Section 4.4.4. Sources of error identified by the authors are most likely resulting from the dynamometer set up, see Section 4.4.1. Alignment is an unavoidable problem. As a single post system is used, which is fairly flexible, the leeway angle set when the model is static is not necessarily the angle undertaken when the forces are measured. The hydrodynamic forces can be sufficient to displace the model from the set leeway angle. This problem is a more significant for larger models [Claughton *et al.* (1998)]. There can also be problems if there is interference between sensors designed to measure a particular force by other forces. It is thought that this could certainly be a problem with the yacht heel fitting used, as the results from some of the channels are meaningless. Although these are not the channels needed for the sideforce and resistance, this interference could have affected the measurements.

The resistance is broken up into components as suggested by Campbell & Claughton (1987),

$$R_{TOT} = R_U + R_I + R_H, \tag{4.19}$$

where R_U is the upright resistance; R_I is the induced resistance due to leeway and R_H is the resistance due to heel. This breakdown is perhaps better understood when considering Figure 4.17.

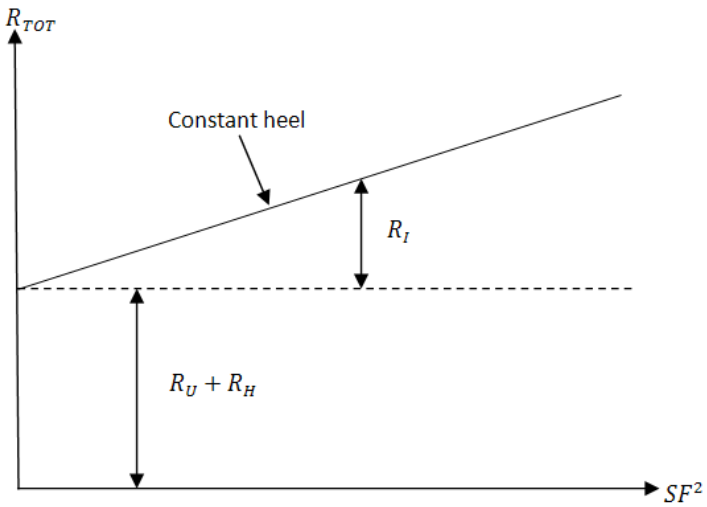

Figure 4.17 – Illustration of resistance components due to heel and leeway as a function of sideforce

For the case of zero heel $R_U + R_H \rightarrow R_U$, by obtaining the intersection of the best fit line with the R_{TOT} axis and by subtracting the upright resistance R_U the error can be determined. This is corrected by adjusting the data points until the best fit line in this case goes through R_U. This is applied to the other two heel cases at this speed and another correction is determined for the other speed tests. Note that although R_H is zero at zero heel does not mean that it increases as a ship is heeled. At small angles of heel a negative R_H can be observed. Campbell & Claughton (1987) report differences in measured data due to this method of breaking down the components and states 'It should not be assumed that the measured data will conform neatly to this description of resistance'.

Scaling procedure to full scale

A scaling procedure is adopted using Froude scaling, as suggested by Campbell & Claughton (1987). This is applied to R_I and R_H as the full scale value of R_U is already known from Section 4.4.1. The Froude scaling is implemented by expressing the resistances in non-dimensional coefficient form. It is not really important how these are non-dimensionalised as there is no interest in the coefficient value. It is simply used to obtain a ship scale force, say

$$C_I = \frac{R_I}{1/2\,\rho A_I V_S^2}, \tag{4.20}$$

where A_I can be the projected area relative to the incident flow or the wetted area. In any case, when one applies Froude scaling the result is

$$R_{IS} = \frac{\rho_S}{\rho_M}\Lambda^3 R_{IM} \tag{4.21}$$

where Λ is the model scale factor. Similarly R_H and SF are given by

$$R_{HS} = \frac{\rho_S}{\rho_M}\Lambda^3 R_{HM} \tag{4.22}$$

and

$$SF_S = \frac{\rho_S}{\rho_M}\Lambda^3 SF_M \tag{4.23}$$

respectively.

Results

All results presented are those at full scale. Table D.4, Appendix D, gives the values of the resistance components and sideforce for each heel and leeway combination tested at both the high (25.5 knots) and low (15.9 knots) speeds. These results are presented as proposed in Figure 4.18.

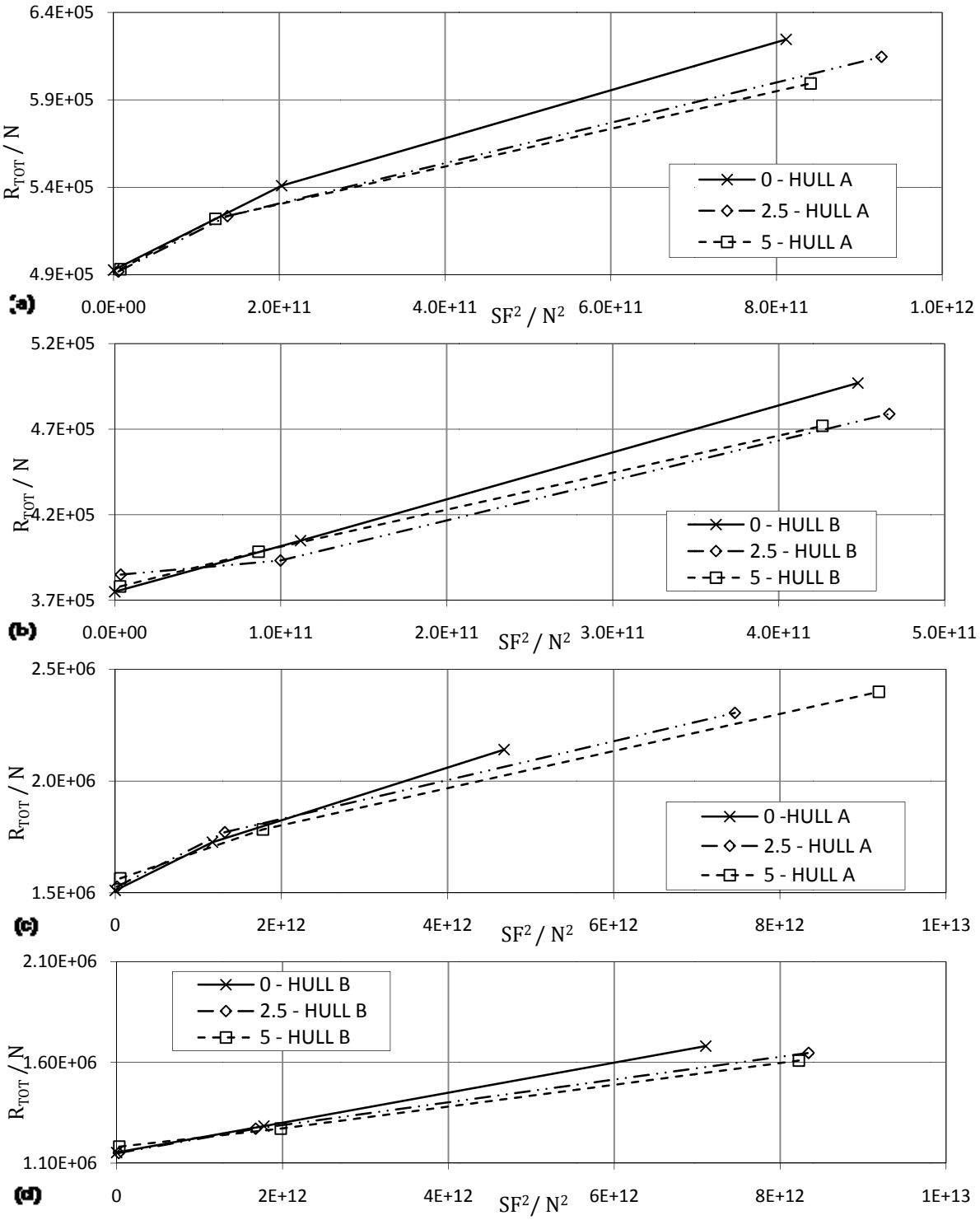

Figure 4.18 – Evaluation of side force and resistance, (a) *Hull A* – 15.9 knots; (b) *Hull B* – 15.9 knots; (c) *Hull A* – 25.5 knots; (d) *Hull B* – 25.5 knots

From Figure 4.18 it can be seen that the trends are approximately linear as is expected. However, *Hull B* seems to fit this trend better. For *Hull A* the resistance value at zero side force tends to fall below the linear fit, this

has been observed by Campbell & Claughton (1987). It is difficult to draw any conclusion about this from the results as there are only three data points for each data set and hence it cannot be clear which of the points is in fact straying from the linear trend. It should be no surprise that the sideforce and resistance get larger with speed and leeway angle. It is also seen, and somewhat expected, that the sideforce and resistance are lower for *Hull B* than they are for *Hull A* at the same speed, this is due to the 'Hogner' stern of *Hull A*. A large side force is desirable as it will prevent significant leeway angles existing when the ship is using the sails. However, this accompanies a large resistance which is not desirable. Hence evaluating hull form performance is not trivial and is dependant on the wind conditions and the sail design. This is considered in detail in Section 6.1.1

That said one can quickly compare the relative magnitude of the results for each hull. If one compares Figure 4.18 (a) and (b) for the low speed case, bearing in mind that sideforce is squared, the difference in the side force between the hulls is around twice the difference in the resistance. This suggests then that *Hull A* will perform well, as the increase in sideforce, which is desirable, is approximately twice the increase in resistance, which is not desirable, and hence the benefits may outweigh the drawbacks. For the high speed case, comparing Figure 4.18 (c) and (d), there is not a very significant difference in the side force between the two hulls, however, *Hull A* still has a significantly larger resistance than *Hull B*. This suggests that *Hull A* will not perform so well at high speed.

In most instances the resistance is greater, at high leeway, for the low heel angles. This is thought to be attributable to the wetted surface area changes as the ships heel. This has not been examined. However, it would seem (from the high leeway results) that it is reducing as the ship heel increases.

Aside from uncertainties and error sources in the experimental procedure (discussed in Section 4.4.4) there are some reasons to believe that the analysis method could be affecting the results. An allowance for model roughness has only been made in the determination of R_U however roughness will certainly affect the other components of resistance and the sideforce. Hence the resistance and the sideforce will be overestimated. This can only be rectified by adding some allowance, however no 'standard' allowance is known to the authors. This is possibly a consequence of the increased complexity of the nature of the viscous boundary layer in these conditions. The Froude scaling method used is somewhat standard, however it is noted that it is difficult to develop a scaling procedure to take full account of viscous flow differences between model and full scale [Campbell & Claughton (1987)].

4.4.3 Added resistance in waves

The resistance of the model advancing in waves of prescribed length has been measured. This allows possible performance in waves and hence the operational capability in certain weather conditions to be assessed. The added resistance at model scale has been determined using Equation (4.24) for values at the same speed.

$$R_{AW} = D_M - R_U \tag{4.24}$$

The added resistance is presented in a non-dimensional form that has been proven by Strom-Tejsen *et al.* (1973) to give consistent results when implemented on model test results of varying scale. This gives confidence that this coefficient form can be used to scale values of added resistance to ship scale and for the necessary wave amplitude. The added resistance coefficient is thus defied as

$$\sigma_{AW} = \frac{R_{AW}}{\rho g (B^2/L_{WL})\zeta^2}. \tag{4.25}$$

Added resistance has been tested at two speeds; a low speed (*Hull A* – 15.9 knots; *Hull B* – 16.0 knots) and a high speed (*Hull A* – 25.5 knots; *Hull B* – 25.6 knots). These speeds are similar and are to be assumed the same for purposes of hull comparison. The differences simply arise from inaccuracy in the carriage control between set and achieved speed. Table 4.11 presents the results for the tested situations.

Table 4.11 – Non-dimensional added resistance for *Hull A* and *Hull B* at both tested speeds

	Hull A		*Hull B*	
Speed	λ/L_{WL} / %	σ_{AW}	λ/L_{WL} / %	σ_{AW}
Low	52.05	0.527	48.21	1.086
	104.37	3.923	103.25	3.732
	155.60	1.606	153.92	1.853
	220.72	0.691	181.25	0.394
High	50.31	1.107	49.74	1.164
	101.13	3.415	100.09	2.963
	151.42	3.522	149.86	4.627
	196.91	0.656	194.71	1.433

Figure 4.19 represents Table 4.11 graphically. The data points have been joined with straight lines as insufficient wavelengths were examined to realistically represent the added resistance profile. Attempts have been made to test at wavelengths where the peak in the added resistance exists, however this has not quite been achieved and due to restrictions in the testing schedule there has been no time to re-run other conditions. It seems likely that the peaks in each of the cases exist somewhere between the second and third data point. As an approximation one expects the peaks to exist for the low speed case at a wave length 120% of ship length and for the high speed case 140% of the ship length for both hulls. This trend of decreasing wavelength peak with decreasing speed is also noticed by Salvesen (1978). A numerical assessment of the added resistance will be carried out in Section 7.1. This should provide some validation of the locations of the peaks to help the assessment of the efficiency of the fast feeder's operations (Chapter 6). In any case one expects the magnitude of the added resistance peaks to be larger at higher ship speed.

The magnitude of the added resistance is essentially a measure of the seakeeping characteristics (heave and pitch) of each of the hulls [Wilson (1985)] when operating in a specified seaway. In a qualitative sense, these results can be used to compare the seakeeping qualities of each hull. One should bear in mind the difference in the ship speed between the two hulls, however the effect of this is expected to be small.

At low speed *Hull A* seems to performs better at low wavelengths (below 80%) but not as well at larger wavelengths (above 155%). At high speed for wave lengths below 100% the performance of the hulls is similar with Hull B performing marginally better. For wave lengths greater than 160% Hull B performs better. A comparison cannot be made in the wavelength range 100-160% as the profile is not sufficiently defined.

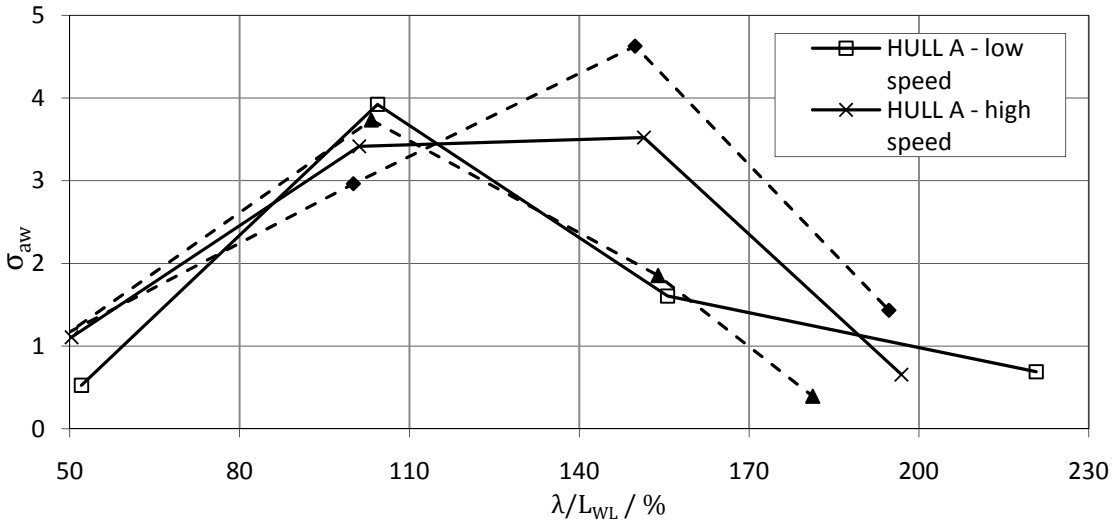

Figure 4.19 – Non-dimensional added resistance profiles for *Hull A* and *Hull B* at both tested speeds

4.4.4 Uncertainty analysis of testing data

Uncertainty analysis (resistance estimates)

An uncertainty analysis was conducted on the calm water resistance, side force and yaw moment experimental results following the ITTC Procedure for Uncertainty Analysis of Resistance Tests [ITTC (2008c)]. The procedure makes an estimate for the effect of various uncertainties in the experimental procedure on test results due to bias (systematic error) and precision (random error), see Figure 4.20.

The uncertainty in a resistance test can be broadly grouped into five components, namely:

- the model geometry, which includes errors in manufacturing, deformation during testing (including the addition of ballast), the effect of residual waves from previous runs and running attitude. These uncertainties lead to variation of the real wetted surface area from the nominal wetted surface area which is one of the most important parameter in resistance estimates;
- the model installation, including alignment, weight, draught and trim verification. Misalignment has direct influences on resistance, trim and sinkage measurements while weight and buoyancy have the direct influences on the wetted surface area and displacement. Variation of weight, displacement, draught and trim can arise due to differences in expected water density and temperature as well as ballasting errors;
- Calibration, which occurs because most instrumentation is linear. The linear regression equations used during calibration leads to an element of uncertainty. There is also a level of uncertainty associated with the masses used during calibration [ITTC (2008a)];
- Direct measurement, which arises due to the uncertainty in the time history of the sampled data which is affected by length of time signal, sampling rate and tow speed measurement. Although the resistance test is steady, the measured resistance will vary due to turbulent boundary layer flow, hull wake, test rig vibrations, drift of the measurement system, fluctuating power supply and electronic noise etc. The average resistance is obtained by averaging the time trace of resistance over the course of the measured run. The level of this uncertainty can be reduced considerably by repeating runs;
- Data reduction, arising from blockage and tank wall effects.

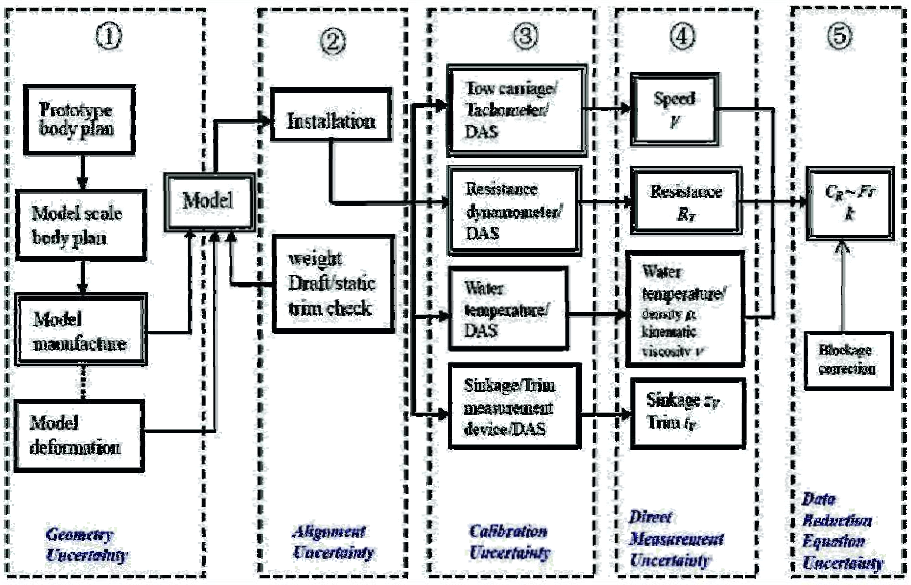

Figure 4.20 – Schematic of test system grouped into areas of uncertainty [ITTC (2008c)]

To simplify the uncertainty analysis it has been assumed that since the model was manufactured to within ITTC procedures [ITTC (2002)] no account of errors from machining tolerances need to be taken into account. In addition to this, no allowance has been made for uncertainties arising from extrapolation to full scale, turbulence simulation, blockage and wall effects or scaling of form factor.

The process of determining the uncertainty in total resistance coefficient[8] involves calculating the maximum amount of uncertainty arising from system error (bias limit) and also measurement uncertainty (precision limit) assuming there is no error correlations between variables. A summary of the process used to determine the uncertainty of the resistance test estimates is given in Appendix D.

Plots of calm water resistance against speed, side force against yaw angle and yaw moment[9] against yaw angle with associated error bars are given in Appendix D. The coverage factor, K, has been chosen as 1.645 to yield a 90% confidence level in the results.

It was found that there is a high level of uncertainty surrounding the experimental results being typically between 600% at slow speeds and 60% at high speeds, with the average being 200% for *Hull A* and 250% for hull B. The uncertainty is dominated by the random errors associated with the processing of the time trace into values of resistance, with the system bias typically accounting for only a few percent of the total error. This uncertainty could be reduced significantly by repeating runs more than once. For example, as a verification exercise hull A was run at 19 knots on three occasions as a calibration exercise. Table 4.12 shows how the uncertainty of each test run on its own is between 86 and 132%, however, when considered together the uncertainty is only 6.7%.

Table 4.12 – The reduction of uncertainty in experimental results due to repeats

	C_T (15 deg C)	$U_{CT}^{15\ deg\ C}$ (Resistance Coefficient C_T, % of $C_T^{15\ deg\ C}$)
Run 1	0.00708	116.933
Run 2	0.00617	85.666
Run 3	0.00680	131.873
Combined	0.00668	6.686

Uncertainty analysis (wave probes)

In a similar manner to the calm water resistance estimates bias and precision limits were calculated for the experimental measurements of wave profile in order to access to level of certainty with the added resistance runs. A summary of the process to determine the uncertainty of the wave probe measurements is given in Appendix D.

The significant wave height was calculated from the mean square of the wave elevation and compared to the value requested from the wavemaker. The error values are given in Table 4.13.

It is evident that there is a deviation of the requested wave height from the requested value at the lower wave frequencies. This is consistent with observations of other researchers using the SSU towing tank wave maker who put the errors down to a difference between the input transfer function and the transfer function used by the wavemaker. The deviation in wave height has been included as a correction in the analysis of the added resistance of the two hulls.

[8] A correction is required to correct C_T to a temperature of 15°C using ${C_T}^{15deg} = {C_T}^{tw} + \left({C_F}^{15deg} - {C_F}^{tw}\right)(1 + k$ where water properties at different temperatures are calculated with [ITTC (2006)].

[9] Yaw moment has been non-dimensionalised with respect to $0.5\rho V^2 L^3$

Table 4.13 – Error in wave height between requested and measured waves

Wavelength / $\%L_{WL}$	*V_S / knots*	*Hull A*		*Hull B*	
		Measured wave height / cm	*Error / cm*	*Measured wave height / cm*	*Error / cm*
50	15	2.893	1.041	2.888	0.813
	25	2.870	1.078	3.047	0.927
100	15	3.335	1.085	3.567	0.977
	25	3.369	1.018	3.634	0.980
150	15	4.013	1.200	4.213	0.999
	25	4.061	1.083	4.294	0.999
200	15	4.848	1.133	4.823	1.030
	25	4.773	1.159	4.918	1.060

A spectral analysis was conducted on the wave probe time traces using a fast Fourier transform to yield the frequency spectrum. The frequency spectrum for all of the runs for the two hulls can be found in Figure D.4, with the peak frequencies summarised in Figure 4.21.

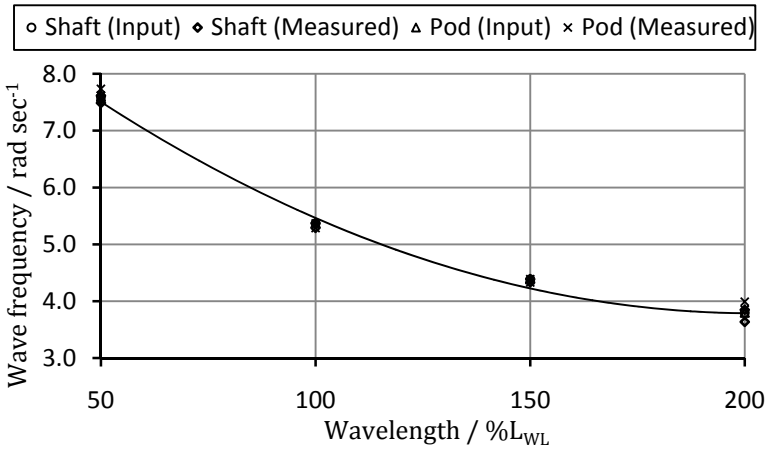

Figure 4.21 – Comparison of generated wave frequency to requested wave frequency

The measured wave frequencies are very close to those requested with the maximum deviation from those requested being 4.4% although most are typically within 2% of the requested value.

5. Sail System Design

5.1 Initial design

5.1.1 Concepts review

The basic concept for the sail system is to design a sail plan that can provide a substantial amount of thrust reduction at the design speeds of 15 and 25 knots. To design such a system, the requirements need to be outlined first. A case design study on wind-assisted cargo ships [Smulders (1985)] is taken as a guide to identify the key features that an efficient wind propulsion system should include :

- a 10% thrust reduction at 15 knots and 3% at 25knots;
- guaranteed stability; maximum heeling of five degrees;
- no interference with loading and unloading;
- strength standards maintained;
- adequate profitability;
- high reliability and low maintenance;
- no restrictions on design requirements of the ship in other respects.

Typical sail systems

Based on the design requirements an investigation of existing typical and innovative sail systems was undertaken. Typical sail rigs are illustrated along with their aerodynamic parameters in Table 5.1.

Table 5.1 - Typical aerodynamic parameters of some basic rig types. [Schenzle (1985)]

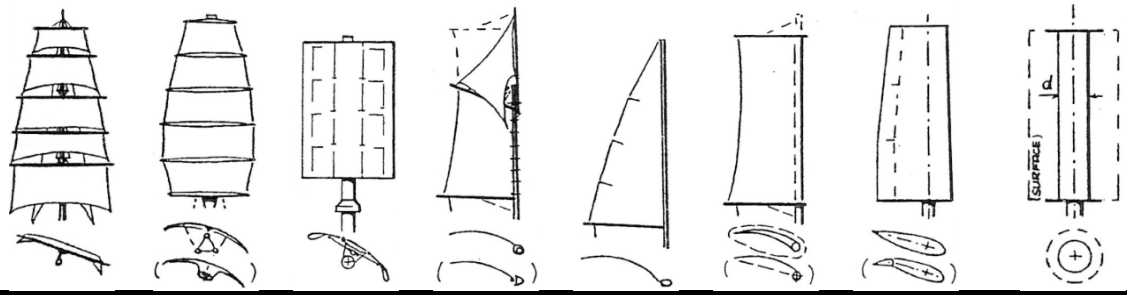

	TS	*MS(DS)*	*RS*	*TG(MS)*	*BM*	*SW(MR)*	*WS(WF)*	*FR*
Rig type	Traditional Square Rig	Modern Square (DYNA)	Rigid Square Rig	Traditional Gaff (MOD.G.)	Bermuda Mainsl.	Sail Wing (Mastrol)	Wing Sail (TE. FLAP)	Flettner Rotor (Surface)
C_{Do}	0.13	0.1 (0.07)	0.10	0.10 (0.07)	0.08	0.05 (0.06)	0.02	0.6 (0.2)
C_{D1}	0.65	0.46 (0.43)	0.58	0.35 (0.37-0.27)	0.28-0.23	0.36-0.26	0.27-0.17 (0.65-0.45)	4.0-5.6 (1.3-3.2)
C_{CM}	0.9	1.5	1.5	1.1 (1.2-1.5)	1.0-1.3	1.7 (1.6)	1.1-1.4 (1.8-2.0)	7.0-10.0 (2.2-3.2)
FR_E	0.5 $\approx FR_{SING}$	2.0 $\approx FR_{GEOM}$	1.5 $\approx FR_{GEOM}$	1.6 (2-3) $\approx FR_{SING}$	2-3 $\approx \frac{2}{3}FR_{GEOM}$	2-3 $\approx FR_{GEOM}$	2-3 $\approx FR_{GEOM}$	6-9 (2-3) $\approx FR_{GEOM}{}^{+(1-3)}$

Among the rig systems considered, 'Sail Wing' and 'Wing Sail with trailing edge flap' show the highest maximum lift but the former has lower drag at maximum lift resulting in greater lift-drag ratio. However the two dimensional section data, shown in Table 5.2 together with lift-drag ratio trends summarise the different characteristics. The 'Wing Sail with plain flap' shows a maximum lift coefficient of 2.0 and drag coefficient at maximum lift of 0.051 which is significantly smaller than those values seen in Table 5.1.

Table 5.2 - Sail rig aerodynamic performance, 2-D section data [Bergeson & Greenwald (1985)]

Rig type	C_{D1}	C_{CM}	C_{Do}
Stayed Fore and Aft	1.5	0.091	0.092
Unstayed Cat	1.5	0.084	0.063
Rigid Square	1.5	0.122	0.107
Sail Wing	1.6	0.035	0.075
Wing Sail (no flap)	1.0	0.037	0.022
(plain flap)	2.0	0.051	0.011
Flettner Rotor	10.0	--	0.113

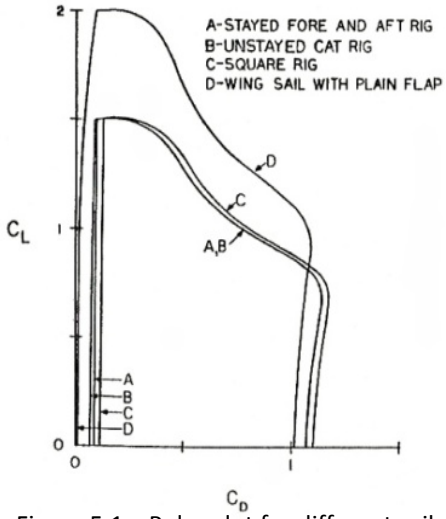

Figure 5.1 – Polar plot for different sail rig designs

Through investigation two design candidates, Sail Wing and Wing Sail are chosen based on their superior drag-lift ratio performance. The Sail Wing can be improved with the aid of a slat forward of the leading edge [Fujiwara *et al.* (2003)]. Since these systems have mainly been used for general cargo ships with speed up to 15 knots it is necessary to study more innovative and efficient systems for reasonable reduction at high speed.

Innovative sail systems

In recent years, there has been an increasing interest in kite assisted propulsion such as the *SkySails system*. The basic idea of this system, as depicted in Figure E.1, is to use a large kite to generate thrust with minimum heeling force using more favourable high altitude wind conditions. The company claims that savings of 10 to 35% in annual fuel consumption are possible, and that upwind sailing is possible from 50 degrees true wind angle. Other major advantages of this system claimed by the company are the flexibility in operation due to the launch and recovery system and a simple installation process. However, limits on the operation of kites near the shore or when approaching the port of call may arise in the near future, as demonstrated on 15th September 2009, when a near miss incident occurred with a helicopter in the southern North Sea. Due to the high service speed of the feeder and resulting low average apparent wind angles (less than 50 degrees), it was decided not to consider kites further.

The NYK Super Eco Ship 2030 and *E/S Orcelle* concepts were also examined. Both designs feature technologies intended to improve the propulsion and cargo handling efficiency. In terms of wind propulsion the *NYK Super Eco Ship* concept is designed for downwind sailing, as declared by the company, and uses a rigid wing system with a folding mechanism and solar panels. It is interesting that both the *Eco Ship* and *Skysails* concepts have a foldable sail mechanism which may be applicable to the fast feeder concept however there is lack of the sail system description. These concept designs are illustrated in Figure E.2.

Finally, the *Multi-wing* system designed by Walker Wing Sail System Ltd. (see Figure 5.2) was investigated. The designer of this system claims a maximum thrust coefficient above 3.0 whereas that of soft sail is only 2.0 [Walker (1985)]; Nautical Innovation Services undertook an economic evaluation of *Wing Sail* and *Multi-wing* System on cargo ships and the analysis concluded that a *Multi-wing* system produces twice as much power per unit sail area than a wing sail at an average wind speed of 15 knots [Smulders (1985)].

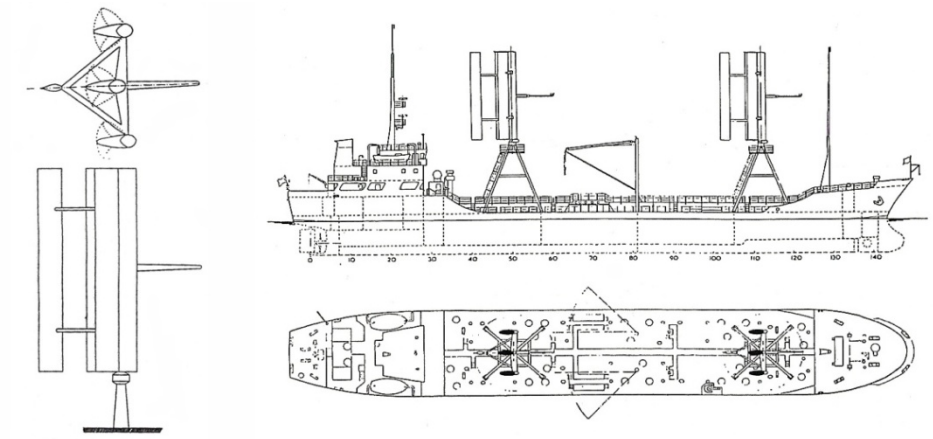

Figure 5.2 – Multi-wing system and general arrangement of cargo ship [Walker (1985)]

Since the sail design is to be optimised for upwind sailing due to the high operational speed a foldable *Multi-wing system* is suitable for the wind propulsion system as it allows retraction during stormy weather and cargo handling. This type of system generally has smaller overall dimensions compared to single wing system therefore preventing excessive height of the installation. In this project a conventional NACA section for the wings was used when assessing performance of different wing configuration cases, also avoiding patent right issue of *Walker Wing Sail*. The following sections will discuss the sizing of the sailplan and the choice of the wing section.

5.1.2 Design

Target sail area

The initial design began with an estimation of the sail area required to give the desired thrust reduction. At the preliminary design stage an average propulsive force per sail area is used based on data provided by Schenzle (1985). Since the data range is 10 to 15 knots, linear extrapolation is applied to obtain data up to 30 knots. Based on the extrapolated data (Figure E.3), the sail area required for the thrust reduction requirement is calculated at different speeds using the hull resistance calculation from Section 4.1.5. The results are summarised in Table 5.3, giving a total required sail area of 945 square metres at 25 knots ship speed.

Table 5.3 – Total sail area estimation

V_S / knots	Required P_B / kW	Required P_E / kW	Thrust reduction / %	P_E from wind / kW	Total sail area / m^{-2}	Hull V_S/ knots	Hull P_D / MW
5	189.00	157.44	100	157.44	1181.07	5.25	0.189
10	1030.00	857.99	27	231.66	914.56	10	1.03
15	4160.00	3465.28	10	346.53	928.28	15	4.16
20	11300.00	9412.90	5	470.65	954.07	20.25	11.3
25	23200.00	19325.60	3	579.77	945.33	24.75	23.2
30	40089.60	33394.64	2	667.89	910.80	--	--

Structural considerations

The maximum bending moment is estimated from the assumed maximum lift coefficient for a two dimensional wing section with flap, obtained from Table 5.1. This is then used in a simple beam analysis of a mast structure attached to the deck to determine the dimensions of the mast, deflection and maximum stresses, in order to identify any relevant constraints. Prior to this analysis the extrapolated driving force was used for the calculation (Appendix E.2).

Table 5.4 – Mast and main stock bending moment, deflection and maximum stress using a lift coefficient of 2.2

	Wind speed / knots	*Max. bending moment / MNm*	*Max. stress / MNm^{-2}*	*Max. deflection / mm*	*% Max / Yield stress*
Mast	30	1.62	8.13	0.073	5.8
	70	8.82	44.27	0.395	31.6
Main	30	0.51	30.00	0.090	21.4
stock	70	0.84	163.34	0.500	116.7

Table 5.4 shows the maximum deflection of the mast to be 0.395 metres and maximum stress of 31.6% of lower yield stress limit of 5083 Aluminium alloy at 70 knot wind speed. A similar analysis is carried out for the main wing stock assuming all wind loading is transferred to the stock. Using pinned-pinned beam with uniformly distributed load, the estimated deflection and maximum stress at a wind speed of 70 knots are 2.5 metres and 116.7% of lower yield stress limit respectively. This shows that the mast provides good structural rigidity and strength but the wing structure requires stocks with higher strength and additional stiffeners. The dimensions can be seen in Table E.1.

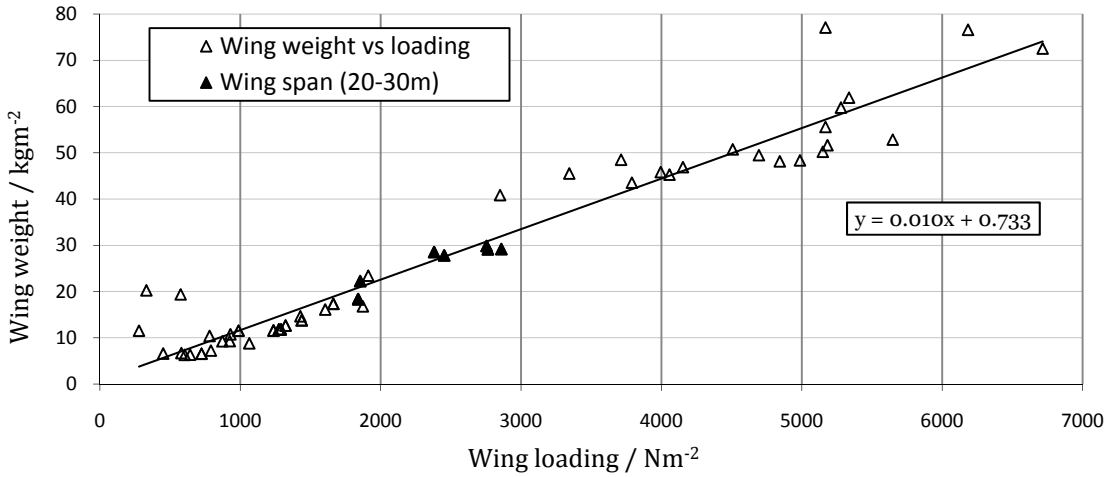

Figure 5.3 – Aluminium aircraft wing loading against wing weight per unit area

To estimate the weight of the wing, a database of 61 different types of aircraft wing is taken as reference [Svoboda (1999)]; the wing weight of seven regional aircraft with 20 to 30 metre wing span is used; the average of these, 26.44 kgm^{-2}, results in a single wing weight of 4.1 tonnes. The averaged wing loading of these structures is equivalent to the wing loading at 90 knots wind speed for the *Multi-wing system.* However as the sail wing has a much simpler structure and additional structure on the top, this wing weight can be reduced. For further analysis total wing weight of 10 tonnes was assumed.

Dimensional constraints and sail stowage

To avoid issues with cargo handling and to improve the safety and reliability of the sail system concept, the rig had to be designed to be stored either below the deck, or folded on deck so that the maximum height is below the level of the top of the container stacks when not in operation. Alternative means of achieving this were considered as below.

- A fixed rigid mast with:
    - the mast fixed at double bottom level and the sails able to retract fully by being lowered down around the mast into the hold;
    - the mast fixed at deck level and the sails telescoped / folded onto deck when not in operation;
    - the sails made of a soft material that can be easily lowered and stored on deck.
- A rigid mast which is jackable where:
    - the jacking system is located at deck level and the mast is lowered into a cavity below the jacking system and the sails are telescoped / folded onto the deck when not in operation;
    - the jacking system is located at mid depth in the hold and the sail and mast are lowered and stored in the hold.
- The mast and sails are both capable of folding / telescoping.

Jacking systems are commonplace in the offshore industry and fall into three categories, summarised below.

- Rack and pinion - these are used on drilling rigs and can have a very high capacity (say 10,000 tonnes each), are capable of continuous running, are relatively fast, but are very expensive.
- Linear jack - these use holes in the legs and linear jacks that move a pin in the legs, and then the leg is locked, the pin is removed, the jack retracted and then the process starts again. This is a slow, cheaper system used on 'lower grade' drilling jack ups and maintenance/production/accommodation jack-ups which cannot justify the high cost of a rack and pinion unit.
- Wires - these use deck mounted winches and wires and sheaves to raise the deck against the legs. This is a quick and cheap system, used on coastal jack-ups with low loads.

The sail system under consideration is not a substantial structure compared to offshore rigs and thus the most realistic system for the hoisting of the sails will be a wire system. A benefit of storing the sails between container stacks is that during cargo operations, the container cell guides can be employed as a ‘cover’ to protect the sails from damage during cargo operations. More consideration of the folding of the sails shall be given, along with consideration of the necessary ship structure required to support the sail system and the vessel layout (Section 7.2.3 and Appendix M respectively).

In addition to the hoisting system there will have to be some form of hydraulics in order to operate the sails and orientate them with the prevailing wind direction. Space within the vessel close to the sail location will need to be allocated for these machinery requirements.

The design of the connection between the sail and the ship should be such to avoid excessive loads on the deck; another issue that often arises during the development of wind assisted ships [Tanneberger (2009)]. This shall be considered later in the report with a finite element analysis investigation (Section 0).

Assuming the sails will be stowed within the hold, dimensional constraints for the span and chord of the wing-sail can be defined. From the preliminary dimensions and deck arrangement, the clearance between the double bottom and the top of the containers is estimated as 30 metres. The sum of the chord length of the wing is then limited to the moulded beam of 26.7 metres.

Geometry of wing sail

The taper ratio is an important factor to consider when designing a wing sail as it affects the load distribution as well as the induced drag. In the development of this rig, only the rectangular planform was considered due to the method of manufacture of the wings (Section 5.2) and the added cost that producing tapered wings with flaps would have incurred. The aspect ratio (AR) is another geometrical proportion which must be considered when designing a sailplan; this ratio affects the efficiency of any wing or soft sail and controls the magnitude of the lift coefficient and the induced drag due to the lift. A high aspect ratio increases the total aerodynamic force coefficient when sailing close to the wind [Marchaj (2003)] whilst it reduces the performance when running downwind or when the foils operate in the stalled condition. The aspect ratio is defined as

$$\mathrm{AR} = \frac{\text{span length}}{\text{chord length}}. \tag{5.1}$$

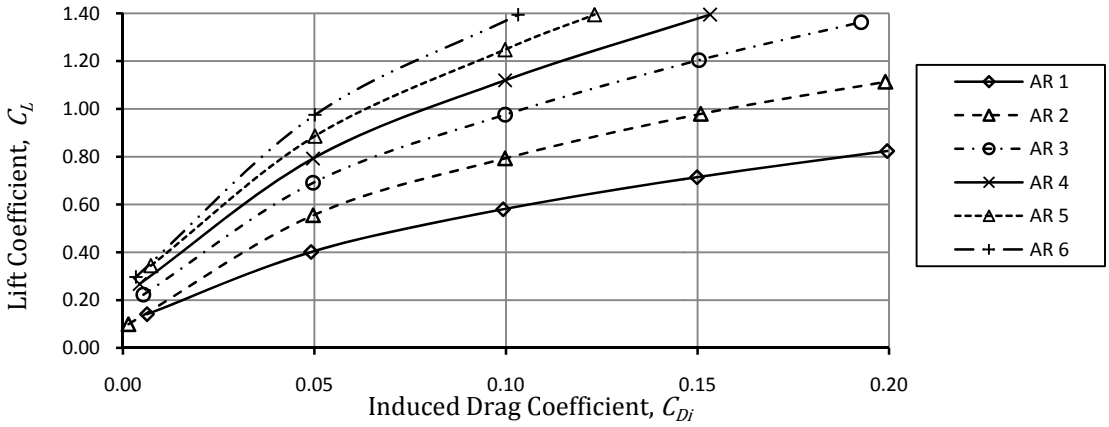

Figure 5.4 – Variation of Induced Drag Coefficient with aspect ratio

Early prototypes of rigid wing sails had a relatively low aspect ratio of between two and three [Bergeson & Greenwald (1985)], in the attempt to maintain good downwind characteristics. The fast feeder concept has to maintain a service speed of 25 knots; therefore the downwind performance is less relevant as the apparent wind speed will be lower. The advantages in selecting a high aspect ratio are clear; however, an initial estimate of the weight and dimensions of the supporting structure had to be addressed to identify any structural constraints. The ratio was set to four, enough to ensure low drag characteristics on the relevant courses.

The dimensional constraints, combined with the choice of aspect ratio and target sail area define the wing dimensions as shown below in Table 5.5.

Table 5.5 – *Multi-wing system* dimensions

No. of system	2
No. of wings per system	3
Height / m	26.5
Wing span / m	25
Chord / m	6.25
Aspect Ratio	4
Taper Ratio	1
Total sail area / m^2	937.5
Width / m	13.86
Extreme width / m	21
Wing weight / tonnes	10
Linkage structure weight / tonnes	2

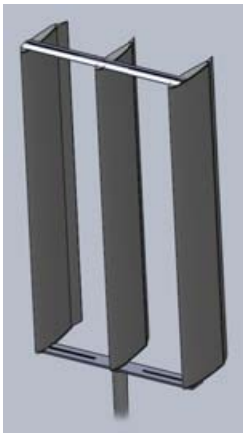

Figure 5.5 – *Multi-wing* system

Wing Section Design

The commercial code *X-Foil* is used to create a database of NACA four digits section at various Reynolds numbers which cover the range of full scale apparent wind speeds. Initially no flaps are included and the polar plots are examined by looking at the:

- maximum lift coefficient for beam reach performance;
- best lift to drag ratio at (L_{SAIL}/D_{SAIL}) for windward sailing;
- lift coefficient after stall accounting for incidence changes along the span due to rolling of the ship;
- thickness to chord ratio for structural integrity and mast allowance.

NACA 0014, 0015 and 0016 sections are selected as candidates. For the addition of the trailing edge flap, hinge points of 70%, 75% and 80% of the chord length were compared on the same basis as above. The plots showed that the maximum L/D ratio would be achieved by the 0015 section with the flap deflected at 22.5 degrees, whilst the maximum lift for beam winds is achieved with a deflection of 45 degrees.

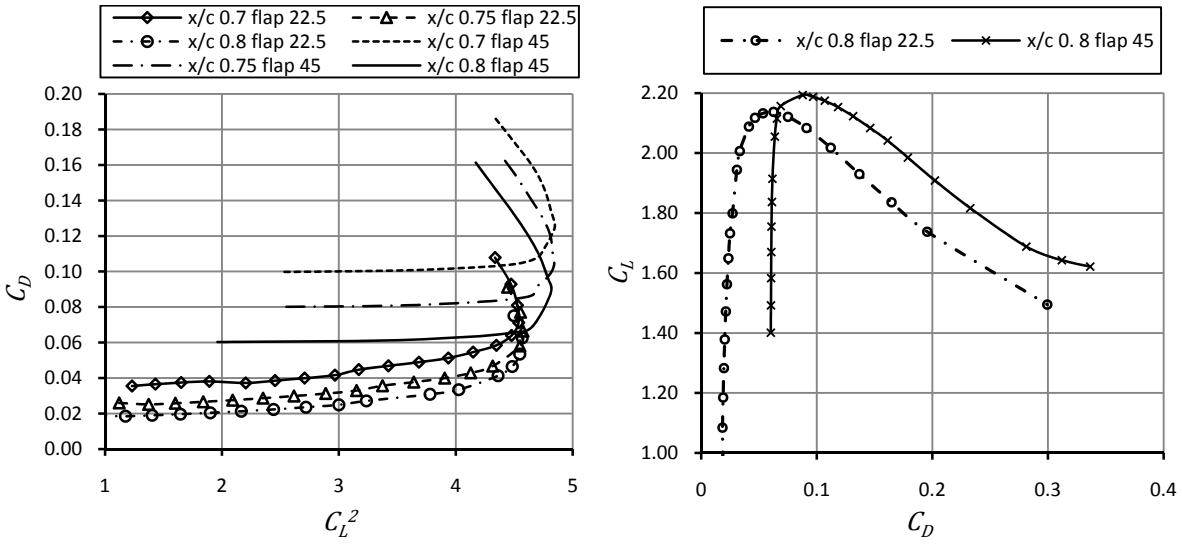

Figure 5.6 – Comparison of drag coefficient against lift coefficient squared for different flap chord positions (left) and; NACA 0015 polar plot for flap angles 22.5 and 45 degrees (right)

Wind Data

Statistical data for wind strength was obtained from NOAA Satellite and Information Service (2009). The sea wind data is processed for an elevation of ten metres above the sea surface by blending data from up to six satellites to reduce the sub-sampling aliases and random errors. The data is complete from 1987 to the present day with a time resolution varying from six-hourly, daily to monthly, with data on a 0.25 degree grid which gives 1,036,800 data items per time snapshot.

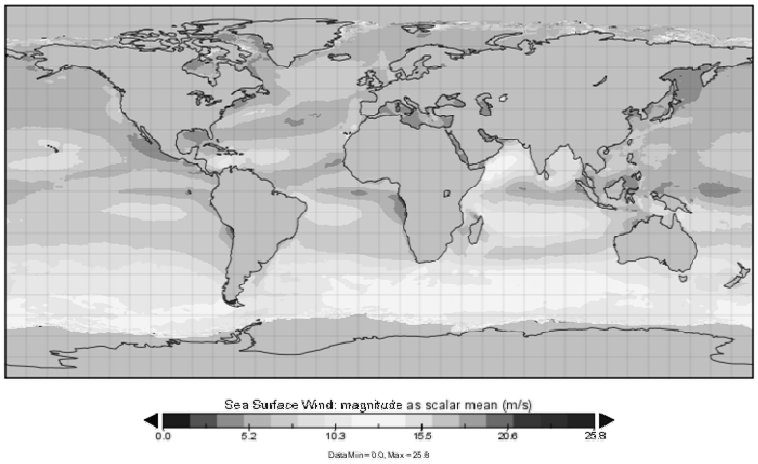

Figure 5.7 – Sea surface wind for 2002: magnitude as scalar mean [NOAA Satellite and Information Service (2009)]

Monthly mean values of easterly and northerly components of speed for the year 2008 were taken and processed to obtain absolute wind speed and direction. Scatter diagrams of average speed and direction were then produced for worldwide and region specific wind statistics on a month by month basis and a yearly cumulative total. A summary of yearly wind strength for the Caribbean showing a clear prevailing wind direction is shown in Figure 5.8. Equivalent plots showing the variation of wind strength with direction for the whole world, South East Asia and the North Atlantic are given in Appendix E.

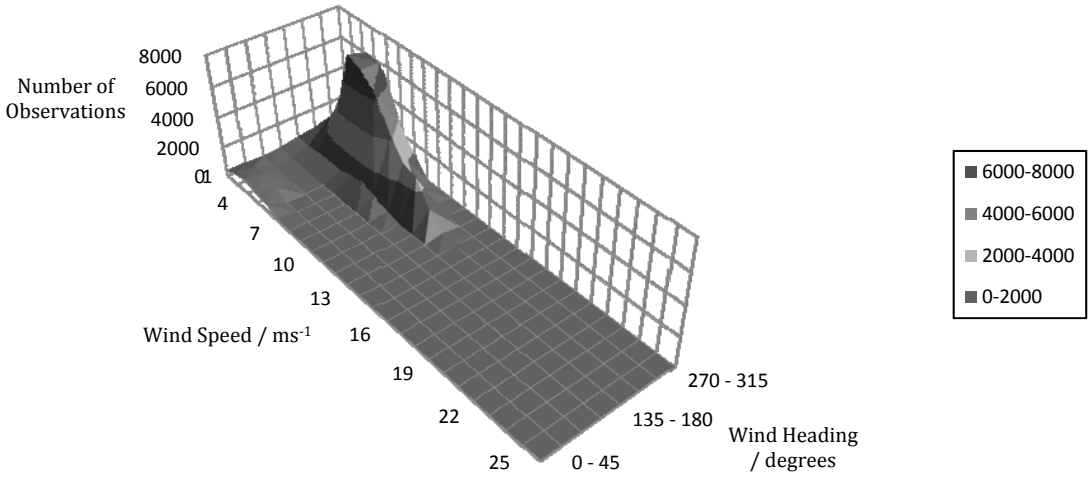

Figure 5.8 – Wind by strength and direction for the Caribbean (annual)

The yearly mean wind speed and standard deviation for the regions being considered and the whole world is given in Table 5.6.

Table 5.6 – Mean wind speed by region

Region	*Mean wind speed / m/s*	*Standard deviation*
Caribbean	5.962	4.652
South East Asia	5.802	4.647
North Atlantic[10]	8.827	6.572
Whole World	6.108	4.8525

[10] Based on sea areas 23, 24, 25 and 16 only [NOAA Satellite and Information Service (2009)].

5.1.3 Theoretical performance

It is necessary to make an evaluation of the sailing performance at an early stage of the project as it enables the designer to quantify the decrease in brake power that can be achieved to maintain the feeder at a constant speed. Another important aspect that needs to be addressed is the effect that the *Multi wing* system has on the dynamics of the vessel whilst at sea. A Performance Prediction Program (PPP) was created in *FORTRAN90*; the underlying principle at the base of the calculations is that under steady sailing conditions, the horizontal and vertical forces and moments acting on hull and sails are balanced. The code uses the aerodynamic data obtained from *X-Foil* to calculate the aerodynamic forces generated by the sails. The angle of heel can be also estimated using the initial hydrostatic data, whilst heave and pitch are neglected in this analysis as less significant. The thrust reduction is computed combining the hydrodynamic drag data from Section 4.1. In Section 6.1.1, the program will be modified to assess the vessel performance using the experimental results.

Aerodynamic Index

The code consist of three main loops for ship speed V_s , true wind speed V_T and true wind direction γ; the apparent wind speed V_A and the apparent wind angle β are calculated as shown in Appendix E. The lift coefficient is taken as, $C_L = 2.1$ and the base drag coefficient is taken from the *X-Foil* database as $CD_0 = 0.019$. The aerodynamic coefficients are then transformed in to the ship axis coefficients $C_X \; and \; C_Y$ to obtain the forward thrust and the heeling force. At this stage of the project only empirical relationships are available to estimate the leeway angle; these are based on hydrodynamic derivatives of old hull forms with fixed rudders and hence cannot be applied to the fast feeder. The formula used to calculate the leeway angle is taken from Schenzle (1985) and is shown in Appendix E 3. In Section 6.1.1, towing tank results will be used to compute the leeway angle to a higher degree of accuracy.

Thrust Reduction

The thrust generated by the sails in the direction of motion can be regarded as an effective reduction in resistance. Since the speed of the ship and the wind speed are known at every time, it is possible to calculate the reduction in brake power requirement, given that the total hydrodynamic resistance of the hull is also known. Table 5.7 presents the typical thrust reductions, heel and leeway for a range of true wind angles. The thrust reduction is calculated as,

$$TR = \frac{Thrust_{no\ sails} - Thrust_{with\ sails}}{Thrust_{no\ sails}}. \qquad (5.2)$$

Table 5.7 – Theoretical thrust benefit prediction (V_S=15 knots, V_T=16.5 knots)

γ / deg	V_A/ knots	β / deg	φ / deg	ψ / deg	*Thrust reduction / %*	
					Hull A	*Hull B*
20	17	11	2.50	0.008	0.0	0.0
40	16.2	22	2.26	0.007	7.5	7.3
60	14.9	33	1.85	0.006	16.4	16.0
80	13.2	45	1.34	0.004	20.3	19.8
100	11.2	57	0.83	0.003	19.2	18.7
120	8.7	70	0.41	0.001	14.3	13.9
140	6.1	86	0.14	0	7.8	7.6
160	3.5	110	0.01	0	2.4	2.3
180	1.8	180	0	0	0.1	0.1
			average:		9.8	9.5

The estimate of the thrust reduction is done assuming an average wind speed of 16.5 knots, as the wind data presented in Section 5.1.2 was not yet available. The reductions are then averaged over the range of true wind angles γ as shown in Table 5.8. One limitation to this assessment is the lack of any drag data for the mast and the supporting structure; also the ship resistance used in the calculation does not include additional resistance due to air, waves, side force and heel. On the other hand the sailing point is kept fixed for all headings, whilst a gain in thrust would be obtained by optimising the sail incidence for each course (see Section 6.1.1).

Table 5.8 – Initial thrust reduction prediction

Ship speed / knots	*Thrust reduction / %*
10	27
15	10
20	5
25	3

5.2 Wind tunnel testing

5.2.1 Introduction

The preliminary estimate of the performance of this *Multi-wing* system relies on the accuracy of the aerodynamic coefficients. Testing a model of the rig in the wind tunnel enables the verification of the predictions and to assess the potential of this type of rig by optimising the spacing between the wings and the stagger angle. The designers believe that an increase in lift coefficient can be achieved thanks to the slot effect which should increase the efficiency of the upwind wings [Chéret (2000)]. Testing the model also allows the assessment of the magnitude of the windage for this particular structure hence increasing the fidelity of the final prediction. A recent study on the feasibility of a sail assisted bulk carrier [Fujiwara *et al.* (2005)], suggested that sail-sail and sail-hull interactions need to be investigated when designing wind assisted ships. The aim of this is to assess the change in performance due to the surrounding environment, thus improving the validity of the results. Due to the dimensional constraints, outlined in Section 5.2.2, the rig has been tested in isolation and successively in the presence of containers; the aim of this is to investigate the potential change in performance caused by the addition of a bluff body upstream, and a reflection plane close to the base of the sails. A computational fluid dynamics (CFD) study will provide the required sail-sail interactions, assessing the shedding effect between the two rigs when sailing to windward and optimising the angle of attack (AoA) of the individual wings. (see Section 5.3)

5.2.2 Model design

A scaled model of the *Multi-wing system* is to be designed and tested in the wind tunnel. A number of considerations need to be made. Firstly, the model must be geometrically identical. Since the geometry is simple it is not an issue. Secondly to determine the scale the constraints derived from the wind tunnel size and the dynamometer capacity need to be investigated. The initial idea was to design two rigs and investigate the interaction between them, but due to insufficient budget, complexity of testing and time constraints a single rig of larger scale has been designed. The model scale is determined based on the following constraints [Claughton & Campbell (1994)]:

- the wind tunnel size - low speed section: 4.6 metres wide by 3.7 metres high by 3.7 metres long;
- a maximum model height of two metres*;*
- a maximum test wind speed of eight metres per second;
- individual dynamometer limit of 1000 N*;*

- the need to adjust the flaps manually - maximum height of 2.3 metres*;*
- model strength;
- model weight.

The rationale behind the choice of the model scale is to maximise the dimensions of the model under the constraints outlined above, so that the tests are performed at a higher Reynolds number, thus increasing the quality of the results. The scale was final set to 1:15.To minimise the weight of the wing sections and flaps, low density foam is used for the manufacture, whilst the rest structure is made from aluminium. When designing the mast, the height was maximised in order to have enough clearance to fit the containers below the sails. To avoid excessive heeling force due to the higher centre of effort, the mast was limited to 0.4 metres. The weight of the system is calculated from the volume and density of the components. This weight produces approximately equally distributed vertical force of 76.62 N on each dynamometer block.

Table 5.9 – Wind tunnel model weight estimation

Item	*Weight / kg*	*Number*	*Total weight / kg*
Wing	0.766	3	2.30
Stock A (main)	1.283	3	3.85
Stock B (flap)	0.499	3	1.50
Wing plate	0.245	6	1.47
Top bar	1.285	1	1.28
Bottom bar	2.677	1	2.68
Mast	3.193	1	3.19
Base	3.513	1	3.51
Mast fitting ring	0.373	1	0.37
Transverse fitting rod	0.936	1	0.94
Longitudinal fitting rod	1.338	1	1.34
Mast key	0.500	1	0.50
Bolts, screws	0.500	1	0.50
Overall total weight			23.43

Using the maximum lift coefficient of 2.10 obtained from *X-Foil,* predictions of the resultant maximum vertical force on the side dynamometers due to moment produced by lift is calculated. This is shown in Appendix F.1, where the maximum resultant force on an individual dynamometer remains under the maximum allowance for wind speeds up to nine metres per second.

Finally, the strength of the model is evaluated. Since the geometry of the components is simple, Euler beam theory can be applied (see Appendix F.1). For Stock A and B (Appendix F.2) the maximum deflections are 4.2 mm and 40.0 mm respectively, while the mast deflection is negligible. It is noticed that Stock B has large maximum deflection. However once assembled, tension will be acting on the stock so the additional support structure at midspan is considered sufficient to restrain this deflection. The maximum stresses are considerably lower than the yield stress and so plastic deformation is not expected. The results are summarised in Appendix F.1. For the model manufacturing drawings BSI (2007) are used (F.2). The overall view of the assembled model is illustrated in Figure 5.9.

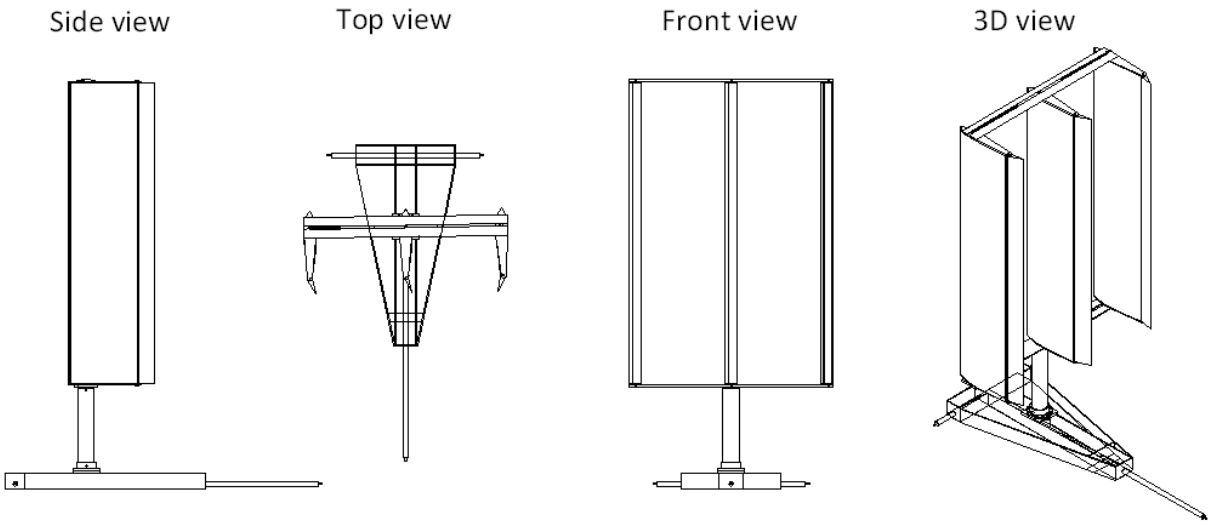

Figure 5.9 – Wind tunnel model assembled view

5.2.3 Model manufacture

Wings

The first components to be manufactured were the wings. It was decided to use Styrofoam, low density foam used for insulation and readily available from local suppliers. This choice was dictated by the low cost of the raw material, the simplicity of the manufacture using the EDMC hot wire cutter (Figure F.1) and the restrained weight. DXF drawings of the main section and the flaps were imported to the numerical cutter; due to the limited length of the wire, the sections had to be cut in three parts and then joined together with epoxy-bonding. A sample section was created to verify the cutter's tolerance for cutting the internal features of the section. To achieve a good surface finish, an essential feature to ensure low skin friction drag characteristics, a high-build primer and non-vinilic paint were applied on the trial wing, but both had the effect of corroding the surface. The alternative solution of covering the entire surface with a thin plastic cover was discarded due to the presence of the trailing edge flap and the corresponding gap which would exist also at full scale. Wet and dry paper was eventually used to smooth the surface. To cut the circular slot for the stocks the hot wire cutter cut through the leading edge along the chord until the pivot point at 20% of the chord. Due to the high sensitivity of this material, inert body filler was used to fill the gap, then wet and dry paper was used to remove the excess filler.

Structure

The supporting structure of the wings was manufactured in the EDMC using CNC milling machines (Figure F.1) which operate from a file input converted from *CAD* software. The aluminium base structure, supporting the mast and used to connect the dynamometers bar, was welded by the EDMC using the Tungsten Inert Gas (TIG) technique (Figure F.2). The mast and transverse bars were assembled together using standard fasteners. A view of the final assembled model is shown in Figure 5.10.

= 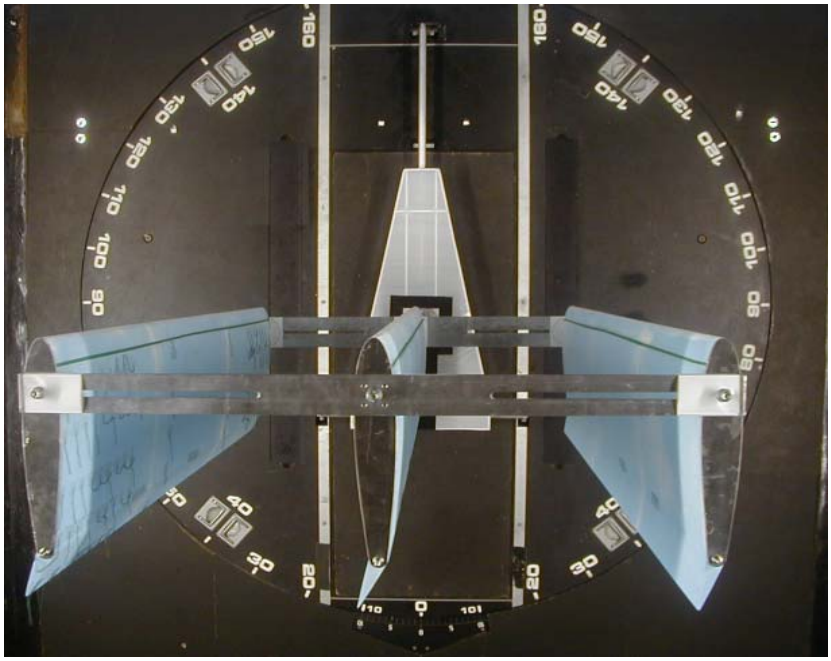

Figure 5.10 – Model assembled in the wind tunnel

Flow Stimulation

The maximum speed achievable in the low speed section of the wind is this eight metres per second, implying a test Reynolds number of 230,000 which is too low to stimulate the transition of the flow from laminar to turbulent at the same location that would occur operating at the full scale Reynolds number. The scope of inducing flow transition affects the accuracy of the data, in particular the magnitude of lift and drag. There are different methods to trip the flow that are used in common practice, the one chosen here for its simplicity and repeatability, is the carbondurum grit strip. *X-Foil* is used to identify the natural transition point of the NACA-0015 at the full scale Reynolds number. At an AoA of five degrees the transition point is found to be at 11% of the chord decreasing to 2% at 15 degrees. The location of the grit strip is therefore fixed at 10% of the chord from the leading edge and the width at five millimetres, as suggested in Barlow *et al.* (1999). The method used here to calculate of the size of the grit is given by Braslow & Harris (1966):

$$h = \frac{12\ ks}{R_{eft}} \tag{5.3}$$

where R_{eft} is the Reynolds number per foot based on the free stream velocity; k is a constant based on the grit roughness. This is also a function of the laminar Reynolds number based on the free stream velocity and the distance from the trip strip to the leading edge. The height h is derived as 0.0075 inches which converts to grit number 80.

Flow Visualisation

To verify the efficiency of the grit an attempt was made to use paraffin; in the turbulent flow, the oil applied after the strip would have evaporated quicker than before the strip. However due to the porosity of the foam this method could not be applied as the oil soaked in too deeply to evaporate in a reasonable time. To visualize the flow wool tufts were used instead; a smoke machine was prepared to visualize the flow characteristic before and after the addition of the containers, but on the day of the testing, it was found unusable due to a problem with the oil pump.

5.2.4 Experimental setup

Measurement system

The measurement system consists of the control room equipment (Figure 5.11) and the dynamometer mounted in the wind tunnel (Figure 5.12).

- Amplifier (1);
- Filter (2);
- Analogue to digital card (3);
- Acquisition software (*LASSO*) (4);
- Roof camera and remote control system (5);
- Laptop for temperature-pressure acquisition;
- Side video camera.

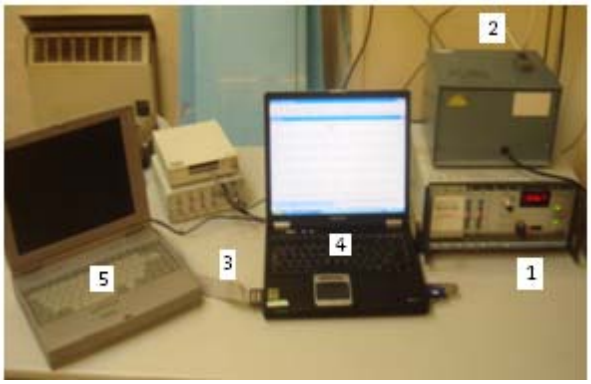

Figure 5.11 – Experimental setup in wind tunnel control room

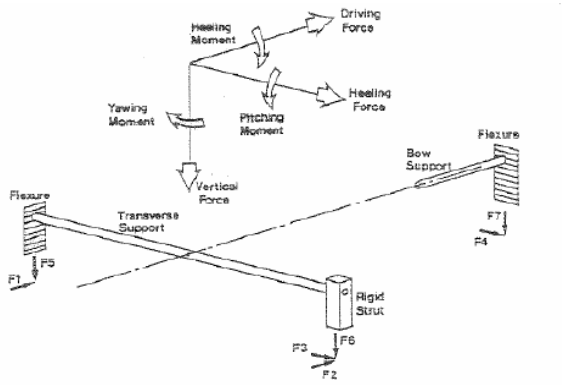

Six Components Dynamometer:

- Channel 1: Drive force starboard;
- Channel 2: Heeling force port;
- Channel 3: Heeling force forward;
- Channel 4: Vertical force forward;
- Channel 5: Vertical force starboard;
- Channel 6: Vertical force port.

Figure 5.12 – Six component dynamometer in the low speed wind tunnel [Campbell (2009)]

Calibration

The acquisition software used for this experiment is the *LASSO* suite provided by *WUMTIA*. This allows user defined channels to be created in which the signals are processed to give the desired output; this also allows corrections to be made for the interactions between forces and moments in the dynamometer. Extensive calibration was necessary before the experiment began; this was done to avoid the necessity of repeating the calibration procedure in the successive days of testing, hence saving time. The procedure can be summarized as follows:

1. Mount calibration rig and position pulley at the drive force link;
2. Take zero reading;
3. Append one kilogram and acquire data;
4. Control measured value;
5. Repeat steps 3 and 4 up to a total of five kilos;
6. Remove 1 kilo, acquire again and compare with previous measurement;
7. Repeat step 6 for the remaining weights.

The rig is then positioned at the heeling force starboard link and the procedure is repeated. The first calibration showed an error of 1.9% for the drive force and 0.5% for the heeling force. The expressions for the user channel were hence modified to compensate for the error. In the second iteration the error was reduced to 0.5% and 0.1% respectively.

Test Matrix and Procedure

The original schedule for the testing was modified due to a delay in the manufacturing of the rig; the first day of testing was postponed to the 17th of February and the experiment could resume only on the 23rd of the same month. This gave plenty of time to improve the test matrix which was updated at the end of the first day.

Table 5.10 shows the final test matrix. Excluding the calibration, the total number of useful runs is 116; the remaining 59 runs are repetitions for zeroing errors and problems with the signal of two channels.

Table 5.10– Wind tunnel test matrix. Rig tested at a range of angles of attack up to stall

Day	Run description	No. of runs	Speed / ms^{-1}	Interaction
1	calibration	66	-	-
1	speed calibration	21	4,6,8	no
2	windage	5	8	no
2	Wing spacing - 100% chord length	21	8	no
2	Wing spacing - 70% chord length	15	8	no
2	Wing spacing - 50% chord length	19	8	no
2	Wing spacing - 110% chord length	15	8	no
3	Wing spacing - 110% chord length	15	8	yes
3	Wing spacing - 110% chord length	13	8	yes
3	Wing spacing - 110% chord length	10	8	yes
3	110% - 30 degrees stagger	11	8	yes
3	110% - 60 degrees stagger	10	8	yes
3	flat sail configuration	11	8	yes
3	windage	6	8	yes
3	single foil	3	8	no
	Total runs	241		

Wind tunnel layout for sail – hull interactions

The dimensional constraints derived by the large scale factor of the model, allowed covering only a part of the testing that would be required to achieve a complete sail-hull interaction experiment. It was decided to replicate the stack of containers using large cardboard boxes. Due to the mast height having to be limited because of the excessive heeling moment that would have generated, only the last three rows of containers could be simulated. The gap between the top of the boxes and the base of the sails replicates the full scale clearance of 2 metres; this value is based on the initial estimates of the full scale rig deflection. The headings that were simulated in the wind tunnel are based on the average apparent wind angles seen by the fast feeder sails at an advance speed of 15 and 25 knots, covering mainly reaching and broad reaching courses. Figure F.3 and Figure F.4 show the layout when simulating containers.

5.2.5 Wind tunnel post processing

Throughout the duration of the experiment it was possible to cover all the relevant configurations and additional runs that were scheduled, despite the time lost in calibrating the equipment and repeating some of the runs. The correction of the raw data to investigate the free-air performance of this *Multi-wing* system is

now addressed. The drive and heeling force of the supporting structure are subtracted from the measured data leaving the forces due to the wings only.

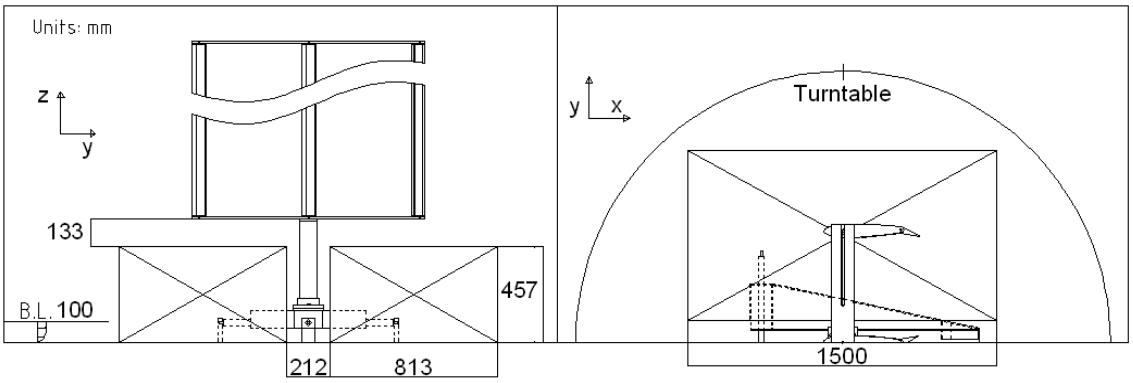

Figure 5.13 – Containers layout and dimensions for sail-hull interaction tests

This enables the data to be non-dimensionalised and to obtain the lift and drag coefficients of the wings which are then used for comparing the different configurations. The wing data must then be corrected to account for the closed environment of the wind tunnel and scale effects as both affect the forces measured.

Dynamometer misalignment

Figure 5.14 (left) shows an average error of between 3.5% and 18% between port and starboard tacks for the lift and drag respectively. The difference is marginal at moderate AoAs and increases towards the stall region. This kind of uncertainty can have multiple causes; such as a small misalignment of the dynamometer or surface defects due to the presence of the wool tufts only being on one side of the wings.

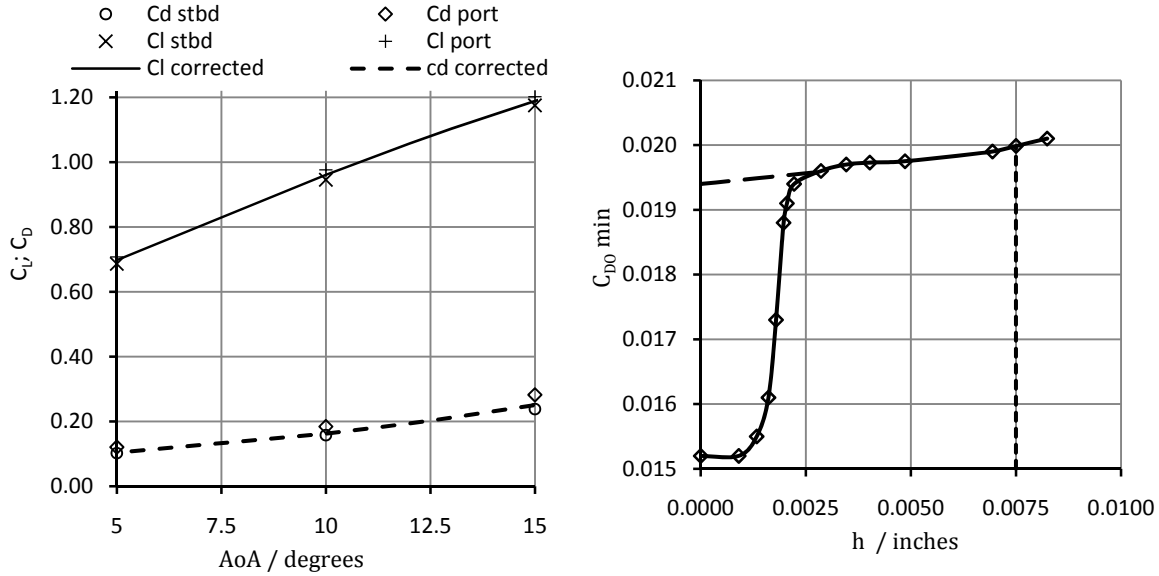

Figure 5.14 – Dynamometer misalignment from port and starboard tacks (left); and variation of base drag with grit size (right) [Braslow & Harris (1966)]

Grit drag

The addition of the grit strip will increase the base drag of the wing sails; at zero AoA, the drag of lifting surfaces is dominated by the skin friction, hence the increase in drag will be proportional to the roughness or the grit size. This increase can be corrected using published data on the variation of base drag coefficient with variable grit size [Braslow & Harris (1966)]. The curve in Figure 5.14 (right) shows an net increase in drag at a grit size of 0.003 inches; this demonstrates that no turbulent boundary layer has developed upstream of the

grit. After this point the rise in drag is lower and constant. The grit size used in this experiment is 0.007 inches and the difference in drag is obtained extrapolating the curve back to zero grit size, as shown by the dashed line. The correction is simply the difference from the drag at 0.0075 inches and the extrapolated zero grit size drag $\Delta C_{D0} = 0.01998 - 0.0194 = 0.0006$. The presence of the wool tufts would also contribute to increasing the roughness of the lifting surface, and therefore a correction should be applied; however no procedure was found in the literature to account for this added roughness. The 1.5 millimetre thick tufts were used in a sparse manner and only on the wing visible from the control room of the wind tunnel and from the cameras; therefore the effect on the wing sail performance should be limited.

Windage

To calculate the aerodynamic coefficients of the wing in isolation, the drive force and heeling force of the supporting structure alone is measured at 0, 5, 10 and 15 degrees to the wind direction. These values are then subtracted from the total forces measured with the wings; within the range covered. The data shows a linear trend, therefore linear interpolation is used at intermediate angles.

$$C_{D'} = \left[\left(Hf - W_{Hf}\right)\sin\beta - \left(Df - W_{Df}\right)cos\beta\right]\frac{\Lambda^2}{\rho g A \frac{q}{5^2}} \tag{5.4}$$

and

$$C_{L'} = \left[\left(Hf - W_{Hf}\right)\cos\beta + \left(Df - W_{Df}\right)sin\beta\right]\frac{\Lambda^2}{\rho g A \frac{q}{5^2}}. \tag{5.5}$$

Here A is the full scale sail area and q is the dynamic head in millimeters of water. The pitôt tube which measures the dynamic head is located in the high speed section of the wind tunnel, where the contraction in cross sectional area is five, therefore q must be corrected by ${C_A}^2$ as the head is proportional to V^2. The windage data can also be transformed into the wind axes system and non-dimensionalised with respect to the sail area. Thus the windage can be added to the forces due to the sails when assessing the different configurations with the Performance Prediction Program (PPP) (see Section 6.1.1).

Only the windage data from the interactions layout is presented in this section. Figure F.6 shows the windage data without the containers. As only a few angles were tested, the windage coefficients had to be extrapolated as shown by the dotted line in Figure 5.15 (left). A peak at 90 degrees apparent wind angle can be observed; this is readily explained if we observe Figure F.4. As the wind moves aft and forward of the beam the containers gradually shed the contribution of the base and mast until only the transverse bars and the top end of the mast contribute to the forces measured. Whilst a lot of work has been carried out to assess the scale effects of lifting surfaces, and standard procedures have been outlined, very little is known on scaling procedures of windage data. If more time had been available, the mast should have been removed to measure the forces due to the base alone; this would have allowed using the correct C_L and C_D for the mast in the PPP. It is important to notice that the model scale structure will be different from the full scale, as the mast would be larger, therefore the addition of the base may compensate for this difference.

Downwash correction

The component of induced flow in the lift direction at the model is changed due to the finite distance from the walls of the wind tunnel [Barlow et al (1999)]. Closed section tunnels, like the 15' x 12' low speed section at the University of Southampton tend to increase the incidence of the wings and the measured drag. Appendix F.5 shows the equations used to calculate this correction.

Solid blockage correction

Solid-body blockage is a function of the volume of the body and the cross sectional area. Continuity of mass flow through the channel requires increases in the flow velocities near the body compared with the velocities

in unconfined flow; the surface stresses are hence higher and the data needs to be corrected to account for this.

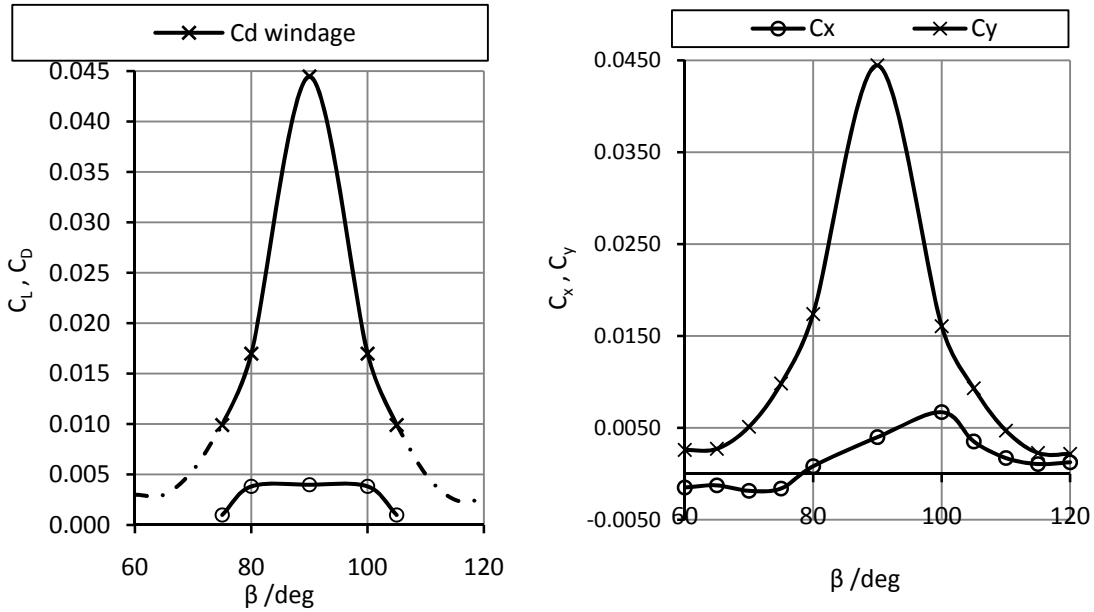

Figure 5.15 – Windage data: wind (left) and ship (right) axes coefficients of the supporting structure. Boundary corrections are applied

The Herriot formula is used to estimate the magnitude of the correction [Barlow *et al.* (1999)]. Table 5.11 summarizes the results; note that wind tunnel cross sectional area C, is taken as the geometric area minus the area of the boundary layer at a mean thickness of 0.1 metres.

Table 5.11 – Wind tunnel wake blockage correction

Item	*Wings*	*Mast*	*Boxes*
Blockage ratio %	2.2	0.5	4.0
Wings volume / m^3	0.0839	0.003	0.87
Wind tunnel area	16.1	-	-
Boundary layer thickness / m	0.1		
Boundary layer thickness area / m^2	1.48		
Jet area / m^2	14.62		
K_1	1.034	0.962	2.42
t_1	0.794	0.791	0.831
Solid blockage correction ε_s	0.00123	0.00004	0.0313

Appendix F.5 shows the calculation of K_1 and t_1 which are correction factors which relate the model geometry to the wind tunnel area (Figure F.7); the correction for the runs where no containers are used is very small, however the volume of the boxes has a larger effect despite the decrease in frontal area due to the boundary layer thickness; the volume of the base also does not contribute to the blockage correction as it remains embedded in the boundary layer. The blockage correction for the windage data is calculated using a simplified formula for unusual shapes according to Barlow *et al.* (1999), (see Appendix F.5).

Wake blockage correction

The rationale behind this correction is similar to the solid blockage, the walls of the section constrain the wake behind the wings thus causing an increase in drag; this correction is based on the drag measured after separation, C_{DS} and increases proportionally to the wake size [Campbell (2009)]. ε_{wb} is the function of the model body shape used to calculate this correction, Appendix F.5 shows its derivation which follows the procedure outlined in [ESDU (1980)].

Speed calibration runs

The choice of the scale has played a fundamental role in obtaining sensible results. The test Reynolds number always dictates the accuracy of the lift and drag data when testing lifting surfaces; to investigate the effects of varying Reynolds number (Figure 5.16) and to verify that the test Reynolds number is high enough to obtain good data, it was decided to test the rig at four, six and eight metres per second.

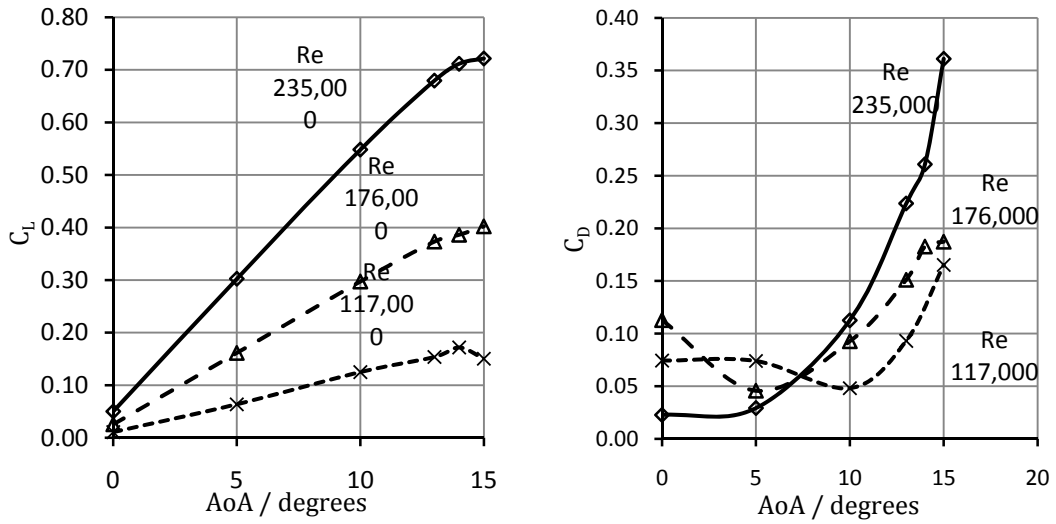

Figure 5.16 – Lift (left) and drag (right) curves with varying Reynolds number; wing spacing 100% of the chord zero stagger, zero flap deflection

At $Re = 117{,}000$ the drag at ten degrees is lower than the base drag at zero degrees. At $Re = 176{,}000$ the same behavior is observed at an angle of attack of ten degrees. Barlow *et al.* (1999) suggests that laminar separation with periodical vortex shedding is the reason of this anomaly, which has been encountered also in the testing of other airfoils as reported in Marchmann & Werme (1994) (see Appendix F.6). Flow visualization over the downwind surface of the wings has enabled the author to observe the behaviour of the tufts at the different speeds. Figure F.9 and Figure F.10 shows that at the lower speeds a mild separation occurs at 30 % of the chord, whilst at 8 ms^{-1} the flow separates at approximately 80% of the chord. Table 5.12 shows the magnitude of the separated drag used in the wake correction. At $Re = 235{,}000$ this component is only present at 15 degrees AoA, where the foil stalls. At the lower speeds C_{Ds} appears from moderate AoAs. The lift coefficient curve increases proportionally with Reynolds number; as the wind speed increases the gradient of the lift coefficient curve rises, but the maximum lift coefficient is still smaller as compared to the published data on the 0015 section [Jacobs & Sherman (1937)] and to *X-Foil*. This leads to the conclusion that scale effects partially limited the performance of the *Wing-sail*. Having outlined the procedure to evaluate the free-air performance of the sail, an attempt will be made to extrapolate the data to higher Reynolds numbers which corresponds to average wind speeds found in service.

Table 5.12 – Separated drag, C_{Ds}

	Reynolds number		
β / degrees	117,000	176,000	235,000
0	0.0	0.0	0.0
5	0.043	0.087	0.0
10	0.041	0.102	0.0
13	0.043	0.087	0.0
14	0.009	0.092	0.0
15	0.082	0.081	0.048

Extrapolation to full-scale Reynolds number

The method commonly used is to extrapolate wind tunnel results to full scale is based on the effective Reynolds number Re_{ef} rather than the test Reynolds number; this accounts for the dynamic pressure fluctuations across the test section. Re_{ef} is calculated by multiplying the test Re by the turbulence factor TF. As suggested by Campbell (2010a) the addition of a grid increases the turbulence in the tunnel; Sinmons & Salter (1934) measured the turbulence factor downstream of a grid using a hot wire anemometer. The mean value in the free stream region ($x > 38\,mm$ from the grid) was found to be 5.92. It follows that $Re_{ef} = 1.39 \times 10^6$ using $test\ Re = 235 \times 10^3$. Research conducted so far suggests that the rig will perform better at higher Reynolds numbers. Barlow *et al.* (1999) gives an overview of the methods used by aerodynamicists to obtain full-scale characteristics of wings. These can be applied only when extensive published data is available for the required section. A large number of tests were conducted at NACA for common airfoil sections and hence an attempt can be made to correlate lift and drag data to higher Reynolds numbers. The average apparent wind speeds for the selected routes are calculated using the PPP (see Section 6.1.1) the reference Reynolds number is 6.1×10^6. A turbulence factor of 1.7 is assumed [Choi (2004)] relating to an effective Reynolds number $Re_{ef} = 10.3 \times 10^6$. The plots shown in Appendix F.8 are taken from Jacobs & Sherman (1937) and summarise the NACA 0015 performance at Reynolds numbers up to $Re_{ef} = 8.3 \times 10^6$, close enough to the target value. At full scale, the maximum lift coefficient is increased by 0.4 whilst the base drag C_{D0} decreases by 0.0015. Figure 5.17 (a) shows the polar plot for $Re_{ef} = 1.39 \times 10^6$; a horizontal line can be drawn through the estimated full scale maximum lift coefficient C_{Lmax}, the linear part of the test lift curve is extended with the same slope and the curved part of the polar is then raised up to coincide with C_{Lmax}. The drag curve is modified by plotting C_L versus C_D [Figure 5.17 (b)] the induced drag is then subtracted to leave the base drag C_{D0}; this is then increased to C_{Lmax} in the same way as the lift curve. The base drag is then decreased by an amount estimated in Appendix F.8 and the induced drag is added back up to C_{Lmax}.

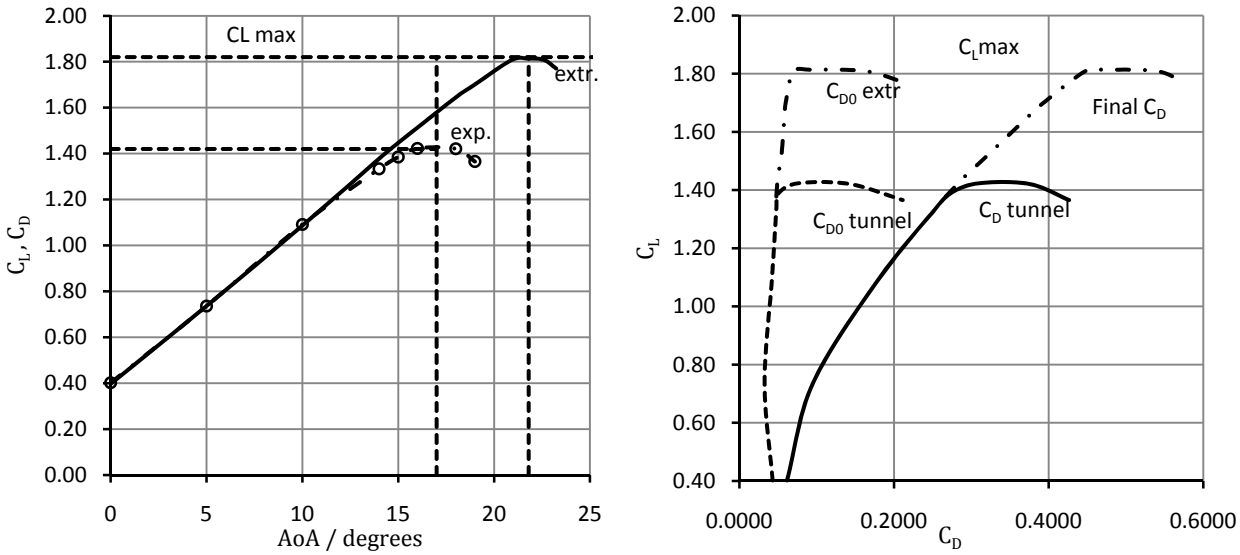

Figure 5.17 – (a) Lift curve extrapolation to full-scale Re; and (b) Drag curve extrapolation to full-scale Re

The limit to the result obtained is that the angle of maximum lift increases excessively, and the stall would also be more abrupt [Jacobs & Sherman (1937)]; moreover the data used for the extrapolation regards the airfoil section performance and not the wing. For this reason, the results presented in the next section do not include the extrapolation process. However, the designers believe that this result can give an indication of the potential increase in lift for the full scale rig. For the application of the proposed wing sail system, the improvement would regard only beam reaching and reaching courses as the best aerodynamic drag at lower AoA remains unchanged.

5.2.6 Analysis of the Results

Wing spacing effect

In this set of experiments the lift variation of the model with decreasing wing spacing is investigated. General Biplane Theory [Munk (1923)] provides lift variation with spacing due to AoA and curvature effects, based on Prandtl's vortex theory using two dimensional inviscid flow. A similar trend was anticipated, however direct comparison is not possible since the pressure distribution on the wings was not measured in the tests, and due to the presence of a third wing. The lift variation due to changes in spacing is plotted in Figure 5.18 (right) from Biplane Theory. The constants G and G_0 are related to lift due to AoA and curvature respectively and are defined by the relationships; lift produced by AoA, $\mathrm{L} = 2\pi \mathrm{AqG} \sin\alpha$ and lift produced by curvature $\mathrm{L}_0 = 2\pi \mathrm{SqG}_0 \sin\beta_0$, where $\beta_0 = \mathrm{C}_{\mathrm{Lo}}/2\pi$. Assuming there is no curvature to generate lift, $G = 1.0$ indicates the lift at infinite spacing and $G = 0.5$ at zero spacing. This is because zero spacing represents a single wing with the reference area of two wings.

The experimental data in Figure 5.18 (left) shows the lift coefficient variation with spacing at three angles of attack. All three trend lines depict a loss in lift coefficient as the gap decreases. At an AoA of ten degrees the trend is parabolic as in General Biplane Theory [Munk (1923)]; showing 22%, 23% and 24.6% decrease in lift as the spacing decreases from 100% to 50% chord length at an AoA of 15, 10, 5 degrees respectively. This verifies that the decrease in spacing results in a reduction in lift and that this trend is proportional to the decrease in AoA.

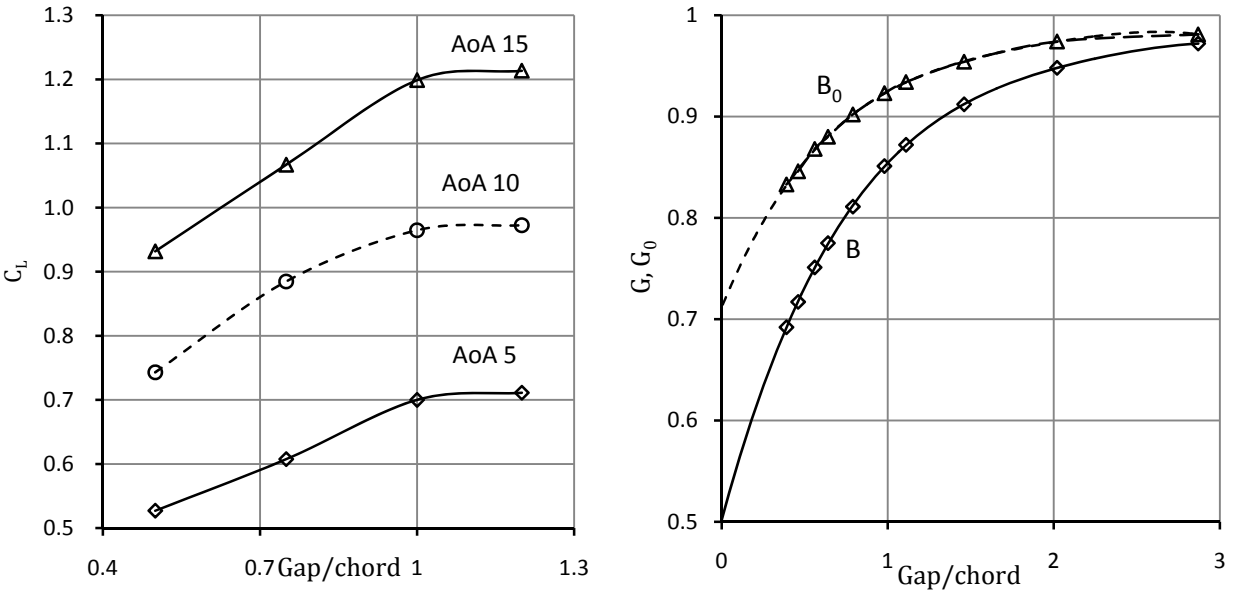

Figure 5.18 –*Multi-wing* lift coefficient experimental data with change in spacing (left), and Biplane theory data (right)

In Figure 5.18 (left) the relationship between lift coefficient and AoA is illustrated at four different spacings. The results show that apart from zero AoA the lift increases with increased spacing. The stalling angle ranges from 16 to 18 degrees and before stall the lift increases linearly. The drag coefficient variation does not show clear trend with changing spacing, however there is no significant change in overall trend. At 50% and 75% spacing the drag coefficient variation is similar but between 100% and the maximum spacing (120%) there is substantial difference in drag. At a wing spacing of 100% of the chord length, the drag coefficient is lower throughout the range of AoA, showing an average 13% reduction. The average lift is only 0.8% greater at 120% wing spacing and the maximum lift is at 16 degrees. 100% spacing shows 0.2% greater lift coefficient resulting

in a higher L/D. Biplane Theory [Munk (1923)] indicates that a wing spacing close to 100% is the most efficient. In the drag breakdown plot, Figure 5.20, it can be seen that the 100% spacing shows better performance in terms of lift-drag ratio. The aerodynamic characteristics of the proposed sails system are illustrated in Figure 5.19.

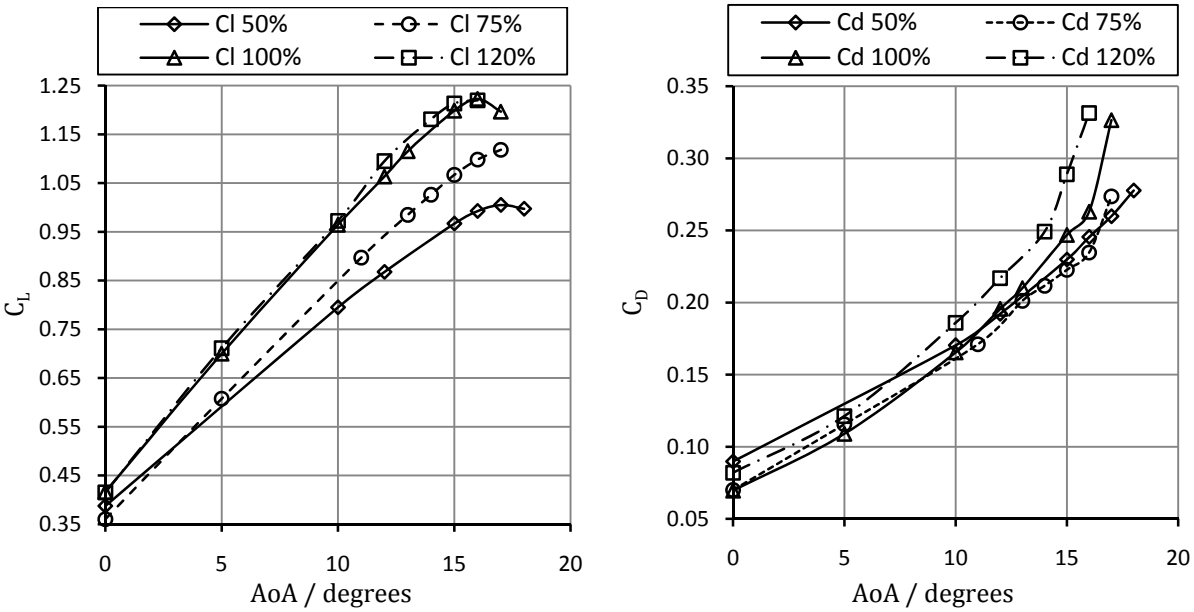

Figure 5.19 – Lift (left) and drag (right) coefficient against AoA at four spacings

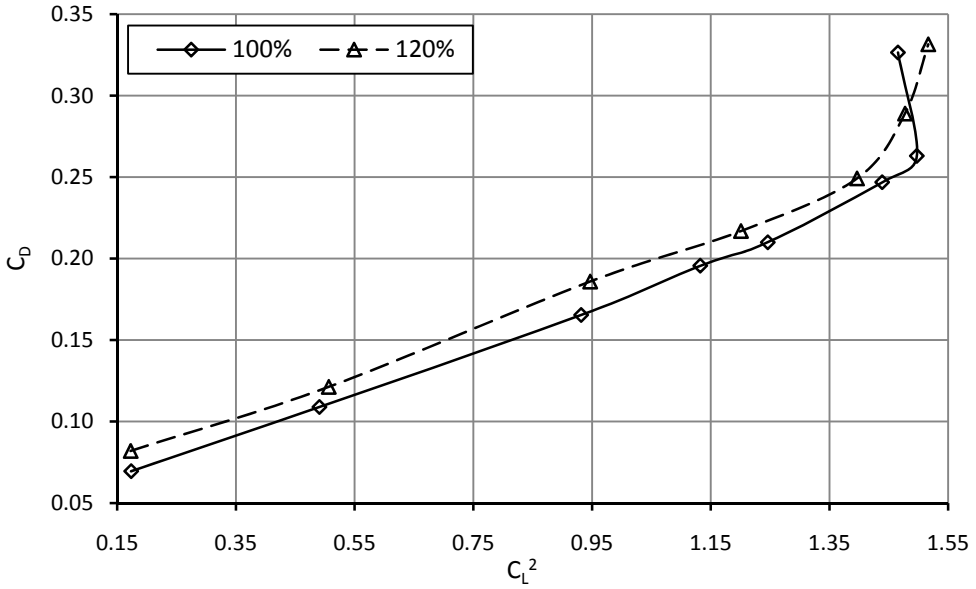

Figure 5.20 – Drag breakdown trend at 100% and 120% spacing

Stagger effect

At the end of the first set of experiments, model containers were added to investigate the interaction with the sails. As no time was available to repeat all the initial configurations, only the maximum chord spacing was tested again in order to provide data for a comparison with the results of the isolated wing. The maximum wing spacing configuration tested with the containers will be referred to as *Wing A*

General Biplane Theory [Munk (1923)] also investigated the effect of stagger position. Figure 5.21 shows the variation of G for non-stagger biplane and small, medium and large stagger positions at three different

gap/chord regions. The plot shows a slight increase in *G* hence increasing in lift but the trend is not consistent, showing a linear increase in lift at gap/chord ratio of around 1.1 and 1.4 and as the stagger to chord ratio increases, *G* shows a non-linear trend at a gap/chord ratio about 0.7. It can be said that the effect due to spacing change is dominant where there is a slight increase in lift for stagger position as summarised in General Biplane Theory [Munk (1923)].

During testing the stagger position and spacing are linked since the distance between the wing stocks are fixed at maximum spacing. The two stagger configurations indicated with relative angle to the top and bottom bar can be redefined relative to percentage chord length as shown in Table 5.13.

Table 5.13 – Three stagger configuration in percentage chord

Stagger	*Gap / chord*	*Stagger / chord*
0	1.2	0
30	1.039	0.6
60	0.6	1.039

The experimental results summarised in Figure 5.22 – Aerodynamic coefficients and drag breakdown for three stagger configurationsshow that, *Stagger 60* produces the highest lift and drag coefficient; From now on this configuration will be referred to as *Wing B*. The staggered cases also have higher lift curve slope within the linear region. In terms of lift-drag ratio the drag breakdown plot in Figure 5.21 illustrates that below C_L^2 of 1.8 *Stagger 30* gives best performance and beyond this *Wing B* shows better performance. An interesting result is *Wing B* shows higher lift coefficient than *Stagger 30* although the amount of decrease in spacing and increase in stagger position relative to the chord length was the same. Therefore with the existence of the third wing the stagger effect is greater than the spacing effect in lift coefficient variation. However the overall performance of these staggered configurations varies with the range of lift coefficient produced.

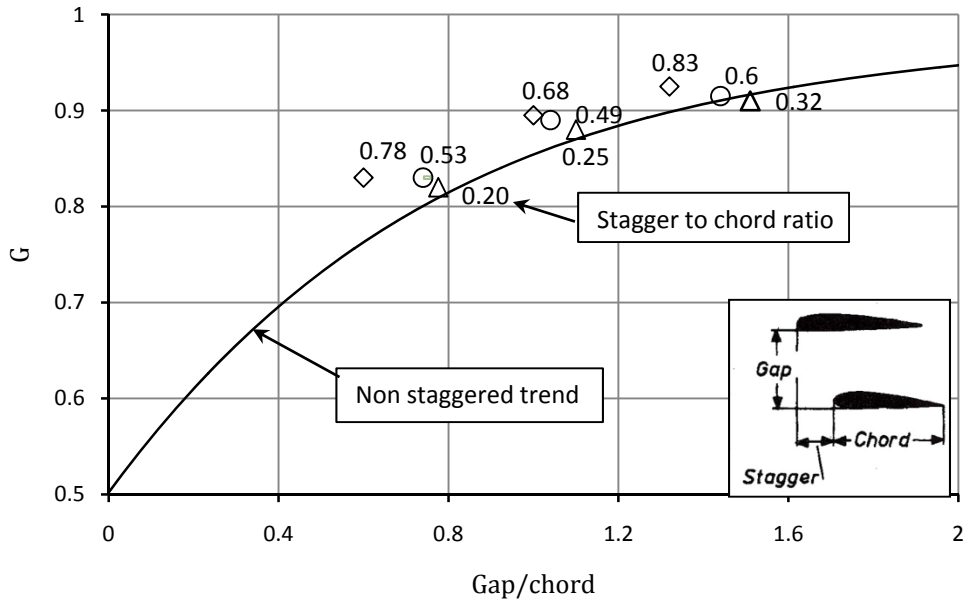

Figure 5.21 – Variation in biplane stagger position lift constant G with gap/chord ratio

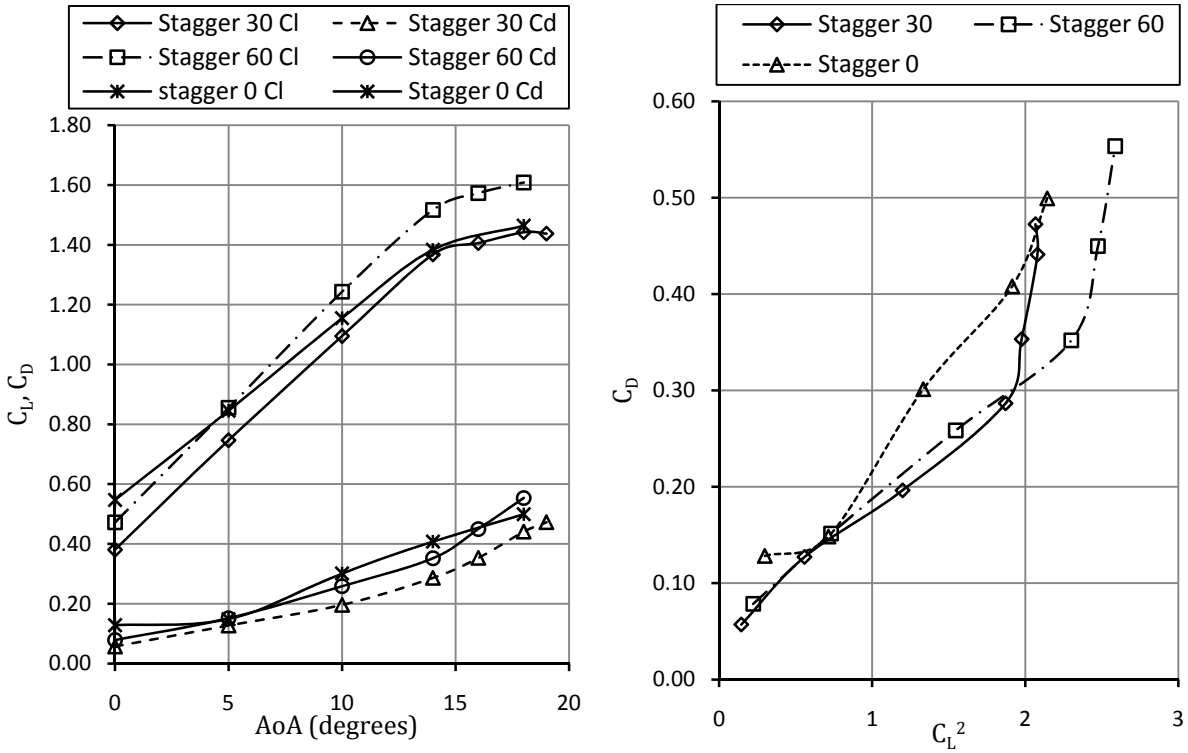

Figure 5.22 – Aerodynamic coefficients and drag breakdown for three stagger configurations

Flat sail configuration

This configuration was originally set to represent continuous single wing shape, aligning the three wings in line. However, due to screws and nuts for the flaps the complete alignment could not achieved. The aerodynamic coefficients and drag breakdown results illustrated in Figure 5.23 show lower lift coefficient and higher drag coefficient than the other configurations and the lift-drag ratio is also poor. However *Wing C* stalled at very high AoA behaving as a conventional sail. This configuration may be used for downwind sailing at low operational speed (see Appendix F.3).

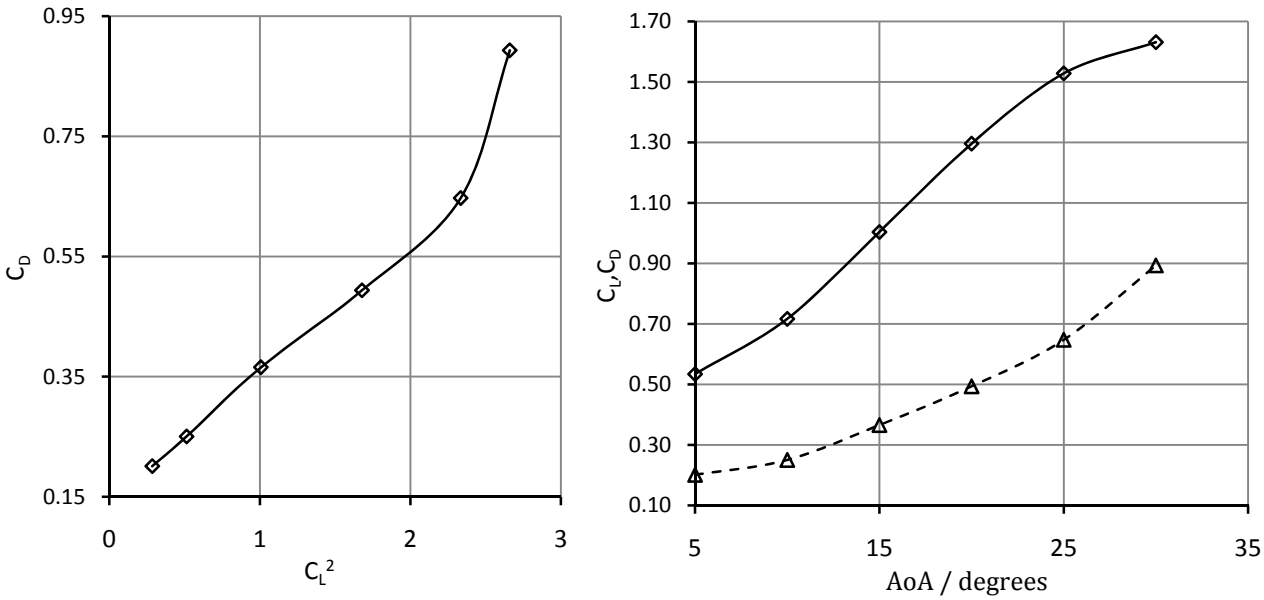

Figure 5.23 – Flat sail configuration: drag coefficient against lift coefficient squared (left) and; lift and drag coefficient against AoA (right)

Containers – Sail Interactions

The experiments on the effect of wing spacing were performed with the rig in isolation, whilst the investigation on the stagger effect was carried out simulating the presence of the container stack. The interaction between the sails and the flat surface increased the lift because the top of the containers worked as a reflection plane, decreasing the end vortexes on the wings and hence increasing the overall efficiency of the rig.

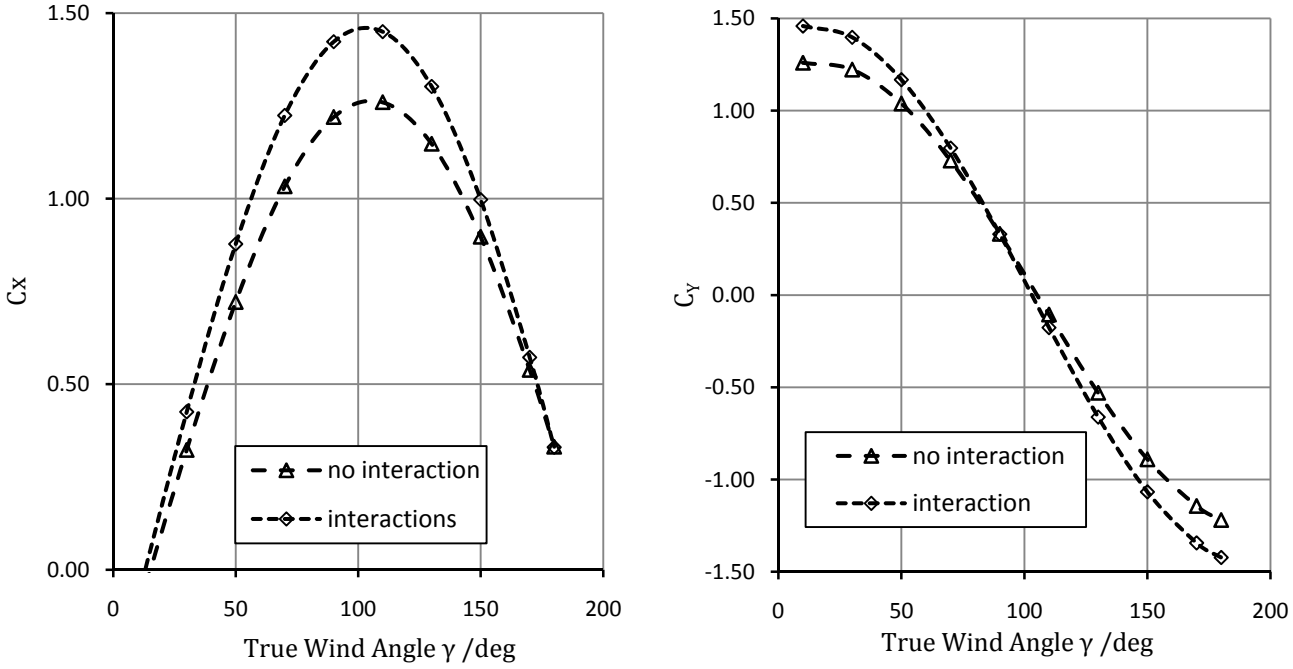

Figure 5.24 – Ship axes coefficients for maximum wing spacing spacing. The plots highlight the benefices deriving from the presence of the containers under the base of the wing

When the wing was tested in isolation, the end vortexes generate a cross-flow at the lower and upper part of the wing, thus contributing to the induced drag and reducing the efficiency of the wing. Once the reflection plane is added, the flow becomes uniform also at the extremities thus increasing the efficiency, due to viscous effects this gain in performance extends towards the top of the wing [Chéret (2000)]. The effective rig height, which the magnitude of the induced drag depends on, is found to increase by 8.6% with the addition of the containers; for the maximum wing spacing case, He increased from 2.21 metres to 2.4, 38% more than the geometric centre at midspan. Appendix F.7 shows the attempt to visualize the flow in the wind tunnel. The result of this investigation proved to be beneficial to the scope of the feeder concept as the maximum thrust coefficient C_X, was found to increase by 15% (Figure 5.24), thus improving the efficiency of the auxiliary propulsion.

Design Selection

While examining the polar plots for the different configurations, the best performing arrangements can be readily identified. As the efficiency and hence viability of the feeder has been assessed simulating a voyage on designated routes (Section 6.1.1), it is necessary to follow the same approach for the selection of the best configuration; this will enable the choice of the most suitable sailing point and wing configuration. Figure 6.1 shows a flow diagram representing the program used to predict the feeder voyage performance. An additional loop is created to run the code for every sailing point and configuration tested in the wind tunnel. The choice is mainly based on the average thrust generated for the routes. As expected, the best results are given by *Wing A,* and *Wing B.*

Table 5.14 – Design choice. Wing A correspond to maximum chord spacing, zero stagger whilst Wing B corresponds to a stagger angle of 60 degrees

Parameter	*Wing A*	*Wing B*
$C_{L\,max}$ at 18 degrees of attack	1.423	1.608
C_D at $C_{L\,max}$	0.426	0.553
C_{D0}	0.062	0.079
$(C_L / C_D)_{max}$ at five degrees AoA	7.7	5.6
Minimum aerodynamic drag angle / deg.	7	10
Centre of effort / % span	35	33
Effective centre of effort / % span	111	106

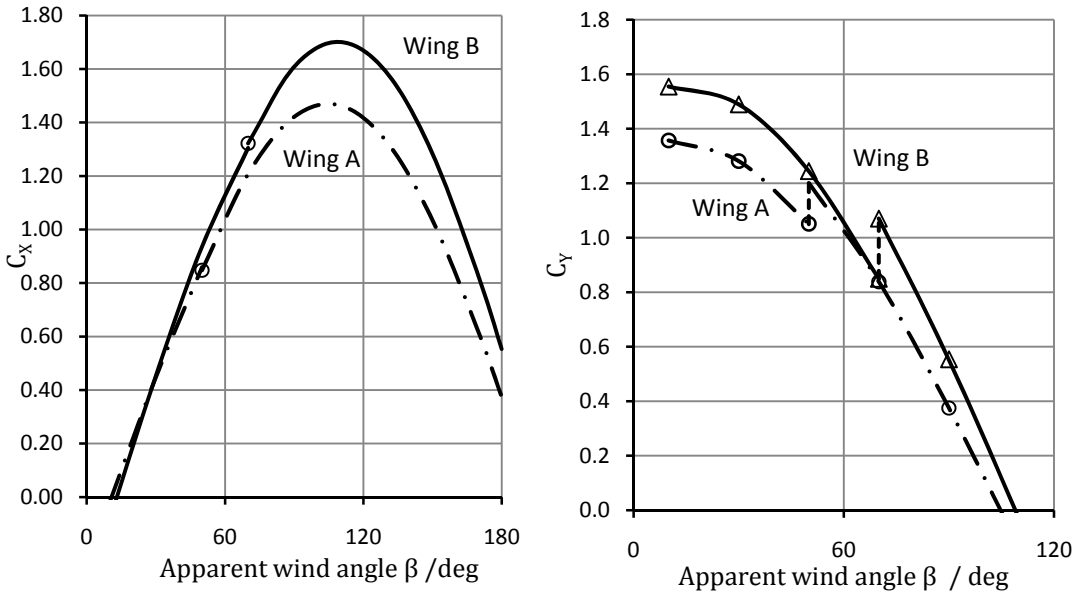

Figure 5.25 – Ship axes coefficients [lift (left); drag (right)]of the selected configurations; the marker indicates the change from the sailing point from windward to beam reaching

The best windward sailing point for both the configurations is at 14 degrees, despite having $(C_L/C_D)_{MAX}$ at five degrees angle of attack. At this angle $(C_L/C_D)_{MAX}$ is 5.2 and 4.3 for *Wing A* and *Wing B* respectively, but the higher lift coefficient overcomes the disadvantage of having a smaller aerodynamic drag angle. Figure 5.25 shows only the positive values since along the abscissa the curve is almost symmetrical. A negative heel coefficient at $\gamma > 170\ C_L$ is not realistic. When running downwind the flat sail configuration (*Wing C*) would be used in the stalled condition, unfortunately this configuration was tested only up to 30 degrees because the heeling force would have increased to near half of the dynamometer limit and hence no risk was taken. At 30 degrees this configuration has $C_L = 1.63$.

When selecting the final design, performance is the main driver; however, the dimensional envelope of the two configurations is also considered (See Appendix F.4). In this case both the criteria favour the choice of *Wing B*. Figure 5.26 compares the ship axes lift coefficient for different sailplans at the maximum lift coefficient sailing point. The *Multi-wing* sail and the rigid square rig generate similar thrust and both are more efficient than the *Dyna rig*. However, it is necessary to remember that the data taken from Table 5.1 reflects the characteristics of the rigs at the time of publication and therefore does not include the developments of the past 20 years. The hybrid rectangular sails [Fujiwara *et al.* (2005)], outclass the former rig types in terms of maximum thrust generated. In the graph the thrust coefficient of *Wing B* is also plotted using the sail coefficients after the full scale extrapolation.

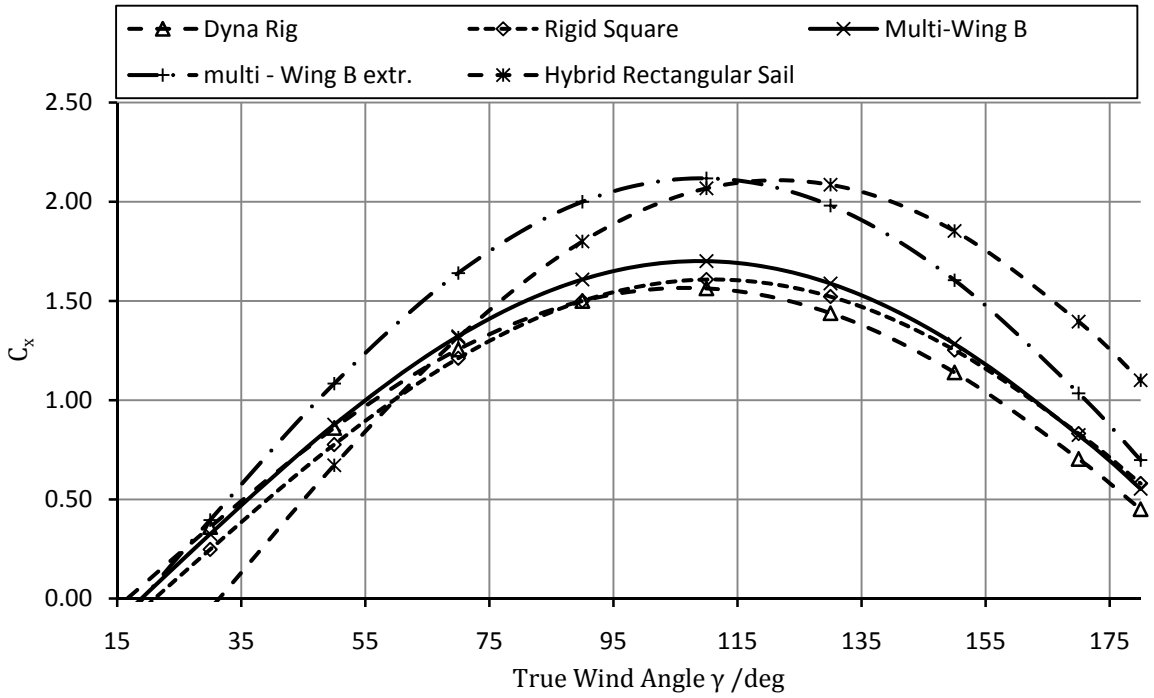

Figure 5.26 – Comparison of *Multi-wing* rig with other existing rigs. The graph shows only the sailing point at maximum lift coefficient

Single foil

Following the last day of testing, the containers and the side wings were removed in order to measure the forces of a single foil in isolation. Figure 5.27 compares the sail coefficients between the single and *Multi-wing* arrangements. The slope of the lift curve is lower for the *Multi-wing* resulting in a higher stall angle. The base drag is lower for the single wing but for angles of attack greater than seven degrees, the *Multi-wing* shows lower drag. The maximum lift of the *Multi-wing* is also slightly lower than the single wing. Note that in Figure 5.27, *Wing A* does not include the interaction effects.

This section also addresses the comparison of the wind tunnel data with that generated using *X-Foil* and from published data for the same section. However, during the testing the wing was left with the flap deflected at 25 degrees. The consequence is that less experimental data is available for the validation. Sears & Liddel (1942) contains data for the required flap deflection of 25 degrees at a $Re_{ef}\ \ is\ \ 2.76 \times 10^6$, but the flap is 30% of the chord length and not 20% as for the sail tested. In Figure 5.27 the *X-Foil* polar seems to overestimate the lift since the flap length is 20% of the chord length, however the *X-Foil* analysis is based on an ideal geometry where the gap at the flap hinge point is sealed; this increases the performance and balances out the difference in flap length. On the other hand a gap was intentionally left at the hinge point of the *Multi-wing* model, to replicate the full scale rig. Therefore the lower drag curve of the single foil could be explained by the different flap lengths.

The lift curve of the experimental single wing has similar gradient in the linear region to the *X-Foil* and NACA polars. However, the angle of stall for the NACA polar is considerably higher than for *X-Foil* and the tested wing, this can be partly explained by the higher Reynolds number of the former polar. A larger discrepancy is found in the drag curves; the base drag of the experimental foil is quite low and the curve gradient is also higher. Part of this error can be explained by the fact that both *X-Foil* and NACA data reflect the performance of sections with ideal surface finish; the surface finish of the model tested in the wind tunnel was certainly not ideal due to the material used and the presence of the tufts. The leading edge geometry may have contributed to this decrease in efficiency due to the sanding process required to remove the excess filler.

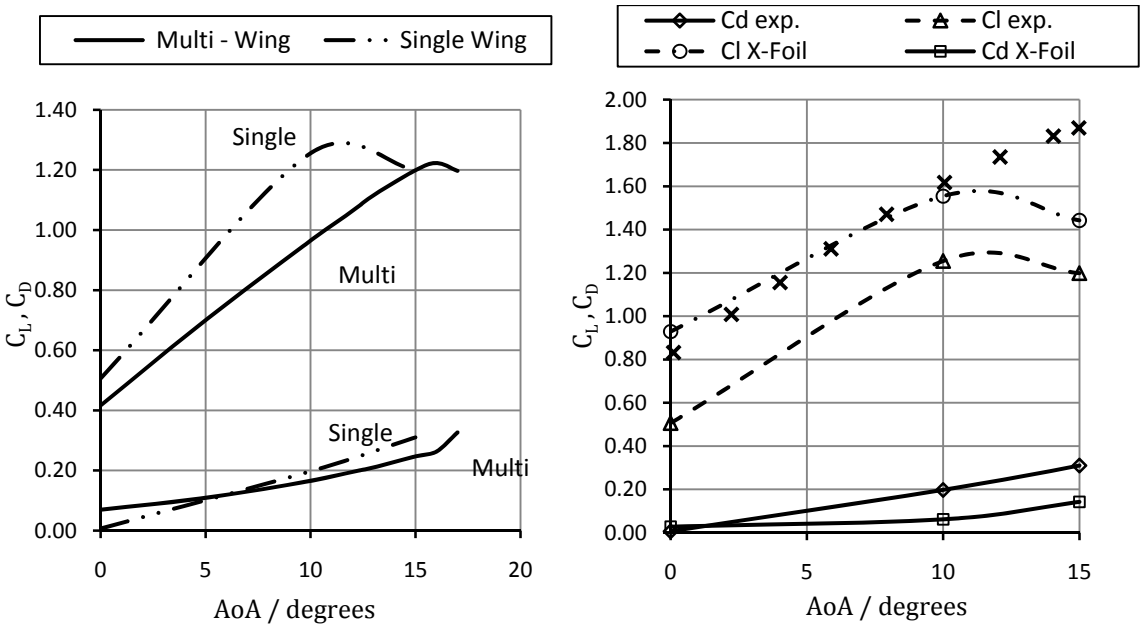

Figure 5.27 – Single and *Multi-wing (Wing A)* comparison (left) and; Single foil comparison, lift curve (Experimental and *X-foil* data is for Re = 235,000 whilst the NACA data points are for $Re_{ef} = 2.76x10^6$ (right)

Uncertainty Analysis

The same rationale as the towing tank uncertainty analysis addressed in Section 4.4.4 can be applied to assess the accuracy of the wind tunnel measurements. Here only the precision component of the total uncertainty is evaluated as the number of repeated runs was too small to provide a significant bias analysis. Appendix F.10 shows the polar plot after the error bars are applied.

Sources of uncertainty include model geometry, which includes dimensional tolerance of the hot wire cutter, the addition of grit and poly-filler to seal the leading edge gap, and the presence of the tufts. The result is variation of the surface roughness which in turn increases the drag, hence altering the performance. A correction for the grit strips has been applied, whilst the tufts were removed after their initial tests. Further uncertainty arises from the time trace of the sampled data, due to anomalies with two of the channels used to derive the output; this uncertainty was reduced by repeating runs.

Discussion

The initial concept of *Multi-wing* system was targeted for upwind sailing performance. The proposed system has been developed by considering wing spacing; magnitude of stager and flap length to optimise the *Walker Multi-wing* sail [Walker (1985)]. To ensure the structural integrity simple beam theory has been used at both ship and model scale. The sail plan geometry has been optimised within dimensional constraints. Through *X-Foil* aerodynamic analysis and structural consideration NACA0015 with 20% chord length trailing edge flap is selected for the wing section. Using the obtained section aerodynamic characteristics and average wind data for the operating regions an overall performance was analysed and a 3% thrust reduction at 25 knots and 10% at 15knots of ship speed is predicted as defined in the initial requirements. However the performance estimate was based on two dimensional section coefficients of a single NACA 0015; any further improvement in the quality and fidelity of the projections necessitated model scale wind tunnel testing.

Throughout the duration of the experiment, it has been possible to complete the test matrix originally planned. The results of the performance when varying wing spacing suggested that the optimal gap corresponds to 100% of the chord length. The results were found to agree with General BiplaneTheory, despite the additional wing.

The second set of experiments proved that the addition of an angle of stagger increases the efficiency of the rig thanks to the slot effect which favours the performance of the upwind wings. Along with this second series of tests, boxes were positioned under the wings to replicate container stacks on the fast feeder. From this experiment the efficiency of the sail plan was found to increase due to a reduction of the induced drag component. The results presented in this chapter contribute to the assessment of the overall design feasibility presented in Section 6.2. The methods and results presented are not common in the literature and therefore act as a useful resource aiding future research and design.

5.3 - Computational fluid dynamics study of *Multi-wing* system

Computational fluid dynamics (CFD) is potentially an alternative method to model experiments for performance prediction, in terms of time efficiency. Due to difficulties in simulating realistic flow conditions experimentally some degrees of uncertainty exist in the results. Using CFD one can visualise the flow around objects. In this project two dimensional CFD is used to undertake further investigation of full scale *Multi-wing*, particularly from an optimisation perspective, which was not available during the testing. Since the analysis is in two dimensions conducted at full-scale and has a different environmental conditions to the wind tunnel, hence the results may not match. To carry out this analysis, the commercial software *Star CCM+* is used.

5.3.1 Mesh generation and physical model

In mesh generation fifteen prism layers are used for the boundary layer and three sizes of unstructured tetrahedral mesh for main domain as shown in Figure 5.28. Using a flat plate empirical formulae the boundary layer thickness of 0.12 metres and first layer thickness of 0.95 millimetres were obtained assuming wall function, Y^+ of 50 and inlet velocity of 15.432 ms^{-1} equivalent to 30 knots [Tu *et al.* (2008)]. Finer meshing is placed around the wing sections and in the downwind region to compute the turbulent flow in the wake. The same method has been applied to all of the CFD meshes used.

Due to high Reynolds number (6.2×10^6) of the flow turbulent modelling is required. In the optimisation of the *Maltese Falcon* sail rig [Doyle *et al.* (2002)] *realisable k-epsilon* and *Spalart-Allmaras* turbulence models showed little difference in results so *Spalart-Allmaras* model was used to increase the efficiency of the iteration. In this *Multi-wing* analysis full optimisation was not considered so for the physics model *k-epsilon turbulent* with *Segregated flow* is used due to the geometrical change around the flaps which may cause more turbulent flow in the wake region.

5.3.2 Simulations

Wing spacing of 100% chord and flap angle of 22.5 degrees

The above defined model showed best lift-drag ratio in the wind tunnel testing in the non-staggered configurations more detailed characteristics of this configuration are investigated using CFD modelling.

The overall lift and drag coefficient trends are similar to the wind tunnel results but the individual wings show different trends around stalling angle. The drag values show insignificant change at AoA of less than eight degrees and at higher AoA they start to increase at different rates, as seen in Figure 5.29. This implies the stalling of one wing changes the flow regime around the other wings. In terms of lift-drag ratio with reasonable lift generated eight degrees AoA shows the best performance but the maximum lift is produced at ten degrees AoA.

In Figure 5.30 increase in separation on the wings at ten degrees AoA can be seen. Since the lift and drag vary at different rates *Multi-wing* can be optimised by adjusting the AoA of each wing for best lift-drag ratio or

maximum lift. Furthermore the staggered configurations and the flap angle of the wings can be optimised for different sailing conditions.

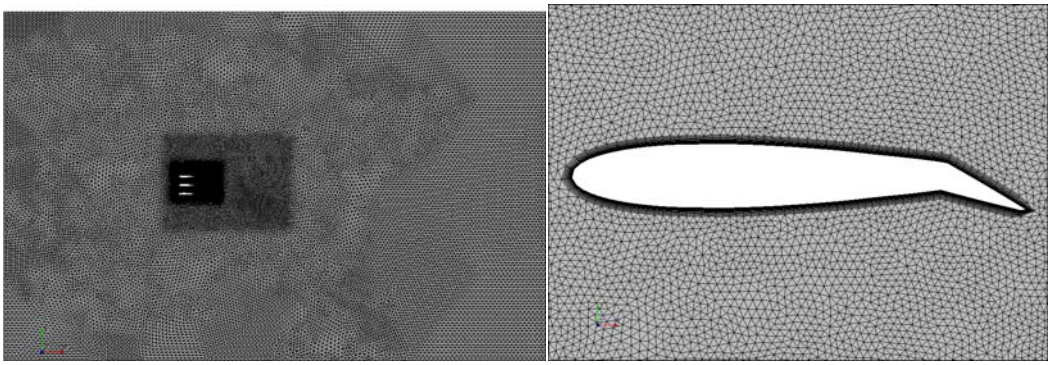

Figure 5.28 – Mesh generation of whole domain (left) and single wing (right)

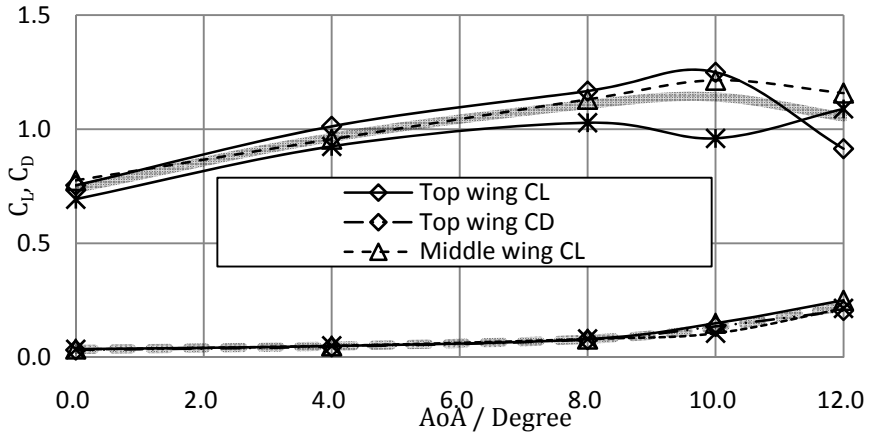

Figure 5.29 – Aerodynamic characteristics of 100% chord spacing with 22.5 degree flap model

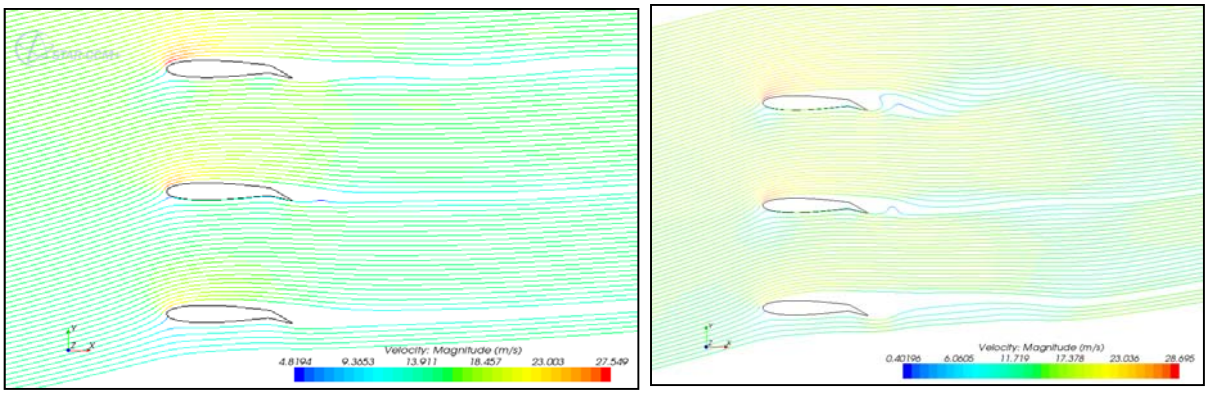

Figure 5.30 – Streamlines at an AoA of: eight degrees (top left), ten degrees (bottom left); and pressure coefficient at eight degrees (right)

Forward and aft sail system interaction

In the upwind sailing condition the air flow behind the forward sail system may affect the aft system performance. Based on the performance prediction the average apparent wind angle of 30 degrees was selected for the analysis. At this angle the flow interaction between the rigs may be more significant than in other sailing conditions. Two dimensional rigs are modelled to have relative apparent wind angle of 30 degrees and AoA of ten degrees. The domain size was increased by 20% overall from the single rig model and shifted to accommodate two rigs ensuring sufficient wake region. To measure the interaction the entry flow angle and magnitude, total lift and drag coefficient and streamline of forward and aft system are obtained in post-

processing. A vertical line probe was derived at five metres (80% chord length) before each rig with 19 metre length (300% chord length).

From the horizontal and vertical flow velocity components the magnitude and angle of flow along the probes were calculated. In Table 5.15 the magnitude and angle of the entry flow are summarised and the results show 1.53% flow velocity reduction and 6.04% reduction in AoA. In aerodynamic characteristics the forward rig produced less lift and more drag than the aft rig due to stalling. In the streamline in Figure 5.31 separation is smaller in the aft rig due to reduction in flow velocity and AoA. This implies that in upwind operation the AoA of the aft rig can be increased to produce more lift when the forward rig is in optimum sailing condition.

Table 5.15 – Entry flow characteristics of forward and aft rig with total lift and drag coefficient

	Flow velocity / ms^{-1}	*Flow angle / degree*	C_L	C_D
Forward rig	15.66	17.89	0.96	0.143
Aft rig	15.42	16.81	1.03	0.127
Reduction / %	1.53	6.04	-6.80	12.60

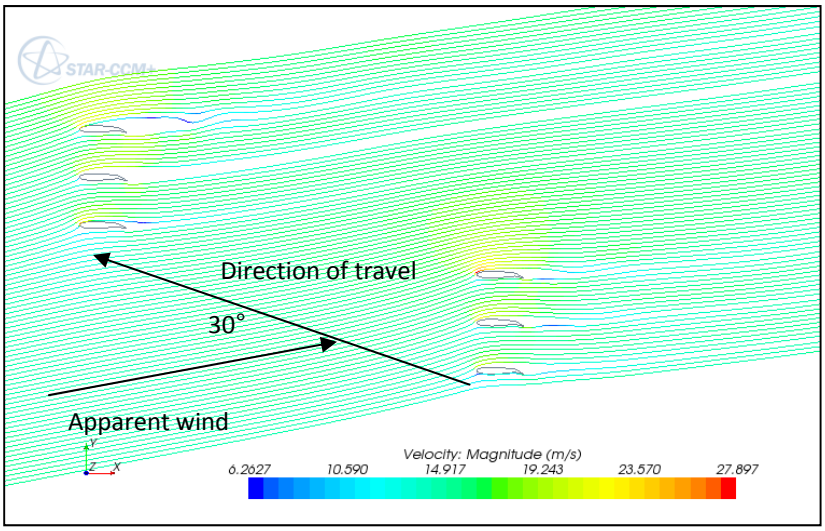

Figure 5.31 – Streamline for forward and aft *Multiwing* system at apparent wind angle of 30 degrees

6. Performance Predictions

This Chapter deals with the prediction of the aero-hydrodynamic performance of the fast feeder. The experimental results from both Chapters 4 and 5 are combined in conjunction with estimates of propulsive efficiency allowing final hull form selection and comparison of performance against existing vessels.

6.1 Design selection

6.1.1 Sailing performance

The program described in Section 5.1 can now be expanded to encompass the aero-hydrodynamic data obtained in the experiments. Initially, the algorithm performs the aerodynamic calculations, where the rig and hull windage are combined with the forces generated by the sails to compute the resulting angle of heel and leeway. The code then calculates the total resistance of the ship which is defined as:

$$R_T = R_U + R_{AAS} + \overline{R_{AW}{}'} + R_H + R_I \tag{6.1}$$

where $\overline{R_{AW}{}'}$ is the added resistance in waves averaged over the selected routes, and $\mathrm{R_{AAS}}$ is the air drag of the above water structure. The code is then used to compare the different configurations of the *Wing-sail* tested in the wind tunnel; this enables the assessment of the efficiency of the rig on an operational basis rather than just from the point of view of pure aerodynamic performance.

Rig Windage

The ship axis coefficients of the rig windage presented in Section 5.2.5 are dimensionalised with respect the sail area and the resulting forces are added to the forces resulting from the sails.

Wind lever

The wind heeling moment is estimated using Equation (6.2) [IMO (2008)].

$$M_H = \frac{1}{2}\rho C_{DH} A H_0 \frac{H}{H_0} V^2 \tag{6.2}$$

The code interpolates the projected area for the corresponding apparent wind angle; a gustiness factor of 1.23 is included to represent fluctuating wind speed. The angle of heel induced by the wind load is once again calculated separately, and then added to the sail component.

Added resistance in waves

The annual wave data for Singapore and the Caribbean are initially converted into probability of occurrence regarding significant wave height and zero crossing period. Using Equation (4.6), $P(T_0)$ can be transformed into $P(\lambda/L_{wL})$ for both *Hull A* and *Hull B* (Table G.1 and Table G.2). On this basis, the non dimensional added resistance σ_{AW}, which was tested over a range of λ/L_{wL}, can be matched to the sea state and dimensionalised for the spectrum of wave amplitude using Equation (4.25). The aim of this is to calculate an "instantaneous" added resistance for Singapore and the Caribbean, which can be added to the calm water resistance in the PPP. Table 6.1 and Table 6.2 shows $\overline{R_{AW}}$ for both hulls operating in the Singapore region at 25 knots speed, Appendix G shows the summary for the Caribbean and the 15 knot speed case for the Singapore region.

Table 6.1 – Averaged added resistance for *Hull A* sailing at 25 knots in Singapore (values in N)

Hull A, 25 knots	*Wave length/wetted length*									
$h_{1/3}$ / *m*	*12*	*20*	*30*	*42*	*55*	*71*	*89*	*109*	*130*	*Total*
2.5	0.0	0.0	686.8	3149.2	3689.2	2317.8	1009.7	302.0	76.3	11231.1
1.5	0.0	0.0	584.8	1838.8	1531.6	719.9	227.2	54.4	0.0	4956.6
0.5	0.0	0.0	41.4	71.4	35.7	9.1	2.5	0.0	0.0	160.1
Total	0.0	0.0	1339.1	5271.3	5658.8	3046.8	1239.4	896.9	76.3	*16347.9*

Table 6.2 – Averaged added resistance for *Hull B* sailing at 25 knots in Singapore (values in N)

Hull B, 25 knots	*Wave length/wetted length*									
$h_{1/3}$ / *m*	*12*	*20*	*30*	*42*	*55*	*71*	*89*	*109*	*130*	*Total*
2.5	0.0	137.9	1751.5	3831.4	3703.0	2150.7	896.3	283.9	86.8	12841.6
1.5	0.0	176.1	1491.4	2237.1	1537.4	668.0	201.7	51.1	0.0	6362.7
0.5	0.0	25.7	105.5	86.9	35.8	8.4	2.2	0.0	0.0	264.6
Total	0.0	339.8	3348.4	6155.3	5276.2	2827.1	1100.2	335.0	86.8	*19468.8*

Only significant wave heights up to 2.5 metres are considered as this represents 89.3% of observations. Some of the wave length ratios from the sea charts fall outside of the range of waves covered in the towing tank testing; the values of σ_{AW} are therefore extrapolated for $\lambda/L_{WL} < 50$. Linear interpolation is used to find σ_{AW} within the range covered by the experiments. No added resistance can be appreciated at $\lambda/L_{WL} < 30$ and $\lambda/L_{WL} < 20$ for *Hull A* and *Hull B* respectively. At 25 knots ship speed, the average drag amounts to 1.1% and 1.7% of the upright resistance for *Hull A* and *Hull B* respectively. A large discrepancy in the performance of the two hulls is observed at a ship speed of 15 knots (see Appendix G) where the percentage of added resistance amounts to 1.6% and 4.9% of the upright resistance for *Hull A* and *Hull B* respectively. The average added resistance is then weighted for the probability of head seas, assuming that the waves will follow the same direction as the wind. To calculate the weighting factor the probability of head winds relative to the ship heading X is multiplied by a factor which accounts for the number of miles the feeder sails at each heading. The calculated weighting corresponding to the route in the Singapore region is shown in Table 6.3.

$$Weighting = \sum_{i=1}^{8} \left\{ [P(bow\ waves)] \times \frac{distance}{total\ distance} \right\} \tag{6.3}$$

Table 6.3 – Calculation of the probability of head waves for Singapore region

Course(X)	*Distance /miles*	*distance / total distance*	*P (bow waves)*	*Weight*
0-45	1716	0.082	0.1326	0.0109
45-90	1721	0.083	0.2258	0.0187
90-135	1454	0.070	0.1659	0.0116
135-180	5511	0.265	0.0546	0.0145
180-225	1716	0.082	0.0915	0.0075
225-270	1721	0.083	0.1217	0.0101
270-315	1454	0.070	0.1101	0.0077
315-360	5511	0.265	0.0979	0.0259
SUM	20803	1.00	1.00	*Weight = 0.107*

In the algorithm, the "instantaneous" resistance in waves is therefore estimated as $\overline{R_{AW}}' = \overline{R_{AW}} \times 0.107$.

Induced and heeled resistance

The results of the runs where the models were tested at angles of heel and leeway are input into the code and using a double interpolation technique it is possible to match the hydrodynamic and aerodynamic sideforce and knowing the extent of vessel heel determining the magnitude of the leeway. This process is illustrated in Figure 6.1.

PPP flow diagram

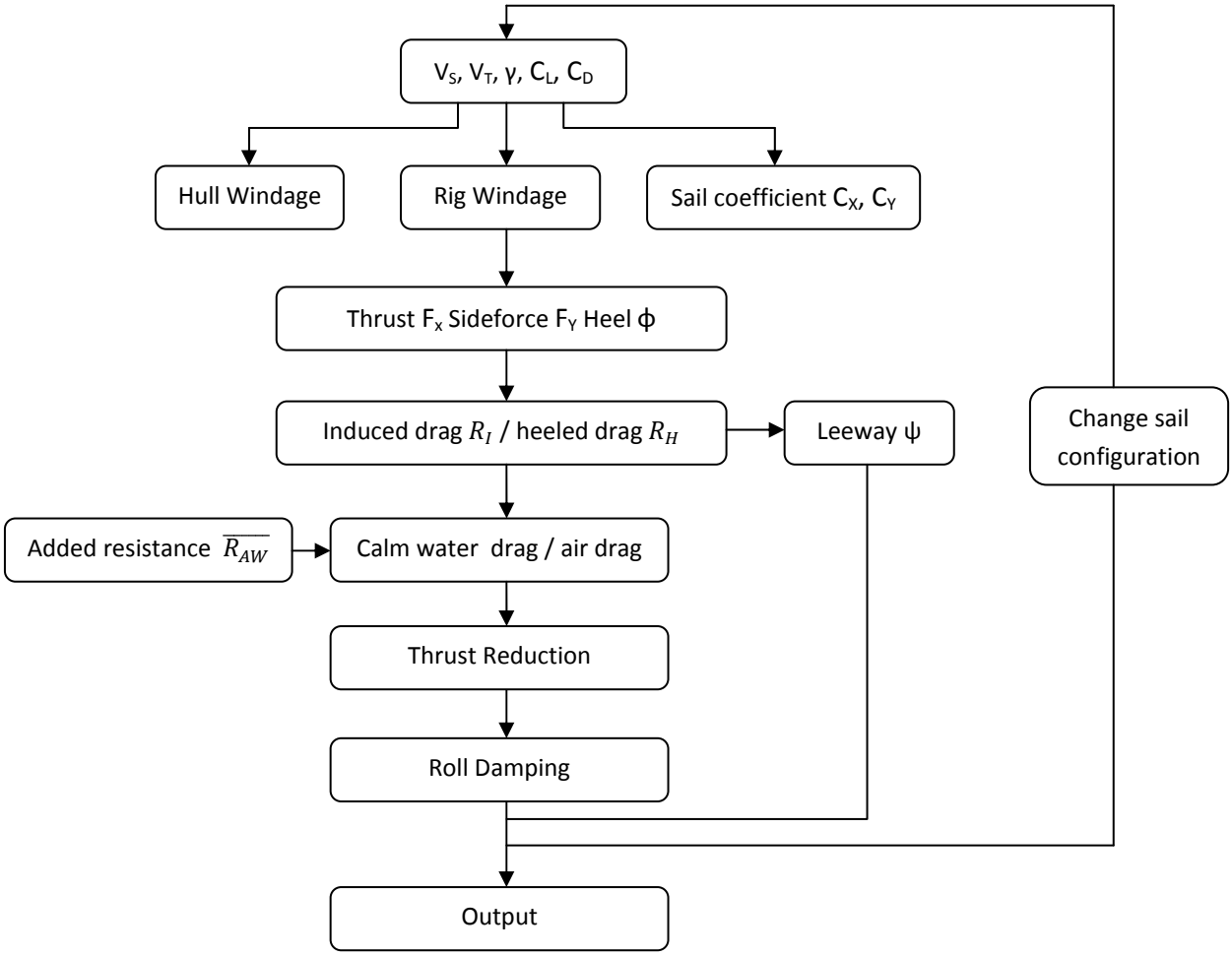

Figure 6.1 – Flow diagram for performance prediction program . The source code is not included in the appendices for practical reasons. It will be included in the CD-rom attached to the main report.

Voyage simulation

The performance of the feeder is to be assessed over the selected routes in the Singapore and Caribbean regions. The output file of the PPP describes the performance of the proposed hull forms in arbitrary wind conditions. This is then fed into a spreadsheet which averages this data over the 24 selected routes combining the probability of wind speed and direction relative to the ship heading. Table 6.4 shows one of the routes for Singapore. The average thrust reductions, angle of heel, leeway and motion damping can be calculated for individual routes or for the entire area. The following calculations are undertaken using the most efficient sail configuration, *Wing B* (see Section 5.2.5).

Table 6.4 – Voyage details for Singapore area

Waypoint	*Sail Use*	*Position*				*Speed / knots*	*miles*	*Course X / deg*	*Reverse course X / deg*
Singapore	Y	1.2	100.5	1.09	100.7	25			
Singapore (Port)	Y	1.2	103.5	1.09	103.7	25	1.6	90.04	270.04
E of Sakijang (LH)	Y	1.1	103.5	1.08	103.7	25	1.9	155.04	335.04
S of Raffles (LH)	Y	1.1	103.4	1.05	103.3	25	9.6	266.15	86.15
Malacca (Strait)	Y	1.1	103.3	1.07	103.2	25	17.5	283.01	103.01
Malacca (Strait)	Y	2.2	101.5	2.10	101.3	25	119.7	298.76	118.76
One Fathom Bank	Y	2.5	100.6	2.30	100.7	25	59.2	289.55	109.55
N/A	Y	3.6	99.3	3.75	99.2	25	105.3	312.94	132.94
Belawan (Port)	Y	3.5	98.5	3.71	98.3	25	40.7	267.80	87.80
Belawan	Y	3.5	98.4	3.28	98.3	25	8.8	185.57	5.57

$$Route\ Average = \sum_{i=1}^{8} \left\{ [P(\gamma) \times P(V_T)] \times TR(\gamma, V_T) \times \frac{distance}{total\ distance} \right\} \qquad (6.4)$$

The annual average includes all routes and the probability matrix reflects annual wind data. The seasonal average reflects summer and winter wind data and is based on one route which is selected for its favourable wind direction relative to the ship heading. The spreadsheet can be used to average other voyage data with results given in Table 6.5 and Table 6.6.

Table 6.5 – Performance summary for both hull forms in Singapore region

	Hull A						*Hull B*					
	Annual			Seasonal			Annual			Seasonal		
Speed	<4	15	25	<4	15	25	<4	15	25	<4	15	25
Thrust benefit / %	80.0	2.5	0.9	80.0	4.1	1.5	81.0	3.5	1.1	81.0	5.9	1.9
Angle of heel / deg.	0.1	0.2	0.6	0.1	0.3	0.7	0.1	0.2	0.6	0.1	0.3	0.7
Leeway angle / deg.	0.0	0.3	0.9	0.0	0.4	1.0	0.0	0.4	1.3	0.0	0.6	1.4
Induced – heeled drag / % R_T	0.	0.7	0.3	0.0	0.7	0.3	0.0	1.6	1.3	0	1.7	1.5
Roll Damping / %	9.4	16.3	30.1	10.0	20.9	31.1	9.4	16.3	30.1	9.4	20.9	31.1

Table 6.6 – Performance summary for both hull forms in Caribbean region

	Hull A						*Hull B*					
	Annual			Seasonal			Annual			Seasonal		
Speed / knots	<4.0	15.0	25.0	<4.0	15.0	25.0	<4.0	15.0	25.0	<4	15.0	25.0
Thrust benefit / %	70.0	2.0	0.9	70.0	3.4	1.1	72.0	2.8	1.0	72.0	4.9	1.4
Angle of heel / deg.	0.1	0.2	0.5	0.1	0.3	0.7	0.1	0.2	0.5	0.1	0.3	0.7
Leeway angle / deg.	0.0	0.3	0.8	0.0	0.4	1.0	0.0	0.4	1.3	0.0	0.5	1.4
Induced – heeled drag / % R_T	0.0	1.4	1.1	0.0	1.6	1.3	0.0	1.5	1.4	0.0	1.7	1.5
Roll Damping / %	7.5	16.0	32.1	8.5	16.4	30.6	7.5	16.0	32.1	8.5	16.4	30.6

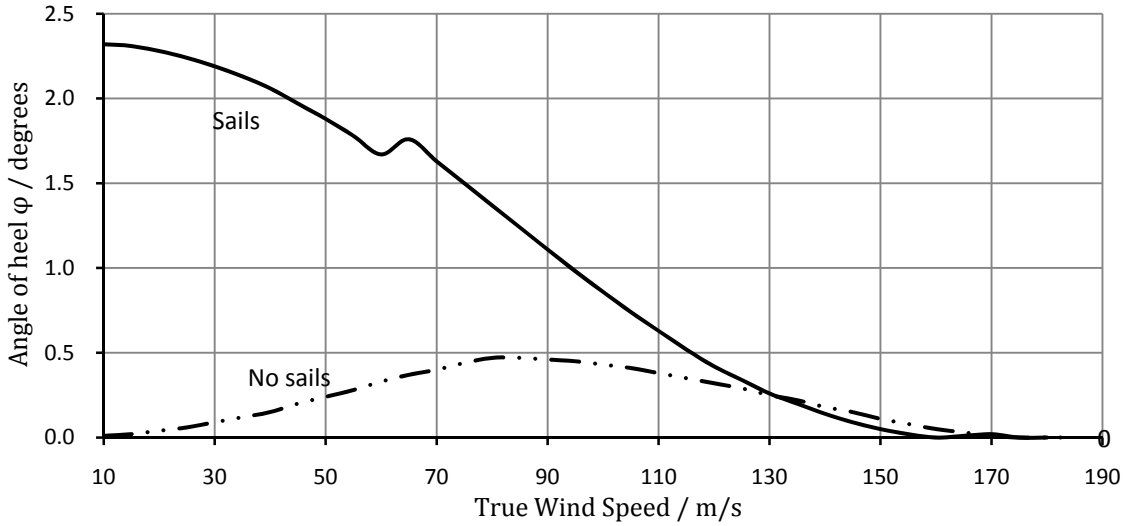

Figure 6.2 – Heel angle *Hull A,* V_S =25 knots, V_T = 30 knots. The step in the 'sail' curve is the change in sail coefficients C_L and C_D. A higher wind speed is chosen in order to appreciate the hull windage component

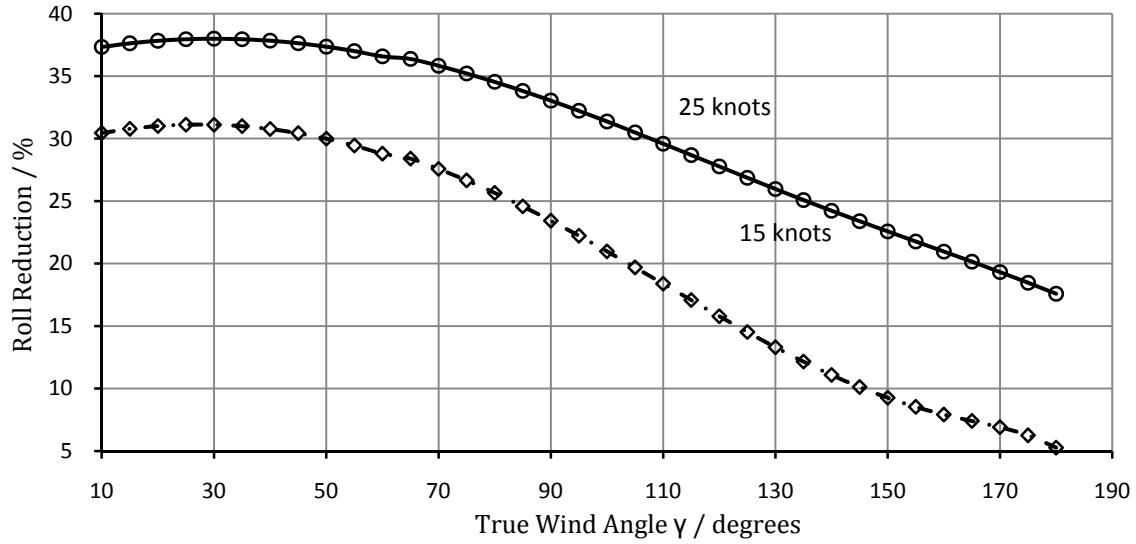

Figure 6.3 – Variation in roll damping with true wind angle (Singapore mean wind speed of 5.9 ms-1)

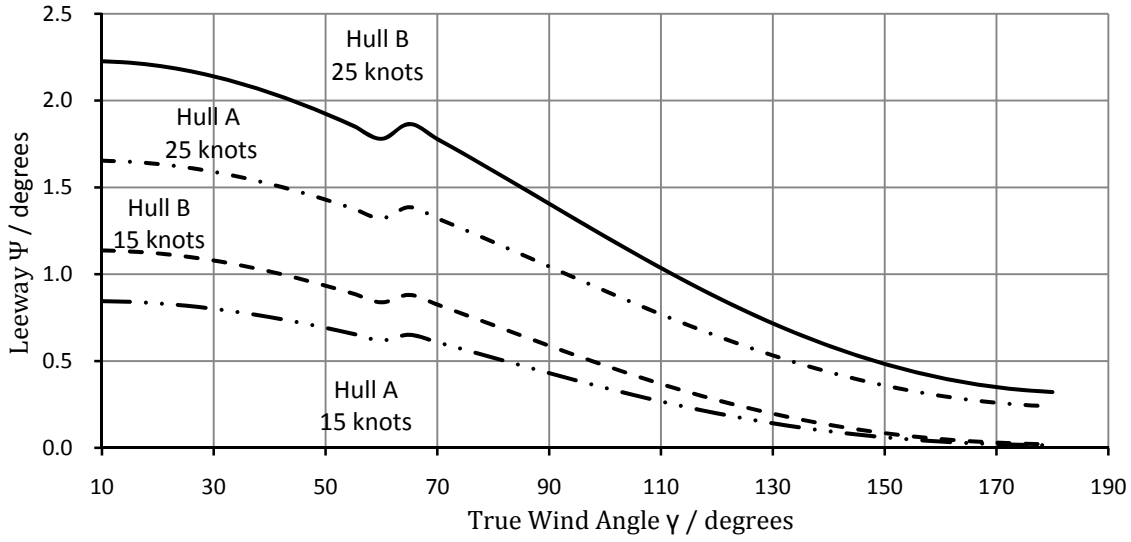

Figure 6.4 – Variation in leeway angle with true wind angle (Singapore mean wind speed of 5.9 ms^{-1})

Figure 6.2 shows the plot of the heel angle at a wind speed of 30 knots, the limit for the safe operation of the sails at a ship speed of 25 knots arising from the structural limitations (see Section 7.2.3). Note how the angle of heel remains below the limit defined in Section 5.1. the small amount of heel is explained by the small sail area, meaning that additional sideforce could be taken by the hull without compromising stability and generating excessive container lashing loads. The average angle of heel is quite small due to the average low wind speeds of 12 knots, the heel angle of *Hull B* is the same as for *Hull A* since the metacentric heights GM_T are assumed to be equal.

The method used to calculate the roll damping is outlined in Section 7.1.7. Figure 6.3 proves that positive damping is maintained throughout the range of true wind directions. Further analysis of the motion damping action of the sails is provided in Section 7.1.7.

Observing Figure 6.5 it is possible to note that the average leeway of *Hull B* is higher than for *Hull A*, as this hull form generates less hydrodynamic sideforce. This is due to the 'Hogner' stern which acts a lifting surface, whilst the flat stern of *Hull B* does not contribute significantly to the production hydrodynamic lift. The stern arrangement of *Hull A* also generates a higher induced resistance. Due to flow separation at the after end the difference in combined heeled and induced resistance between the hulls when generating the same sideforce is 16%, meaning that *Hull B* generates sideforce more efficiently. Figure 6.5 and Figure 6.6 confirm this view showing the plot of the effective draught for the two hulls; this is a direct measure of the efficiency of the hull form and is calculated as shown in Equation (6.5). At 15 knots the two hull forms have similar behaviour, whilst at 25 knots, *Hull A* as a much higher induced drag component, as noted in Section 4.4.2. It is necessary to remember that the models were tested without appendages, therefore it is not possible to estimate the increase in induced or heeled drag resulting from the addition of the pods, thus no definitive conclusion can be drawn on which hull performs better when sailing to windward.

$$T_e = \sqrt{\frac{L^2}{R_I \rho \pi V_S{}^2}} \tag{6.5}$$

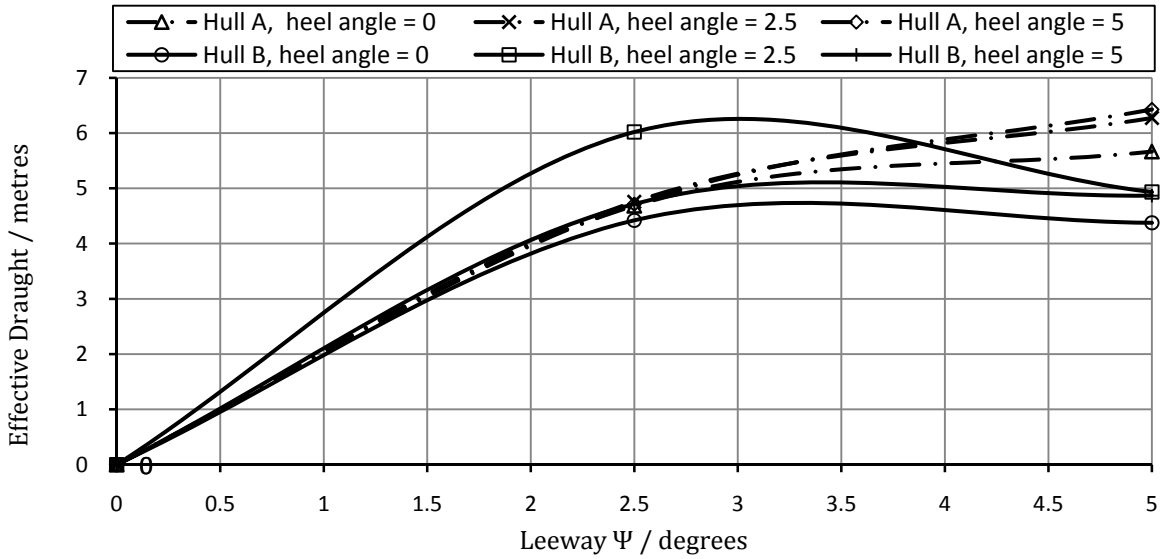

Figure 6.5 – Variation in effective draught with leeway angle, at V_S = 15 knots.

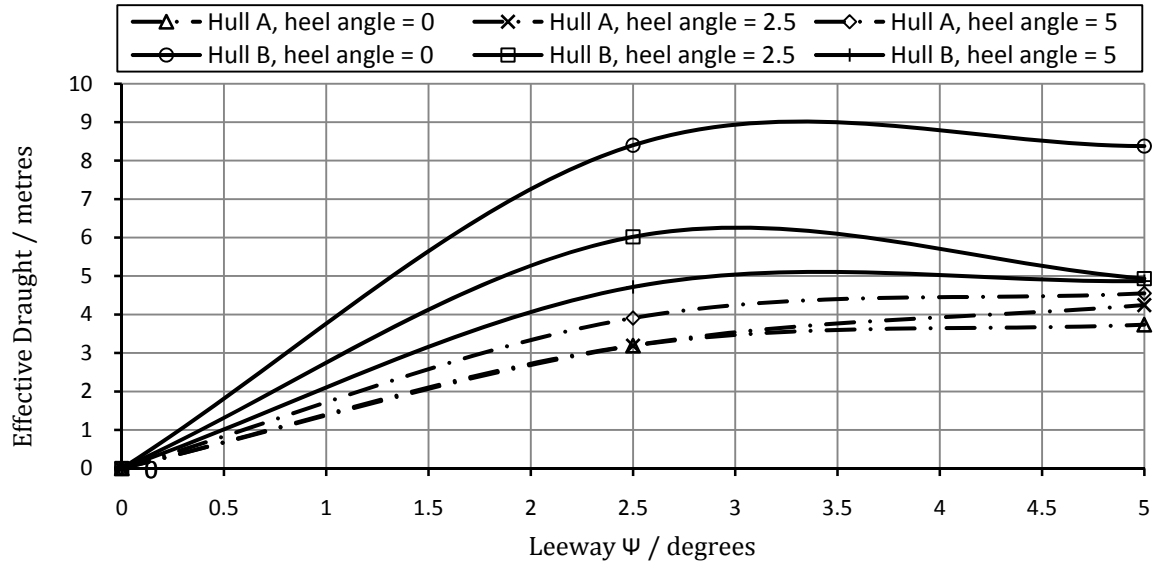

Figure 6.6 – Variation in effective draught with leeway angle, at V_S = 25 knots

In order to obtain a unique reduction figure for the entire voyage, it is possible to average the thrust reduction for different speeds using the round trip breakdown shown below in Table 6.7. Originally two different schedules were simulated to investigate the effects of delays on the average reductions. In such a case, the feeder would slow down to 15 knots to increase the propulsive benefits from the sails; however the difference in thrust reduction between schedules was found to be only 0.2% and therefore only the schedule which reflects a realistic loading and unloading time is included in the report.

Table 6.7 – Round trip speed weightings

	Speed/ knots	*Hours*	*Weight*
Approaching port & manoeuv.	<4	2.24	0.027
Slow speed	15	45.92	0.55
High speed	25	35.84	0.43
Port	0	28	0
Total		112	

The choice of including a third low speed is based from the possibility of using the vectored thrust of the sails for manoeuvring, thus reducing the use of the bow thruster. This is the case for the *MV Ashington* which used a *Walker Wingsail* system fitted on top of the superstructure removing the need to use of tugs [Satchwell (1986)]. The necessity of having bow thrusters however remains as the sail system would not be able to sway the feeder straight into the wind. At lower speeds the thrust reduction is unrealistically high; this is explained by the fact that no experimental drag data is available for that speed, therefore the Holtrop estimate used to compute the reductions, may not be very accurate at such low speeds. For these reasons, the reductions at the manoeuvring speeds are not included in the main economic analysis.

Table 6.8 – Percentage thrust reduction weighted for round trip

	Singapore		*Caribbean*	
	Annual	Seasonal	Annual	Seasonal
Hull A thrust reduction / %	3.9	5	3.3	4.2
Hull B thrust reduction / %	4.6	6.4	3.9	5.4

Table 6.8 summarises the thrust reduction for the selected areas of operation, the reductions in thrust are considerably small respect to the initial estimate of Section 5.1.3. At 15 knots the estimated 10% reduction,

has decreased to 2-6% whilst at 25 knots the 3% estimate has decreased to 1-2%. The factors that determined these changes are summarised below:

- experimental C_D was found to be lower than theoretical estimate thus increasing the thrust reduction;
- experimental calm water resistance at 15 knots is higher than the original Holtrop estimate thus decreasing the thrust reduction;
- addition of windage data decreases the rig propulsive efficiency;
- addition of induced and heel drag decreases the sail propulsive benefits;
- lower average wind speed for the selected areas limits the thrust reductions.

North Atlantic routes

One of the factors which limited the thrust reductions is the average wind speed. The aim of this section, is to undertake an environmental sensitivity analysis and show how the performance of the feeder (mainly fuel consumptions), would improve if it was to operate in a different area. Using data from the initial economic analysis it has been possible to identify 12 routes in the North Atlantic region which would be suitable for the fast feeder. Table 6.9 presents the voyage details for the selected routes including the improvement in thrust reduction respect to the annual estimate for Singapore (Table 6.1). The increase is due to the higher average true wind speed (+34%), which in turn increases the apparent wind angle by 16% and moves the average sailing point towards beam reach, where the maximum thrust is generated.

Table 6.9 – Annual North Atlantic voyage simulation

	Hull A		*Hull B*	
Speed / knots	15	25	15	25
Thrust reduction / %	4.73	1.66	6.4	2.15
Improvement	+2.2	+0.7	+2.9	+1.0
Angle of heel / deg.	0.32	0.69	0.32	0.69
Leeway angle / deg.	0.44	1.04	0.58	1.22
Induced – heeled drag / % R_T	1.68	1.33	1.84	1.45
Roll Damping / %	17.95	30.5	17.95	30.5

A significant improvement of the thrust reduction is observed at the lower speed, whilst at 25 knots the reductions remain quite low. This result enables the designers to draw some conclusions about the effectiveness of the proposed rig and the limits to its application for the fast feeder concept. The reductions achieved at the lower speed can partially justify the use of sails, however higher savings would be required to make the use of sails profitable (see Section 6.2.2 for further details). If a second iteration of the design spiral was undertaken the sail area would have to be increased and the possibility of adding a third sail may be considered. Both solutions would imply radical changes to the fast feeder concept in terms of safety and capacity. Increasing the span and the chord of the wings would exclude the possibility of stowing the rigs below the deck; hence the structural analysis would change to assess the loads on the ship structure. The addition of a third foldable rig would decrease the cargo capacity and the whole economic case would have to be revised. Decreasing the service speed would certainly improve the viability of the existing sail system, but the initial specification prevents this. Section 6.1.2 addresses the comparison of the two hull form designs in terms of propulsive efficiency.

6.1.2 Propulsive efficiency

The efficiency of the propulsion system must be estimated in order to predict the total installed power requirement of a ship, in this case providing a major measure by which to compare the two designs. This requires estimates of the performance of the propeller and transmission system, as well as the flow in the wake and the drag of the podded drives. In this case, propeller performance is calculated using the commercial software *WINPROP*, transmission efficiencies taken from manufacturer's guidelines and all other calculations made using empirical methods.

General theoretical basis

The relationship between effective power and delivered power (at the propeller), is given by:

$$P_D = \frac{P_E}{QPC}. \tag{6.6}$$

The quasi-propulsive coefficient (QPC) is defined as:

$$QPC = \eta_H \eta_O \eta_R = \frac{(1-t)}{(1-w_T)} \eta_O \eta_R. \tag{6.7}$$

η_O is the efficiency of the propeller without the presence of the hull, whilst η_H and η_R account of the interaction between hull and propeller. Values of t, w_T and η_R for each hull are estimated using empirical formulae. The references containing these are summarised in Table 6.1.

Table 6.10 – References used for estimating propulsive coefficients

Coefficient	*Hull A*	*Hull B*
t	Holtrop & Mennen (1978)	Holtrop & Mennen (1978)
w_T	Henschke (1965)	Schneekluth (1988)
η_R	Holtrop (1984)	Holtrop & Mennen (1978)

The coefficient η_O is calculated using *WINPROP* which uses standard series propeller charts to derive performance data for a given set of input parameters. The Wageningen B4.70 series data is used for four-bladed propellers, while B5.75 is used for the five-bladed podded propeller. These series were chosen as they provide a relatively high BAR and therefore are less likely to encounter problems involving cavitation. However, detailed design of the propellers is not carried out in this case. Having obtained all the propulsive coefficients, the brake (or installed) power is estimated by:

$$P_B = \frac{P_D}{\eta_T} \tag{6.8}$$

The transmission efficiency (η_T) in the case of electric propulsion is made up of a number of component efficiencies, with the values given in Table 6.11 taken from those quoted by ABB (2009). Note η_T is simply the product of the first five values.

Table 6.11 – Electrical efficiency components of the transmission efficiency

Efficiency component	*Value*
Frequency converter	0.990
Generator	0.970
Motor	0.970
Switching gear	0.999
Transducer	0.995
Overall transmission	0.926

Since both the propulsion systems proposed utilise two motors powering two propellers, the transmission efficiency is assumed the same for both designs.

Accounting for podded drives

The simple design procedure outlined in the previous section must be modified to account for the drag of the podded drives for both hulls. The procedure followed is that outlined by ITTC (2008e), which estimates the drag of the pod(s) and accounts for this by reducing the values of η_0 and K_T attributed to the propeller. Note this is a slight departure from standard performance estimates, which normally include appendage drag in the total resistance of the ship. However, there is a considerable difference between a propeller operating behind a 'standard' merchant hull form and one mounted on a pod, which this method must account for. The pod dimensions are estimated using ABB (2009) and are assumed the same for both *Hull A* and *Hull B* since an even power distribution was initially assumed for *Hull A*. Where required values were not available, dimensioning ratios supplied by Molland *et al.* (unpublished) were employed. Figure G.1 and Figure G.2 provide the values used in all calculations. Note that, having checked for adequate clearances on the general arrangement, the largest possible propeller diameter was selected in both cases so as to maximise efficiency.

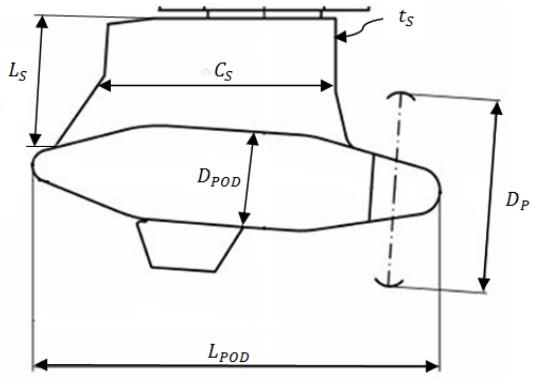

Figure 6.7 – Pod dimensions used in drag estimate [ABB (2009)]

Table 6.12 – Summary of dimensions used in estimation of podded drive drag (*Hull A* uses *VO1800* and *Hull B* uses *VO2100*) [ABB (2009)]

Symbol	*Dimension*	*VO1800*	*VO2100*
D_P	Propeller diameter	3.8 – 5.9	4.4 – 6.4
D_{POD}	Pod diameter	2.33	2.68
L_{POD}	Pod length	10.10	11.60
C_S	Strut chord	5.76	6.60
L_S	Strut length	2.59	2.97
t_S	Strut thickness	1.73	1.99

Using these values and the ITTC '57 skin friction line, the drag of the pod can be calculated based on three components: pod body drag; pod strut drag; and interference drag. Any component due to lift is neglected since the propeller is assumed to be lightly loaded at the design speed of 25 knots. During this process, the value of interference drag obtained proved unreliable, and far too large. Therefore, based on values presented by ITTC (2008e) the interference drag was assumed to be equal to the pod body drag as a conservative estimate. Note that this method takes into account the difference in the velocity impinging on the pod inside and outside of the propeller diameter.

Accounting for contra-rotating propellers

The main consideration when predicting contra-rotating propeller design is the increase in inflow velocity into the aft propeller. In this case, this was calculated in the same way as the velocity impinging on the pod, based on Molland *et al.* (unpublished):

$$V_{a,aft} = V_{a,fwd} + K_R V_{a,fwd} \left\{ \left[1 + \left(\frac{8K_T}{\pi J^2} \right) \right]^{0.5} - 1 \right\}, \tag{6.9}$$

where V_a is the advance speed, equal to $V_S(1 - w_T)$; $K_R = 0.5 + \{0.5/[1 + (0.15/J)]\}$; K_T is the propeller thrust coefficient, equal to $T/(\rho n^2 D_P^4)$; and J is the advance coefficient, equal to V_a/nD_P. Note this serves to increase the total pod drag. van Gunsteren (1971) describes an alternative approach, using a blade element

momentum (BEM) model to evaluate contra-rotating propeller performance, and optimise propeller diameter. Whilst this would have been the preferred method, it was considered too complex and could not be successfully implemented in the time available, and as such was disregarded.

The second design issue to selecting the distribution of power between the forward and aft propellers. Praefke *et al.* (2001) recommend that the designer keep the forward and aft blade passing frequencies the same to avoid broad band excitation and optimise efficiency by eliminating swirl from the slipstream using a torque identity. This implies:

$$\frac{NB_{fwd}}{NB_{aft}} = \frac{n_{aft}}{n_{fwd}} = \frac{P_{D,aft}}{P_{D,fwd}}. \tag{6.10}$$

Since it is desirable to minimise the size, and therefore drag, of the installed pod, and upon finding most CPPs to be four-bladed, a ratio of NB_{fwd}/NB_{aft} = 0.8 was chosen. Taking into account the propeller speed and shaft power ratings of the pods in (see Figure G.1), this assumption allowed the smaller *VO1800* model to be selected for *Hull A*. Finally, the forward propeller was sized to have a larger diameter than the aft one, taking account of slipstream contraction.

Having derived the power distribution between forward and aft propellers for the *Hull A*, a suitable CPP could be selected. Based on delivered power requirement and suitability for fast ships, the Wärtsilä *LIPS E-HUB 4E1300* was chosen, providing up to 16 MW delivered power, and a favourable boss diameter/overall diameter ratio of 0.2 [Wärtsilä Corporation (2008)].

Estimating installed power requirement

Applying the theoretical approach described, the required installed power of each ship for calculated. Important values are summarised in Table 6.13.

Table 6.13 – Summary of values used in estimation of installed propulsive power for both hulls

	Shaft		*Pod*
	fwd	*aft*	
$stern\ form\ coeff.$	-18	-18	-25
t	0.07965	0.07965	0.09822
w_T	0.2883	0.2883	0.1263
η_R	0.9975	1.1658	0.9600
$D\ /\ m$	6.3	5.9	6.4
NB	4	5	4
η_O	0.700	0.657	0.706
QPC	0.847	0.990	0.664
P_D / MW	11.371	9.093	11.676
η_T	0.926	0.926	0.926
$P_{B,prop}\ (90\%\ MCR) / MW$	12.280	9.821	11.792
$P_{B,total}\ / MW$	25.42		27.12

An operational power margin of 15% is assumed based on the recommendation ITTC (2005a). Auxiliary load was assumed from Buhaug *et al.* (2009) who estimate the auxiliary power requirement of 1000 to 2000 TEU container ships as one generator of 985 kW running at 60% utilisation equivalent to approximately 0.6 MW. However, Wärtsilä Ship Power R&D (2009) claim overall savings of at least 10% in installed power when using electric propulsion which is larger than the total estimated auxiliary power requirement. Therefore this figure is not included in the total installed power estimate, although it can be seen that the plant selected would be able to provide this power if necessary.

Based on the final values of installed power in Table 6.13, plant were chosen for each concept. As the calculated installed power is the assumed maximum power requirement, it is desirable not to over-size the installed plant so as to reduce efficiency, yet there are obvious limitations in the number of units available within a certain power range. Considering the Wärtsilä dual-fuel 50DF range [Wärtsilä Ship Power Technology (2009a)], the following installations are proposed:

- *Hull A:* 2 x 6L50DF @ 5.70 MW and 2 x 8L50DF @ 7.60 MW totalling 26.6 MW.
- *Hull B:* 2 x 6L50DF @ 5.70 MW and 2 x 9L50DF @ 8.55 MW totalling 28.5 MW

Full specifications of these plant are included in Figure G.2 and Table G.7. It can be seen that total installed power for *Hull A* is closer to the target value than for *Hull B*, as well as being lower. In addition, a 40 tonne saving in total weight for the four units is seen with the former configuration. As well as improving efficiency, the use of four plant instead of two larger units increases overall system redundancy, although a penalty is paid in terms of total weight and overall footprint area.

Off-design cases

Based on the estimates of thrust reduction provided by the sail system (see Table 6.5), the analysis of the main propulsion system was repeated for speeds of both 15 knots and 25 knots. These are considered 'off-design cases' since the propulsion system has been optimised to provide 100% of the propulsive power requirement at the service speed of 25 knots. A summary of the power savings in terms of both power requirement and percentage reductions is given in Table 6.14.

Table 6.14 – Savings in power requirement for *Hulls A* and *B* based on annual and seasonal wind conditions, Singapore region (power margin not included)

Wind condition	*No wind*		*Annual*				*Seasonal*			
	P_B / *MW*		P_B / *MW*		*% reduction*		P_B / *MW*		*% reduction*	
Speed / knots	*15*	*25*	*15*	*25*	*15*	*25*	*15*	*25*	*15*	*25*
Hull A	3.94	22.10	3.88	22.02	-1.52	-0.36	3.82	21.97	-2.28	-0.59
Hull B	4.66	23.58	4.38	23.45	-6.01	-0.55	4.32	23.37	-7.30	-0.89

The percentage reduction in power requirement is larger for *Hull B* than *Hull A.* However, the power requirement for *Hull B* is still higher in all cases. The values presented in Table 6.14 are used in Section 6.2.1 as part of the voyage simulation to assess the total emissions of the ship during a typical round trip.

Discussion

It must be remembered that the method used to estimate the propulsive efficiency of both hull forms is based on empirical formulae and standard series propeller charts. Whilst the accuracy of the method employed is not fully quantifiable, it is recognised that the estimates presented are sensitive to both the assumptions that have been made, and the choice of formulae and input values used.

This is particularly true for *Hull B* where the novel hull form means the empirical estimates of propulsive coefficients for twin-screw ships may not be appropriate. However, with a lack of any other data, these were considered the best estimate available to the designer. A more detailed insight into the wake velocity profile would allow improvements in the design and optimisation of the propulsors, yet this would require the use of specialised equipment such as wake traverse probes, which were not available to the project.

6.1.3 Justification of hull form choice

Since the concept is required to improve efficiency and reduce environmental impact compared to existing ships, the main criteria for selecting a hull form is the installed power requirement, as presented in Table 6.13. This leads to *Hull A* being chosen for further development, since it's installed power requirement is estimated to be approximately 6% lower than *Hull B.* This is due to the twin pods of *Hull B* providing significantly more drag than the CRP-pod propulsion arrangement of *Hull A. Hull A* has also been shown to perform better when operating in waves, again reducing overall fuel consumption.

Although it has not been modelled here, the CRP-pod propulsion arrangement of *Hull A* has an additional advantage; when operating at low speed, the CPP can be disengaged and feathered so as to reduce drag, with all the propulsive power delivered through the pod. Due to the twin pod layout of *Hull B* this cannot be achieved and thus both pods must be run at low power and thus efficiency than the single pod of *Hull A.* It should be emphasised that both concepts have not been optimised for low speed (15 knots) operation since it is assumed that the installation of CPPs of podded drives is not possible due to the high complexity of such a system. If this were possible, then both of the propulsion arrangements considered could be optimised for two speed operation.

Whilst this choice has been based on those factors already mentioned, it should be noted that *Hull B* performs significantly better under sail, as discussed in Section 6.1.1. However, this 'thrust reduction' is not large enough to compensate for the difference in power requirement already described. If the ship were designed to operate at a lower service speed, or more favourable wind conditions were modelled, then the choice of hull form may be different.

6.2 Design feasibility

6.2.1 Round-trip evaluation

Manoeuvrability in port

An important feature of the design is its ability to manoeuvre into a berth without the use of tugboats. This aims to save on berthing costs as well as reduce waiting times when entering port (see Section 2.5). Therefore the requirement set was that the ship be suitably equipped to be able to move in pure sway and pure yaw at slow speed (three knots), and appropriate machinery be installed to achieve this. While the azimuthing podded drive can be used for this purpose, a bow thruster must be specified to augment it.

The approach recommended by Palmer (2010) was to equate the total force and moment in sway and yaw respectively to the equivalent force and moment provided by the manoeuvring devices. This requires assessing both the hydrodynamic and aerodynamic cross-flow drag of the ship. The following assumptions were made in this analysis, that:

- The ship is moving in pure sway or yaw at a velocity, or angular velocity equivalent to, three knots with no current effects;
- The wind speed is taken as the prevailing condition for the regions under investigation of 5.3 metres per second at ten metres above the water surface. The wind heading is assumed to be beam-on with the ship moving into the wind i.e. the worst case scenario;
- Shallow water effects are neglected and calm water is assumed;
- The sail system is folded away and thus provides zero drag.

The hydrodynamic sway force and yaw moment are calculated by adapting the method of Faltinsen (1998) which is designed for assessing current loads, using a strip theory approach, thus:

$$F_v = \frac{1}{2}\rho {V_s}^2 \int_{L_{WL}} C_{D,cf}\,(x) T(x) dx \tag{6.11}$$

and,

$$M_\psi = \frac{1}{2}\rho {V_s}^2 \int_{L_{WL}} C_{D,cf}\,(x) T(x) x\, dx. \tag{6.12}$$

The change in cross-flow drag coefficient ($C_{D,cf}$) along the length of the hull was estimated from Faltinsen (1998) and adapted based on values recommended by Hoerner (1965) to correct for the effect of increased bilge radius. The hull was divided into 20 sections of 7.924 metres length, with the draught $T(x)$ measured at each from the general arrangement drawing.

The aerodynamic drag was calculated assuming the above-water side-on form to be a simple rectangle of 165.8 metres by 19.74 metres, with a drag coefficient a 2.025 taken by interpolating values from Çengel & Cimbala (2006) for rectangles of varying aspect ratio and wind gradient profile according to Molland (2009). The results are summarised in Table 6.6.

Table 6.15 – Hydrodynamic and aerodynamic components of sway force and yaw moment

	Hydrodynamic component	*Aerodynamic component*	*Total*
Sway force / kN	823.7	169.3	993.0
Yaw moment / kNm	2292.4	160.9	2453.2

To equal the forces and moments estimated in Table 6.15, the following procedure was used:

1. Divide the required thrust between the bow thruster and the pod;
2. Calculate the actual thrust achieved and power required by the pod propeller using the method described in Section 6.1.2. Since the pod is operating at 90 degrees to the centreline, t, w_T and η_R are assumed to be zero;
3. Select a bow thruster diameter based on manufacturer's specifications [Rolls Royce (2008)] which produces close to the required thrust, calculated using actuator disc theory [Molland (2009)]. Compare required thrust to achieved thrust. If discrepancy, modify thrust balance between pod and thruster and repeat. If satisfactory, compare yaw moment;
4. Modify yaw moment by moving bow thruster position forward or aft. Check bow thruster location against layout restrictions;
5. Estimate total power requirement. For the pod, assume $P_E = P_D \eta_o$, and bow thruster efficiency to be 0.8 [Bertram (2000)].

Having achieved an agreement between required and device thrust of less than 1%, the following power requirements were derived: 2949.0 kW for the pod; and 2642.6 kW for the bow thruster. This results in a total propulsive power requirement for manoeuvring of 5591.7 kW. Note that this power requirement can be met using one of the 6L50DF plant, rated at 5.7 MW, running at 100% MCR.

The bow thruster installed is the Rolls-Royce TT-CP of 2.8 metre diameter giving a power of 2650 kW. This size of bow thruster is more than twice the power of a typical unit installed on a standard feeder ship, as may be

expected for such a manoeuvrable ship, yet its diameter meets the requirement to be located at least one diameter below the still water surface in order to avoid ventilation [Palmer (2010)].

Cargo handling time

Reducing cargo handling time is also key to improving the efficiency of the design. The requirement is to be able to self-unload, and faster than existing ships, which can spend up to 48 hours being unloaded by quayside cranes. Time is also saved since the ship will not have to wait for a crane-equipped berth to become available.

It is assumed that the ship is equipped with two gantry-type cranes. Information on the operating speeds of similar container terminal gantry cranes was used in estimating the total time at berth (see Table 6.16).

Table 6.16 – Summary of data used for cargo handling simulation [Kalmar (2009)]

	Trolley	*Gantry*	*Hoist*
Speed / $m.min^{-1}$	90.0	270.0	90.0
Ave. dist. per move / m	28.0	26.4	20.6
No. of moves per two TEU	-	2.0	4.0

In addition, the following assumptions were made regarding the loading/unloading pattern, that:

- The average load per lift is equivalent to two TEU;
- Each crane unloads an entire bay before moving to the next, which is located on average one quarter of the length of the cargo area away;
- The average distance moved in the vertical direction per lift is equivalent to eight TEU;
- The average distance moved in the lateral direction per lift is equivalent to half the ship beam plus 13 metres for clearance onto the quayside;
- A 10% margin is assumed for connecting the container(s) to the gantry.

Based on the values and assumptions presented, the total cargo handling time for the fully loaded ship of 1270 TEU is 25.9 hours based on two loading and unloading sequences and an average handling time of 0.28 minutes per TEU. The total time reduces to 23.3 hours if the ship is only utilised to 90%. In a more realistic scenario where the ship is required to use the hub port's own quayside cranes, the total cargo handling time increases to 28.2 hours based on a time of 0.36 minutes per TEU at Singapore [Maritime and Port Authority of Singapore (2009)].

Voyage simulation

In order to provide an assessment of the success of the concept in terms of both economics and emissions, a comparison was made with what were assumed typical existing ships operating in both the Singapore and Caribbean regions. Based on the analysis presented in Section 2.6 and assuming that each ship of the proposed design would replace two existing ships, it was predicted that the concept could meet predicted 2020 container trade demand by sailing three round trips for every two sailed by an existing ship. Table 6.17 illustrates this over a 14 day period, assuming a utilisation factor of 90% for all ships.

The demand in Singapore is met easily, and the utilisation factor can reduce to 84% before a shortfall in delivered TEU is seen. This is a negligible shortfall in the Caribbean region which is assumed allowable, although an increase in utilisation factor of 0.5% would see this negated.

Table 6.17 – Summary of simulated voyage to meet fortnightly container demand

	Singapore comparison	*Caribbean comparison*	*Fast feeder*
Average TEU capacity at 90% utilisation	801	860	1143
No. of ships operating on route (minimum ratio)	2	2	1
No. of round trips per ship per fortnight	2	2	3
Average time per round trip / hours	168	168	112
Total TEU carried to/from spoke port per fortnight	3204	3440	3429
Speed @ 90% MCR / knots	15.2	17	25

A basic voyage simulation was made assuming the operational profile of the typical ship to be similar to that stated by Mash (2009). Cargo handling time was estimated assuming 0.36 minutes per TEU at the hub port [Maritime and Port Authority of Singapore (2009)] and 1.1 minutes per TEU at the spoke port [Chittagong Port Authority (2010); Vietnam Seaports Association (2010)]. This results in total cargo handling time per round trip of 40 hours and 45.9 hours for the Singapore and Caribbean ships respectively. Power requirement and installed plant were selected using the equations presented in Table 3.1 and examination of basis ship data.

The operational profile of the fast feeder was calculated to include the estimates of cargo handling time as well as power savings due to the use of the sail system at speeds of both 15 and 25 knots, calculated from Section 6.1.1 assuming typical annual wind conditions. Note that added resistance in waves of the fast feeder was modelled directly from testing results, while no such effect was included for the comparison ships. It was assumed that any slack in the schedule of these ships was taken up waiting in port using only auxiliary power, while the fast feeder experiences no delays due to weather or waiting time. Note that since the differences in thrust reduction due to sails and distance of route between the two regions was negligible, the fast feeder voyage was modelled identically in both regions. The speed and power profiles modelled are included as Figure H.1 and Figure H.2. Table 6.18 summarises the overall power requirements for the fortnightly period simulated.

Table 6.18 – Summary of power requirements for fast feeder and comparison ships over fortnightly period

	Singapore comparison			*Caribbean comparison*			*Fast feeder*		
Operating Mode	*Time / hours*	*ME power / kW*	*AE power / kW*	*Time / hours*	*ME power / kW*	*AE power / kW*	*Time / hours*	*ME power / kW*	*AE power / kW*
Cargo handling	78.0	0	591	91.7	0	591	77.3	0	-
Manoeuv./waiting	44.2	0	591	51.2	0	591	6.7	5600	-
Low speed	53.5	5656	591	48.3	6567	591	154.6	4880	-
High speed	160.3	7272	591	144.8	8443	591	97.4	22100	-

Note that the comparison ships are assumed to have a power requirement for manoeuvring equivalent to their normal auxiliary load. Although this may seem low, this accounts for the use of tugs in berthing operations. Note also, the fast feeder has zero power requirement during cargo handling since 'cold ironing' is assumed, whereby shore-side power is provided to the ship when berthed.

Based on the profile assumed in Table 6.18 and the values of SFC and emissions specified in Table H.1 and Table H.2 respectively, an estimate of the fuel consumption and emissions of each ship could be made. Fuel costs were estimated using values from Table 3.9 Note that the comparison ships are assumed to be burning MDO fuel to comply with MARPOL Annex VI regulations [IMO (2005b)], whilst the fast feeder concept uses LNG fuel exclusively. The 'percentage difference' values presented are the savings predicted when operating the fast feeder as opposed to the comparison ship in each region.

Table 6.19 – Summary of fuel consumption and cost, and emissions for fast feeder and comparison ships over fortnightly period

	FC / tonnes	*FC / % diff.*	*CO_2 / tonnes*	*CO_2 / % diff.*	*NO_x / tonnes*	*NO_x / % diff.*	*Cost / kUSD*	*Cost / % diff.*
Singapore Comp.	593.3	-32.9	2100.3	-39.7	38.3	-89.2	381.5	-51.5
Caribbean Comp.	618.5	-35.6	2190.5	-42.2	40.0	-89.7	397.7	-53.4
Fast Feeder	398.2	-	1266.5	-	4.1	-	185.0	-

Table 6.19 shows that the overall GHG (CO_2) emissions reduction target of 30% has been exceeded in both regions, meaning the fast feeder is deemed environmentally sustainable within the scope of this analysis. Note that this estimate does not account for any emissions incurred during build or scrappage and in the production and transport of bunker fuel to its point of delivery to the ship. The majority of this saving in emissions is due to the use of LNG fuel and reducing the number of fortnightly sailings from four to three. It can also be seen that the reduction in NO_x emissions estimated is in line with the values presented in Table 3.8. This means the ship complies with MARPOL Annex VI Regulation 13. In addition, Regulation 14 on the Annex, limiting SO_x emissions to 4.5%, is easily met since LNG fuel has zero sulphur content. Buhaug *et al.* (2009) note that most ships currently already comply with Regulation 14, which comes into force in 2020. However, there is currently little incentive for ship owners to reduce sulphur oxide emissions further using diesel fuels, even after this date. Thus the fast feeder concept is considered highly environmentally sustainable in this respect, removing the ship's contribution to acid rain completely.

The performance of the fast feeder was also judged against the comparison ships using performance indices: the transport efficiency index (TEI) and the IMO Energy Efficiency Design Index (EEDI). Modifications have been made to the formulations of these measures to account for the voyage profiles given in Figure H.1 and Figure H.2.

Table 6.20 – Summary of fast feeder performance against comparison ships using design indices.

	TEI	*modified TEI*	*percentage improvement (modified TEI)*	*EEDI*	*modified EEDI*	*percentage improvement (modified EEDI)*
	TEU·knots / kW			*g CO_2 / tonne·nm*		
Singapore comparison	6.88	3.44	63	24.15	27.05	56
Caribbean comparison	7.12	3.56	58	22.63	31.41	62
Fast feeder	4.48	5.61	-	14.82	11.84	-

Table 6.20 shows that unless the decrease in the number of ships is accounted for the TEI for the fast feeder is not favourable. However, since the fast feeder has been designed to replace a feeder service, rather than a specific ship, it is reasonable to include this modification to the TEI. The environmental performance of the fast feeder in terms of the EEDI is better than that of the comparison ships even without the modifications made to the index. Note that the percentage improvement in EEDI is significantly larger in each case than the percentage reductions in CO_2 presented in Table 6.19. This is because the increase in speed of the fast feeder serves to improve the index value, since the calculation is mass of CO_2 per unit speed, as opposed to purely mass of CO_2 emitted.

Using cost data supplied by Ocean Shipping Consultants Ltd (2010) an estimate of the total daily costs of each of the ships could be made in order to assess the economic viability of the proposed concept. The values presented are linearly interpolated to the TEU capacity of each ship using the data provided, and are based on ownership costs rather than charter. The daily costs presented in Table 6.21 represent two comparison ships against one fast feeder. Daily capital charge is based on newbuild prices of 21.85 and 23.45 million US dollars respectively for the Singapore and Caribbean comparison ships. The newbuild price of the fast feeder was

interpolated from the data provided, but a factor was included to account for the increase in capital cost due to the novel systems installed on the ship, including the podded drive, LNG fuel tank and retractable sail system. Thus a total build cost of 45 million US dollars was used, since more accurate estimates of the additional costs were not available.

Table 6.21 – Summary of daily cost estimates comparing fast feeder concept to two typical existing ships

Cost / USD per day	*Singapore Comparison (two ships)*	*Caribbean Comparison (two ships)*	*Fast Feeder*
daily capital charge	18016	19332	18623
manning	2226	2396	1588
repair and maintenance	976	1048	696
insurance	582	626	416
admin/other	890	956	635
fuel	27250	28407	13214
total cost	49940	52765	35172

The daily cost saving based on a typical fortnightly period is 29.6% and 33.3% in case of the Singapore and Caribbean regions respectively. This represents a significant cost saving to the owner, especially considering this estimate includes an estimate of the additional construction costs associated with the fast feeder design. Based on this analysis, the fast feeder will only become un-economical if the price of LNG fuel more than doubles, to USD958 and USD1000 per tonne respectively in Singapore and Caribbean regions.

6.2.2 Economic feasibility of *Multi-wing* system

This section provides an estimate of the capital and operating costs for the *Multi-wing* sail system; a simple Net Present Value (NPV) analysis is also carried out to assess the profitability of using the sails over the assumed time span after which the feeder is sold. Bergeson & Greenwald (1985) summarises building and running costs of different rig configuration including a rigid wing sail of surface area 280m^2, the cost of which is scaled according to the sail area. To obtain the costs at the present day, an annual national inflation rate is taken as 2.91% [Federal Reserve (2010)]. The figures for building costs are available for a single prototype rig, a rig out of a production run of ten and one out of 100, produced in U.S. In the following analysis the cost of one model out of 10 is used as a reference.

Table 6.22 – Building and running cost for two *Multi-wing* rigs

	Capital investment.	*Annual maintenance*
Cost in 1985 / kUSD	881	10.6
Cost in 2010 / kUSD	1806	21.6
Cost (including 50 % margin for hoisting system) / kUSD	2709	32.3

As the data reflects the cost of a wing sail fitted on deck and the required machinery to operate it, a factor of 1.5 is included to allow for the extra cost of the hoisting system, consisting mainly of the generators required to power the lift.

The annual benefits due to the use of the sails are calculated from the associated power reductions derived using *Winpow*. As the reductions for Singapore and the Caribbean are very similar, only Singapore is considered in this economic analysis. Table 6.23 shows the calculated benefits; the breakdown between annual and seasonal reflects different routes and wind conditions as explained in Section 6.1.1. The following assumptions have been made:

- 71 round trips per year;
- SFC of 430 g.(kWh)$^{-1}$;
- Cost of MDO to be 575 USD.ton^{-1} [Hinrichs (2009)];
- Full load condition only.

Table 6.23 – Annual benefits from the use of the *Multi-wing*

	Hull A				*Hull B*			
	Annual		*Seasonal*		*Annual*		*Seasonal*	
Reduction / kW	60	80	90	130	280	130	340	210
Hours per round trip	46	36	46	36	46	36	46	36
Fuel saved / t	1.2	1.2	1.8	2.0	5.5	2.0	6.7	3.2
Savings per round trip / USD	681	709	1022	1152	3179	1152	3860	1861
Annual benefit / kUSD	48.36	50.33	72.55	81.79	225.71	81.79	274.07	132.12
Total Benefit / kUSD	99		154		308		406	

Net Present Value (NPV) analysis

The Net Present Value appraisal method is used to verify whether the operation of the *Multi-wing* would generate a profit at the end of an assumed project time span of 15 years. The calculation will be undertaken considering the *Multi-wing* system as a separate entity, as if it was to be retrofitted on an existing vessel. NPV is equal to the difference between the net global benefit and the investment cost discounted on the same base [Mange (2006)]. In this analysis, the rate of return is the interest that could be earned on an alternative investment with similar risk. It is essential to select a sensible value as this will determine how the discounted cash-flow is calculated. A hypothetical situation can be assumed where a large shipping company commission the building of ten fast feeders, the interest rate the company would receive is the corporate bond rate of 5.31% [Federal Reserve (2010)]. The Internal Rate of Return (IRR) is the discount rate which makes the NPV equal to zero (the break-even point), and reflects the risk involved in the project [Mange (2006)]. The calculation is based on the costs and annual benefits estimated in the previous section and it relies on the same assumptions.

Table 6.24 – NPV analysis for *Hull A*. operating in Singapore region

	Annual	*Seasonal*
NPV	-2034	-1469
Payback period / years	27.44	17.5

Table 6.24 shows a negative NPV for *Hull A*, with a payback period well above the assumed project time span. A sensitivity analysis on the discount rate used and fuel prices confirms this view. Table 6.25 shows the projections for the second hull form. In this case the annual simulation results just above break-even, whilst the seasonal schedule will generate some profit. However the IRR, found to be 1%, reflects the low profitability of this investment.

Table 6.25 – NPV analysis for *Hull B*. Singapore

	Annual	*Seasonal*
NPV	88	1092
IRR	0.057	0.095

A sensitivity analysis based on *Hull B* for the seasonal schedule, is also included in Table 6.26 to improve the economic model. Note that the fuel cost is a fundamental factor as it determines the magnitude of the annual benefits from the sails. While fuel prices are expected to grow by 2020, thus increasing the profitability, there are no means of estimating the price fluctuations over such a time span.

Table 6.26 – NPV sensitivity analysis for *Hull B*, seasonal schedule

		Rate of return				
		3.31%	4.31%	**5.31%**	6.31%	7.31%
Fuel costs / kUSD	375	6	-178	-345	-495	-631
	475	831	591	374	177	0
	575	1656	1359	**1092**	850	631
	675	2481	2128	1810	1522	1262
	775	3305	2897	2528	2195	1893

The economic assessments conducted so far have only included the benefits derived from the thrust reduction generated by the sails. The reduction achieved at a ship speed of 25 knots has proven to be too small to generate enough return on the investment. Section 7.1.7 outlines a procedure from which the thrust reductions derived from the motion damping due to the sails is estimated. This reduction has not been included in the main economic assessment as the method used assumes a series of parameters which are not directly related to the fast feeder hull form. Nonetheless, the designers are of the opinion that if this potential drag reduction was further investigated and proven, the use of sails at this speed would be readily justified and considerable savings would be generated. Table 6.27 shows the NPV analysis based on annual benefits derived from wind propulsion and motion damping. The annual benefits from motion damping are found calculating the fuel saved when sailing in quartering seas. The thrust reductions are weighted with the probability of quartering winds giving a total reduction of 2.14% and 1.93% at 25 and 15 knots respectively.

Table 6.27 – NPV analysis including thrust reductions due to motion damping. The assumed rate of return is 5.31%

	Annual		*Seasonal*	
NPV	*Hull A*	*Hull B*	*Hull A*	*Hull B*
	1736	2302	3973	4976

The application of the *Wing-sail* is now a profitable investment. Since this analysis aim to assess the ability of sails to generate profit, excluding the benefits derived by the reductions in emissions, the penalty arising from the decrease in container capacity due to the foldable system must also be considered. 88 TEUs which are lost to accommodate the sails; using an estimated freight rate (Appendix H.2) of 4316 USD it is possible to calculate the annual loss assuming a 60% utilisation; the annual figure amounts to 13.48 million USD, well above any projected profit from the sails.

7. Design Development

7.1 Seakeeping analysis

A seakeeping analysis has been completed to estimate the extent of the motions experienced by the ship. This will affect the operability of the ship in terms of safety and comfort of crew and regarding structural integrity, due to possible high slamming loads. It is the former reason that is of primary concern. The superstructure of the ship is situated at the forward end, where it is likely that large accelerations will be experienced. This is where the crew spend the majority of their time. Alongside this accelerations are evaluated at the sail mast locations to aid structural analysis (Section 7.2.3) and where the most vulnerable containers are located to allow an assessment of cargo lashing loads (Section 7.1.5).

7.1.1 Modelling

The analysis has been carried out using Strip Theory implemented using the software *Seakeeper*. Strip Theory is commonly used in Naval Architecture to assess a ship's motions. It essentially simplifies the ship by representing it as a number of two dimensional transverse sections (21 have been used in this case). The hydrodynamic coefficients are determined at these sections using conformal mapping and integration is carried out along the ship's length to give the global hydrodynamic coefficients forming the equations of motion. A detailed explanation of Strip Theory is given by Lewis (1989). As this method makes a significant simplification of the ship's hull form there are clearly limitations to its applicability. Better results are obtained at low Froude numbers however good correlation is claimed up to $Fn = 0.53$ [Formation Design Systems (2005b)], but the quality of results is also dependant on hull form type.

The hull is defined by a number of geometric sections determined from the surface definition in *Maxsurf*. Lewis sections are mapped to these for use in the analysis. Two other main inputs are details of the mass distribution and the definition of sea spectra. The mass distribution of the ship is defined by a vertical centre of gravity and a pitch and roll radius of gyration. The VCG is taken from the mass estimate including a factor for free surface effects, 10.377 metres above the keel. The pitch radius of gyration is taken as 25% of the overall length and the roll as 35% of the beam. These are simply estimates based on common practice and expected values [Loukakis & Chryssostomidis (1975)]. The seaway is represented by the ITTC or Two Parameter Bretschneider spectrum [Formation Design Systems (2005b)]. This requires the user to input characteristic wave height and zero crossing period. The characteristic wave height is set to one metre, as accelerations can be scaled linearly for the desired wave height, and the zero crossing periods have been defined from 3.5 to 11.5 seconds in intervals of one second. This range has been chosen in consideration of the annual wave statistics in the proposed operating areas [Hogben (1986)].

7.1.2 Results

Accelerations are to be presented as and when necessary to carry out any further analysis. In this section the responses in heave, roll and pitch will be discussed. These are best represented by RAOs which are plotted against wave frequency in Figure I.1 to Figure I.3 for both 15 and 25 knots ship speed.

Studying Figure I.2 one can see very large roll response motions. At 25 knots the maximum roll occurs in beam seas, seemingly reasonable. At 15 knots large roll motions are predicted in stern quartering seas. Lewis (1989) states that roll motions are worst in large ships in quartering seas when underway, making this a reasonable prediction. The magnitudes of the roll motion however seem excessive. The maximum RAO at 25 knots is 4.25 and for 15 knots is 7.0. These represent large magnitude motions that, especially at 15 knots, would make

operation impossible if not capsize the ship, depending on the wave environment. At 15 knots in stern quartering seas multiple peaks are observed suggesting resonant frequencies that are very close together. This does not seem likely. Less is known about transverse motions and roll is the most difficult to predict being strongly coupled with sway and yaw [Lewis (1989)]. Furthermore Strip Theory is not able to predict roll motions of this amplitude as they will certainly be outside the assumptions of the linear analysis. Evaluating such motions would require time domain simulations. It is possible that *Seakeeper* is over predicting the magnitude of the roll motions. Peaks in the roll response are observed at high frequency in stern quartering seas. Lewis (1989) (p79) states that 'severe roll can occur in lighter seas with shorter period if the ship is underway and the seas and coming from the quarter' which coincides with what is seen from the results. In addition, for a ship with roll damping less than 5%, as in this case (see Section 7.1.7 for naked hull roll damping), it is not unusual to observe peak roll RAOs greater than ten [Lewis (1989)]. On this vein, it is possible that the roll prediction is not inaccurate but the performance of the hull is poor. This seakeeping analysis does not account for any additional damping from the sails. Section 7.1.7 estimates this increase in damping, which significantly improves the roll motions potentially eliminating the need for any additional stabilising mechanisms.

Pitch motions seem reasonable both in terms of magnitude and the effect of wave heading. At both speeds in head and following seas the response is similar in magnitude (peaks at approximately 1.2) as it is in stern and bow quartering seas (peaks at approximately 1.0) and the magnitude of the response in beam seas is significantly lower (peak at approximately 0.6). This behaviour is expected.

At 25 knots there are large heave motion peaks in head (1.4), bow quartering (1.5) and beam seas (1.25). These results are larger than expected, especially in bow quartering and beam seas. It is possible that this could be due to pushing the limits of Strip Theory's applicability at high Froude number as the same problems in head and bow quartering seas are not observed at 15 knots although the large amplitude motions in beam seas exist almost identically. These problems could be resulting from the poor fitting of the Lewis sections in the forward and aft regions of the ship. Lewis sections have not been able to fit the high curvature shape at the bow and stern, hence the sections are not representing the form accurately. This can be seen in Figure 7.1 and is occurring due to Lewis forms being restricted to be horizontal at the keel and vertical at the waterline. This has resulted in changes in the volume distribution that affects the magnitude of the motions at all headings. At both speeds the response for following and stern quartering seas decays quickly from a value of one but then increases and peaks again at higher frequency.

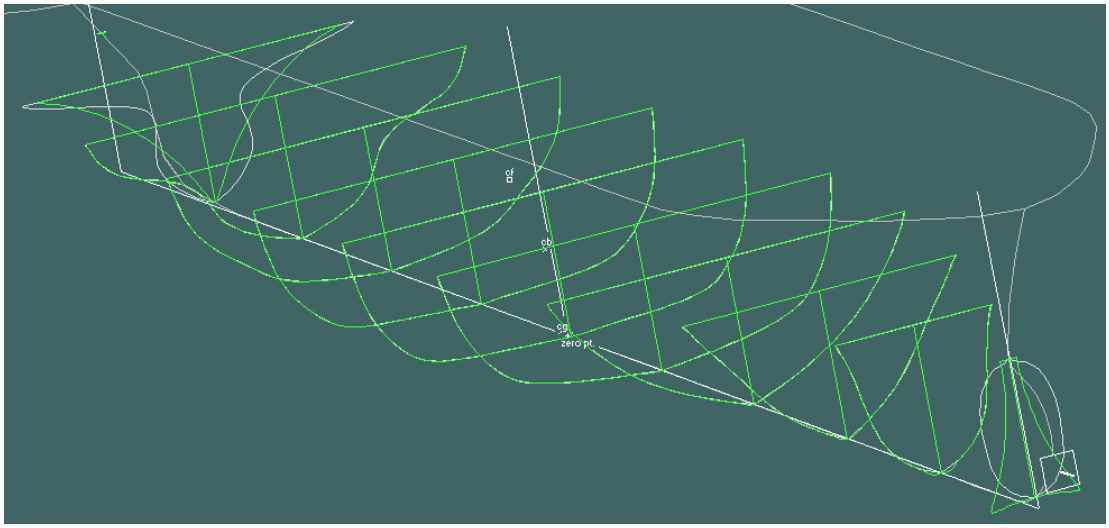

Figure 7.1 – Mapping of 11 Lewis sections to *Hull A* (Ship sections – white; Lewis forms – green)

7.1.3 Theoretical added resistance

A theoretical prediction of the added resistance has been computed in head seas to provide a validation and comparison to the results presented in Section 4.4.3. For this reason the analysis is carried out for both *Hull A* and *Hull B*, seakeeping only considered *Hull A*. *Seakeeper* provides three analysis methods for determining the added resistance in waves; two methods by Gerritsma & Beukelman (1972) and one by Salvesen (1978). Salvesen (1978) provides a comparison of the proposed method against the method of Gerritsma & Beukelman (1972) and results from experiments for a destroyer hull ($C_B = 0.49$) form operating at $F_n = 0.35$. Salvesen (1978) (Figure 7.2 and Figure 7.3) shows that the proposed method gives results that are a lot closer to those from the experiments than the results obtained by the method of Gerritsma & Beukelman (1972). This destroyer form is not significantly different to the proposed hull forms and hence this method is employed. This method is defined by Wilson (1985) as a 'hull pressure method' and uses a distribution of sources and doublets along the centreline of the ship to represent the flow around the hull. The velocity potential has three components due to the

- incoming wave field;
- the singularities in calm water;
- and the wave system of the singularities.

The added resistance is hence given by the sum of six components due to the

- pure heaving of the ship;
- the pure pitching of the ship;
- the wave diffraction off the hull;
- the coupling between heave and pitch;
- the coupling between heave and the reflected wave;
- and the coupling between pitch and the reflected wave.

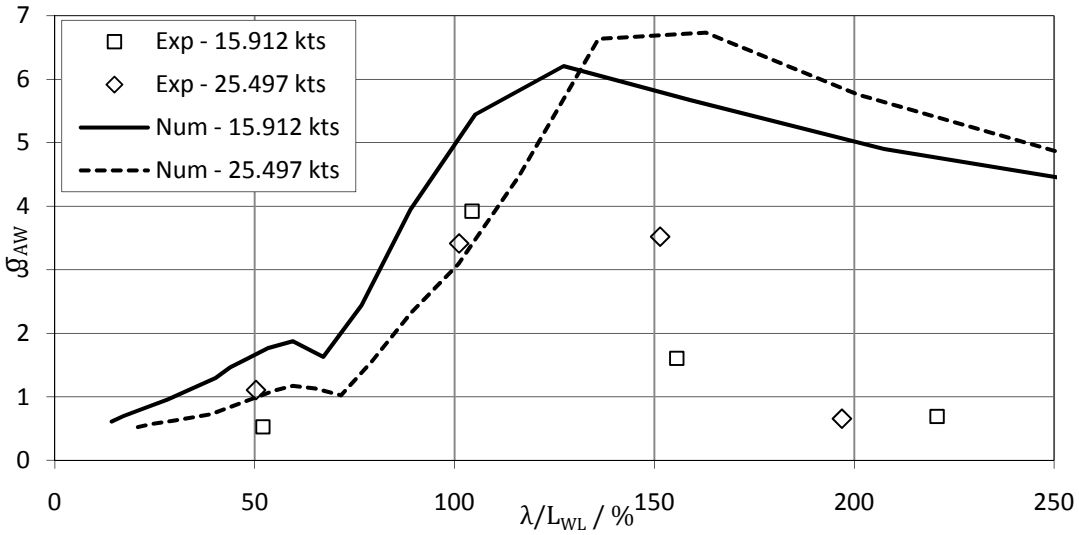

Figure 7.2 – Comparison of numerical and experimental added resistance - *Hull A*

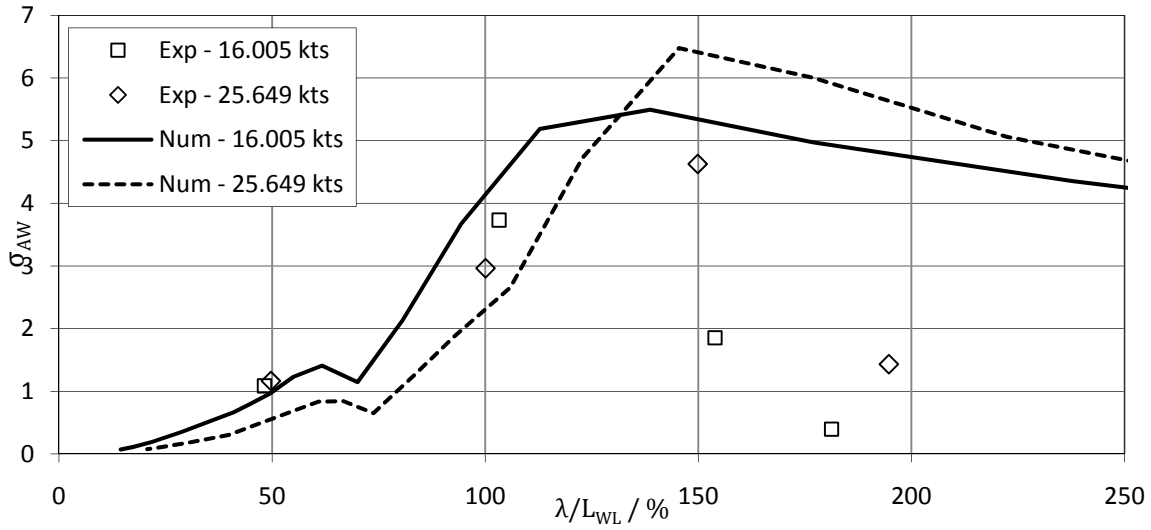

Figure 7.3 – Comparison of numerical and experimental added resistance - *Hull B*

Figure 7.2 and Figure 7.3 illustrate a comparison of the numerical and experimental solutions for *Hull A* and *Hull B* respectively. The input speeds for the numerical analysis match those of the tested runs. The results are relatively similar. However, generally the results from the numerical method are larger. The results for *Hull B* match better. As noted in Section 4.4.3 the peaks of the added resistance in the experimental data have not been captured. One cannot then be sure how the magnitudes of the peaks from the tests would compare to the numerical data. It is probable that the peaks will coincide in terms of what wavelength they occur at. The trend in the peak location as speed increases as mentioned in Section 4.4.3 can be seen clearly in both sets of numerical data. The match between the correlation of the experimental and numerical data at wavelengths less than the peak are good however at wavelengths greater than the peak the correlation is not so good. The numerical data does not show a sharp decrease in added resistance at higher wavelengths than the peak added resistance. The experimental data shows this trend which is somewhat expected, from studying examples presented by Salvesen (1978).

The differences discussed arise from a combination of errors and limitations in both methods. The determination of the numerical added resistance is strongly dependant on the heave and pitch motions [Wilson (1985)] and thus the way they are determined can have a great effect on the results. Although most computations determine ship motions using Strip Theory the accuracy of the solution will have severe effect on the accuracy of the added resistance. Strom-Tejsen *et al.* (1973) has explored this subject and found that, in some cases, vast differences in the added resistance occur; especially near the peak value. This is likely to be a particular problem in the numerical analysis carried out in this thesis as unexpected results have been observed for the heave RAOs in Section 7.1.2. All the forces comprising the total added resistance are dependent on the wave amplitude squared and hence, unlike the motions, the solution is non-linear. This means that any errors incurred in the numerical or experimental analysis are also non-linear and hence their sources are more difficult to identify and their magnitudes larger. There is also the question of the comparability of the pitch gyradius used in each case. In the numerical analysis the pitch gyradius has been used as defined in Section 7.1.1. In the experiments the model was ballasted in an attempt to match this however due to restrictions in time the model was not 'swung' which is the only reliable method in determining the model 'lightship' (model without ballast weights and fittings) gyradius. Any small differences in the gyradii will affect the motions and due to the added resistance's strong dependence on this and the non-linear nature of the problem could pose large discrepancies in the results.

7.1.4 Absolute motions

The *Hull A* roll, pitch and heave RAOs where used with a *Bretschnider* wave spectrum as part of a spectral analysis to calculate the maximum roll, pitch and heave motions for a 7.5m significant wave height at 15 and 25 knots for all wave headings. The roll and pitch angle are important in the determination of forces due to ship motion for both the container securing analysis (section 7.1.5) and also the finite element analysis (Section 7.2.3). A summary of the heave, pitch and roll response in various sea states is given in Table 7.1 and Table 7.2. The highlighted values correspond to the maximum significant motion and seem reasonable and within the limits of empirical values given with Lloyds rules for maximum pitch angle (not greater than 8^o) and roll angles (between 22^o and 30^o) [Lloyd's Register (2009)].

Table 7.1 – Summary of absolute maximum motions at 25 knots for *Hull A*

		Wave heading / deg				
		180	*135*	*90*	*45*	*0*
Heave	m_0 / m^2	1.097	1.796	1.531	1.057	0.779
	sig. motion / m	4.190	5.361	4.950	4.113	3.530
Roll	m_0 / θ^2	0.000	0.133	7.676	4.859	0.000
	sig. motion / θ	0.000	1.460	11.082	8.817	0.000
Pitch	m_0 / θ^2	0.802	0.876	0.407	1.971	1.835
	sig. motion / θ	3.581	3.744	2.552	5.615	5.419

Table 7.2 – Summary of absolute maximum motions at 15 knots for *Hull A*

		Wave heading / deg				
		180	*135*	*90*	*45*	*0*
Heave	m_0 / m^2	0.671	1.189	1.947	0.414	0.187
	sig. motion / m	3.277	4.362	5.581	2.574	1.732
Roll	m_0 / θ^2	0.000	0.408	7.676	52.852	0.000
	sig. motion / θ	0.000	2.553	11.082	29.080	0.000
Pitch	m_0 / θ^2	0.810	0.844	0.329	0.669	0.717
	sig. motion / θ	3.601	3.675	2.296	3.273	3.387

7.1.5 Cargo securing

It is estimated that every year 10,000 containers are lost from container ships [Podsada (2001); Frankel (2002)] which raises environmental and safety concerns. In addition, there is an economic cost to the operator arising from the loss of cargo.

Throughout the design process the main focus has been on the optimisation of hydrodynamic resistance with little attention focussed on the ships seakeeping characteristics. Since the proposed layout is somewhat different to traditional container ships an analysis was conducted to determine the ability of the cargo to resist forces due to static gravity forces; inertial forces generated by accelerations due to roll, pitch and heave motions of the ship; wind forces (taken at a wind speed of 40 metres per second across the beam) and forces imposed by the cargo securing arrangements

The basis of the method is prescribed by Lloyd's Register (2009) Part 3 Chapter 14; Regulations for Cargo Securing Arrangements which the author has modified to account for different stacking heights and lashing arrangements.

The analysis is conducted based on the most severe combination of the forces, where the resultant force acting on a container at tier i (F_i) is the vectorial summation of the individual directional components of all forces acting at a given instant.

A numerical finite element model was created using a spreadsheet which replaced a stack of up to eight containers and lashings with up to 16 elements (depending on the stack size being considered) where the stiffness of the elements was related to the equivalent stiffness of the container and lashings (Figure 7.4). A global stiffness matrix for the container stack and an equilibrium condition for the system was then derived (Equation (7.1)). Using forces calculated using Lloyd's Register (2009) at each tier in the container stack the deflection of the container stack at each tier; the tension in the lashings (T_{Li}); residual forces transmitted laterally through the stack (($F_{i,RES} = F_i - T_{Li}\cos(\alpha_l)$), where α_l is the lashing angle); and the additional vertical forces due the presence of the lashings could be determined.

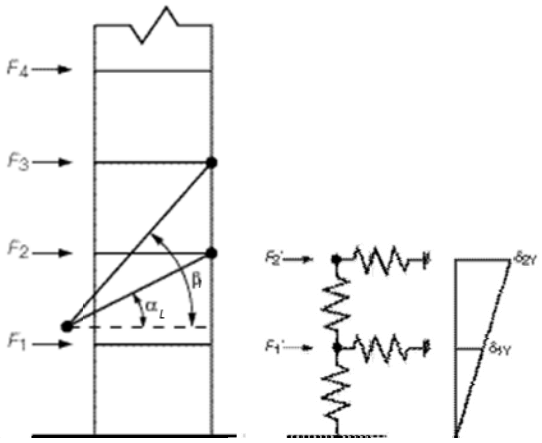

Figure 7.4 – Modelling assumptions required for the analysis of the cargo securing arrangements [Lloyd's Register (2009), Part 3 Chapter 14]

$$\begin{bmatrix} F_{1x} \\ F_{1y} \\ \vdots \\ F_{nx} \\ F_{ny} \end{bmatrix} = \begin{bmatrix} k_{1x} & 0 & \cdots & 0 & 0 \\ 0 & k_{1y} & \cdots & 0 & 0 \\ \vdots & \vdots & \ddots & \vdots & \vdots \\ 0 & 0 & \cdots & k_{nx} & 0 \\ 0 & 0 & \cdots & 0 & k_{ny} \end{bmatrix} \begin{bmatrix} \delta_{1x} \\ \delta_{1y} \\ \vdots \\ \delta_{nx} \\ \delta_{ny} \end{bmatrix}. \quad (7.1)$$

The model assumes that the suitable locking devices are fitted between tiers of containers to resist negative (separation) forces and stacks of containers within the cargo hold are connected together with double stacking cones[MacGregor (2010)] , however, forces have not been transferred from neighbouring stacks through these connections.

This last assumption leads to an underestimate of the racking force in the lower tiers but will still provide correct representation of the compressive forces. It has also been assumed that forces on the container stack will be greater in the transverse direction than longitudinally and thus failure in this plane is the focus of this investigation.

Six container stacks were considered as part of the analysis, whose positions on the ship are indicated in Figure 7.5. The stacks were selected to be representative of the stacks which are expected to experience the highest loading due to their distance from the centre of flotation, centreline and roll centre and also stacking height.

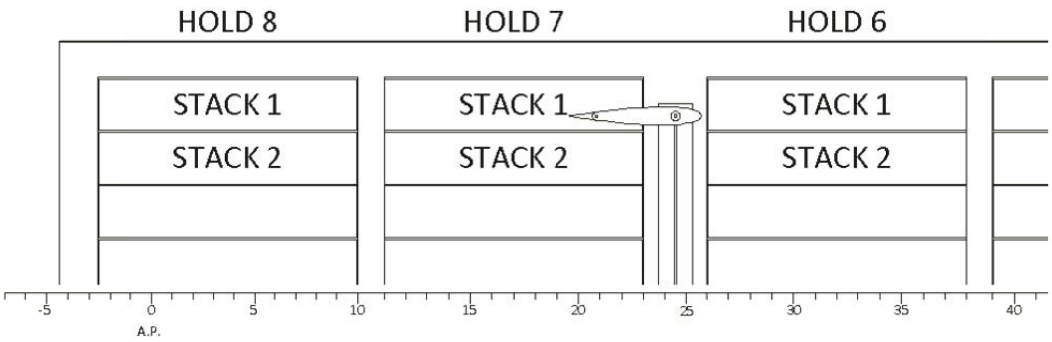

Figure 7.5 – Container stacks considered in container securing analysis

For each of the six stacks the transverse and longitudinal sliding forces and vertical forces imposed on the container stacks due to the motion of the ship[11] where calculated for six separate motion conditions, namely with the ship experiencing a:

1. Rolling motion with
    - maximum roll motion (descending) and maximum heave motion (descending);
    - maximum roll motion (ascending) and maximum heave motion (ascending);
2. Pitching condition with
    - maximum pitch motion (descending) and maximum heave motion (descending);
    - maximum pitch motion (ascending) and maximum heave motion (ascending);
3. Combined condition with
    - 0.71 x [maximum roll motion (descending) and maximum pitch motion (descending)];
    - 0.71 x [maximum roll motion (ascending) and maximum pitch motion (ascending)].

The maximum tension in the lashings, racking force, compressive force in the corner posts and shear forces in the stack for each of the six motion conditions at each tier were compared to acceptance criteria given by American Bureau of Shipping (1988) and Lloyd's Register (2009) and which is summarised in Table 7.3.

Table 7.3 – Acceptance criteria for container securing

	Maximum Load / tonnes	
	TEU	*FEU*
Maximum tension in lashings	12	12
Racking force on container end	15	15
Vertical forces at each bottom corner, tension	25	25
Vertical forces at each corner post, compression	86.4	86.4

The container securing arrangements for the stacks considered were chosen to be representative of current container securing arrangements used on container ships [ClassNK (2008)] and is shown diagrammatically for the six stacks under consideration in Figure 7.6.

[11] Based on the maximum roll angle and pitch angles calculated from the seakeeping analysis (see Section 7.1).

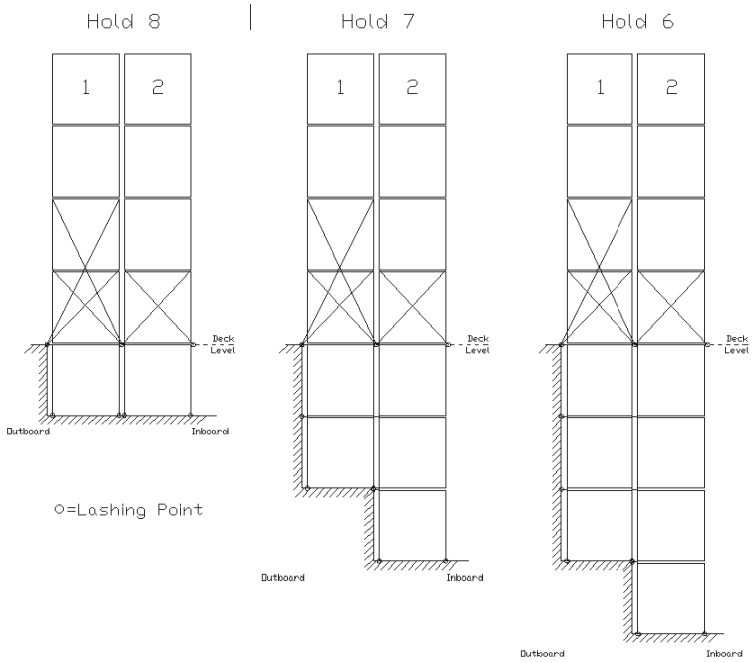

Figure 7.6 – Diagrammatic representation of the cargo securing arrangements [Lloyd's Register (2009)]

Lashing tensions, racking forces and maximum compressive forces for the six container stacks being considered were checked against the allowable values given in Table 7.3 assuming the containers all weigh the design nominal weight of 9.3 tonnes per TEU. It was found that all criteria were met except for three stacks, namely the two stacks in hold six and stack two in hold seven that failed in compression at the lowest tier in at least one motion condition, as summarised in Table 7.4.

Table 7.4 – Maximum compressive force in tier one of the considered container stacks and the motion condition to cause failure

		Max compressive force / tonnes	*Failure motion*
Hold 8	Stack 1	86.31	-
	Stack 2	85.90	-
Hold 7	Stack 1	81.17	-
	Stack 2	88.37	Combined top
Hold 6	Stack 1	86.78	Combined top of motions
	Stack 2	93.48 / 87.96	Combined top / roll top of motions

A more useful analysis is to determine the maximum mean container load to cause failure of the container stack in any of the failure criteria. The results from this investigation are summarised in Table 7.5.

Table 7.5 – Average container mass that causes failure of a container stack

		Maximum Container Mass / tonnes TEU^{-1}	*Failure Criteria*	*Failure Motion*	*Failure Tier*
Hold 8	Stack 1	10.8	Compression	Combined top of motions	1
	Stack 2	11.0	Compression	Combined top of motions	1
Hold 7	Stack 1	9.8	Compression	Combined top of motions	1
	Stack 2	9.0	Compression	Combined top of motions	1
Hold 6	Stack 1	9.2	Compression	Combined top of motions	1
	Stack 2	8.5	Compression	Combined top of motions	1

Table 7.4 and Table 7.5 shows that there are structural concerns with the container stacks principally in lower tiers of the higher container stacks which are susceptible to compressive failure (buckling). There are a number of solutions to this problem including the use of hatchcovers; the careful loading of containers to ensure only light containers are used in susceptible stacks and placing heavy containers at the bottom of a stack. Careful cargo loading also has benefits in reducing racking and shear forces within container stacks which may become important if a non-homogeneous container mass within a stack is considered.

If hatchcovers were used for the second stack in the hold six it would be possible to increase the maximum nominal container mass to 15.4 tonnes per TEU within the cargo hold and 14.7 tonnes per TEU on deck, which is a significant improvement on the 8.5 tonnes per TEU without hatchcovers.

As mentioned Section 07.1.2, the quality of the roll RAO generated by *Seakeeper* is somewhat questionable. Since forces on container stacks are dependent on roll angle it is possible that some of the high forces can be attributed to the inaccuracies in the seekeeping analysis. In addition, any possible beneficial influence of the sails on roll motion has not been considered when determining the forces on the container stacks.

7.1.6 Motions

One of the design parameters laid out in Section 2.5 is that a feeder container ship must be able to keep speed in sea states up to force five. It is thus necessary to determine at what point the ship will have to reduce speed in order to ensure the crews safety and ability to function.

A ship underway in a seaway will typically, due to the phase lag between heave and pitch motions, show the lowest motions at a location 30% of the waterline from the stern, where, the motion will be 30-50% less than other parts of the ship. This is one of the deciding factors for conventional container ships having an accommodation block located near to this point [Keuning *et al.* (2001)]. A key concern with a forward accommodation block position is the effect of the ship motions on the comfort and ability of the crew to perform their duties as the motions will be greater than the motions within a conventionally located accommodation block. There are several measures that can be used to assess the influence of motions on crew comfort and ability to function, namely the:

- Motion Sickness Index (MSI) which predicts the percentage of a people who will feel seasick in a two hour period of sustained vertical motions of given magnitude and frequency;
- Subjective Magnitude (SM) quantifies how severe a motion feels relative to a reference motion of $\pm$0.6 g at 1.0 Hz;
- Motion Induced Interruption (MII) indicated the number of times a crew member will have to stop work to hold on to a suitable anchorage to prevent loss of balance due to sliding or tipping;
- Probability of slamming;
- Probability of deck wetness;
- Probability of exceeding a certain acceleration (e.g. 0.6g at the bow).

To assess the safety and ability of the crew to function the absolute and relative values of acceleration at various positions around the accommodation block were investigated and used to estimate the limiting sea state and speed combinations using the crew performance measures listed above. The positions investigated were;

1. the bridge deck at centreline
2. the bridge deck on wing

3. the officers lounge
4. the mooring deck

The accelerations were evaluated for *Hull A* at speeds of 10, 15, 20 and 25 knots for all wave headings from head seas to following seas in increments of 45 degrees. The analysis was conducted for all combinations of wave height and period that were expected to occur in the operational sea areas [Hogben (1986)], assuming no time is spent in sheltered water close to islands or banks.

The MSI is a poor indicator of performance for the ship because seasickness is dependent on more than just vertical motions as there are secondary factors such as smells that contribute to the feeling of seasickness. In addition, the MSI is derived from a small sample of male student test subjects and thus is not representative of crew members who are accustomed to working at sea and who will not suffer unduly from seasickness [Lloyd (1989)]. For these reasons the results of this analysis have not been presented in this report.

A much more relevant measure of motions is SM, which quantifies a motion into five categories (Table 7.6).

Table 7.6 – Subjective magnitude scale

SM Value	*Description*
Under 5	Moderate
5 to 10	Serious
10 to 15	Severe
15 to 20	Hazardous
Above 20	Intolerable

A motion equivalent to ten on the SM scale is generally deemed unacceptable as this requires crew to support themselves by holding on to a suitable anchorage [Lloyd (1989)]. The SM values at combinations of speed, wave heading and wave height were investigated and plotted on polar plots for the officer's lounge and bridge deck[12]. These two positions were investigated because as although the motions on the mooring deck will be more severe; it is not expected that access to these areas will be required in the most extreme sea states. A typical polar plot showing the SM value for various headings and wave heights at 25 knots is shown in Figure 7.7. Polar plots of SM for speeds of 10, 15 and 20 knots are given in Appendix I.

It is evident from the polar plots in Figure 7.7 and Appendix I that the most severe motion is experienced in head and bow quartering seas and at wave heights above 6.5 metres where the SM in the officer's lounge reaches unacceptable levels. At no combination of speed or wave condition does the SM magnitude on the bridge deck exceed the imposed limit of ten. From an analysis of the polar plots it's possible to define limiting speeds associated with wave height and direction combinations to prevent the SM exceeding ten. The results from this analysis are shown in Table 7.7.

Slamming is an important physical effect because it causes declarations, local structural damage and transient vibratory stresses (whipping) [Lewis (1989)]. The probability of slamming was investigated for all combinations of wave height, wave heading and speeds being considered (Figure 7.8) where the critical velocity for slamming was calculated based on the theory of Ochi for a merchant ship as 3.76 meters per second [Lloyd (1989)].

[12] The presented SM is based on the wave period that creates the worst motion for a given wave height. This was chosen because wave height is a much easier way to describe real sea conditions that wave period.

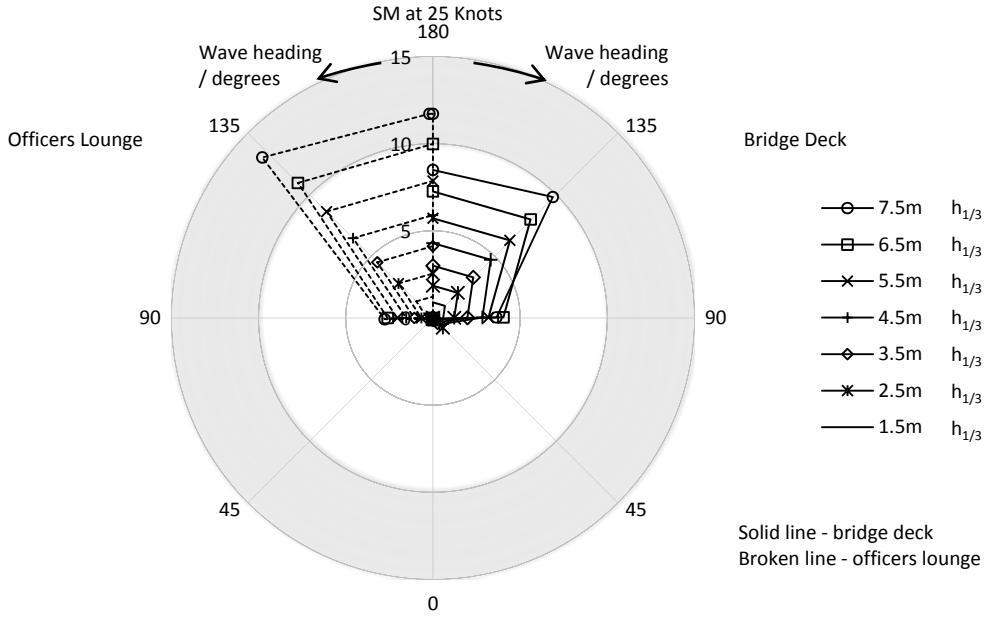

Figure 7.7 – Polar plot of Subjective Motion variation with wave heading height for the bridge deck and officers lounge at 25 knots

Table 7.7 – Summary of maximum ship speed in certain sea states to prevent excessive motions

$h_{1/3}$	*Limiting speed*		
	Head seas	*Bow quartering seas*	*Beam, stern quartering and following Seas*
5.5 metres and below	25 knots	25 knots	25 knots
6.5 metres	20 knots	20 knots	25 knots
7.5 metres	15 knots	10 knots	25 knots

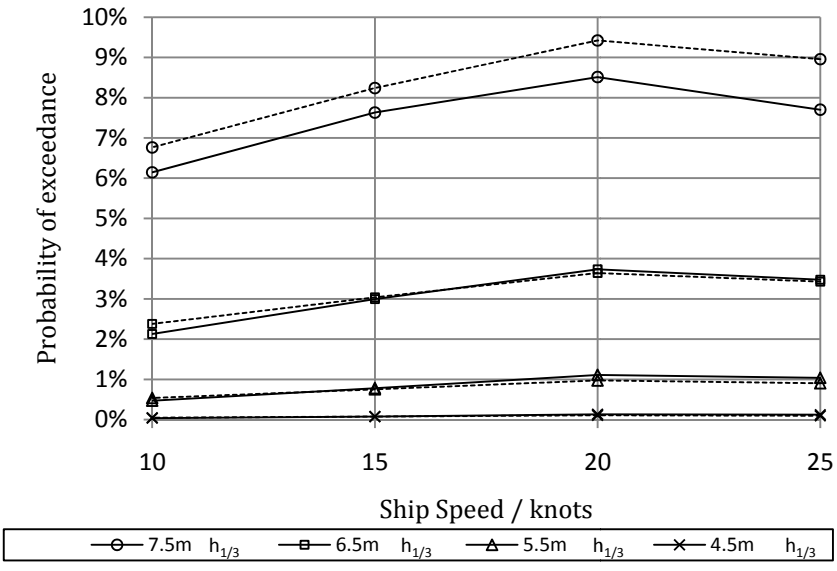

Figure 7.8 – Probability of slamming as a function of ship speed and wave height

These results are generally as expected except for the drop in slamming probability at 25 knots. On closer inspection of the probability of slamming as a function of wave period it was observed that at 25 knots there is an increased probability of slamming over the probability at 20 knots if all wave periods are considered (from 3.5 to 11.5 seconds) as shown in Figure 7.9. However, at 25 knots the wave periods that cause the greatest

probability of slamming do not occur at the large significant wave heights in the considered sea areas and thus the probability of slamming is reduced at 25 knots. This result is similar to the results of Bonafoux *et al.* (2001) who noticed the same pattern when investigating the MSI of fast ferries.

A suitable acceptable probability of slamming is in the order of 3-4% [Harries *et al.* (2003)], thus operation of the ship is possible in all seas up to 6.5m significant wave height with an acceptable level of slamming.

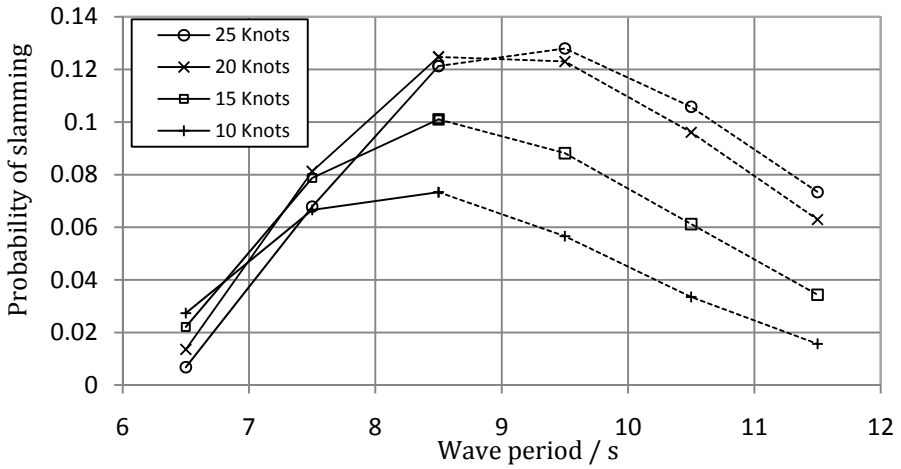

Figure 7.9 – Probability of slamming as a function of wave period and ship speed for a 7.5m significant wave height. Solid lines indicate waves that exist in the investigated sea areas and dashed lines indicate waves that do not exist in the investigated sea states

The MII gives an indication of the number of times a crew member will have to stop work due to tipping or slipping and thus their ability to work effectively. The analysis has been conducted based on transverse and vertical motion (although longitudinal motion could also have been considered) of the ship for all wave height, wave period and wave direction combinations,. The MSI coefficient, μ, for tipping is a ratio of stance width to a person's COG (defined as 0.25 in this investigation) [Lloyd (1989)] and for sliding, is the co-efficient of friction between a crew members shoes and the deck which for a dry weather deck is 0.7 [Graham *et al.* (1992)]. The MII for the mooring deck was judged as the most adequate location to apply this criterion, the results of which are shown in Figure 7.10.

The probability of deck wetness was investigated and found to be 1.56% for a 7.5m significant wave height and 0.42% for 6.5m significant wave height which is considered to be small and not a constraint on operation when compared to criteria such as slamming and SM and thus has not been presented in this report.

The probability of bow acceleration was calculated but because it didn't yield any more information than has already been obtained from other measures has not been presented in this report.

From the results presented, it is evident that the ship should be able to operate safely in seas up to 5.5m significant wave height, equivalent to force 6-7 on the Beaufort scale (providing there is sufficient installed power to overcome the added resistance and the crew can tolerate reasonable ship motion) which more than satisfies the design requirement set in Section 2.5. The problem with the measures discussed in this investigation to measure crew comfort is that the measures are subjective and the limits of what's acceptable will vary widely from person to person.

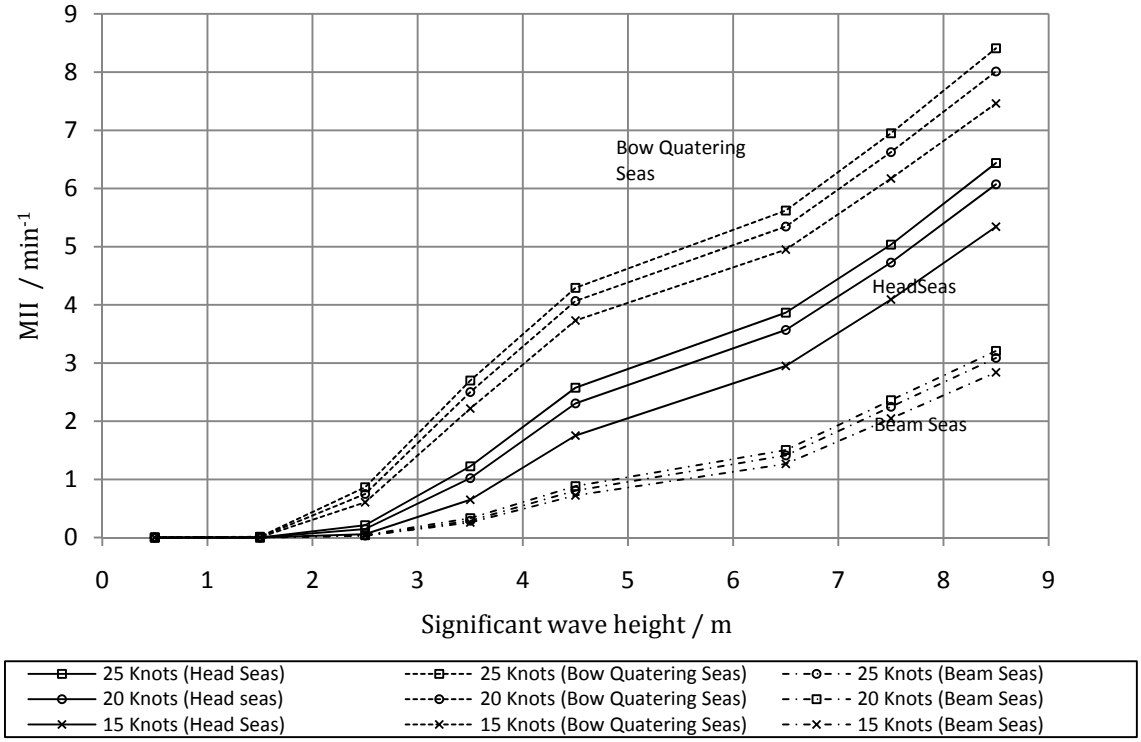

Figure 7.10 – Motion Induced Index (MII) for various wave heights, wave heading and speeds

7.1.7 Roll damping due to sails

Nature of roll damping

So far the *Wing Sail* has been considered exclusively as propulsion auxiliary. However, this sail system will also act as a motion damping device which decreases the roll and yaw motions of the feeder in resonant waves. The Japanese experience in the 80's with sail assisted cargo ships suggests that on top of the fuel savings due to the thrust generated by the sails, there is another five to ten per cent decrease in resistance when sailing to windward associated with a reduction of coupled roll/yaw motions. The otherwise unexplainable decrease in drag is a direct effect of the reduced yaw motion in quartering seas and consequent decrease of induced resistance. Research conducted at the University of Southampton in the 80's by Satchwell (1986) provides guidance for the estimate of the aerodynamic loads and associated roll damping, however very little is known about the correlation of this reduction in motion to the decrease in drag and hence fuel savings. In this section the reduction in coupled roll/yaw for the feeder is estimated using the lifting surface theory and published data based on lifting line theory [Glauert, H. (1930)]. The results are then used to estimate the potential reduction in resistance which would occur when sailing to windward.

Lifting surface method and lifting line analysis

The first estimate of the aerodynamic roll damping was carried out applying the lifting surface method, however the results were found to overestimate the damping. As suggested by Satchwell the accuracy of this method may be limited by the uncertainty related to the hull superstructure, vortex shedding and turbulence at sea level shows the formulae used and plots of the damping components.

The lifting line method proposed here neglects starting vortex effects and any distortion to the planar trailing vortex wake. This quasi-static analysis accounts for unsteady flow effects by a sequence of steady flow

calculations [Satchwell C.J. (1986)]. $N_{\varphi Aa}$ and $N_{\varphi AV}$ are the damping components due to incidence changes and air speed changes respectively, Appendix J shows how these quantities are derived.

Control system

Figure 7.11 shows that in strong following, winds the damping becomes negative. This is a result of the 'airspeed changes' component which becomes negative as the wind moves aft of the beam. However due to the low operational apparent wind angle the negative damping is present only when $\beta > 150$. Figure J.3 shows that incidence damping is always positive if stall is avoided. A simple control system could be used to avoid stall if the change in angle of attack due to the rolling motion is known. Again lifting line theory can be used to estimate the changes in angle of attack along the span of the wing and the result could be used to calculate the required margin to avoid stall [Equation (J.7)].

Roll reduction

A number of components contribute to the total hydrodynamic roll damping. These include the skin friction of the hull in contact with water, moments arising from separation of the flow, hydrodynamic side force, and the moment due to the creation of waves [Lewis (1989)] . The resulting hydrodynamic damping of the feeder, which has been estimated in the previous section, can be used to describe the rolling of a ship as follows suggested by Satchwell (1986).

$$I\ddot{\varphi} + \frac{T_\varphi \nu_\varphi \Delta\overline{GM_T}}{2\pi^2}\dot{\varphi} + \Delta GM_T\varphi = f(1) \tag{7.2}$$

$T_\varphi \nu_\varphi \Delta GM_T$ is a linear hydrodynamic damping and the term $\nu_\varphi = 2K_1$ is introduced to include any non-linear effects, appropriate to a ship rolling through a full cycle. The solution of Equation (7.2) for the maximum angle of heel φ_{MAX} is proportional to the wave slope and $1/\nu_\varphi$. The aerodynamic damping equivalent $\nu_{\varphi a}$ is found by identifying the damping term in Equation (7.1) and equating this to $N_{\varphi A}$ (see Appendix J).

$$\nu_{\varphi A} = \frac{2\pi^2 N_{\varphi A}}{T_\varphi \Delta GM} \tag{7.3}$$

$$\frac{\varphi_{MAX} - \varphi_{MAX\_A}}{\varphi_{MAX}} = \frac{\nu_{\varphi A}}{\nu_{\varphi A} + \nu_\varphi} \tag{7.4}$$

From Appendix I.1, roll resonant frequencies for beam and quartering waves are found at $\lambda/L_{WL} = 280\ and\ 30$, for 15 and 25 knots respectively. Observing the sea state data in Appendix G [Hogben (1986)] we note that there are no observations for the resonant wave lengths at 25 knots, however at 15 knots the peaks in quartering beam coincide with waves, but at 15 knots resonant roll at $\lambda/L_{WL} = 30$ accounts for 31 and 19.5% of the sea state for Singapore and Caribbean respectively, suggesting that for the selected routes the damping action of the wing sail will be particularly beneficial at the low speed.

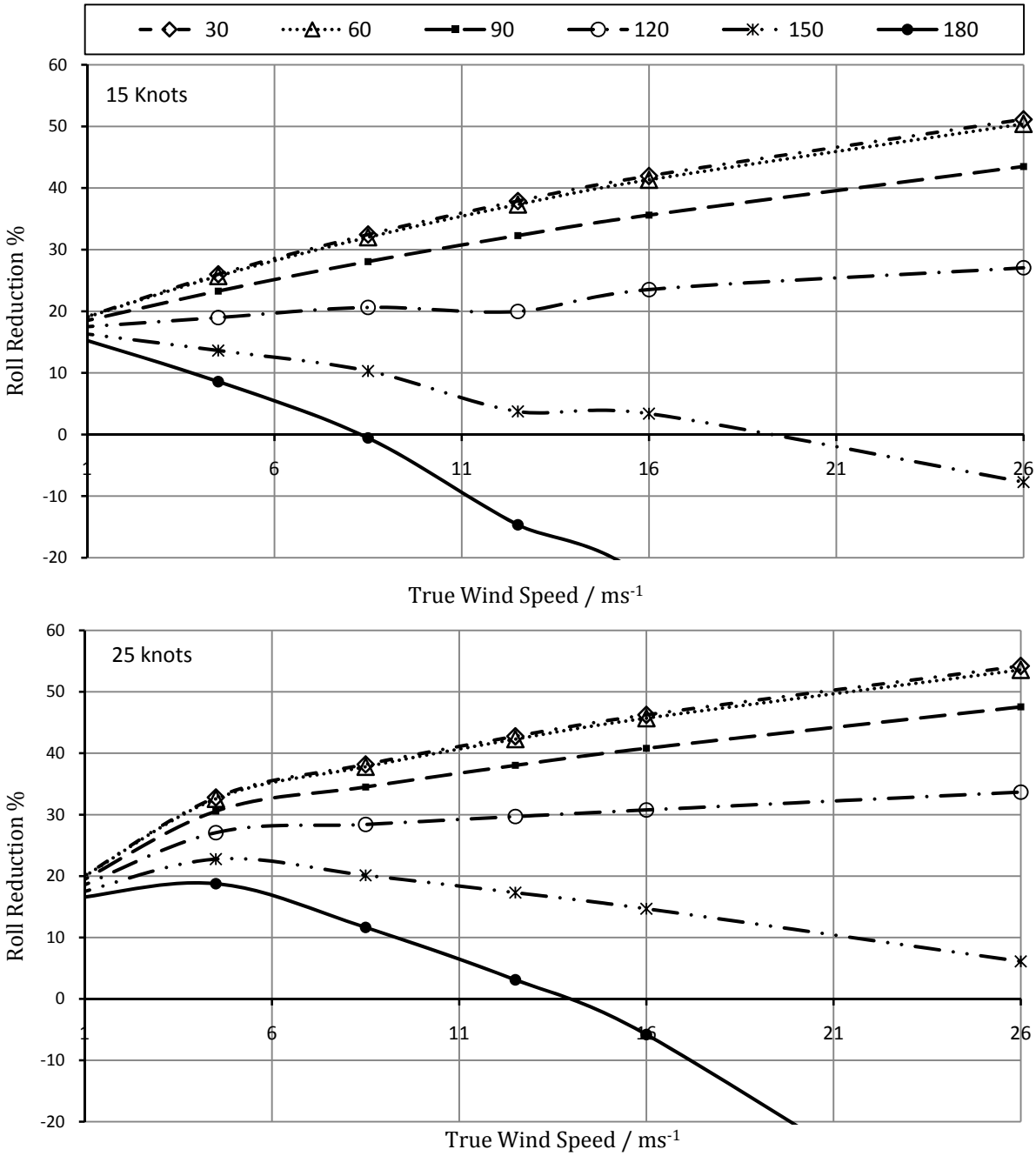

Figure 7.11 – Roll reduction for 15 and 25 knots ship speed at different apparent wind angles

Yaw Component

Clayton & Sinclair (1989) give guidance on how to estimate the yaw aerodynamic derivative of a *wing sail* at different headings. These are used to calculate the corresponding yaw damping coefficient component induced by roll motion $b_{\psi\varphi}$. As no lateral motions were included in the seakeeping analysis, a yaw damping coefficient is assumed as 0.15 from Das *et al.* (2006), comparing this typical value with the aerodynamic component, it is readily seen that a significant damping can be achieved.

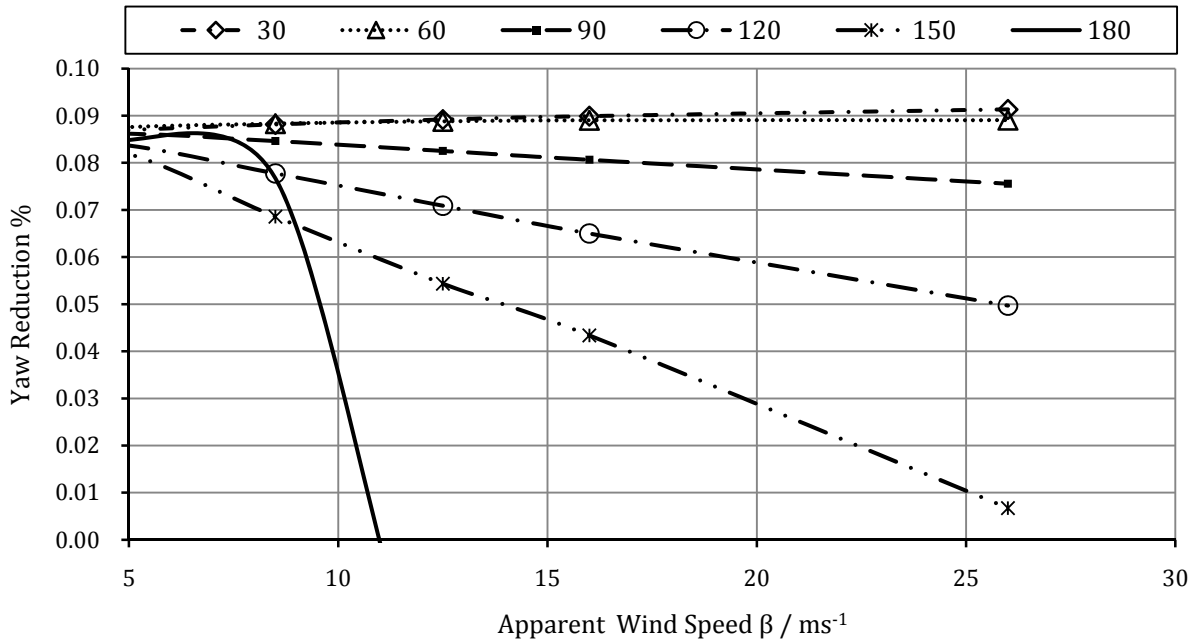

Figure 7.12 – Reduction of Roll Induced Yaw Component. Ship speed 25 knots

Resistance reduction due to motion damping

In the simulation of the voyages performed in Section 6.1.1 the average reduction in roll motion for resonant waves is found to be 16% and 30% at 15 and 25 knots boat speed respectively. In addition to this, the average reduction of the yaw component induced by resonant has also been calculated. With this information is now possible to predict a decrease in induced resistance in resonant waves. The experimental induced drag data can be used to simulate the resistance associated with a sinusoidal 2.5 degrees yaw motion; From Satchwell (1986) a time averaged induced resistance coefficient C_{Ri} is defined as follows:

$$C_{Ri} = \frac{1}{T_\psi} \int_0^{T_\psi} \frac{250\, R_i(t)}{\pi \rho {V_S}^2 \Delta^{2/3}}\,, \tag{7.5}$$

where T_ψ is the period of coupled roll/yaw motion, assumed to be 9 seconds [Das & Das (2007)]. The numerical integration yields $C_{Ri} = 0.25$. Using the same expression in Equation (7.5) the total resistance of the vessel sailing at 25 knots corresponds to a coefficient of $C_{RT} = 1.20$, thus the yawing motion could contribute up to around 20% of the total resistance. Similarly, the reduction at a ship speed of 15 knots is found to be 18%. Removing this yaw motion when sailing to windward would eliminate this source of drag. The expectance probability of sailing in quartering and beam waves calculated in Section 6.1.1 can be used to apply a weight to this reduction to average the value for the selected routes and use the resulting value for an economic case in Section 6.2.2. For Singapore area the averaged benefit is found as 2.14% and 1.93% at 25 and 15 knots respectively. This reduction is not included in the main economic analysis as it relies on assumed hydrodynamic yaw damping coefficients and yaw displacement periods. Future work could involve a detailed seakeeping analysis of the feeder and optimise the aerodynamic motion damping and the associated resistance reduction for the resonant peaks, and aerodynamic pitch damping could be also considered for a decrease if added resistance in waves.

7.2 Structural design

7.2.1 Midship scantlings

It was recognised that only a preliminary design was practical or desirable within the scope of the concept design. Thus the design was limited to primary members and associated stiffening at the midship section, (to facilitate the finite element modelling of a hull module centred amidships). The approach consisted of a combination of direct calculation based on design loads; rule based design from Lloyd's Register's Rules for the Classification of Ships [Lloyd's Register (2009)] (herein "the Rules") and design from basis. Aside from initial arrangement and plate thickness calculations, the structural work was carried out with the assistance of the LR software package *Rulescalc*. The use of *Rulescalc* facilitated an increase in the speed and accuracy of structural property calculations, and improved the fidelity of Rules checks with a more accurate representation of the ship section.

Arrangement

The cue for the design was taken as the Nigel Gee and Associates Ltd. design, NG254, for which a midship section and related structural information were available [Gee (2007)]. Based on the broad similarities of the designs' operational envelopes a number of key assumptions for the concept were made at this stage relating to the structural arrangement.

(v) A duct keel in the double bottom would facilitate maintenance access and provide space for power transmission to the motors at the stern.

(vi) Side girders in the double bottom would be neglected in favour of the bilge box and duct keel.

(vii) Conventional side structure with stringer decks including an underdeck walkway and high scantling 'torsion box' to resist stresses at deck level would be retained – this latter being a requirement particularly stressed by the Rules.

(viii) LR H36 grade high tensile steel ($\sigma_0 = 355$ meganewtons per square metre) was to be used throughout the midship section. The use of H36 throughout the section rather than only at deck and bottom allowed a general reduction in structural mass, in addition to negating construction complexities arising from the joining of high tensile and mild steel strakes.

(ix) The scantling draught used in pressure loading and rule scantling calculations was taken to be the freeboard summer load waterline calculated at the second deck from maximum depth, leading to $T_D = 9.52$ metres. The use of T_D in the design stage effectively serves as a built in safety factor for the ship in its operational condition.

(x) Commercial bulb flats [Corus (2002)] were adopted as the secondary longitudinal stiffening members throughout the section, as while manufactured T-sections can incur significant cost savings [Blomqvist & Forrest (2000)], it was felt that standard bulb sections would improve shipyard viability.

Drawing on these assumptions arising from the basis design and the further requirements of the Rules (Part 4, Chapter 8), the principle structural members were finalised as shown in Figure 7.13 and divided into primary panels as in Table 7.8. The stiffener distribution between and along primary longitudinal members was assumed to be the same as that for the NG254, with one addition on panels 7 and 13 to account for a reduction in the overall depth and a relative increase in the height of the walkway.

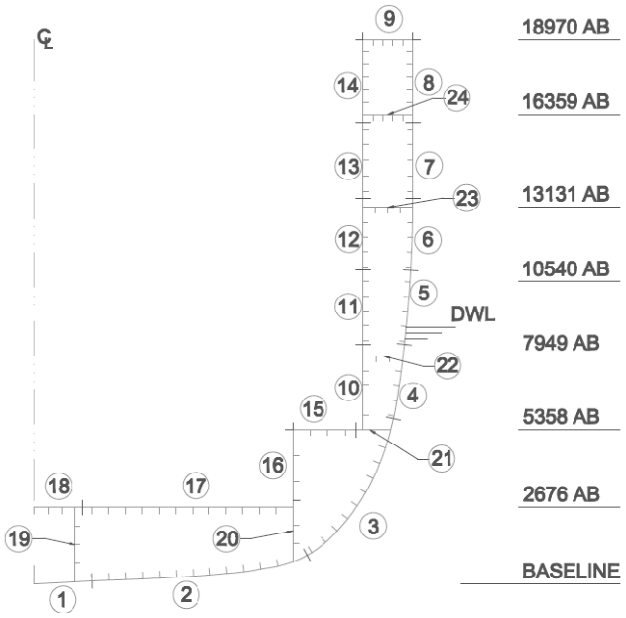

Figure 7.13 – Structural arrangement and principal panels within the midship section

Table 7.8 – Longitudinally effective panels

No.	*Function*	*No.*	*Function*
1	Keel	13	Inner Hull[1]
2	Bottom Shell	14	Inner Hull[1]
3	Bilge	15	Bilge Box Top
4	Side Shell[1]	16	Bilge Box Side
5	Side Shell[1]	17	Inner Bottom[2]
6	Side Shell[1]	18	Inner Bottom[2]
7	Side Shell[1]	19	Duct Keel Side
8	Sheerstrake	20	Girder
9	Main Deck	21	Stringer
10	Inner Hull[1]	22	Stringer
11	Inner Hull[1]	23	Stringer
12	Inner Hull[1]	24	Stringer

Note 1 The side shell and inner hull below the torsion box, while behaving as a single panel in global terms, were divided into individual strakes to facilitate varying thickness.

Note 2 Similarly, the Inner Bottom above the Duct Keel was treated separately to the rest of the cargo region.

Loads

The initial design point was taken from vertical bending global loads for the fully loaded condition combined with local hydrostatic and cargo loadings. The local hydrostatic loadings were calculated from first principles for the scantling draught. Hydrodynamic loads due to motions and waves were estimated from empirical formulae from the rules, while cargo loads were based on n_T assuming a maximum averaged container loading of 14 tonnes and uniformly distributed throughout the hold. A working value of M_S was obtained from the initial mass estimate adjusted for the ship in ballast condition (maximum hogging bending moment), while the design value for M_{VW} was obtained from the Rules. The design loads are summarised in Table 7.9.

Table 7.9 – Design loadings used in initial scantling derivation, external and internal local design loads for individual panels and maximum global bending moments

	External loads, p_H / kNm^{-2}	
Panel	*Hydrodynamic*	*Hydrostatic*
1	32.5	95.7
2	32.5	95.7
3	32.5	88.6
4	32.5	37.9
5	32.3	11.8
6	32.2	-
7	30.6	-
8	27.3	-

	Internal loads, p_V / kNm^{-2}	
Panel	*Ballast head*	*Cargo loads*
10	78.2	-
11	48.1	-
12	22.0	-
15	-	41.6
16	27.0	-
17	-	46.2
18	-	46.2
19	26.1	-
20	46.0	-
21	78.2	-

Global loads / MNm	
M_S	814.6
$M_{WV_{sag}}$	-814.1
$M_{WV_{hog}}$	649.0

Scantlings

Initially modelling the midship section with scantlings derived from the NG254, the longitudinal stresses acting on plating elements were calculated by means of Equation (7.6), where σ_{local} was obtained for a uniformly

loaded plate as in Equation(7.7), defining elements as a panel of width s and with a length of one frame bay. The plate shape factor β_P is taken as 0.5 for a rectangular plate with all edges fixed [Young & Budynas (2002)].

$$\sigma_{Design} = \frac{M_S + M_{WV}}{I_Y} z_i + \sigma_{local} \tag{7.6}$$

$$\sigma_{local} = \beta_P \frac{(p_H + p_V)s^2}{{t_P}^2} \tag{7.7}$$

Comparing this design stress to the permissible longitudinal stress from the Rules, $\sigma_L = 157/k_L$, panel thicknesses were then reduced, balancing the effect on local stress values with that on the section modulus at deck and keel. Once satisfied with these values, the structural arrangement was input into *Rulescalc* for more detailed analysis.

Verification

The initial scantlings were subjected to a number of checks to ensure compliance with the Rules.

(i) Minimum plating thickness requirements were obtained from Part 4, Chapter 8, Section 5 of the Rules and compared to derived scantlings (see Table 7.10).

(ii) Stiffener and attached plating section moduli were obtained from Part 4, Chapter 8, Section 6 of the Rules and used to select appropriate stiffener profiles (see Table 7.11).

(iii) Critical buckling stresses were calculated for plates and stiffeners in accordance with the Rules and compliance verified (Appendix K.1).

Table 7.10 – Plate thickness by direct calculation and minimum rule requirements

Panel No.	t_P / mm	$t_{P_{Rule}}$ / mm		*Panel No.*	t_P / mm	$t_{P_{Rule}}$ / mm	
1	18.0	19.0	FAIL	13	9.0	7.5	PASS
2	16.0	12.0	PASS	14	17.5	13.5	PASS
3	14.0	12.0	PASS	15	10.0	9.0	PASS
4	11.0	10.0	PASS	16	12.0	10.0	PASS
5	11.0	10.0	PASS	17	10.0	8.5	PASS
6	11.0	10.0	PASS	18	8.5	8.5	PASS
7	11.0	10.0	PASS	19	10.5	10.5	PASS
8	17.5	11.0	PASS	20	12.0	10.0	PASS
9	17.5	13.5	PASS	21	12.0	9.0	PASS
10	11.0	7.5	PASS	22	9.0	9.0	PASS
11	7.5	7.5	PASS	23	9.0	9.0	PASS
12	7.5	7.5	PASS	24	17.5	9.0	PASS

Transverse Structure

The transverse structure was obtained similarly to the longitudinal stiffening by design from rule. Required section moduli were calculated for the transverse framing on the shell plating. Suitable Tee-section built-up profiles were then found, assuming a consistent flange plate of 200 x 10 mm. These scantlings were assumed to be repeated on the inboard plating of the double hull structure. Near the main deck, scantlings were increased above rule requirements in accordance with the increased transverse stiffening observed on the NG254, it was expected that this would aid in resisting warping distortions at deck level. The results are shown in Table 7.12.

Table 7.11 – Minimum rule requirements for local section modulus of stiffeners and attached plating

Panel No.	$Z_{i_{Rule}}$ / cm^3	Stiffener profile / mm x mm	*Panel No.*	$Z_{i_{Rule}}$ / cm^3	Stiffener profile / mm x mm
1	-	650 x 12	13	5.0	180 x 8
2	270.1	220 x 10	14	13.5	200 x 10
3	268.9	220 x 10	15	147.5	180 x 8
4	288.9	240 x 10	16	150.9	180 x 8
5	200.8	200 x 8.5	17	412.5	280 x 10.5
6	196.3	200 x 8.5	18	491	260 x 10
7	149.7	180 x 9	19	-	200 x 10
8	117.8	200 x 10	20	220.4	200 x 10
9	103.8	200 x 10	21	-none-	
10	311.8	240 x 10	22	-	180 x 8
11	200.3	200 x 8.5	23	19.8	180 x 8
12	189.5	200 x 8.5	24	-	200 x 10

Table 7.12 – Required section moduli and selected web profiles for transverse stiffening

Panel No.	$Z_{i_{Rule}}$ / cm^3	*Web Profile / mm x mm*	Z_i / cm^3
1	1401.5	730 x 12	1411.0
2	1857.8	850 x 12	1863.0
3	1797.6	840 x 12	1823.0
4	610.4	500 x 10	610.4
5	524.3	510 x 8	526.2
6	407.0	450 x 8	419.3
7	325.5	450 x 10	504.4
8	325.5	450 x 12	586.2

With all rule strength checks deemed satisfactory the scantlings were finalised as shown in the Midship Section drawing in Appendix K.2 and the design progressed to more detailed structural analysis.

7.2.2 Global strength

Once satisfactory scantlings had been established throughout the midship section a further check on the structural design was carried out in the form of a global strength analysis. This consisted in the first part of checking the global properties against LR longitudinal strength requirements detailed in Part 3 Chapter 4 and further, Container Ship specific requirements in Part 4 Chapter 8. Once global properties were confirmed within permissible limits, operational bending moment envelopes were generated and the global loads for a selection of operational conditions assessed. The global properties of the midship section are shown in Table 7.13.

Table 7.13 – Global properties of the midship section

Global Properties	μ / kgm^{-1}	I_Y / m^4	I_Z / m^4	z_{NA} / m	Z_D / m^3	Z_B / m^3	ε / m	I_ω / m^6
	18,143	96.89	234.70	7.611	8.53	12.731	-2.539	20,124

Rule criteria

Global strength properties of the midship section were assessed against two sets of rule criteria in two distinct conditions, a head seas wave condition as that used in the scantling derivation consisting of maximum M_S and

wave induced M_{WV}; and an oblique sea condition incorporating the effects of wave induced horizontal bending moment and torque. The head seas wave condition is applied as a check on the ability of the structure to resist pure vertical bending without exceeding a specified stress level. The criteria for the check are summarised in Table 7.14.

Table 7.14 – Rule Global strength criteria

Criteria	*Rule*	
Minimum hull section modulus, Z_{min} / m^3	5.114	PASS
Minimum hull moment of inertia, $I_{Y_{min}}$ / m^4	57.95	PASS
Permissible stress, σ_L / Nmm^{-2}	218.1	PASS
Permissible SWBM, $\overline{M_S}$/ MNm	1365.4	-

While vertical bending checks were passed, the open section design of container ships means that they are considerably more susceptible to anti-symmetric distortions and stresses and this is accounted for in Lloyd's Rules. Using rule prescribed bending moments and torques (summarised in Table 7.15), the combined stress value at a position within the section is calculated by means of Equation (7.8), in which the warping stresses have been estimated by with [Magnucki *et al.* (2004)] and I_ω and ω_{n_i} were acquired from *Rulescalc*. Results are shown in Table 7.16.

Table 7.15 – Rule derived anti-symmetric global loads.

Global Loads	M_{WH} / MNm	M_{WT} / MNm	M_{ST} /MNm
	284.3	69.9	37.0

$$\sigma_C = \frac{M_S}{I_Y} z_i + 0.6 \frac{M_{WV}}{I_Y} z_i + \frac{M_{WH}}{I_Z} y_i + \frac{M_{ST} + M_{HT}}{I_\omega} \omega_{n_i} \tag{7.8}$$

Table 7.16 – Combined stress calculations

	Deck Edge Inboard	*Bilge Extreme*
y_i/ m	11.39	11.40
z_i / m	11.58	4.72
ω_{n_i} / m^2	206.72	62.84
σ_C	186.4	85.0
	PASS	PASS

All global strength criteria based only on the midship section had been successfully passed, so the next step was to confirm that the likely loading conditions for the concept as a whole were within permissible limits. To do this, the mass estimate derived in Section 3.2 was revised to include a more accurate description of the structural mass total and distribution.

Hull steel mass

The hull steel mass was estimated by means of a coffin diagram, the derivation of which traced the continuity and extent of major structural features. Specifically, the elements considered were the shell girth, strength deck breadth, double bottom breadth and inner hull depth. The contributions from these elements were then summated along the length of the ship and normalised to unity. After being corrected for scantling taper allowances at the fore and aft ends of the ship from the Rules, this distribution was multiplied through by the

value of steel mass per metre (μ) amidships and integrated to give the longitudinal structure mass. Transverse structural mass was estimated from the mass of a frame amidships and distributed by the full depth sectional area of the hull form. The normalised coffin diagram and the resulting lightship mass distribution are shown in Figure 7.14 .

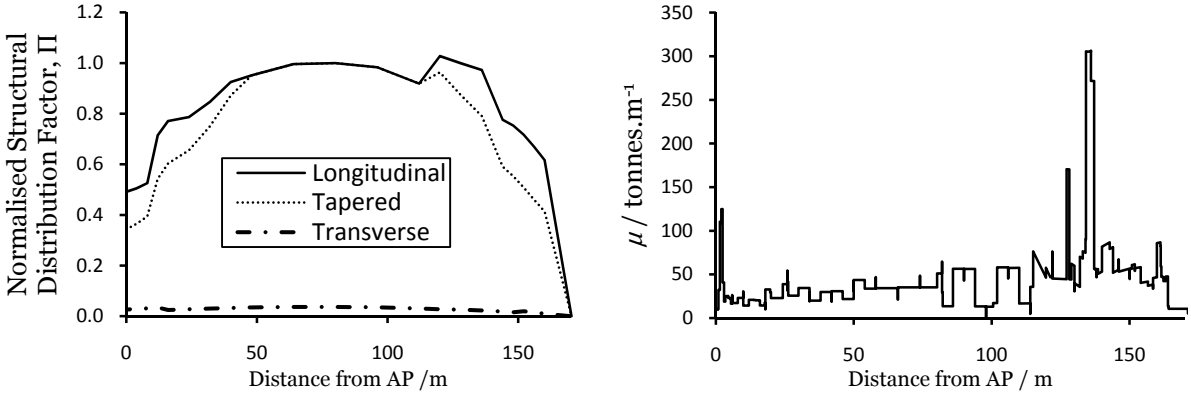

Figure 7.14 – Coffin diagram for structure mass normalised by μ amidships (left) and resulting lightship distribution of μ (right)

Operational conditions

From the revised hull mass estimate and using the load conditions specified in Appendix K.3, SWBM values were calculated for the ship in operation to confirm them beneath the maximum permissible SWBM, see Figure 7.15.

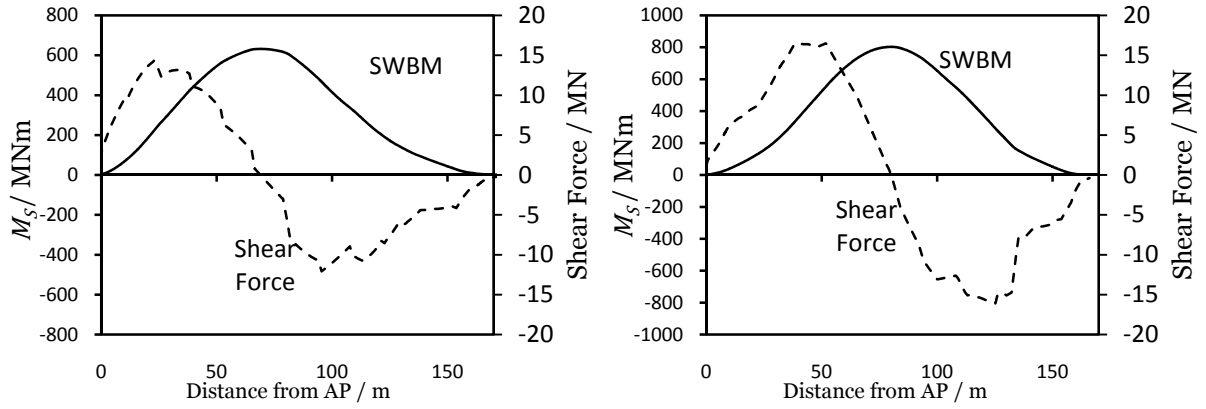

Figure 7.15 – Distribution of still water shear force and SWBM in the loaded arrival condition (left) and ballast arrival (right)

Neither the loaded nor the ballast condition produced SWBM maxima approaching the permissible rule value from Table 7.14 so as such the global strength check was considered passed on all counts and the structural arrangement was now ready for more detailed analysis.

7.2.3 Finite element midship section model

The use of finite element methods (FEM) in the design of ships has become commonplace, giving the designer more power to control the overall and detailed design of a ship structure. FEM are particularly useful in the structural assessment of novel ship structures (such as sail assisted ships) which have geometry or loadings that are different to those normally experienced by a ship and is a mandatory requirement for their classification [Lloyd's Register (2006a)].

In order to assess the structural integrity of the proposed sail system and its effect on the ship structure an Finite Element (FE) model of a short length of the proposed concept including one transverse bulkhead and sail system mast has been modelled in *ANSYS*. The FE model has been used to perform a structural strength assessment of the proposed midship structure in still water; the stresses within the hull due to extreme loading on the sail system; the stresses due to dynamic wave bending and torque loads.

Modelling

The modelling of the sail system and ship section was guided by International Association of Classification Societies (2008) and Lloyd's Register (2006b) which provides guidance on the modelling of structural components; restraint requirements; loading and acceptance criteria required in order to conduct a strength assessment using FEM.

A 28 metre section of the ship was modelled which included the full length of the ships parallel mid body plus a small allowance at either end. The procedure involved modelling the entire primary and secondary support structure, with plates modelled using shell elements and stiffeners and riders modelled with beam elements. The beam and plate elements where connected together between their nodes with rigid links which are beam elements with very high rigidity and very small mass. This effectively welds the beam and plate elements together. Brackets, small lightening holes and small radiuses have not been modelled as recommended by the CSR.

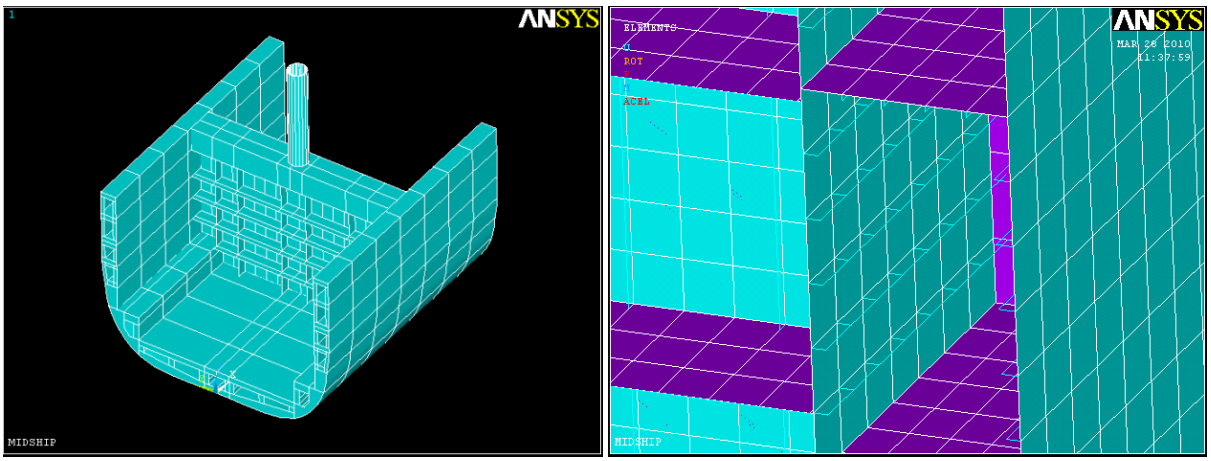

Figure 7.16 – The extents of the finite element model (left); and the modelling of stiffened plates using a combination of beam and plate elements (right)

The mast has been assumed to be fixed rigidly to the cross deck with the sails being lowered down the mast and folded to be stored on deck (Appendix M). From the list of possible sail stowage arrangements given in Section 5.1.2 this is deemed the most practical method of fixing the sail to the ship because it minimises the total bending moment which in turn reduces mast scantlings; minimises mast tip deflection and has the least interference on the ship structure. The same high tensile steel as the hull has been used for the mast, this is a change from the initial material selection of Aluminium 5083 because of the difficulty in welding aluminium to steel.

The sail supporting bulkhead and cross deck was initially assumed to be of equivalent dimensions to that of a standard watertight bulkhead with the addition of additional stiffening on the reverse side to create a cross deck three metres in width rather than 1.25 metres for a standard bulkhead. Effectively this can be seen as two standard watertight bulkheads back to back, a structural drawing of the modelled bulkhead can be seen in Appendix K.2.

FEM discretises a structure into elements with an exact representation of the ship structure only achieved with an infinite number of elements with the accuracy of the solution tending towards reality as the number of

elements is increased; however this comes at the expense of computation time. In order to make FEM a fast and reliable method of strength assessment, acceptance criteria is given based on an assumed mesh size by providing a suitable safety margin to take account of the coarseness of the mesh. The mesh for the hull structure was developed based on the guidelines for a structural strength assessment given in the CSR and LRSDA so the acceptance criteria given in the LR SDA procedures could be applied. The meshing process can be summarised as follows:

- A mesh is generated that follows the stiffening system as far as practicable, hence representing the actual plate panels between stiffeners;
- One element is used between every longitudinal stiffener. Longitudinally, the element length is not greater than two longitudinal spaces;
- One element is used between every vertical stiffener on transverse bulkheads;
- One element is used between every web stiffener on transverse and vertical web frames, cross ties and stringers;
- At least three elements are used over the depth of double bottom girders and floors, transverse web frames, vertical web frames and horizontal stringers on transverse bulkheads;
- The aspect ratio of plates is kept as close to one as is practically possible;
- The plate elements are all defined in the same clockwise direction to ensure the normals are in the same direction;
- The rotation of the local element co-ordinate system for beam elements is chosen to orientate the element correctly in the global co-ordinate system.

In addition to the mesh for the strength assessment a local fine mesh was created to assess the stresses arising around the intersection of the mast to the cross deck from which suitable structure could be designed to prevent failure of the mast under extreme loading events. The mesh for this area was generated with guidance from the CSR and involved creating a mesh with a resolution of 50 millimetres square extending for ten elements in all directions from investigated area (Figure 7.17). The other high stress concentration areas in a container ship such as the intersection of the deck and hatch coamings with the transverse bulkheads which are normally investigated using a fine mesh when analysing a container ship structure (LRSDA procedures, (2006)) have not been considered in this investigation.

The sail mast was modelled from the connection with the cross deck to the bottom of the sails using the same fine mesh size used for the intersection of the mast to the cross deck. The nodes at the top of the mast were connected to an independent point at the centre of the mast section. This point was then used as a location to apply forces and moments to account for the loading on the sails (Figure 7.17).

The model restraint was selected in the most minimal way possible following the guidelines of the LR SDA and CSR to prevent rigid body motion while minimising the amount of additional forces applied to the model. Ground spring elements (an element with one end constrained in all six degrees of freedom (DoF), and stiffness in global Z or global Y degree of freedom depending on the structural member to which it is attached) were used to constrain the intersection of the deck and inner and outer side shell in global Z direction and the deck and transverse floors in the global Y direction (Figure 7.18). The stiffness of the ground springs was calculated using the LR SDA procedures to provide an equivalent shear stiffness of the ship at the model ends.

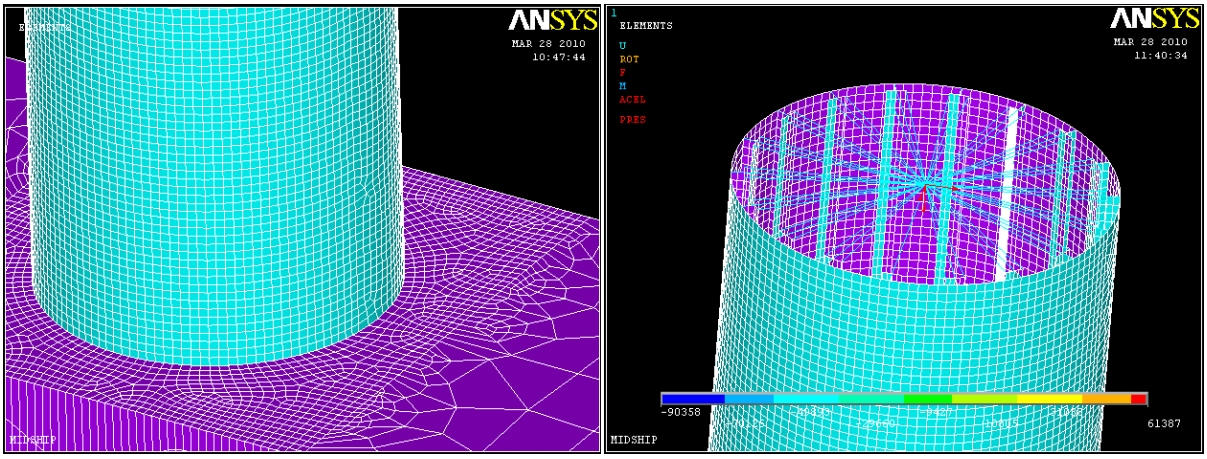

Figure 7.17 –The finite element model showing: the fine mesh region at the intersection of the mast and cross deck (left); and the application of loads to the top of the mast (right)

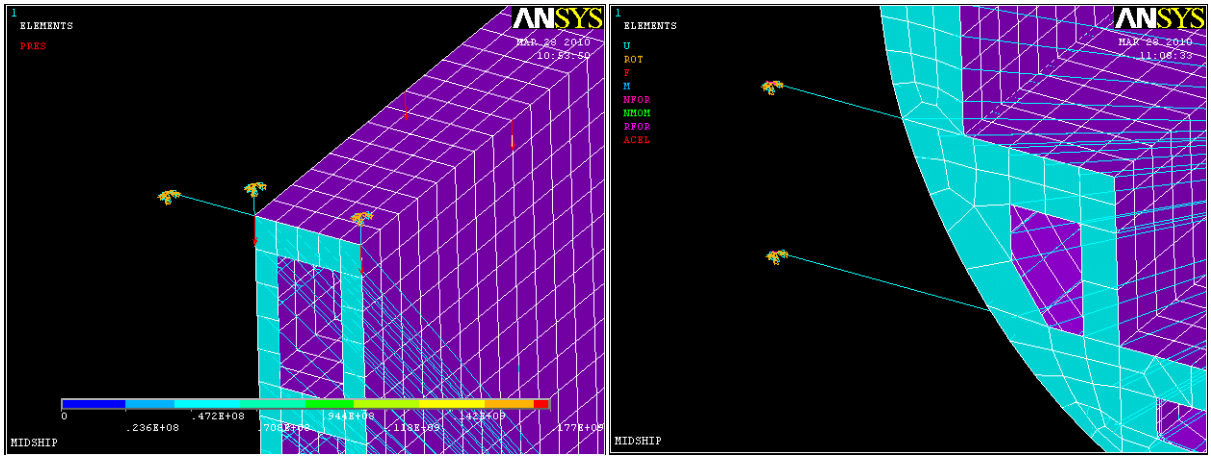

Figure 7.18 – Locations of ground springs used to restrain the model at its ends

The nodes at either end of the model were connected using rigid link elements to an independent point located at the models neutral axis. One end the model was constrained at its independent point in x translation. In a similar manner to the independent point at the top of the mast, moments to replicate the global bending moment of the ship where applied to the independent points at the model ends. The application of end moments in this manner creates large stress concentrations at the model ends near the connection of the rigid links and the ship structure. In order to minimise the effect of these stress concentrations on the stress results the modelled section was extended beyond the parallel mid body.

The modelling of the ship section was performed with the aid of *Microsoft Excel* in order to generate the required ANSYS input file. This gave the author the ability to make dimensional changes to the ship structure, change plate thicknesses, section types and number of stiffeners quickly in order to access the affect of these parameters on the strength of the ship section. It also allowed the author to model the ship section in ANSYS without knowing the scantlings given in Section 7.2.1 which could be input afterwards.

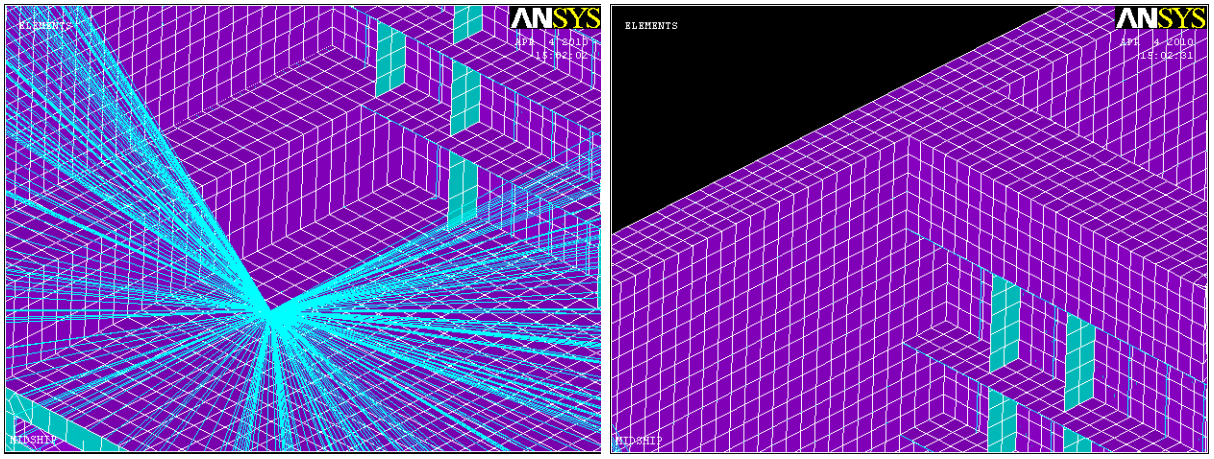

Figure 7.19 – Application of end moments to the independent points at the end of the model (left); and the mesh at the intersection of the transverse bulkhead and side tanks (right)

Loading

Since there is insufficient time to conduct a full analysis of the structure in all the load cases required for a full strength assessment, the LR SDA procedures, the CSR and Lloyd's Register (2008) have been used for guidance to derive load cases that the author feels are representative of the most extreme loading the ship will experience. The loading conditions used to investigate the structural strength of the ship and mast were developed to investigate the ship in the full load departure loading condition[13] in four motion conditions[14], namely:

1. Statically in still water;
2. Dynamically in head seas;
3. Dynamically in beam seas;
4. Dynamically in oblique seas.

The loading applied to the model for the four motion conditions can be broadly be divided in to the following:

- Hydrostatic pressure including the effect of the ship heel and trim;
- A uniform pressure applied to the bottom of the cargo holds representative of the weight of the container stacks. In the dynamic load cases the cargo pressure is factored by the vertical acceleration at the container stacks centre of mass (as calculated by the seakeeping analysis). The affect of longitudinal and transverse accelerations on the cargo have not been considered for simplicity;
- Moments applied to the ends of the model so that the maximum still water bending moment is achieved within the length of the modelled section;
- Dynamic vertical wave bending moments and horizontal wave bending moments;
- Hydrodynamic and cargo torque applied at the model ends;
- Correction loads distributed across the intersection of the transverse web frames and deck plate to ensure no net vertical force on the model;
- Wind loading pressure on sail mast;

[13] The full load departure condition has been selected for analysis as this loading condition produces the highest still water bending moment.

[14] The head seas, beam seas and oblique seas in the LR SDA and CSR for assessing the global strength of the hull have been assumed to be equivalent to the maximum pitching, rolling and combined motions load cases prescribed by Lloyd's Register (2008) Code for Lifting Appliances in the Marine Environment which has been used to derive the extreme loading on the sail system.

- Inertial loading on sail mast due to ship motions;
- Forces and moments applied to top of mast to account for wind loading and inertial loading on sails due to ship motions.

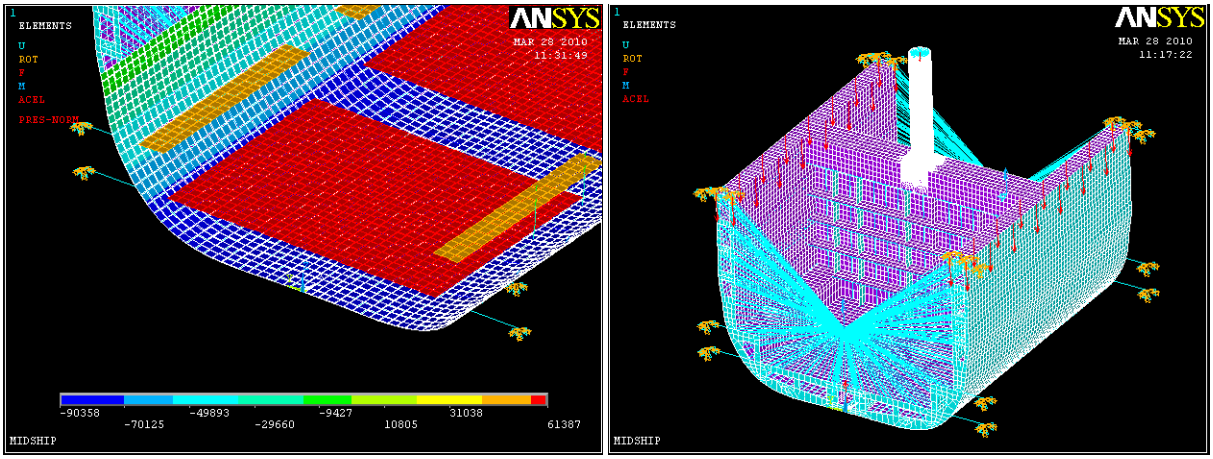

Figure 7.20 – Application of hydrostatic and cargo pressures (left); and correction loads (red arrows) required to ensure no net vertical force on the model (right)

Forces to account for wind loading, inertial loading due to the ship motions and operational loading on the sail and mast were calculated using a procedure to access the strength of cargo handling equipment [Lloyd's Register (2008)] for the four loading conditions being considered using the maximum roll and pitch angles from Section 7.1.4. Loading on the sails was determined and applied as an equivalent set of forces and moments to the independent point at the top of the mast.

The main change from the procedure of Lloyd's Register (2008) rules for cargo securing arrangements was in the selection of design wind speed. Lloyd's Register (2008) defines a design wind speed of 63 metres per second, however it was decided that this is excessive since the rules are prescribed for an offshore installation which will see far harsher conditions than the ship. Instead a 50 year return wind speed was investigated as defined by International Electrotechnical Committee (2005) for a ten minute gust. International Electrotechnical Committee (2005) defines a simple relationship for a 50 year return wind speed as simply five times the yearly mean. This is equivalent to a 23.2 metre per second wind speed in the Caribbean and South East Asia and a 24.2 metres per second wind speed worldwide. A wind speed of 32.6 metres per second has been chosen and used for the calculation of wind loadings which is equivalent to withstanding a force eleven storm and is more onerous than the International Electrotechnical Committee (2005) 50 year return wind speed. This is deemed a more than adequate wind speed in which to access the ship with its sails in the fully extended position.

The maximum vertical wave bending moment, horizontal wave bending moment and cargo and hydrodynamic torque are applied to the motion load cases using the design load combination factors given in the LR SDA procedures. These are factors applied to the maximum wave bending moment in head seas to estimate the wave bending moments in the beam and oblique sea conditions.

The additional loading on the ship structure due to the passing of a wave is usually accounted for with an additional positive (wave crest) or negative pressure (wave trough) superimposed onto the hydrostatic component. The additional loading imposed by green seas[15] (water on deck) is taken account of with relevant

[15]From Section 7.1.4 it was found that the probability of deck wetness was very small and thus supports the decision to neglect this loading condition from the analysis.

pressure loading. To simplify the analysis and due to time constraints the effect of these dynamic wave pressures have not been considered.

Using a similar argument to neglecting dynamic wave components, the assessment of the structure in combinations of different cargo loading conditions and damaged conditions has not been considered, for a full analysis these load cases would need to be undertaken.

The dimensions of the modelled mast section were assumed to consist of a circular cylinder of given thickness with vertical stiffening running its entire vertical height. The principle mast dimensions; plate thickness; diameter and stiffener section were chosen based on the maximum design loads using a beam theory approach and a limiting stress equal to yield at the foot of the mast. Since the mast and sail loading is dependent on sail and mast weight an iterative optimisation procedure was adopted in which the mast diameter, plate thickness and stiffener section (chosen from a list of 450 standard and custom sections [Corus (2002; 2007)]) was chosen in order to minimise the mast weight. A summary of the optimum mast dimensions from a beam theory approach is given in Table 7.17.

Table 7.17 – Summary of optimum mast dimensions

Parameter	*Dimension*
Mast diameter / m	2.00
Mast plate thickness / mm	10.00
Stiffener depth / mm	100.00
Stiffener width / mm	150.00
Stiffener web thickness / mm	25.00
Stiffener flange thickness / mm	25.00
Number of stiffeners	18.00
Mast mass / tonnes	14.14

The buckling capacity of the mast was calculated using beam theory and found to be 413 MN which is more than adequate to resist the calculated maximum vertical load on the mast of 0.596 MN in the head seas motion condition.

Acceptance criteria

The acceptance criterion which details the allowable stresses within different parts of the ship structure was taken from the LR SDA procedures and is summarised in Table 7.18. Results have been considered for a 20 metre section of the model with no results considered for the four metres at either end for reasons discussed previously.

For this investigation only the von Mises stresses (σ_{vm}) have been considered, although within LR SDA procedures acceptance criteria for longitudinal (σ_x), transverse (σ_y) shear (τ) and buckling (σ_{cr}) stresses are given. There are also prescribed stresses for beam elements which have not been evaluated in this investigation for simplicity. It is anticipated that general conclusions regarding the suitability of the ship structure can be obtained from the plate element von Mises Stress results, thus justifying this simplification.

The maximum values of allowable stress within the fine mesh zone, around the intersection of the mast and cross deck are different from the acceptance criteria for primary structure and were taken from the CSR and are summarised in Table 7.19.

Table 7.18 – Acceptance criteria for primary structure [Lloyd's Register (2006b)]

Structural item	*Allowable von Mises stress (σ_{vm}) / Nmm^{-2}*	
Bottom shell plating	0.63 σ_Y[16]	(≡ 223.65)
Double bottom girders	0.63 σ_Y	(≡ 223.65)
Deck Plating	0.75 σ_Y	(≡266.25)
Double bottom floors	0.75 σ_Y	(≡266.25)
Side shell long bulkhead	0.75 σ_Y	(≡266.25)
Side stringers	0.75 σ_Y	(≡266.25)
Side transverses	0.75 σ_Y	(≡266.25)
Transverse bulkhead plating	0.75 σ_Y	(≡266.25)
Cross deck transverses	0.75 σ_Y	(≡266.25)

Table 7.19 – Maximum permissible stresses for fine mesh analysis [International Association of Classification Societies (2008)]

Element stress	*Loading condition*	*Allowable von Mises stress(σ_{vm}) / Nmm^{-2}*	
Element not adjacent to weld	Dynamic loadcase	1.75σ_Y	(≡ 621.25)
	Still water	1.36σ_Y	(≡ 318.24)
Element adjacent to weld	Dynamic loadcase	1.5σ_Y	(≡ 532.5)
	Still water	1.2σ_Y	(≡ 426)

Model validation

The finite element model was verified by comparing the modelled mass to the expected model mass. A summary of the total mass of the finite element model is given in Table 7.20.

Table 7.20 – Finite element model validation by structure mass

Structural component (element type)	*No. of elements*	*Mass / kg*
Plates (shell 93)	90387	561437
Beams (beam 4)	35770	137252
Restraint elements (Link 8)	20	1.19
	Total	698690.19

The expected model mass excluding the additional structure added to the reverse side of the transverse bulkhead is 658.490 tonnes. This seems reasonable since there will be mass associated with the increased scantlings of the transverse bulkhead, if this was considered it is suspected that the model mass and ship mass would be very similar.

The mast deflection was verified by fully restraining the at mast deck level in all directions so it could be considered a fixed-free beam. The tip deflection under a known load was checked to see if was reasonable when compared to a beam theory calculation. The theoretical prediction of deflection from beam theory was found to be 3.965 centimetres. The tip deflection predicted by *ANSYS* was found to be 6.4535 centimetres which is of comparative magnitude to the beam theory estimate.

[16] σ_Y is the yield stress of steel, which for H36 high tensile steel is 355 MNm^{-2}.

The final check of the model geometry for errors came from careful analysis of stress results. It was found in the initial stages of the analysis that many areas of the structure were showing unexpected results. On further investigation of these areas it was possible to trace these errors to incorrectly defined geometry and modelling errors which were subsequently fixed.

Hull structure results

From an initial analysis conducted using the ship scantlings defined in Section 7.2.1 it was found that there were a number of overstressed regions in the hull structure, namely:

- The keel plating (1) for all load cases (Figure 7.23 and Appendix K.4)
- The inner bottom (17, 18) and bilge box top (15) plating around the intersections with the duct keel side (19) and transverse web frames for the roll loadcase (Figure 7.21);
- The intersection of the cross deck with the inner hull (14) in the head seas condition (Figure 7.21);
- The side shell (4, 5) at the intersection with the stringers (22) and transverse frames in the beam sea load case (Figure 7.24).

The author made changes to the hull structure upon analysis of the initial results which principally involved strengthening the pipe trunk. It was observed in Gee (2007) that in the development of the 'Norasia' fast feeder that there was some additional vertical bulkhead stiffeners between frames. The author added these additional structural items to the FE model to relive some of the high stresses in the keel plating (1). The additional structure consisted of plating extending between the centre girder and duct keel side (19) and a vertical stiffener on the duct keel side (19) spaced three between every transverse frame (Figure 7.22 and Appendix K.2).

Closer inspection of the failure region of the inner bottom (17,18) in the beam seas load case revealed that these areas were only marginally overloaded. It is suspected that a factor in the presence of these stress concentrations is due to the way the structure has been modelled and cargo loads applied. In reality, there will be additional reinforcement around the location of container corner posts to support the container stacks. This means the cargo loads could be treated as a series of point masses at the container corner posts and not as a uniform pressure load as has been used in this analysis. For these reasons these overstressed areas shall not be focussed on in this investigation as the overloaded areas are likely to be due to the limitations of neglecting the foundations under the container stacks and the way in which the cargo loads have been applied and not due to a deficiency in the hull structure. It was also commented on in Section 7.1.2 that the ship roll motion is poorly predicted numerically. Since the loading on the FE model is derived from these motions, this may be having an adverse effect on some of the loading conditions which is turn showing that some areas of the structure fail to meet the acceptance criteria in the beam sea load case where the roll motion is dominant.

The intersection of the cross deck and inner hull (14) is a common location to get high stresses within a container ship [Lloyd's Register (2006b)]. As a result this is usually the focus of detailed FE analysis in the design of a conventional container ship. These stress concentrations are usually prevented with detailed design of the intersection and because the failure region is small and only occurs in the head seas load case is not considered an issue for this investigation. The principal concern with this investigation is more with global strength and detailed design of the mast cross deck intersection and not the detailed design of hatch corners.

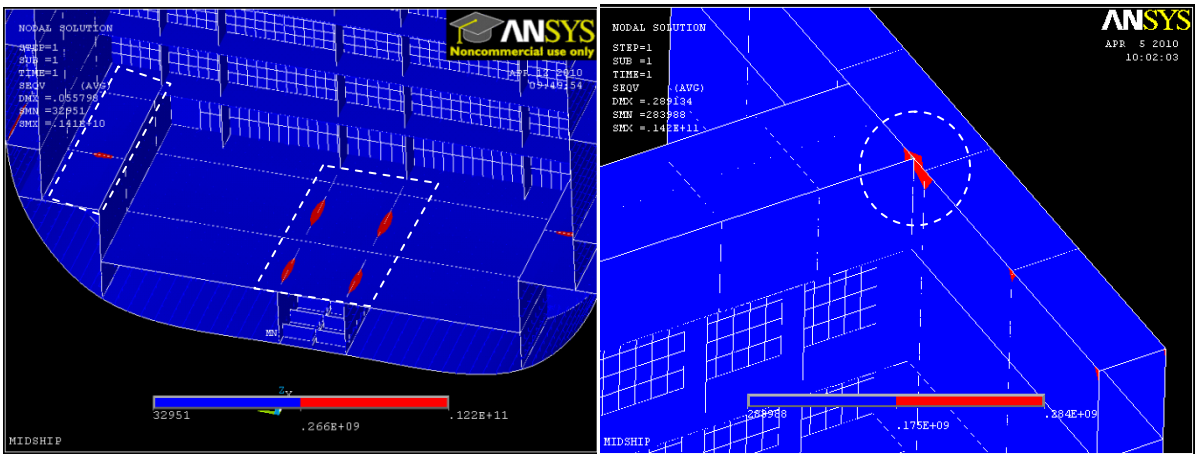

Figure 7.21 – Locations of areas of inner bottom (17,18) and bilge box top (15) plating that do not meet the LR SDA acceptance criteria defined in Table 7.18 (red areas) for the initial analysis in beam seas condition (left); and the stress concentration created at the intersection of the cross deck and inner hull (14) for the head seas condition (right) [Areas in blue indicate structure that meets the LR SDA acceptance criteria]

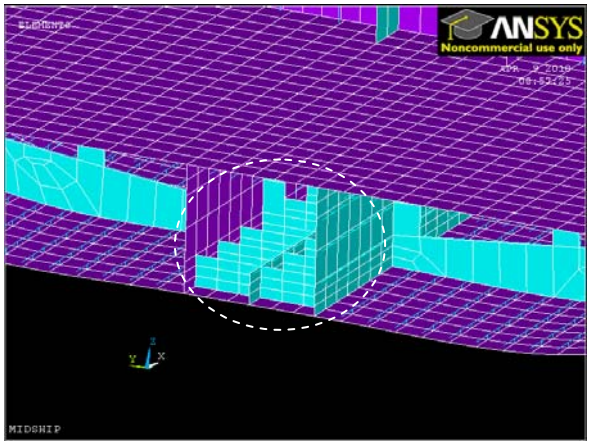

Figure 7.22 – Structural improvements made to ship structure as a result of the initial analysis.

Figure 7.23 shows the typical failure region in the keel plating (1) for the initial analysis and the affect the structural improvements had in reducing the stresses to within acceptable levels. The results presented are for the still water load case, results for the dynamic load cases can be found in Appendix K.4.

In addition to the keel plate (1) and the inner bottom (17,18), the side shell (4,5))on the submerged side of the ship in the beam sea condition failed to meet the criteria of the LR SDA procedures (Figure 7.24). The failure in these areas is very similar in form to the failure regions with the inner bottom (17,18), with the failure region occurring at the intersection of the side shell plating (4,5) with the transverse frames and stringers (22) and were only marginally overloaded. It is anticipated that these failure region are connected to the inaccuracies in the roll response predicted by the sea keeping analysis producing a maximum roll angle which is larger than reality and thus imposing higher pressures on the side shell than will be experienced in reality, and for this reason shall not be considered in this investigation.

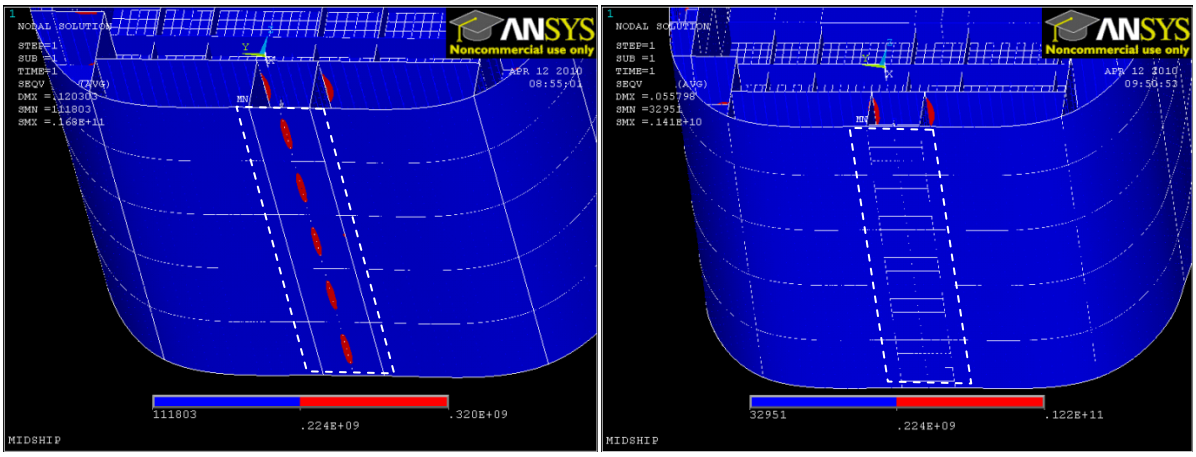

Figure 7.23 – Locations of areas of keel plating (1) that do not meet the LR SDA acceptance criteria (red areas) for the initial structure analysis (left); and the modified structure analysis (right) in beam seas condition [Areas in blue indicate structure that meets the LR SDA acceptance criteria]

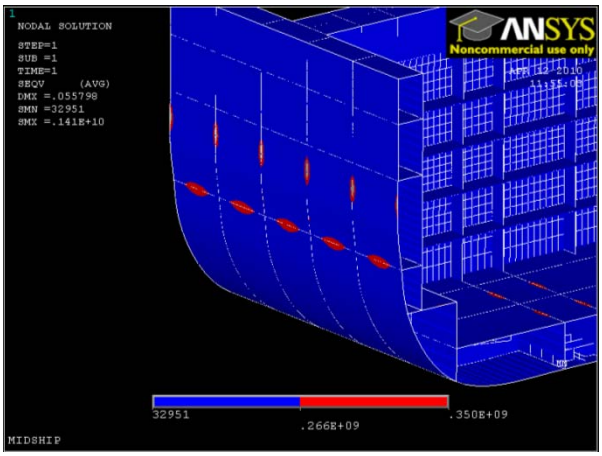

Figure 7.24 – Locations of areas of the side shell (4,5) that do not meet the acceptance criteria of Table 7.19 (red areas) (red areas) for the beam sea condition [Areas in blue indicate structure that meets the LR SDA acceptance criteria]

Mast structure results

From an analysis of the fine mesh region around the mast intersection with the cross deck and mast for the initial model, it is evident; and not unexpected that; there is a significant stress concentration formed at the intersection of the mast, cross deck and underlying vertical support structure and in the lower parts of the mast plating (typical results for the head seas condition are shown in Figure 7.26 results for the other load cases are presented in Appendix K.4). The stresses within the remainder of the mast were within the limits of the LR SDA procedures and these conclusions were consistent across all the dynamic motion conditions.

As a result of the initial analysis of the mast structure the author set about making a series of structural improvements to the mast structure. Four iterations were made around the design loop to arrive at a mast structure that met the requirements of the LR SDA procedures acceptance criteria given in Table 7.19. A summary of the structural improvements made to the mast structure after the last iteration of the design cycle are summarised as follows:

- Increased mast plating thickness around bottom 1 metre section from ten millimetres to twenty millimetres (although for practical purposes the whole mast was modelled as twenty millimetre plate) to relieve high stress areas in the mast plating at the bottom of the mast;

- Addition of horizontal rings of plating 250 millimetres deep and 17.5 millimetres thick spaced at 1000 millimetre intervals vertically within mast (Figure 7.25);
- Addition of 30 millimetre thick support brackets with 120 millimetre wide, 30 millimetre thick riders at the four quadrants of the mast intersection with cross deck (Figure 7.25) to reduce the magnitude of the stress concentrations, reduce the stresses in the lower mast plating and reduce the mast tip deflection.

Structural drawings of the final mast scantlings including these changes can be found in Appendix K.4.

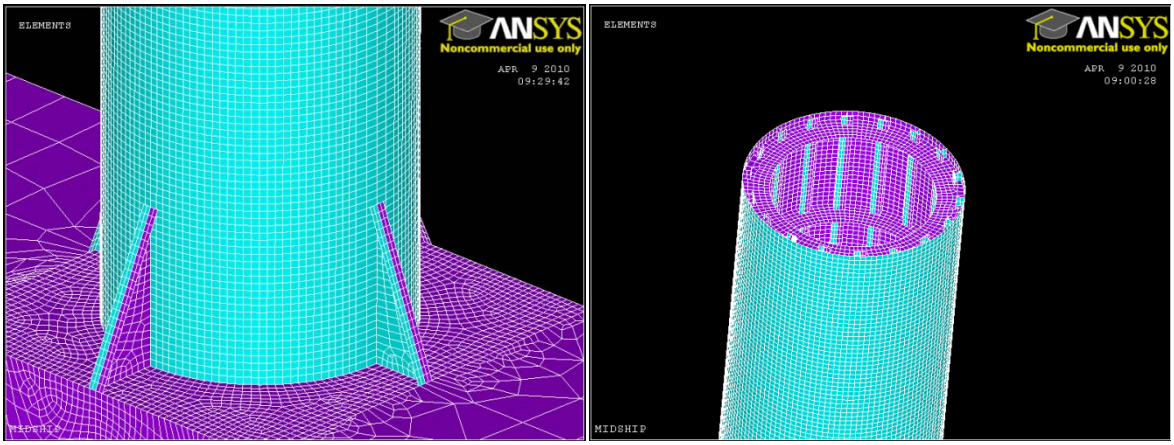

Figure 7.25 – Structural improvements made to mast structure as a result of the initial results, with the addition of brackets at the mast and cross deck intersection (left); and internal ring stiffening (right)

The high stress region created at the intersection of the mast and cross deck for the head seas condition initial analysis can be seen in Figure 7.26. In addition, figures showing the effect of the modified mast structure on reducing the magnitude of the stress in the mast and cross deck plating have also been presented. With all of the presented results the regions of high stress are reasonably symmetrical in size and shape on either side of the mast with one side showing a higher peak stress depending on the direction of loading. Results for the beam and oblique seas load cases can be found in Appendix K.4.

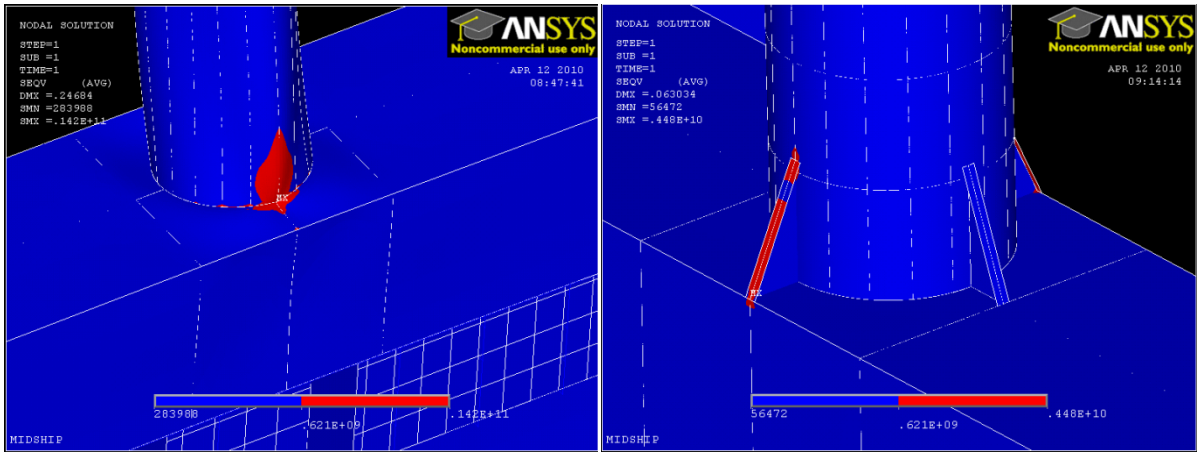

Figure 7.26 – Stress in the fine mesh zone at the base of the mast which does not meet the acceptance criteria of Table 7.19 (red areas) for the initial analysis (left); and the modified analysis (right) in the head seas condition [Areas in blue indicate structure that meets the LR SDA acceptance criteria]

It can be seen from Figure 7.26 and Appendix K.4 that the additional structure has had a significant effect on reducing the magnitude of the stress around the intersection of the mast and cross deck. There are still small areas where the requirements of the LR SDA procedures acceptance criteria have not been met. The head seas load comparatively case shows a much larger failure region (Figure 7.26) than the beam and oblique sea

load cases presented in Appendix K.4. It is the opinion of the author that these areas could be eliminated with increased dimensions of the brackets at the four quadrants of the mast intersection with the cross deck which due to time constraints have not been made within this project. It has however been demonstrated that significant improvements can be made with the addition of very small amounts of additional supporting structure.

The mast tip deflection was investigated for the considered load cases and compared to an allowable limit of 50 centimetres at the mast tip to prevent the mast striking the container stacks. The results of this investigation are shown in Table 7.21.

Table 7.21 – The mast deflection in the dynamic load cases for the initial and modified analysis

Load case	*Initial deflection / m*	*Modified deflection / m*	*% reduction*
Head seas	0.406	0.116	71.8
Beam seas	0.267	0.0726	73.1
Oblique seas	0.335	0.124	63.0

It can be seen from Table 7.21 that at all times the deflection of the mast is within the limits to prevent the mast striking the container stacks. It can also be seen that the mast tip deflection is reduced by between 63% and 73% with the addition of the additional structure at the base of the mast which is a significant improvement.

Discussion on stress concentrations

From the results presented for the mast intersection with the cross deck it is evident that there are some very extreme stress concentrations (Figure 7.27). It is well known that stress concentrations are not well modelled by FE programs which, is in part due to neglecting brackets and radius's when modelling. It can be seen in stress contours presented in Figure 7.27 show how the stress concentration increases very rapidly as the stress concentration is approached (left of Figure 7.27).

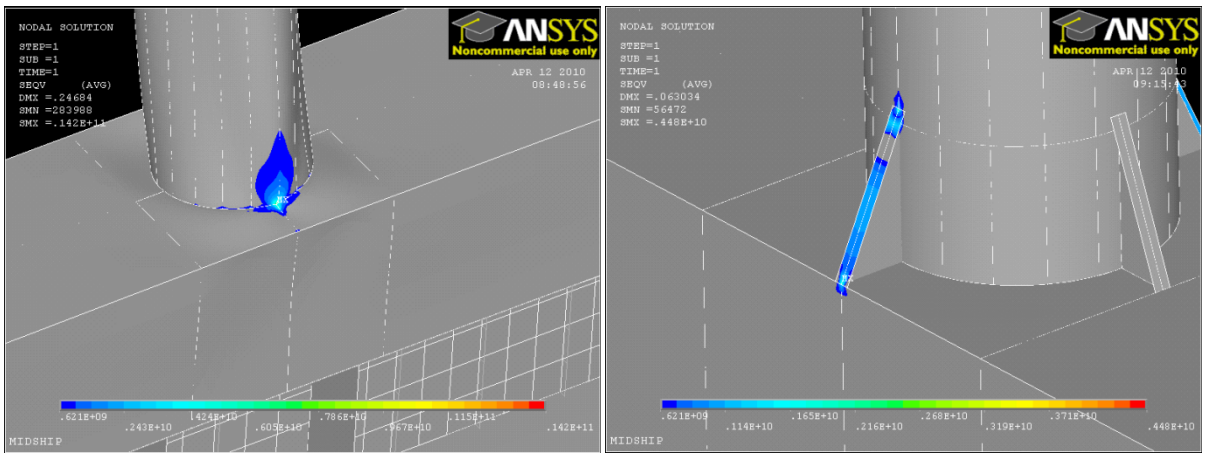

Figure 7.27 – High stress concentration regions around the mast and cross deck intersection for the initial analysis (left); and the modified analysis (right) for the head seas condition

A influential factor in the modelling of these stress concentrations is the choice of modelling scheme, be it, a solid, shell of shell-beam hybrid model, the latter of which has been used to model the ship structure while a shell modelling scheme has been used for the mast. Of these methods the solid model is the most representative of the ship geometry, but it is also the most computationally expensive, where as the shell-beam model is the most efficient but least representative of reality. A sub-investigation conducted by the author to investigate the effect of modelling scheme on the stress concentration factor created between the

mast and the cross deck plate revealed that the peak stress of the solid model was 47-52% of that of the shell model. The sub investigation was conducted using FE models which included the full extent of the mast, an area of cross deck plating around the mast foundation and the top supporting plating underneath using the same load cases as used for the main FE investigation, see Table 7.22.

Table 7.22 – Error in peak stress due to the choice of modelling scheme for the three motion loadcases

Modelling Scheme	*Peak stress for a considered dynamic load case*		
	Roll	*Pitch*	*Comb*
Shell	18.85 σ_N	19.02 σ_N	22.65 σ_N
Solid	9.23 σ_N	9.02 σ_N	11.84 σ_N
Shell-beam	24.91 σ_N	25.90 σ_N	39.70 σ_N

These results indicate as to how much *ANSYS* is overestimating the concentration created at the intersection of the mast and the cross deck due to the choice of modelling scheme. For further analysis of the mast structure careful consideration to the location of the stress concentrations and the reasons for their occurrence would need to be made to ensure the stresses are not a result of the chosen modelling scheme. It is suspected by the author that a significant proportion of the peak stress's observed in the presented fine mesh results can be attributed to this effect.

Discussion

FEM has been used in this investigation to investigate the global strength of the proposed hull form. A number of deficiencies were found and either solved with additional structure or attributed to modelling errors that cannot be resolved within the time frame of this project. The intersection of the mast with the cross deck has been investigated and suitable improvements suggested to prevent failure of the mast under extreme loading. It appears from an analysis of all the results that there are no significant influences of loading on the sails on the ultimate strength of the hull and that with the right structural design the proposed concept is viable. There are however a number of local areas of structure which still fail to meet the requirements of the LR SDA procedures. It is hoped that with further work these small areas could be eliminated with increased scantlings and careful detailed design of key areas.

The analysis conducted is only a small portion of what is required for a full analysis and verification of the hull structure. In a full analysis of the hull structure many more load cases and detailed investigations into critical areas of the design would need to be undertaken.

There are more considerations to the structural design of the proposed sail system than just ultimate strength. Wind is cyclic in nature which creates large fluctuating stresses in the mast and hull structure and combined with significant stress concentrations around the mast intersection with the cross deck mean there are likely to be problems from fatigue. It is likely that before any ship will use sails for propulsion an in depth fatigue analysis will have to be undertaken using FEM to redesign the mast cross deck intersection to improve its fatigue performance.

It has been demonstrated in this investigation how FEM is a useful tool that can be used to prove the reliability of a novel feature of a ship structure, a procedure which is a mandatory requirement for the classification of a ship with unusual or novel structure. There are however, in the opinion of the author, a number of limitations with the use of FEM for ship design, that include:

- The results are very sensitive to manner in which the model is restrained; meshed; loads are applied and results obtained. Throughout this investigation every effort has been made to eliminate errors as much as possible, however, a number of simplifications and assumptions have had to be made to complete the project within the time frame which will all have an influence on the final results;

- There is a large potential for errors in modelling, principally due to user error due to the large number of considerations that need to be made throughout the process;
- The process is slow and labour intensive compared to conventional rule based design. This has been demonstrated by the two design methods running side by side in this thesis. There are specialist classification societies computer programs such as GL Ship Model [Germanischer Lloyd (2010)] that can be used to speed up the process when compared to traditional FE programs such as *ANSYS.*

There are however a number of benefits to the use of FEM for ship design, namely:

- A reduction in scantlings to achieve a more efficient design (both steel weight and production costs) [Germanischer Lloyd (2010)].
- The ability to investigate fatigue life, buckling capacity and vibration characteristics along with ultimate strength.

7.2.4 Finite element sail rig model

In the preliminary design stage Euler beam theory was applied to validate the strength of major components of *Multi-wing* structure. However the assembled structure has some degree of complexity and this necessitates use of alternative methods. Therefore to evaluate the structural rigidity of the rig, finite element methods (FEM) used in the midship section analysis will be reintroduced.

The rig model of *Multi-wing system* will be simplified to increase the efficiency maintaining the general structural features. The rig is to be modelled for two conditions which represent upwind and downwind or storage configuration. For the loading 20 knots (15knots for downwind) and 70 knots of wind speed are applied for the average operational condition and for the worst weather condition respectively. The results will illustrate the maximum deflection, stress and stress concentration for each case and buckling behaviour in storage configuration.

Modelling

The *ANSYS* model of the full scale system consists of shell, beam and pipe elements. Since the mast and stocks are of conventional pipe shape, the *PIPE16* element is used and for the top and bottom bar *BEAM4* is applied. To simplify the structure thin plates are created to represent the wing surfaces using *SHELL6*3 and the connectivity of these elements is verified. The model generation is illustrated in Figure 7.28.

Then the 'real constants 'are calculated and applied to the model with material properties of 5083 aluminium alloy and 0.4% carbon steel considered [Calvert & Farrar (1999)]. In the initial modelling 5083 aluminium alloy is used for all the components to ensure the lightweight of the structure.

Loading

The loading applied to the structure is calculated using Equation (F.1) with appropriate lift coefficient. For the wing section the lift coefficient of 2.20 in upwind condition from *X-Foil* analysis and lift coefficient of flap plate, 1.28 is used in downwind condition. In this analysis it is assumed that the wind loading on the mast and connecting structure is negligible therefore only the pressure on the wing plate is to be applied. From the equation the pressures applied are 138 Pa, 45 Pa for the upwind and downwind operational condition and 1689 Pa and 982 Pa for upwind and downwind worst weather condition. The pressure is applied normal to the plate surface and evenly distributed. For the boundary conditions of the mast ends all DoF are constrained in both cases and the top of the structure is free end.

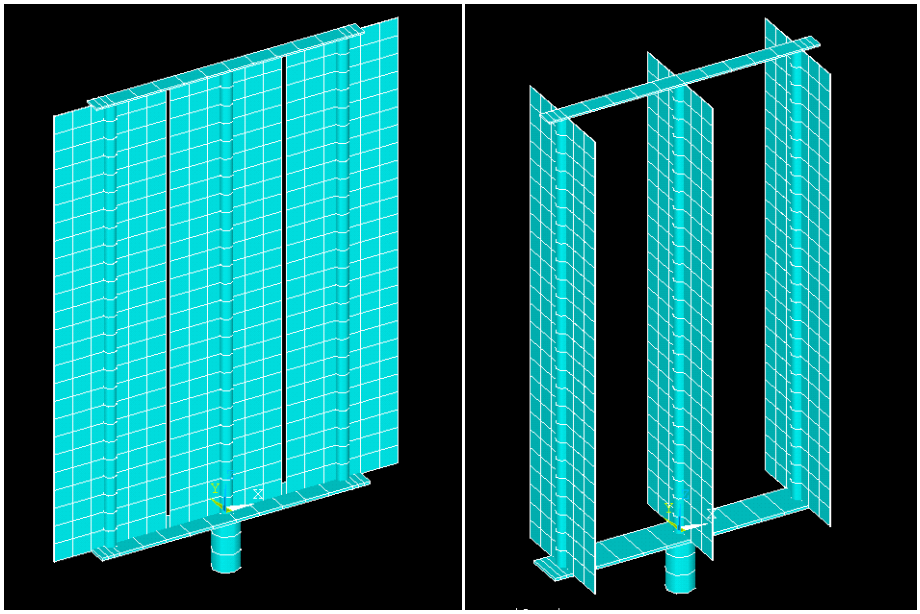

Figure 7.28 – Upwind mode (left) and downwind/storage model (right) in ANSYS

Results

Having applied nodal solution the results in four cases are shown in Figure 7.29 and Figure 7.30. Since the displacement and stress distribution trend are identical in both wind conditions, for operational wind speed, stress distribution is displayed, and for worst weather, the displacement is displayed. The results are summarised in Table 7.23 together with theoretical prediction of a single main wing stock using Euler beam equations for fixed-free end with evenly distributed load which is more reasonable than the preliminary design analysis since the top bar is not constrained.

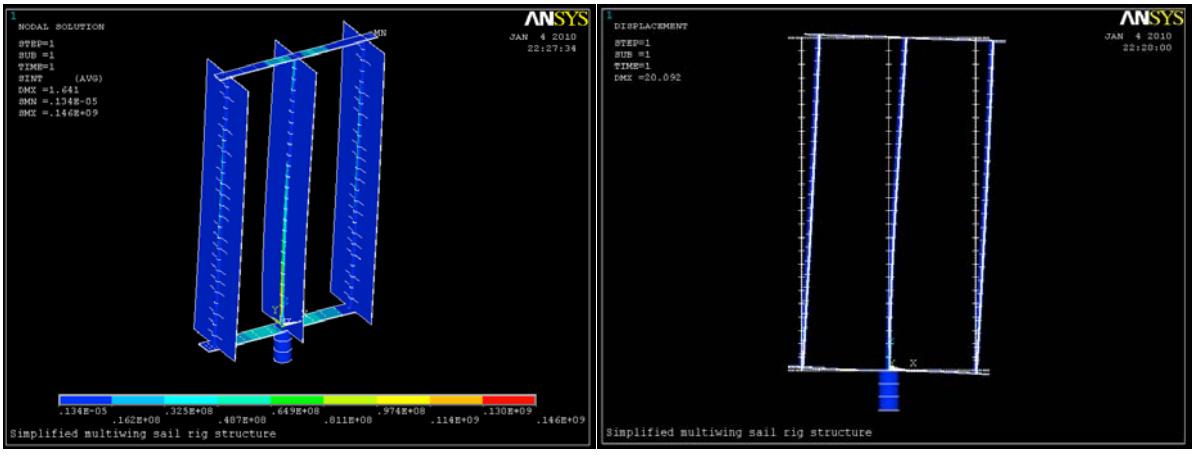

Figure 7.29 – Upwind model solution in operational condition(left) and worst condition(right)

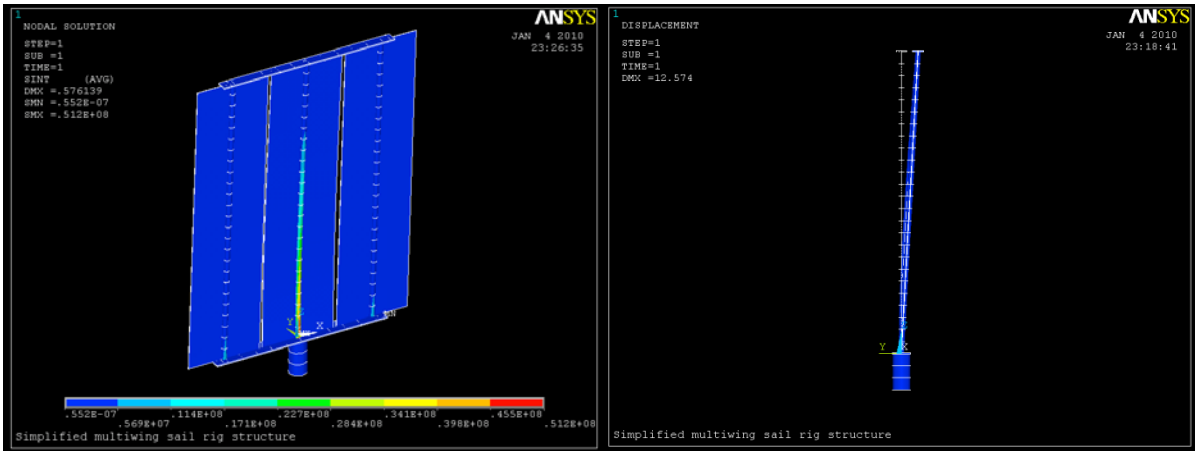

Figure 7.30 – Downwind/storage model solution in operational condition (left) and worst condition (right)

Table 7.23 – Theoretical and *ANSYS* solution in operational and worst weather condition

Model		*Theoretical estimation*		*ANSYS solution*	
		Max. deflection / m	*Max. stress / MPa*	*Max. deflection / m*	*Max. stress / MPa*
Operational	Upwind	0.68	68.73	1.641	146.0
	Downwind	0.22	22.54	0.576	51.2
Worst weather	Upwind	8.26	845.00	20.100	1790.0
	Downwind	4.80	492.00	12.574	1120.0

The worst weather condition results in excessive deflection and stress since the target maximum deflection and maximum stress were one metre and half the yield stress respectively. The *ANSYS* solution produced results of more than twice the maximum allowable deflection and stress. This requires some modification of the models.

Modification

To maximise the efficiency the simplest and straightforward modifications will be undertaken before considering design modifications involving additional structure or remodelling. Two modifications, changing material with higher Young's modulus and increasing dimensions are undertaken. Two components, the stocks and bottom bar are modified.

A direct way to reduce the stress concentration on the stock is to increase the diameter from 0.45 to 0.7 metres and the thickness of the wall from 0.03 to 0.05 metres within the design allowance for wing fitting. This results in 6.2 times higher second moment of area hence smaller maximum deflection and stress are expected.

By observation of the upwind model deflection it is noticed that small inclination of the bottom bar may produce large deflection on the top bar. One degree inclination of the bottom bar results in 0.43 metres deflection on the top bar. Therefore the bottom bar second moment of area needs to be increased. By changing the material from aluminium to 0.4% C steel and increasing the width from 1.5 to 2 metres and the thickness from 0.09 to 0.15 metres the second moment of area is improved in all directions. Figure 7.31 illustrates the change in stress distribution.

It can be seen that after modification the stress is distributed to mast and other components. The results summarised in Table 7.24 shows significant improvement in both maximum stress and deflection. Although the modification does not satisfy the target values it was clearly observed which structural elements are critical so it can contribute the efficiency of further modification. The modification involves significant weight increase due to change in dimension and material but since second moment of area can be increased using stiffeners

and geometric modification without significant increase in weight the original weight estimation using existing aluminium wing data is used in other structural analysis of this project.

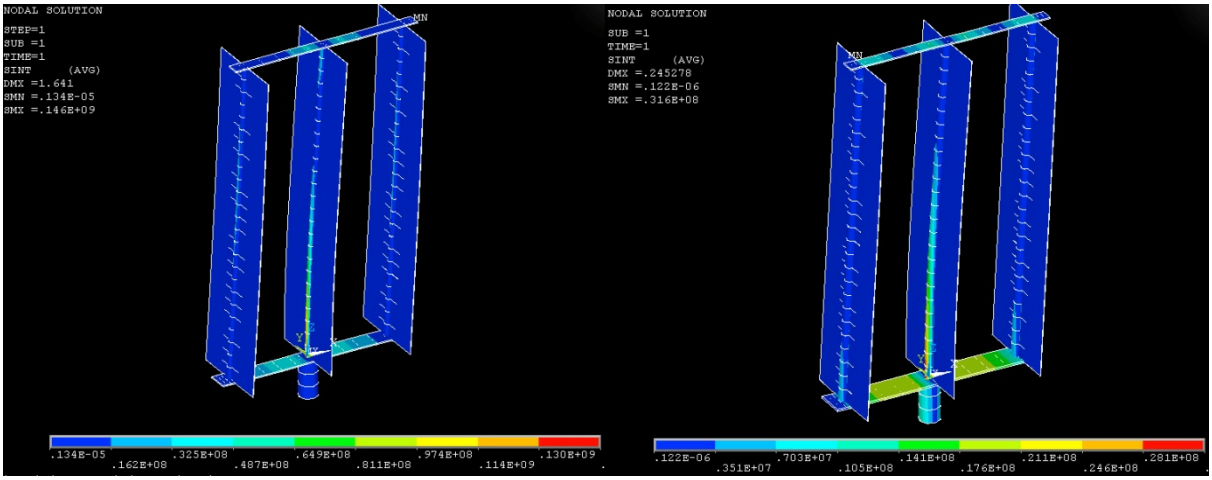

Figure 7.31 – The stress distribution before (left); and after (right) modification

The last case to investigate is buckling in modified downwind/storage model. When the stored rig elevates collision may happen due to obstacles on the way. Therefore this buckling analysis can determine the maximum speed or limit of lifting force to avoid buckling. To simulate buckling unit force, 1 N is applied on the top of each stock. Using the buckling factor the buckling load of 1480 kN is calculated which is bigger than theoretical value of 821 kN for a single wing plate. Figure 7.32 illustrates the buckling phenomenon.

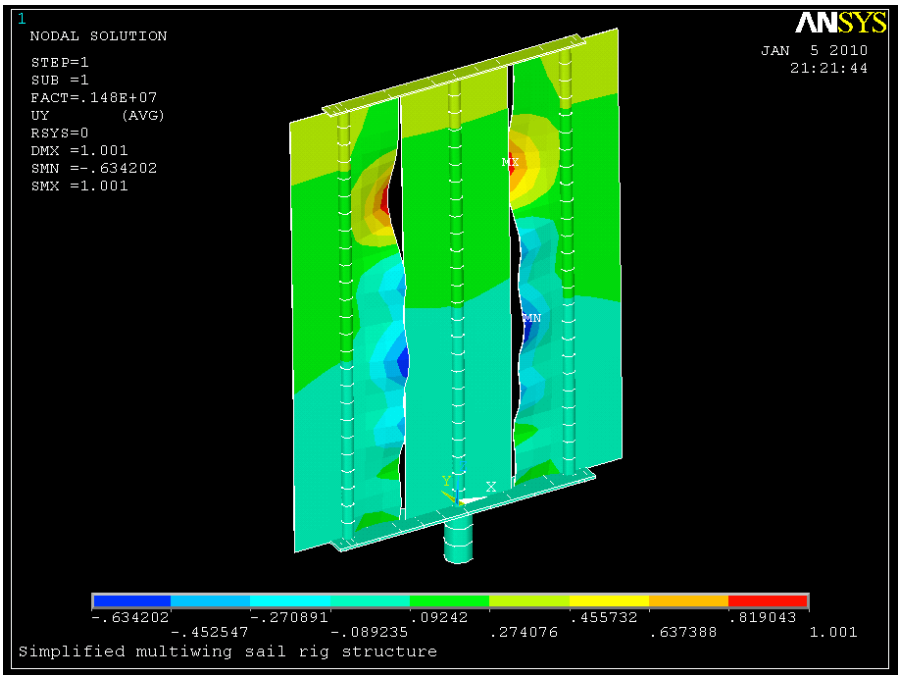

Figure 7.32 – Buckling mode of downwind/storage model

The figure shows the buckling occurs on the inner plates of the side wing plates. This may be caused by the deflection of the top and bottom bar since there is no gap between the plate and the bars in the model. Therefore when designing the real rig structure a reasonable amount of clearance between these two elements needs to be taken into account to avoid wing buckling. The buckling load calculated may not be valid in real wing section but the procedure may be required to determine the lifting speed and force limit of the rig.

Table 7.24 – Sumary of maximum deflection and stress comparing original and modified sail rig designs

Model		*Original design*		*Modified design*			
		Max. deflection / m	*Max. stress / MPa*	*Max. deflection / m*	*% of original*	*Max. stress / MPa*	*% of original*
Operational	Upwind	1.641	146.0	0.245	14.9	31.60	21.6
	Downwind	0.576	51.2	0.079	13.7	9.76	19.1
Worst weather	Upwind	20.100	1790.0	3.002	14.9	387.00	21.6
	Downwind	12.574	1120.0	1.716	13.6	213.00	19.0

Model validation

To validate the model generated the results are reproduced in different mesh sizes. Four different element numbers are used as shown in Table 7.25. The smallest element number 251 produced larger maximum deflection and stress but from element number 339 the change in value is insignificant. As 451 elements are used in both models the error due to mesh size will be insignificant to the overall analysis.

Table 7.25 – Effect of changing mesh size on maximum deflection and stress

No. of Element	*Max. deflection / m*	*Max. stress / MPa*
251	0.283270	36.7
339	0.245389	31.6
451	**0.245273**	**31.6**
592	0.245278	31.6

7.3 Stability

7.3.1 Intact stability

For the intact stability of the fast feeder concept, IMO (2008b) regulations were applied and additional criterions from LY2 [MCA (2007)] were used to look at the differences due to the sail system. However it should be noted that the fast feeder concept is not required to meet the LY2 criterion since it is in different category. The analysis was undertaken using a commercial software, *Hydromax* using the built in criteria analysis tool.

Tank and compartment definition

Prior to the analysis, the tanks, compartments and main items were defined to determine the longitudinal and vertical centre of gravity based on the weight estimation. This model, defined using *Hydromax,* is illustrated in Figure L.1. Then four load cases were created ensuring that the draft range lies within the maximum draft limit of 9.5 metres for operating in some ports and the minimum draft limit for complete emergence of the propellers which requires 6.4 metres including clearance. The four load cases are summarised in Table 7.26 with hydrostatics in equilibrium condition and the full item lists are in Appendix K.3.

IMO intact stability criteria

The IMO codes used for the intact stability comprise *Annex – International Code on Intact Stability,* 2008 Chapter 3.2 for all ships and Chapter 4.9 for container ships greater than 100 metres. With coefficients calculated in Appendix L.2, the required criterions were obtained and updated on the IMO criteria database ready for the large angle of heel analysis. To obtain the wind heeling lever, l_{w1} or severe wind and rolling criteria, the windage area and heeling lever are required. Therefore the worst case is assumed where all six wings are exposed to the wind direction having the largest area.

Table 7.26 – Hydrostatics of four load conditions in equilibrium condition

	Full load departure	*Full load arrival*	*Ballast departure*	*Ballast arrival*
Draft Amidships / m	8.942	8.935	7.004	7.011
Displacement / t	20483	20416	14506	14522
Draft at FP / m	**8.871**	**9.04**	**6.483**	**6.618**
Draft at AP / m	**9.013**	**8.829**	**7.525**	**7.405**
Draft at LCF / m	8.947	8.927	7.014	7.018
Trim (+ve by stern) / m	0.143	-0.211	1.042	0.787
WL Length / m	158.719	158.097	158.239	157.779
Wetted Area / m^2	4821.082	4804.151	3954.269	3949.572
Waterplane Area / m^2	3236.991	3217.485	2831.904	2819.949
KB / m	5.219	5.207	4.078	4.079
KG fluid / m	9.874	9.805	8.434	8.55
BMt / m	7.251	7.218	8.099	8.059
Trim angle (+ve by stern) / degree	0.0512	-0.0757	0.3735	0.282

Table 7.27 – values used in calculation of wind heeling lever

	Area / m^2	*Z / m*
Hull	1664.75	14.00
Superstructure	246.67	23.82
Container Bay	118.35	23.82
Mast	21.6	24.37
Sail (single wing)	151.44	42.39
Total sail area	908.64	42.39
Worst condition	**3035.73**	**18.44**

Four load cases were analysed and satisfied all criteria in the codes. The GZ curves for all conditions are given in Appendix L.2. The results are summarised in Table 7.28 and further details, including percentage margin, are given in Table L.2.

Table 7.28 – Summary of stability charateristics for analyisd ship conditions

Condition	*Initial GM @ $\Phi = 0$ / m*	*Max. GZ / m*	*Φ (Max. GZ) / deg*
Full load departure	2.596	2.520	59.1
Full load arrival	2.620	2.576	59.1
Ballast departure	3.743	4.180	68.2
Ballast arrival	3.588	4.061	68.2

LY2 intact stability criteria

Since there is no stability criteria developed for sail assisted container ships, LY2 for monohull sailing vessels [MCA (2007)] was used to investigate the difference between IMO and LY2 criteria. There are three criterions from LY2, which involve the range of positive stability, angle of equilibrium and angle of downflooding as shown in Table 7.29.

Table 7.29 – LY2 Monohull sailing ship criteria

Code	*Criteria*		*/degree*
11.2.2.1.2	Range of positive stability	Shall be greater than	90
11.2.2.1.3	Angle of equilibrium - derived wind heeling arm	Shall be greater than	15
11.2.2.1.3b	Angle of downflooding	Shall not be less than	40

The range of positive stability is satisfied in all load conditions but the other two criterion are not satisfied. This is due to non-watertight walkway compartments along the side of the ship, which cause low downflooding angle. The relatively high downflooding angle required may be due to the nature of sailing yachts' where 20 to 25 degree heel is normal upwind sailing condition which is not acceptable in most commercial vessels. The main difference between the severe wind in IMO and rolling criteria and LY2 is the former uses the actual windage area, wind heeling lever and dynamic pressure whereas the latter derives the heeling lever from downflooding angle or 60 degrees whichever is least as shown in Figure 7.33 and the following equations.

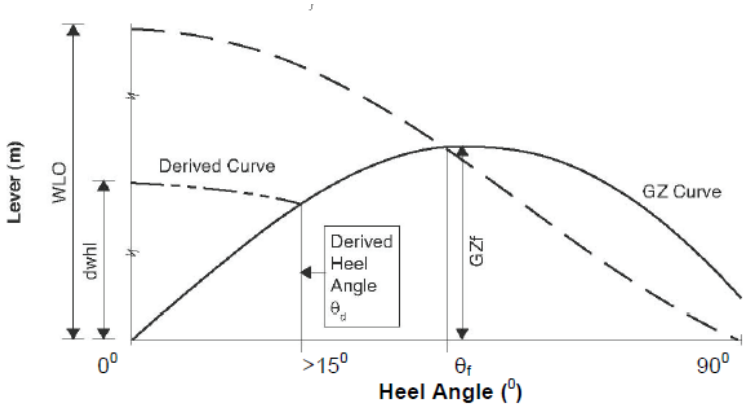

Figure 7.33 – Derived wind heeling lever with typical GZ curve

The derived wind heeling lever (dwhl) at angle $\theta°$ is equal to $0.5 \cdot \mathrm{WLO} \cdot \cos^{1.3}\theta_f$ where $\mathrm{WLO} = \mathrm{GZ_f}/\cos^{1.3}\theta_f$. Noting that: WLO is the magnitude of the actual wind heeling lever at zero degrees which would cause the vessel to heel to the 'down flooding angle' θ_f or 60 degrees whichever is least; θ_f is the angle at which the 'derived wind heeling' curve intersects the GZ curve.

7.3.2 Damage stability

Compartment definition

Bulkheads were defined in accordance with the requirement from Part 3, Chapter 3 of Lloyd's Rules [Lloyd's Register (2009)] that the ship have at least eight watertight bulkheads over its length. For consistency of loading it was decided that all cargo hold bulkheads would be assumed fully watertight, giving a total of nine full bulkheads. A watertight bulkhead was also located under the engine room floor forwards of the LNG plant room.

The damage stability of the concept was assessed against IMO probabilistic damage stability criteria from SOLAS Chapter II-1, Part B-1 [IMO (2009)]. This relies at its core on the ship being divided into a series of longitudinally defined damage zones which in this case were chosen to align with the major transverse bulkheads. As a result of the minor subdivision forward of the LNG spaces, the engine room compartment was included in two damage zones. The definition of longitudinal damage zones with is shown in Figure 7.34.

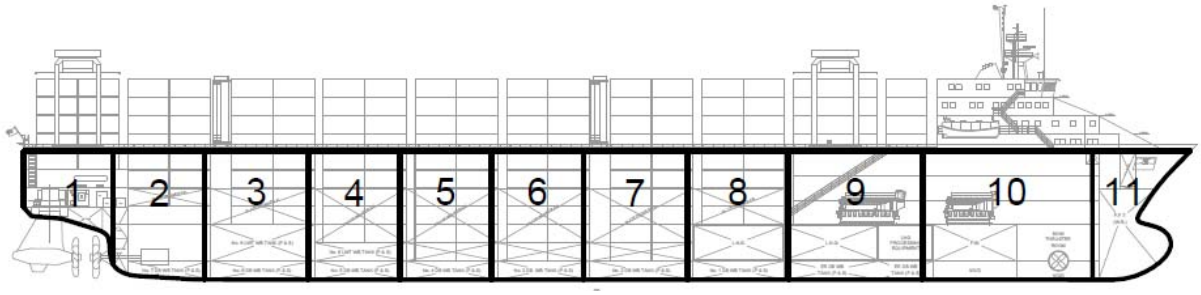

Figure 7.34 – Location of damage zones along the ship, aligned with watertight subdivision

Probabilistic calculations

SOLAS probabilistic stability considers a vessel to be suitably subdivided if its attained 'subdivision index', is not less than a required value [see Equation (7.9)] which is dependent on the subdivision length L_{SD}. The attained index is calculated by assessing the probability of occurrence of a particular damage case (p_i) and subsequent survival (s_i) at three operational draughts, the deepest subdivision draught d_s, a partial subdivision draught d_p and a light service draught d_l, and summating weighted contributions of the partial subdivision indices [Equation (L.3)].

$$R = 1 - \frac{128}{L_{SD} + 152} = 0.60335 \tag{7.9}$$

$$A_{si} = 0.4A_s + 0.4A_p + 0.2A_l\,, \tag{7.10}$$

where $$A_{s,p,l} = \sum p_i s_i.$$

Calculations for a damage case may be based on a single damage zone, or a combination. While the damage zones account only for transverse subdivision along the ship, the factor p_i incorporates the influence of longitudinal, based on an IMO statistical analysis. The probability of survival,s_i, is then calculated from the positive righting lever range in the damaged condition, with a reduction factor accounting for horizontal subdivision.

The attained index will tend to increase as more damage cases are investigated, though the contributions from larger damage lengths will clearly reduce as s_i reduces. Anticipating that the length of the engine room compartment might lead to too low a survival probability to attain the required index, a number of combinations were assessed as shown in Table 7.30.

Table 7.30 – Damage cases considered in the stability analysis and their constituent longitudinal damage zones

Damage Case, i	1	2	3	4	5	6	7	8	9	10	11	12	13	14
Zone(s)	1	2	3	4	5	6	7	8	9	10	11	8,9	9,10	10,11

The probabilities $p_i$and s_i were calculated in accordance with the procedure from SOLAS Chapter II-1, Part B-1 [IMO (2009)] given in Appendix L.3, with the resulting index values summarised in Table 7.31. It is clear that with the initial compartment definition, the required subdivision index is not only attained but substantially exceeded, suggesting that a lesser extent of subdivision might be possible without jeopardising the damage stability of the ship.

Table 7.31 – Calculated subdivision indexes

R_{SD}	0.603
A_{SD}	0.784
A_{SD_s}	0.737
A_{SD_p}	0.804
A_{SD_l}	0.838

7.3.3 Freeboard and tonnage

Freeboard

The freeboard for the concept design has been determined in conjunction with the Load Line Convention [IMO (1966/1988)]. This convention essentially prescribes the safe loading limit of a ship and markings that represent where the maximum draughts are located have to be displayed on the ship's hull, for each operating water type, as can be seen in the General Arrangement (Appendix M). This has been done to conform to international regulations, however the results is not crucial to the development of the concept. This is due to the maximum allowable draught being much larger than the ship is designed to operate. The freeboards are summarised in Table 7.32.

Table 7.32 – Summary of freeboard requirements

Summer freeboard / mm	4488.5
Summer draught / mm	14500.0
Tropical freeboard / mm	4186.4
Winter freeboard / mm	4790.6
Fresh water freeboard / mm	4160.9

Tonnage

Tonnage is of more interest as it is these values that port dues and other costs are often based in the operational maritime environment. It is therefore often desirable to minimise the tonnage. However, the determination of this is prescribed by the International Tonnage Convention [IMO (1969)] which aims to prevent conflicting measurements of tonnage for a particular ship. It should be noted that different tonnage certificates exist for transit thought the Suez Canal, for example. This is essentially for the gain of that state and need not be considered for this concept. Using the International Convention there are two measures of tonnage, gross and net. Gross is essentially a measure of the entire enclosed volume of the ship and net a measure of the cargo volume, although for a container ship this does not include containers stowed above deck. Both of these tonnages, although being measures of volume, are dimensionless and are summarised in Table 7.33.

Table 7.33 – Tonnage measurements

Gross tonnage	18463.7
Net tonnage	8284.6

7.4 Layout and arrangement

What follows is a brief explanation of areas of the vessel arrangement not discussed in the previous chapters.

The design methodology behind the layout was to locate the accommodation and engine room forward to maximise the container stowage and minimise aerodynamic drag through the use of an aerodynamic

accommodation block shape. All the main external features of the accommodation block, such as lifeboats and external stairs are enclosed within the outer skin of the accommodation block to reduce aerodynamic resistance. Crewing and space requirements within the accommodation block were sized using basis vessels, Watson & Gilfillan (1977), International Labour Organisation (1970) and a Nigel Gee concept design vessel [Centre for the Commercial Deployment of Transportation Technologies (2006)] .

During the arrangement of the vessel it was found that the overall length of the vessel had to be increased (by two metres) to fully accommodate the azipod and allow for a bulwark at the bow. This arose due to insufficient consideration to the dimensions of the azipod and final layout at the initial design stages. This dimensional change will only have small influences on the rest of the concept as the underwater form remained unaffected with the most notable change being a small increase in structure mass.

The cargo stowage arrangements were arranged within eight hatchcoverless cargo holds with two additional rows of reefer containers on deck just aft of the accommodation block. The use of hatchcoverless holds were used because it places no restrictions on the stowage of high cube containers[17] [Mash (2009)] for which there is increasing demand due to their greater transport efficiency. Currently 29% of 20ft containers and 55% of 40ft containers are high cubes. By 2020 it is predicted that 80% of containers could be high cube [Lloyd's Register (2006a)].

The storage of LNG was located within a tank underneath the engine space allowing for a 5.4 metres cofferdam to the side shell (Section 7.3.1) and assumed to be unrestricted by shape requirements. The use of containerised LNG was also considered but neglected due the larger volume and resulting loss in cargo space.

The unusual form of the engine room due to its position within the ship and propulsion machinery installation warranted special consideration to the engine room layout. Machinery was selected from manufacturer's websites to cover the main groups of:

- machinery, including
    - engines;
    - power take offs;
    - exhaust system and silencer;
    - electric motors;
- electrical, including
    - switchboard and cycloconverters;
    - transformers;
    - frequency converter;
- systems, including
    - cooling systems;
    - fresh water system;
    - waste system;
    - lubricating oil system;
    - refrigeration system;

[17] A high cube container is 2896mm in height rather than 2591mm for a standard container [Hapag-Lloyd (--)].

- fire fighting systems;
- ballast systems;
- LNG processing plant;
- engine room crane;

Spaces were also allocated to a machinery control room, electrical and engineering workshops; spare gear store; changing and laundry areas. The layout was arranged in a manner to determine the feasibility of a LNG diesel electric propulsion system located in this location and not intended as a detailed arrangement. Sufficient space has been left around the various machinery items to account for the smaller items of machinery that have not been considered.

A machinery arrangement for the three machinery spaces is illustrated on the general arrangement drawing in Appendix M and demonstrates that adequate space has been achieved with a forward located accommodation block to accommodate all of the required machinery.

The general arrangement and tank plan along with a diagrammatic illustration of the deck layouts is given in Appendix M

To demonstrate the feasibility of the cargo handling equipment, diagrammatic representation of the gantry crane operation around a folded sail system is shown in Appendix M. Little attention has been paid in this thesis to the detailed engineering of the sail system folding mechanism. At this stage an initial indication of a likely folding mechanism has been given with the detailed design a future consideration.

8. Conclusions

The fast feeder concept has been shown to be both economically and environmentally feasible based on the analyses detailed in this report. The best improvement in performance over typical existing ships is seen in the Caribbean region. Here a 42% reduction in CO_2 emissions has been predicted as well as a 33% reduction in daily costs, whilst meeting the market share for the 2020 container market initially assumed. It should be noted that the assumption of maintaining a constant number of sailings has not been adhered too. In order to replace two existing ships with one fast feeder the number of sailings has decreased by 25% so as not to under-utilise the vessel. The performance of the ship in the Singapore region is also favourable and only slightly lower in terms of CO_2 and cost savings compared to the Caribbean.

It is noted that numerous environmentally conscious ship concepts are currently being proposed within the maritime industry [Byklum (2010); NYK (2010); Wärtsilä Corporation (2009b)], and as such the fast feeder reflects changing attitudes towards ship design. Of particular interest is the novel container ship concept developed by DNV [Byklum (2010)] which reflects many of the unconventional design features present in this report. These include low block coefficient, LNG-fuelled engines, podded drives and improved cargo handling efficiency. This leads to the conclusion that the fast feeder concept has adopted design and operational approaches that will be commercially viable in the future, further justifying this study.

The main conclusions regarding the achievements of the project are summarised as follows. Regarding hydrodynamic model testing:

- Aside from the quantified uncertainty the results from the model tests are give an accurate naked hull form performance prediction following appropriate post processing. No account has been taken for appendages. In terms of upright resistance this is accounted for by adjusting the propulsive efficiency. The effect on side force and induced resistance when the ship is under sail is not considered. It is expected that the effect of the appendages is significant, due to the large size of the podded drive(s);
- The testing of the two ship models is justified by the novel form of *Hull B.* Validation of the numerical resistance predictions was important since *Hull B* was poorly represented by the *Holtrop.* regression;
- Model testing of both hull forms in waves was important to evaluate voyage performance more realistically. This also provides comparison to numerical methods whose validity has been found to be questionable;
- In hindsight the numerical prediction of the added resistance in waves should have been carried out prior to model testing. This may have allowed more reasonable estimation of the wave lengths to test, possibly enabling the capture of the peak in added resistance for each hull at both tested speeds;

Regarding aerodynamic model testing:

- The choice of the model scale played a fundamental role in obtaining accurate results. The analysis proves that the forces generated by the sails are highly dependent on the Reynolds number and a further increase in the sail coefficient would be expected for the full scale rig;
- The investigation of optimum sail rig configuration has been valuable in increasing the lift generated. The results of the spacing optimisation agree with General Biplane Theory [Munk (1923)] whilst the investigation on the stagger effect shows that the performance of the *Multi-wing* can be improved by the slot effect created between the upwind and downwind wings;
- Examining sail-container interaction has also led to a benefit in terms of performance, due to the reduction of the induced drag component. This has been predicted as a 15% increase in generated thrust;

- The limitations of the wind tunnel testing meant detailed rig-rig interaction could not be achieved. These effects are not fully accounted for in the overall prediction of performance. Thus the use of CFD has been valuable in showing that the two rigs must be independently controlled to maintain optimum overall sail system performance;

Regarding concept feasibility:

- A detailed study into 2020 container market has been carried out. This analysis does not include extrapolation past this date. As such, the growth in the container market throughout the operating life of the fast feeder has not been taken into account when assessing feasibility. However, since the comparison ships are operating in the same environment, this simplification is not considered too onerous.
- The thrust provided by the sails is low, as expected, especially at high speed. An additional limitation on the sail rig was the requirement to fold inside the hull so as not to hinder cargo handling. This is largely due to the ship type, and non-retractable sails could have provided larger sail area. However, the influence of the sails on ship stability is the ultimate limitation;
- The attained thrust reduction due to the auxiliary sail propulsion is not as large as initially estimated. At 25 knots a 3.0% reduction was predicted where as only 1-2% reduction was achieved; at 15 knots a 10.0% reduction was predicted whereas only 2-6% reduction was achieved, depending to the route. Although the wind tunnel results show improved rig efficiency, in terms of drag, compared to initial estimates, other factors that were crudely accounted for or disregarded in the initial design stages have resulted in a net reduction in the magnitude of thrust reduction. These factors include estimations of calm water, induced and added resistance;
- The final concept can operate safely in conditions up to 30 knots true wind speed (force seven) and 6.5 metres significant wave height, without affecting the scheduling of the service. This is considerably better than existing feeder ships (Section 2.5);
- Account has been taken of the typical operation of feeder services and attitudes of operators. It is acknowledged that many of the design and operational concepts introduced in this study will not be feasible immediately. However, the conservative nature of the maritime industry has not been allowed to hinder the design development, and it is assumed that many of the technologies proposed will be commonplace in 2020. It is noted that marine LNG terminals already exist in both the Singapore and Caribbean regions [Wärtsilä Corporation (2009b)], so in this respect, the adoption of LNG as a main propulsion fuel is considered entirely feasible;
- While the performance evaluation of the fast feeder concept is considered to be realistic, since the probability of wind and wave conditions is included in the PPP, no account is taken for these effects on the performance of the comparison ships. This means that efficiency gains may have been under-predicted, since the margin included in the comparison ship's schedule has been assumed to be due to waiting time in port, not weather delays;
- The economic feasibility analysis is considered to be fairly simplistic. This is due to a lack of cost data for the fast feeder, especially relating to the added construction cost attributed to the podded drives and LNG-electric propulsion system. Thus the confidence placed in the results of the economic assessment is not as high as that for the environmental analysis. The operation of the *Multi-wing* proves to be profitable when the benefits derived from motion damping are considered;

The design implications of the novel concept were not fully realised at the outset and were not accounted for early on in the project. These include:

- The unconventional mass distribution of the ship due to the stern-mounted podded drives and forward engine room leads to hogging. However, the structural design passes all class rules regarding global strength. In addition, this leads to difficulties in getting the vessel to float on an even keel as is desirable for efficient operation.
- The optimisation of the hull form for use with sails The performance of the candidate hull forms in this condition was not understood until after the results of the model testing had been analysed. It is anticipated that a greater thrust benefit could have been achieved if this had been considered during hull form development. However numerical techniques to evaluate this were not available.
- An additional benefit of the sail system was also not initially foreseen. The ability of the sails to provide motion damping has the advantage of reducing roll and yaw motions, which in turn reduces induced resistance when sailing to windward, as well as structural and cargo loads. Since the analysis of motion damping was not carried out until late on in the design development, these effects could not be incorporated into the resistance and seakeeping predictions, or FEA midship section model.
- Computational techniques, namely CFD and FEA, have been used to great advantage in the demonstration of the fast feeder concept viability. This is important, since in such unconventional designs simple design methods may not be rigorous enough. Novel design aspects are not always covered by rules and regulations that the vessel must adhere to and thus more intense numerical methods must be applied to prove the concept viability.

One full loop of the 'design spiral' has been completed, as proposed at the outset of the project. However, this means that the final design could be further refined by iterating through the spiral. The focus in this report has been on reducing resistance through hull form optimisation, yet an additional pass through the design spiral could focus on reducing structural mass. This could allow deadweight to be maximised or ship size to be reduced, both of which would improve efficiency.

From a reflective point of view, the organisation of, and constraints on the project, have directly affected the outcome. This has manifested in both positive and negative effects.

- The efficient organisation and early allocation of tasks within the group has meant a broad scope of work has been completed in the time available. The use of a quality checking system has also improved the quality of the final design.
- The submission of model plans by week 7 meant that the hull forms developed are not necessarily considered the most appropriate in hindsight. The limited time available resulted in unsatisfactory hull fairing. Ideally, more detailed design would have been carried out during the hull form development. This could have included: design for sailing performance; detailed propulsion calculations to inform stern design (avoiding the problems encountered (Section 7.4); and the use of a genetic algorithm to rapidly optimise the hull form based on multiple requirements.

9. Future Work and Recommendations

The recommendations listed can be divided under two main headings: those that would have benefited this project but were not carried out; and those that are outside the scope of this work but would enhance the robustness of the proposed concept.

Significant improvements could have been made to the investigation by:

- Conducting hull form optimisation for performance in waves, as well as reduced vessel motions. In addition, the PPP has not accounted for added resistance in stern quartering seas, and thus the total magnitude of added resistance over a typical voyage may be under-estimated. A reduction in added resistance, as well as pitch motions, may be evaluated from an analysis of the pitch damping due to the sails. This has not been carried out here since the appropriate inputs to the theoretical model are not available.
- Incorporating roll damping predictions into cargo securing and midship FE analyses, providing more realistic results.
- Incorporating the concept of 'weather routing' into the PPP so as to optimise the voyage simulation in terms of minimising power requirement.
- Making improvements in manufacturing techniques. The main concern is in refining the surface finish exhibited by the models so as to reduce the reliance on roughness corrections and increase confidence in the test results.
- Researching and quantifying other methods for improving efficiency such as hull coatings [Willsher & Solomon (2010)].
- Investigating of the effect of the gap size between the containers and rig on thrust increase. It is expected that further reducing the gap will increase the thrust, based on the container-sail interaction results already obtained.
- Completing more cases investigating the interaction between the forward and aft sail rigs using CFD. This will allow a greater understanding of the level of interaction for a range of wind speeds and angles. The results of such an investigation could also be incorporated into the PPP to improve performance prediction.

Improvements in performance through more detailed design that were not possible in this project include:

- Re-iteration of the design spiral. This would aim to optimise the hull form in the sailing condition as well as for calm water resistance.
- Detailed numerical simulation or physical testing of the propulsor hull interaction. This could include model self-propulsion tests; wake traverse measurements; tests with appendages (podded drives); and CFD simulations of the inflow into the propellers.
- More detailed investigation and understanding of the feasibility of using LNG as a marine fuel. In addition, the environmental cost incurred in producing and transporting the fuel to the bunkering location should be accounted for. The viability and environmental impact of using bio-fuels could also be considered. It follows that the life cycle emissions of the fast feeder, including construction and scrappage should be estimated. This has not been considered at all in this work, however a truly environmentally sustainable ship should take account of all emissions incurred throughout its life.

References

ABB (2009) Project Guide for Azipod® VO and VI Series.

American Bureau of Shipping (1988) Guide for Certification of Container Securing Systems.

Andersen, P. and Kristensen, H.O. (2009) Design for Efficiency of Performance. Proceedings of the 10th International Marine Design Conference, Trondheim.

Barlow, J.B., Rae, W.H. and Pope, A. (1999) *Low-Speed Wind Tunnel Testing.* Third edition. Wiley, New York.

Bergeson, L. and Greenwald, K.C. (1985) Sail Assists Developments 1979-1985. *Journal of Wind Engineering and Industrial Aerodynamics*, 19 (1-3), pp45-114.

Bertram, V. (2000) *Practical Ship Hydrodynamics.* Butterworth-Heinemann, Oxford.

Blomqvist, P.A. and Forrest, D.L. (2000) Laser Cutting and Welding of DDG-51 Structural Shapes. *The Journal of Ship Production*, 16 (4), pp183-92.

BMT Nigel Gee (1998) Norasia Data Sheet. Available from: http://media.bmt.org/bmt_media/resources/29/NG254-Norasia.pdf, accessed 15/10/2009.

Bonafoux, J., Dudson, E. and Sherwood, D. (2001) An Evaluation of the Effect of Hull Form Choice on the Operability of Fast Ferries. Proceedings of the 6th International Conference on Fast Sea Transport (FAST), Southampton.

Braslow, A.L. and Harris, R.V. (1966) Use of Grit Type Boundary Layer Transition Trips on wind Tunnel Models, NASA.

BSI (2007) Engineering Drawing Practice: A Guide for Further and Higher Education to BS 888:2006, Technical Product Specification,

Buhaug, Ø., Corbett, J.J., Endresen, Ø., Eyring, V., Faber, J., Hanayama, S., Lee, D.S., Lee, D., Lindstad, H., Markowska, A.Z., Mielde, A., Nelissen, D., Nilsen, J., Palsson, C., Winebrake, J.J., Wu, W. and Yoshida, K. (2009) IMO Second GHG Study 2009, International Maritime Organisation.

Byklum, E. (2010) Quantum – A Container Ship Concept for the Future, Container Update. *http://www.dnv.com/industry/maritime/publicationsanddownloads/publications/dnvcontainershipupdate/2010/1-2010/Quantumacontainershipconceptforthefuture.asp.* Accessed: 19/04/2010

Calvert, J.R. and Farrar, R.A. (1999) *An Engineering Data Book.* Palgrave, Basingstoke.

Campbell, I. (2009) Yacht Experimental Techniques Lecture Notes, University of Southampton.

Campbell, I. (2010a).Personal communication: Discussion in University of Southampton wind tunnel. 22/02/2010.

Campbell, I. (2010b).Personal communication: SSU towing tank. 24/02/2010.

Campbell, I. and Claughton, A. (1987) The Interpretation of Results from Tank Tests on 12m Yachts. Proceedings of the Eighth Chesapeak Sailing Yacht Symposium, pp91-107.

Carlton, J.S. (2007) *Marine Propellers and Propulsion.* Butterworth-Heinemann, Oxford.

Çengel, Y.A. and Cimbala, J.M. (2006) *Fluid Mechanics - Fundamentals and Applications.* McGraw-Hill, New York.

Centre for the Commercial Deployment of Transportation Technologies (2006) Pentamaran Concept Design Lift-on/Lift-off Containership, California State University. Available from: http://www.ccdott.org/transfer/projresults/2004/...31/task%202.31_1.pdf, accessed 20/04/2010.

Cheng, F. (2009).Personal communication: Sustainable shipping talk, University of Southampton. 15/10/2009.

Chéret, B. (2000) *Les Voiles: Comprendre, Régler, Optimiser.* Gallimard, Paris.

Chittagong Port Authority (2010) Turn Around Times of Vessels During the Fiscal Year 2007-2008. Available from: http://www.cpa.gov.bd/new/index.php?option=com_content&view=article&id=95&Itemid=64, accessed 09/04/2010.

Choi, E.C.C. (2004) Report on the Status of Codification on Wind Loading in Singapore. Proceedings of the Workshop on Regional Harmonisation of Wind Loading and Wind Environmental Specifications in Asia-Pacific Economies. Available from: http://www.wind.arch.t-kougei.ac.jp/APECWW/Report/2004/SIN.pdf, accessed 13/04/2010.

ClassNK (2008) Guidelines for Container Stowage and Securing Arrangements.

Claughton, A. and Campbell, I. (1994) Wind Tunnel Testing of Sailing Yacht Rigs. Proceedings of the 13th International HISWA Symposium on Yacht Design and Yacht Construction, Amsterdam. pp89-106.

Claughton, A., Wellicome, J. and Shenoi, A. (1998) *Sailing Yacht Design: Theory.* Addison Wesley Longman Limited, Harlow.

Clayton, B.R. and Sinclair, F.M. (1989) Motion Damping of Ships Fitted with Marine Aerofoils. *Transactions of the Royal Institution of Naval Architects*, 131 pp121-33.

Comstock, J.P. (1967) *Principles of Naval Architecture.* The Society of Naval Architects and Marine Engineers, New York.

Corus (2002) Corus Special Profiles Brochure : Bulb Flats for Plate Stiffening. Available from: http://www.corusgroup.com/file_source/StaticFiles/Business%20Units/Special%20Strip/Bulbflat.pdf, accessed 10/02/2010.

Corus (2007) Corus Advance Sections Brochure. Available from: http://www.corusconstruction.com/file_source/StaticFiles/Construction/Library/Sections/Advance_brochure.pdf, accessed 10/02/2010.

Cyberiad (2009) Michlet. *http://www.cyberiad.net/michlet.htm*. Accessed: 23/10/2009

Das, S.K. and Das, S.N. (2007) Modeling of Coupled Roll and Yaw Damping of a Floating Body in Waves. *Mathematical Problems in Engineering*.

Das, S.K., Das, S.N. and Sahoo, P.K. (2006) Investigation of Sway, Roll and Yaw Motions of a Ship with Forward Speed. Proceedings of the 5th International Conference on High Performance Marine Vehicles, Tasmania.

Dataloy (2009) Dataloy Distance table. *http://www.dataloy.com/*. Accessed: 31/11/09

Degerlund, J. (2004) *Containerisation Yearbook 2004.* Informa, London.

Degerlund, J. (2006) *Containerisation Yearbook 2006.* Informa, London.

Degerlund, J. (2008) *Containerisation Yearbook 2008.* Informa, London.

Doyle, T., Gerritsen, M. and Iaccarino, G. (2002) Optimization of Yard Sectional Shape and Configuration for a Modern Clipper Ship. Proceedings of the 17th International HISWA Symposium on Yacht Design and Yacht Construction, Amsterdam. pp73-83.

Engineering Sciences Data Unit (1980) ESDU 80024 Blockage Corrections for Bluff Bodies in Confined Flow.

Engineering Sciences Data Unit (1995) ESDU 76028 A Lift-interference and Blockage Corrections for Two-dimensional Subsonic Flow in Ventilated and Closed Wind-tunnels.

Faltinsen, O.M. (1998) *Sea Loads on Ships and Offshore Structures.* Cambridge University Press, Cambridge.

Federal Reserve (2010) Federal Reserve Statistical Release. *http://www.federalreserve.gov/releases/h15/data.htm*. Accessed: 16/04/2010

Formation Design Systems (2005a) Hullspeed User Manual.

Formation Design Systems (2005b) Seakeeper User Manual.

Francesetti, D.G. and Foschi, A.D. (2002) The Development of Hub and Spoke Systems in the Mediterranean: a Problem of Sustainable Development, Available from: http://ssrn.com/abstract=385183 or doi:10.2139/ssrn.385183, accessed 14/03/2010.

Frankel, E.G. (2002) The Challenge of Container Transhipment in the Caribbean. Proceedings of the IAME Panama 2002 International Steering Committee, Panama. Available from: http://www.eclac.cl/Transporte/perfil/iame_papers/papers.asp, accessed 14/03/2010.

Fujiwara, T., Hearn, G.E., Kiramura, F. and Ueno, M. (2005) Sail-sail and Sail-hull Interaction Effects of Hybrid - Sail Assisted Bulk Carrier. *Journal of Marine Science and Technology*, 10 (2), pp82-95.

Fujiwara, T., Hirata, K., Ueno, M. and Nimura, T. (2003) On Aerodynamic Characteristics of a Hybrid-Sail with Square Soft Sail. Proceedings of the 13th International Offshore and Polar Engineering Conference Hawaii. pp326-33.

Gee, N. (2007) New Developments in Container Vessel Design, BMT Nigel Gee, Available from: http://www.ngal.co.uk/Documents%20&%20Resources/?/126/2865/2865, accessed 03/04/2010.

Germanischer Lloyd (2010) GL Ship Model. Available from: http://www.germanlloyd.org/en/maritime_software/15450.php, accessed 11/04/2010.

Gerritsma, J. and Beukelman, W. (1972) Analysis of the Resistance Increase in Waves of a Fast Cargo Ship. *International Shipbuilding Progress*, 19 pp285-93.

Graham, R., Baitis, A.E. and Meyers, W.G. (1992) On the Development of Seakeeping Criteria,. *Naval Engineering Journal*, 104 (3), pp259-75.

Harries, S. (2006) Fundamentals of Advanced Hydrodynamic Design. *The Naval Architect, April 2006*, pp48-54.

Harries, S., Heimann, C.A.J. and Hochkirch, K. (2006) Advanced Hydrodynamic Design of Container Carriers for Improved Transport Efficiency. Proceedings of the Design and Operation of Container Ships Conference, London. pp121-29.

Harries, S., Heimann, J. and Hinnenthal, J. (2003) Parento Optimal Routing of Ships, Technical University of Berlin. Available from: http://www.futureship.net/downloads/2003_NAV_ParetoOptimalRoutingofShips.pdf, accessed 01/04/2010.

Henschke, W. (1965) Schiffbautechnisches Handbuch, Verlag Technik.

Hinrichs, R. (2009) Cost of MDO in Singapore. *HANSA International Maritime Journal*, 146 (6), p.15.
Hoerner, S. (1965) *Fluid Dynamic Drag.* published by the author, Brick Town, New Jersey.
Hogben, N. (1986) *Global Wave Statistics.* Unwin Brothers, Feltham, Middlesex.
Holtrop, J. (1984) A Statistical Re-analysis of Resistance and Propulsion Data. *International Shipbuilding Progress*, 31 (363), pp272-76.
Holtrop, J. and Mennen, G.G.J. (1978) A Statistical Power Prediction Method. *International Shipbuilding Progress*, 25 (603), pp253-56.
Holtrop, J. and Mennen, G.G.J. (1982) An Approximate Power Prediction Method. *International Shipbuilding Progress*, 29 (335), pp166-70.
Hoyle, J.W., Cheng, B.H., Hays, B., Johnson, B. and Nehrling, B. (1986) A Bulbous Bow Design Methodology for High-Speed Ships. *Transactions of the Society of Naval Architects and Marine Engineers*, 94 pp31-56.
Hughes, G. and Allan, J.F. (1951) Turbulence Stimulation on Ship Models. *Transactions of the Society of Naval Architects and Marine Engineers*, 59 pp281-314.
International Maritime Organisation (1966/1988) International Convention on Load Lines, 1966, as Amended by the Protocol of 1988
International Maritime Organisation (1969) International Convention on Tonnage Measurement of Ships.
International Maritime Organisation (2005a) MEPC/Circular.471 - Interim Guidelines for Voluntary Ship CO2 Emission Indexing for Use in Trials - (29 July 2005) - Annex - Interim Guidelines for Voluntary Ship CO2 Emission Indexing for Use in Trials - Appendix - Calculation of CO2 index based on operational data.
International Maritime Organisation (2005b) Resolution MEPC.132(53) - Amendments to the Annex of the Protocol of 1997 to Amend the International Convention for the Prevention of Pollution from Ships, 1973, as Modified by the Protocol of 1978 Relating Thereto - (Adopted on 22 July 2005).
International Maritime Organisation (2008a) Explanatory Notes to the SOLAS Chapter II-1 Subdivision and Damage Stability Regulations, Resolution MSC.285(86).
International Maritime Organisation (2008b) International Code on Intact Stability, Resolution MSC.267(85).
International Maritime Organisation (2009) International Convention for the Safety of Life at Sea.
International Association of Classification Societies (2008) Common Structural Rules for Double Hull Oil Tankers (CSR). Available from: http://www.iacs.org.uk/document/public/Publications/Common_rules/PDF/CSR_Double_Hull_Oil_Tanker_pdf778.pdf accessed 30/03/2010.
International Electrotechnical Committee (2005) IEC 61400-12-1: Wind Turbines – Part 21-1: Power Performance Measurements of Electricity Producing Turbines.
International Labour Organisation (1970) ILO 133 - International Labour Conference (ILO) Convention No. 133 - Convention Concerning Crew Accommodation on Board Ship (Supplementary Provisions), Part II. Crew Accommodation Requirements - Article 5
International Shipping Corporation (2010) Fleet Specs. Available from: http://www.intship.com/wp-content/uploads/2009/09/Container_Specs_ISH.pdf, accessed 17/03/2010.
ITTC (2002) Recommended Procedures and Guidelines: 7.5-01-01-01 Model Manufacture Ship Models.
ITTC (2005a) Recommended Procedures and Guidelines: 7.5-02-03-01.5 Testing and Extrapolation, Propulsion, Performance, Prediction. Power Margins.
(2005b) Recommended Procedures and Guidelines: 7.5-02-07-02.1 Testing and Extrapolation Methods, Loads and Responses, Seakeeping.
ITTC (2006) Recommended Procedures and Guidelines: 7.5-02 01-03 Testing and Extrapolation Methods, General Density and Viscosity of Water.
ITTC (2008a) Recommended Procedures and Guidelines: 7.5-01-03-01 Uncertainty Analysis Instrument Calibration.
ITTC (2008b) Recommended Procedures and Guidelines: 7.5-02-02-01 Testing and Data Analysis Resistance Test.
ITTC (2008c) Recommended Procedures and Guidelines: 7.5-02-02-02 Testing and Extrapolation Methods, General Guidelines for Uncertainty Analysis in Resistance Towing Tank Tests.
ITTC (2008d) Recommended Procedures and Guidelines: 7.5-02-03-01.4 Performance, Propulsion 1978 ITTC Performance Prediction Method.
ITTC (2008e) The Specialist Committee on Azimuthing Podded Propulsion. Proceedings of the 25th ITTC. Available from: http://ittc.sname.org/proc25/assets/documents/VolumeI/Volume1_5PropulsionCommittee.pdf, accessed 23/03/2010.

Jacobs, E.N. and Sherman, A. (1937) Airfoil Section characteristics as Affected by Variation in Reynolds Number, NACA Report 586.

Kalmar (2009) Automatic Stacking Crane Systems: Maximise Your Capacity. Available from: http://www.kalmarind.com/source.php/1261239/ASC-Systems_0909.pdf, accessed 27/03/2010.

Keuning, A., Toxopeus, S. and Pinkster, J. (2001) The Effect of Bow Shape on a Fast Monohull. Proceedings of the 6th International Conference on Fast Sea Transport (FAST), Southampton. p.197.

Kim, E.-C., Koh, C.D., Lee, C.-J., Kim, S.Y. and Choi, Y.-R. (2003) Development of a 30 knot Class High-Speed Container Ship CHUNGHAE-30. Proceedings of the Design and Operation of Container Ships Conference, London. pp105-11.

Kirkman, K.L. and Pedrick, D.R. (1974) Scale Effects in Sailing Yacht Hydrodynamic Testing. *Transactions of the Society of Naval Architects and Marine Engineers*, 82 pp77-101.

Koi Yu Ng, A. and Kee, J.K.Y. (2008) The Optimal Ship Sizes of Container Liner Feeder Services in Southeast Asia: a Ship Operator's Perspective. *Maritime Policy and Management*, 35 (4), pp353-75.

Kracht, A.M. (1978) Design of Bulbous Bows. *Transactions of the Society of Naval Architects and Marine Engineers*, 86 pp197-217.

Kyriazis, G. (1996) Bulbous Bow Design Optimisation for Fast Ships, Massachusetts Institute of Technology.

Levander, O. (2002) LNG-fuelled RoPax Vessels. *The Ship Power Supplier: Wärtsilä Corporation*, pp10-15. Available from: http://www.wartsila.com/ Wartsila/global/docs/en/ship_power/ media_publications/marine_news/ 2002_2/levander.pdf, accessed 04/03/2010.

Levander, O. (2008a) Alternative Fuel and Machinery Technologies for Ferries. Proceedings of the RoRo 2008, Gothenburg. Available from: http://www.wartsila.com/ Wartsila/global/docs/en/ship_power/ media_publications/presentations/ alternative-fuel-and-machinery-concepts-for-ferries-presentation.pdf, accessed 27/02/2010.

Levander, O. (2008b) Alternative Fuels for Ships. Proceedings of the Hållbara transporter 2008, Stockholm. Available from: http://www.wartsila.com/ Wartsila/global/docs/en/ship_power/ media_publications/presentations/alternative-fuels-for-ships-presentation.pdf, accessed 28/02/2010.

Levander, O. (2009) New Concepts in Ferry Propulsion, Wärtsilä Corporation. Available from: http://www.wartsila.com/Wartsila/global/docs/en/ship_power/media_publications/brochures/product/general/2009/Ferry-propulsion-2009.pdf, accessed 23/03/2010.

Lewis, E.V. (1989) *Principles of Naval Architecture.* Volume 3. Second edition. The Society of Naval Architects and Marine Engineers, Jersey City.

Lloyd's Register (2006a) Containers Push Size and Shape Boundaries.

Lloyd's Register (2006b) New ShipRight Procedure for Container Ships Helps to Assess Hull Stresses (LR SDA).

Lloyd's Register (2008) Code for Lifting Appliances in the Marine Environment.

Lloyd's Register (2009) Lloyd's Register Rules and Regulations - Rules and Regulations for the Classification of Ships.

Lloyd, A.R.J.M. (1989) *Seakeeping: Ship Behaviour in Rough Weather.* Ellis Horwood Series in Marine Technology,

Loukakis, T.A. and Chryssostomidis, C. (1975) Seakeeping Standard Series for Crusier-Stern Ships. *Transactions of the Society of Naval Architects and Marine Engineers*, 83 pp67-127.

MacGregor (2010) Lashing Systems Data Sheets. Available from: http://www.macgregor-group.com/?id=7176, accessed 21/03/2010.

Magnucki, K., Szyc, W. and Stasiewicz, P. (2004) Stress State and Elastic Buckling of a Thin-walled Beam with Monosymmetrical Open Cross-section. *Thin-Walled Structures*, 42 (1), pp25-38.

MAN Diesel (2010) Marine Engine IMO Tier III Programme. Available from: http://viewer.zmags.com/htmlCat/index.php?mid=rpwhph, accessed 23/03/2010.

Mange, E. (2006) Short Sea Shipping Cost Benefit Analysis. Proceedings of the European Transport Conference, Strasbourg.

Marchaj, C.A. (2003) *Sail Performance.* Adlard Coles Nautical, London.

Marchmann, J.F. and Werme, T.D. (1994) Clark-Y Performance at Low Reynolds Numbers. Proceedings of the VA.AIAA 22nd Aerospace Science Meeting, Reno.

Maritime and Port Authority of Singapore (2009) Port Statistics. Available from: http://www.mpa.gov.sg/sites/global_navigation/publications/port_statistics/port_statistics.page, accessed 09/04/2010.

Mash, C. (2009).Personal communication via e-mail, Borchard Lines Ltd. 13/11/2009.

MCA (2007) LY2 - The Large Commercial Yacht Code, Maritime and Coastguard Agency. Available from: http://www.ukshipregister.co.uk/msn_1792_edition_2.pdf, accessed 14/04/2010.

Michell, J.H. (1898) The Wave Resistance of a Ship. *Philosophical Magazine*, 45 (5), pp106-23.
Molland, A.F. (2008) Ship Design and Economics Lecture Notes, University of Southampton
Molland, A.F. (2009) Marine Propulsion Engineering Notes, University of Southampton.
Molland, A.F., Turnock, S.R. and Hudson, D.A. (unpublished) *Ship Resistance and Propulsion.* Cambridge University Press, Cambridge.
Molland, A.F., Wellicome, J.F. and Couser, P.R. (1994) Ship Science Report 71: Resistance Experiments on a Systematic Series of High Speed Displacement Catamaran Forms: variation of Length-Displacement Ratio and Breadth-Draught Ratio, University of Southampton.
Munk, M.M. (1923) General Biplane Theory, NACA.
U.S. Department of Commerce (2009) Global Ocean Observations. Available from: http://www.aoml.noaa.gov/phod/goos.php, accessed 14/03/2010.
Noteboom, T.E. and Vernimmen, B. (2009) The Effect of High Fuel Costs on Liner Service Configurations in Container Shipping. *The Journal of Transport Geography*, 17 (5), pp325-36.
NYK (2010) NYK Super Eco Ship 2030. *http://www.nyk.com/english/csr/envi/ecoship.htm.* Accessed: 19/04/2010
Ocean Shipping Consultants Ltd (2006) Is the Growth of the East Asian Container Port Markets Sustainable?
Ocean Shipping Consultants Ltd (2010) Deep-Sea Containership Trading Costs, obtained from David Tozer of Lloyd's Register with the permission of the authors.
Palmer, A. (2010).Personal communication, via e-mail. 19/03/2010.
Percival, S., Hendrix, D. and Noblesse, F. (2001) Hydrodynamic Optimisation of Ship Hull Form. *Applied Ocean Research*, 23 (6), pp337-55.
Podsada, J. (2001) Sea Cargo: Beach Bounty or Junk? . *http://news.nationalgeographic.com/news/2001/06/0619_seacargo.html.* Accessed: 14/03/2010
Praefke, E., Richards, J. and Engelskirchen, J. (2001) Counter Rotating Propellers Without Complex Shafting for a Fast Monohull Ferry. Proceedings of the 6th International Conference on Fast Sea Transport (FAST), Southampton. pp1-10.
PSA Singapore Terminals (2009) Transhipment. *http://www.singaporepsa.com/corporate/transhipment.html.* Accessed:
Rolls Royce (2008) Kamewa Propulsion Brochure. Available from: http://www.rolls-royce.com/marine/downloads/propulsion/prop_broc.pdf, accessed 10/12/2008.
Salvesen, N. (1978) Added Resistance of Ships in Waves. *Journal of Hydronautics*, 12 (1), pp24-34.
Satchwell, C.J. (1986) Marine Aerofoil Motion Damping and Related Propulsive Benefits, University of Southampton.
Satchwell, C.J. (1989) Windship Technology and its Application to Motor Ships. *Transactions of the Royal Institution of Naval Architects*, 131 pp121-33.
Schenzle, P. (1985) Estimation of Wind Assistance Potential. *Journal of Wind Engineering and Industrial Aerodynamics*, 20 (1-3), pp97-109.
Schneekluth, H. (1988) *Hydromechanik zum Schiffsentwurf.* Koehler,
Schneekluth, H. and Bertram, V. (1987) *Ship Design for Efficiency and Economy.* Butterworth-Heinemann, Oxford.
Sears, R.I. and Liddel, R.B. (1942) Tunnel Investigation of Control Surface Characteristics. VI A 30-Percent-Chord Plain Flap on the NACA 0015 Airfoil, NACA Report 454.
Sinmons, L.F.G. and Salter, C. (1934) Experimental Investigation and Analysis of the Velocity Variations in Turbulent Flow. *Proceedings of the Royal Society of London*, 145 (854), pp212-33.
Sipila, H. and Brown, A. (1997) Application of the Slender Monohull to High Speed Container Vessels. Proceedings of the 4th International Conference on Fast Sea Transport (FAST), Sydney. pp247-53.
SkySails (2010) SkySails: Turn Wind into Profit. *http://www.skysails.info/.* Accessed: 19/04/2010
Smulders, F. (1985) Exposition of Calculation Methods to Analyse Wind-Propulsion on Cargo Ships. *Journal of Wind Engineering and Industrial Aerodynamics*, 19 (1-3), pp187-203.
Strom-Tejsen, J., Yeh, H.Y.H. and Moran, D.D. (1973) Added Resistance in Waves. *Transactions of the Society of Naval Architects and Marine Engineers*, 81 pp109-43.
Svendsen, J. and Tiedemann, J. (2009) Containership-Info. *http://www.containership-info.com/.* Accessed: 11/11/2009
Svoboda, C. (1999) Aluminium Structural Member Component Weight as a Function of Wing Loading. *Aircraft Design 2*, 2 (4), pp231-37.
Tanneberger, K. (2009).Personal communication: Meeting at Lloyd's Register 71 Fenchurch Street, London. 16/12/2009.

Townsin, R.L. (2003) The Ship Hull Fouling Penalty, International Marine Coatings.
Tozer, D. (2009).Personal communication: Meeting at Lloyd's Register 71 Fenchurch Street, London. 16/12/2009.
Tu, J., Yeoh, G.H. and Liu, C. (2008) *Computational Fluid Dynamics: A Practical Approach.* First edition. Butterworth-Heinemann, Oxford.
Tuck, E. and Lazaukas, L. (2008) Drag on a Ship and Michell's Integral. Proceedings of the XXII International Congress on Theoretical and Applied Mechanics, Adelaide. pp1-2.
Tuck, E.O. and Lazaukas, L. (1996) Unconstrained Ships of Minimum Total Drag, University of Adelaide.
Tuck, E.O., Lazaukas, L. and Scullen, D.C. (1999) Sea Wave Pattern Evaluation, Part 1 Report: Primary Code and Test Results (Surface Vessels), University of Adelaide.
van Duivendijk, L. (2009) Container Ships. *http://www.duivendijk.net.* Accessed: 10/11/2009
van Gunsteren, L.A. (1971) Application of Momentum Theory in Counterrotating Propeller Design. *International Shipbuilding Progress*, 18 (206), pp359-72.
Veldhuis, I. (2007) Application of Hydrogen Marine Systems in High-speed Sea Container Transport. Thesis, University of Southampton.
Vietnam Seaports Association (2010) Shipping Schedules. Available from: http://www.vpa.org.vn/english/information/info_schedure.htm, accessed 09/04/2010.
Walker, J.G. (1985) A High Performance Automatic Wingsail Auxiliary Propulsion System For Commercial Ships. *Journal of Wind Engineering and Industrial Aerodynamics*, 20 (1-3), pp83-96.
Wärtsilä Corporation (2008) Wärtsilä Controllable Pitch Propellers. Available from: http://www.wartsila.com/Wartsila/global/docs/en/ship_power/media_publications/brochures/product/propulsors/controllable-pitch-propellers-wartsila-brochure.pdf, accessed 24/03/2010.
Wärtsilä Corporation (2009a) Flexibility in a Small Package. Available from: http://www.wartsila.com/ Wartsila/global/docs/en/ about_us/in_detail/1_2009/ flexibility-in-a-small-package-article.pdf, accessed 23/02/2010.
Wärtsilä Corporation (2009b) Shipping in the Gas Age. Available from: http://www.wartsila.com/Wartsila/global/docs/en/ship_power/media_publications/brochures/shipping-in-the-gas-age-brochure.pdf, accessed 19/04/2010.
Wärtsilä Corporation (2010) Fuel Cells for Marine Applications. Available from: http://www.wartsila.com/Wartsila/global/docs/en/products_services/fuel_cells/wartsila_fuel_cells_for_marine_applications_leaflet.pdf, accessed 23/03/2010.
Wärtsilä Ship Power R&D (2009) Boosting Energy Efficiency. Available from: http://wartsila.eu/Wartsila/ global/docs/en/ship_power/energy-efficiency/boosting-energy-efficiency-presentation.pdf, accessed 01/03/2010.
Wärtsilä Ship Power Technology (2009a) Wärtsilä 50DF Main Data. Available from: http://www.wartsila.com/ Wartsila/global/docs/en/ ship_power/products/2009/ main-data-wartsila50df.pdf, accessed 26/02/2010.
Wärtsilä Ship Power Technology (2009b) Wärtsilä 50DF Product Guide. Available from: http://www.wartsila.com/wartsila50DF, accessed 24/02/2010.
Watson, D.G.M. and Gilfillan, A.W. (1977) Some Ship Design Methods. *Transactions of the Royal Institution of Naval Architects*, 119 p.45.
Willsher, J.D. and Solomon, T. (2010) Operational and Environmental Benefits of Foul Release Coatings. Proceedings of the Ship Design and Operation for Environmental Sustainability, London. pp51-54.
Wilson, P.A. (1985) A Review of the Methods of Calculation of Added Resistance of Ships in a Seaway. *Journal of Wind Engineering and Industrial Aerodynamics*, 20 (1-3), pp187-99.
Young, W.C. and Budynas, R.G. (2002) *Roark's Formulas for Stress and Strain.* Seventh edition. McGraw-Hill, New York.

Appendices

Appendix A – Basis Ships

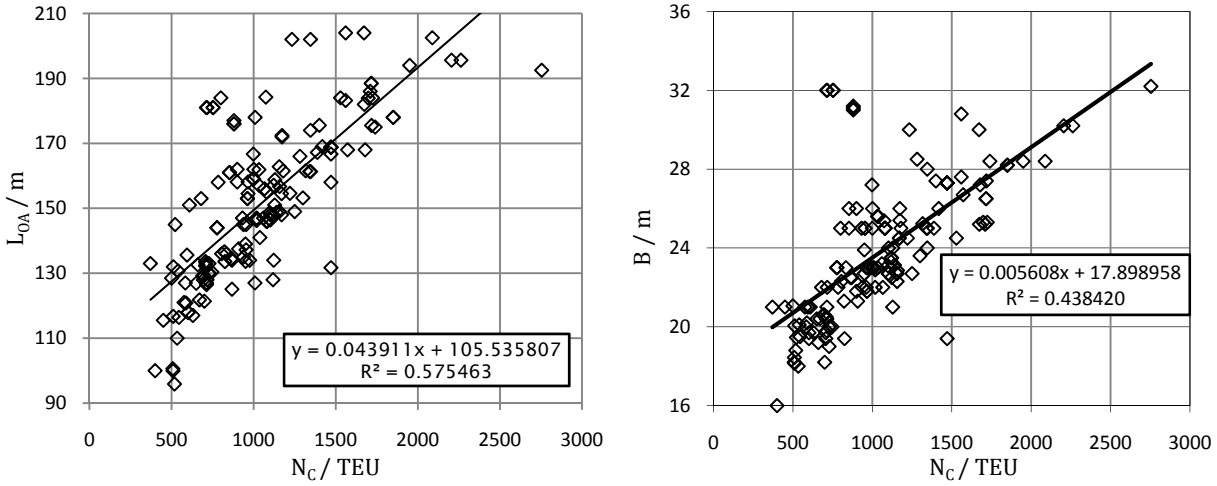

Figure A.1 – L_{OA} as a function of cargo capacity (left); and B as a function of cargo capacity (right)

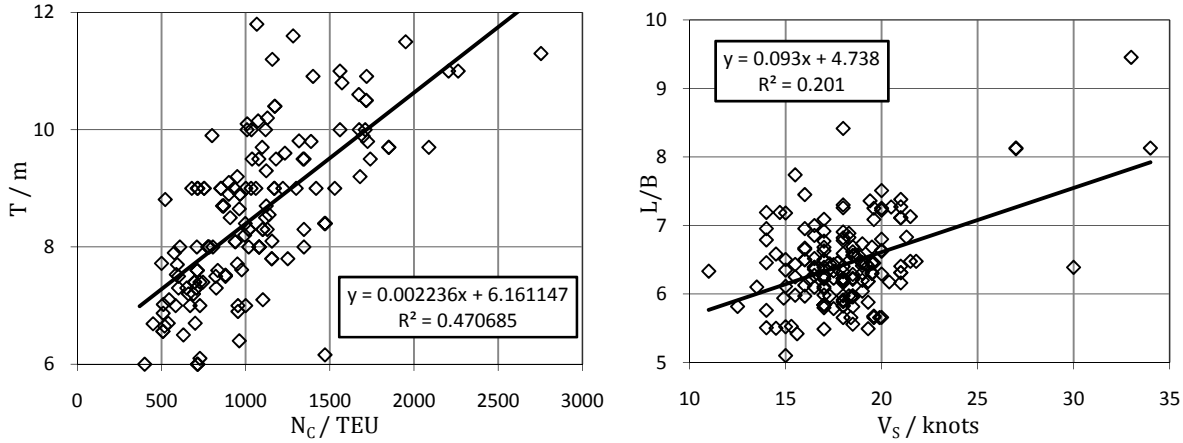

Figure A.2 – Draught as a function of cargo capacity (left); and L_{OA}/B as a function of ship speed (V_S) (right)

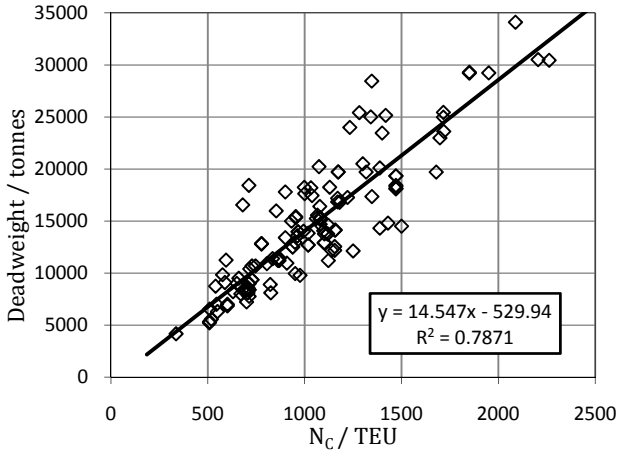

Figure A.3 – Deadweight as a function of cargo capacity

Appendix B – Hull Form Development

B.1 – Bulbous bow optimisation

Table B.1 – Hull A; Total resistance coefficient for all bulb variants

Bulb variant		1	2	3	4	5	6	7	8	9	10	11	12	13	14	15
V_S/ knots	Fn	$C_{TS} \times 1000$														
0.4	0.0049	3.560	3.560	3.538	3.556	3.551	3.535	3.557	3.551	3.530	3.566	3.561	3.535	3.533	3.526	3.529
1.5	0.0196	3.172	3.166	3.083	3.150	3.132	3.070	3.151	3.127	3.050	3.180	3.164	3.063	3.052	3.026	3.038
3.0	0.0391	3.160	3.147	2.995	3.117	3.084	2.970	3.118	3.074	2.932	3.170	3.140	2.954	2.933	2.884	2.907
4.5	0.0587	3.195	3.176	2.975	3.139	3.094	2.943	3.139	3.080	2.892	3.205	3.164	2.919	2.889	2.825	2.855
6.0	0.0783	3.207	3.183	2.954	3.143	3.090	2.917	3.143	3.073	2.859	3.214	3.166	2.887	2.851	2.777	2.811
7.5	0.0978	3.195	3.167	2.927	3.128	3.071	2.888	3.127	3.052	2.827	3.198	3.145	2.853	2.814	2.737	2.771
9.0	0.1174	3.157	3.126	2.887	3.091	3.032	2.849	3.090	3.013	2.787	3.156	3.102	2.811	2.771	2.693	2.727
10.5	0.1370	3.105	3.074	2.843	3.043	2.984	2.806	3.041	2.965	2.746	3.103	3.048	2.767	2.728	2.652	2.684
12.0	0.1566	3.055	3.024	2.805	2.996	2.939	2.770	2.994	2.921	2.713	3.050	2.998	2.732	2.696	2.624	2.654
13.5	0.1761	3.018	2.988	2.785	2.964	2.911	2.753	2.961	2.893	2.700	3.013	2.964	2.718	2.686	2.620	2.647
15.0	0.1957	3.006	2.979	2.793	2.957	2.909	2.765	2.954	2.891	2.715	3.003	2.959	2.736	2.710	2.651	2.675
16.5	0.2153	3.028	3.006	2.837	2.984	2.942	2.814	2.981	2.926	2.767	3.030	2.991	2.793	2.776	2.726	2.747
18.0	0.2348	3.082	3.066	2.916	3.044	3.009	2.898	3.040	2.994	2.855	3.090	3.059	2.888	2.882	2.842	2.860
19.5	0.2544	3.183	3.174	3.046	3.150	3.125	3.033	3.147	3.111	2.995	3.201	3.179	3.040	3.048	3.020	3.035
21.0	0.2740	3.358	3.358	3.253	3.331	3.317	3.247	3.327	3.304	3.211	3.388	3.377	3.273	3.301	3.287	3.298
22.5	0.2935	3.516	3.524	3.437	3.496	3.490	3.436	3.490	3.475	3.402	3.555	3.552	3.477	3.525	3.522	3.527
24.0	0.3131	3.588	3.601	3.529	3.572	3.572	3.532	3.565	3.558	3.501	3.633	3.636	3.584	3.643	3.648	3.650
25.5	0.3327	3.654	3.675	3.621	3.642	3.653	3.629	3.637	3.641	3.602	3.710	3.722	3.695	3.762	3.779	3.782
27.0	0.3523	3.821	3.855	3.826	3.815	3.840	3.841	3.813	3.832	3.819	3.898	3.922	3.933	4.014	4.049	4.052
28.5	0.3718	4.150	4.204	4.206	4.152	4.199	4.233	4.154	4.196	4.217	4.258	4.302	4.365	4.472	4.534	4.536
30.0	0.3914	4.661	4.741	4.784	4.674	4.749	4.825	4.679	4.749	4.816	4.811	4.881	5.011	5.159	5.255	5.254

Table B.2 – *Hull B*; Total resistance coefficient for all bulb variants

Bulb variant		1	2	3	4	5	6	7	8	9	10	11	12	13	14	15
V_S/ knots	Fn	$C_{TS} \times 1000$														
0.4	0.0049	3.526	3.536	3.505	3.538	3.529	3.505	3.543	3.534	3.504	3.556	3.549	3.511	3.507	3.496	3.500
1.5	0.0195	3.181	3.225	3.107	3.226	3.195	3.104	3.242	3.208	3.095	3.286	3.262	3.114	3.092	3.049	3.068
3.0	0.0389	3.215	3.294	3.080	3.298	3.239	3.074	3.324	3.262	3.055	3.400	3.354	3.087	3.042	2.964	2.999
4.5	0.0584	3.286	3.386	3.107	3.393	3.315	3.098	3.427	3.343	3.072	3.519	3.457	3.109	3.049	2.946	2.991
6.0	0.0778	3.320	3.426	3.113	3.439	3.348	3.103	3.475	3.378	3.072	3.572	3.499	3.109	3.039	2.923	2.972
7.5	0.0973	3.310	3.415	3.090	3.433	3.335	3.080	3.468	3.364	3.048	3.562	3.483	3.080	3.005	2.885	2.934
9.0	0.1167	3.268	3.367	3.046	3.388	3.290	3.036	3.422	3.316	3.004	3.509	3.427	3.031	2.955	2.836	2.883
10.5	0.1362	3.210	3.300	2.993	3.324	3.227	2.983	3.355	3.252	2.952	3.433	3.353	2.974	2.900	2.786	2.830
12.0	0.1557	3.150	3.232	2.944	3.257	3.164	2.934	3.286	3.187	2.906	3.355	3.277	2.924	2.854	2.747	2.787
13.5	0.1751	3.104	3.178	2.911	3.202	3.115	2.902	3.229	3.137	2.877	3.290	3.218	2.892	2.829	2.731	2.767
15.0	0.1946	3.082	3.149	2.906	3.171	3.091	2.897	3.198	3.113	2.877	3.253	3.186	2.892	2.838	2.749	2.782
16.5	0.2140	3.093	3.156	2.937	3.174	3.102	2.928	3.201	3.127	2.914	3.252	3.192	2.931	2.889	2.812	2.840
18.0	0.2335	3.137	3.197	3.003	3.210	3.146	2.993	3.239	3.175	2.987	3.286	3.234	3.008	2.980	2.915	2.939
19.5	0.2529	3.227	3.288	3.120	3.292	3.238	3.108	3.324	3.274	3.114	3.371	3.329	3.141	3.130	3.080	3.100
21.0	0.2724	3.386	3.449	3.309	3.443	3.400	3.294	3.481	3.446	3.314	3.528	3.498	3.350	3.364	3.330	3.345
22.5	0.2919	3.531	3.594	3.476	3.579	3.544	3.458	3.622	3.598	3.490	3.668	3.646	3.533	3.570	3.549	3.557
24.0	0.3113	3.596	3.659	3.561	3.638	3.611	3.541	3.683	3.669	3.581	3.728	3.713	3.628	3.677	3.667	3.672
25.5	0.3308	3.659	3.726	3.649	3.696	3.679	3.629	3.745	3.744	3.677	3.792	3.787	3.732	3.791	3.794	3.798
27.0	0.3502	3.820	3.896	3.846	3.853	3.849	3.825	3.911	3.927	3.890	3.963	3.971	3.957	4.033	4.057	4.060
28.5	0.3697	4.137	4.228	4.215	4.164	4.179	4.189	4.237	4.279	4.280	4.299	4.326	4.369	4.476	4.527	4.527
30.0	0.3891	4.629	4.740	4.771	4.649	4.686	4.740	4.742	4.818	4.866	4.819	4.869	4.985	5.137	5.225	5.221

B.2 – Numerical resistance prediction

Table B.3 – Breakdown of coefficients of resistance and effective power for optimised hulls

	Hull A						*Hull B*					
V_S / knots	Fn	C_T	C_W	C_F	C_V	P_E / kW	Fn	C_T	C_W	C_F	C_V	P_E / kW
1.5	0.0196	3.050	0.169	2.074	2.464	3.4	0.0195	3.104	0.242	2.071	2.448	3.1
3.0	0.0391	2.932	0.281	1.881	2.235	26.3	0.0389	3.074	0.439	1.879	2.220	23.0
4.5	0.0587	2.892	0.361	1.781	2.115	87.6	0.0584	3.098	0.582	1.778	2.102	76.4
6.0	0.0783	2.859	0.406	1.714	2.036	205.3	0.0778	3.103	0.666	1.712	2.023	176.1
7.5	0.0978	2.827	0.433	1.665	1.977	396.5	0.0973	3.080	0.701	1.663	1.965	372.9
9.0	0.1174	2.787	0.439	1.626	1.932	675.6	0.1167	3.036	0.702	1.624	1.920	763.8
10.5	0.1370	2.746	0.435	1.595	1.894	1057.1	0.1362	2.983	0.687	1.593	1.882	1430.0
12.0	0.1566	2.713	0.434	1.568	1.862	1559.0	0.1557	2.934	0.669	1.566	1.851	2651.5
13.5	0.1761	2.700	0.448	1.545	1.835	2208.6	0.1751	2.902	0.664	1.543	1.824	3335.3
15.0	0.1957	2.715	0.487	1.525	1.811	3046.7	0.1946	2.897	0.683	1.523	1.800	5371.4
16.5	0.2153	2.767	0.561	1.507	1.790	4133.6	0.2140	2.928	0.734	1.505	1.779	8968.4
18.0	0.2348	2.855	0.667	1.491	1.771	5536.0	0.2335	2.993	0.818	1.489	1.760	10344.1
19.5	0.2544	2.995	0.824	1.477	1.754	7382.9	0.2529	3.108	0.950	1.475	1.743	14912.0
21.0	0.2740	3.211	1.056	1.463	1.738	9887.5	0.2724	3.294	1.152	1.462	1.727	15168.2
22.5	0.2935	3.402	1.262	1.451	1.724	12884.9	0.2919	3.458	1.331	1.449	1.713	19221.4
24.0	0.3131	3.501	1.374	1.440	1.710	16091.2	0.3113	3.541	1.427	1.438	1.700	23627.2
25.5	0.3327	3.602	1.487	1.429	1.698	19858.5	0.3308	3.629	1.527	1.428	1.687	27803.8
27.0	0.3523	3.819	1.716	1.420	1.686	24994.9	0.3502	3.825	1.734	1.418	1.676	37000.8
28.5	0.3718	4.217	2.125	1.411	1.675	32460.8	0.3697	4.189	2.110	1.409	1.665	54638.0
30.0	0.3914	4.816	2.734	1.402	1.665	43234.2	0.3891	4.740	2.671	1.400	1.655	80225.6

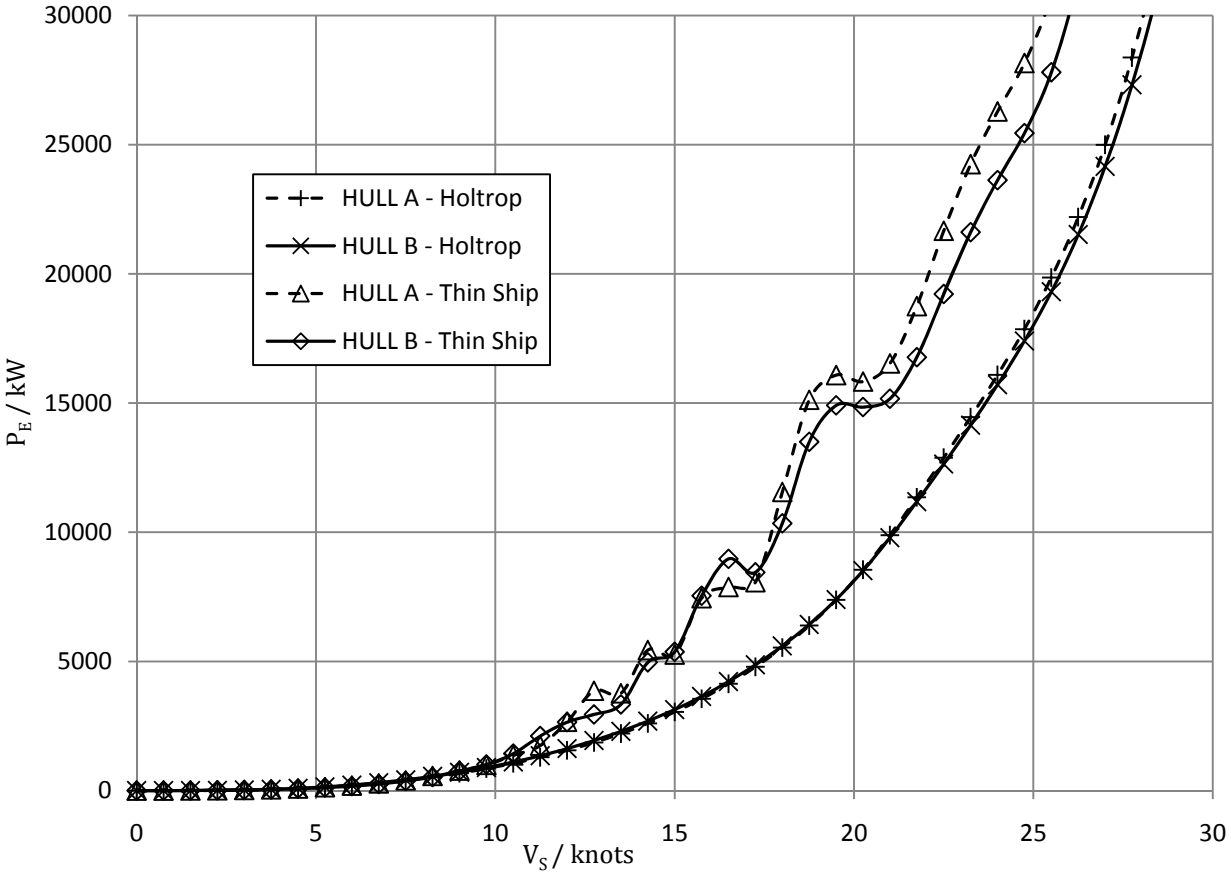

Figure B.1 – Comparison of results using Holtrop regression and Thin Ship Theory

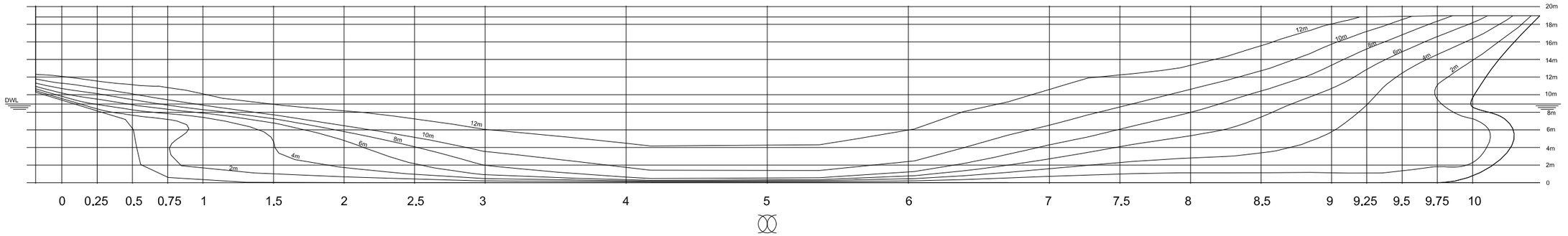

PROFILE

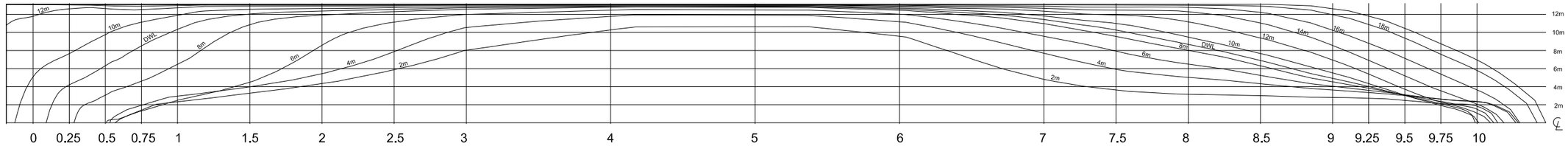

PLAN

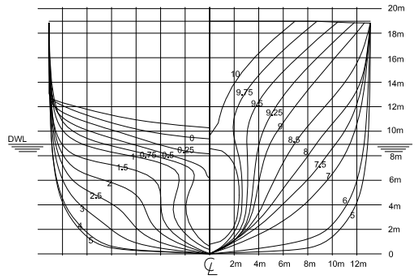

BODY PLAN

PRINCIPAL DIMENSIONS	
LOA	170.70m
LBP	160.09m
LWL	158.47m
BREADTH MOULDED	26.2m
DEPTH MOULDED	18.97m
DRAUGHT	8.94m
DISPLACEMENT	20466.05 tonnes
LCB	0.604m aft ST 5
LCF	5.833 aft ST 5
VCB	5.213m above keel

HULL A LINES PLAN

Designed by	Drawn by	Date	Scale
AB	AB	13/04/10	1:500
APPENDIX B3		Edition A	Sheet 1 of 1

UNIVERSITY OF Southampton
School of Engineering Sciences
University of Southampton
University Road
Highfield
Southampton
SO17 1BJ

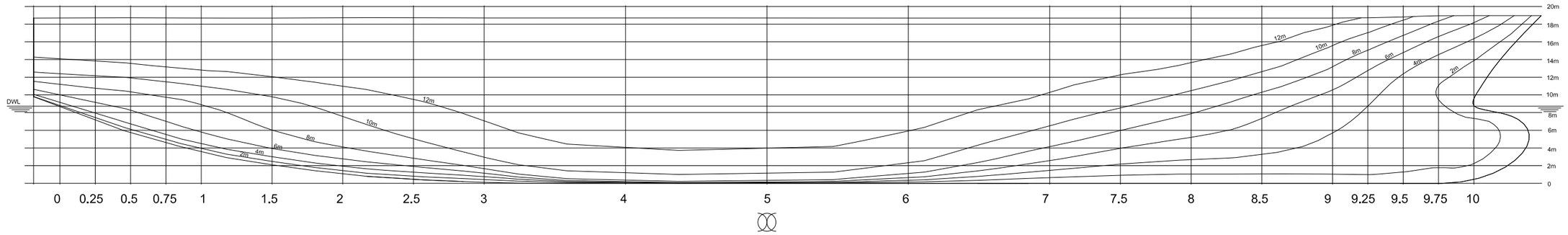

PROFILE

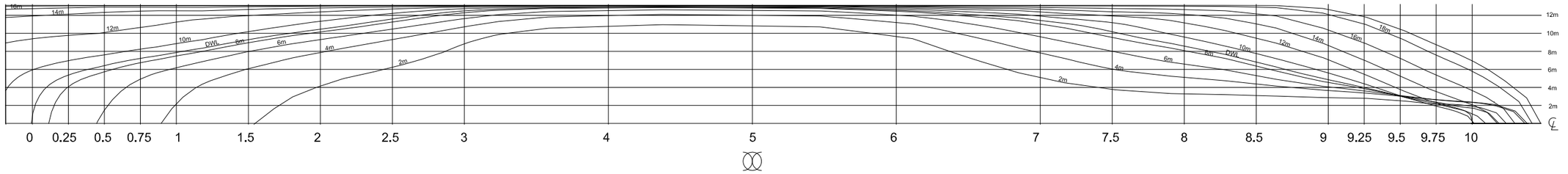

PLAN

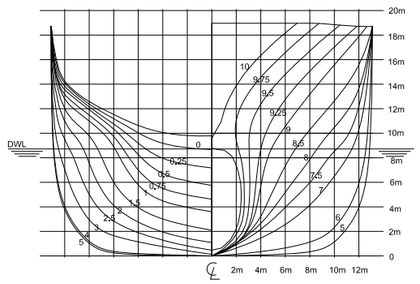

BODY PLAN

PRINCIPAL DIMENSIONS	
LOA	170.70m
LBP	160.09m
LWL	160.3m
BREADTH MOULDED	26.2m
DEPTH MOULDED	18.97m
DRAUGHT	8.72m
DISPLACEMENT	20344 tonnes
LCB	0.893m aft ST 5
LCF	4.214 aft ST 5
VCB	5.082m above keel

HULL B LINES PLAN

Designed by	Drawn by	Date	Scale
SM	AB	13/04/10	1:500
APPENDIX B4		Edition A	Sheet 1 of 1

UNIVERSITY OF Southampton
School of Engineering Sciences
University of Southampton
University Road
Highfield
Southampton
SO17 1BJ

Appendix C – Model Design, Manufacture and Testing Preparation

C.1 – Design

Depth Froude number calculation

Depth effects will become increasingly important as the depth Froude number, defined as

$$Fn_D = \frac{V_m}{\sqrt{gd}}, \tag{C.1}$$

approaches and exceeds a value of one. Assuming the critical value of Fn_D, the required model speed is $V_m = \sqrt{gd}$, which is equal to 4.26 ms^{-1}. Based on a Froude number scaling approach,

$$\frac{V_s}{V_m} = \sqrt{\Lambda} \tag{C.2}$$

and the corresponding scale factor is $\Lambda = 9.12$. This equates to a model L_{WL} of 17.38 metres for *Hull A*.

3-D model views

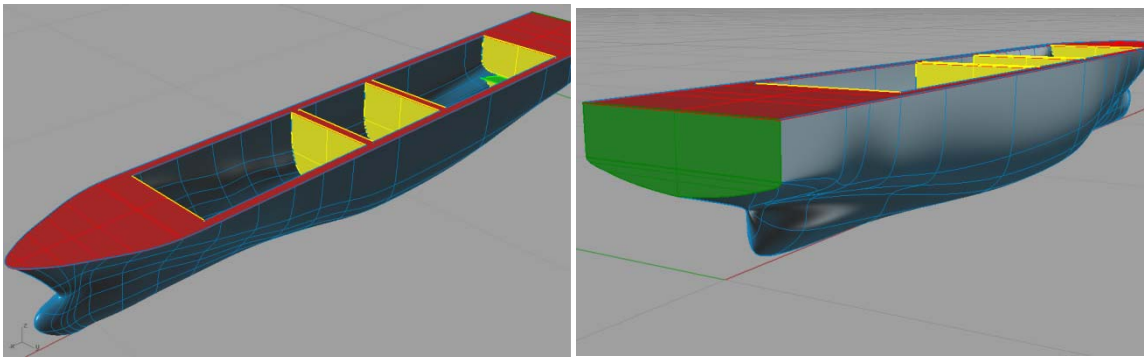

Figure C.1 – Views of *Hull A*: bulbous bow shape and internal detail (left); and stern shape (right)

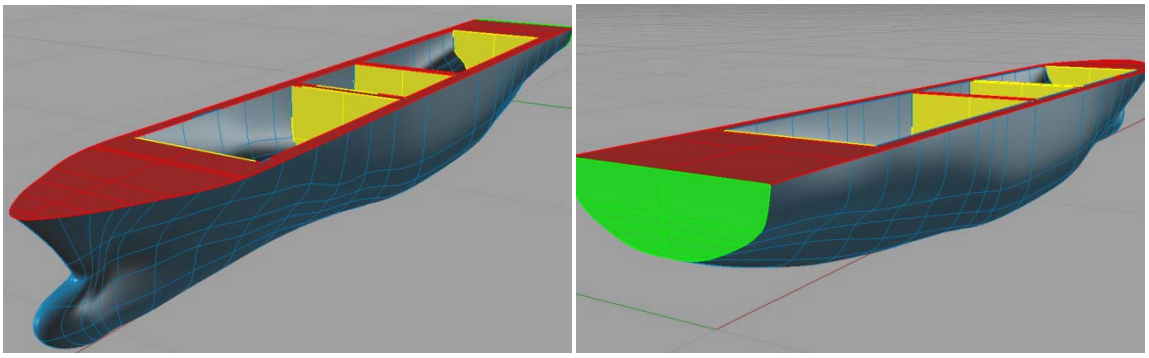

Figure C.2 – Views of *Hull B*: bulbous bow shape (left); and stern shape (right)

JIGSAW CONNECTOR

4 X JIGSAW PIECES CNC-MACHINED FROM 200 kg/m³ FOAM TO FIT CUT-OUTS IN MODEL PARTS.

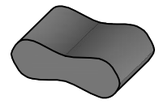

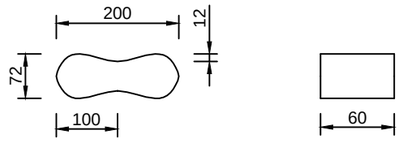

SCALE 1:5

HULL A MODEL

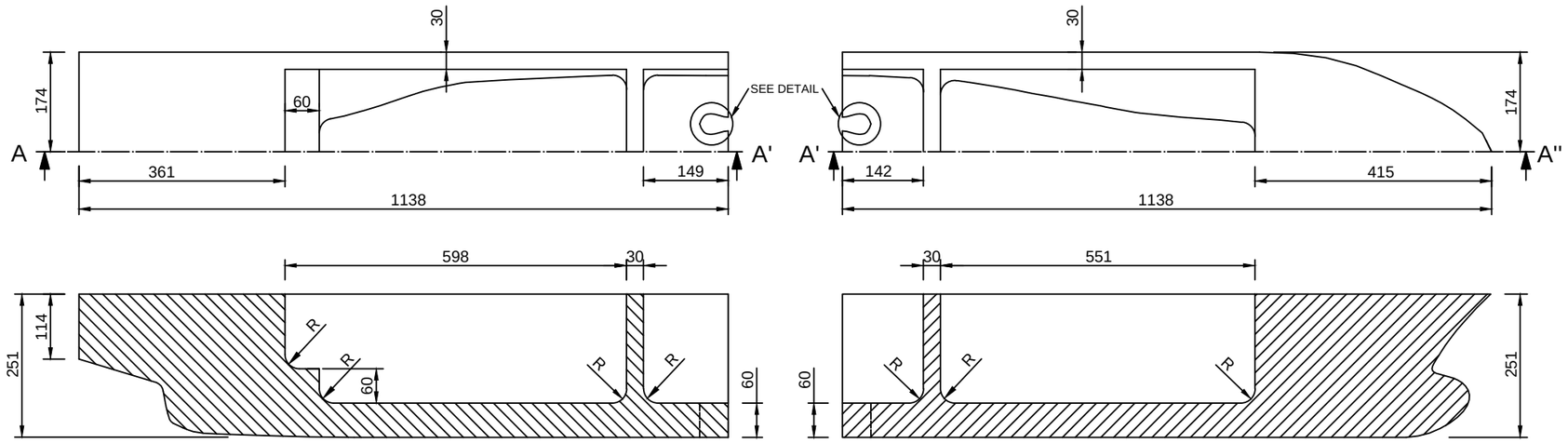

SECTIONS ON
A-A' & A'-A''

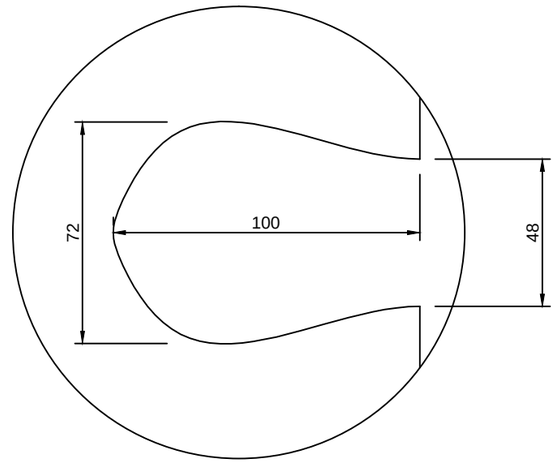

DETAIL
SCALE 1:2

HULL B MODEL

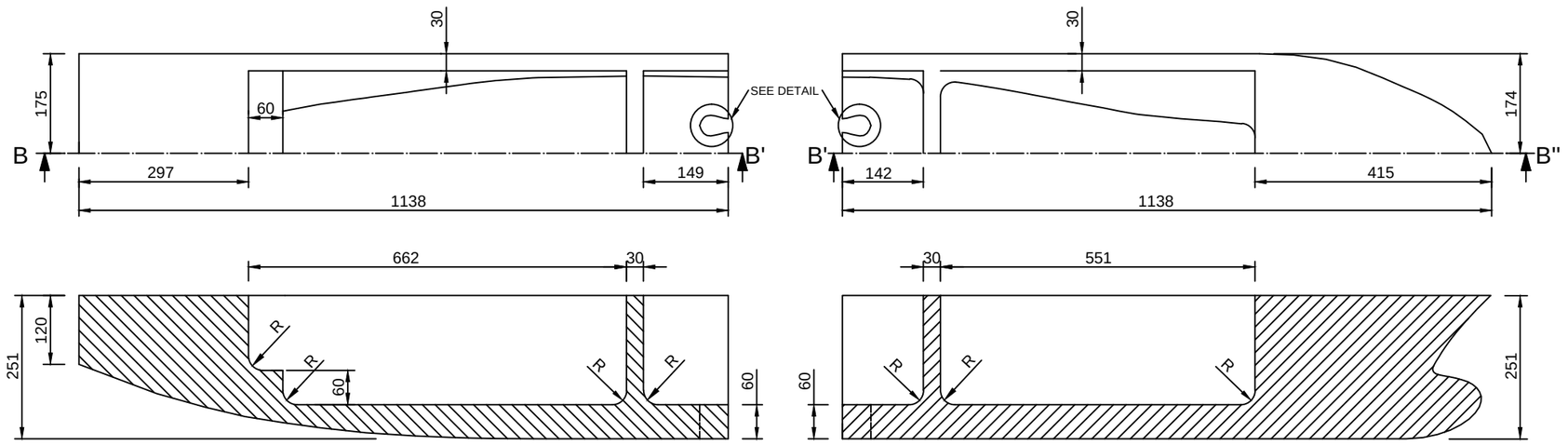

SECTIONS ON
B-B' & B'-B''

FORE AND AFT SECTIONS OF HULL MODELS TO BE CNC MACHINED WITH 'JIGSAW' DETAIL. SECTIONS TO BE ALIGNMENED WITH JIGSAW PIECES AND JOINED WITH SILICON ADHESIVE.

TOWING TANK MODEL PLANS

Designed by	Checked by	Date	Scale
SM	TL	19/04/10	1:10

Units	Materials		APPENDIX C.2	Edition	Sheet
mm	120 kg/m³ FOAM	200 kg/m³ FOAM	UNIVERSITY OF Southampton School of Engineering Sciences	A	1 of 1

University of Southampton
University Road
Highfield
Southampton
SO17 1BJ

C.3 – Manufacture

a)  b) 

c) 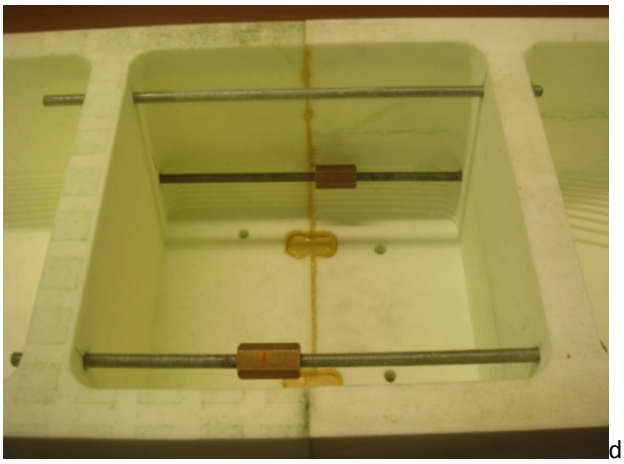 d) 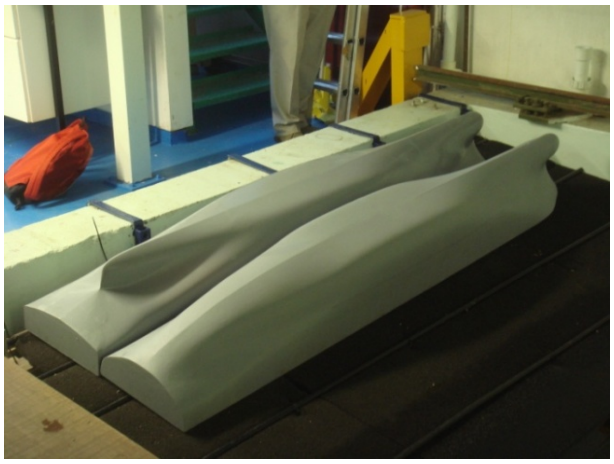

e) 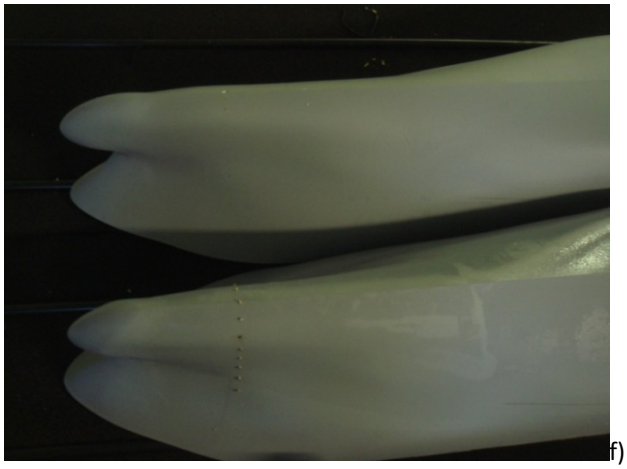 f) 

Figure C.3 – (a) *Hull A* stern section during milling; (b) *Hull A* at 'pre-finishing' stage; (c) Bulkheads and join of forward and aft model sections during gluing; (d) Comparison of stern forms of *Hulls A* and *B*; (e) Turbulence stimulator locations and fairing issues at intersection of bulb and hull; (f) Heel fitting and trimming moment rail attached to *Hull A*

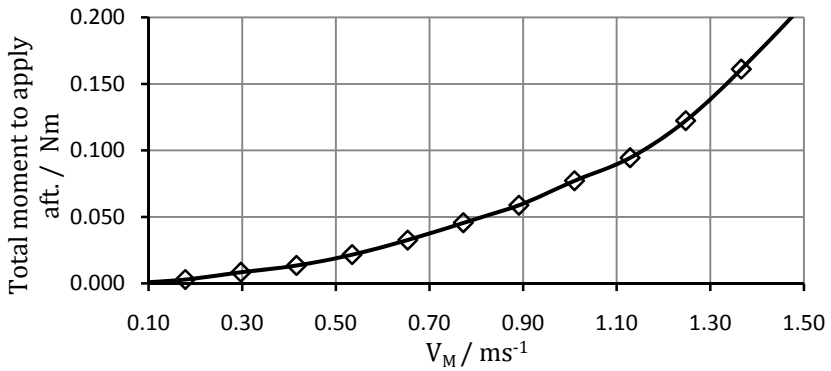

Figure C.4 – Total trim moment correction applied for range of model speeds tested

C.4 – Testing preparation

Table C.1 – Conservative estimate of possible tests during three days (total of 64 runs)

Day	*Time*	*Run description*	*No. of runs*	*No. of speeds*	*Waves?*
1	08:30-12:00	Calibration and ballasting	-	-	-
1	12:00-13:40	*Hull A*: Calm water	10	10	no
1	13:40-15:40	*Hull A*: Sailing condition, calm water	7	1	no
1	15:40-17:00	*Hull A*: Added resistance in waves	4	2	yes
2	08:30-09:00	Calibration check	-	-	-
2	09:00-11:00	*Hull A*: Added resistance in waves	8	2	yes
2	11:00-13:00	Change over	-	-	-
2	13:00-14:40	*Hull B*: Calm water	10	6	no
2	14:40-16:40	*Hull B*: Sailing condition, calm water	7	1	no
3	08:30-09:00	Calibration check	-	-	-
3	09:00-13:00	*Hull B*: Added resistance in waves	12	2	yes
3	13:00-14:00	*Hulls A/B*: Low speed (Prohaska) tests	6	3	no
3	14:00-17:00	Sailing condition at additional speed?			no

Table C.2 – Estimate of maximum required tests during three testing days (total of 80 runs)

Day	*Time*	*Run description*	*No. of runs*	*No. of speeds*	*Waves?*
1	08:30-12:00	Calibration and ballasting	-	-	-
1	12:00-13:10	*Hull A*: Calm water	10	10	no
1	13:10-16:40	*Hull A:* Sailing condition, calm water	15	1	no
1	16:40-17:00	*Hull A*: Low speed (Prohaska) tests	3	3	no
2	08:30-09:00	Calibration check	-	-	-
2	09:00-12:00	*Hull A*: Added resistance in waves	12	2	yes
2	12:00-14:00	Change over	-	-	-
2	14:00-15:10	*Hull B*: Calm water	10	10	no
2	15:10-17:00	*Hull B*: Sailing condition, calm water	11	2	no
3	08:30-09:00	Calibration check	-	-	-
3	09:00-09:40	*Hull B*: Sailing condition, calm water	4	2	no
3	09:40-12:40	*Hull B*: Added resistance in waves	12	2	yes
3	12:40-13:00	*Hull B*: Low speed (Prohaska) tests	3	3	no
3	13:00-17:00	Sailing condition at additional speed?	-	-	-

Appendix D – Towing Tank Results Processing

D.1 – Turbulence stimulation correction

The measured drag were corrected for the drag due to turbulence studs by means of the method outlined by Molland (1994), wherein a correction based on model boundary layer thickness in laminar and turbulent regions is applied to the measured drag to allow accurate scaling with the ITTC correlation line. Calculating the drag contribution for both flow regions as D_{lam} and D_{turb} respectively, the correction may be obtained as indicated in Equation (D.1), where D_{stud} is the frictional drag acting on the stimulation studs themselves and $D_{CF_{ITTC}}$the frictional drag according to the ITTC correlation line.

$$Drag\ correction\ =\ D_{CF_{ITTC}}\ -\ D_{stud} - D_{lam} - D_{turb} \tag{D.1}$$

Although in the yawed sailing condition tests the boundary layer thickness at the studs will clearly vary between the leeward and windward sides, it was assumed for the purposes of the correction that this effect was to an extent self-cancelling and that the upright resistance correction could be applied with relative confidence. The corrections obtained from the method are shown in Table D.1.

Table D.1 – Example drag correction calculations for both hulls

	V_M /ms^{-1}	R_{TM} / N	$D_{M,ITTC}$ / N	$D_{M,Lam}$ / N	$D_{M,Turb}$ / N	D_{stud} / N	*Correction*	
							/ N	/ %
Hull A	0.940	2.414	1.608	0.097	1.437	0.016	0.048	2.00
	1.515	6.758	3.796	0.199	3.386	0.057	0.131	1.94
Hull B	0.936	2.254	1.522	0.098	1.347	0.015	0.050	2.23
	1.510	5.981	3.599	0.201	3.180	0.055	0.136	2.28

Having obtained a positive correction, it was assumed that the transition to turbulent flow was in fact occurring forwards of the position considered. Retrospectively, it is thus possible to examine the effect of stud location on drag correction to be applied, (see Figure D.1).

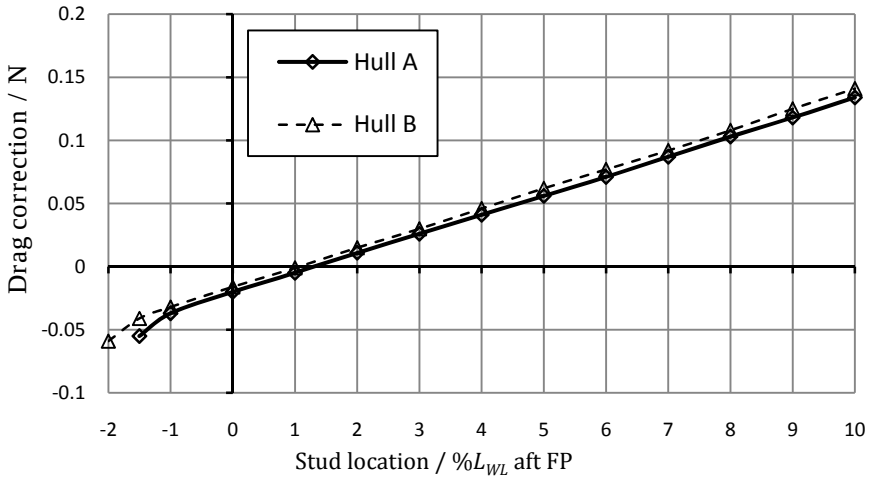

Figure D.1 – Variation in empirical drag correction with trip stud location

The slight difference between the two hulls is to be expected, due to the increased submerged length and differing surface area of *Hull B*. From this result it is proposed that a better representation of full scale flow around the hull might have been obtained from placing the trip studs further forwards, specifically within the length of the bulbous bow.

D.2 – Upright resistance

Table D.2 – *Hull A* effective power and resistance component breakdown

V_S / $knots$	Fn	$C_{TS} \times 1000$	$C_W \times 1000$	$C_{FS} \times 1000$	$C_{VS} \times 1000$	P_E / kW
5.07	0.066	4.370	1.934	1.717	1.966	192.73
6.22	0.081	3.397	1.027	1.671	1.914	277.05
7.15	0.093	2.841	0.516	1.642	1.880	350.49
10.14	0.132	2.352	0.141	1.570	1.798	828.13
11.32	0.148	2.685	0.512	1.549	1.774	1318.86
13.34	0.174	2.788	0.668	1.518	1.738	2235.42
13.45	0.175	2.840	0.723	1.516	1.736	2335.58
13.45	0.175	2.796	0.679	1.516	1.736	2299.61
13.90	0.181	2.993	0.887	1.510	1.729	2719.87
15.82	0.206	2.903	0.840	1.486	1.702	3886.61
15.91	0.208	3.038	0.978	1.485	1.701	4138.93
17.83	0.233	3.144	1.121	1.465	1.677	6024.36
17.91	0.234	3.083	1.062	1.464	1.676	5986.72
19.39	0.253	3.435	1.440	1.450	1.660	8463.05
21.22	0.277	3.317	1.352	1.434	1.642	10710.04
23.23	0.303	3.452	1.518	1.419	1.625	14625.44
25.50	0.333	3.661	1.758	1.403	1.607	20524.07

Table D.3 – *Hull B* effective power and resistance component breakdown

V_S / $knots$	Fn	$C_{TS} \times 1000$	$C_W \times 1000$	$C_{FS} \times 1000$	$C_{VS} \times 1000$	P_E / kW
6.26	0.081	3.297	0.929	1.669	1.911	256.76
7.26	0.094	2.545	0.225	1.637	1.875	309.34
7.26	0.094	2.330	0.010	1.637	1.875	283.56
10.20	0.132	2.333	0.125	1.568	1.796	786.89
11.44	0.148	2.231	0.060	1.546	1.770	1060.49
13.53	0.174	2.411	0.296	1.514	1.734	1895.32
15.85	0.204	2.540	0.478	1.485	1.700	3212.65
16.01	0.206	2.438	0.379	1.483	1.698	3174.35
17.95	0.232	2.765	0.744	1.462	1.675	5082.24
19.50	0.251	2.954	0.961	1.448	1.658	6957.38
21.37	0.276	2.844	0.881	1.432	1.640	8811.47
23.33	0.301	2.848	0.915	1.417	1.623	11481.95
25.57	0.330	2.921	1.019	1.402	1.605	15509.72

D.3 – Sailing condition

Table D.4 – Resistance breakdown in sailing condition

			Hull A					*Hull B*				
V_S / *knots*	Φ / *deg*	Ψ / *deg*	R_U / *N*	R_I / *N*	R_H / *N*	R_{TOT} / *N*	*SF* / *N*	R_U / *N*	R_I / *N*	R_H / *N*	R_{TOT} / *N*	*SF* / *N*
15.9	0	0	4.926E+05	0.000E+00	0.000E+00	4.926E+05	0.000E+00	3.750E+05	0.000E+00	0.000E+00	3.750E+05	0.000E+00
		2.5		4.822E+04		5.409E+05	4.505E+05		2.988E+04		4.049E+05	3.345E+05
		5		1.319E+05		6.245E+05	9.009E+05		1.219E+05		4.969E+05	6.691E+05
	2.5	0		0.000E+00	-8.368E+02	4.918E+05	7.618E+04		0.000E+00	3.929E+03	3.789E+05	6.005E+04
		2.5		3.169E+04		5.235E+05	3.707E+05		1.437E+04		3.933E+05	3.160E+05
		5		1.228E+05		6.146E+05	9.627E+05		9.998E+04		4.789E+05	6.831E+05
	5	0		0.000E+00	4.535E+02	4.931E+05	9.012E+04		0.000E+00	3.120E+03	3.781E+05	5.686E+04
		2.5		2.885E+04		5.219E+05	3.504E+05		2.031E+04		3.984E+05	2.943E+05
		5		1.062E+05		5.993E+05	9.171E+05		9.384E+04		4.719E+05	6.530E+05
25.5	0	0	1.531E+06	0.000E+00	0.000E+00	1.531E+06	0.000E+00	1.153E+06	0.000E+00	0.000E+00	1.153E+06	0.000E+00
		2.5		2.157E+05		1.746E+06	1.082E+06		1.312E+05		1.284E+06	1.333E+06
		5		6.294E+05		2.160E+06	2.163E+06		5.278E+05		1.681E+06	2.665E+06
	2.5	0		0.000E+00	1.657E+04	1.547E+06	1.483E+05		0.000E+00	-2.583E+03	1.150E+06	1.620E+05
		2.5		2.435E+05		1.791E+06	1.149E+06		1.208E+05		1.271E+06	1.295E+06
		5		7.772E+05		2.325E+06	2.731E+06		4.970E+05		1.647E+06	2.888E+06
	5	0		0.000E+00	5.412E+04	1.585E+06	2.461E+05		0.000E+00	2.183E+04	1.175E+06	1.790E+05
		2.5		2.186E+05		1.804E+06	1.333E+06		9.685E+04		1.272E+06	1.407E+06
		5		8.341E+05		2.419E+06	3.032E+06		4.341E+05		1.609E+06	2.868E+06

D.4 – Uncertainty analysis

Nomenclature

ITTC-based nomenclature pertinent to appendix, other parameters as per principal nomenclature.

B_{C_T}	Resistance co-efficient bias limit		$B_{\zeta x}$	Bias on x position	cm
B_{Mx}	Resistance mass bias	kg	P_{C_T}	Precision limit on resistance co-efficient	
B_{MX1}	Resistance calibration bias	kg	P_ζ	Precision limit on wave profile measurement	
B_{MX2}	Resistance curve fit bias	kg	t_w	Water temperature	^oC
B_{MX3}	Resistance load cell misalignment bias	kg	U_{C_T}	Uncertainty of resistance co-efficient	
B_{MX4}	Resistance towing force inclination bias	kg	θ_M	Sensitivity coefficient for resistance mass	m/Ns^2
B_S	Wetted surface area bias	m^2	θ_S	Sensitivity coefficient for wetted surface area	m^{-2}
B_{s1}	Assumed error in hull form bias	m^2	θ_V	Sensitivity coefficient for speed	$1/ms^{-1}$
B_{s2}	Error in displacement bias	m^2	θ_X	Sensitivity coefficient for x position	cm^{-1}
B_{tw}	Water temperature bias	^oC	θ_ρ	Sensitivity coefficient for water density	m^3kg^{-1}
B_ρ	Bias on water density	kgm^{-3}	$\theta_{\rho tw\rho}$	Sensitivity coefficient for water temperature	$^oC^{-1}$
B_ζ	Bias on wave profile measurement	cm	θ_ζ	Sensitivity coefficient on wave amplitude	cm^{-1}
$B_{\zeta 1}$	Bias on scale placement	cm	ζ	Measured wave amplitude	cm
$B_{\zeta 2}$	Bias on marker placement	cm	$\zeta_{1/3}$	Significant wave amplitude	cm
$B_{\zeta 3}$	Bias on marker reapplication	cm	σ_{C_T}	Standard deviation of resistance co-efficient measurement	
$B_{\zeta 4}$	Bias on wave elevation reading	cm	σ_ζ	Standard deviation of wave profile measurement	

Resistance tests uncertainty estimation

The total uncertainty is a combination of the precision limit (P_{C_T}) and the bias limit (B_{C_T}) i.e.

$$\left(U_{C_T}\right)^2 = \left(B_{C_T}\right)^2 + \left(P_{C_T}\right)^2 \tag{D.2}$$

where,

$$\left(B_{C_T}\right)^2 = (\theta_S B_s)^2 + (\theta_V B_V)^2 + (\theta_{Mx} B_{Mx})^2 + \left(\theta_\rho (B_\rho + \theta_{\rho tw\rho} B_{tw})\right)^2 \text{ and } P_{C_T} = \frac{K\sigma_{C_T}}{\sqrt{M_r}}. \tag{D.3}$$

The bias limit is the sum of errors from speed variation (B_V), resistance mass (B_{Mx}) and water properties (B_ρ) (B_{tw}) and wetted surface area variation (B_S) which includes error in hull form and error in displacement i.e.

$$(B_s)^2 = \left({B_{s1}}^2 + {B_{s2}}^2\right). \tag{D.4}$$

The resistance mass bias limit includes effect of calibration (B_{MX1}), curve fit bias (B_{MX2}), load cell misalignment (B_{MX3}) and tow force inclination (B_{MX4}) i.e.

$${B_{Mx}}^2 = {B_{Mx1}}^2 + {B_{Mx2}}^2 + {B_{Mx3}}^2 + {B_{Mx4}}^2. \tag{D.5}$$

The θ's are sensitivity coefficients obtained from the differential of the total resistance coefficient, C_T, with respect to required parameter i.e.

$$\theta_V = \frac{\partial C_T}{\partial V} = \frac{R_T}{0.5\rho S}\left(-\frac{2}{V^3}\right), \qquad \theta_M = \frac{\partial C_T}{\partial (R/g)} = \frac{g}{0.5\rho V^2 S},$$

$$\theta_S = \frac{\partial C_T}{\partial S} = \frac{R_T}{0.5\rho V^2}\left(-\frac{1}{s^2}\right), \qquad \theta_\rho = \frac{\partial C_T}{\partial \rho} = \frac{R_T}{0.5\rho V^2}\left(-\frac{1}{\rho^2}\right),$$

and

$$\theta_{\rho t w \rho} = \frac{\partial \rho}{\partial t_w}(t_w = 15°\mathrm{C}) = |0.0638 - 0.017 t_w + 0.0001897 {t_w}^2| \,. \tag{D.6}$$

Within the precision limit equation, σ is standard deviation on C_T, K is coverage factor which controls the level of confidence in the result and M_r is number of runs. In this analysis the coverage factor was chosen to yield a 90% confidence level in the results ($K = 1.645$).

Uncertainty results – resistance tests

The following figures contain experimental results for resistance, side force and yaw moment with appropriate error bars.

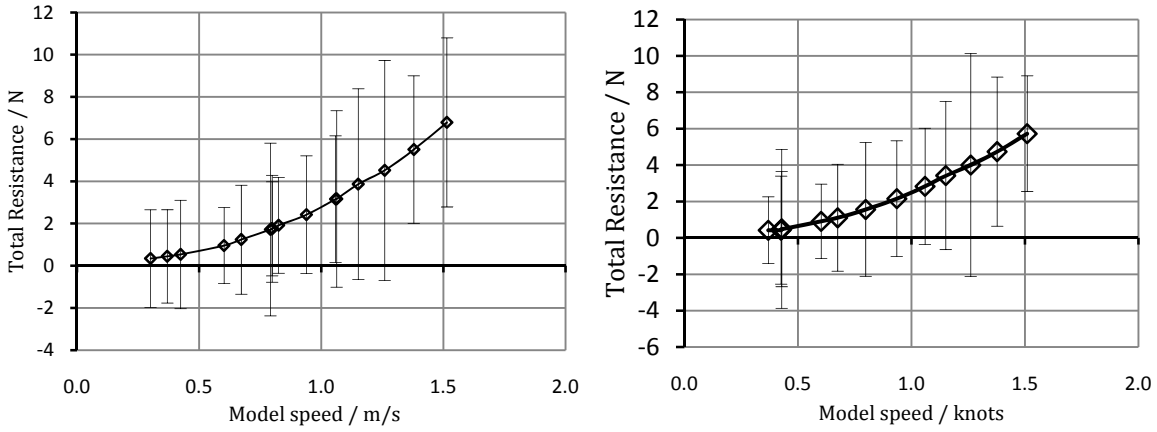

Figure D.2 – Resistance estimates of *Hull A* and *Hull B* with error bars

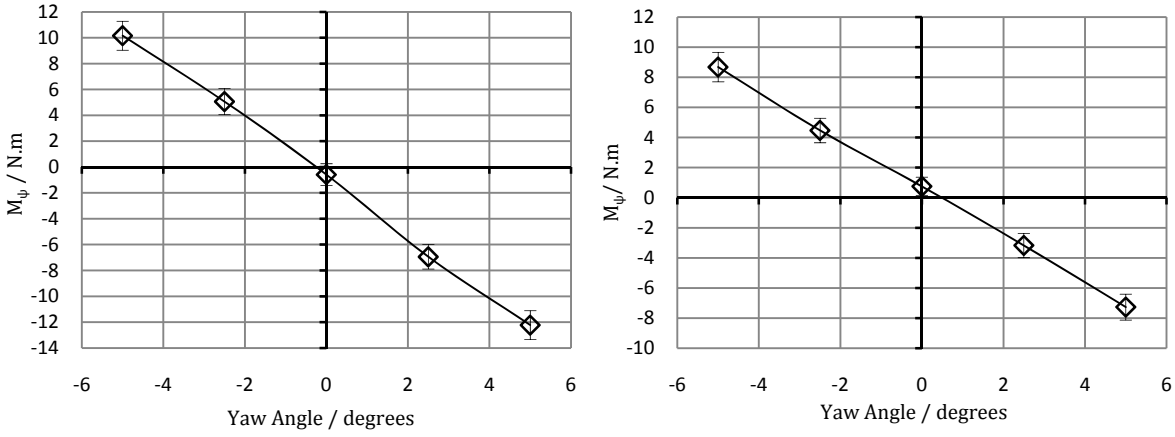

Figure D.3 – Yaw moment variation with yaw angle of *Hull A* and *Hull B* with error bars

Table D.5 – Summary of uncertainty in total resistance and side force measurements for tests in sailing condition

V_S /	Φ /	Ψ /	*Hull A*				*Hull B*			
knots	*deg*	*deg*	R_T / N	*Error / N*	*SF / N*	*Error / N*	R_T / N	*Error / N*	*SF / N*	*Error / N*
15.9	0	0	2.488	4.355	0.020	5.129	2.157	3.495	-0.171	4.682
		2.5	2.628	4.726	0.750	4.752	2.227	3.098	0.523	2.848
		5	2.827	3.406	2.155	4.432	2.445	2.274	1.414	2.850
	2.5	0	2.485	3.453	0.090	4.922	2.188	2.560	-0.048	2.863
		2.5	2.585	4.143	0.788	4.235	2.208	2.382	0.559	2.746
		5	2.801	3.476	2.191	4.502	2.411	2.403	1.429	2.929
	5	0	2.493	2.805	0.129	4.504	2.184	3.136	-0.047	4.158
		2.5	2.586	3.454	0.746	5.834	2.232	3.312	0.516	4.415
		5	2.770	3.852	2.089	4.106	2.407	2.829	1.366	4.416
25.5	0	0	8.054	3.418	-4.700	4.260	5.725	3.178	-0.525	4.498
		2.5	7.172	3.778	-1.553	5.121	5.953	3.945	2.290	3.446
		5	6.790	4.006	0.486	3.457	6.805	3.416	5.848	4.152
	2.5	0	7.625	3.756	2.551	3.546	5.716	5.206	-0.200	6.151
		2.5	8.704	3.609	6.069	3.041	6.037	3.504	2.485	6.586
		5	6.913	4.434	0.790	3.071	6.928	3.519	6.262	5.083
	5	0	7.686	3.840	3.161	2.255	5.855	3.033	-0.152	5.701
		2.5	8.951	3.774	6.912	2.562	6.067	3.486	2.759	7.110
		5	7.082	3.418	0.600	2.861	6.867	3.149	6.222	8.793

Wave probe uncertainty estimation

The uncertainty in wave profile measurement can be expressed as the sum of the precision and bias limits, i.e.

$$U_\zeta{}^2 = B_{\zeta P}{}^2 + P_\zeta{}^2 \tag{D.7}$$

where

$$B_{\zeta P}{}^2 = (B_\zeta \theta_\zeta)^2 + (B_x \theta_x)^2 \text{ and } P_\zeta = \frac{K\sigma_\zeta}{\sqrt{M_r}}. \tag{D.8}$$

The bias limit on the wave profile, B_ζ, consists of bias limits from scale placement ($B_{\zeta 1}$), marker placement ($B_{\zeta 2}$), mark reapplication ($B_{\zeta 3}$), wave elevation reading ($B_{\zeta 4}$) and longitudinal position in the tank (x) bias ($B_{\zeta x}$) i.e.

$$B_\zeta{}^2 = B_{\zeta_1}{}^2 + B_{\zeta_2}{}^2 + B_{\zeta_3}{}^2 + B_{\zeta_4}{}^2. \tag{D.9}$$

The sensitivity coefficients on wave profile and x position are

$$\theta_\zeta = \frac{\partial \zeta_P}{\partial z} = \frac{1}{L} \quad \text{and} \quad \theta_X = \frac{1}{L}\frac{\partial z}{\partial x}. \tag{D.10}$$

Typical error bars on a wave profile trace are given in Figure D.4.

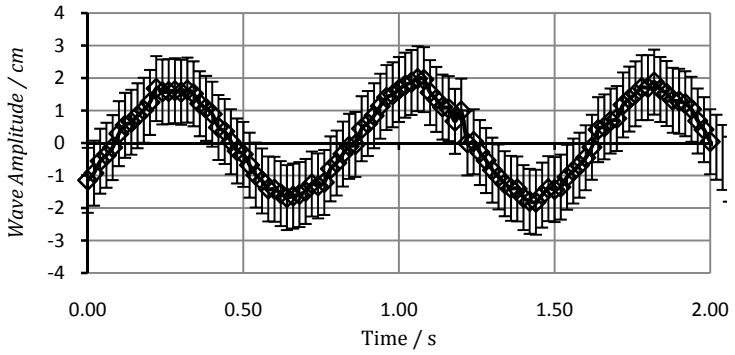

Figure D.4 – Error bars on wave profile measurements

The frequency spectrums for the added resistance test runs are given in the Figure D.5 and Figure D.6

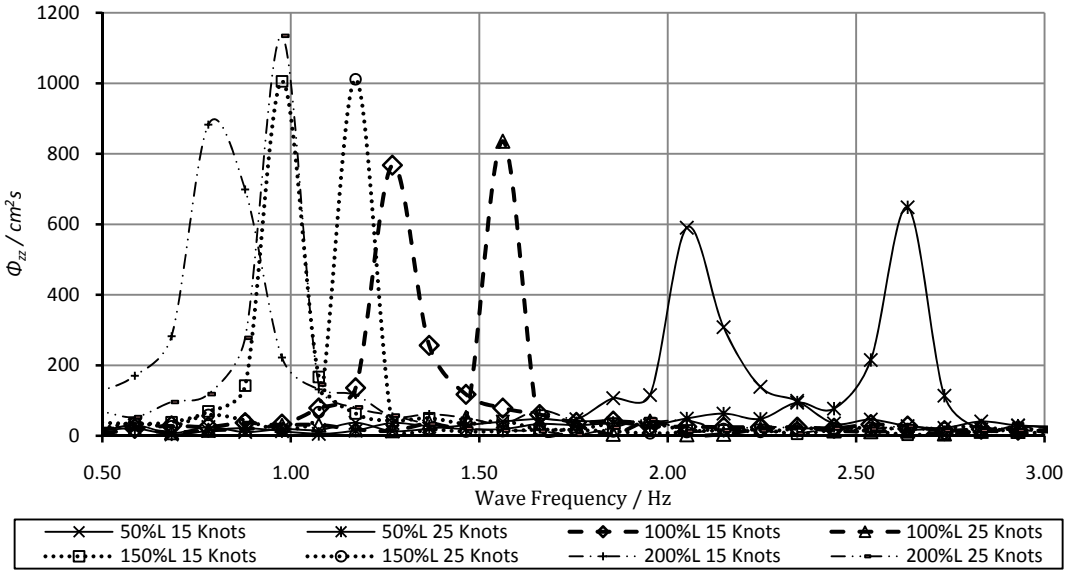

Figure D.5 – Frequency spectrums for Hull A added resistance tests

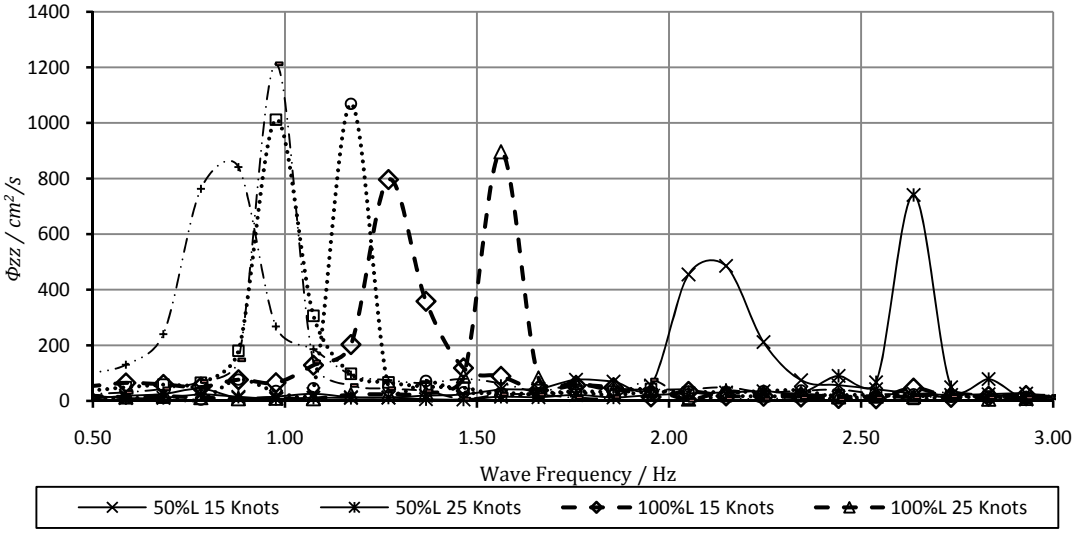

Figure D.6 – Frequency spectrums for *Hull B* added resistance tests

Appendix E – Sail Design

E.1 – Concept review

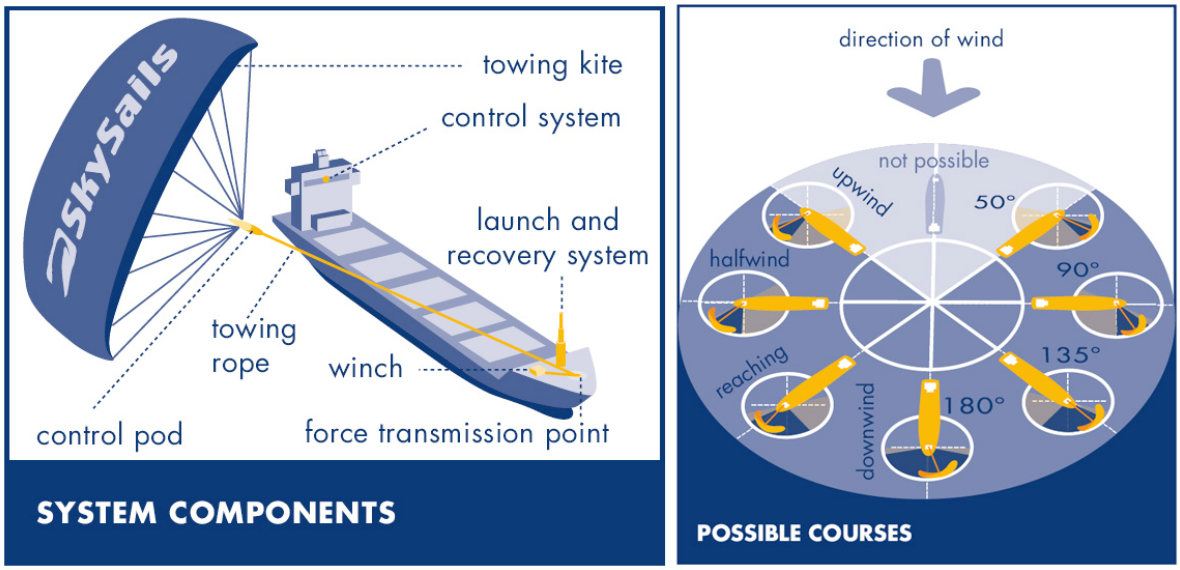

Figure E.1 – SkySails System[18]

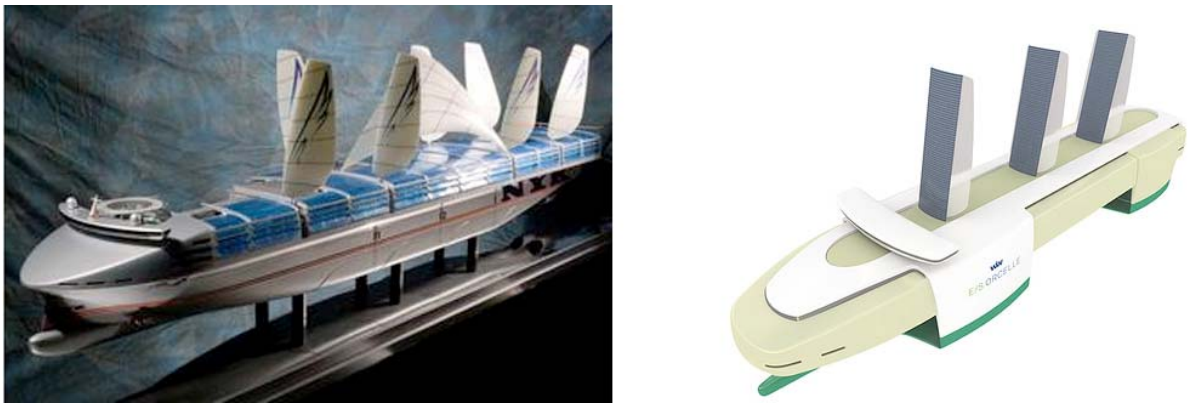

Figure E.2 – NYK Super Eco Ship 2030 (left) and E/S Orcelle (right)[19] concepts

[18] Picture obtained from: http://www.skysails.info/fileadmin/user_upload/documents/Dokumente/SKS_Broschueren/EN/EN_Technology_Information.pdf, accessed 15/04/2010.

[19] Pictures obtained from: NYK Super Eco Ship 2030 - http://www.nyk.com/english/release/31/NE_090422.html, accessed 15/04/2010; E/S Orcelle - http://www.ecofriend.org/entry/esorcelle-cargo-ship-gets-its-juice-from-sun-wind-and-water/, accessed 15/04/2010.

E.2 – Design

Sail area estimation

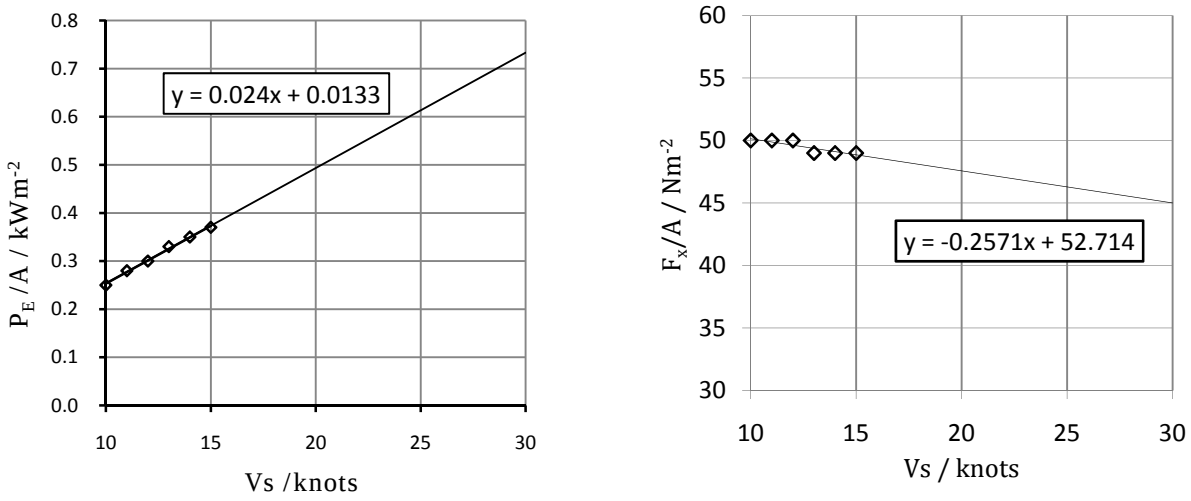

Figure E.3 – Extrapolation of data for *Wingsail*: effective power (left); and average propulsive force (right) at an average wind speed of 15 knots

Structural Design

Table E.1 – Sail mast dimensions

Dimensions (Deck to base)	
Inner radius / m	0.5
Outer radius / m	0.7
Section area / m^2	1.26
Second moment of Area / m^4	0.14
Deck to system base / m	11
Weight /kg	36907

Lift force is calculated using the following equation:

$$L = \frac{1}{2}\rho A V^2 C_L \quad \text{(E.1)}$$

The moment lever is the distance from deck to sail rig system base, ten metres.

Table E.2 – Mast bending moment, deflection and maximum stress using driving force estimation

Vs / knots	*Max. bending moment / Nm*	*Max. stress / Nm^{-2}*	*Max. deflection/ m*	*% Max / Yield stress*
5	334074.40	1676518.69	1.36E-03	1.20
10	252222.49	1265753.10	1.03E-03	0.90
15	249444.70	1251813.04	1.02E-03	0.89
20	249629.80	1252741.98	1.02E-03	0.89
25	240656.89	1207712.34	9.80E-04	0.86
30	225429.05	1131292.97	9.18E-04	0.81

* Maximum deflection $\delta_{max} = WL^3/3EI$

E.3 – Theoretical performance

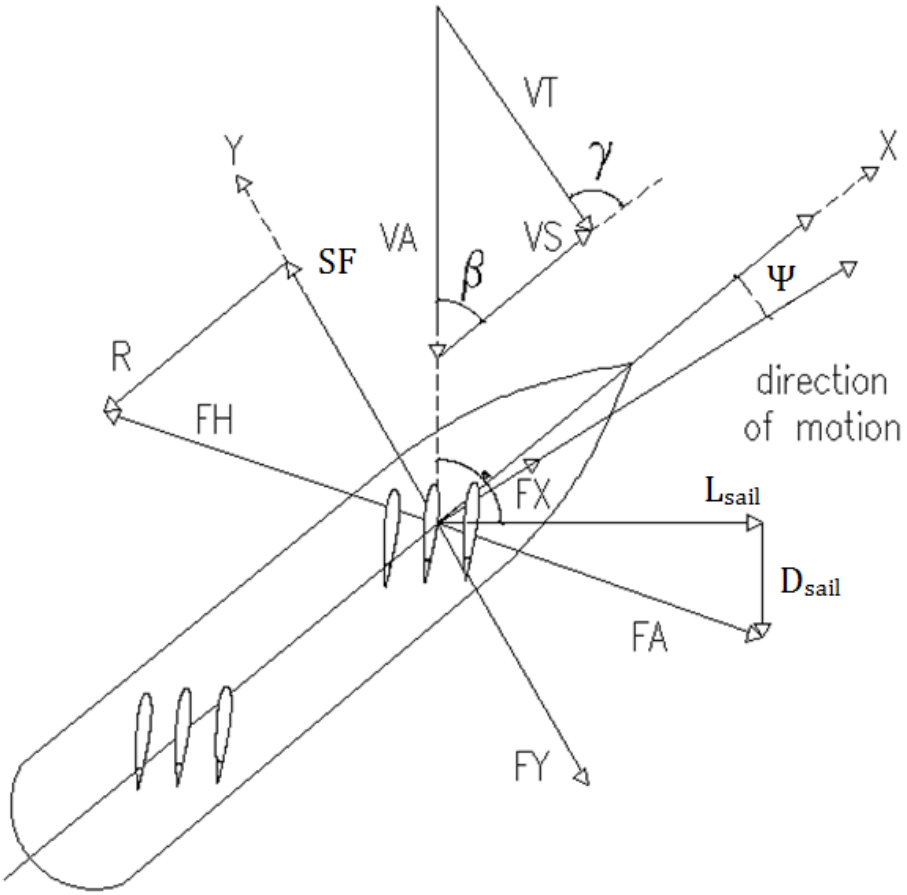

Figure E.4 – Forces acting on sail-assisted ship [Satchwell (1989)]

Nomenclature

Nomenclature pertinent to appendix, all other parameters defined in principal nomenclature

D_{sail}	Sail drag	N	F_X	Sail thrust	N
C_X	Drive coefficent ship axis)		F_Y	Aerodynamic side force	N
C_Y	Heeling coefficent (ship axis)		L_{sail}	Sail lift	N
F_A	Total aerodynamic force	N	γ	True wind angle	deg
F_H	Total hydrodynamic force	N			

$$\beta = \tan^{-1}\left({sin\gamma}/{cos\gamma + V_S/V_T}\right) \quad \text{(E.2)}$$

$$V_A = \frac{sin\gamma}{sin\beta} V_T \quad \text{(E.3)}$$

$$C_D = \frac{{C_L}^2}{\pi AR} + 0.005\ {C_L}^4 + C_{D0} \quad \text{(E.4)}$$

$$C_X = \ C_L sin\beta - C_D\ cos\beta\ ; C_Y = \ C_L cos\beta + C_D sins\beta \quad \text{(E.5)}$$

$$F_X = \frac{1}{2} C_X \rho {V_A}^2 A \; ; \; F_Y = \frac{1}{2} C_Y \rho {V_A}^2 A \tag{E.6}$$

Formula from Schenzle (1985) are used to estimate sideforce, rearranged for leeway. The values $k_1 = 2$ and $k_2 = 0.25$ are constants selected for hulls with fixed rudder and operating propeller to account for an offset in lift.

$$SF = k_1 S {V_S}^2 T^2 \Psi \left(1 + \frac{k_2}{k_1} \cdot \frac{L}{T} |\Psi|\right) \tag{E.7}$$

The angle of heel is estimated by rearranging the following equation:

$$M_H - GM_T gm \sin\Phi = 0 \tag{E.8}$$

E.4 – Wind statistics

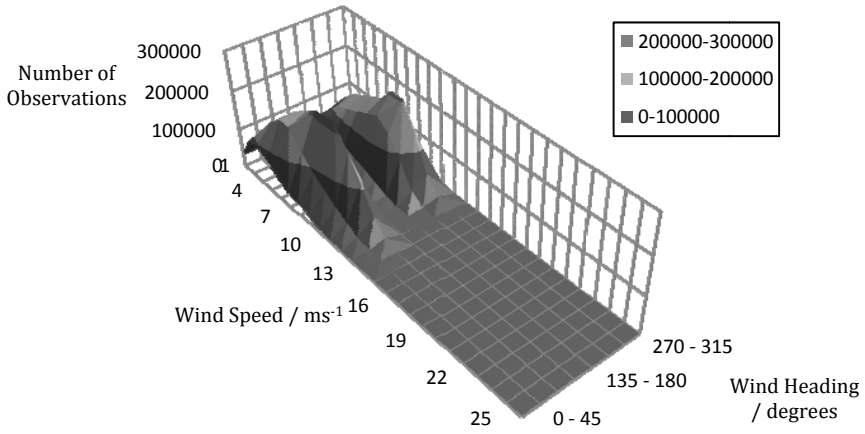

Figure E.5 – Wind by strength and direction for the whole world (annual)

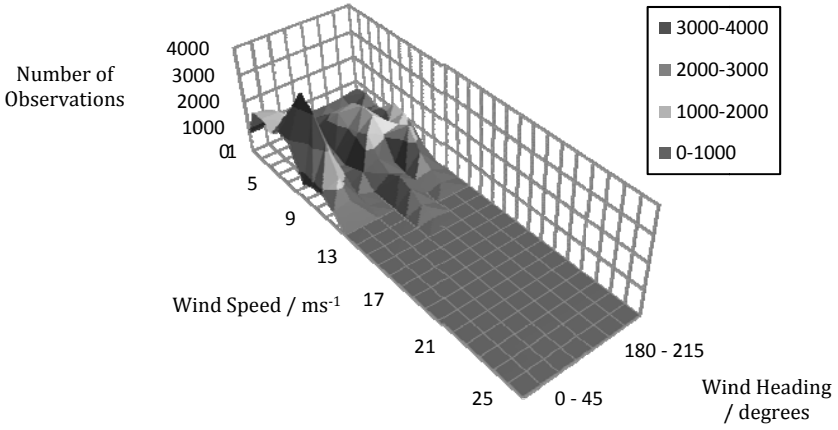

Figure E.6– Wind by strength and direction for South East Asia (annual)

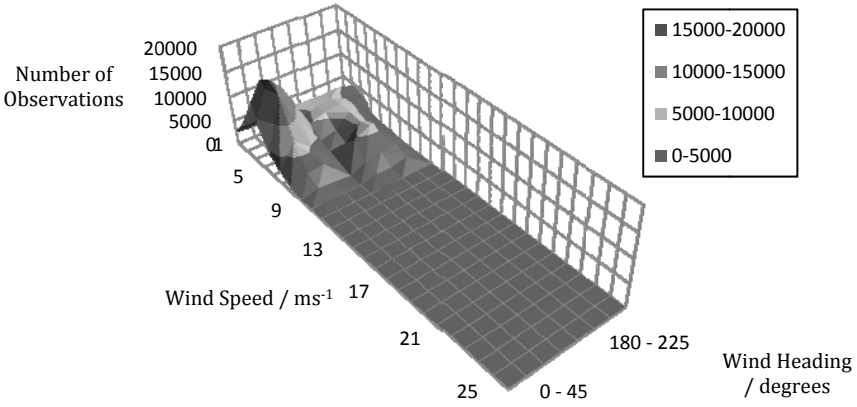

Figure E.7– Wind by strength and direction for the North Atlantic (annual)

Appendix F – Wind Tunnel

F.1 – Design and manufacture

Table F.1 – Estimation of maximum force experienced by individual wind tunnel dynamometer

Wind speed/ ms^{-1}	*Max. Side force / N*	*Moment / Nm*	*Vertical force due to Moment / N*	*Weight / kg*	*Vertical force due to weight / N*	*Maximum resultant force / N*
5	68.45	91.38	261.09	23.43	76.62	337.70
6	98.57	131.59	375.97	23.43	76.62	452.58
7	134.16	179.11	511.73	23.43	76.62	588.35
8	175.23	233.93	668.39	23.43	76.62	745.00
9	221.78	296.07	845.93	23.43	76.62	922.54

Wind tunnel model structural analysis

The mast is assumed to be a fixed – free end beam with a point load. Thus $\delta_{max} = WL^3/3EI$ (where δ_{max} is maximum deflection, W is point load, L_M is mast length and I is the second moment of area of the mast) and $M_{max} = WL$ (where M_{max} is the maximum bending moment). The sail wing stocks are modelled as fixed - fixed end beam with evenly distributed load. Thus: $\delta_{max} = wL^4/384EI$ (where w is a uniformly distributed load) and $M_{max} = wL^2/12$.

Table F.2 – Stock bending moment, deflection and maximum stress for wind tunnel model

Component	*Sail area / m^2*	*Force / Nm^{-1}*	*Max. bending moment / Nm*	*Max. stress / MNm^{-2}*	*Max. deflection / m*	*Yield Stress / MNm^{-2}*	*% Max /Yield Stress*
Stock A (Main)	0.6972	44.2671	10.2880	5.4570	0.00042	285.0	1.9148
Stock B (Flap)	0.1394	8.8534	2.0576	97.0307	0.03970	285.0	34.0459

Table F.3 – Mast structure calculation for wind tunnel model

Shear force / N	Bending moment / Nm	Weight above mast / kg	Vertical force / N	Max. bending stress / MNm^{-2}	Max. deflection / m	Max. normal stress / MNm^{-2}	Max resultant stress / MNm^{-2}	Yield stress / MNm^{-2}	% Max. yield stress
222	110	14	138	3.2	9.47E-05	0.063	3.3	285	1.15

Manufacture

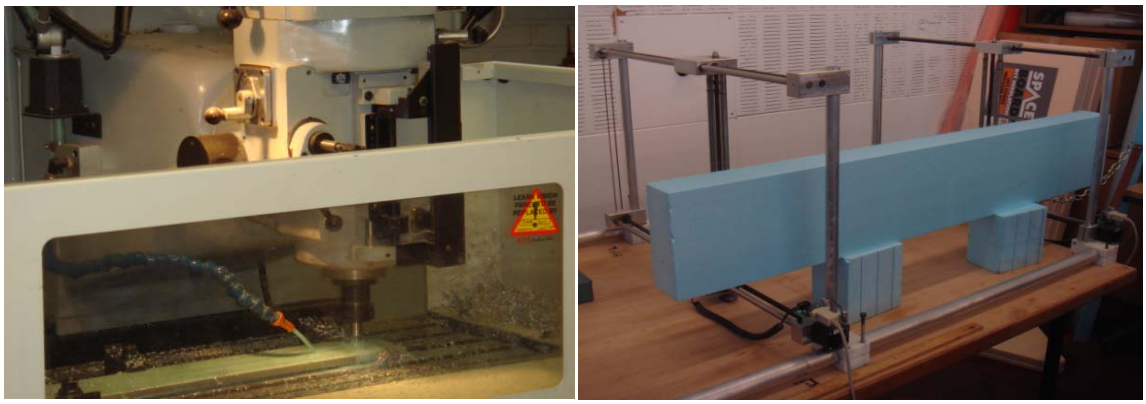

Figure F.1 – CNC milling machine (left); and hot wire cutter (right)

Figure F.2 – Model manufacture: wing with stock (left); and base (right)

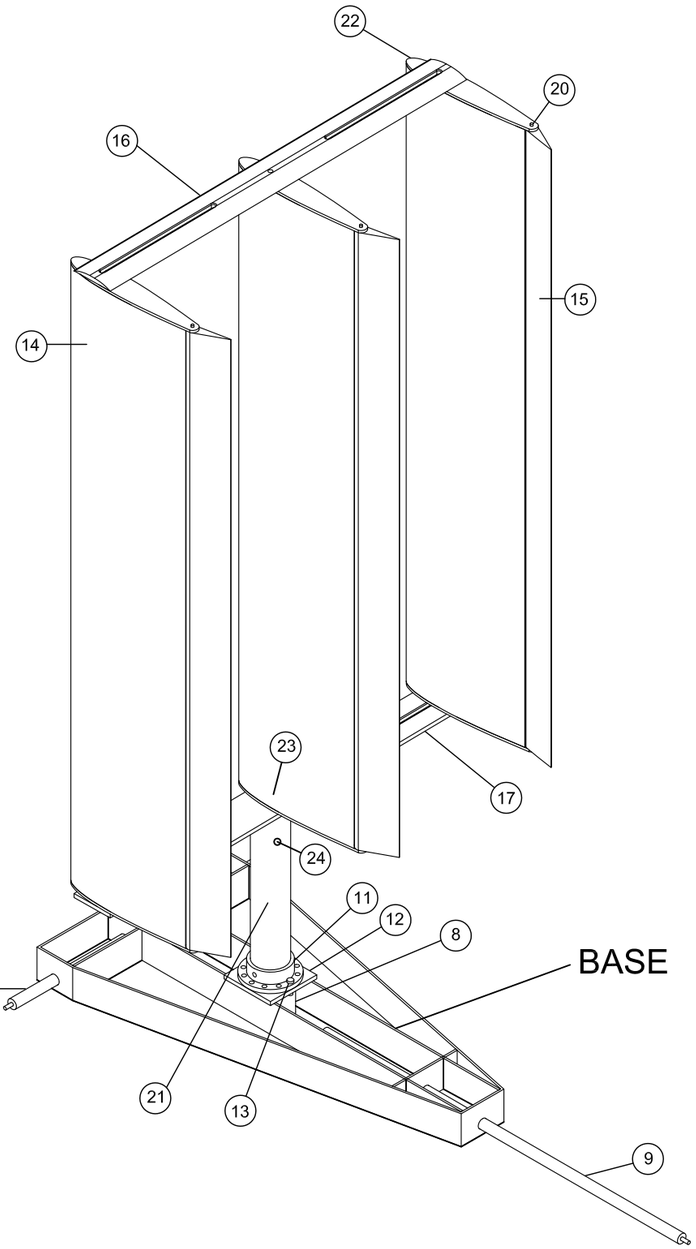

ASSEMBLY PERSPECTIVE VIEW

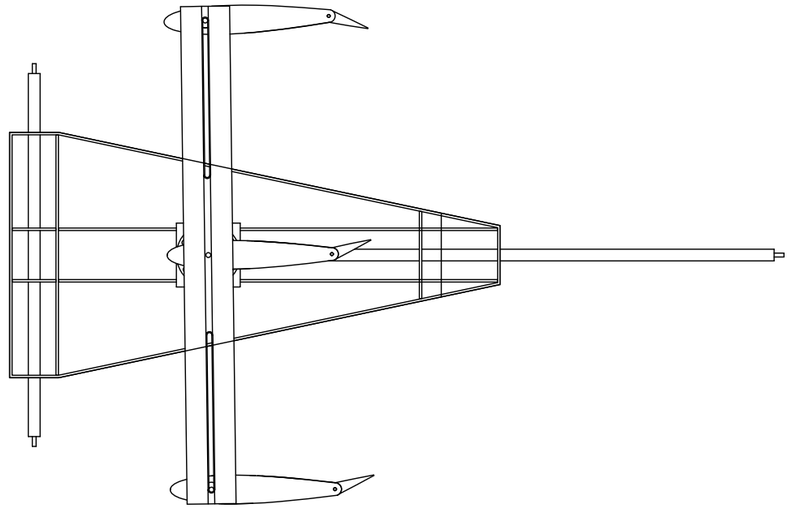

ASSEMBLY TOP VIEW

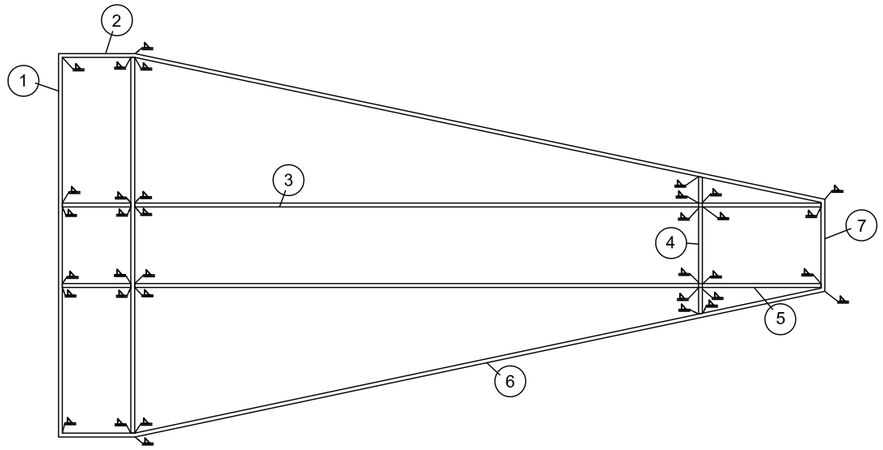

BASE ASSEMBLY TOP VIEW

MODEL ASSEMBLY DRAWING

Designed by	Checked by	Date	Scale
LM - IBS - BS	Mike Street	20/04/10	N/A
Appendix F2		Edition A	Sheet 1 of 3

UNIVERSITY OF Southampton
School of Engineering Sciences

University of Southampton
University Road
Highfield
Southampton
SO17 1BJ

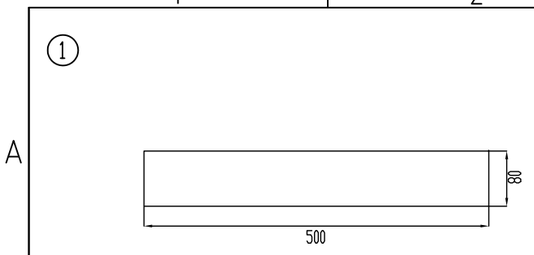

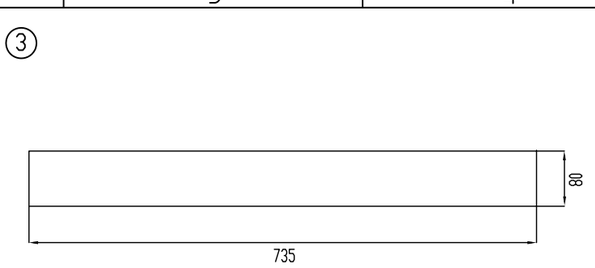

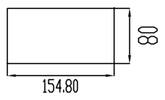

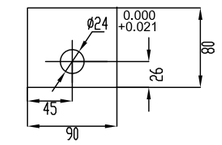

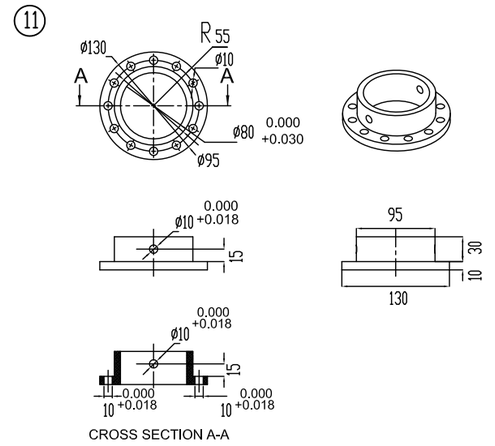

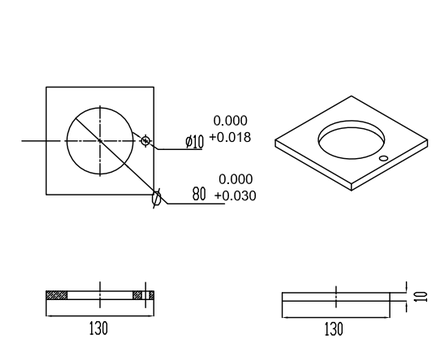

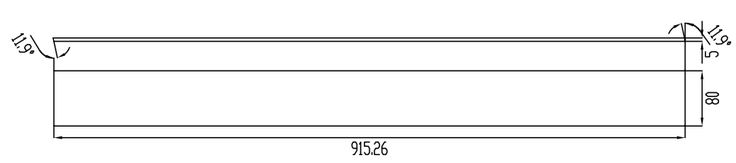

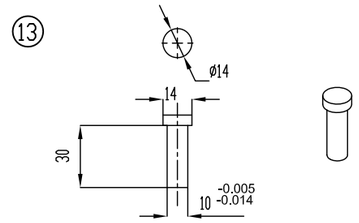

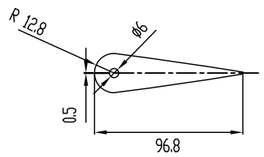

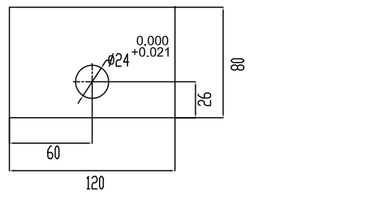

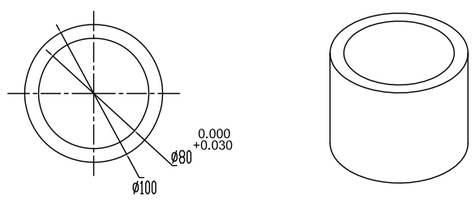

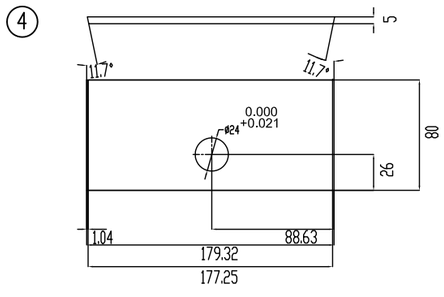

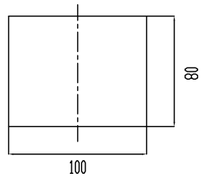

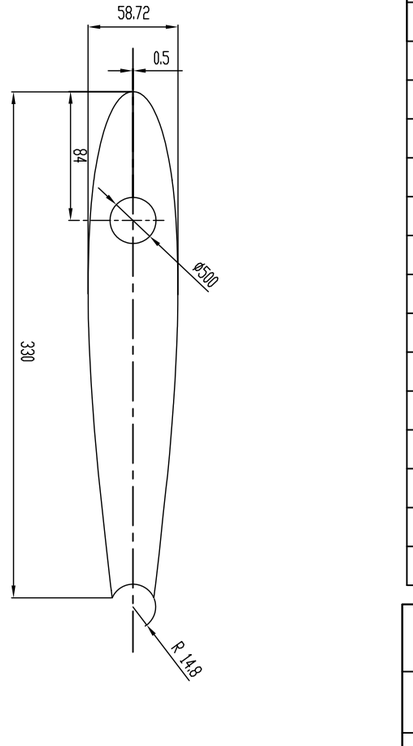

ITEM NO.	QTY	DESCRIPTION	MATERIAL
①	2	Base Component 1	aluminium plate
②	4	Base Component 2	aluminium plate
③	2	Base Component 3	aluminium plate
④	1	Base Component 4	aluminium plate
⑤	2	Base Component 5	aluminium plate
⑥	2	Base Component 6	aluminium plate
⑦	1	Base Component 7	aluminium plate
⑧	1	Mast Fitting Ring	aluminium plate
⑨	1	Longitudinal Bar	aluminium plate
⑩	1	Transverse Bar	aluminium plate
⑪	1	Mast Connecter	aluminium
⑫	1	Base Top Plate	aluminium
⑬	1	Pin	aluminium rod
⑭		Main Wing Section	Blue foam
⑮		Flap Section	Blue foam

COMPONENTS DRAWING

Designed by: LM - IBS - BS	Checked by: Mike Street	Date 20/04/10	Scale N/A
Appendix F2	Dimension: mm	Edition A	Sheet 2 of 3

UNIVERSITY OF Southampton
School of Engineering Sciences
University of Southampton
University Road
Highfield
Southampton
SO17 1BJ

16

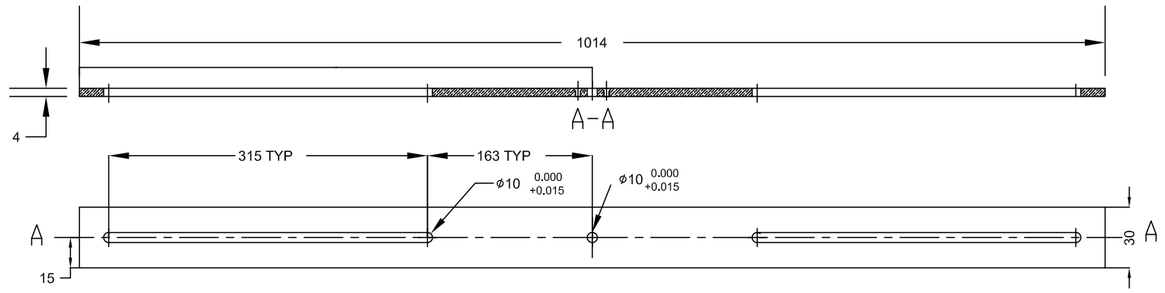

17

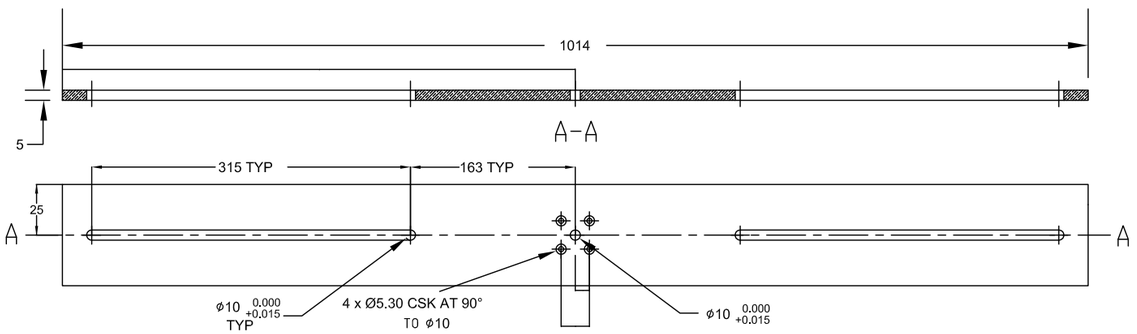

18

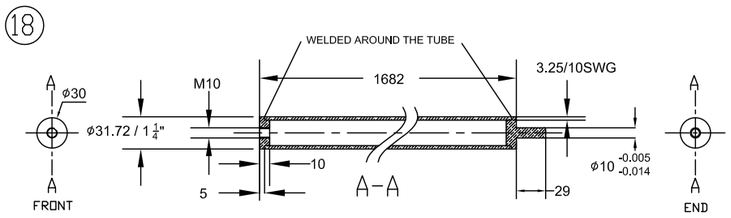

19

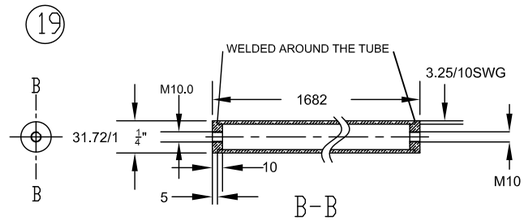

20

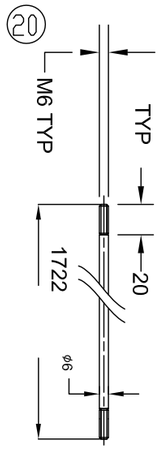

21

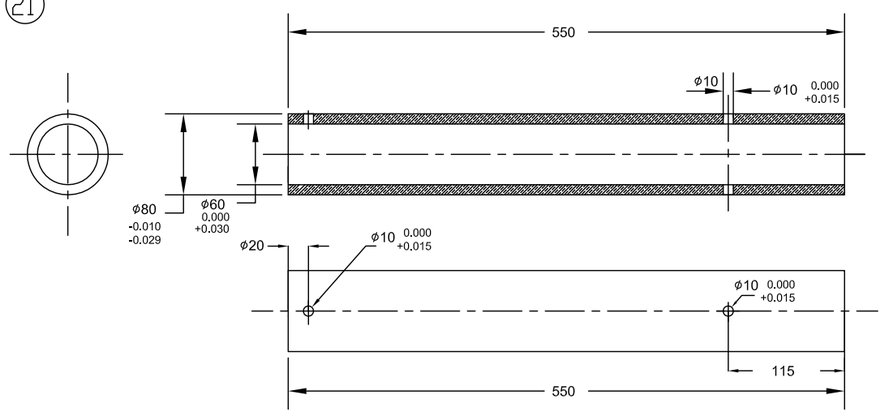

22

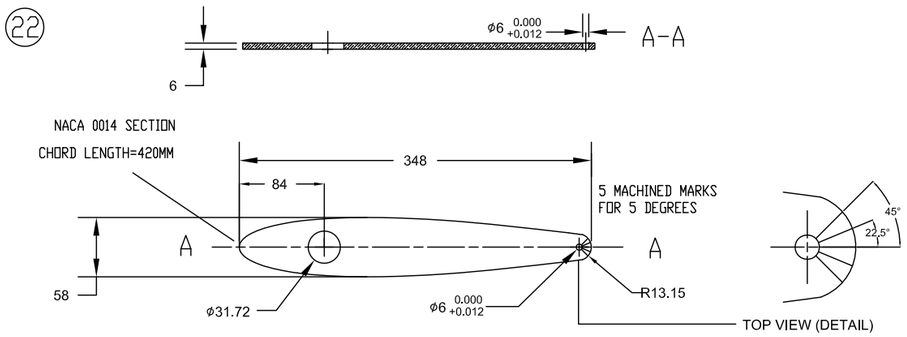

23

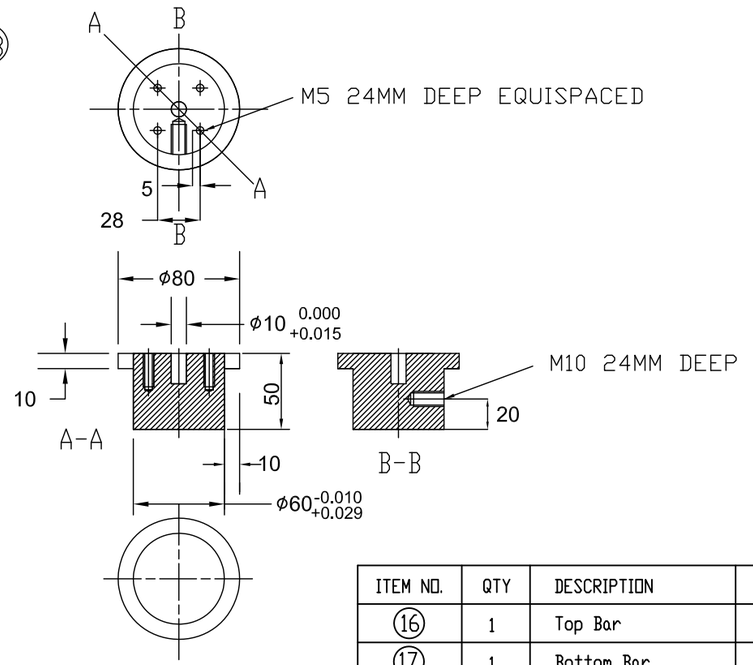

24

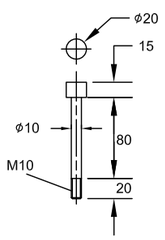

ITEM NO.	QTY	DESCRIPTION	MATERIAL
16	1	Top Bar	aluminium plate
17	1	Bottom Bar	aluminium plate
18	1	Central Wing Stock	aluminium tube
19	2	Side Wing Stock	aluminium tube
20	3	Flap Stock	aluminium rod
21	1	Mast	aluminium tube
22	6	Wing Plate	aluminium plate
23	1	Mast Key	aluminium
24	1	Mast Pin	aluminium rod

COMPONENTS DRAWING

Designed by	Checked by	Date	Scale
LM - IBS - BS	Mike Street	20/04/10	N/A
Appendix F2	Dimensions : mm	Edition A	Sheet 3 of 3

UNIVERSITY OF Southampton
School of Engineering Sciences
University of Southampton
University Road
Highfield
Southampton
SO17 1BJ

F.3 – Wind tunnel calibration results

Table F.4 – Summary of wind tunnel calibration measurements

Weight / kg	*Heeling force / N*	*Error / %*	*Drive force / N*	*Error / %*	*Heeling force / N*	*Error / %*	*Drive force / N*	*Error / %*
1	9.93	-0.7	10.32	3	9.95775	-0.4	10.01546	0.2
2	19.92	-0.4	20.60	3	20.00216	0.0	20.21857	1.1
3	29.65	-1.2	30.91	3	29.98211	-0.1	30.30577	1.0
4	39.65	-0.9	41.37	3	39.82752	-0.4	40.09646	0.2
5	49.51	-1.0	51.59	3	49.78548	-0.4	50.05789	0.1
4	39.75	-0.6	40.79	2	39.98039	0.0	40.04002	0.1
3	29.86	-0.5	30.40	1	30.21798	0.7		
2	20.03	0.1	19.98	0	20.13961	0.7		
1	10.05	0.5	9.78	-2	10.06070	0.6		
	Average	-0.5		1.9		0.1		0.5

F.4 – Sail-container interaction figures

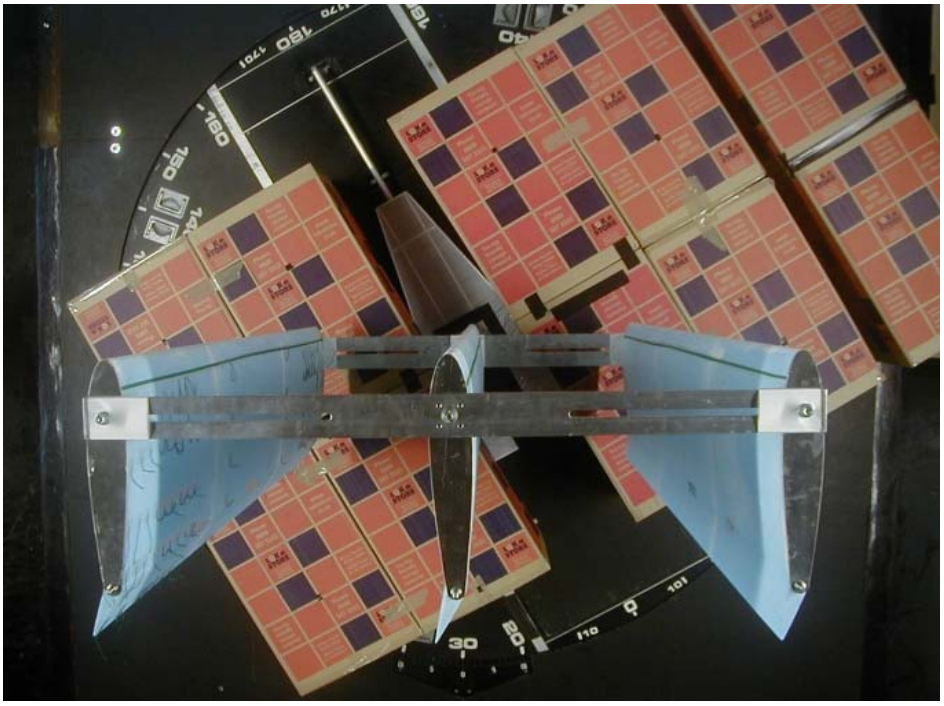

Figure F.3 – Sail - container interaction at apparent wind angle of 60 degrees (Wing A, maximum chord spacing) The boxes which cover the base had to be trimmed to avoid any contact with the dynamometer link

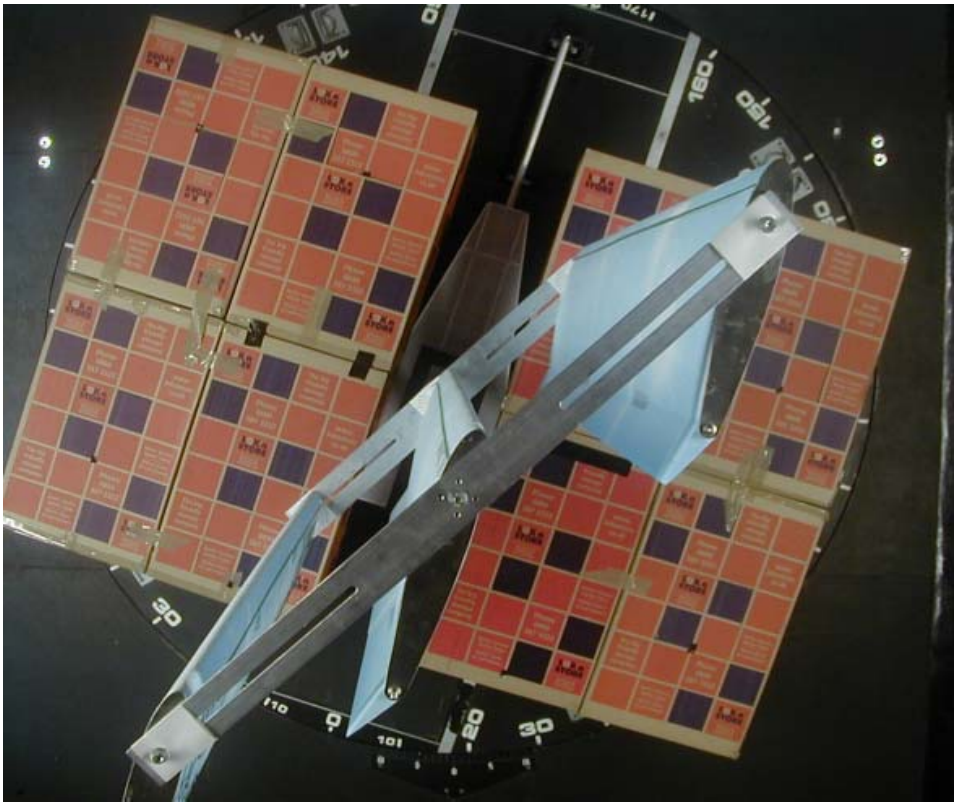

Figure F.4 – Sail - container interaction at apparent wind angle of 109 degrees (Wing B, 60 degrees of stagger)

Figure F.5 – Flat sail configuration (Wing C) for downwind performance

F.5 – Wind tunnel corrections

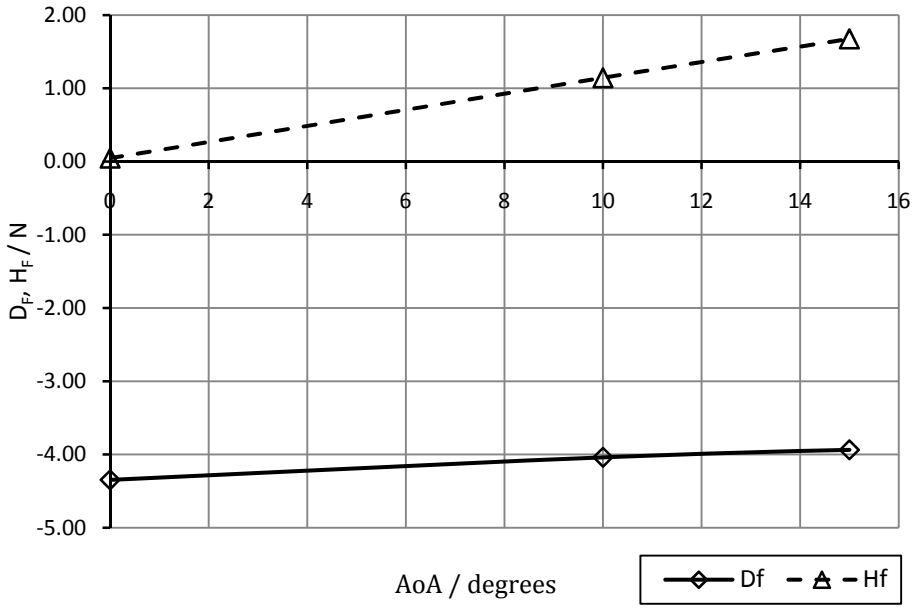

Figure F.6 – Windage data of rig supporting structure, no interactions

Nomenclature

Nomenclature pertinent to appendix, all other parameters defined in principal nomenclature

C	Wind tunnel cross section area	m^2	K_1	Solid blockage model geometry factor	
C_{bt}	Total blockage correction		He	Effective rig height	
c_{wb}	Wake blockage correction		β''	Apparent wind angle, downwash correction	deg
c_{sbw}	Solid blockage correction, windage data		δ	Downwash correction factor	
$C_{D''}$	Drag coefficient, downwash correction		c_{sb}	Solid blockage correction	
$C_{D'''}$	Drag coefficient, blockage correction		ε_{wb}	Wake blockage correction factor	
C_{DS}	Separated drag coefficient		τ_1	Solid blockage test section factor	

Downwash correction [ESDU (1995)]

$$C_{D''} = C_{D'} + \frac{\delta A {C_L}^2}{C\Lambda^2} \quad \text{(F.1)}$$

$$\beta'' = \beta + \frac{\delta A {C_L}^2}{C\Lambda^2} \quad \text{(F.2)}$$

δ is a coefficient based on the ratio of the span of the wings to the width of the jet and the test section shape. 0.113 is the value for octagonal sections [ESDU (1995)].

Solid blockage correction

Figure F.7 shows the calculation of the dimensional ratios K_1 and τ_1 for the solid blockage correction:

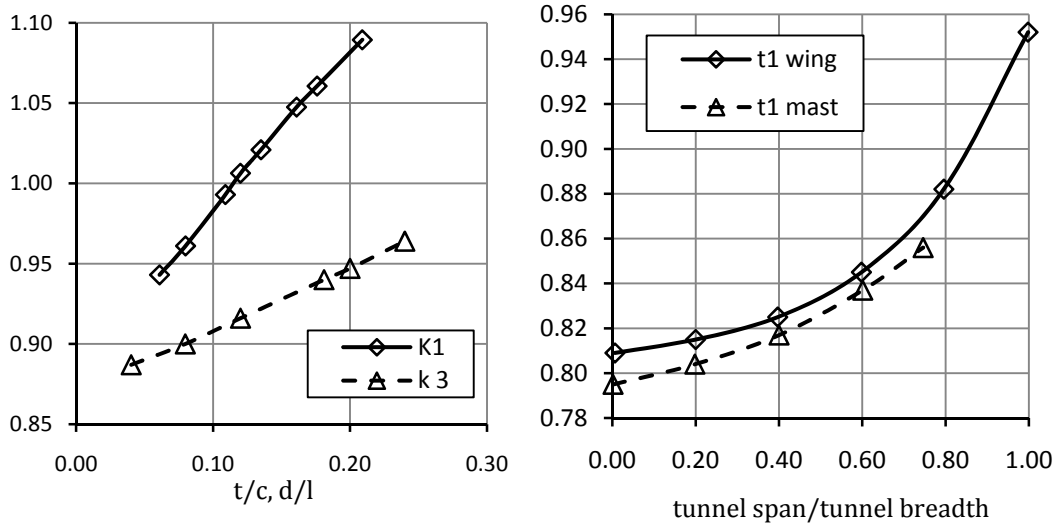

Figure F.7 – Variation in solid blockage correction parameters K_1 and τ_1

$$c_{sb} = \frac{K_1\tau_1 \cdot wing(structure)\ \ volume}{C^{3}/_{2}} \quad \text{(F.3)}$$

Windage solid blockage

$$c_{sbw} = \frac{1}{4} \cdot \frac{structure\ frontal\ area}{wind\ tunnel\ test\ section\ area} \quad \text{(F.4)}$$

Wake blockage

Table F.5 – Body shape factors used for wake blockage correction [ESDU (1980)]

Body shape	ε; m; *maximum* S/A*
Flat plate, centre-mounted 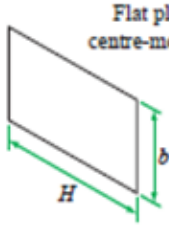	$\varepsilon = 2.84 - 0.07H/b$ and $m = 3.20 - 0.05\ H/b$ for $H/b \le 20$; for $S/A \le 0.10$.
Flat plate, surface-mounted 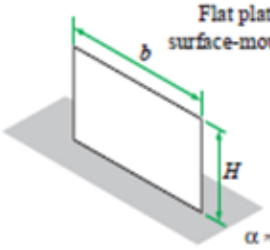	$\varepsilon \approx 2.37$; $m \approx 2.84$ for $\frac{1}{3} \le H/b \le 3$; for $S/A \le 0.10$ For $H/b > 3$ use value for centre-mounted plate of $2H/b$ aspect ratio.

Table F.6 – Model frontal area at zero AoA

Component	*Height / m*	*Width / m*	*Area / m^2*
Wings x3	1.670	0.189	0.31563
Top bar	0.008	1.014	0.008112
Bottom bar	0.010	1.014	0.01014
Mast	0.420	0.080	0.033600
Base	0.080	0.500	0.040000
Total			0.407482

Table F.7 – Calculation of wake blockage correction factor ε_{wb}

Item	*Wings*	*Top bar*	*Bottom bar*	*Mast*	*Base*
S	0.319032	0.00811	0.01014	0.033600	0.04000
A	16.09500	16.09500	16.09500	16.09500	16.09500
S/A	0.019821	0.000504	0.00063	0.00209	0.00249
H	0.18900	1.01400	1.01400	0.08000	0.5000
b	1.68800	0.00800	0.01000	0.42000	0.0800
H/b	0.11197	126.75000	101.40000	0.19048	6.2500
ε_{wb}	2.83216	-	-	2.82667	2.4025

$$C_{DS} = C_D'' - \frac{A \cdot {C_L}^2}{\pi \cdot He^2} - C_{D0} \quad \text{(F.5)}$$

$$He = \sqrt{\left[A/\pi \cdot \left(\delta C_D/\delta {C_L}^2\right)\right]} \quad \text{(F.6)}$$

$$c_{wb} = MAX\left(1 + C_{DS}\frac{\varepsilon_{wb} \cdot A}{C \cdot scale^2}, 1\right) \quad \text{(F.7)}$$

Total Blockage Correction

$$C_{bt} = c_{sb} + c_{wb} \quad \text{(F.8)}$$

$$C_{D'''} = {C_D''}/{C_{bt}} \quad \text{(F.9)}$$

$$C_{L''} = {C_L'}/{C_{bt}} \quad \text{(F.10)}$$

F.6 – Low Reynolds number testing

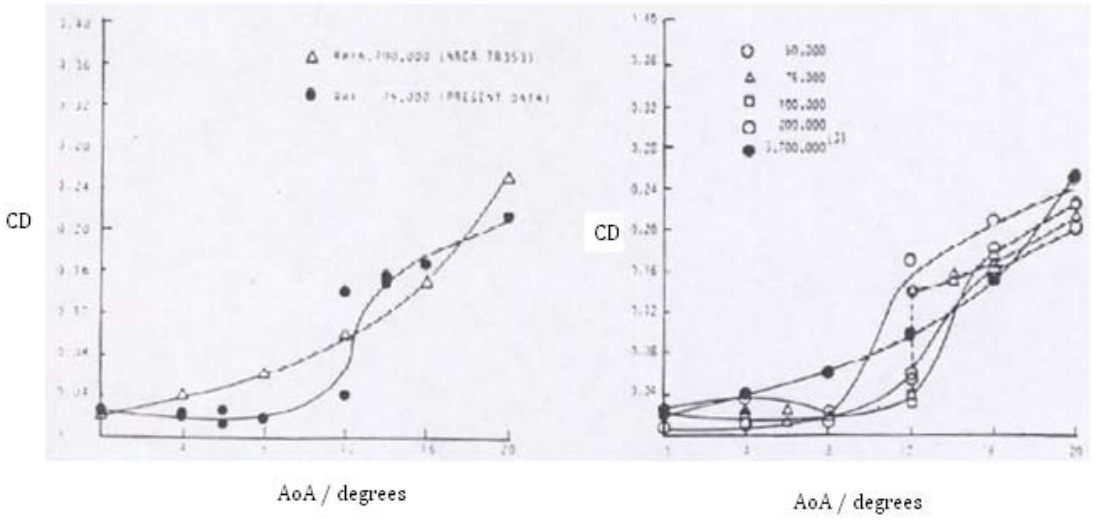

Figure F.8 – Low Reynolds number drag curve for CLARK Y type airfoil [Marchmann & Werme (1994)] In particular the curve on the right for Re 200,000 shows similar trend to the *Multi-wing* in the speed calibration runs

F.7 – Flow visualisation

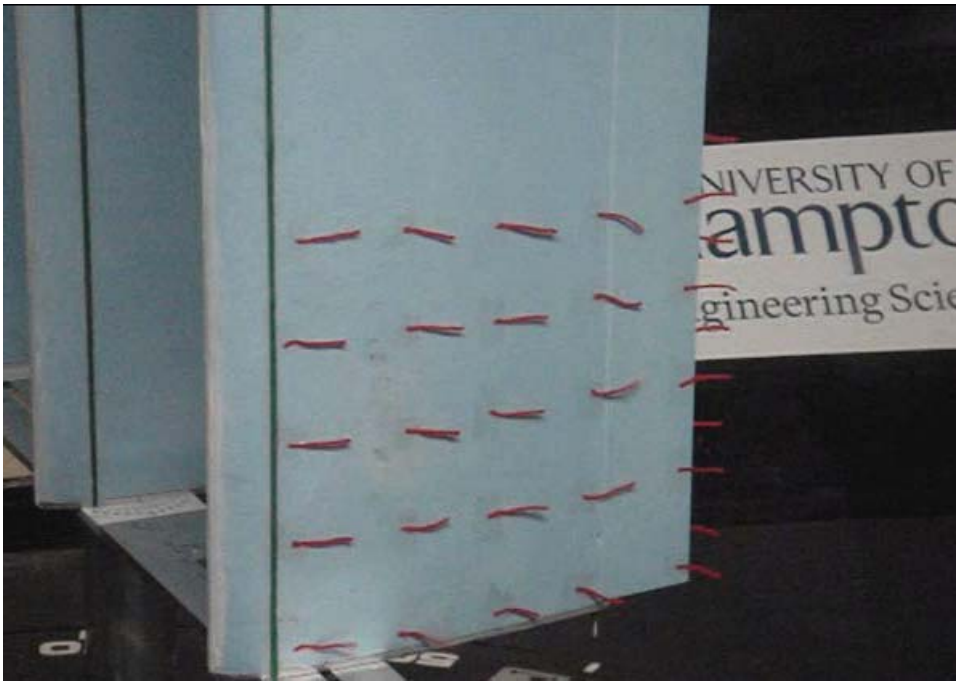

Figure F.9 – Low Reynold number testing. Va = 6ms^{-1}, AoA = 14 degrees.The first column of tufts (20 % chord) is attached to the wing, whilst separation start at 30 % of the chord. Note how the alignment of the second and third column of tufts change from Figure 125, unfortunately the picture is not clear enough, however observing the video it is possible to see the tufts vibrate.

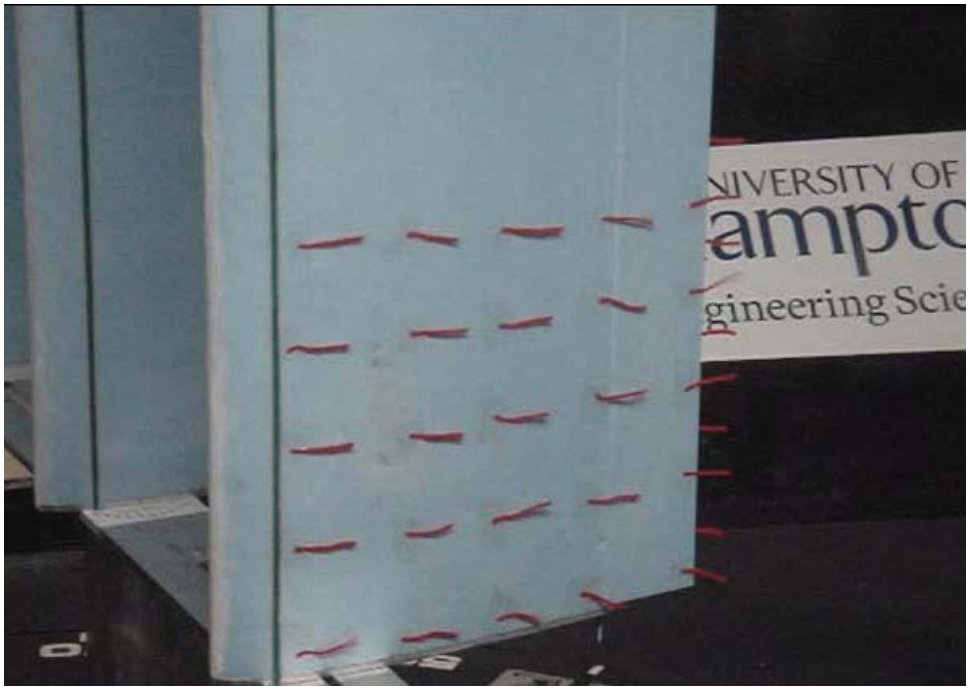

Figure F.10 – Low Reynolds number testing. Va = 8 ms^{-1}, AoA = 14 degrees. Here the tufts are aligned with the flow and are attached to the surface. Observing the bottom row is possible to note the end vortex coming off the wing; the first two tufts of this row are separating from the surface due to the interference of the bottom bar

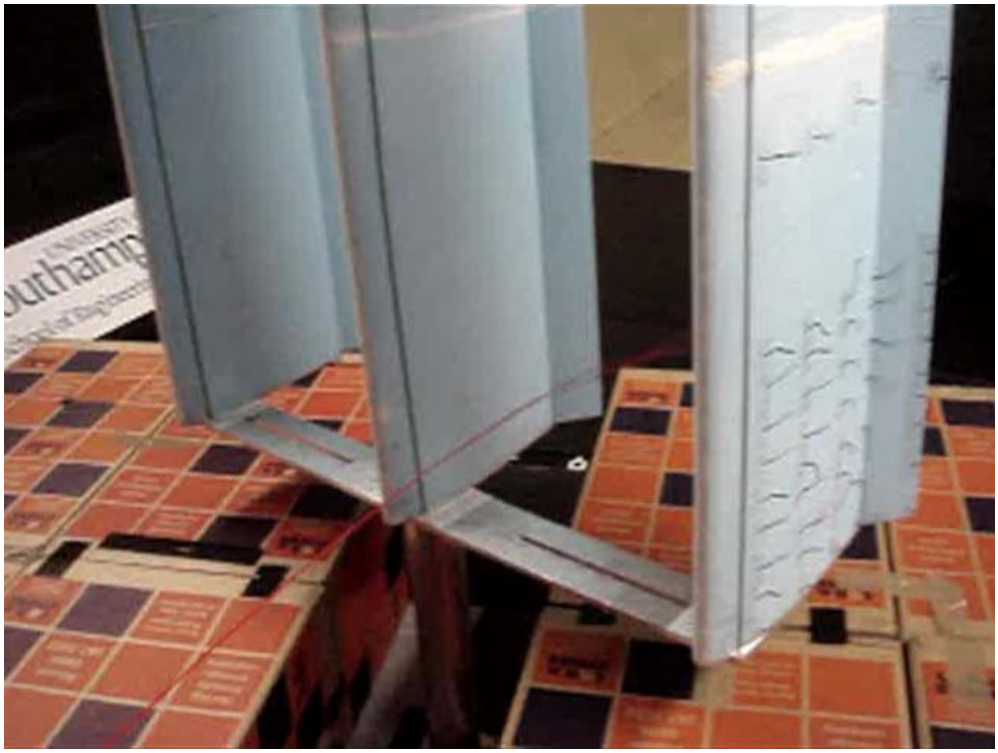

Figure F.11 – Container - Sail interaction study. the gap between the boxes and the base of the wing replicates the full scale gap of 2 metres. Note the red wire which was used instead of the smoke to visualize the flow near the gap; unfortunately this intrusive method had limited effectiveness.

F.8 – Extrapolation to full-scale Reynolds number

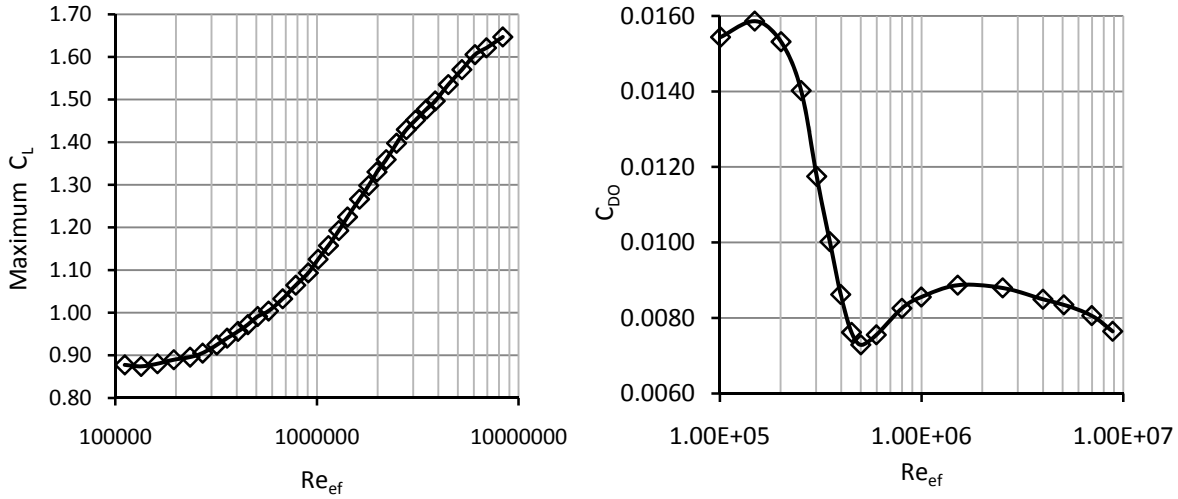

Figure F.12 – NACA 0015 maximum lift coefficient (left); base drag coefficient (right) at different effective Reynolds Numbers [Jacobs & Sherman (1937)]

F.9 – Aerodynamic characteristics from wind tunnel results after correction

Wind Speed Calibration

Table F.8 – Measured lift and drag coefficient with wing spacing of 100% chord (no flap angle; no container interactions)

U = 4 ms^{-1}			
AoA / deg (Stbd)	C_D	C_L	C_L^2
0	0.0102	0.0108	0.0001
5	0.0736	0.0625	0.0039
10	0.1312	0.1228	0.0151
13	0.1754	0.1508	0.0227
14	0.1752	0.1709	0.0292
15	0.2055	0.1454	0.0211
U = 6 ms^{-1}			
AoA / deg (Stbd)	C_D	C_L	C_L^2
0	0.0249	0.0255	0.0007
5	0.1608	0.1556	0.0242
10	0.1526	0.1455	0.0212
13	0.3894	0.3603	0.1298
14	0.4130	0.3722	0.1385
15	0.4297	0.3893	0.1515
U = 8 ms^{-1}			
AoA / deg (Stbd)	C_D	C_L	C_L^2
0	0.0221	0.0501	0.0025
5	0.0301	0.3022	0.0913
10	0.1167	0.5476	0.2998
13	0.2303	0.6786	0.4605
14	0.2682	0.7106	0.5050
15	0.3615	0.7069	0.4997

Wing A

Table F.9 – Measured lift and drag coefficient, and lift-to-drag ratio, for wing spacings of 100% and 75% chord (22.5 degree flap angle; no container interactions)

chord spacing		*100%*				*75%*			
	AoA / deg	C_L	C_D	C_L^2	C_L / C_D	C_L	C_D	C_L^2	C_L/C_D
Starboard	0	0.4162	0.0695	0.1734	5.9869	0.3602	0.0700	0.1298	5.1448
	5	0.7000	0.1089	0.4906	6.4271	0.6075	0.1156	0.3690	5.2562
	10	0.9645	0.1654	0.9315	5.8328	-	-	-	-
	11	-	-	-	-	0.8971	0.1711	0.8048	5.2441
	12	1.0634	0.1956	1.1323	5.4354	-	-	-	-
	13	1.1155	0.2100	1.2460	5.3125	0.9848	0.2012	0.9698	4.8952
	14	-	-	-	-	1.0262	0.2116	1.0530	4.8487
	15	1.1987	0.2469	1.4388	4.8561	1.0669	0.2226	1.1382	4.7918
	16	1.2228	0.2630	1.4971	4.6496	1.0981	0.2347	1.2059	4.6797
	17	1.1966	0.3265	1.4654	3.6656	1.1183	0.2736	1.2507	4.0872
Port	0	0.4373	0.0856	0.1912	5.1091	0.4118	0.0983	0.1696	4.1880
	5	0.7077	0.1257	0.5009	5.6299	0.6436	0.1145	0.4142	5.6219
	10	0.9763	0.1887	0.9532	5.1744	0.8847	0.1809	0.7827	4.8893
	15	1.2018	0.2863	1.4444	4.1975	1.0573	0.2618	1.1178	4.0391
	16	1.2286	0.3269	1.5094	3.7578	-	-	-	-

Table F.10 – Measured lift and drag coefficient, and lift-to-drag ratio, for wing spacings of 50% and 120% chord (22.5 degree flap angle; no container interactions)

chord spacing		*50%*				*120% (maximum)*			
	AoA / deg	C_L	C_D	C_L^2	C_L/C_D	C_L	C_D	C_L^2	C_L/C_D
Starboard	0	0.3082	0.0976	0.0951	3.1567	0.4019	0.0724	0.1617	5.5536
	5	0.5272	0.0910	0.2782	5.7936	0.6802	0.1139	0.4632	5.9712
	10	0.7430	0.1347	0.5527	5.5155	0.9417	0.1539	0.8879	6.1184
	12	0.8210	0.1699	0.6749	4.8323	1.0350	0.1891	1.0726	5.4746
	15	0.9318	0.1974	0.8693	4.7213	1.1714	0.2347	1.3738	4.9914
	16	0.9786	0.2103	0.9590	4.6546	-	-	-	-
	17	0.8784	0.3175	0.8123	2.7668	-	-	-	-
Port	0	0.3875	0.0898	0.1503	4.3143	0.4152	0.0820	0.1726	5.0650
	5	-	-	-	-	0.7111	0.1213	0.5063	5.8642
	10	0.7950	0.1703	0.6328	4.6669	0.9724	0.1859	0.9468	5.2306
	12	0.8677	0.1922	0.7547	4.5146	1.0952	0.2169	1.2009	5.0493
	14	-	-	-	-	1.1810	0.2492	1.3966	4.7400
	15	0.9669	0.2298	0.9425	4.2073	-	-	-	-
	16	0.9926	0.2455	0.9970	4.0439	-	-	-	-
	17	1.0051	0.2598	1.0267	3.8679	-	-	-	-
	18	0.9973	0.2777	1.0191	3.5916	-	-	-	-

Table F.11 – Single wing with 22.5 degree flap angle without containers

	AoA / deg	C_L	C_D	C_L^2	C_L/C_D
Starboard	0	0.505956	0.00665	0.2563191	76.08051
	10	1.254967	0.197406	1.5769551	6.357274
	15	1.198690	0.310085	1.4921586	3.865683

Table F.12 – Measured lift and drag coefficient, and lift-to-drag ratio for wing spacing of 120% of chord and flap of angle of 22.5 degrees

AWA of containers / deg	*90-119*				*69-79*			
AoA / deg (Stbd)	C_L	C_D	C_L^2	C_L / C_D	C_L	C_D	C_L^2	C_L/C_D
0	0.402	0.062	0.16	6.519	0.547	0.128	0.299	4.263
5	0.736	0.095	0.54	7.738	0.845	0.148	0.715	5.700
10	1.091	0.179	1.19	6.081	1.155	0.301	1.334	3.833
14	1.333	0.253	1.78	5.271	1.384	0.408	1.914	3.391
15	1.385	0.271	1.92	5.112	-	-	-	-
16	1.423	0.308	2.02	4.621	-	-	-	-
18	1.421	0.375	2.02	3.792	1.464	0.499	2.143	2.932
19	1.366	0.426	1.86	3.203	-	-	-	-

Table F.13 – Measured lift and drag coefficient, and lift-to-drag ratio for wing spacing of 120% of chord and flap angle of 45 degrees with containers at 90 to 119 degrees apparent wind angle

AoA / deg(Stbd)	C_L	C_D	C_L^2	C_L/C_D
0	0.720	0.175	0.519	4.124
5	1.074	0.266	1.153	4.034
10	1.397	0.337	1.953	4.144
14	1.634	0.417	2.671	3.916
16	1.729	0.486	2.989	3.558
18	1.751	0.572	3.066	3.063

Wing B

Table F.14 – 30 degree stagger configuration with wing spacing of 120% of chord with 22.5 degrees flap angle with containers at 90 to 119 degrees apparent wind angle

AoA / deg(Stbd)	C_L	C_D	C_L^2	C_L/C_D
0	0.381	0.057	0.145	6.663
5	0.747	0.127	0.557	5.872
10	1.095	0.196	1.198	5.577
14	1.368	0.287	1.871	4.773
16	1.406	0.353	1.976	3.979
18	1.442	0.441	2.080	3.270

Table F.15 – 60 degree stagger configuration with wing spacing of 120% of chord with 22.5 degrees flap angle with containers 90 to 119 degrees apparent wind angle

AoA / deg(Stbd)	C_L	C_D	C_L^2	C_L/C_D
0	0.472	0.079	0.223	6.010
5	0.855	0.151	0.731	5.646
10	1.243	0.259	1.546	4.809
14	1.517	0.352	2.300	4.310
16	1.573	0.450	2.474	3.498
18	1.608	0.553	2.587	2.906

Table F.16 – Extreme stagger configuration with wing spacing of 120% of chord with containers at 90 to 119 degrees apparent wind angle

AoA / degree(Stbd)	C_L	C_D	C_L^2	C_L/C_D
5	0.534	0.201	0.285	2.658
10	0.716	0.250	0.513	2.863
15	1.003	0.366	1.007	2.745
20	1.296	0.494	1.679	2.625
25	1.528	0.647	2.334	2.360
30	1.631	0.893	2.660	1.826

F.10 – Uncertainty analysis – random error component

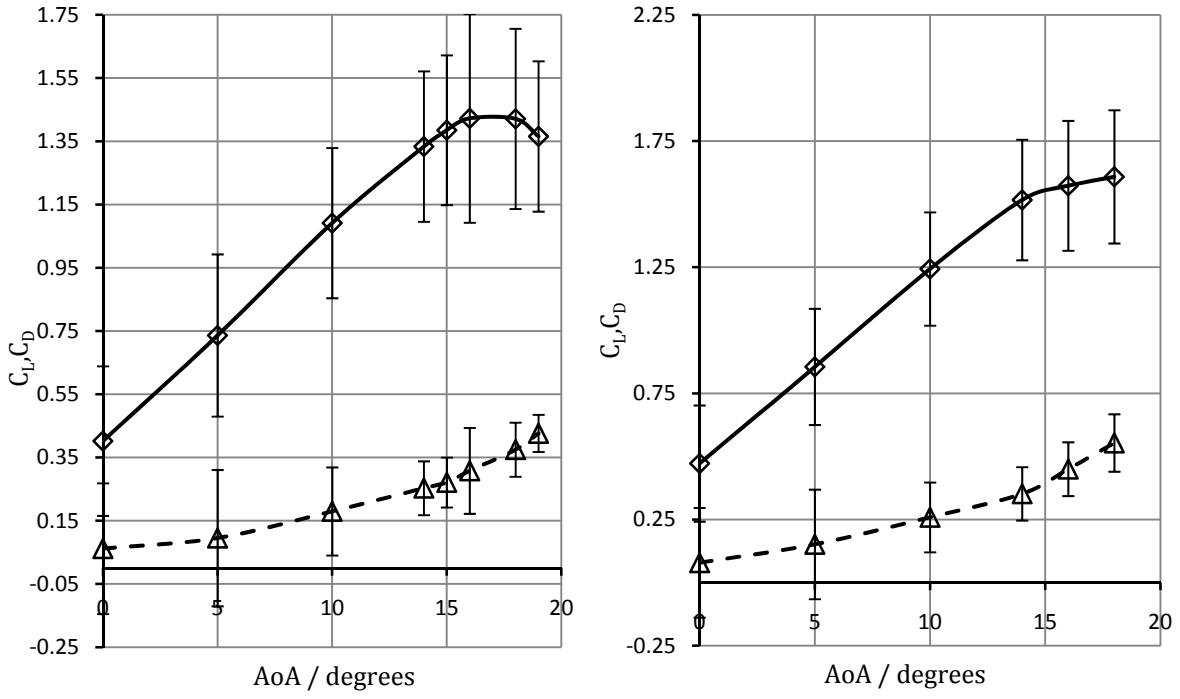

Figure F.13 – Standard deviation of wing performance coefficients for *Wing A* (left); and *Wing B*, 60 degrees of stagger (right)

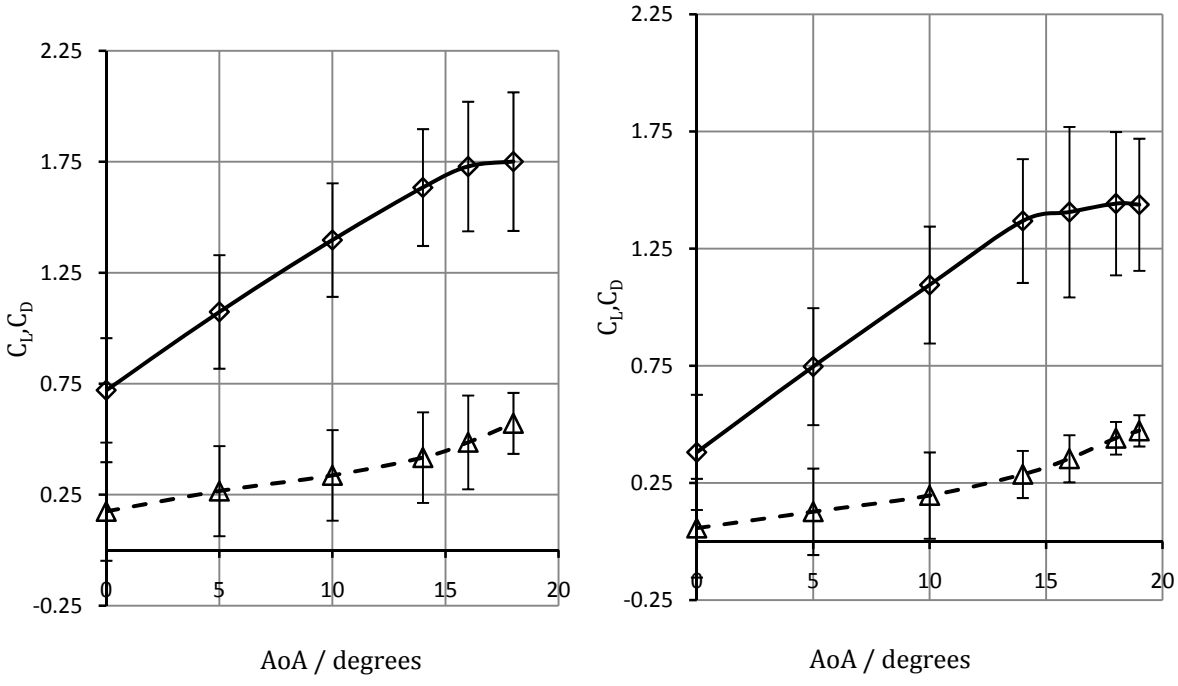

Figure F.14 – Standard deviation of wing performance coefficients for *Wing A,* flap at 45 degrees (left); and *Wing B,* 30 degrees of stagger (right)

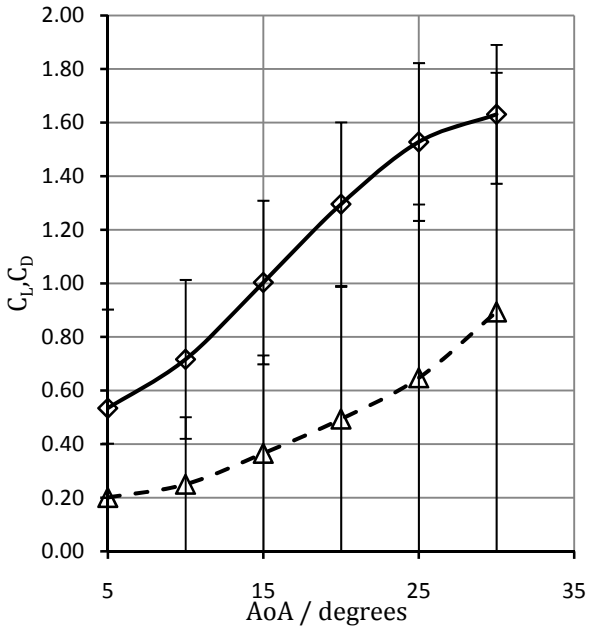

Figure F.15 – Standard deviation of wing performance coefficients for *Wing C*

F.11 – Computational fluid dynamics study on *Multi-wing* sail system

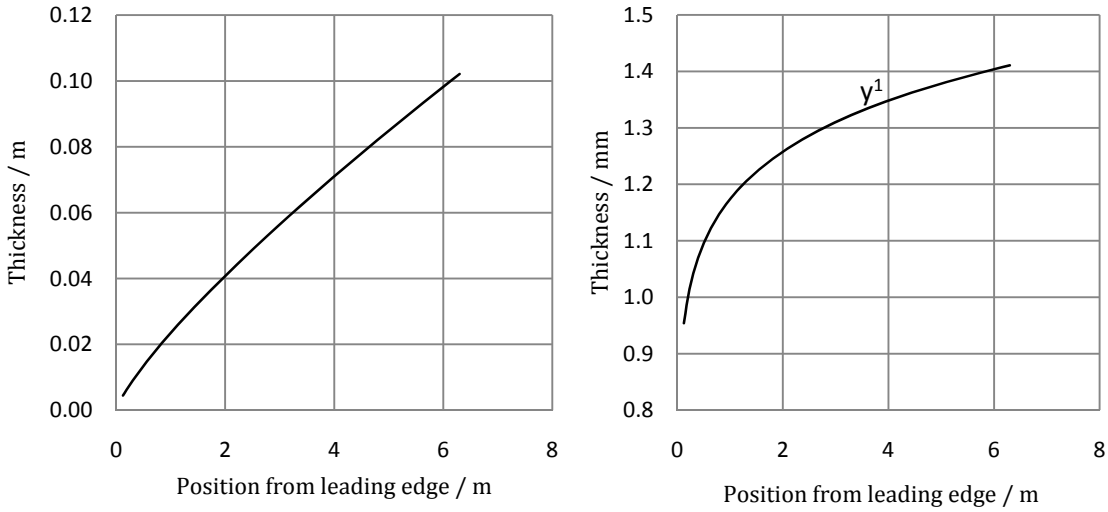

Figure F.16 – Boundary layer (left) and first wall (right) thicknesses

Table F.17 – Aerodynamic characteristics of wing spacing of 100% of chord with 22.5 degree flap angle model

	Total			*Top wing*			*Middle wing*			*Bottom wing*		
AoA / degree	C_L	C_D	C_L/C_D	C_L	C_D	C_L/C_D	C_L	C_D	C_L/C_D	C_L	C_D	C_L/C_D
0.0	0.74	0.03	21.33	0.75	0.03	23.12	0.78	0.03	22.15	0.69	0.04	18.96
4.0	0.96	0.05	19.67	1.01	0.05	21.79	0.96	0.05	18.90	0.92	0.05	18.47
8.0	**1.11**	**0.08**	**13.94**	**1.17**	**0.08**	**15.00**	**1.13**	**0.08**	**14.03**	**1.03**	**0.08**	**12.82**
10.0	1.14	0.13	8.75	1.25	0.14	9.22	1.21	0.11	11.46	0.96	0.15	6.41
12.0	1.05	0.22	4.72	0.91	0.21	4.46	1.16	0.21	5.39	1.09	0.25	4.35

Appendix G – Performance Predictions

G.1 – Sailing performance

Table G.1 – Probability of significant wave length to waterline length for Singapore area

	Wave length/wetted length									
$h_{1/3}$ / *m*	*12*	*20*	*30*	*42*	*55*	*71*	*89*	*109*	*130*	*Total*
6.5	0.0000	0.0000	0.0003	0.0007	0.0007	0.0000	0.0000	0.0000	0.0000	0.0016
5.5	0.0000	0.0003	0.0010	0.0017	0.0020	0.0010	0.0003	0.0000	0.0000	0.0063
4.5	0.0000	0.0010	0.0043	0.0063	0.0053	0.0030	0.0017	0.0003	0.0000	0.0220
3.5	0.0003	0.0050	0.0170	0.0237	0.0177	0.0087	0.0033	0.0007	0.0003	0.0768
2.5	0.0017	0.0214	0.0595	0.0671	0.0414	0.0170	0.0053	0.0013	0.0003	0.2150
1.5	0.0100	0.0758	0.1406	0.1089	0.0478	0.0147	0.0033	0.0007	0.0000	0.4018
0.5	0.0371	0.0995	0.0895	0.0381	0.0100	0.0017	0.0003	0.0000	0.0000	0.2762
Total	0.0491	0.2031	0.3123	0.2465	0.1249	0.0461	0.0144	0.0030	0.0007	1

Table G.2 – Probability of significant wave height and wave length to waterline length for the Caribbean area

	Wave length/wetted length									
$h_{1/3}$ / *m*	12	20	30	42	55	71	89	109	130	Total
6.5	0.000	0.000	0.000	0.000	0.001	0.000	0.000	0.000	0.001	0.002
5.5	0.000	0.000	0.000	0.001	0.002	0.001	0.000	0.000	0.002	0.007
4.5	0.000	0.000	0.002	0.005	0.005	0.004	0.002	0.000	0.007	0.026
3.5	0.000	0.002	0.011	0.020	0.018	0.010	0.004	0.001	0.025	0.090
2.5	0.001	0.012	0.044	0.059	0.040	0.017	0.005	0.001	0.077	0.256
1.5	0.004	0.044	0.098	0.083	0.037	0.011	0.002	0.000	0.147	0.427
0.5	0.013	0.041	0.040	0.017	0.004	0.001	0.000	0.000	0.076	0.191
Total	0.018	0.099	0.195	0.186	0.107	0.043	0.013	0.004	0.334	*0.874*

Table G.3 – Averaged added resistance for *Hull A* sailing at 15 knots in Singapore - values in Newtons

Hull A 15 knots	*Wave length/wetted length*									
$h_{1/3}$ / *m*	12	20	30	42	55	71	89	109	130	Total
2.5	0.00	0.00	0.00	0.00	2047.1	1997.0	1034.2	326.7	62.4	5467.5
1.5	0.00	0.00	0.00	0.00	849.9	620.3	232.7	58.8	0.0	1761.7
0.5	0.00	0.00	0.00	0.00	19.8	7.8	2.6	0.0	0.0	30.2
Total	0.00	0.00	0.00	0.00	3140.1	2625.1	1269.5	970.4	62.4	*7259.4*

Table G.4 – Average added resistance for *Hull B* sailing at 15 knots in Singapore - values in Newtons

Hull B 15 knots	*Wave length/wetted length*									
sig wave height / m	12	20	30	42	55	71	89	109	130	Total
2.5	0	0	720.94	3282.92	3799.00	2397.35	1046.76	312.79	60.84	11620.60
1.5	0	0	613.86	1916.83	1577.20	744.59	235.52	56.30	0.00	5144.30
0.5	0	0	43.42	74.48	36.76	9.40	2.62	0.00	0.00	166.68
Total	0	0	1378.22	5274.23	5412.97	3151.33	1284.90	369.09	60.84	*16931.5*

Table G.5 – Average added resistance for *Hull A* sailing at 15 knots in the Caribbean area – values in Newtons

Hull A, 15 knots	*Wave length/wetted length*									
$h_{1/3}$ / *m*	12	20	30	42	55	71	89	109	130	Total
2.5	0.0	0.0	0.0	-585.7	1979.8	1995.7	968.9	326.5	14343.3	19028.5
1.5	0.0	0.0	0.0	-294.9	659.3	450.8	162.8	29.4	9900.6	10907.9
0.5	0.0	0.0	0.0	-6.6	7.9	3.1	0.0	0.0	566.2	570.7
Total	0.0	0.0	0.0	-909.4	2870.0	2714.1	1568.3	1260.4	25653.3	*30507.1*

Table G.6 – Averaged added resistance for *Hull B* sailing at 15 knots in the Caribbean area – values in Newtons

Hull B 15 knots	*Wave length/wetted length*									
$h_{1/3}$ / *m*	11.9	19.7	30.0	42.0	54.8	71.0	89.0	109.0	130.0	Total
2.5	0.0	0.0	611.2	3323.5	4202.9	2740.6	1121.9	357.6	15996.7	28354.3
1.5	0.0	0.0	488.4	1673.7	1399.6	619.1	188.5	32.2	11041.9	15443.3
0.5	0.0	0.0	22.2	37.3	16.8	4.3	0.0	0.0	631.5	712.2
Total	0.0	0.0	1121.8	5034.6	5619.2	3364.0	1310.3	389.8	27670.1	*44509.8*

G.2 – Propulsion

Propulsor and plant selection

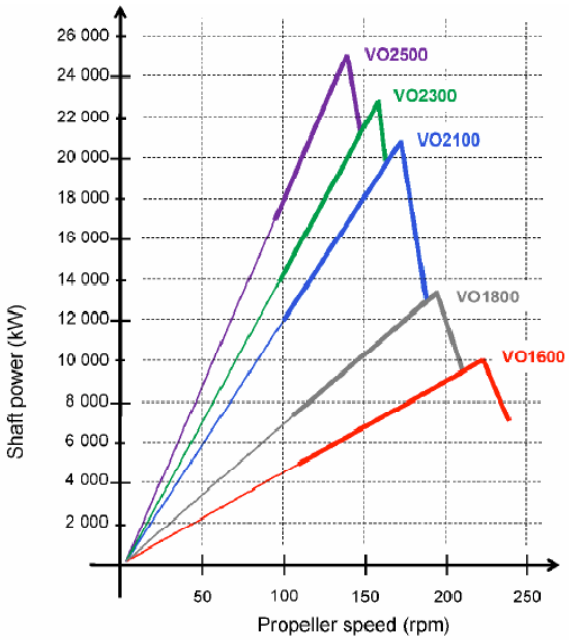

Figure G.1 – Manufacturer's VO series poded drive specifications [ABB (2009)]

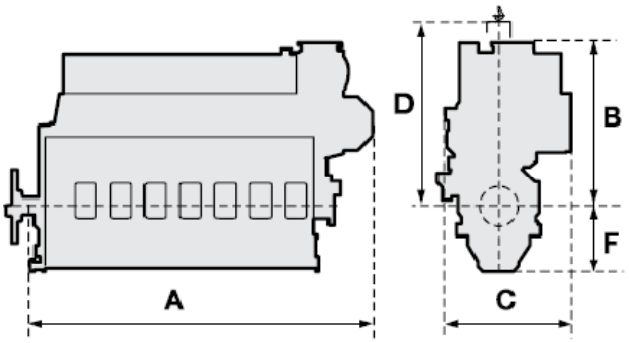

Figure G.2 – L50DF engine drawing [Wärtsilä Ship Power Technology (2009a)]

Table G.7 – L50DF engine series dimensions in millimetres, and weights [Wärtsilä Ship Power Technology (2009a)]

Engine	*A*	*B*	*C*	*D*	*F*	*Weight / tonnes*
6L50DF	8115	3580	2850	3820	1455	96
8L50DF	9950	3600	3100	3820	1455	128
9L50DF	10800	3600	3100	3820	1455	148

Appendix H – Design Feasibility

Table H.1 – Summary of plant specifications used in voyage simulation [data obtained from Wärtsilä Ship Power Technology (2009a) and MAN Diesel (2010)]

	Typical (Singapore)	*Typical (Caribbean)*	*Fast Feeder*
ME	MAN MC-C8 6 cylinder	MAN MC-C8 7 cylinder	Wärtsilä 6L50DF/8L50DF
power / kW	8280	9660	2 x 5700; 2 x 7600
SFC @ MCR / g.kWh^{-1}	177	177	135.2
SFC @ part load / g.kWh^{-1}	175	175	-
AE	MAN 5L21/31	MAN 5L21/31	-
power / kW	950	950	-
SFC @ MCR / g.kWh^{-1}	190	190	-
SFC @ 85%MCR / g.kWh^{-1}	188	188	-

Table H.2 – Emissions estimates used in voyage simulation [data obtained from Wärtsilä Ship Power Technology (2009a) and MAN Diesel (2010)]

	LNG (MCR)	*LNG (part load)*	*MDO (MCR)*	*MDO (part load)*
CO_2 / g.kWh^{-1}	430	450	630	630
NO_x / g.kWh^{-1}	1.4	2	11.5	12

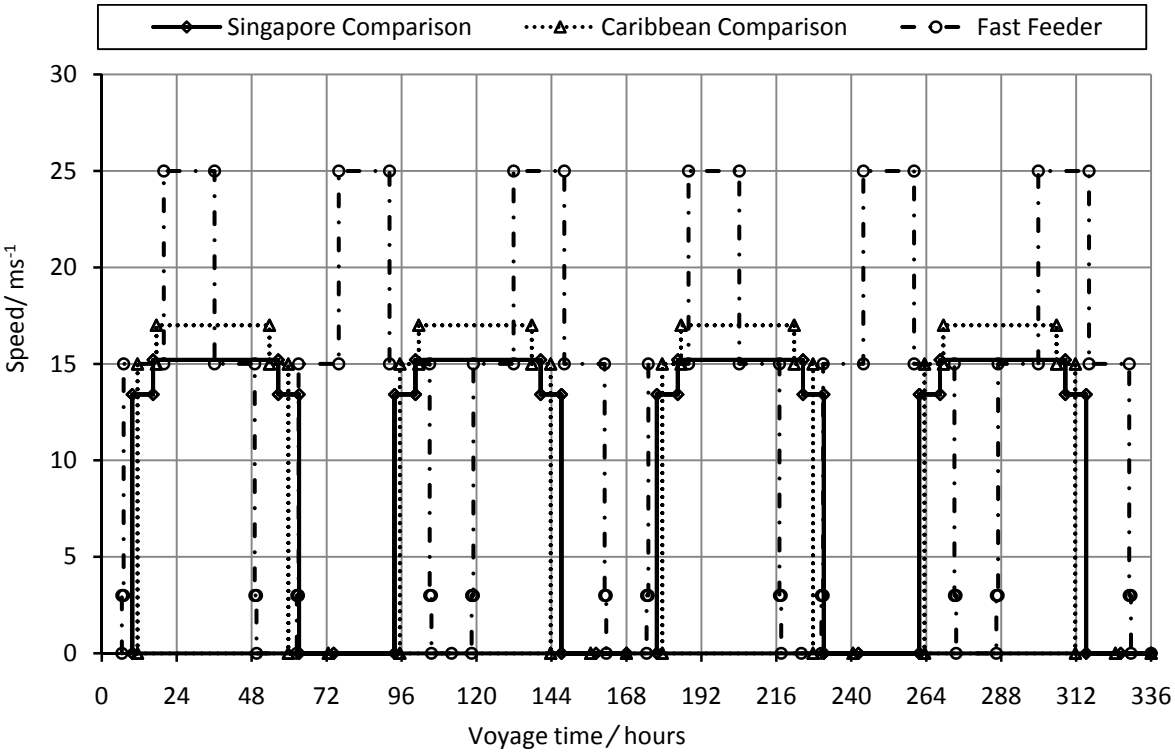

Figure H.1 – Speed profile for fast feeder and comparison ships over fortnightly operating period

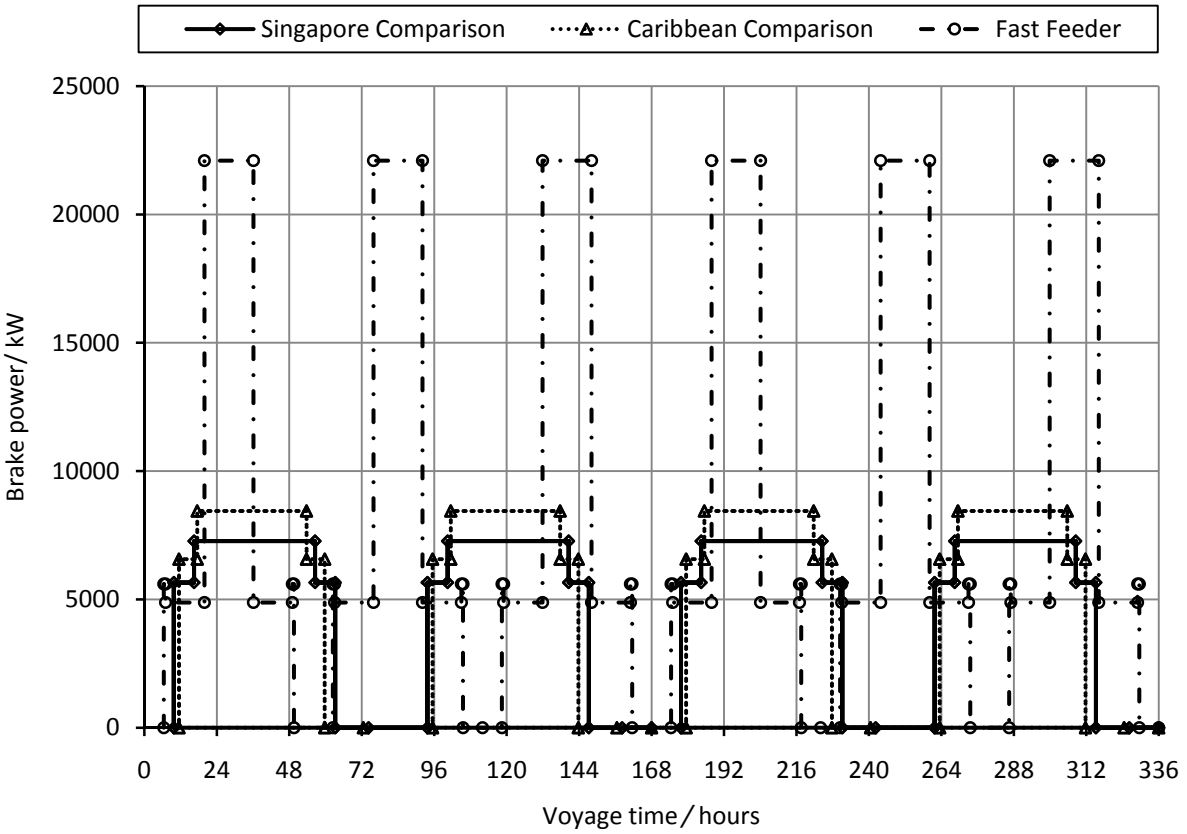

Figure H.2 – Power profile for fast feeder and comparison ships over fortnightly operating period

H.1 – Performance indices

Nomenclature

Nomenclature pertinent to appendix, previously defined symbols

C_C	Carbon factor (g CO_2 / tonne fuel)	N_S	Number if ships
$EEDI$	Energy efficiency design index	TEI	Transport efficiency index
h	high speed (subscript)	w_h	weighting for high speed operation
l	low speed (subscript)	w_l	weighting for low speed operation

Transport efficiency index

This simple measure of ship efficiency is often defined as the ratio between 'volume rate' of cargo and the power requirement, thus

$$TEI = \frac{N_c V_s}{P_B} \; (TEU \cdot knot/kW). \tag{H.1}$$

No account is taken in Equation (H.1) for the number of ships carrying the cargo, or operation at different speeds or power requirements. It is deemed appropriate to modify

$$modified\ TEI = \frac{N_c\left(V_{s,l} w_l + V_{s,h} w_h\right)}{N_s\left(P_{B,l}^{(ME)} w_l + P_{B,h}^{(ME)} w_h\right)} \tag{H.2}$$

Energy Efficiency Design Index

This measure of environmental performance is defined as

$$EEDI = \frac{\sum C_c \cdot SFC \cdot P_B}{DWT \cdot V_s} \ (g\ CO_2/\ tonne \cdot nm), \tag{H.3}$$

where the summation is used to take in to account all of the installed engines. The calculation is to be carried out for a design load condition at a ship speed and power rating corresponding to 75% MCR. Rules accounting for auxiliary engines are also defined [Andersen & Kristensen (2009)]. Taking a weighted approach when calculating the EEDI leads to the following modified formulation:

$$modified\ EEDI = \frac{C_c\left(P_{B,l}^{(ME)} SFC_l^{(ME)} w_l + P_{B,h}^{(ME)} SFC_l^{(ME)} w_h + P_B^{(AE)} SFC^{(AE)}\right)}{DWT \cdot \left(V_{s,l} w_l + V_{s,h} w_h\right)}. \tag{H.4}$$

The carbon factor values used for LNG and MDO are 2931200 and 320600 respectively [IMO (2005a)] Whilst this version of the EEDI cannot be used to compare the fast feeder to values published for existing ships, it provides a more accurate assessment of performance against the comparison ships within the context of this report.

H.2 – Freight rate estimate

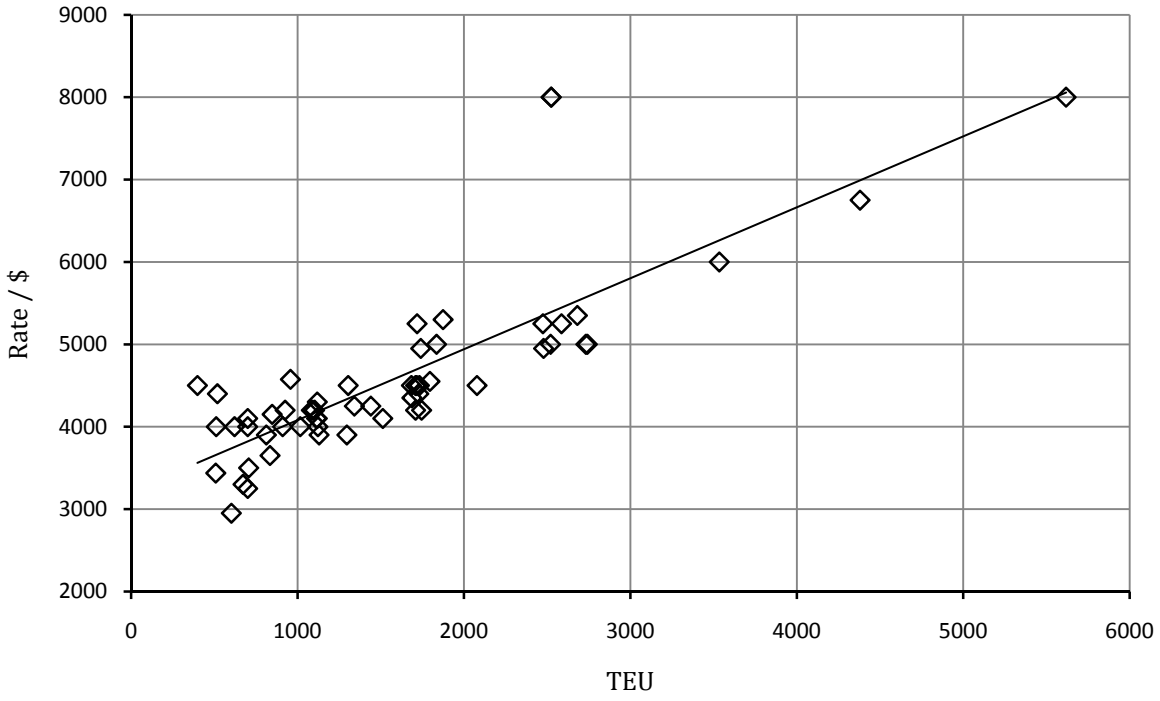

Figure H.3 – Freight rate basis [Hansa (2009)]

Appendix I – Seakeeping

I.1 – Predicted RAO curves

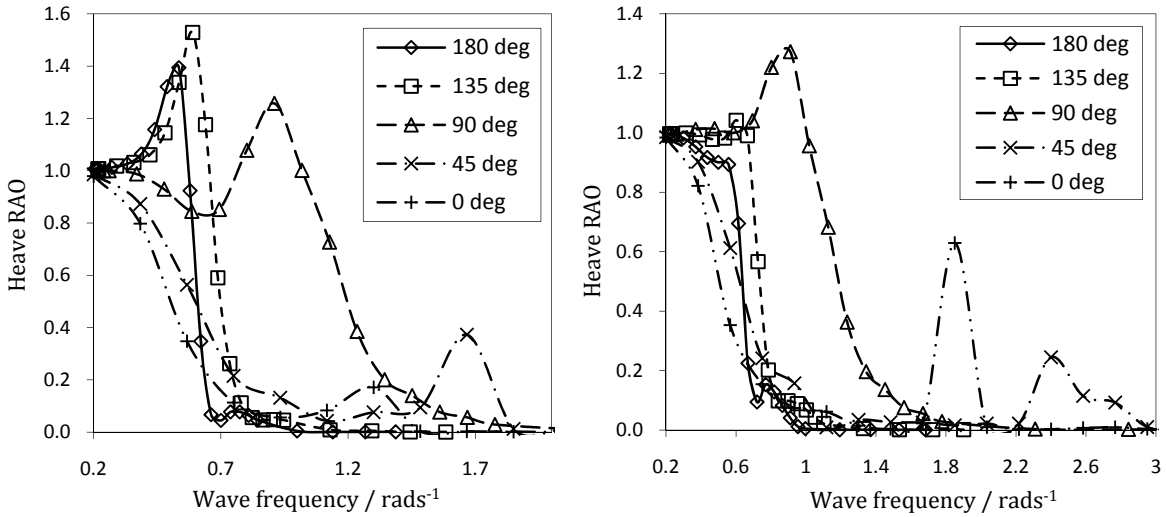

Figure I.1 – Heave RAO at 25 knots (left); and 15 knots (right)

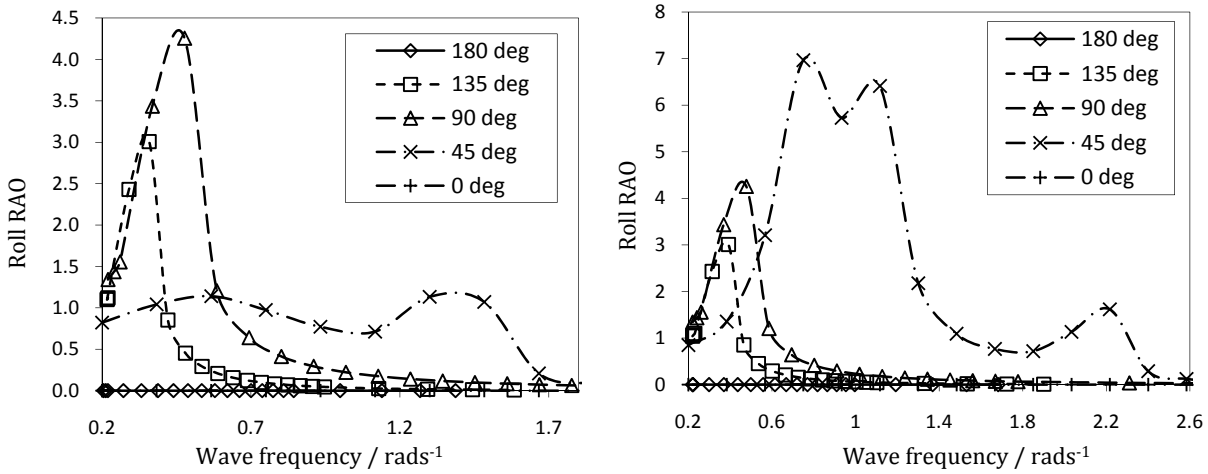

Figure I.2 – Roll RAO at 25 knots (left); and 15 knots (right)

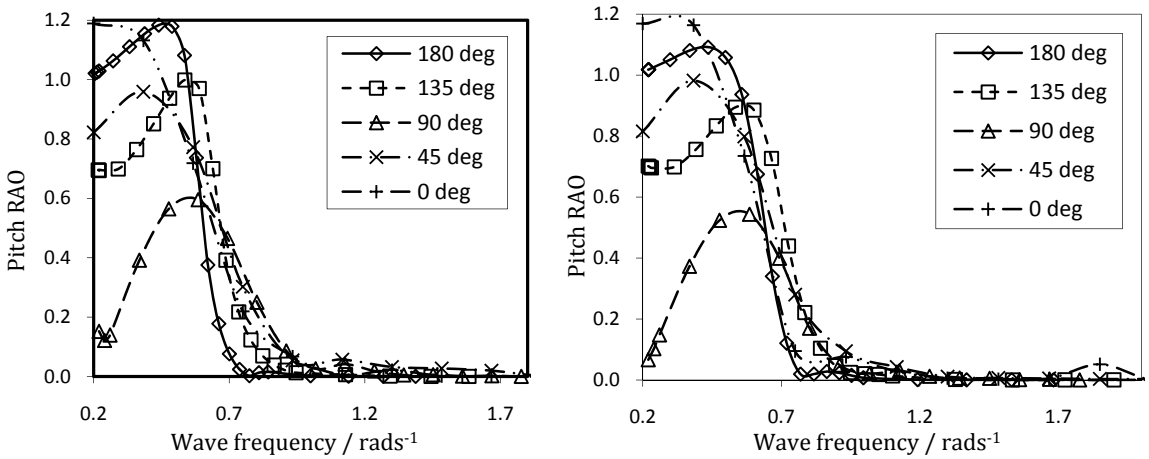

Figure I.3 – Pitch RAO at 25 knots (left); and 15 knots (right)

I.2 – Subjective motion (SM) polar plots

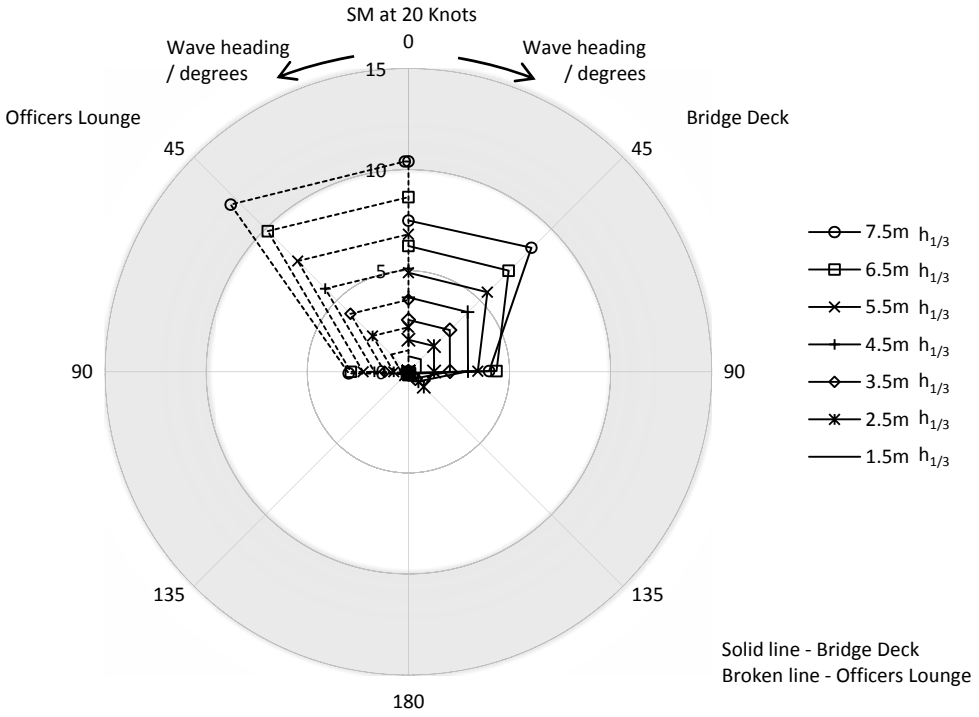

Figure I.4 – Polar plot of SM variation with wave heading height for the bridge deck and officers lounge at 20 knots for *Hull A*

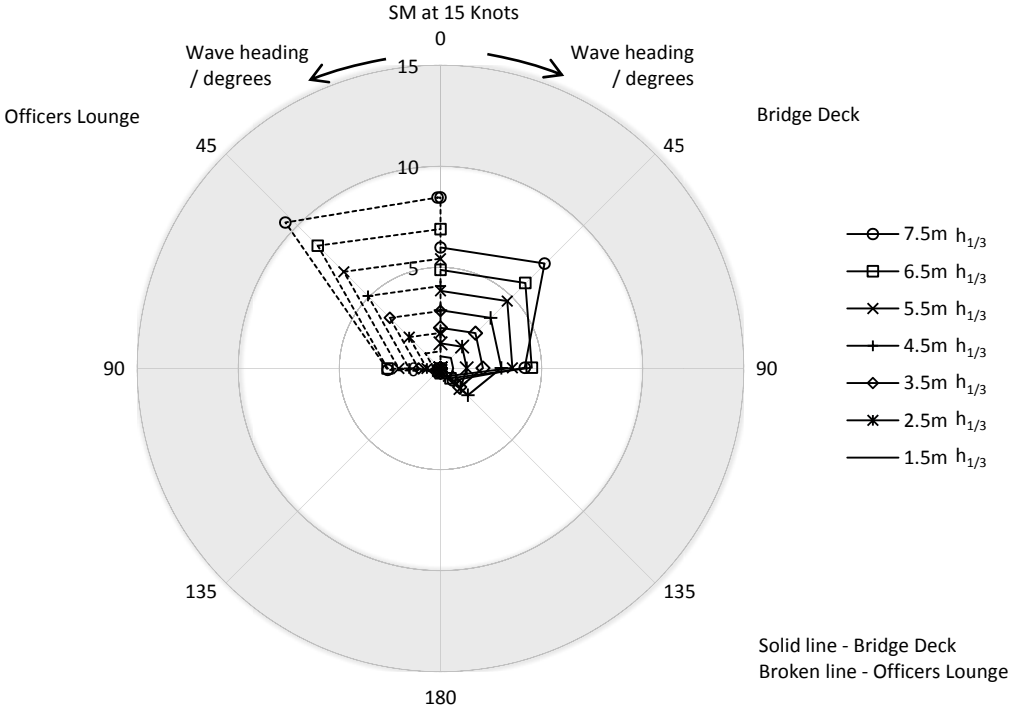

Figure I.5 – Polar plot of SM variation with wave heading height for the bridge deck and officers lounge at 15 knots for *Hull A*

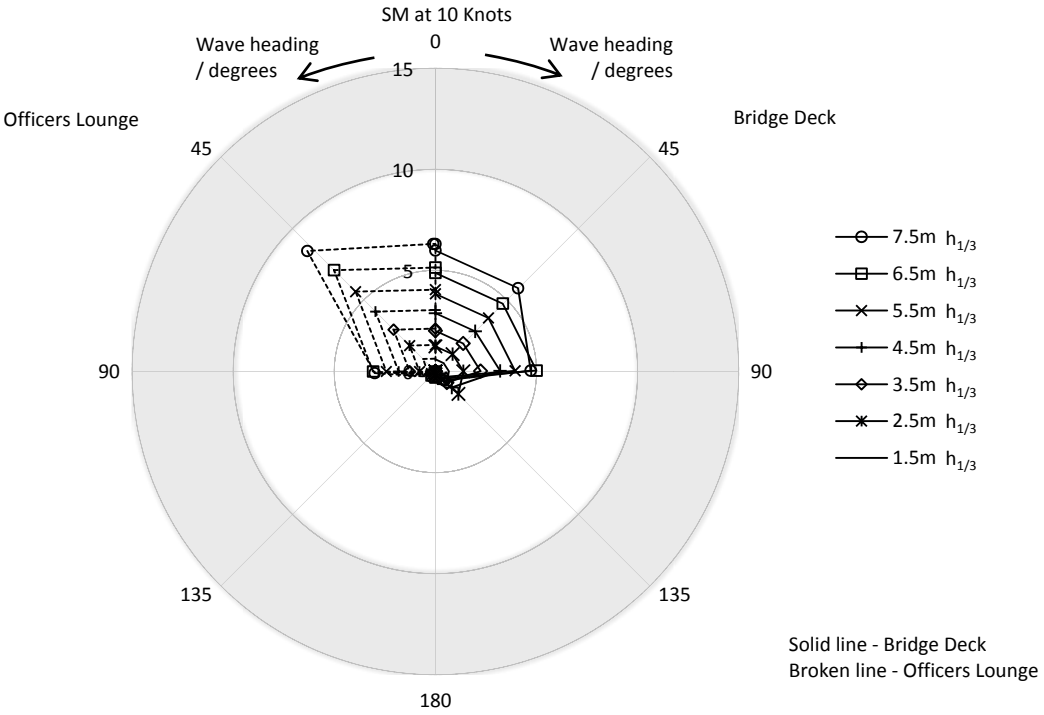

Figure I.6 – Polar plot of SM variation with wave heading height for the bridge deck and officers lounge at 10 knots for *Hull A*

Appendix J – Predicted Roll Damping

J.1 – Naked hull roll damping

Table J.1 – Roll damping time series

Time / s	*Peak angle /deg*	*Period / s*	*ξ*
12.13	25.67	14.48	0.043
26.61	18.74	14.43	0.043
41.04	13.68	14.53	0.043

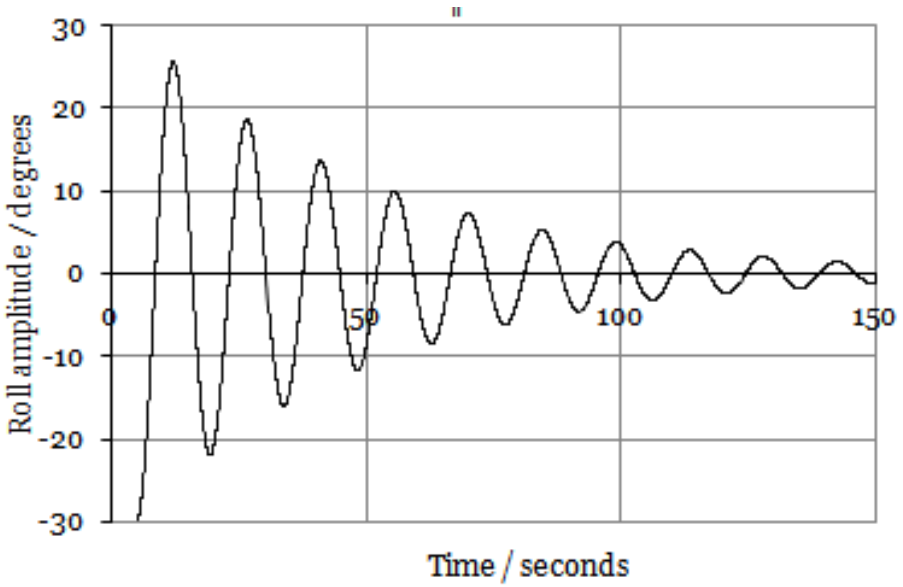

Figure J.1 – Roll decay curve

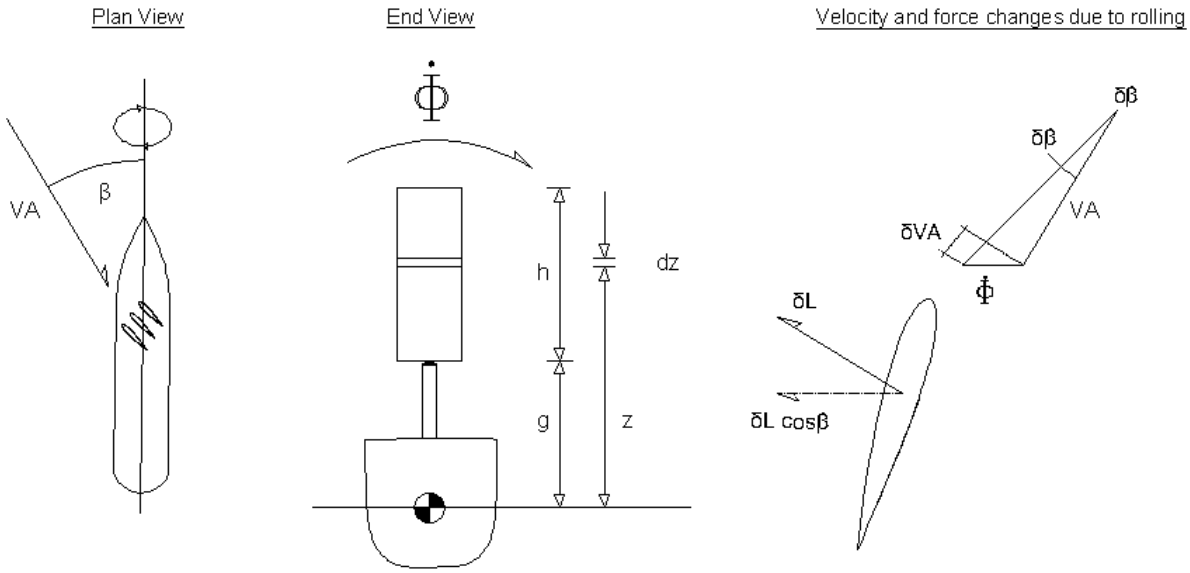

Figure J.2 – Frame of reference for roll damping calculations

J.2 – Lifting surface method

$$N_{\varphi Aa} = \frac{1}{2}\,\rho_A V_A c \int_{h0}^{h} \frac{dC_L}{d\alpha}(z) z^2\, cos\beta^2\, \delta z \tag{J.1}$$

$$N_{\varphi AV} = \frac{1}{2}\cdot\, V_A c \int_{h0}^{h} 2C_L(z)\, z^2\, cos\beta sin\beta\, \delta z \tag{J.2}$$

$$N_{\varphi A} = N_{\varphi AV} + N_{\varphi Aa} \tag{J.3}$$

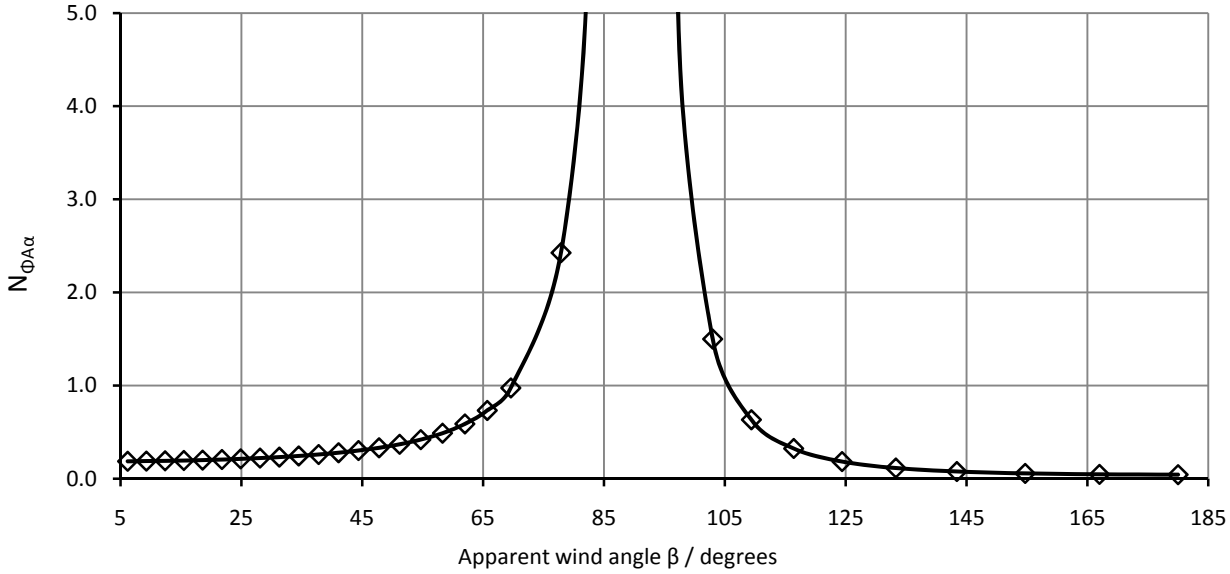

Figure J.3 – Variation in aerodynamic roll damping 'incidence changes' coefficient component with apparent wind angle

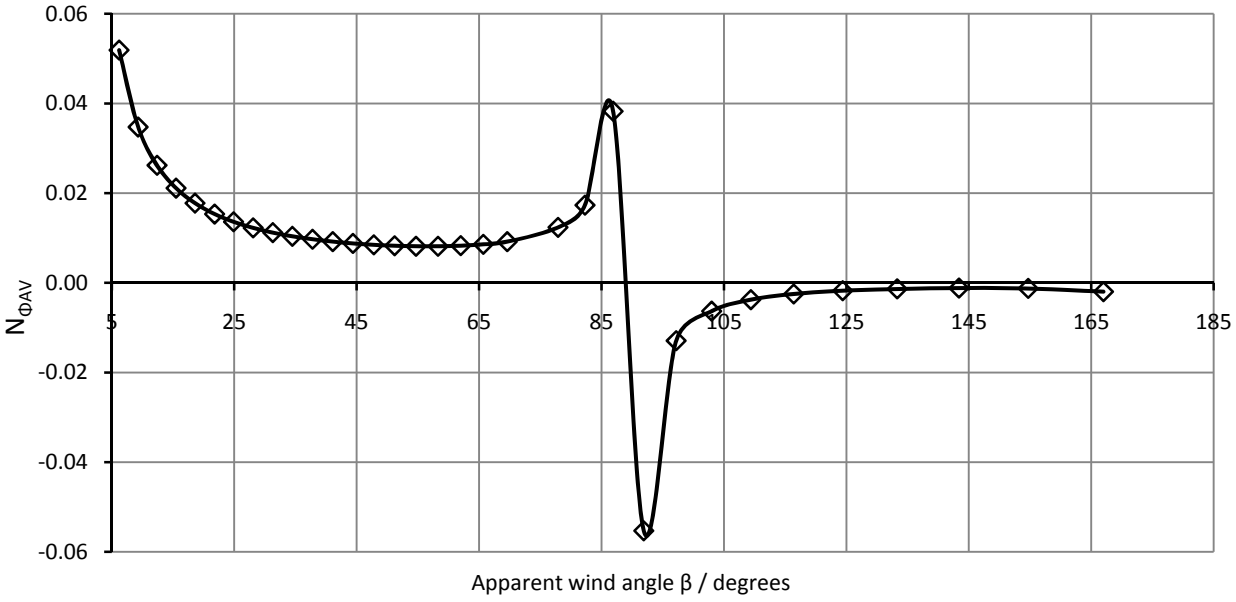

Figure J.4 – Variation in aerodynamic roll damping 'air speed changes' component with apparent wind angle

J.3 – Lifting line method

The components of roll damping were calculated based on a regression analysis of a 20 metre rectangular planform aerofoil. The components are given by

$$N_{\varphi Aa} = \frac{1}{2}\rho_A V_A c(g+h)^3 cos\beta^2 \cdot f(1) \tag{J.4}$$

and

$$N_{\varphi AV} = \frac{1}{2}\,\rho_A V_A c(g+h)^3 cos\beta \cdot sin\beta \cdot C_L f(2), \tag{J.5}$$

where $f(1)$ and $f(2)$ are a function of the span/air gap ratio. The total aerodynamic damping coefficient is found as:

$$N_{\varphi A} = N_{\varphi AV} + N_{\varphi Aa}\,. \tag{J.6}$$

J.4 – Control system

The calculated lift coefficient is subtracted from the operational lift coefficient to obtain the required margin to avoid stall:

$$C_L(z)|_{rolling} = C_L(z)|_{steady} + \frac{\delta C_L}{\delta \alpha}(z)\,\delta\alpha = C_L(z)|_{steady} + \frac{\delta C_L}{\delta \alpha}(z)\,\frac{\dot{\varphi} z}{V_A}|cos\beta|. \tag{J.7}$$

Appendix K – Structural Design

K.1 – Midship scantling calculations

Nomenclature

σ_A	Design bending stress
σ_{CRB}	Critical buckling stress
σ_E	Elastic buckling stress (from Part 3, Chapter 3, Section 7 of the Rules)

Arrangement

Table K.1 – Panel particulars derived from the NG254 basis ship

Panel No.	*Function*	*Panel length,*	*Vertical depth,*	*Height above base,*	*s*	t_P	*No. Stiffeners*	*Stiffener profile*
		/ m	*/ m*	*/ m*	*/ mm*	*/ mm*		*/ mm*
1	Keel	2.000	0.139	0.050	965	19.0	1	650 x 12 [1]
2	Bottom Shell	7.538	0.967	0.258	580	16.0	12	240 x 10
3	Bilge	5.749	4.738	3.078	575	16.0	9	240 x 10
4	Side Shell	2.627	2.599	7.047	525	15.0	4	220 x 10
5	Side Shell	2.602	2.593	9.641	434	12.5	5	180 x 8
6	Side Shell	2.492	2.491	12.185	498	12.5	4	180 x 8
7	Side Shell	2.629	2.629	14.745	438	18.0	5	180 x 10
8	Sheerstrake	2.911	2.911	17.515	485	20.0	5	200 x 11
9	Main Deck	1.708	-	18.970	342	20.0	4	200 x 11
10	Inner Hull	2.989	2.989	6.852	598	12.0	4	220 x 10
11	Inner Hull	2.593	2.593	9.643	432	10.0	5	180 x 8
12	Inner Hull	2.491	2.491	12.185	498	10.0	4	180 x 8
13	Inner Hull	2.629	2.629	14.745	438	16.0	5	180 x 10
14	Inner Hull	2.911	2.911	17.515	485	20.0	5	200 x 11
15	Bilge Box Top	2.188	-	5.358	547	10.0	3	200 x 10
16	Bilge Box Side	2.682	2.682	4.017	894	12.0	2	220 x 10
17	Inner Bottom	6.949	-	2.676	535	10.0	12	220 x 10
18	Inner Bottom	1.669	0.000	2.676	477	10.0	3	200 x 11
19	Duct Keel Side	2.602	2.602	1.375	651	15.0	3	220 x 10
20	Girder	1.895	1.895	1.729	632	12.0	2	220 x 10
21	Stringer	1.205	0.000	5.358	600	11.0	-	-
22	Stringer	1.308	0.000	7.949	436	10.0	2	200 x 11
23	Stringer	1.708	0.000	13.131	427	18.0	3	180 x 10
24	Stringer	1.708	0.000	16.359	342	20.0	4	200 x 11

Note 1 Keel stiffener is single flat bar positioned on centreline, all other profiles are Corus bulb flats.

Direct calculations

Table K.2 – Panel plating design stresses for the midship section

Panel No.	σ_{local} / Nmm^{-2}	I_{y_i} / m^4	σ_{Design} / Nmm^{-2}	*Panel No.*	σ_{local} / Nmm^{-2}	I_{y_i} / m^4	σ_{Design} / Nmm^{-2}
1	137.5	2.600	242.1	13	-	2.509	90.6
2	125.5	9.391	227.4	14	-	6.672	127.3
3	116.5	3.074	180.9	15	93.3	0.195	127.4
4	64.1	0.068	75.7	16	112.3	0.603	164.2
5	39.1	0.147	61.9	17	99.0	2.875	168.7
6	38.5	0.722	95.0	18	78.8	0.650	148.5
7	13.6	2.757	104.2	19	36.9	2.076	123.9
8	12.0	6.672	139.4	20	95.6	1.105	177.9
9	0.0	5.513	146.7	21	174.4	0.087	208.5
10	145.5	0.090	159.8	22	-	0.000	0.3
11	67.4	0.124	90.2	23	-	1.016	69.1
12	41.0	0.606	97.6	24	-	3.214	112.0

Rule calculations

Rule checks for buckling strength of plate strakes and stiffeners were conducted in accordance with Part 3, Chapter 4, Section 7 of the Rules. The Design bending stress σ_A was calculated by means of Equation (K.1), and critical buckling stresses σ_{CRB} by Equation (K.2).

$$\sigma_A = \sigma_D + \frac{z_i}{z_D}, \text{ for structural members above the neutral axis, or}$$
$$\sigma_A = \sigma_B + \frac{z_i}{z_B}, \text{ for structural members below the neutral axis} \quad \text{(K.1)}$$

$$\sigma_{CRB} = \sigma_0\left(1 - \frac{\sigma_0}{4\sigma_E}\right) \; if \; \sigma_E > \frac{\sigma_0}{2}, otherwise \; \sigma_{CRB} = \sigma_E, \quad \text{(K.2)}$$

Table K.3 – Rule buckling checks for panel plate and longitudinal stiffeners

		Plate Buckling		*Stiffener Buckling*			
Panel No.	*Design* σ_A / *Nmm*$^{-2}$	*Elastic* σ_{CRB} / *Nmm*$^{-2}$		*Elastic* σ_{CRB} / *Nmm*$^{-2}$	*Torsion* σ_{CRB} / *Nmm*$^{-2}$	*Web* σ_{CRB} / *Nmm*$^{-2}$	
1	187.3	219.7	PASS	347.2	348.7	224.2	PASS
2	182.4	282.1	PASS	295.4	308.8	330.3	PASS
3	114.7	275.6	PASS	300.2	315.1	337.5	PASS
4	41.7	247.6	PASS	318.3	310.2	334.2	PASS
5	41.7	281.8	PASS	297.6	315.0	334.6	PASS
6	51.3	258.4	PASS	293.7	313.0	334.6	PASS
7	81.6	280.3	PASS	277.5	318.4	340.4	PASS
8	114.5	327.3	PASS	271.7	329.7	340.6	PASS
9	131.8	341.3	PASS	286.9	330.9	340.6	PASS
10	41.7	216.0	PASS	316.3	310.4	334.2	PASS
11	41.7	193.1	PASS	306.1	300.1	334.6	PASS
12	51.3	146.4	PASS	303.7	296.0	334.6	PASS
13	81.6	242.1	PASS	283.9	309.7	336.2	PASS
14	114.5	327.3	PASS	271.7	329.7	340.6	PASS
15	60.1	158.6	PASS	270.9	299.2	325.7	PASS
16	92.2	92.8	PASS	224.4	264.9	325.7	PASS
17	124.4	166.1	PASS	331.6	274.1	319.6	PASS
18	124.4	204.1	PASS	328.9	282.4	330.6	PASS
19	155.6	174.4	PASS	288.3	292.3	340.6	PASS
20	147.1	185.5	PASS	284.0	295.2	334.6	PASS
21	60.1	202.1	PASS	-	-	-	-
22	41.7	190.2	PASS	284.1	299.3	325.7	PASS
23	62.5	196.9	PASS	284.7	298.1	325.7	PASS
24	100.8	341.3	PASS	286.9	331.3	340.6	PASS

TYPICAL WATERTIGHT BULKHEAD AMIDSHIPS

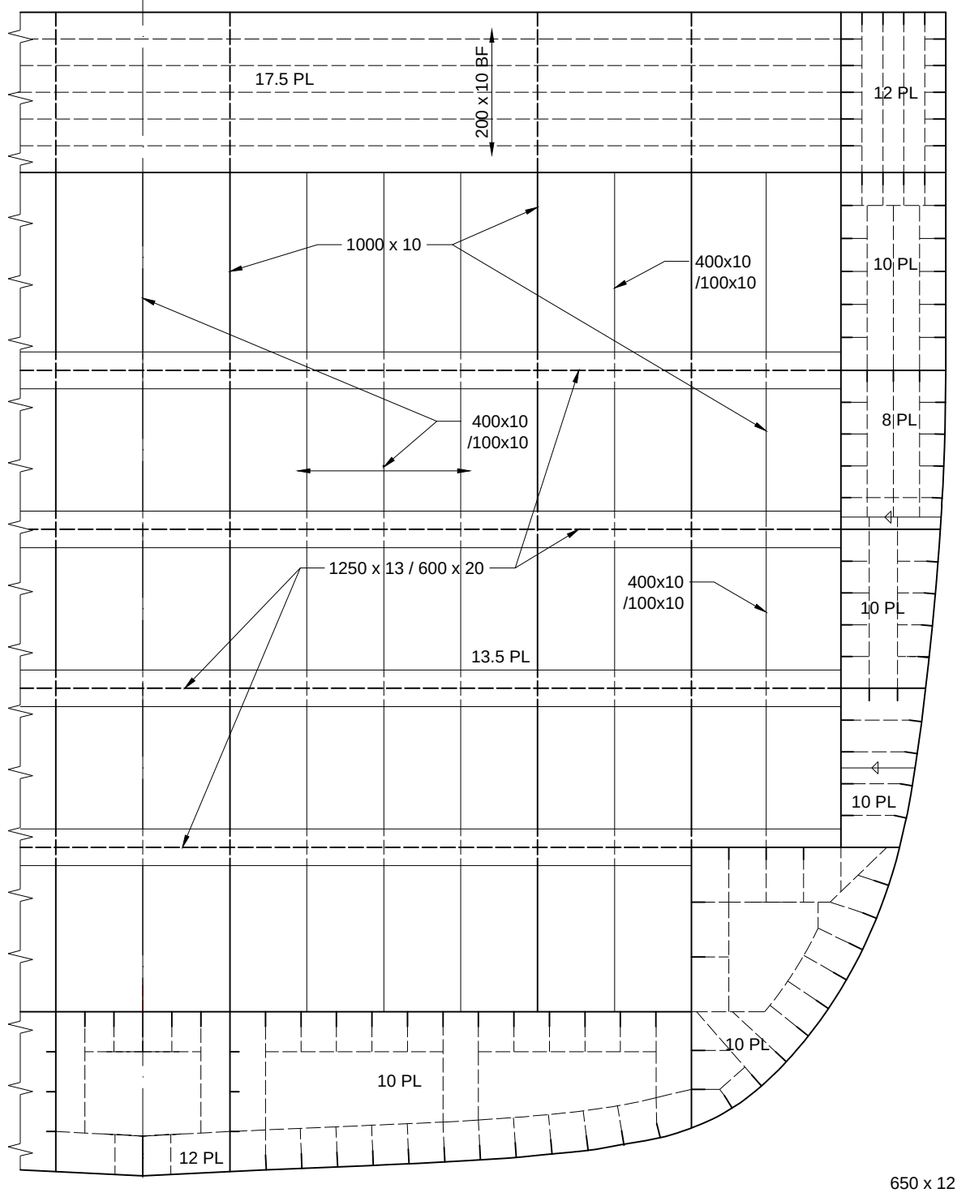

TYPICAL FRAME AMIDSHIPS

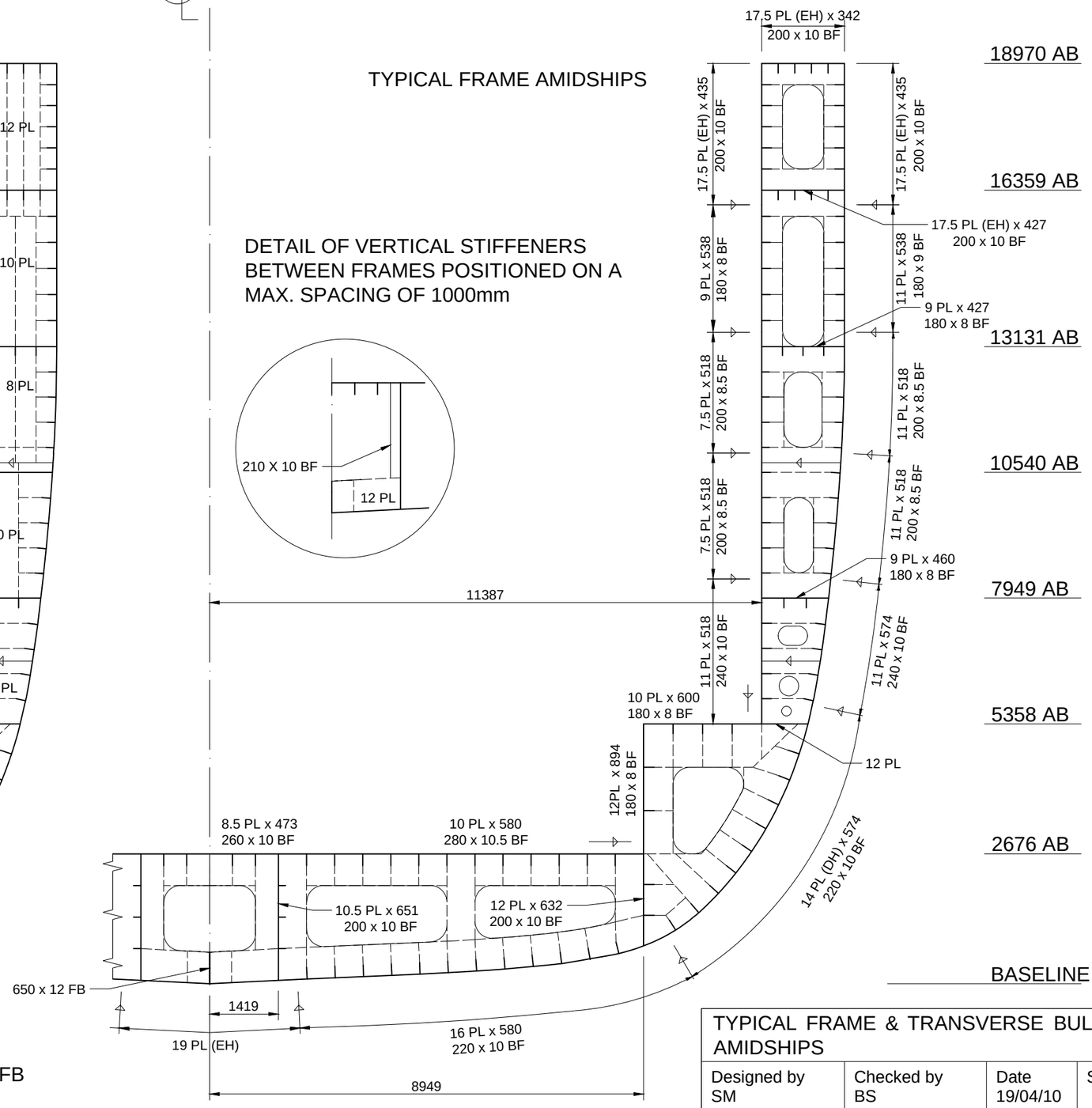

DETAIL OF VERTICAL STIFFENERS BETWEEN FRAMES POSITIONED ON A MAX. SPACING OF 1000mm

ALL UNMARKED TRANSVERSE STIFFENING 100 x 10 FB

FB - FLAT BAR
BF - CORUS SHIPBUILDING FLAT BAR
ALL STEEL LR GRADE H36, YIELD STRESS 355 N/mm²

TYPICAL FRAME & TRANSVERSE BULKHEAD AMIDSHIPS			
Designed by SM	Checked by BS	Date 19/04/10	Scale 1:100
APPENDIX K.2		Edition A	Sheet 1 of 2

UNIVERSITY OF Southampton
School of Engineering Sciences
University of Southampton
University Road
Highfield
Southampton
SO17 1BJ

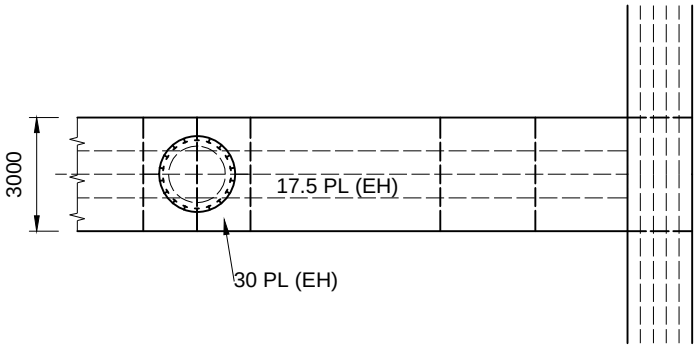

MAST STIFFENER
(CUSTOM SECTION)

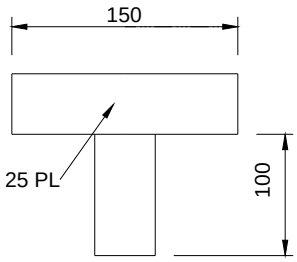

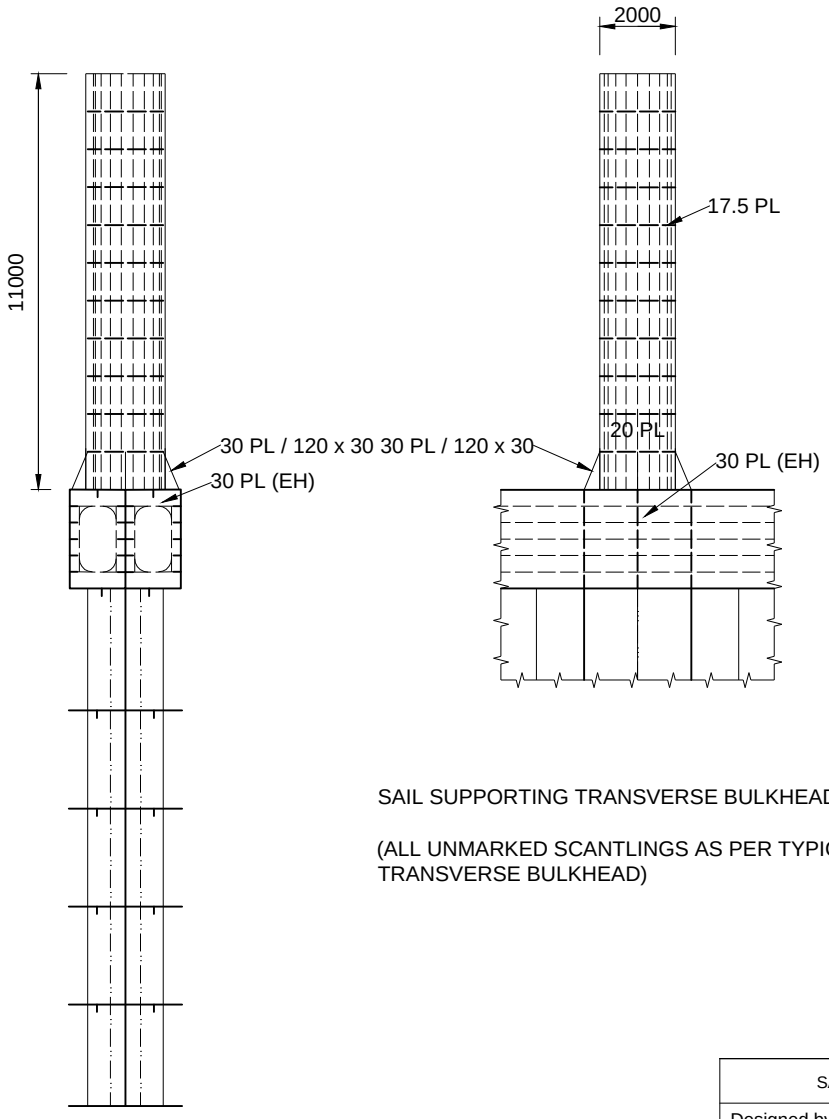

SAIL SUPPORTING TRANSVERSE BULKHEAD

(ALL UNMARKED SCANTLINGS AS PER TYPICAL TRANSVERSE BULKHEAD)

SAIL MAST AND SUPPORTING BULKHEAD			
Designed by BS	Checked by SM	Date 19/04/10	Scale 1:200
APPENDIX K.2		Edition A	Sheet 2 of 2
UNIVERSITY OF Southampton School of Engineering Sciences	University of Southampton University Road Highfield Southampton SO17 1BJ		

K.3 – Global strength

Nomenclature

Π	Longitudinal structural area normalised to amidships

Hull mass estimate

The structural area distribution factor used to calculate the hull coffin diagram is shown in Table K.4, along with the assumed structural element extents from which it is derived. The tapered factor is obtained by applying the thickness taper ratios from Part 3, Chapter 3, Section 2 of the Rules.

Table K.4 – Assumed extent of major structural elements along the length of the ship and structural distribution factor

x / m	Shell Girth / m	Deck Beam / m	Inner Hull Depth / m	Bottom Breadth / m	Π	Π_{Taper}
-2.98	38.71	6.60	7.21		0.464	0.317
0.00	39.30	6.60	9.70		0.491	0.343
4.00	40.41	6.60	10.14		0.505	0.365
8.01	42.40	6.60	10.49	0.00	0.526	0.394
12.01	53.42	6.60	11.08	9.68	0.714	0.543
16.01	53.63	6.60	16.06	10.94	0.771	0.603
24.02	52.92	6.60	16.06	13.45	0.787	0.656
32.02	51.90	6.60	21.25	15.97	0.846	0.750
40.03	52.39	6.60	27.23	18.49	0.925	0.872
48.03	54.07	6.60	27.23	19.80	0.952	0.952
64.04	56.43	6.60	27.23	22.42	0.996	0.996
80.05	56.89	6.60	27.23	22.42	1.000	1.000
96.06	55.04	6.60	27.23	22.42	0.984	0.984
112.07	50.19	6.60	27.23	19.91	0.919	0.919
120.08	48.45	26.19	24.09	17.55	1.028	0.963
128.08	47.55	26.19	24.09	15.20	0.999	0.874
136.09	46.91	26.19	24.09	12.84	0.973	0.791
144.09	46.71	25.23	11.08	4.76	0.776	0.591
148.09	46.63	23.58	10.26	4.76	0.753	0.553
152.10	46.23	20.89	9.24	4.76	0.717	0.509
156.10	45.48	17.48	8.09	4.76	0.670	0.460
160.10	45.39	12.99	6.66	4.76	0.617	0.414
170.40	0.00	0.00	0.00	0.00	0.000	0.317

Load conditions

The load conditions used in the global strength analysis were based on those required by the IMO Intact Stability Code IMO (2008b) as they most adequately represented the likely behaviour of the ship. These consisted of fully loaded and ballast conditions, modelled at both departure (with full stores and fuel) and arrival (with 10% stores and fuel remaining). Subject to propeller immersion and restrictions on maximum draught, the load conditions were ballasted to attain suitable trim.

Table K.5 – Lightship mass distribution (including crew and stores)

Item	*Quantity*	*Unit Mass / tonnes*	*Total Mass / tonnes*	*Long. Arm / m*	*Vert. Arm / m*
Fwd Sail	1	14.00	14.00	79.290	43.470
Aft Sail	1	14.00	14.00	23.315	43.470
Fwd mast	1	18.00	18.00	79.290	24.470
Aft mast	1	18.00	18.00	23.315	24.470
Crew	1	1.8.00	1.80	0.000	0.000
Stores	1	50.00	50.00	147.480	20.650
Accom. Tier 1	1	93.35	93.35	148.480	20.650
Accom. Tier 2	1	91.72	91.72	145.440	23.241
Accom Tier 3.	1	85.17	85.17	142.830	25.832
Accom Tier 4	1	86.80	86.80	139.660	28.423
Accom Tier 5	1	65.51	65.51	136.480	31.014
Crane	1	126.00	126.00	125.730	0.000
Crane	1	126.00	126.00	115.200	0.000
Pod propulsion module	1	78.00	78.00	0.000	4.500
Steering Module	1	44.0	44.00	0.000	11.700
Slip Ring Unit	1	3.00	3.00	-1.130	11.700
Cooling Air Unit	1	7.00	7.00	2.500	11.700
Hydraulic Power Unit	1	4.50	4.50	2.500	11.700
Oil Treatment Unit	1	0.60	0.60	2.500	11.700
GTU+AIU+LBU+ACU	1	0.50	0.50	2.500	11.700
Pod propeller	1	5.00	5.00	3.700	4.000
Shaft propeller	1	5.00	5.00	6.290	4.000
Refrigeration system	1	81.00	81.00	130.000	12.900
Shaft motor	1	6.50	6.50	16.740	4.000
Shaft/m	1	0.77	0.77	10.000	4.000
Bow Thruster	1	7.50	7.50	137.780	2.767
Aft Engine	2	93.00	186.00	118.400	12.930
Forward Engine	2	148.00	296.00	133.740	12.940
Misc. engine weight	1	641.00	641.00	133.740	12.90
Weight margin	1	135.50	135.50	160.000	15.290
Hull mass	1	4577.02	4577.02	80.430	11.510
Anchors	2	4.32	8.64	164.100	0.000
Chain	1	36.93	36.93	164.100	0.000

Table K.6 – Tank mass distribution for each loading condition (for tank names and positions see the general arrangement, Appendix M)

		Full load departure		*Full load arrival*		*Ballast departure*		*Ballast arrival*	
Tank	*Unit Mass / tonnes*	*Quantity*	*Mass / tonnes*	*Quantity*	*Mass / tonnes*	*Quantity*	*Mass / tonnes*	*Quantity*	*Mass / tonnes*
FW	329.112	98%	322.530	9%	29.620	98%	322.530	9%	29.620
LNG 1	123.643	98%	121.170	9%	11.128	98%	121.170	9%	11.128
LNG 2	273.418	98%	267.950	9%	24.608	98%	267.950	9%	24.608
LOT	50.437	98%	49.428	9%	4.539	98%	49.428	9%	4.539
FPT	407.295	98%	399.149	98%	399.149	0%	0.000	98%	399.149
DBT 1	167.432	10%	16.744	98%	164.084	0%	0.000	98%	164.080
DBT 2	355.310	0%	0.000	0%	0.000	98%	348.200	98%	348.200
TS 1	192.236	0%	0.000	0%	0.000	0%	0.000	98%	188.390
LWT 1	625.370	0%	0.000	0%	0.000	98%	612.860	98%	612.860
DBT 3	532.754	0%	0.000	98%	522.098	98%	522.100	98%	522.100
LWT 2	281.832	0%	0.000	0%	0.000	98%	276.200	98%	276.200
TS 2	316.282	0%	0.000	0%	0.000	0%	0.000	0%	0.000
DBT 4	494.182	0%	0.000	0%	0.000	98%	484.300	98%	484.300
LWT 3	271.502	0%	0.000	0%	0.000	98%	266.070	98%	266.070
TS 3	297.024	0%	0.000	0%	0.000	0%	0.000	0%	0.000
DBT 5	445.340	0%	0.000	0%	0.000	98%	436.430	98%	436.430
LWT 4	192.336	0%	0.000	0%	0.000	98%	188.490	98%	188.490
TS 4	280.386	0%	0.000	0%	0.000	0%	0.000	0%	0.000
DBT 6	303.812	0%	0.000	0%	0.000	98%	297.740	98%	297.740
LWT 5	814.392	0%	0.000	0%	0.000	98%	798.100	98%	798.100
TS 5	234.908	0%	0.000	0%	0.000	98%	230.210	98%	230.210
DBT 7	143.300	0%	0.000	0%	0.000	98%	140.430	98%	140.430
LWT 6	1305.876	0%	0.000	0%	0.000	98%	1279.800	98%	1279.800
TS 6	187.594	0%	0.000	0%	0.000	98%	183.840	98%	183.840
DBT 8	104.681	0%	0.000	0%	0.000	98%	102.588	98%	102.588
LWT 7 P	187.026	0%	0.000	0%	0.000	98%	183.285	98%	183.285
LWT 7 S	187.026	0%	0.000	0%	0.000	98%	183.285	98%	183.285
	374.052	0%	0.000	0%	0.000	98%	366.570	98%	366.570
APT	277.829	0%	0.000	0%	0.000	98%	272.272	98%	272.272
Total	9756.400		1177		1155.2		7933.800		7994.300

Table K.7 – Full load cargo mass distribution (zero cargo mass assumed in ballast condition)

Item	*Mass / tonnes*	*Long. Arm / m*	*Ver. Arm / m*
Hold 10	677	5.302	10.582
Hold 9	1054	18.742	9.468
Hold 8	1284	34.012	8.853
Hold 7	1484	47.542	8.237
Hold 6	1692	61.062	7.621
Hold 5	1734	74.582	7.621
Hold 4	1773	89.932	7.621
Hold 3	1442	103.532	8.853
Hold 2	809	117.142	10.470
Hold 1	418	127.672	20.212

K.4 – FE midship section model results

Hull strength results

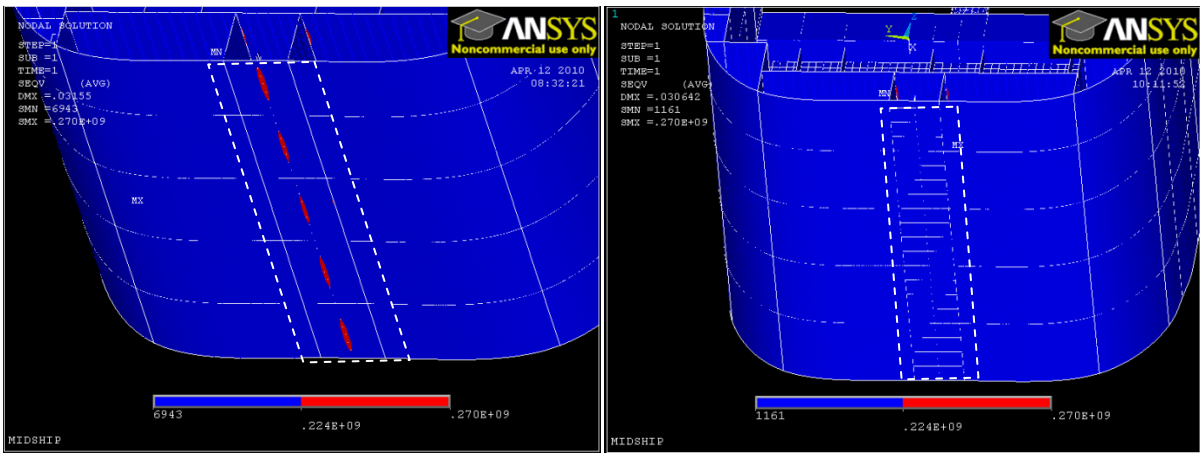

Figure K.1 – High stress region in the bottom shell that do not meet the acceptance criteria of Table 7.18 in the initial analysis (left); and the modified analysis (right) for the still water condition

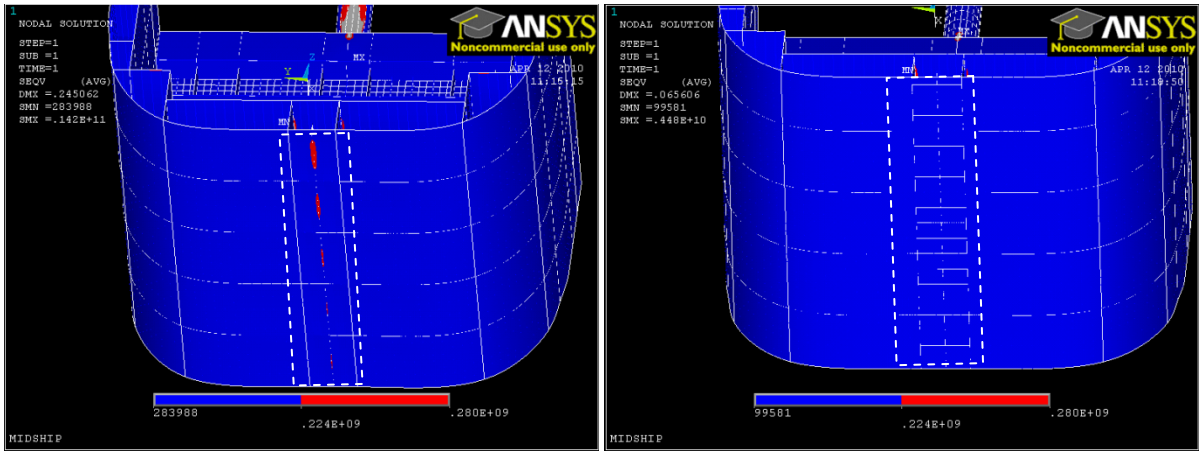

Figure K.2 – High stress region in the bottom shell that do not meet the acceptance criteria of Table 7.18 in the initial analysis (left); and the modified analysis (right) for the head seas condition

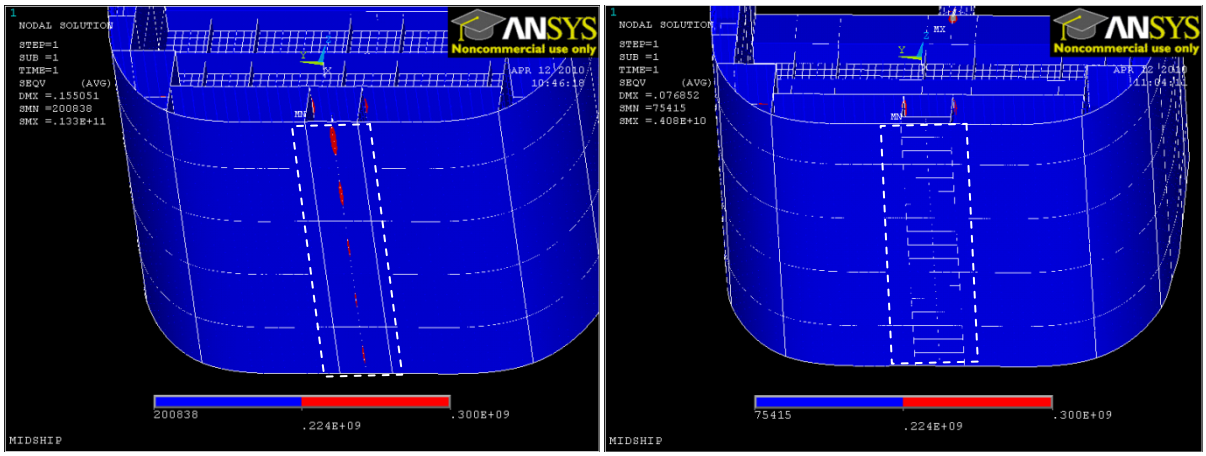

Figure K.3 – High stress region in the bottom shell that do not meet the acceptance criteria of Table 7.18 in the initial analysis (left); and the modified analysis (right) for the oblique seas condition

Mast Strength Results

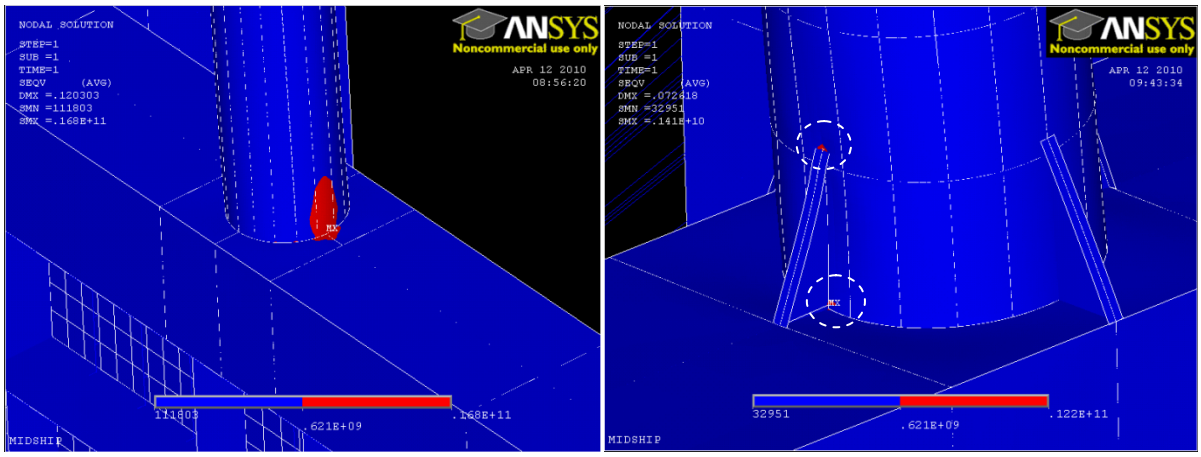

Figure K.4 – Stress in the fine mesh zone at the base of the mast which does not meet the acceptance criteria of Table 7.19 for the initial analysis (left); and the modified analysis in the beam seas condition

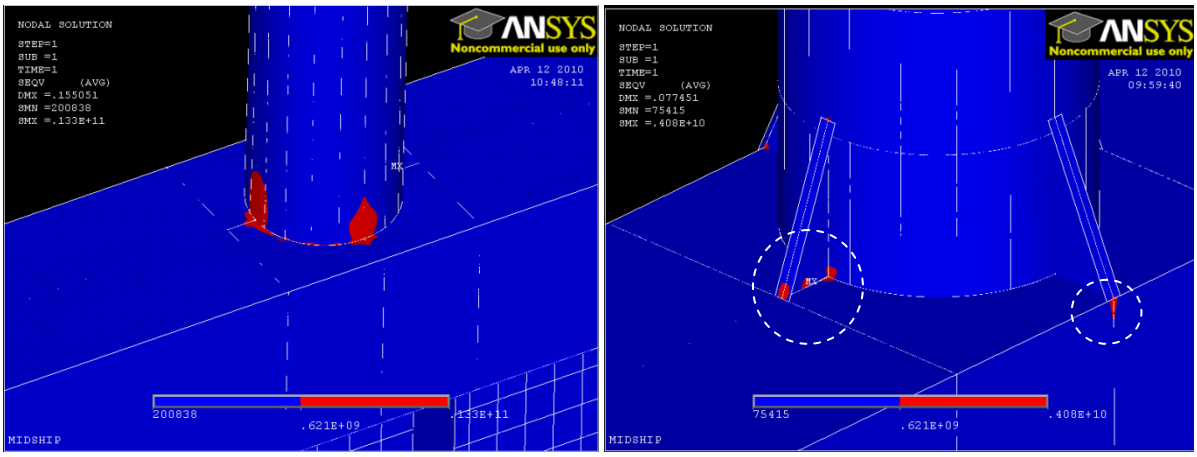

Figure K.5 – Stress in the fine mesh zone at the base of the mast which does not meet the acceptance criteria of Table 7.19 for the initial analysis (left); and the modified analysis in the oblique seas condition

Appendix L – Stability

L.1 – Stability model definition

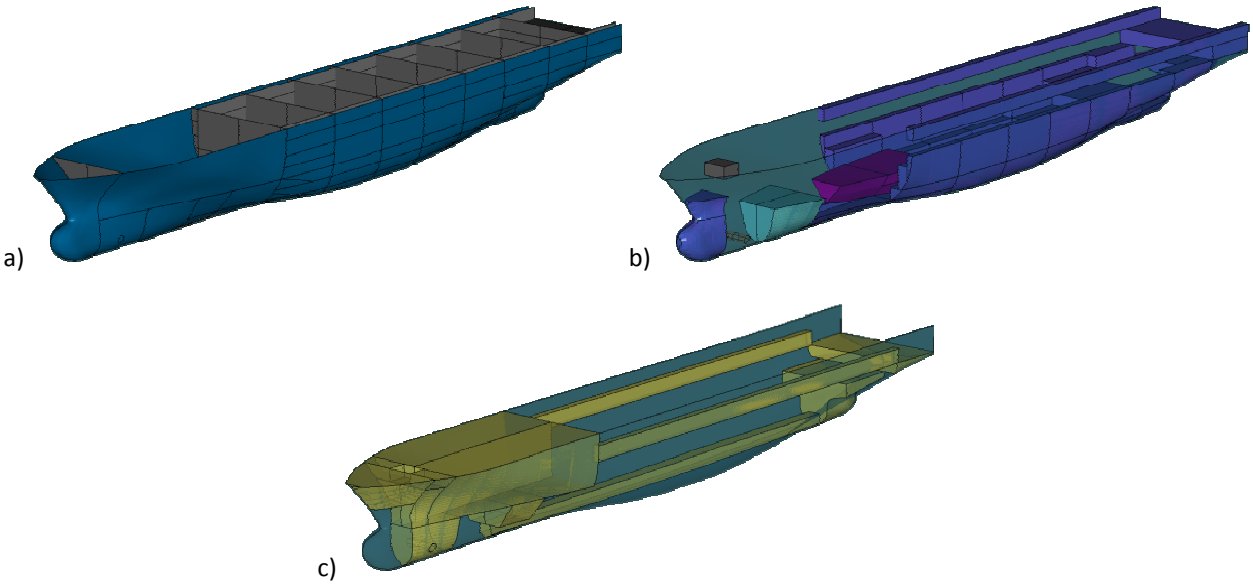

Figure L.1 – Stability model used in the analysis (refer to Appendix M for arrangement and function of spaces), showing: (a) distribution of internal subdivision; (b) disposition of tank spaces; and (c) allocation of internal compartments

L.2 – Intact stability

Nomenclature

Nomenclature pertinent to appendix. Other parameters defined in principal nomenclature or report text.

B_D	Moulded breadth	m	d	Mean draught.	m
B_m	Breadth of ship on the waterline at half mean draught.	m	h_H	Mean height of hatch coamings within $L/4$ forward and aft of amidships.	m
b_H	Mean width of hatch coamings within $L/4$ forward and aft of amidships .	m	l_H	Length of each hatch coaming within $L/4$ forward and aft of amidships.	m
C	Form factor for GZ.		KG_{cor}	Height of centre of mass above base, corrected for free surface effect, not to be taken as less than d.	m
D'	Moulded depth of the ship, corrected for defined parts of volumes within the hatch coamings.	m	L	Length of ship.	m

Calculation of coefficients

Table L.1 – Summary of values used in intact stability analysis

$d\ /\ m$	9.482
D/m	18.970
$b_H\ /\ m$	0.000
$h\ /\ m$	0.000
$B_D\ /\ m$	26.190
$l_H\ /\ m$	0.000
$L\ /\ m$	159.890
$KG_{cor}\ /\ m$	9.760
C_B	0.551
C_{WP}	0.806
$B/\ m$	25.847
$B_m\ /\ m$	24.420

Moulded depth is calculated as

$$D' = D + h\left(\frac{2b - B_D}{B_D}\right)\left(\frac{2\sum l_H}{L}\right) = 18.97. \quad \text{(L.1)}$$

The form factor is thus derived:

$$C = \frac{dD'}{{B_m}^2}\sqrt{\frac{d}{KG}}\left(\frac{C_B}{C_{WP}}\right)^2\sqrt{\frac{1000}{L}} = 0.109916. \quad \text{(L.2)}$$

GZ curves

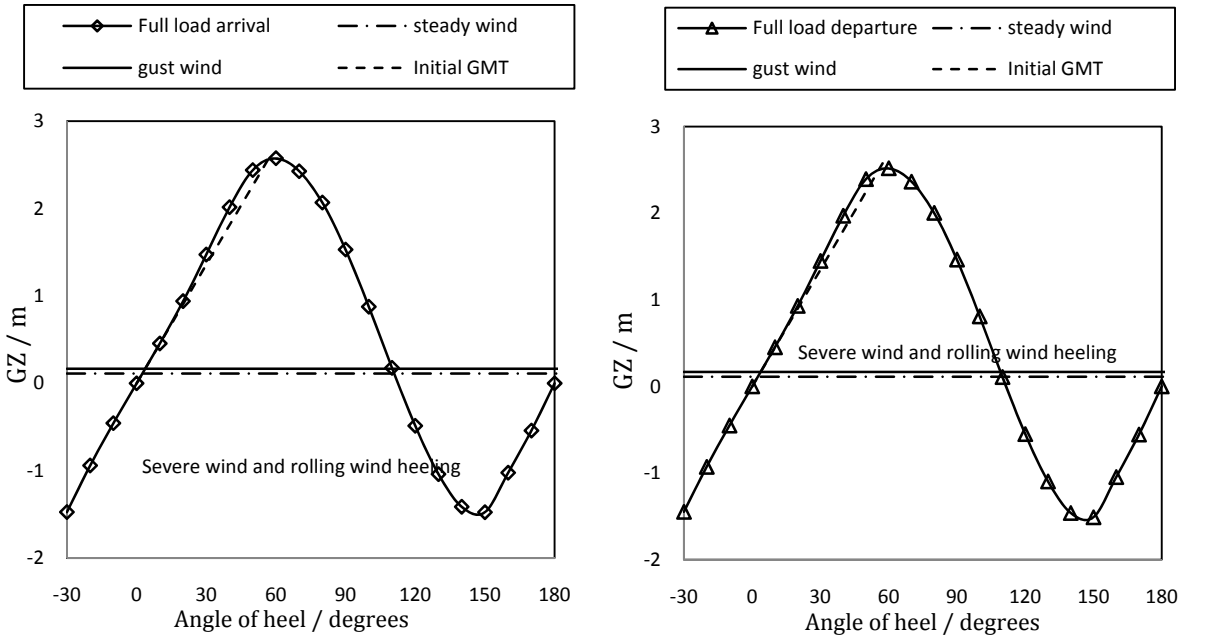

Figure L.2 – Full load departure (left) and arrival (right) GZ curves

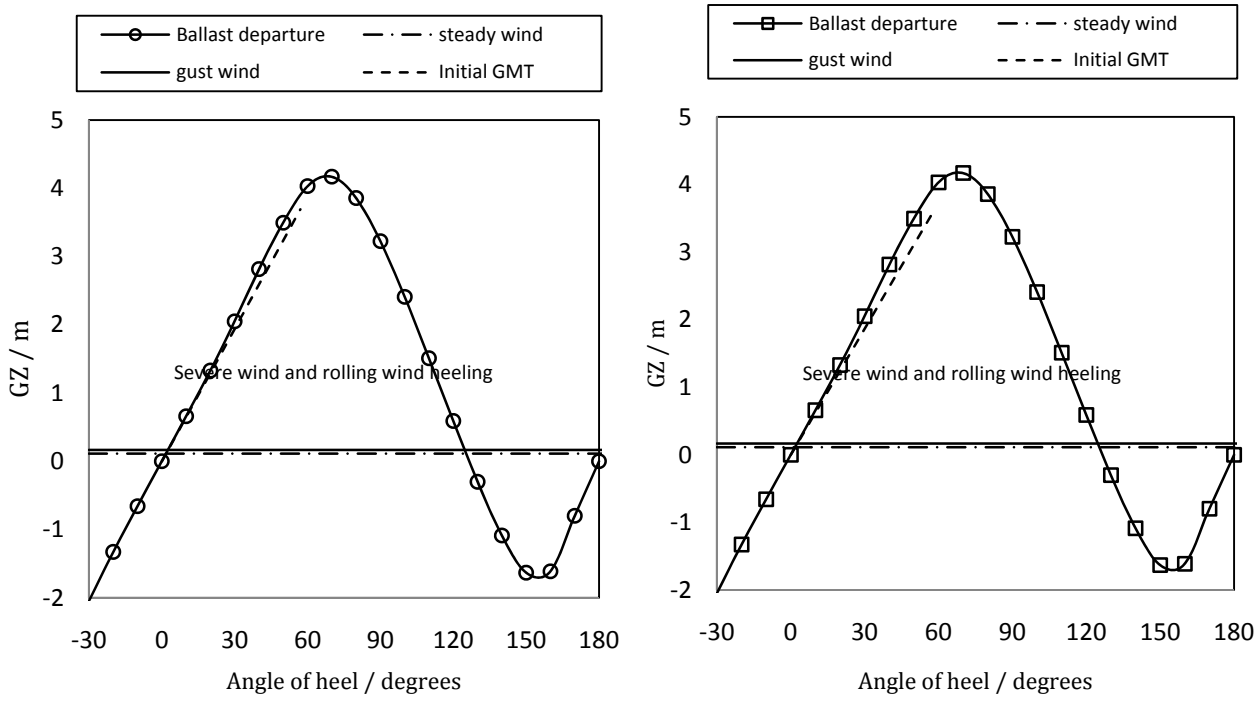

Figure L.3 – Ballast departure (left) and arrival (right) GZ curves

Table L.2 – Intact stability results summary, applying IMO A.749(18) Ch3 and 4.9 code

Code				*Full load departure*		*Full load arrival*		*Ballast departure*		*Ballast arrival*		*Status*
A.749(18) Ch3 - Design criteria applicable to all ships	*Value*		*Unit*	*Actual*	*Margin/ %*	*Actual*	*Margin/ %*	*Actual*	*Margin/ %*	*Actual*	*Margin/ %*	
3.1.2.1: Area 0 to 30	≥	3.1513	m.deg	21.8192	592.39	20.4465	548.83	30.4195	865.30	27.7395	780.26	Pass
3.1.2.1: Area 0 to 40	≥	5.1566	m.deg	39.6537	668.99	37.3356	624.04	55.2814	972.05	50.4755	878.85	Pass
3.1.2.1: Area 30 to 40	≥	1.7189	m.deg	17.8346	937.56	16.8892	882.56	24.8619	1346.38	22.736	1222.71	Pass
3.1.2.2: Max GZ at 30 or greater	≥	0.2	m	2.584	1192.00	2.484	1142.00	4.213	2006.50	3.916	1858.00	Pass
3.1.2.3: Angle of maximum GZ	≥	25	deg	58.20	132.80	59.10	136.40	67.300	169.20	67.300	169.20	Pass
3.1.2.4: Initial GMt	≥	0.15	m	2.687	1691.33	2.514	1576.00	3.773	2415.33	3.431	2187.33	Pass
3.2.2: Severe wind and rolling Criteria												
Angle of steady heel	≤	16	deg	2.20	86.25	2.40	85.00	2.30	85.63	2.60	83.75	Pass
Angle of steady heel / Deck edge immersion angle	≤	80	%	12.37	84.54	13.06	83.67	8.62	89.22	9.55	88.06	Pass
Area1 / Area2	≥	100	%	497.48	397.48	492.17	392.17	486.43	386.43	472.63	372.63	Pass
4.9 Container ships larger than 100m												
4.9.2.1: Area to 30	≥	4.6925	m.deg	21.8192	364.98	20.4465	335.73	30.4195	548.26	27.7395	491.15	Pass
4.9.2.1: Area 0 to 40	≥	8.3423	m.deg	39.6537	375.33	37.3356	347.55	55.2814	562.66	50.4755	505.05	Pass
4.9.2.2: Area 30 to 40	≥	3.1283	m.deg	17.8346	470.11	16.8892	439.88	24.8619	694.74	22.7360	626.78	Pass
4.9.2.3: Maximum GZ at 30 or greater	≥	0.3	m	2.5840	761.33	2.4840	728.00	4.2130	1304.33	3.9160	1205.33	Pass
4.9.2.4: Value of maximum GZ	>	0.382	m	2.5840	576.44	2.4840	550.26	4.2130	1002.88	3.9160	925.13	Pass
4.9.2.5: Area under GZ curve to downflooding	>	15.114	m.deg	172.032	1038.19	161.743	970.11	308.705	1942.43	276.85	1731.69	Pass

L.3 – Damage stability

Nomenclature

Nomenclature pertinent to appendix. All other parameters defined in principal nomenclature or report text.

j	Damage zone number	$r(x1_j, x2_j, b_k)$	Reduction factor based on longitudinal subdivision
$x1$	Aft extent of damage zone	θ_e	Equilibrium heel angle for damage case
$x2$	Forward extend of damage zone	θ_v	Downflooding heel angle for damage case
$p(x1_j, x2_j)$	Probability of damage based on transverse subdivision	GZ_{max}	Maximum positive righting lever up to angle θ_v
k	Longitudinal bulkhead number in from shell, $k = 0$ at shell	$r(x1_j, x2_j, b_k)$	Reduction factor based on longitudinal subdivision
b	Distance from sideshell to longitudinal bulkheads in zone *j*		

Calculation of p_i

The probability p_i for a particular damage case is calculated by either

$$p_i = p(x1_j, x2_j) \times \left[r\left(x1_j, x2_j, b_k\right) - r\left(x1_j, x2_j, b_{k-1}\right)\right] \tag{L.3}$$

when the damage involves a single zone, or

$$\begin{aligned} p_i = p\left(x1_j, x2_{j+1}\right) \times \left[r\left(x1_j, x2_{j+1}, b_k\right) - r\left(x1_j, x2_{j+1}, b_{k-1}\right)\right] \\ -p\left(x1_j, x2_j\right)\left[r\left(x1_j, x2_j, b_k\right) - r\left(x1_j, x2_j, b_{k-1}\right)\right] \\ -p\left(x1_{j+1}, x2_{j+1}\right) \times \left[r\left(x1_{j+1}, x2_{j+1}, b_k\right) - r\left(x1_{j+1}, x2_{j+1}, b_{k-1}\right)\right] \end{aligned} \tag{L.4}$$

if the damage involves two adjacent damage zones. In all cases, $r(x1, x2, b_0) = 0$.

Values of and $p(x1_j, x2_j)$ and $r(x1_j, x2_j, b_k)$ were calculated by the method in SOLAS Chapter II-1, Part B-1, Regulation 7-1 for all damage zones. The longitudinal extents and longitudinal bulkhead position for each damage zone are shown in Table L.3 with the lowest value for b_k being used for the calculation of values of $r(x1_j, x2_j, b_k)$ in accordance with the procedure outlined in the IMO's explanatory notes to damage stability [IMO (2008a)]. Table L.2 shows the resulting probabilities p_i obtained for all damage cases by Equations (L.3) and (L.4) as appropriate.

Table L.3 – Longitudinal extents of damage zones and location of longitudinal bulkhead considered for damage limitation, measured from the aft extent and the side shell respectively

Zone	*1*	*2*	*3*	*4*	*5*	*6*	*7*	*8*	*9*	*10*	*11*
$x1$	00.00	12.39	25.92	41.19	54.71	68.23	81.79	97.15	112.00	129.61	156.83
$x2$	12.39	25.92	41.19	54.71	68.23	81.79	97.15	112.00	129.61	156.83	170.70
b_1	- n/a-	3.06	3.37	1.27	1.43	1.49	1.43	3.33	5.72	5.81	- n/a -

Table L.4 – Probabilities p_i for all damage cases, with intermediate results for single zone damages

Damage Case	*Zone(s)*	$p(x1, x2)$	$r(x1, x2, b_k)$	p_i
1	1	0.0508	1.0000	0.0508
2	2	0.0345	1.9936	0.0688
3	3	0.0440	1.7327	0.0763
4	4	0.0345	1.0364	0.0358
5	5	0.0345	1.1475	0.0396
6	6	0.0347	1.1818	0.0410
7	7	0.0445	0.9333	0.0415
8	8	0.0416	1.8000	0.0749
9	9	0.0586	1.7262	0.1011
10	10	0.1395	1.0742	0.1499
11	11	0.0588	1.0000	0.0588
12	8,9	0.1905	1.0000	0.0144
13	9,10	0.2871	1.0000	0.0361
14	10,11	0.2578	1.0000	0.0492

Calculation of s_i

For cargo ships, s_i is calculated from the final equilibrium stage of flooding only, ignoring intermediate stages and neglecting the influence of heeling moments. Probability of survival at the final stage is defined as shown in Equation (L.5). The heel angle and righting lever values obtained for all damage cases and draughts are shown in Table L.5 along with the resultant probabilities.

$$s_i = K \times \left[\frac{GZ_{max}}{0.05} \times \frac{\theta_v - \theta_e}{16}\right]^{\frac{1}{4}}, \tag{L.5}$$

where

$$K = \begin{cases} 1, & \theta_e \leq 25 \\ \sqrt{\frac{30-\theta_e}{5}}, & 25 \leq \theta_e \leq 30 \\ 0, & \theta_e \geq 30 \end{cases}.$$

Table L.5 – Probabilities s_i for all damage cases and the three loading conditions

	Deepest subdivision draught, d_s				*Partial subdivision draught, d_p*				*Light service draught, d_l*			
Case	θ_e/°	θ_v/°	GZ_{max}	s_i	θ_e/°	θ_v/°	GZ_{max}	s_i	θ_e/°	θ_v/°	GZ_{max}	s_i
1	0.0	17.4	1.176	1.0000	0.0	20.4	2.175	1.0000	0.0	27.2	2.269	1.0000
2	0.4	13.4	1.185	0.9494	0.0	19.4	2.325	1.0000	-1.9	25.8	2.653	1.0000
3	3.2	13.8	1.143	0.9022	1.9	19.1	2.254	1.0000	-3.0	26.0	2.693	1.0000
4	3.0	15.7	1.204	0.9439	0.4	19.3	2.337	1.0000	-1.4	26.1	2.668	1.0000
5	2.7	14.7	1.134	0.9306	0.5	19.0	2.224	1.0000	0.3	25.4	2.439	1.0000
6	3.0	13.9	1.134	0.9085	0.6	17.7	2.182	1.0000	0.4	24.6	2.390	1.0000
7	3.2	12.6	1.061	0.8755	1.5	16.4	2.018	0.9824	0.5	24.1	2.332	1.0000
8	0.8	14.3	1.153	0.9584	0.6	18.0	2.223	1.0000	1.2	25.5	2.520	1.0000
9	4.1	12.1	0.725	0.8409	2.1	14.8	1.539	0.9439	0.0	24.2	1.996	1.0000
10	4.7	10.6	0.656	0.7793	2.4	13.4	1.436	0.9106	0.0	21.9	1.873	1.0000
11	0.0	17.7	1.396	1.0000	0.0	19.2	2.269	1.0000	0.0	26.4	2.475	1.0000
12	0.7	12.7	1.161	0.9306	0.5	16.0	2.217	0.9921	0.9	24.1	2.550	1.0000
13	5.8	8.6	0.582	0.6468	3.5	10.8	1.299	0.8219	1.2	19.2	1.796	1.0000
14	4.6	10.7	0.672	0.7858	3.2	11.4	1.274	0.8461	0.7	19.8	1.749	1.0000

FAST SAIL ASSISTED FEEDER CONTINER SHIP CONCEPT

B DECK

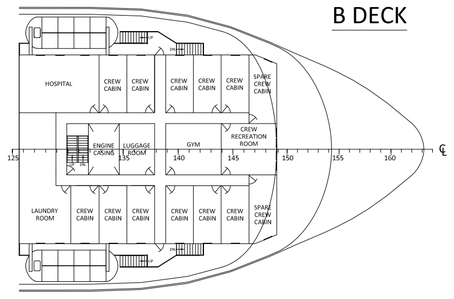

C DECK

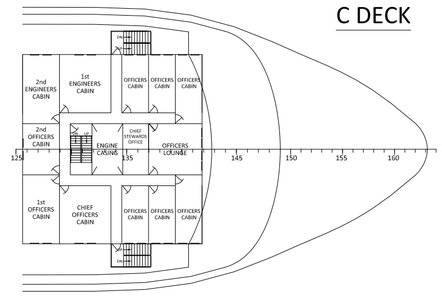

D DECK

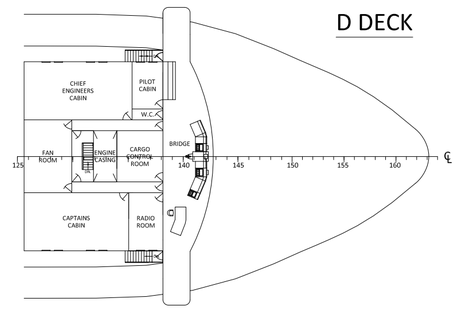

PROFILE

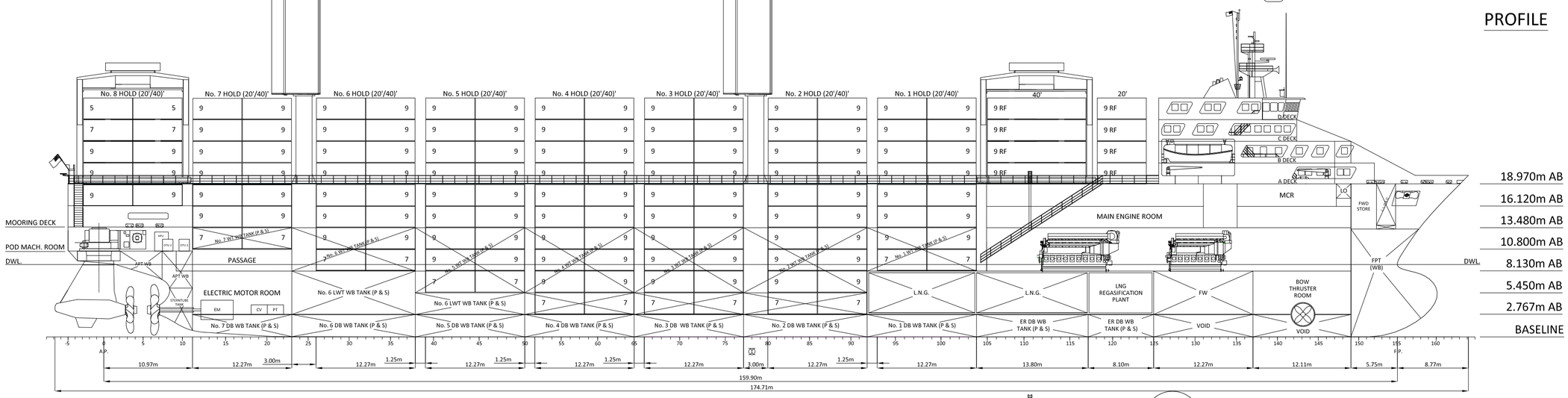

DECK LAYOUT (A DECK)

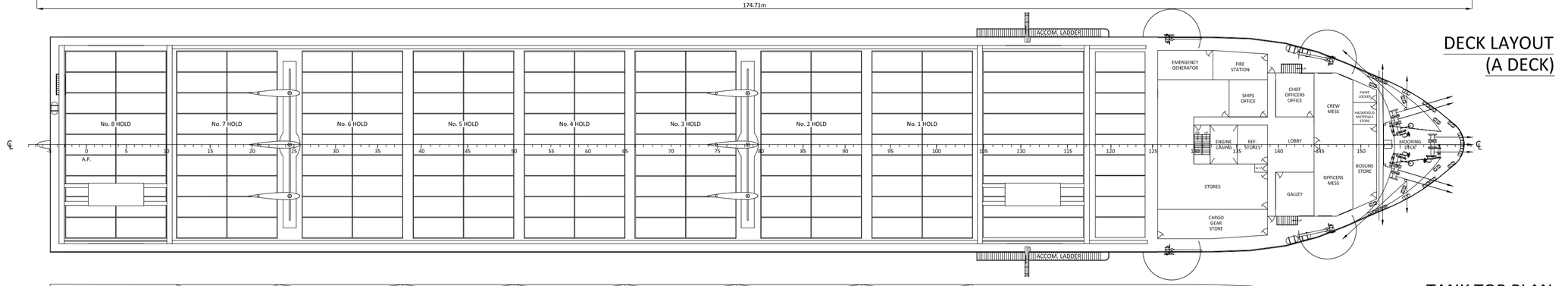

TANK TOP PLAN

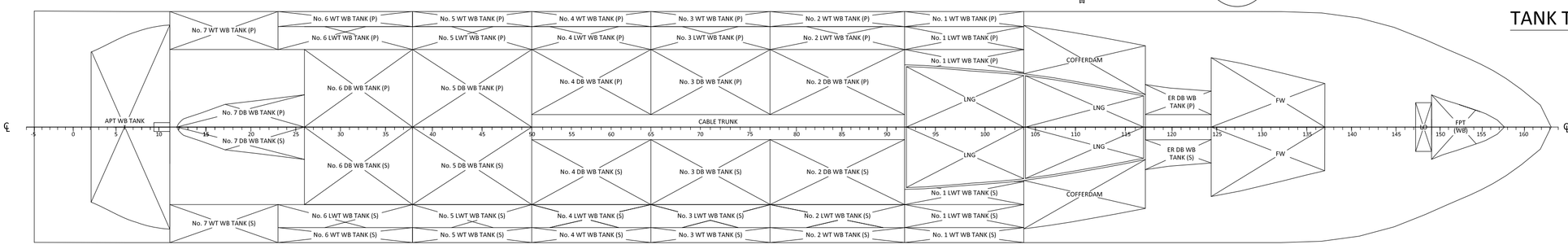

MAIN MACHINERY ROOM (LEVEL 3)

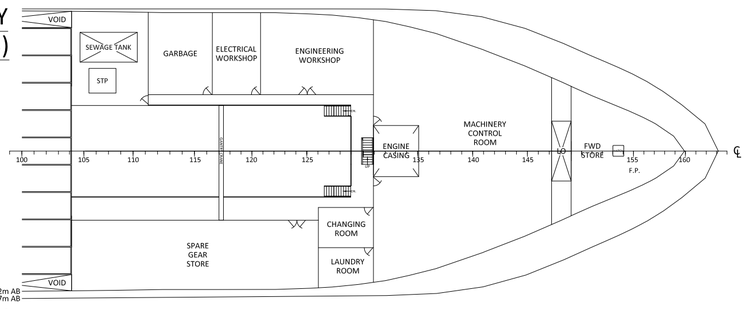

MAIN MACHINERY ROOM (LEVEL 2)

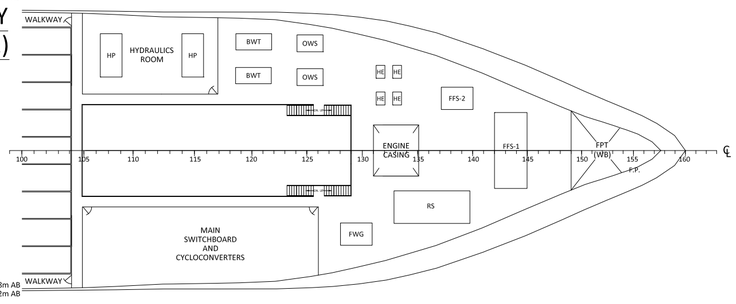

AFT MOORING DECK

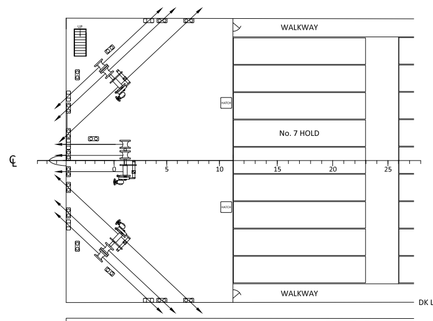

MAIN MACHINERY ROOM (LEVEL 1)

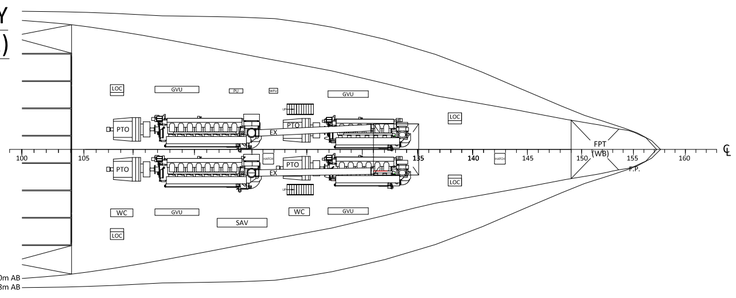

POD MACHINERY ROOM

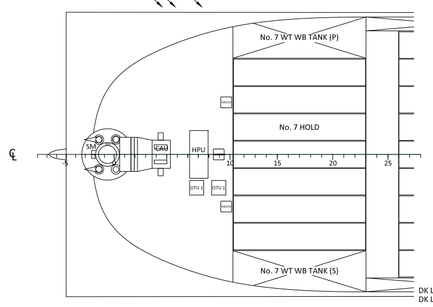

LNG PROCESSING ROOM

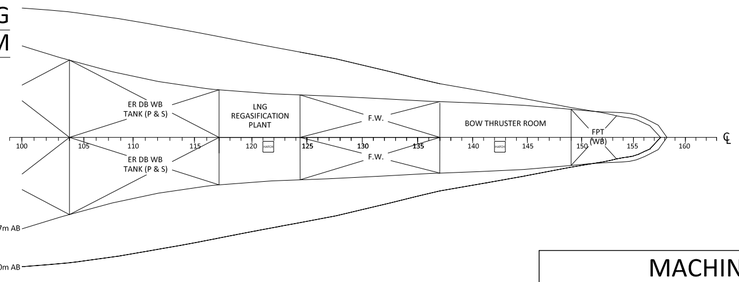

ELECTRIC MOTOR ROOM

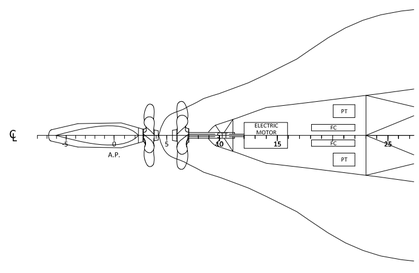

TANK SYMBOLS

APT	AFT PEAK TANK	LWT	LOWER WING TANK
DB	DOUBLE BOTTOM	P	PORT
ER	ENGINE ROOM	S	STARBOARD
FPT	FORE PEAK TANK	STU	STERNTUBE TANK
FW	FRESH WATER	WB	WATER BALLAST
LNG	LIQUIFIED NATURAL GAS	WT	WING TANK
LO	LUBRICATING OIL		

MACHINERY SYMBOLS

BWT	BALLAST WATER TREATMENT UNIT
CAU	COOLING AIR UNIT
EM	ELECTRIC MOTOR
EX	EXHAUST
FC	FREQUENCY CONVERTER
FFS-1	ER FIRE FIGHTING SYSTEM
FFS-2	ACCOM. FIRE FIGHTING SYSTEM
FWG	FRESH WATER GENERATION SYSTEM
GVU	GAS VALVE UNIT
HE	HEAT EXCHANGER
HP	HYDRAULIC PUMP
HPU	HYDRAULIC POWER UNIT
LOC	LUBRICATING OIL COOLER
OTU	OIL TREATMENT UNIT
OWS	OIL WATER SEPARATION UNIT
PT	PROPULSION TRANSFORMERS
RS	REFRIGERATION SYSTEM
SAV	STARTING AIR VESSEL
SM	STEERING MODULE
SRU	SLIP RING UNIT
STP	SEWAGE TREATMENT PLANT
WC	WATER COOLER
WFU	WATER FEED UNIT

PRINCIPAL PARTICULARS

LENGTH OVERALL	174.7m
LENGTH B.P.	159.9m
BREADTH MOULDED	26.2m
DEPTH MOULDED	18.97m
SUMMER DRAUGHT	8.94m
GRT	18464
NRT	8285
CONTAINER (NOMINAL)	1270 TEU
MAIN ENGINES	
2 x Wärtsilä 8L50DF & 2 x Wärtsilä 6L50DF DUAL FUEL MEDIUM SPEED	
COMBINED MCR	26600kW
SERVICE SPEED	25 kts
RANGE	3000 n.m

AFT VIEW

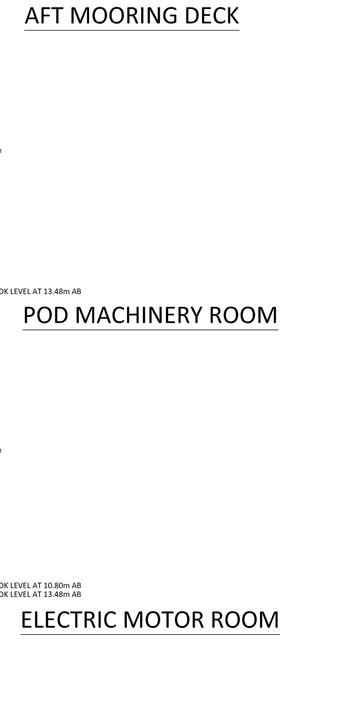

FWD VIEW

MIDSHIP LAYOUT

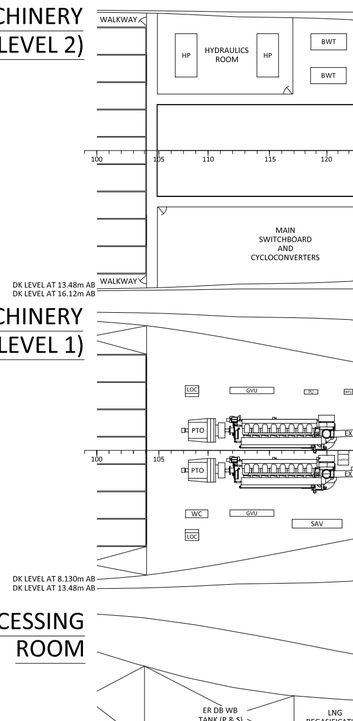

GENERAL ARRANGEMENT DRAWING

Designed by BS	Checked by AB TL LM SM IS	Date 10/04/10	Scale 1:400
APPENDIX M		Edition A	Sheet 1 of 2

University of Southampton
School of Engineering Sciences
University of Southampton
University Road
Highfield
Southampton
SO17 1BJ

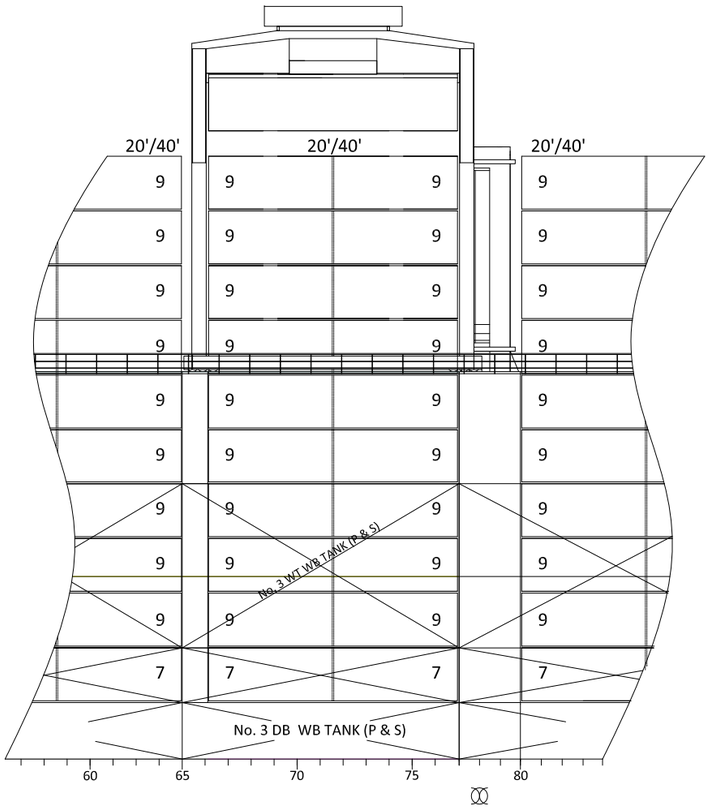

PROFILE VIEW

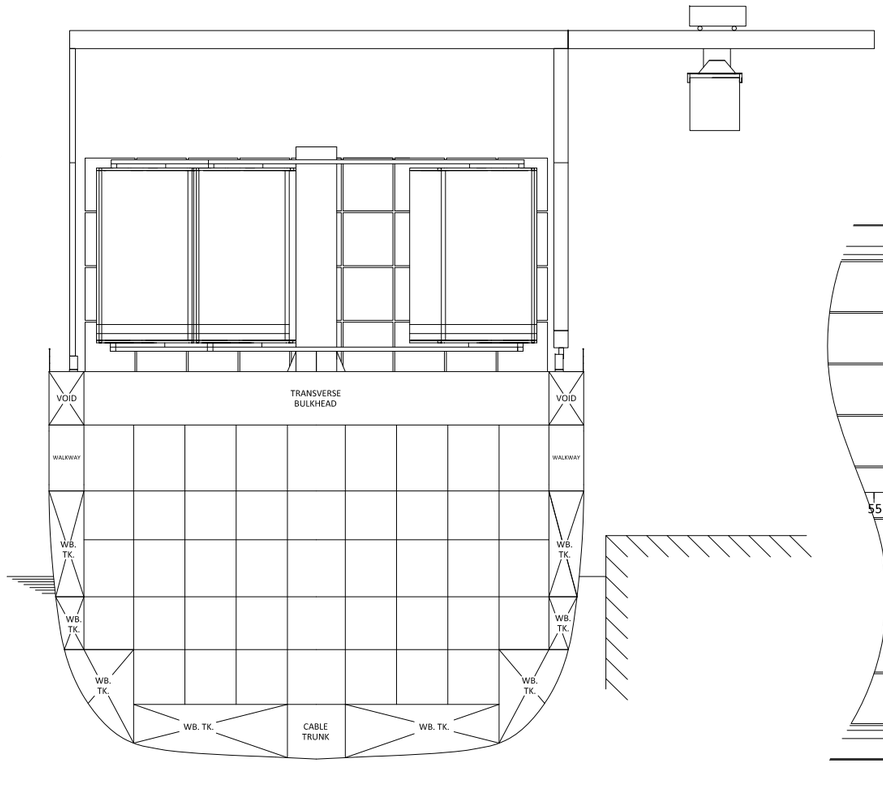

SECTION VIEW

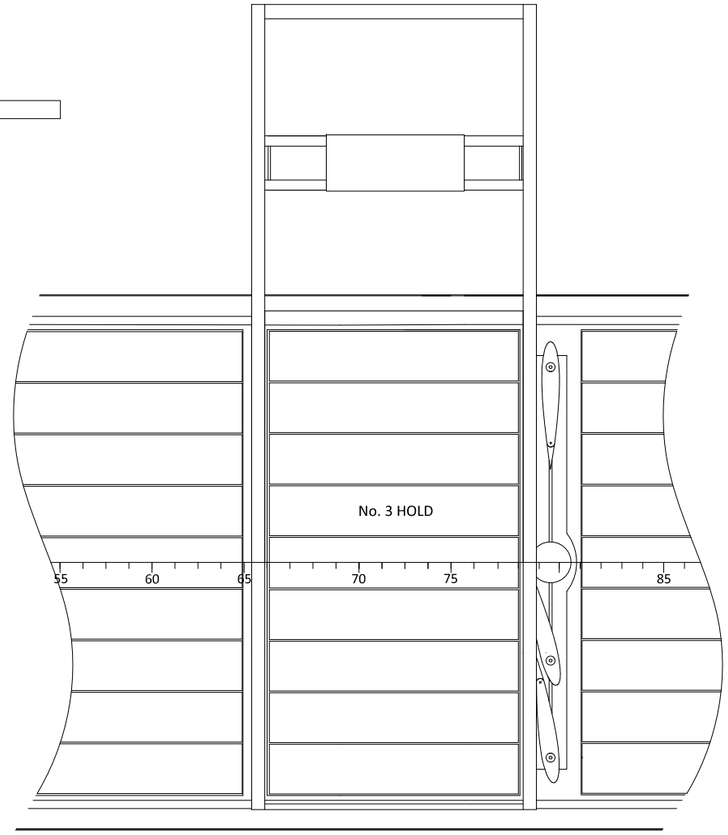

PLAN VIEW

PRINCIPAL PARTICULARS	
LENGTH OVERALL	174.7m
LENGTH B.P.	159.9m
BREADTH MOULDED	26.2m
DEPTH MOULDED	18.97m
SUMMER DRAUGHT	8.94m
GRT	18464
NRT	8285
CONTAINER (NOMINAL)	1270
MAIN ENGINES:	
2 x Wärtsilä 8L50DF & 2 x Wärtsilä 6L50DF DUAL FUEL MEDIUM SPEED	
COMBINED MCR	26600 kW
SERVICE SPEED	25 ktS
RANGE	3000 n.m

NOTE : THESE DRAWINGS DEMONSTRATE HOW THE STOWED SAIL SYSTEM DOES NOT INTERFERE WITH CARGO HANDLING OPERATIONS.

GENERAL ARRANGEMENT DRAWING

Designed by	Checked by	Date	Scale
BS	AB TL SM LM IS	10/04/10	1:300
APPENDIX M		Edition A	Sheet 2 of 2

UNIVERSITY OF Southampton
School of Engineering Sciences
University of Southampton
University Road
Highfield
Southampton
SO17 1BJ

Appendix N – Budget Summary

Table N.1 – Budget summary

	Item	*Qty*	*Price per item / £*	*Subtotal / £*
Towing tank models	*Homeblown* High Density Foam (2 x 120kg.m^3 + 2 x 200 kg.m^3)	1	1432.00	1432.00
	SP 'Ampreg 22' Resin	1	31.98	31.98
	Araldite	3	4.10	12.30
	High Build primer spray paint	3	4.32	12.96
	Car wing mirror	1	3.99	3.99
Wind tunnel rig	Grip paper and tape	1	16.10	16.10
	Blue foam for wings	2	23.00	46.00
	Bolts	1	26.98	26.98
	Boxes for containers	1	59.80	59.80
	Aluminium rod for flap stock	1	11.50	11.50
	Aluminium plate	1	58.80	58.80
	Aluminium tube	1	46.00	46.00
	Aluminium flat bar	1	10.99	10.99
	Aluminium rod	1	32.82	32.82
	Aluminium rod	1	11.75	11.75
	Poly-filler	1	6.56	6.56
Hire of wind tunnel and towing tank	Wind tunnel hire (academic rate)	3	1716.00	5148.00
	SSU towing tank hire	3	300.00	900.00
Transport	Train ticket to Lloyds Register in December	6	27.80	166.80
	Train ticket to Lloyds Register in June	6	27.80	166.80
	Transport to SSU towing tank	12	2.00	24.00
Photocopying, printing & binding	Printing report	3	16.00	48.00
	Printing GA drawings	3	12.00	36.00
Deductions	Initial budget	1	- 780.00	-780.00
	Elevator pitch	1	- 160.00	- 160.00
	Lloyds sponsorship	1	- 523.52	- 523.52
	Wind tunnel hire	3	- 1716.00	- 5148.00
	Towing tank hire	3	- 300.00	-900.00
	Individual contribution for train tickets to Lloyds	12	- 27.80	- 333.60
	Individual contribution to model parts	6	- 32.61	- 195.64
	Individual contribution for transport to SSU towing tank	6	- 4.00	- 24.00
	Individual contribution for printing	6	- 14.00	- 84.00
		Total spent		**£ 8310.14**
		Deductions		**-£ 8148.76**
		Project deficit		**£ 161.38**

The deficit of £161.38 indicated in Table N.1 is attributed to an underestimate for the price of the *Homeblown* High Density Foam which was initially estimated to cost £1045.45 but cost £1432 when ordered, adding £386.55 to the project costs. A total of 18 days of manufacturing time were required by the EDMC for the manufacture of the towing tank models and wind tunnel rig. An additional 15 days of manufacturing time was required by team members on model manufacture. The required manufacturing time in the EDMC was greater than the initial project allocation of five days, however, it was agreed in advance that the EDMC would be able to undertake the work on our behalf.